observations and modeling of disk winds in galactic black holes

Maxime Parra

THÈSE

Pour obtenir le grade de

DOCTEUR DE L'UNIVERSITÉ GRENOBLE ALPES
et de l'UNIVERSITÀ DEGLI STUDI ROMA TRE

École doctorale : PHYS - Physique
Spécialité : Astrophysique et Milieux Dilués
Unités de recherche :
Institut de Planétologie et d'Astrophysique de Grenoble
&
Dipartimento di Matematica e Fisica, Università Roma Tre

Observations et Modélisation des vents dans les disques des trous noirs galactiques

Observations and Modeling of Disk Winds in Galactic Black Holes

Présentée par :

Maxime Parra

Direction de thèse :

Pierre-Olivier Petrucci Directeur de Recherche, Université Grenoble Alpes	Directeur de thèse
Stefano Bianchi Associate Professor, Università Roma Tre	Co-Directeur de thèse

Rapporteurs :

Melania Del Santo
Primo Ricercatore, INAF/IASF PAlermo
María Díaz Trigo
ALMA Programme Scientist, European Southern Observatory

Thèse soutenue publiquement le **02-10-2024**, devant le jury composé de :

Melania Del Santo Primo Ricercatore, INAF/IASF Palermo	Rapporteure
María Díaz Trigo ALMA Programme Scientist, European Southern Observatory	Rapporteure
Olivier Godet Maitre de Conférence, Université Toulouse III Paul Sabatier	Examinateur
Julien Malzac Directeur de Recherche, Institut de Recherche en Astrophysique et Planétologie	Examinateur
Gilles Henri Professeur des Universités, Université Grenoble Alpes	Président du Jury

, , « - ».
, ,
, , .
, , .

You only have a few minutes

Astrophysical Black Holes are not just among the most fascinating objects in the universe: they have grown along with it since the very beginning, shaping its constituents from stars to galaxies, and beyond. One of the most important goals of modern astrophysics is thus to understand their growth mechanisms. The main process of this evolution, governed by gravitational forces, is called "**accretion**", and in the case of Black Holes, the extreme physics that take place in their vicinity lead to powerful ejections of matter and energy. They greatly hamper and fundamentally change the structures by which Black Holes accrete matter, called accretion disks. The slower and more massive type of ejections, dubbed "**winds**", were only discovered half a century ago, and for now remain very poorly understood. The focus of this work is to improve the understanding of winds in **Black Hole Low Mass X-ray Binaries** (BHLMXBs), a subset of the stellar mass Black Hole population. For this, I used two complementary approaches: data analysis and modeling.

A decade ago, the first and only global study of BHLMXB wind properties (Ponti et al. 2012) used their main signatures, blueshifted absorption lines in the X-rays, to highlight how these winds were connected to the evolution of the accretion processes in these objects. Since then, the observational landscape became much more complex, and a new large-scale study was direly needed. Thus, after developing tools to detect and characterize these signatures in a systematic manner for a large sample of objects, **I analyzed all publicly available observations** of the two X-ray instruments most sensitive to lines, XMM-*Newton*'s EPIC and *Chandra*'s HETG. With ten times more sources than before and a very thorough line detection process, I was able to **refine** previously found **dichotomies**, showing that the detection and properties of these absorption lines are indeed very dependent on both the structure of the accretion disk, and the viewing angle of the source. These results also allow for a very important **comparison** with more exotic wind detection, and the **colder outflows** recently detected in other energy bands.

First, I identified the most promising sources for a more thorough analysis, with new and unpublished results. I thus followed with a very **in-depth study of an archetypal wind source**, 4U 1630-47, with a one-of-a-kind sampling of its wind evolution. **Combining** the data of **seven** different X-ray **telescopes**, I was able to probe an unmatched **20 years of wind evolution**. This allowed to quantify the evolution of the absorption lines over large time scales, with a near complete outburst coverage. Moreover, the **hard X-ray** coverage **removes the degeneracy** between the illumination of the source and the absorption line evolution, which allows to **distinguish several structures** where the outflow itself could remain constant between different outbursts. In parallel, I **identified several outliers** in recent outbursts, whose detailed analysis reveals both complex dipping structures and very fast evolution of ionized absorbers on unusually short timescales.

Meanwhile, a team at the "Institut de Planétologie et d'Astrophysique de Grenoble" (IPAG) has been developing solutions of accretion-ejection structures for **magnetized** disks, named **Jet Emitting Disks**. After two decades, a **new**, low-magnetization subset of **solutions** proved capable of **creating outflows** that could match observations of accreting Black Holes. Building on previous codes developed in Chakravorty et al. (2016); Datta et al. (2024), I developed a framework that from these theoretical models, computes **synthetic spectra** at high resolution for a wide range of physical parameters, in the form of tables that can be used to **fit real observations**. This allows to study how wind signatures are linked to the physical properties of the outflow, and prepare for **comparisons**, using both archival observations and future **high-resolution data** that will become available thanks to the telescope on board the *XRISM* space mission.

Tu n'as que quelques minutes

Les Trous Noirs astrophysiques ne sont pas seulement parmi les objets les plus fascinants de l'univers : ils ont grandi avec lui depuis ses débuts, façonnant ses constituants, des étoiles aux galaxies, et au-delà. L'un des objectifs les plus importants de l'astrophysique moderne est donc de comprendre leurs mécanismes de croissance. Cette évolution, gouvernée par les forces gravitationnelles, invoque souvent des processus dits "d'**accrétion** », et dans le cas des trous noirs, s'accompagne de processus extrêmes donnant lieu à de puissantes éjections de matière et d'énergie. Ces dernières entravent et modifient fondamentalement les disques d'accrétion via lesquels les trous noirs évoluent. Les "**vents**", le type d'éjection plus lent et le plus massif, ont été découverts récemment et restent encore mal compris. Cette thèse vise à améliorer la compréhension des vents dans les **binaires X de faible masse à trous noirs** (BHLMXB), un sous-ensemble de trous noirs de masse stellaire. Pour cela, j'ai utilisé deux approches complémentaires : l'analyse des données et la modélisation.

Il y a près de dix ans, la première et unique étude globale des propriétés des vents de BHLMXB (Ponti et al. 2012) a utilisé leurs principales signatures, des raies d'absorption décalées vers le bleu en rayons X, pour lier l'évolution des vents à celle des processus d'accrétion. Depuis lors, le paysage observationnel est devenu beaucoup plus complexe, et requérait une nouvelle étude à grande échelle. **J'ai analysé l'intégralité des observations d'archive** des deux instruments les plus sensibles aux raies en rayons X, l'EPIC de XMM-*Newton* et l'HETG de *Chandra*. Cela m'a permis d'**affiner** les **dichotomies** précédemment trouvées, montrant que la détection et les propriétés de ces raies dépendent à la fois de la structure du disque d'accrétion et de l'angle de vision de la source. Ces résultats permettent également une **comparaison** avec les détections de vents plus exotiques, et les **éjections "froides"** récemment détectées à plus basse énergie.

Ce premier projet a permis d'identifier les sources les plus prometteuses pour une analyse plus approfondie, et j'ai poursuivi avec une **étude détaillée d'une source** à vent bien connue, 4U 1630-47, dont la couverture observationnelle est inégalée. En **combinant** les données de **sept télescopes X** différents, j'ai pu sonder l'**évolution des vents** dans cette source sur une durée inédite de **20 ans**. Cela a permis de quantifier l'évolution des raies d'absorption sur de grandes échelles de temps, mais aussi d'avoir une couverture quasi complète des éruptions. En outre, les observations en **rayons X durs lèvent la dégénérescence** entre l'illumination de la source et l'évolution des raies, permettant de **distinguer plusieurs structures** au sein desquelles les éjections resteraient similaires entre les éruptions. J'ai aussi **identifié plusieurs anomalies** au cours des éruptions récentes, dont l'analyse détaillée révèle à la fois des structures d'obscuration complexes et des absorbeurs ionisés évoluant sur des échelles de temps inhabituellement courtes.

En parallèle, l'Institut de Planétologie et d'Astrophysique de Grenoble (IPAG) développe depuis deux décennies des solutions de structures d'accrétion-éjection de disques **magnétisés**, appelés **Jet Emitting Disks**. Récemment, un **nouveau** sous-ensemble de **solutions à faible magnétisation** s'est avéré capable de **créer des éjections** pouvant correspondre aux observations de trous noirs accrétants. En m'appuyant sur les codes précédemment développés dans Chakravorty et al. (2016); Datta et al. (2024), j'ai développé un outil, qui, à partir de ces modèles théoriques, calcule des **spectres synthétiques** à haute résolution pour une large gamme de paramètres physiques, sous forme de tables pouvant être directement **comparées aux observations**. Cela permet d'étudier le lien entre les propriétés des raies et celles des éjections, et de préparer des comparaisons, déjà avec les observations précédemment identifiées, et les **données à haute résolution** qui seront fournies par le télescope à bord du satellite en rayons X *XRISM*.

Acknowledgements

A PhD is meaningless without a subject, and a student useless without a teacher. I've had the privilege to work with two advisors. In all subjectivity, they not only provided me the best subject I could ever ask for, but eased my entry into the world and methods of research so much that I cannot imagine ever wanting to leave it. My constant bickering in our day to day interactions is only equaled by the pleasure and drive I've felt through the entire process, and you both have my utmost respect for the trust and independence you've deliberately given me from the get go. I'll try to repay that by writing more papers. Maybe. Thanks Pop and Stefano.

Of course, the work environment is another important component that can make students thrive or cower. The SHERPAS[1] team and its members (past and present) were as welcoming to me as one could be, be it for scientific, social, or administrative interactions. The same thing could be said about the rest of the lab, from GAD members to IT and HR personnel, and particularly David and Bruno, who got me out of innumerable material and administrative issues. On the younger side, I'd like to believe that the PhD group that arose after the arrival of the 2021 batch was something special. I'll hold fond memories of every member of Gang Poivrons.

The Roman half of the story feels shorter than ever now that I've left it, but the Italian researchers and students of Roma Tre, and more generally the Italian affiliated community made me feel like I belonged despite a long lasting language skill issue on my part. Grazie per l'aiut**O** e il benvenuto, particularmente nel Coffice. I could also speak about every the ever expanding "nice people seen few times a year during conferences" category, but I'll see most of you next year anyway, so let's move on.

I've been told that humans are social creatures, and tend to regroup into herds when given the occasion. Several of them deserve to be mentioned. First, among the Gang Poivrons group of PhDs and its extended family, many colleagues became real friends over these fragmented 3 years. Julien, Thomas, Lucie, Célia, Antoine, Valentina, Dorian, Marc, Thibault, Adrien, Jonah, Nathan, Myriam, Simon, Philip, Lisa, Alejandro, les Maximes, among many others. Honorable mentions to ClarArt and Clara B. for tolerating this group of morons. Secondly, among the climbing faces turned friends, in Grenoble, Jakob and Miriam, Thomas and Alice, Romain, and the kilter board du Perchoir, in Roma, the oh so welcoming coaches and climbers in Monkey Island, for being my gateway into socializing in this giant city. Rome was also a suprisingly good place to meet frenchies, including but not limited to Sacha, Mathilde, Isaure, Edoardo. And it would be unfair to forget the og Toulouse crew and its newest members, the AstroJeunes teams over the last 3 years, and the masochistic kids that kept coming back to hear from us. That's it for the long lists.

This last paragraph is for the cream of the crop, le nec plus ultra, la crema del raccolto. First, my parents, who, aside from a constant practical support, must have done a few good things in my education if their kid managed to reach the dream he was always aiming for. Merci Maman, Merci Papa.

Then, to the ally of everyday, in work and in pain, at home and foreign, the lover of AGNs. Now a dear friend. These years wouldn't have been the same without you. Grazie Vittoria.

Finally, to the girlfriend that makes an uncertain future into a certain pleasure. My life won't be the same thanks to you. Dziekuje Gosia.

I was almost going to forget the kid stuck on the first floor, who thinks things are over and regrets what was before. This one is for you.

[1] There's too many people to cite here, just go check the wayback machine for https://ipag.osug.fr/french/recherche/equipes/sherpas/membres-de-l-equipe-sherpas

Contents

List of Figures

Page

List of Tables

Page

List of notations

Notation	signification	value/unit(s)
	Constants	
c	speed of light (vacuum)	299792.458 m s^{-1}
G	Gravitational constant	6.6773×10^{-11} m^3 kg^{-1} s^{-2}
h	Planck constant	6.6261×10^{-34} m^2 kg s^{-1}
	Units	
$M_\odot$	Mass of the sun	$\sim 2 \cdot 10^{30}$ kg
L_{Edd}	Eddington Luminosity	erg/s | $\propto$ M
R_g	Black Hole Gravitational Radius	m | $\propto$ M
(k)pc	(kilo) parsec | distance	$(1000\times)$ 3.086×10^{18} m
(k)eV	(kilo) Electronvolt | photon energy	$(1/1000\times)$ 1.2398×10^{-6} m
	Mathematical terms	
M	Mass (astrophysical object)	$M_\odot$
R	Radius (particle - central object)	R_g
d	Distance (observer - central object)	kpc
L	Luminosity	erg/s | L_{Edd}
T	Temperature	K
θ	Inclination angle	deg/rad
ξ/U	Ionization parameter	variable
N_H	Column density	cm^{-2}
n	Density	cm^{-3}
EW	Line Equivalent Width	eV
v	velocity ($\rightarrow$ central object)	km/s | c

List of acronyms

Main Physical Acronyms

Notation	signification
AGN	Active Galactic Nuclei
AMD	Aborption Measure Distribution
BH	Black Hole
BP	Blandford-Payne
CO	Compact Object
CV	Cataclysmic Variable
DIM	Disk Instability Model
EW	Equivalent Width
FWHM	Full-Width at Half Maximum
GW	Gravitational Waves
HID/HLD	Hardness-Intensity/Luminosity Diagram
HR	Hardness Ratio
HS	Hard State
ISM	Intestellar Medium
JED	Jet Emitting Disk
IMBH	Intermediate Mass Black Hole
ISCO	Innermost Stable Circular Orbit
MHD	MagnetoHydroDynamics
NHP	Null Hypothesis Probability
MJD	Modified Julian Day
MRI	Magneto-Rotational Instability

NS	Neutron Star
PCC	Power-Colour Diagram
LMXB/HMXB/XRB	(Low-Mass/High-Mass) X-ray Binary
OIR	Optical-Infrared
QPO	Quasi Periodic Oscillation
RMS	Root Mean Square
SAD	Standard Accretion Disk
SED	Spectral Energy Distribution
S-E	Super-Eddington
SMBH	SuperMassive Black Hole
SS	Soft State
SPL	Steep Powerlaw (State)
UFO	Ultra-Fast Outflows
U/HLX	Ultra/Hyper-Luminous X-ray Source
WA	Warm Absorber
WED	Wind-Emitting Disk
WD	White Dwarf
(Δ)-C/-χ^2	(Delta) C-statistic/Chi-squared statistic

Main Instrumental Abbreviations

Notation	signification
(FI/BI)-CCD	(Front/Back-Illuminated) Charge Coupled Device
PSF	Point Spread Function
SNR	Signal-To-Noise Ratio
GTI	Good Time Interval
AstroSat	AstroSat multi-wavelength Observatory
Chandra	Chandra X-ray Observatory
ACIS	Advanced CCD Imaging Spectrometer (Chandra)
L/M/HETG	Low/Medium/High-Energy Transmission Gratings (Chandra)
INTEGRAL	International Gamma-Ray Astrophysics Laboratory
IXPE	Imaging X-ray Polarimetry Explorer
HXMT	Hard X-ray Modulation Telescope
MAXI	Monitor of All-sky X-ray Image
NICER	Neutron Star Interior Composition Explorer
NuSTAR	Nuclear Spectroscopic Telescope Array
FPM	Focal Plane Module (NuSTAR)
RXTE	Rossi X-ray Timing Explorer
Suzaku	Suzaku (*lit.* Vermilion Bird) X-ray Observatory
XIS	X-ray Imaging Spectrometer (Suzaku)
PIN	part of the Hard X-ray Detector (Suzaku)
Swift	Neil Gehrels Swift Observatory
BAT	Burst Alert Telescope (*Swift*)
XRT	X-ray Telescope (*Swift*)
XMM(-*Newton*)	X-ray Multi-Mirror satellite
EPIC	European Photon Imaging Camera (XMM)
PN/MOS	"PN"/Metal Oxide Semi-conductor CCD (EPIC)
XRISM	X-ray Imaging and Spectroscopy Mission

You have an hour or two

Introduction

The study of **compact objects**, particularly Black Holes, is critical for understanding extreme astrophysical phenomena. Compact objects, including **White Dwarfs**, **Neutron Stars**, and **Black Holes**, are defined by their **compactness**, a **dimensionless ratio** describing the gravitational energy relative to the mass energy of an object. This property distinguishes compact objects from less dense astrophysical bodies and makes their study pivotal for exploring **high-energy processes**, **relativistic effects**, and the **evolution of stellar systems**. Compact objects form through processes tied to the life cycle of stars, and their properties depend on the mass and composition of their progenitor. Stars achieve stability through a balance between outward pressure from nuclear fusion and inward gravitational forces. As stars evolve, this balance shifts, eventually leading to the creation of remnants and compact objects.

Black Holes, with their immense gravitational pull and event horizon that trap even light, represent the most extreme outcome of stellar evolution, embodying the limits of known physics. This thesis aims to add a stone to the ever-growing pyramid of our understanding of the formation, growth and behavior of these fascinating objects. This requires a detailed description of accretion processes, relativistic effects, and interactions between angular momentum and magnetic fields in disk-driven systems.

This part is for anyone wise enough to not do a PhD in compact object astrophysics, yet foolish enough to be truly interested in my work. The section below introduces the notions necessary to understand the overviews of my works that will follow.

Formation and characteristics of compact objects

Compact objects are classified based on their compactness parameter, which measures the intensity of their gravitational fields. This parameter spans a wide range, with **White Dwarfs** (WD) exhibiting values of approximately 10^{-4}, **Neutron Stars** (NS) between 0.2 and 0.4, and **Black Holes** (BHs) at 1.

White Dwarfs form from low- to intermediate-mass stars (below approximately 8–10 solar masses), where fusion ceases at elements between helium and carbon/oxygen. The remnants of these stars are sustained by electron degeneracy pressure, with radii of the order of 1% of their progenitor. Neutron stars, on the other hand, arise from the collapse of more massive stars (around 10–20 solar masses), in which only the strong nuclear force and neutron degeneracy pressure could counteract the gravitational shrinking.

Finally, when the initial mass of the star exceeds approximately 20 solar masses, the gravitational collapse typically leads to the formation of a **Black Hole**, an object with no physical surface and an event horizon that isolate its interior from the rest of the universe. The formation of Black Holes is strongly tied to parameters such as angular momentum, metallicity, and binary interactions, adding complexity to their evolutionary pathways.

For more details see Sections 1.1.1 and 1.1.2.

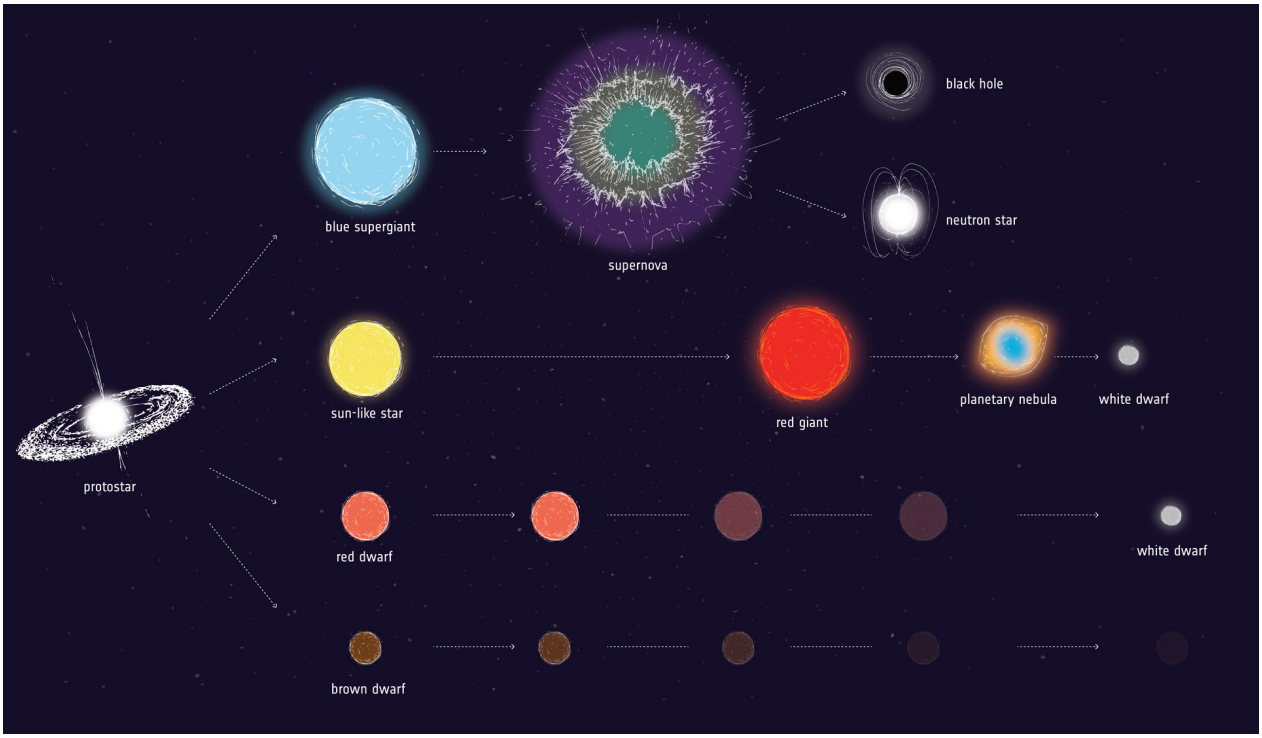

Figure 1: Simplified view of stellar evolution pathways. The specific case of brown dwarfs, stars of very low masses, is irrelevant to the field of compact objects.
From https://www.esa.int/ESA_Multimedia/Images/2018/03/Stellar_evolution

Accretion processes and disk formation

Accretion is one of the fundamental processes governing the growth and evolution of compact objects: the gradual accumulation of matter onto an astrophysical body due to gravitational attraction. In most astrophysical systems, accretion involves matter with angular momentum, leading to the formation of a **disk**-like structure around the central object. The dynamics of these accretion disks depend on the interplay of gravitational forces, angular momentum transfer, and dissipative processes that convert potential energy into heat and radiation.

In binary stellar systems, accretion can occur through two primary mechanisms: the capture of stellar winds or Roche lobe overflow. The later is due to the way the gravitational interaction affects orbits in two body systems. This shapes a complex landscape, characterized by **Roche Lobes**, which delimit for each star the neighboring region where its gravitational pull is predominant. The size of these lobes is primarily determined by the mass ratio of the stars and the distance separating them. When a material body, such as a particle from an expanding star, crosses the contact point (L1) between the two Roche Lobes, it transitions to a region dominated by the gravitational pull of the second object. This puts the particle orbit around this accretor, moving at a velocity dictated by **Kepler's laws**.

In more realistic scenarios, instead of a single particle, a continuous flow of gas crosses the L1 point, and will initially settle into a ring structure. This ring then expands into an **accretion disk** as angular momentum transfer occurs, due to dissipative processes (e.g. friction) within the accreting material. Matter within the disk drifts inward up to the surface of the central object, leading to a dynamic structure that sustains mass transfer onto the accretor, and plays a pivotal role in the evolutionary paths of both stars in the binary system.

Accretion onto compact objects, such as **Neutron Stars** or **Black Holes**, is recognized as one of the most efficient energy conversion processes in the universe. This efficiency is often compared to the rest mass energy of the particles using the **accretion efficiency** parameter, η, and varies based on the nature of the compact object. For Neutron Stars, η is approximately 0.15, and can reach 0.4 for fast rotating Black Holes. In comparison, even the efficiency of nuclear *fusion* processes is below $\eta = 1\%$.

For more details see Sections 1.1.3 and 1.2.1.

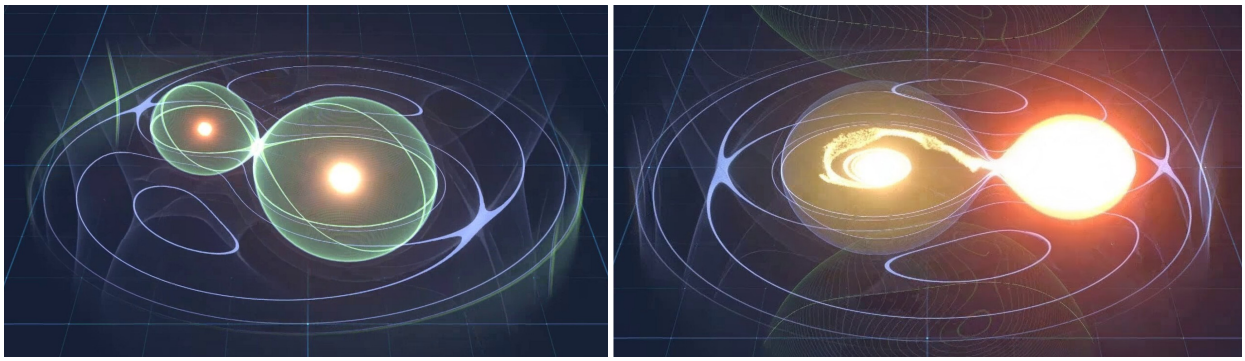

Figure 2: **(Left)** Gravitational equipotentials (blue) and Roche Lobes (green) in a binary stellar system. **(Right)** Advanced binary stellar system undergoing Roche Lobe overflow from one star to the other. From https://www.artstation.com/artwork/v26KeO

Evolution and classification of binary systems

The evolution of compact binary systems is a complex process influenced by factors such as the mass and nature of their components. If the core of the most evolved star in such a system is not massive enough, it can become a White Dwarf, often leading to the formation of Cataclysmic Variables (CVs). CVs are characterized by the transfer of matter from a companion star onto the WD, resulting in various X-ray emissions. These systems are the most common type of **X-ray Binaries**, with thousands of objects censused within a few hundred parsecs (our galactic neighborhood). CVs include subtypes like Dwarf Novae, with frequent disk-driven outbursts, and classical Novae, marked by rare, brighter explosions due to nuclear fusion on the WD's surface.

If instead the core of the evolved star is more massive, it can collapse into a Neutron Star (NS) or Black Hole (BH) after a supernova, potentially disrupting the system. X-ray Binaries involving compact objects are thus primarily located in the Galactic plane, but can also be found at higher latitudes due to ejections of compact objects following supernovae.

Low-Mass X-ray Binaries (LMXBs) form when a NS or BH accretes matter from a low-mass star, in this case via Roche-lobe overflow. Although brighter than CVs, LMXBs are less common, with a few hundred detected in the Milky Way. These systems often exhibit transient behavior, with long quiescent phases punctuated by occasional outbursts. Distinguishing between NS and BH accretors in LMXBs is challenging due to their similar accretion disk properties. The best method to distinguish them is direct mass estimates, with NS capped at approximately 2.5 solar masses ($M_\odot$) and BHs theoretically exceeding this threshold. In addition, some phenomena remain specific to NS, notably thermonuclear X-ray bursts, magnetic accretion-induced pulsations, and thermal emission from the NS surface.

High-Mass X-ray Binaries (HMXBs) differ from LMXBs in having massive companion stars that transfer matter through strong stellar winds. These systems are either persistent or exhibit high-frequency outbursts. Notable subtypes include Be-HMXBs, involving Be-type stars, Supergiant HMXBs, and Wolf-Rayet HMXBs, where the companion evolves into a Helium core star with huge winds and will soon collapse into a compact object.

For more details see Sections 1.2.2 and 1.2.1.
Relevant figure (full page): Fig. 1.3

Triggering outbursts in X-ray Binaries

In **X-ray Binaries** with **accretion disks**, the **Disk Instability Model** (DIM) explains the recurring cycle of **outbursts** and **quiescence** due to **thermal instability** in the disk. This instability arises from the balance between **radiative cooling** (temperature-dependent) and viscous heating (dependent on surface density Σ and viscosity parameter α). At specific temperatures (∼5000–6900 K), hydrogen becomes ionized, changing the cooling rate to become negatively correlated with temperature. This makes the disk unstable and leads to a temperature jump to a hotter state, initiating an outburst.

During an outburst, the entire disk becomes ionized, the viscosity increases, and matter is rapidly accreted until the disk cools and returns to quiescence. The outburst dynamics depend on the ratio of α in the "hot" and "cold" states. The propagation of instability across the disk leads to characteristic heating and cooling fronts, which dictate the disk's behavior over the transition.

The DIM aligns well with observed **Cataclysmic Variables** and **Low-Mass X-ray Binaries**, particularly in **distinguishing transient systems**. However, irradiation from inner disk regions plays a very significant role in LMXBs, requiring adjustments to the model. Moreover, despite its successes, the DIM has limitations. It relies on many simplifying assumptions and does not provide an explanation for the physical origin of angular momentum transport (the source of the viscosity α). This role may be played by **Magneto-Rotational Instability** (MRI), but for now, simulations fail to reproduce the observed evolution. Including **outflows** of matter —which transport angular momentum—shows promise in bridging this gap but fundamentally alters disk structure, requiring new models.

Additionally, DIM alone cannot describe the **spectral evolution** observed during outbursts in LMXBs, especially transitions between "hard" and "soft" X-ray states associated respectively with jets and thermal disk emission (see below). Future models must incorporate more complex magnetized structures and outflows to reproduce more characteristics of real outbursts.

For more details see Section 1.2.3.

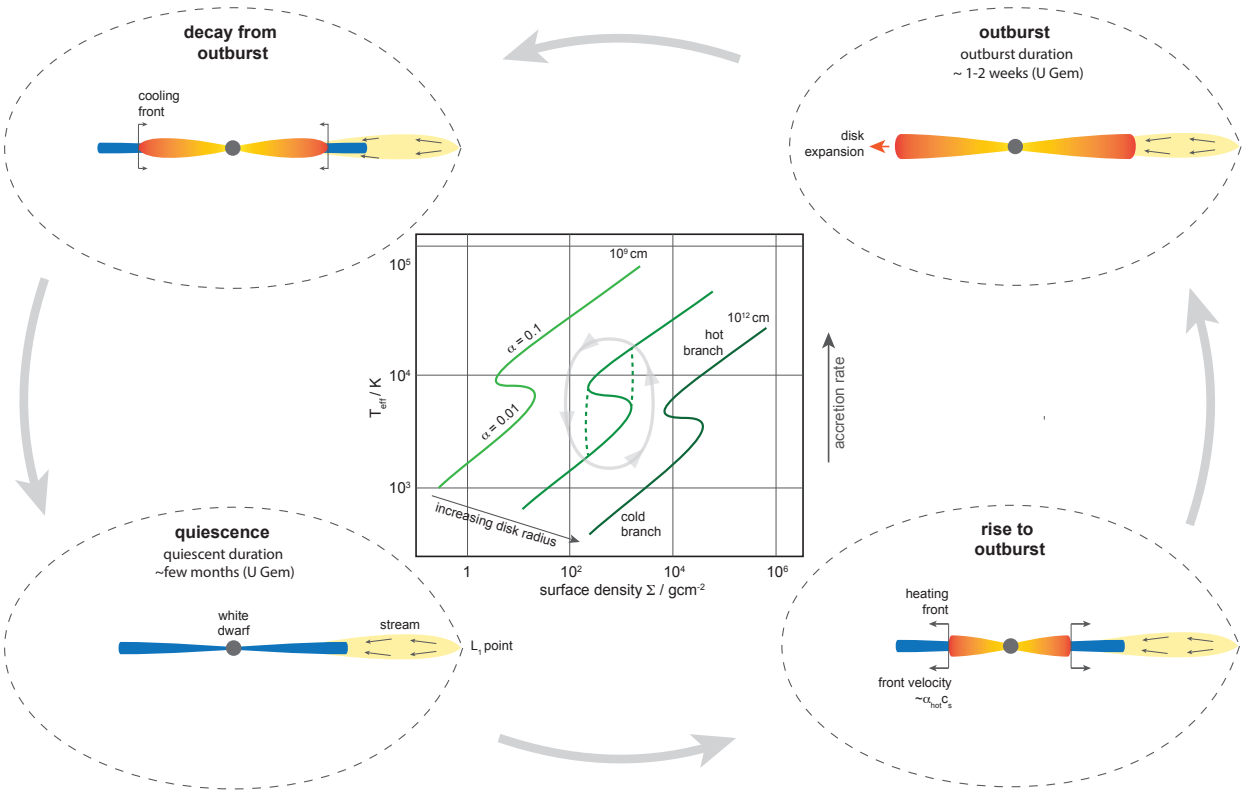

Figure 3: Evolution of the accretion disk structure along a DIM cycle, from Armitage (2022).

Spectral properties of Black Hole Low-Mass X-ray Binaries

Let us now focus on the subcategory of Black Hole Low Mass X-ray Binaries (BHLMXB), the subject of this manuscript. While they emit radiation across multiple wavelengths, their emission peaks in X-rays, and this energy band is essential for understanding their behavior. X-rays reveal strong spectral and timing evolution, due to the variety of physical mechanisms contributing to emission in this band. Soft X-rays (0.1–10 keV[2]) hold particular significance because they exhibit the richest diversity of spectral features, and most studies of Black Hole outbursts focus on this band.

During outbursts, the X-ray luminosity increases dramatically, often by more than five orders of magnitude, and is accompanied by spectral-timing state changes. These transitions are commonly represented using a Hardness Intensity Diagram (HID), which plots X-ray intensity (or luminosity) against a flux ratio between two energy bands called Hardness Ratio.The evolution in the HID typically follows a distinct "Q-shape", reflecting transitions between hard and soft states, dominated by more (hard) or less (soft) energetic X-rays.

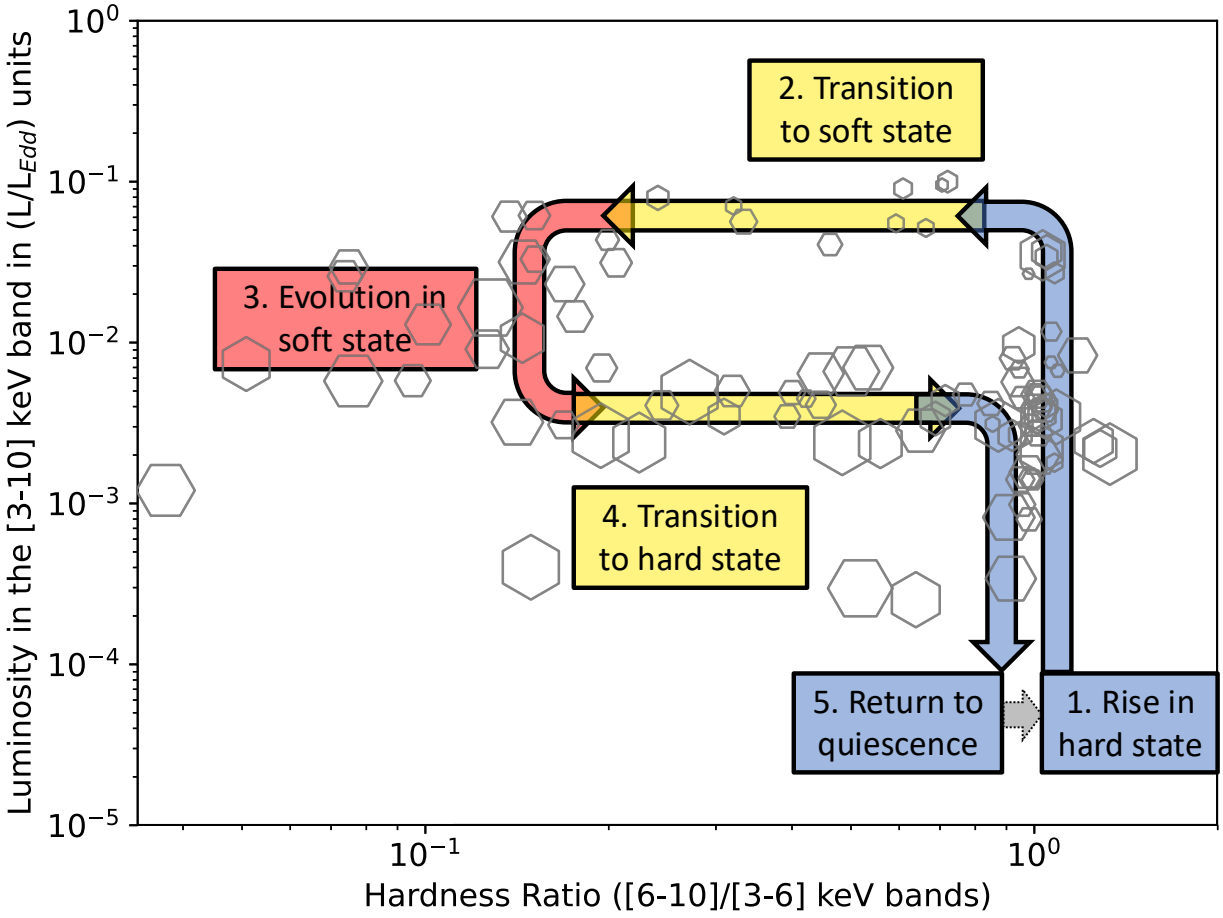

Figure 4: Typical evolution of a "standard" Black Hole Low-Mass X-ray Binary outburst represented in a soft X-ray Hardness Luminosity Diagram. Normalizing the luminosity (y-axis) to the Eddington limit allows to remove the dependency of the source luminosity on the mass of the Black Hole.

[2] in astrophysics, it is common to characterize light by the energy of each photon, $E = hc/\lambda$, with h the Plank constant and c the speed of light. 0.1-10 keV corresponds to a wavelength λ between 0.12 and 12 nm.

In the hard state, the X-ray spectrum (or SED) is dominated by Comptonization processes originating in a hot, optically thin plasma near the BH. Reflection of this emission on the accretion disk notably adds fluorescent iron lines, and a jet signature is seen in radio. As the luminosity increases beyond $\sim 10\%$ of the Eddington limit (L_{Edd}, the maximum luminosity that can be emitted with standard accretion), a transition to the soft state occurs, and the spectrum becomes dominated by thermal emission from an optically thick, geometrically thin disk. Jets are suppressed during this phase, and a "hard tail" appears at high energies. As the system evolves in the soft state, luminosity decreases over weeks to months, and the source eventually transitions back to the hard state after reaching $\sim 1-2\% L_{Edd}$, before returning to quiescence and a negligible amount of X-ray emission.

Not all outbursts follow this standard pattern. About 40% of events, termed "failed" or "hard-only" outbursts, reach or come close to the transition luminosity but fail to transit to the soft state, instead returning to quiescence. In contrast, some outbursts exhibit extended soft or Very-High States (VHS) with steep X-ray spectra. Rarely, systems exceed the Eddington limit, entering "Ultra-Luminous" states, which involve distinct accretion configurations and spectral properties. Conversely, obscured outbursts feature heavily absorbed spectra, often linked to massive outflows that hide the central emission.

For more details see Section 1.3.

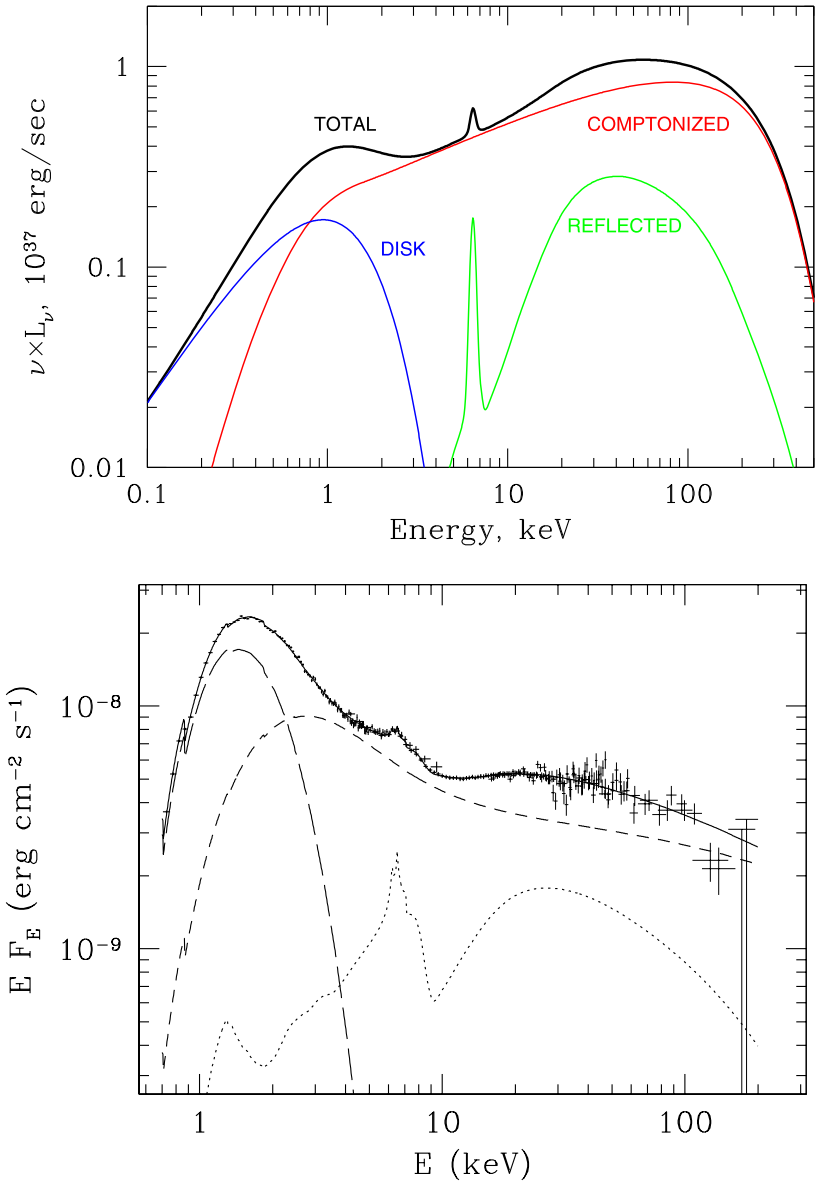

Figure 5: Typical X-ray spectra in hard **(left)** and soft **(right)** states of a BHXRB.
From Gilfanov & Merloni (2014) and Gierliński et al. (1999).

Winds

Wind signatures in X-rays

The study of **X-ray spectroscopy** has significantly advanced the understanding of a type of matter ejection dubbed **winds** in **Black Hole Low-Mass X-ray Binaries**. The definition of these winds remains nevertheless incomplete, and becomes clearer as new instruments and observations become available.

By the late 20th century, understanding of stellar phenomena was already significant, thanks to high-resolution optical and ultraviolet spectroscopy, which allow to study detailed spectral features. Among them, absorption and emission lines, linked to the presence of matter in the line of sight, can probe the density, ionization, and chemical composition of outflowing material. In contrast, technological limitations bound X-ray astronomers to far lower spectral resolutions, delaying their ability to identify similar processes in X-ray wavelengths.

The advent of the Japanese ASCA satellite in 1994 marked a turning point. Equipped with a high-resolution spectrometer, ASCA achieved groundbreaking detections of X-ray absorption lines, tracing highly ionized elements like iron. Then, in the early 2000s, the *Chandra* X-ray Observatory showed that these absorption lines are blueshifted, which means the matter is moving at *millions* of kilometers per hour in our direction. This identified a new type of outflow in X-ray Binaries, which took the name of similarly "slow" and massive ejections already identified in the vicinity of star and protoplanetary disks, "winds". This penomenon, although poorly understood, quickly became an important component of the accretion-ejection paradigm of X-ray Binaries.

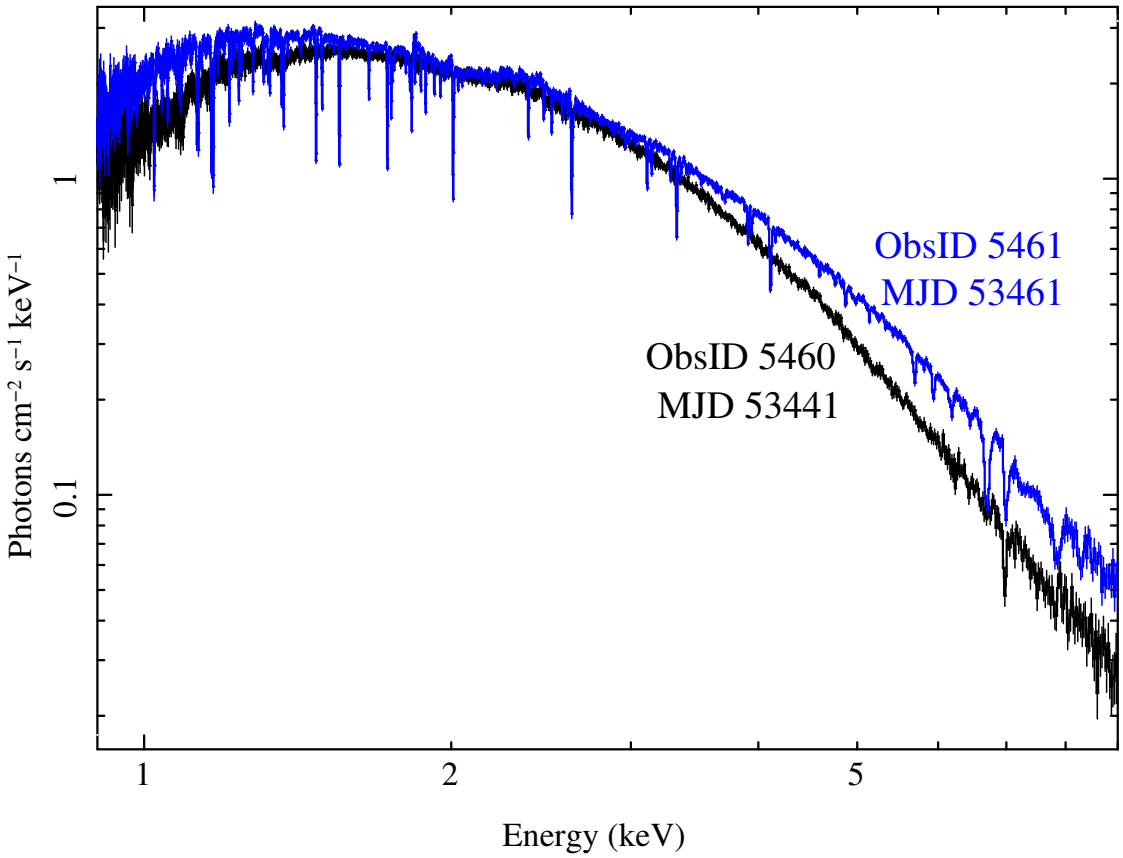

Figure 6: Example spectra of BHLMXB observations with blueshifted absorption lines, from Miller et al. (2008). The two observations in blue and black are only 20 days apart yet have completely different lines, showing how quickly this phenomenon evolves in a single source.

In the following decade, more observations linked these phenomena to specific accretion states, with studies showing winds predominantly arose in soft states of high inclined sources (seen close to the axis of the disk). This strongly supports the scenario of equatorial, disk-driven outflows.

However, despite substantial progress, many questions surrounding X-ray winds remain unresolved. For example, the interplay between winds and jets —the other main type of ejection, much faster but less massive, often observed in hard spectral states- has proven more intricate than expected. In parallel, recent detections in hard states challenge earlier assumptions of a strict dichotomy. Additionally, limitations in resolving detailed outflow structures in observations forbid any real constrain on wind models (see below). Finally, current observables often rely on narrow ionization ranges, limiting their ability to capture the full dynamics of wind emitting systems.

For more details see Section 2.1.1.

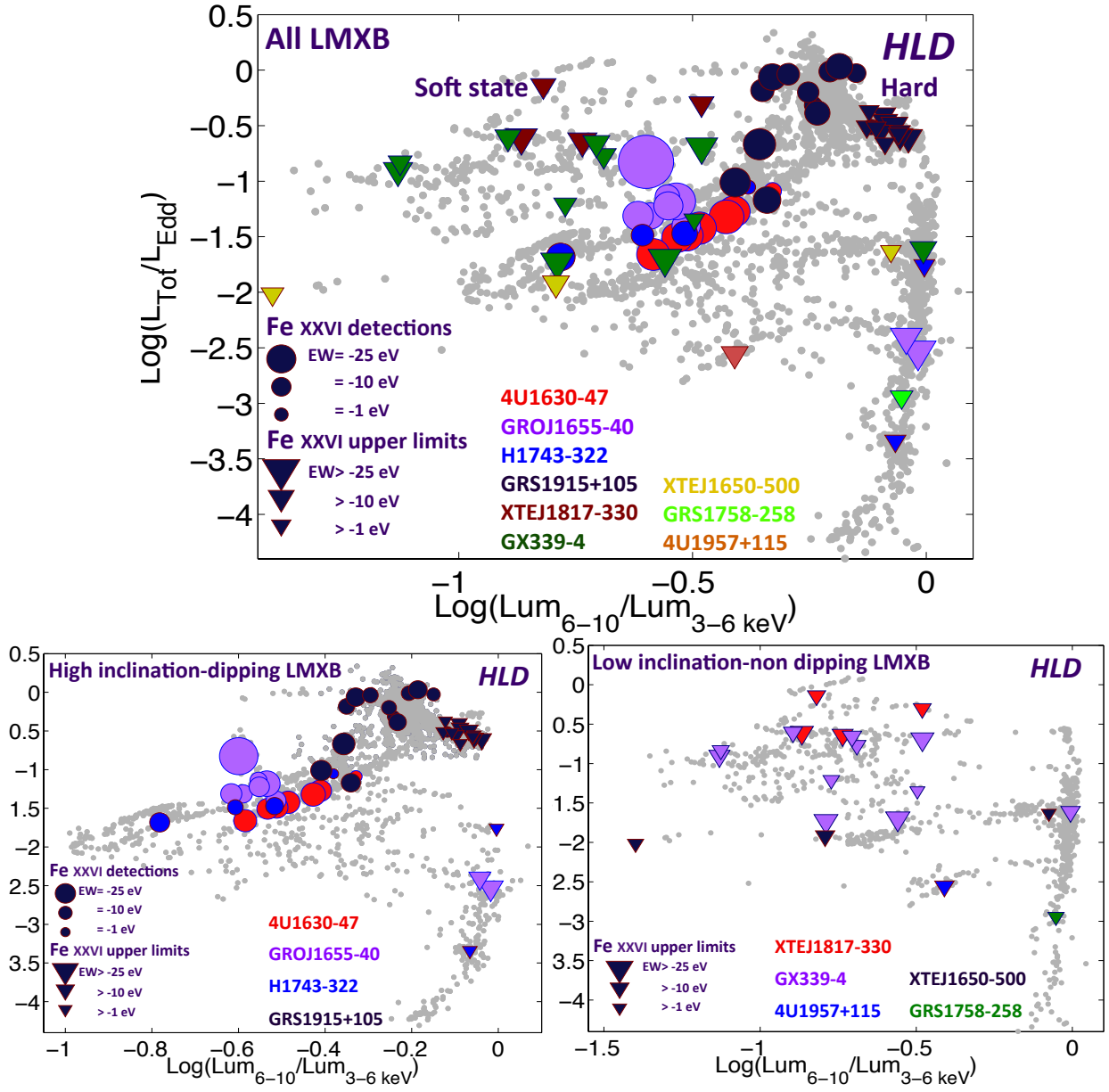

Figure 7: **(Left)** Hardness-Luminosity Diagram with wind detections and upper limits in a sample of BHLMXBs. The grey points highlight lower SNR observations. Aside from one notable exception, all detections come from soft state observations. **(Right)** HLDs from the same sample, but restricted to high and low inclination sources respectively. Only high-inclined sources show feature absorption lines. From Ponti et al. (2012)

Optical-Infrared counterparts and cold winds

In the last decade, new studies have identified **optical and infrared (OIR) wind features** in X-ray Binaries, showcasing a range of blueshifted absorption and emission profiles, with some properties at odds with their X-ray counterparts. Indeed, optical (visible wavelengths) wind features are predominantly observed in the **hard state** of BHLMXBs. Infrared signatures are also primarily tied to the hard state, though some persist across the **entire outburst**. This dichotomy suggests a shift from high-energy "hot winds", seen at high energies in the soft state, to low-energy "cold winds" seen at low energies in the hard state. However, it remains unclear whether these winds arise from a unified phase, considering the lack of simultaneous detections in standard accretion states.

The geometry of these winds is debated, with recent evidence suggesting a **less equatorial distribution** for cold winds. This could explain the absence of X-ray wind detections in some XRBs which show optical and infrared signatures, although the sample of sources with detections in either band is for now very limited. In parallel, While Ultraviolet (UV) wind signatures are prominent in active Supermassive Black Holes, no such detections have been confirmed in BHLMXBs. However, recent findings in high-inclination Neutron Star LMXBs have shown hints of wind signatures, sparking hope for future discoveries in sources out of the galactic plane whose UV emission is not absorbed by the interstellar medium.

For more details see Section 2.1.2.

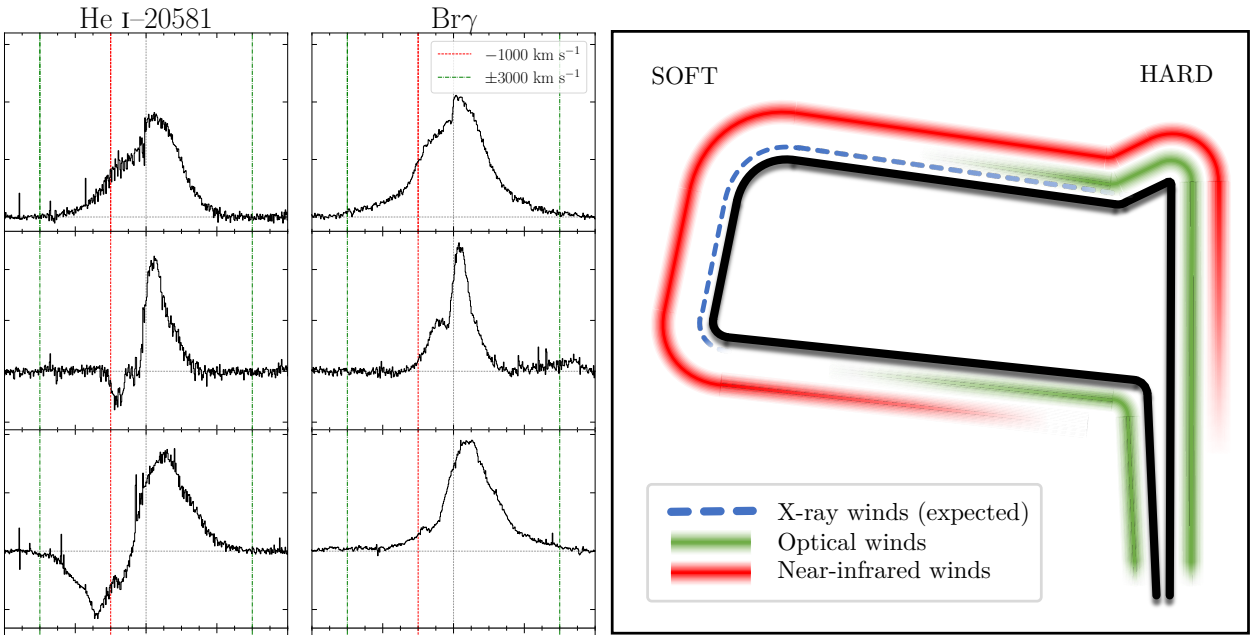

Figure 8: **(Left)** Example of infrared blueshifted P-Cygni (emission + absorption) profiles, from Sanchez-Sierras et al. (2023b). **(Right)** Repartition of wind detections along the outburst track in a Hardness Luminosity Diagram. From Sanchez-Sierras & Munoz-Darias (2020).

Wind launching mechanisms

Several physical phenomenon are susceptible to launch winds from the disks of accreting Black Holes. **Thermal winds** in X-ray Binaries arise from **irradiation-induced heating** of the outer accretion disk by X-rays from the inner regions. This heating creates an ionized layer, where thermal motions (∼1000 km/s) may exceed the **escape velocity**, enabling outflows. The **Compton radius** R_{IC} defines the threshold where material transitions from bound to unbound: material below remains bound, while regions beyond R_{IC} can support **isothermal winds** if the luminosity exceeds a critical threshold (L_{crit}). At very high luminosities, the wind can have a double thermal and radiative origin, due to the non-negligible influence of **radiation pressure**, which increases the wind speed and mass-loss rate.

Despite being restricted to large radii and velocities of a few hundred km/s, **thermal winds can explain most X-ray wind detections in Black Hole Low-Mass X-ray Binaries**. Current models predict **symmetric line profiles**, that can only be tested against high-resolution datasets. However, some observations of winds with **high velocities** or at **low luminosities** remain **incompatible** and require further study.

The spectral energy distribution and accretion flow geometry both have an impact on the wind dynamics: hard states reduce the wind launching radius and luminosity thresholds, widening the wind's parameter space. However, in this state, a highly opaque inner disk atmosphere can also stop ejections altogether. In parallel, **thermal instabilities** (see below) within the disk can influence wind launching in a more subtle manner.

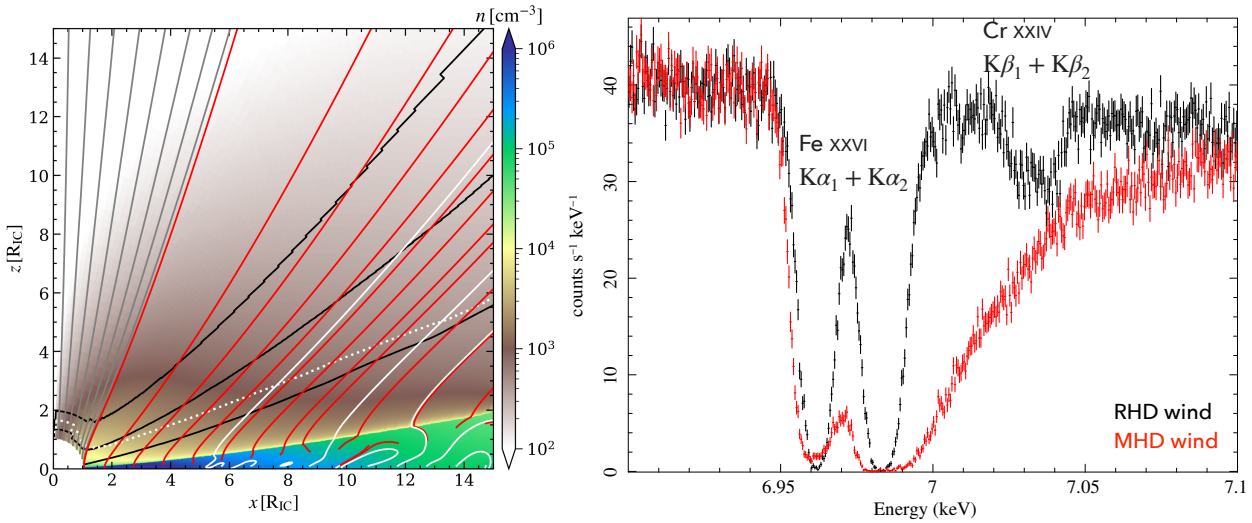

Figure 9: **(Left)** Radial view of a thermal wind emitting disk, with density structures and streamlines highlighted, from Waters et al. (2021). **(Right)** Comparison of expected profiles of thermal (RHD, black) and magnetic (MHD, red) winds, from Tomaru et al. (2023)

Magnetic outflows were first theorized as relativistic jets emerging from magnetized disks, then were expended to more diverse configurations. A **first class of models** focuses on the **ejections alone**, treating the disk as a boundary condition. Recent refinements to this paradigm were **successfully compared** to X-ray wind signatures observed **both in X-ray Binaries and SuperMassive Black Holes**.

The **second approach** integrates the entire accretion-ejection system, leading to more self-consistent solutions at the cost of a much more restricted parameter space. The **Jet Emitting Disk (JED)** semi-analytical model developed at IPAG incorporates several turbulent parameters and allows to derive a **supersonic accretion flow** coupled with **jet ejections**. A subsequent extension of the solutions to lower magnetization, dubbed the **Wind Emitting Disk (WED)**, achieves **much higher mass loads** supported by more standard disks. The mass loss ratio **p** and the magnetization μ, which are the main free parameters in the model, influence the transition between jet-like (fast, light) and wind-like (dense, slow) flows, shaping complementary structures.

Since magnetic winds are launched with varying speeds across the entire disk, they produce distinct X-ray absorption features with characteristic **blueshifted tails**. These signatures are easily distinguishable from thermal winds in the most extreme cases, but can overlap in weaker cases, and only high-resolution data from new and future observatories like XRISM and Athena will be able to distinguish them.

For more details see Section 2.2.

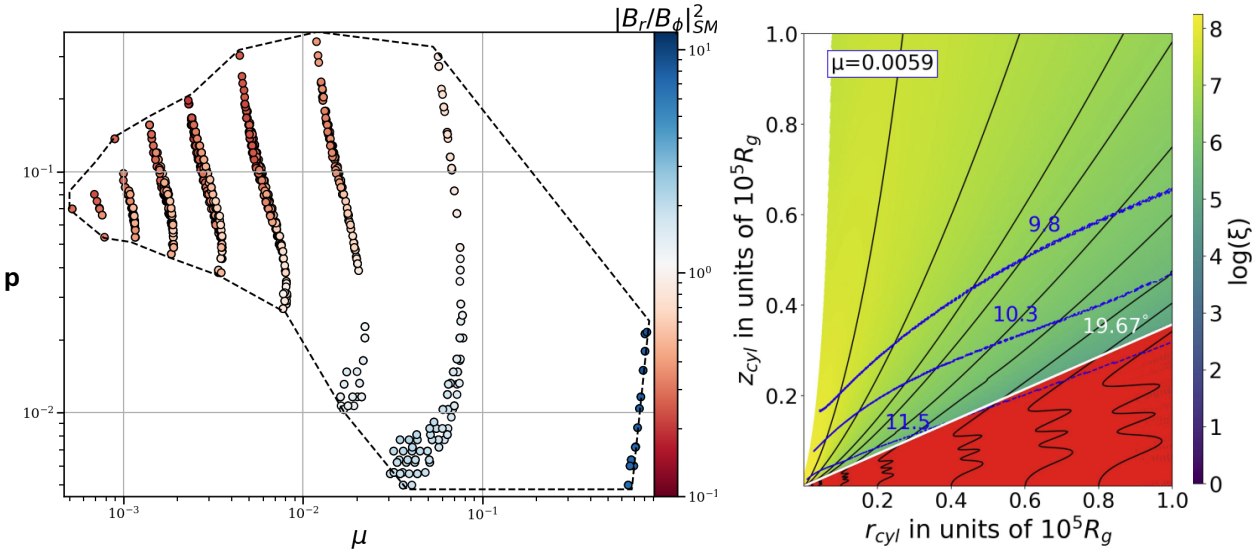

Figure 10: **(Left)** Parameter space of the JED-WED solutions, with a color scale showing the level of bending of the magnetic field lines, from Jacquemin-Ide et al. (2019). **(Right)** Density contours (blue) and magnetic field lines (black) of a single WED solution, from Datta et al. (2024).

Absorption lines and atomic processes

The quantization of **atomic energy levels** explains the origin of **emission and absorption lines** in spectra. Atoms in low-energy states absorb specific radiation frequencies, producing absorption lines, while energized atoms emit radiation as they return to their ground states, forming emission lines. The characteristics of these lines depend heavily on the **ionization levels** and **column density (NH, density integrated over the line of sight)** of the material. Ionization levels dictate the strength of atomic transitions, while NH affects both ion availability and the path of radiation.

Line profiles are influenced by **Doppler broadening** and **turbulence**, determining their **equivalent widths (EW)**, a quantity which measures line absorption "depth". Line profiles evolve from Gaussian (low densities) to Lorentzian wings at high densities, transitioning through saturation regimes. Turbulence is necessary to explain observed high EWs, as thermal broadening alone is insufficient. Measurements of EW depend on the ionic column density, ionization fraction, and elemental abundances. The **Ionization parameter** (ξ), representing the flux-to-density ratio, helps to assess ionization states but its influence varies with the SED, complicating direct calculations.

A material's **optical depth** determines its opacity to radiation. Soft X-rays in low-ionized matter are absorbed via the **photoelectric effect**, whereas hard X-rays are primarily scattered by **Compton scattering**. For highly dense gases, the material becomes **Compton thick**, blocking X-rays above 10 keV. In parallel, the strongest atomic transitions in X-rays are found in the so-called "iron-band" between 6 and 9 keV, among which Fe xxv Kα and Fe xxvi Kα at 6.7 and 7.0 keV. Their energies, determined by electron transitions to or from the K-shell, are crucial for velocity diagnostics.

Accurate diagnostics often require **photoionization grids** generated by dedicated tools like **XSTAR, Cloudy**, or **SPEX**. These models assume simplified slab geometries, but more advanced methods address **multi-dimensional geometries** and variability in irradiating sources. The approach chosen must balance computational cost and physical realism. High-resolution instruments will further clarify ambiguities in line identification and velocity diagnostics.

For more details see Sections 2.3.1 and 2.3.2.

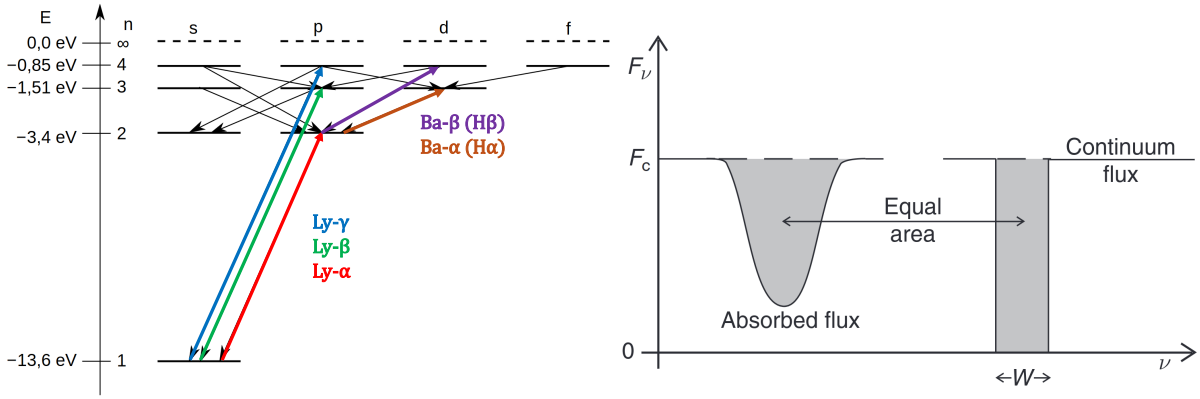

Figure 11:
(Left) Energy levels, transitions and line names for the Hydrogen atom. For Fe xxvi, which has a similar structure, the first transitions are often called with the letter K. Adapted from wikimedia.
(Right) Representation of the Equivalent width of an absorption line. From Pradhan & Nahar (2011)

Thermal stability and line visibility

The appearance of absorption lines in astrophysical winds is influenced by the **thermal stability** of the outflowing material. Stability curves, typically plotted in a $\log(\xi/T)$-T plane, represent the balance between **radiative and gas pressures**. These curves are crucial for understanding wind behavior under perturbations, either stabilizing or destabilizing the gas. In regions with a positive slope ($d\log T/d\log(\xi/T) > 0$), perturbations are counteracted, maintaining stability. Conversely, in regions with a negative slope, runaway heating or cooling occurs, leading to **instabilities**. This dynamic defines the material's migration across stability zones bounded by the lowest and highest stable branches. The Compton temperature marks the upper limit of these branches.

Changes in the Spectral Energy Distribution between hard and soft states profoundly **alter stability zones**. In the **soft state**, most of the curve is **stable**, allowing certain ionization states like Fe XXV and Fe XXVI to remain observable. In contrast, the **hard state destabilizes** these regions, **preventing the formation of associated absorption lines**. During state transitions, the material's evolution remains nuanced, with isobaric processes causing condensation into dense clumps within a hotter, diffuse medium. The timescale for these transitions, dictated by local conditions like the sound velocity and the thickness of unstable gas clumps, may only be accessible to the latest generation of instruments.

Broadband SED evolution plays a pivotal role in shaping stability curves. Variations in the high-energy cutoff significantly affect gas stability. However, constrains on the **hard X-ray component** are often incomplete if present, which complicates stability modeling.

Understanding these instabilities is essential to disentangle wind visibility, driving mechanisms, and the formation of clumps. The latter, supported by observations in SuperMassive Black Holes, enhances wind densities and can explain specific absorption line profiles. In **Black Hole X-ray Binaries**, clumping is being studied for its relevance to **cold outflows** at low luminosities, inaccessible to traditional thermal or magnetic winds.

For more details see Sections 2.3.3.

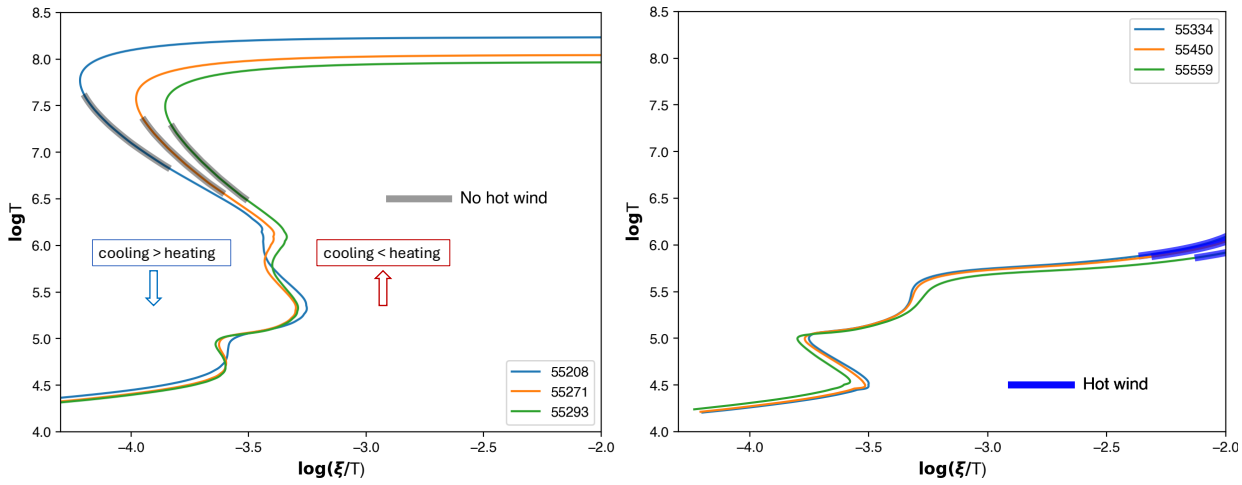

Figure 12: Evolution of the stability curves for hard **(left)** and soft **(right)** states of a Black Hole Binary BHLXMB. Different curves highlight different observations. Adapted from Petrucci et al. (2021)

Global study of X-ray winds in BHLMXBs

The new generation of X-ray telescopes is expected to put significant constrains on launching mechanisms and probe deeper the influence of other elements such as the evolution of the wind structure along the outburst. Nevertheless, many answers can still be found in the existing observations, and more constraints can obtained using large datasets. Indeed, observational studies and modeling efforts often focus on either single observations or select samples with very precise analysis or modeling of the existing features, and they mostly cover observations with the most prominent lines. Moreover, no detailed study of a large sample of sources, with exhaustive, multi-instrument data coverage, has been performed in the last decade, despite an extensive increase in the number of observations and sources, and a greater understanding of winds as a physical process.

One of my first objectives was thus to get a global, up-to-date view of the wind signatures in a large sample of objects and observations. This would not only allow to draw new conclusions on the observations from a much larger dataset than previously studied, but also to identify the best sources, outburst and datasets in which the line signatures would be susceptible to put constrains on wind launching mechanisms.

In order to maximize the number of BHLMXB candidates, I drew my sample from the two most up to date galactic Black Hole catalogs, *BlackCAT* and *WATCHDOG*, for a total of 88 sources. In parallel, there are many telescopes susceptible to detect lines in the soft X-ray band: when restricting ourselves to the ones with easily accessible archival data, that leaves *Chandra*, *NICER*, *NuSTAR*, *Suzaku*, XMM-*Newton*, *Swift*, and *HXMT*. Among them, XMM-*Newton* and *Chandra* had the advantages of being well established and (relatively) well calibrated, suited for line detections in the iron band, and having well documented studies of most archival line detections to confront my results. Further choosing to restrict myself to the most relevant instruments of each telescope, I ended up analyzing all XMM-*Newton* EPIC-PN and *Chandra*-HETG observations of currently known BHLMXBs, made public as of October 2022. This restricted the sample to 42 sources.

As of the writing of this manuscript, the literature for BHLMXBs remains very fragmented, and none of the BH catalogs are fully up to date with the literature. I thus listed in Tab. 3.1 the relevant physical properties and an overview of iron band absorption line detections for the **full sample of 88 sources** identified as BHLMXBs in the literature as of mid-2024, and will be discussed at different points of the study.

The data reduction procedures of the relevant telescopes, along with other instruments used for subsequent analysis, are detailed in Appendix 6.1.

For more details see Section 3.2.

Line detection methodology

To detect absorption lines in the iron band with sufficient signal-to-noise (S/N) ratios, a threshold of **5000 counts** in the 4-10 keV energy range was applied to XMM-*Newton* and *Chandra* spectra, corresponding to a detectability limit matching the high end of the EW distribution in the dataset. Following this refinement, **242 exposures** remained, of which **137 EPIC-pn and 105 HETG spectra**. I then applied an automatic procedure for each observation, whose main steps are summarized below.

- **1. Broadband Modeling**

  The continuum is modeled using a combination of powerlaw, diskbb, and phabs (neutral absorption) components, to represent the hard comptonized emission, the disk, and the galactic absorption respectively. They are iteratively added and evaluated through F-tests, requiring a 99% confidence threshold for inclusion.

- **2. Blind Search**

  To identify narrow line features in the iron band, we test by how much an additional line component improves or worsens the fit (the comparison between the model in the data), along a variety of energies and EWs. This leads to a 2D ΔC statistic map, where regions with statistically significant changes highlight potential absorption or emission lines.

- **3. Line Fitting Procedure**

  We model significant features in detail, with up to seven lines components. These include the strongest Fe absorption lines (notably Fe xxv Kα and Fe xxvi Kα) and neutral Fe Kα and Kβ emission lines. All lines of a single ion are assumed to originate from the same material, with velocity shifts constrained to avoid overlap or degeneracy. After storing the errors on the parameters of each line, which will be our main results, a second blind search confirms the absence of residual line features.

- **4. Line Significance Assessment**

  Monte Carlo simulations are necessary to properly assess the statistical significance of detected lines. We thus create 1000 synthetic spectra that reproduce the observation currently analyzed, based on the continuum model that we obtained, **without absorption lines**, and assess whether the photon noise of the instrument can create residuals significant enough to be comparable to the line measurement in each line's energy range. Only lines exceeding **99.7% confidence (3σ)** are considered valid detections. For observations with no significant lines, we instead compute 3σ upper limits for line equivalent widths in the initial observation.

Relevant figure (full page): Fig. 3.1.
For more details, see Section 3.3.

Global results

Favorable conditions for absorption line detection

Our results are in good agreement with standard expectations: all the wind signatures are found in luminous ($L_X > 0.01 L_{Edd}$) soft states ($HR_{[6-10]/[3-10]} < 0.8$) of five high-inclined (dipping) sources. The absence of Fe XXV and Fe XXVI absorption line detections in the hard state agrees with theoretical studies suggesting that the ionization range compatible with these ions should be thermally unstable when the gas is illuminated by a hard state SED. Thus, even if the wind itself were present, it would not be detectable through these absorption lines.

For more details, see Section 3.4.2.

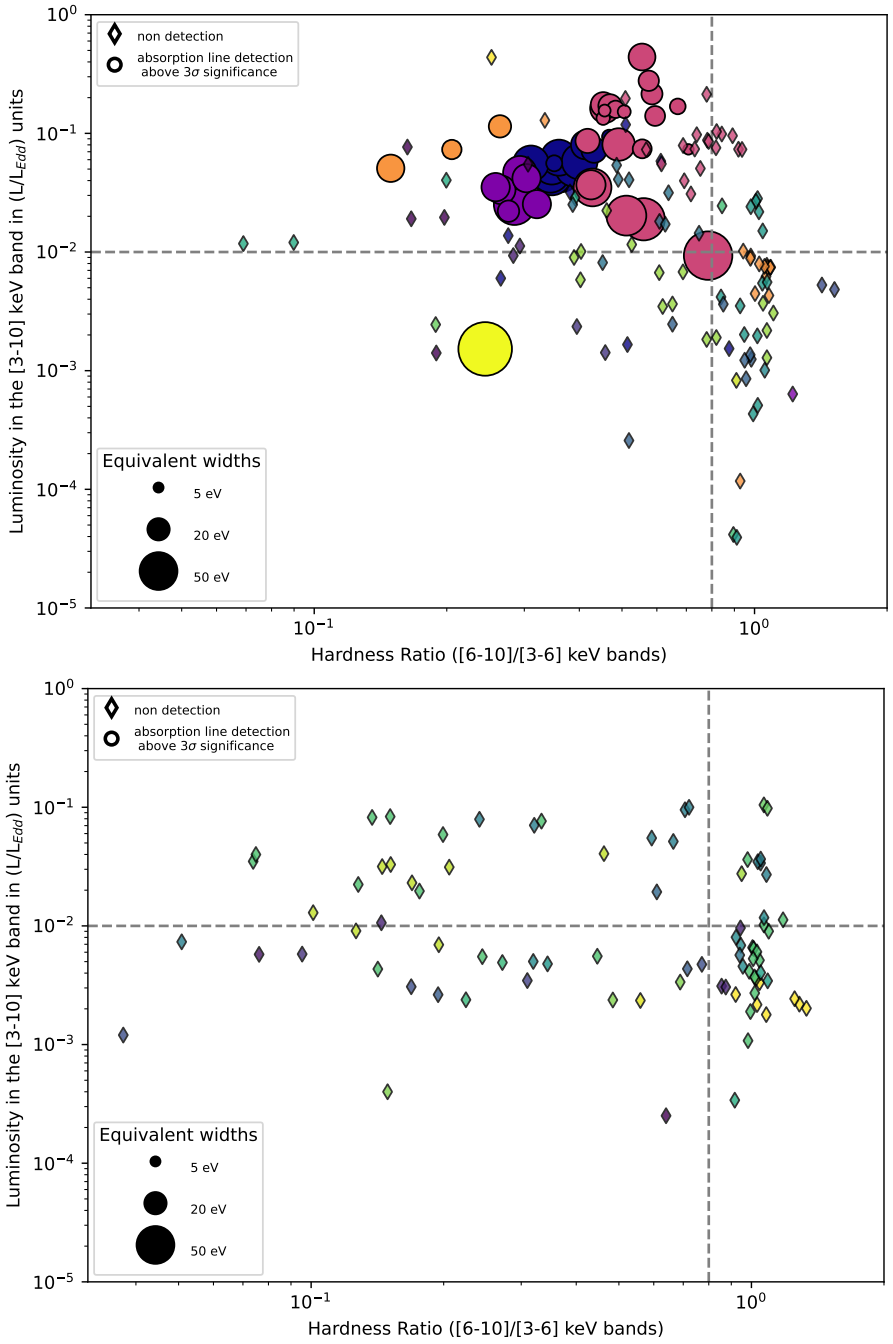

Figure 13: Hardness Luminosity Diagram with the position of all line detections (circles) in the sample, split between high-inclined sources **(left)** and low-inclined (or unknown) sources **(right)**.

Parameter distribution and correlation

With the *Chandra* instrument, precise measurements of outflow velocities reveal a global trend of slight blueshifts in absorption signatures, with velocity shifts averaging -200 ± 60 km s^{-1} and up to -1000 km s^{-1} (negative values indicate blueshifts). These findings align with prior studies on lower-energy lines and highlight consistency in velocity shift measurements despite the limits of *Chandra*'s accuracy.

The few line width detections, with full widths at half maximum (FWHMs) reaching several 1000 km s^{-1}, indicate significant turbulence velocities in the winds, which are estimated around 1000 km s^{-1} under simple geometric assumptions.

In parallel, we find few significant correlations between line and continuum parameters, among which a very strong anti-correlation between X-ray luminosity (in Eddington units) and Fe xxv Kα equivalent widths. This suggests a consistent wind structure across sources, potentially driven by ionization states above the ionic fraction peak for Fe xxv Kα.

Finally, the notable lack of detection for lower luminosities may reflect ionization changes, sparse data, or the outflow's dependency on high illumination, as proposed by thermal wind models.

For more details, see Section 3.4.1.

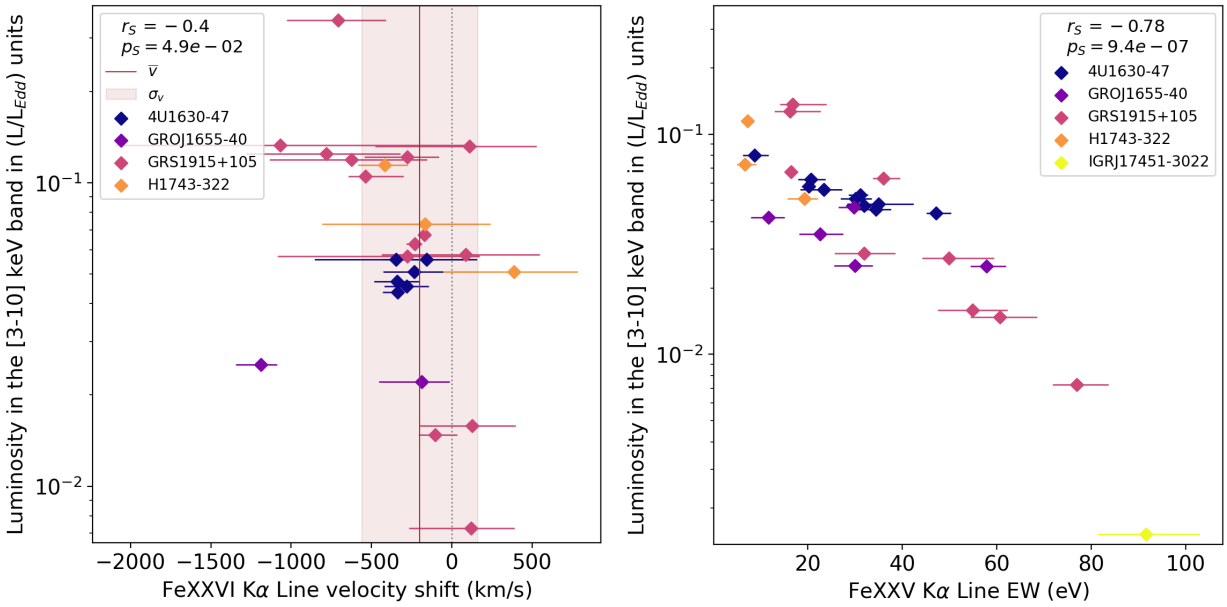

Figure 14: Evolution of the Fe xxvi Kα blueshift **(left)** and Fe xxv Kα EW **(right)** with luminosity in the sample. The r_S and p_S values in each graph give the Spearman test rank and p-value for each graph, which assesses monotonous relations between parameters. The p-value gives the probability that the correlation is due to random spread. Here, no correlation is present on the left panel, but a very significant correlation (p-value below 10^{-6} and strong rank) is present in the right panel.

Contextualization in the global observational landscape

In order to investigate the differences between results obtained in our sample and the rest of the literature, I compiled in Tab. 3.3 the reports of absorption lines in all wavebands, associated accretion states, and potential issues among all known BHLMXBs candidates.

In the iron band, the majority of the literature agrees with our findings, with a notable exception for occasional reports of high-velocity, hard-state absorption features, sometimes for low-inclined sources. Aside for having physical properties at odds with the canonical detections in every single aspect, these detections stem primarily from *NuSTAR* spectra, where blending with reflection components makes significance assessments difficult. *NuSTAR*'s limited spectral resolution and reliance on model-dependent residuals raise additional concerns, as conflicting results between reflection models are common. More over, important calibration issues that can affect both reflection and absorption studies have not been considered in any of those reports.

While other hard state detections were reported in the X-rays at lower energies, they exhibit low-enough ionization parameters to remain thermally stable even with hard state SEDs, and thus align with theoretical predictions. However, interpretations are hindered by the lack of consideration for multiphase interstellar medium contributions, which may explain a portion of the features. To distinguish static and dynamic absorbing phases, broader datasets spanning multiple spectral states are required.

Optical and infrared absorption lines provide a complementary perspective on winds as they often appear in hard states. These features are observed in high-inclination systems and align with X-ray detections in some sources, but display significant differences (notably in velocity shifts) in others. The scarcity of multi-band detections forbids any definitive conclusion but current datasets already points to a multi-phase type of outflow, with different behaviors for X-ray and OIR winds.

I also used my extensive compilation of source parameters to investigate additional links with wind properties, notably with the orbital periods. Cold winds, linked to outer disk regions, may be influenced by the disk's maximum size, yet no clear pattern emerges from current data due to limited inclination and orbital measurements. However, some of the systems with the shortest periods have shown significant outflow, which may already constrain wind-launching mechanisms.

For more details, see Section 3.6.

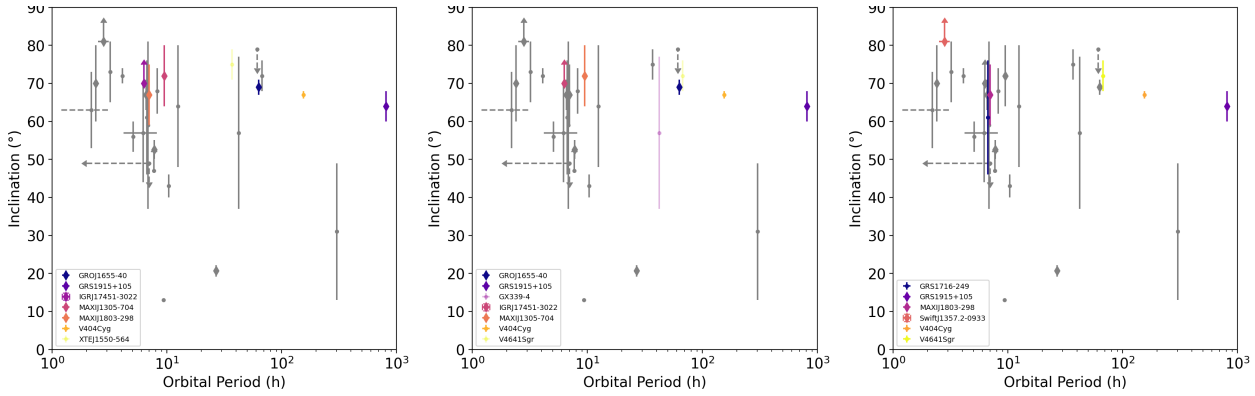

Figure 15: Distribution of the orbital period and inclination measurements of BHLMXB candidates with clear wind detections in the iron band **(left panel)**, at lower energy in soft X-rays **(middle panel)** and OIR **(right panel)**, compared to the rest of the sample (in grey). Diamond markers indicate dippers, and dashes tentative orbital period measurements.

20 years of disk winds in 4U 1630-47

The global study detailed previously had two direct applications: either perform a detailed study aiming to fill some of the gaps identified in the observational landscape, or focus on models and comparisons with the data. Unlike what the structure of this document suggests, I ended up leaning towards the second option first. After finishing the groundwork on the modeling project (which we will come back to later), I returned to observations and focused on one of the sources whose archival data had the most potential: 4U 1630-47.

4U 1630-47, a transient X-ray source with recurring outbursts every 600-700 days, has been classified as a Black Hole Low-Mass X-ray Binary based on spectral and timing properties. Despite some similarities to other sources of the same kind, its behavior deviates significantly from the norm, with irregular "super-outbursts" of extended duration, atypical spectral evolution, and rare occurrences of proper hard states. The source instead transitions erratically between soft/thermal, intermediate, flaring and "steep power-law" (SPL) states, each with distinct high-energy components and timing properties. It has also a history of fully soft outbursts. These properties, combined with a very high inclination, have made the source one of the most well observed wind emitters.

Wind detections began with *Suzaku* observations in 2006, with earlier hints in *Chandra*-HETG data. Subsequent campaigns during the 2012-2013 outburst included observations with many instruments such as XMM-*Newton*, *Chandra*, *Suzaku*, and *NuSTAR*, revealing absorption features and possible relativistic emission lines, although the latter remains debated. More recently, a continuous *NICER* monitoring through 2018 and into a prolonged 2022-2024 outburst confirmed wind signatures and complemented X-ray polarization studies. These observations underscore a near-decadal recurrence of super-outbursts over three decades.

Archival data includes over 200 "high-quality" epochs where lines can be detected, spread across nine outbursts, combining many different instruments (*Chandra*, *NICER*, *NuSTAR*, *Suzaku*, and XMM-*Newton*), and significant additional high energy coverage (notably via *Swift*-BAT and *INTEGRAL*). These datasets can provide unparalleled insights into the evolution of the wind in an outbursting BHLMXB, but until now, studies have focused on single outbursts or instruments. In an effort to understand the long-term evolution of the source, I thus analyzed all publicly available data until the end of 2023.

For more details, see Section 4.1.

Note: The data reduction procedures are listed in Appendix 6.1.2, and the details of the spectral analysis are presented in section 4.2. The line detection procedure in itself remains identical to what was used for the previous study.

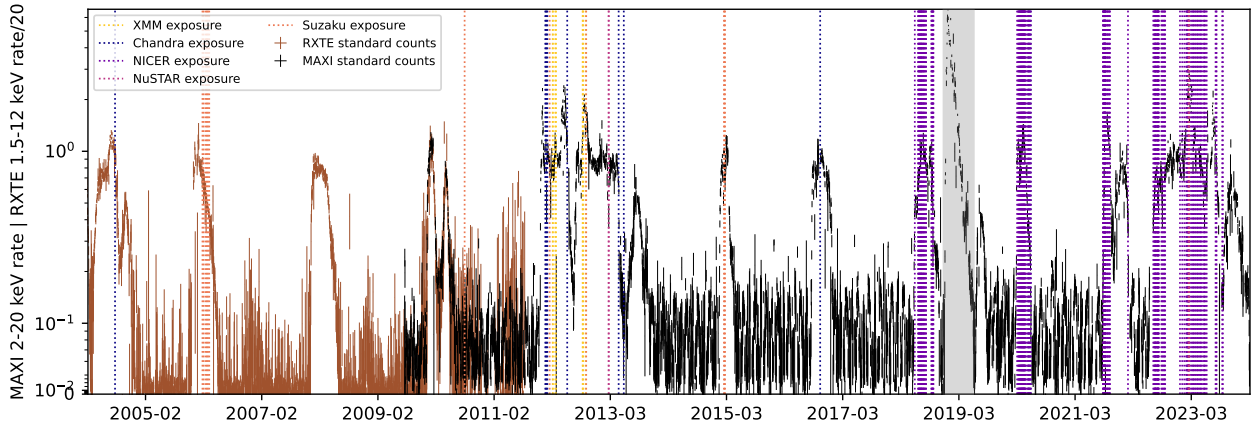

Figure 16: Long-term lightcurve of 4U 1630-47 using two monitoring telescopes, with exposures used in this study highlighted with vertical lines. The grey period is contaminated by a nearby source.

Global results

HLD evolution at low and high energies

I first constructed the standard Hardness-Luminosity Diagram of 4U 1630-47 using the intrinsic luminosities in the [6-10] and [3-6] keV bands for the Hardness Ratio (HR) and the [3-10] keV luminosity in Eddington units. Thanks to an aggregated dataset spanning multiple outbursts, we reach a near-complete coverage of the source's evolution at high luminosities (above $\sim 10^{-2} L_{Edd}$). Observations in the soft state predominantly align along a narrow diagonal, consistent with expectations for highly inclined binaries. The high-cadence *NICER* monitoring corroborates earlier findings, notably the diminished presence or disappearance of absorption lines above HR values of ~0.4–0.45 and $L_{3-10} \sim 10^{-1}\ L_{Edd}$. However, many *NICER* observations in softer states yield non-detections with upper limits incompatible with detections at identical HR and luminosity values.

As the influence of hard X-rays above 10 keV was the likely culprit, I implemented a new "hard" HLD, substituting the [6-10]/[3-6] keV HR (HR_{soft}) with a [15-50]/[3-6] keV Hardness Ratio (HR_{hard}), only accessible thanks to the high-energy monitoring. The resulting diagram, with shaded markers indicating epochs where [15-50] keV estimates are not significant, provides a much better distinction between states with and without detectable absorption lines. Indeed, their equivalent width exhibits a clear anti-correlation with HR_{hard}, confirmed by a null hypothesis test (Spearman rank) below 10^{-9}. Above $HR_{hard} \sim 0.1$, the expected EWs of absorption lines decrease to levels undetectable with current instruments in most observations, explaining the scarcity of detections.

For more details see Section 4.3.1.

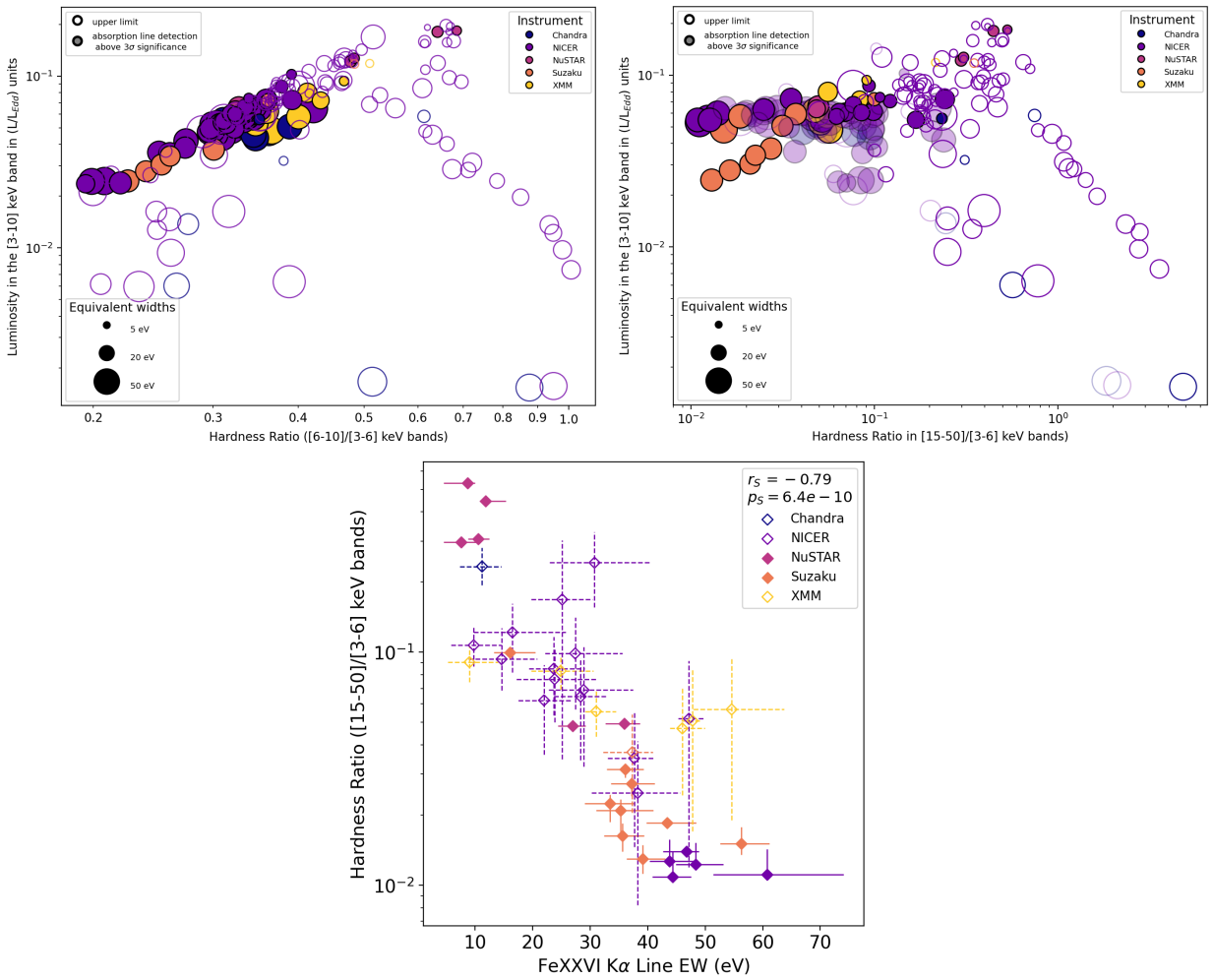

Figure 17: **(Top)**Multi instrument "soft" **(left)** and "hard" **(right)** HLDs of 4U 1630-47, colored according to instruments. **(Bottom)** Scatter plot of the Fe xxvi Kα line EWs and HR_{hard}

Correlations and structures

The distributions and properties of the lines detected with *NICER*, *Suzaku* and *NuSTAR* remain mostly consistent with the smaller XMM-*Newton* and *Chandra* set of observations of the source already analyzed for the previous study. The blueshift distribution of the most precise satellite remains most notably significantly distinct from zero, with $\overline{v_{out}} \sim -560 \pm 60$ km/s.

When examining correlations between line parameters and continuum properties, the soft X-ray luminosity ($L_{[3-10]}$) shows strong relationships with the EWs of Fe xxv Kα, to a lesser extent Fe xxvi Kα, and their ratio. These correlations are significant (significance $\sim 10^{-5}$) and align with prior findings for global wind emitting sample. In parallel, the "soft" Hardness Ratio does not correlate to any line parameters, unlike the "hard" Hardness Ratio.

The notable difference with the previous study is the appearance of significant deviations appear at the highest and lowest luminosities, most likely due to our order of magnitude increase in sampling. Indeed, excluding observations below $L/L_{Edd} \sim 4 \cdot 10^{-2}$ and above $L/L_{Edd} \sim 10^{-1}$ significantly enhances the soft X-ray luminosity correlations, highlighting these regions as outliers. Most notably, the low luminosity portion significantly departs from the main trends. Regression analysis confirms observations in this substructure lie well outside the confidence interval of the main structure, and also show distinct behavior in hardness-luminosity diagrams (HLDs). Observations in this substructure are typically part of the initial rises or final declines of each outburst, contrasting with the brighter portions of the soft-state diagonal.

Finally, highlighting the time evolution further distinguishes outburst types, as super outbursts appear to have more structured correlations than normal outbursts. However, more uniform and systematic observations are required to assess whether this phenomenon is a byproduct of uneven sampling.

For more details see Sections 4.3.2 and 4.3.3.

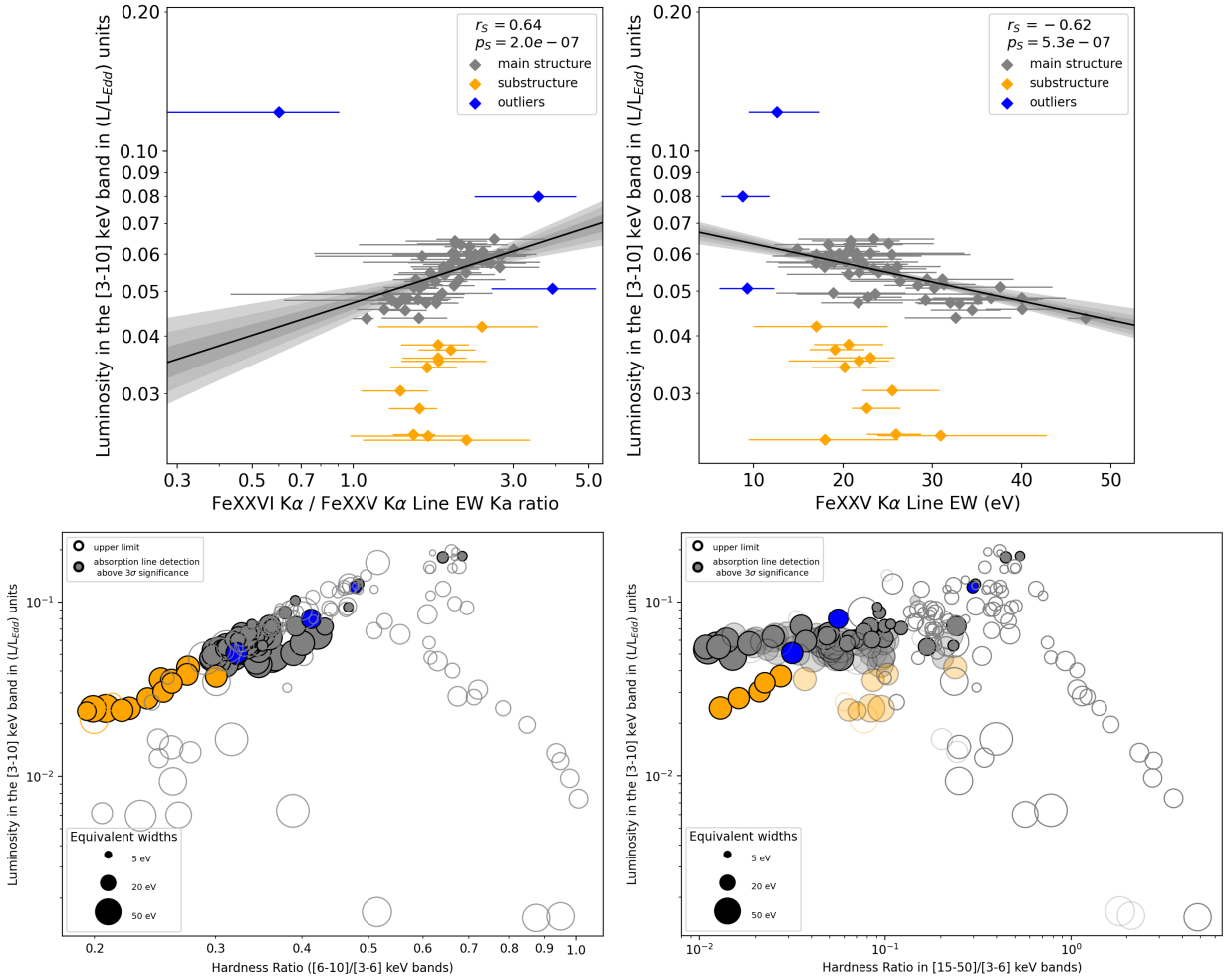

Figure 18: **(Top)** Scatter plots of line EWs and luminosity highlighting the proposed substructure and outliers.**(Bottom)** Multi instrument "soft" **(left)** and "hard" **(right)** HLDs of 4U1630-47, using the same color scheme.

Wind evolution along spectral states

The evolution of the absorption lines seen in the observations can be the sign of intrinsic changes in the outflow properties, but also the consequence of the changes in the spectrum. To distinguish the two, two main effects need to be considered: the stability of the plasma, and the evolution of its ionization. We thus regroup the behavior of the source in five spectral states (soft, intermediate, SPL, QRM, hard) before testing how the SED of each state affects the appearance of the lines.

For more details see Section 4.4.

Influence of plasma stability

By computing stability curves with CLOUDY, we identified thermally stable regions at varying ionization parameters in a range of observations of each state, focusing on those with robust high-energy measurements. Our results show that the ionization ranges of Fe XXV and XXVI ($\log \xi \sim 3.5-4$) remain thermally stable in all spectral states except the canonical "hard". The observed decline in equivalent widths of Fe XXV and Fe XXVI absorption lines when transitioning to intermediate and SPL states can thus not be due to instability effects. Unexpectedly, even some fully hard states retain a thermally stable region for Fe XXV. This discovery marks the first report of such stability in BHXRB hard states, and diverges from the typically thermally unstable hard states seen in other sources.

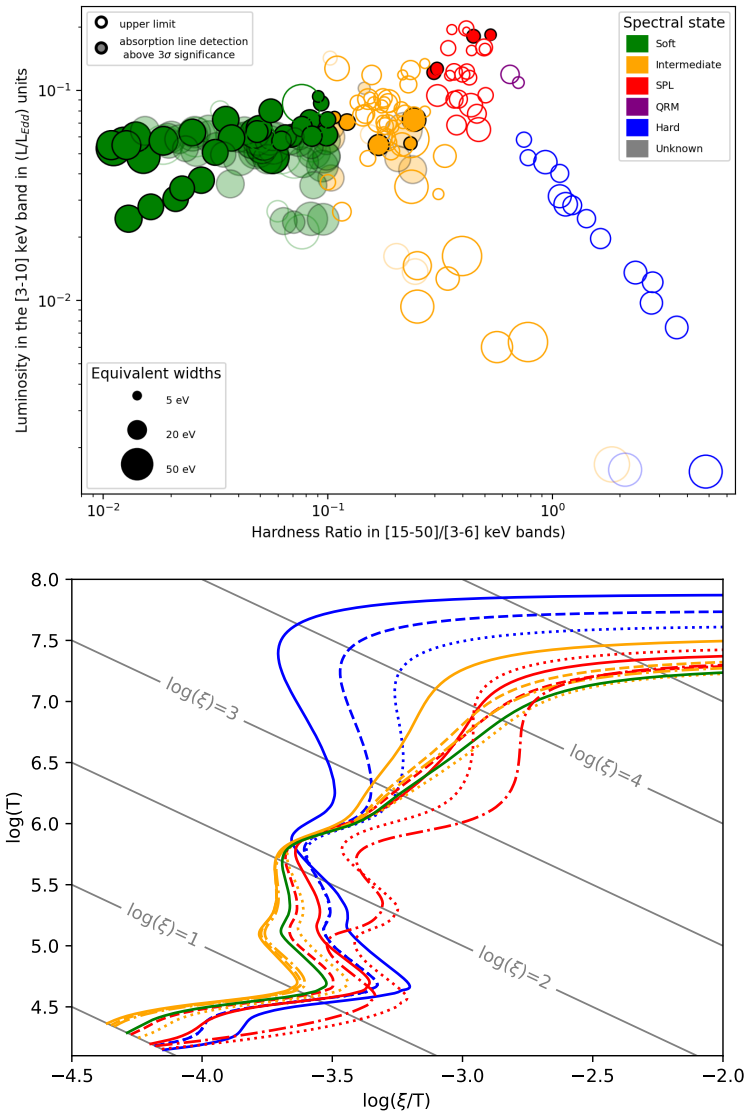

Figure 19: Hard Hardness Luminosity Diagram **(top)** and stability curves of SEDs in each spectral state **(bottom)** of 4U 1630-47, colored according to the spectral states.

Influence of ionization changes

To further isolate SED-independent wind parameters, we computed for several observations the curve of growth of the EW of each absorption line across a fixed N_H and turbulence, scaling these by ionization parameters and luminosity. This approach was applied to a number of exposures with varying line properties and HLD positions. The results show that a significant change in the intrinsic parameters of the outflow is required to explain the discrepancies between observations of either different luminosity, or different HR_{hard}.

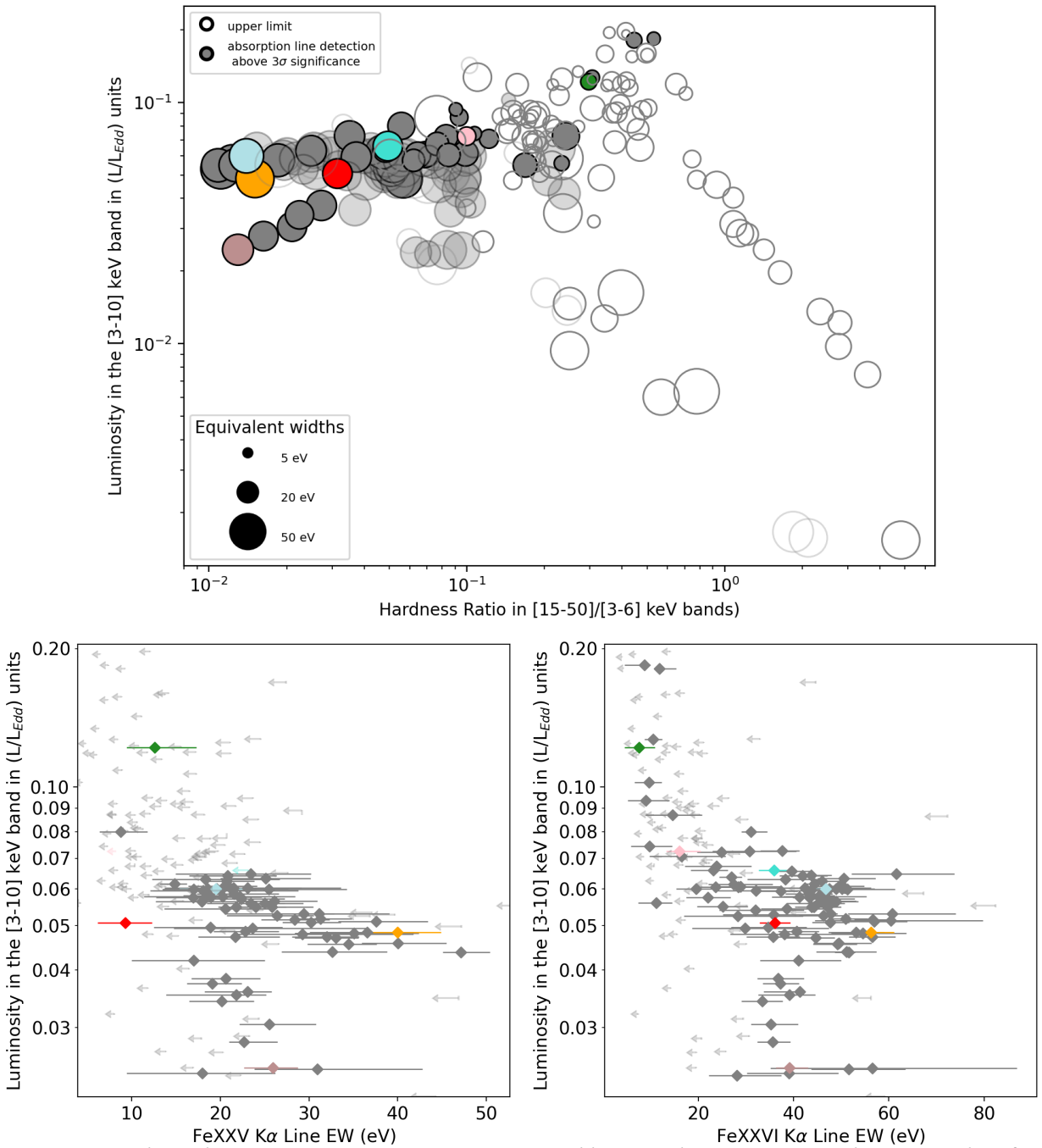

Figure 20: Hard Hardness Luminosity Diagram **(top)** and line EW-luminosity correlation graphs of 4U 1630-47 **bottom)**, highlighting the observations tested for differences in wind parameter.

Outstanding line variability in recent outbursts

Until this point, we've limited ourselves to the variability of the source on the timescale of daily-averaged epochs. However, a more detailed look at the individual *NICER* orbits reveals of a number of peculiar short-lived spectral-timing evolutions related to the presence of lines. One of them is detailed below.

For more details see Section 4.5.

February 2023: Highly variable dipping

NICER observed 4U 1630-47 on February 23, 2023 during 6 different periods (orbits). While the last 3 exhibit a standard thermal state spectrum without detectable absorption lines, suggesting an intermediate or SPL state, the first 3 show very strong absorption features, as well as erratic flux variability on sub-minute timescales. Orbit-integrated spectra reveals a progressive decrease in luminosity to 10% of the initial flux in the 3–10 keV range, accompanied by deep absorption lines and a broad iron emission line. However, time-resolved spectroscopy shows that the flux drops are systematically softer, despite similar absorption line properties. This is inconsistent with standard absorption-driven dimming due to very dense material entering the line of sight. The other scenario, namely a change in continuum due to variations of the accretion flow, would require very rapid changes in the disk structure, an extremely rare occurrence in non-pulsating sources.

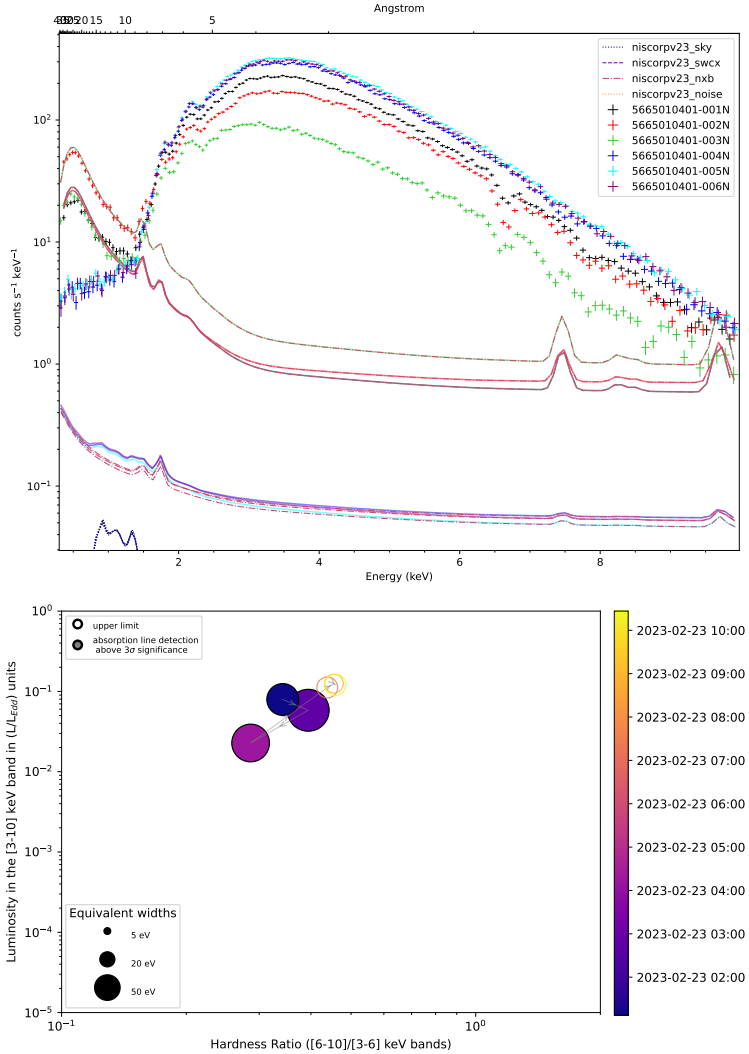

Figure 21: **(Left)** Time-integrated spectra of the individual orbits. **(Right)** soft HLD of the individual orbits and corresponding EWs for Fe xxv Kα, color-coded with time.

Observational signatures of Wind Emitting Disks

The Wind Emitting Disks solutions developed at IPAG are among the very few physical models of magnetically launched winds, and their self-similar description provides a very promising way of accessing key physical parameters of the accretion-ejection structure via the outflow signatures. However, despite few pilot studies in the last decade, the observational signatures of the WED parameter space have yet to be fully characterized, and comparisons with existing data have yet to be performed. One of the main objectives of my PhD was to continue this project.

I ended up restricting myself to laying the groundwork, namely creating the tools necessary to produce tables of synthetic high-resolution spectra, to compare against relevant datasets. The study of the wind signatures available with the current version of the WED parameter space, as well as comparisons against present and future datasets, are both ongoing projects that will be the focus of my upcoming JSPS fellowship, in collaboration with IPAG and members of the XRISM team.

WED synthetic signatures: improvements and scaling

The computation of synthetic Wind Emitting Disc (WED) spectral signatures requires a radiative transfer code with precise atomic data to assess the impact of outflowing material on transmitted spectra. Axisymmetric WED solutions provide a 3D self-similar structure for disks and outflows, which ideally should be analyzed with full 3D radiative transfer codes. However, such codes are way too computationally expensive, which forbids using them for parameter space exploration and direct dataset fitting. A simpler approach developed by my predecessors utilizes a discretized 1D method. Synthetic spectra are calculated iteratively along each line of sight (LoS), therefore divided into a range of radial steps or "boxes". Each step's transmitted spectrum is used as input for subsequent calculations, until the final transmitted spectrum is obtained.

Our approach has several drawbacks. First, it ignores off-axis material, a limitation whose importance can only be assessed via comparisons with 3D models (which are currently in progress). Additionally, the current solutions are fully "cold", meaning that they don't consider any effect of the central emission on disk or wind structures. One of the main consequences is that the scale height of the disk becomes a free parameter instead of being solved. Moreover, unstable Spectral Energy Distributions should alter gas ionization structures, but the current solving method disregards such instabilities and they must be implemented as post processing.

The initial WED algorithm, developed as a wrapper the XSTAR radiative transfer code, suffered from limited scalability and portability across XSTAR versions or alternative codes. The rewritten implementation is much more flexible, supports multidimensional sets of solutions and can be plugged into any radiative transfer code. It also incorporates additional effects, among which relativistic corrections, and optimized radial and spectral sampling.

For more details see Section 5.1.

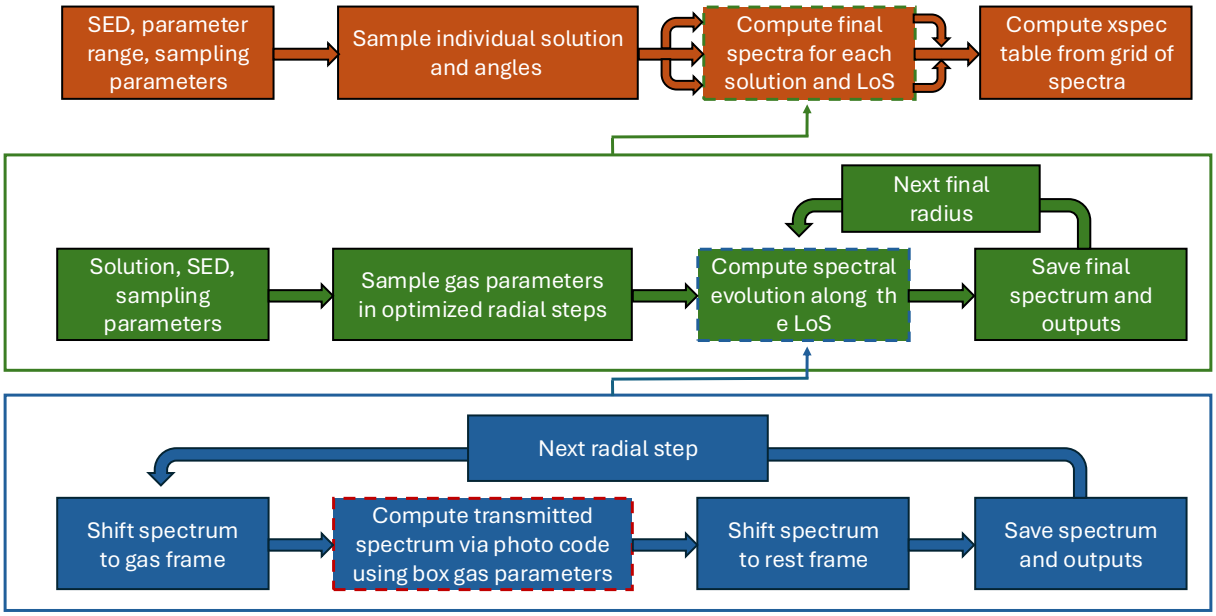

Figure 22: Overview of the logic of the grid creation framework. The cycle in blue represents individual radial computations along a line of sight, the cycle in green the computation of a single solution, and the one in brown the computation of a grid of synthetic spectra. We highlight in red dashes the fundamental step which involves an external photionization code, for now assured by XSTAR.

Exploring the WED parameter space

Radial distribution for single solutions

One of the approaches I used to characterize the 3D wind structure was to sample various angles within a single solution and compare the radial distributions of parameters pertinent to wind computations.

First, the ionization structure remains independent of luminosity due to the linear dependence of density on the mass accretion rate. In practice, a constant ionization structure is constant in each WED solution allows to map the maximum velocities available in the WED parameter space for a given SED without extensive spectral computations. Combining this with ionization computations could reveal whether the observed velocity landscape of BHLMXBs is consistent with the current WED parameter space, without having to directly compare with spectra.

In a single solution, the column density scales linearly with the accretion rate, meaning that between observation where the SED only evolves in flux, the intensity of absorption lines should predictably correlate with the luminosity. However, the evolution of the luminosity of XRBs in soft states often involves spectral changes (such as for 4U 1630-47). In parallel, the effects of the inclination angle effect are very pronounced, both in terms of column density and velocities. The important decrease of density for angles below $\sim 50°$ restricts observations with significant absorption features to very high inclination angles. In parallel, the velocity range available for non-fully ionized material remains below few 1000 km/s no matter the inclination angle.

For more details see Section 5.2.2.

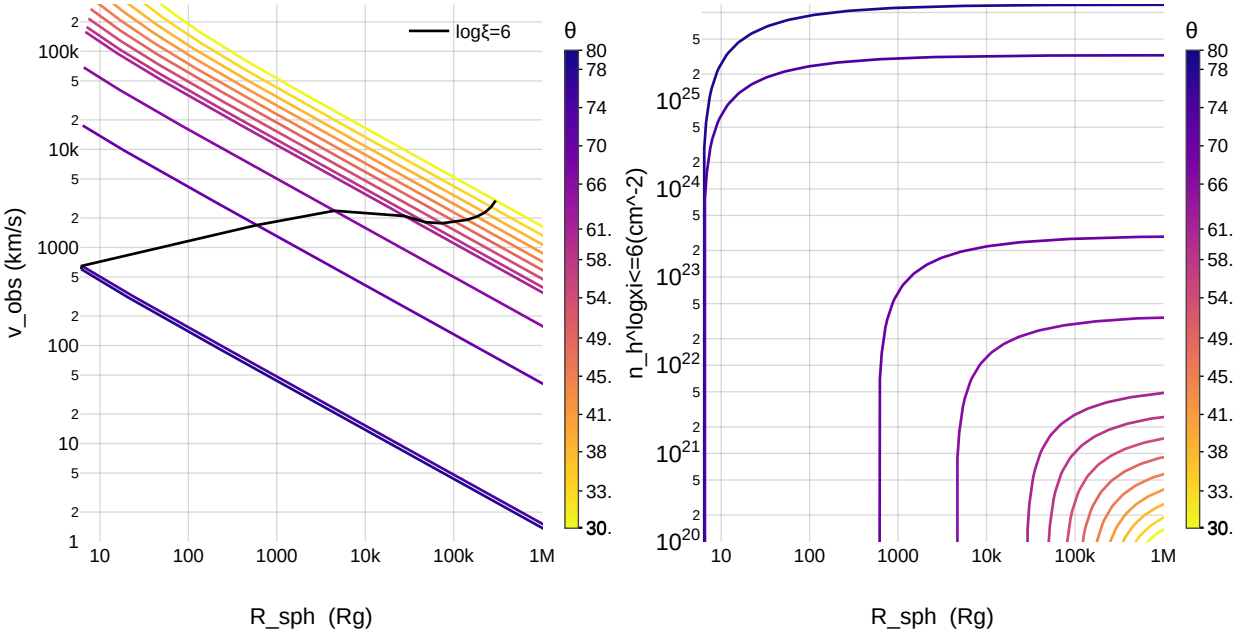

Figure 23: Overview of the radial dependence of the wind velocity in the line of sight **(left)** and the portion of the column density that is not fully ionized **(right)**, using a linear angle sampling of a single WED solution. Here, the dense region above the disk rises to around $\sim 75°$, which explains the changes between the second and third angle sampling.

Thermal structure

One physically verifiable WED parameter is the disk's aspect ratio or scale height (ϵ). Since theoretical models for accretion disk structures typically exclude the outer regions where the wind creates the absorption lines, due to their negligible amount of emission, I developed tools to compute a first order of the thermal structure of WED-like solutions analytically.

After solving for a range of different solutions, the evolution of ϵ with radius in the typical wind-emitting region visible in X-rays ($\sim 10^3 - 10^5$ Rg) is relatively small, and thus the assumption of a constant scale height used for the WED grid computations is a decent approximation. However, it remains significantly lower than the canonical values of $\epsilon = 0.1$ typically assumed in the literature.

We further asses the influence of different parameter on these conclusions by sampling the effect of changes in the accretion rate (through the Eddington fraction) and the evolution in the main parameters of the WED solutions, the ejection index p and the magnetization μ. While the influence of each parameter is fundamentally different, individually, none of the changes are very significant, and the aspect ratio of the disk typically remains in a range of ϵ ~0.01-0.03. However, special care should be taken when comparing solutions with extreme combinations, such as high luminosity, high ejection index, and low magnetization, or low luminosity, low ejection index, and high magnetization, as the difference between the assumed value of ϵ and the real values in the outer disk may become the source of significant inaccuracies.

For more details see Section 5.2.3.

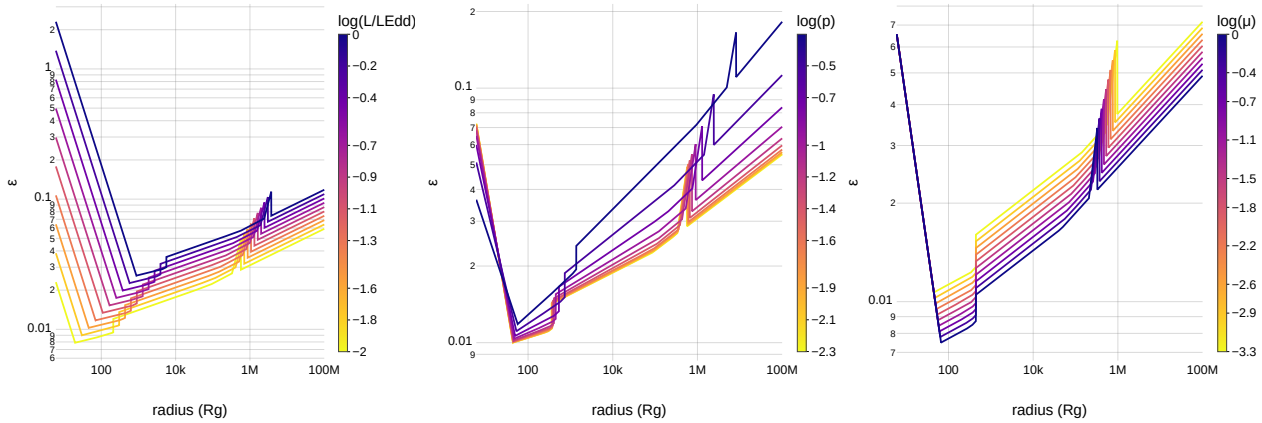

Figure 24: Radial evolution of the aspect ratio when varying a single of the parameters of the solution. Variations of L/L_{Edd} are translated in accretion rates to reflect the typical luminosity range of the soft states in a BHLMXB outburst.

Tu as une heure ou deux

Introduction

L'étude des **objets compacts**, en particulier des Trous Noirs, est essentielle pour comprendre les phénomènes astrophysiques extrêmes. Le terme objet compact comprend **les Naines Blanches (WD), les Etoiles à Neutrons (NS) et les Trous Noirs (BH)**, en raison de leur **compacité**, un rapport sans dimension entre leur énergie gravitationnelle et leur énergie de masse. Cette propriété distingue les objets compacts des corps astrophysiques moins denses, et rend leur étude cruciale pour l'exploration des **processus à haute énergie**, des **effets relativistes** et de l'**évolution des systèmes stellaires**. En effet, les objets compacts se forment par des processus liés au cycle de vie des étoiles, et leurs propriétés dépendent de la masse et de la composition de leur progéniteur. Les étoiles maintiennent leur stabilité grâce à un équilibre entre la pression due à la fusion nucléaire (vers l'extérieur) et les forces gravitationnelles (vers l'intérieur). Au cours de leur vie, cet équilibre se modifie et, une fois à son terme, peut transformer l'astre en objet compact.

Les Trous Noirs, avec leur immense attraction gravitationnelle et leur horizon des événements qui piège même la lumière, représentent l'issue la plus extrême de l'évolution stellaire, et les limites de la physique connue. Cette thèse vise à rajouter une brique à la pyramide en perpétuelle extension de notre compréhension de la formation, la croissance et le comportement de ces objets fascinants. Cela implique une description détaillée des processus d'accrétion, des effets relativistes et de l'interaction des champs magnétiques et du moment angulaire dans les systèmes dits "à disque".

Cette partie s'adresse à quiconque a été assez sage pour ne pas faire une thèse en astrophysique des objets compacts, mais assez sot pour s'intéresser réellement à mon travail. La section ci-dessous introduit les notions et les enjeux permettant de comprendre les aperçus de mes travaux, qui seront présentés par la suite.

Formation et caractéristiques des objets compacts

Les objets compacts sont classés en fonction de leur paramètre de compacité, qui mesure l'intensité de leur champ gravitationnel. Ce paramètre s'étend sur une gamme assez large: Les **Naines Blanches** restent aux environs de 10^{-4}, les **Etoiles à Neutrons** entre 0.2 et 0.4, et les **Trous Noirs** à 1.

Les **Naines Blanches** se forment à partir d'étoiles de masse faible à intermédiaire (inférieure à environ 8-10 masses solaires), où la fusion s'arrête aux éléments situés entre l'hélium et le carbone/oxygène. Ces cadavres stellaires sont maintenus stables par la pression de dégénérescence des électrons, et mesurent près d'un pour cent de la taille de leur progéniteur. Les **Etoiles à Neutrons**, quant à elles, résultent de l'effondrement d'étoiles plus massives (environ 10 à 20 masses solaires), pour lesquelles seule la force nucléaire forte et la pression de dégénérescence des neutrons ont pu s'opposer à l'effondrement gravitationnel.

Enfin, lorsque la masse initiale de l'étoile dépasse environ 20 masses solaires, l'effondrement gravitationnel conduit le plus souvent à la formation d'un **Trou Noir**, un objet dépourvu de surface physique, dont l'intérieur est isolé du reste de l'univers par un horizon des événements. La formation des Trous Noirs est influencée par de nombreux paramètres, tels que le moment angulaire, la métallicité et les interactions dans les systèmes binaires, qui peuvent rendre leur création bien plus complexe.

Pour plus de détails, voir les Sections 1.1.1 et 1.1.2.

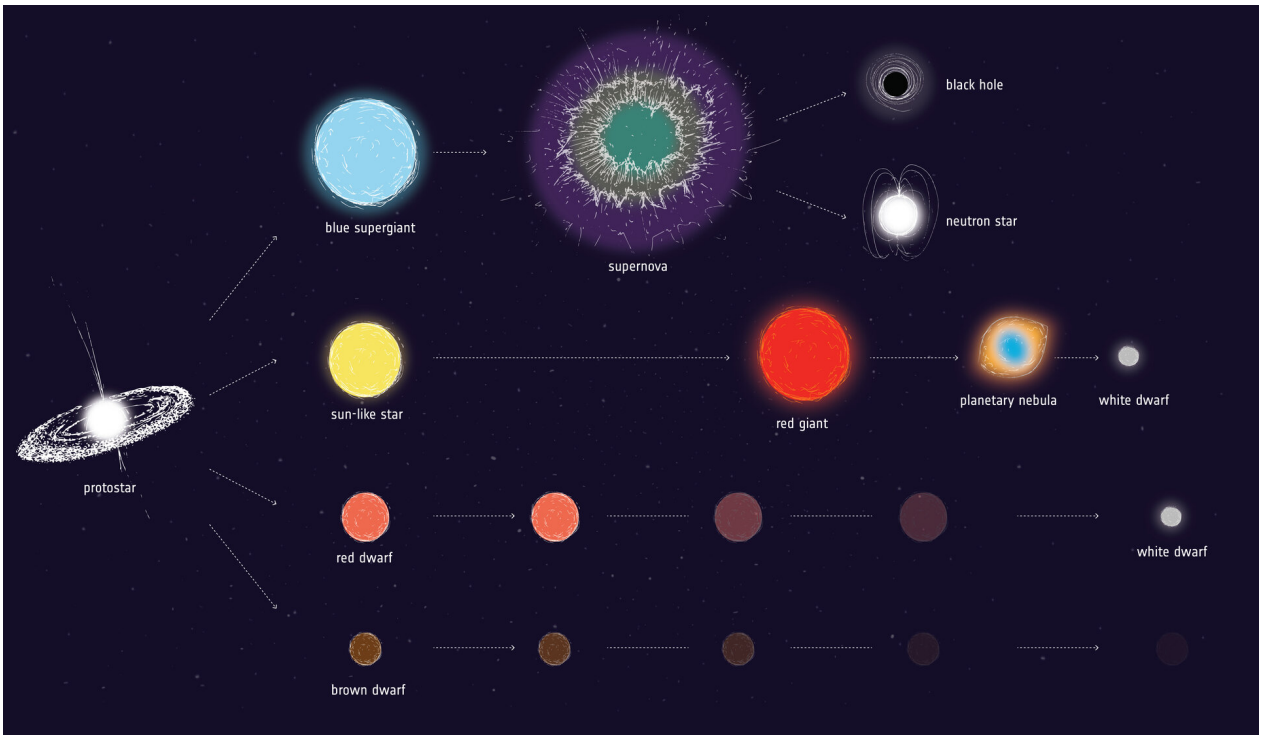

Figure 25: Vue synthétique des scénarios d'évolution stellaire. Le cas spécifique de l'évolution des naines brunes, des étoiles de très faible masse, n'est pas pertinent pour l'étude des objets compacts.
Source : https://www.esa.int/ESA_Multimedia/Images/2018/03/Stellar_evolution

Processus d'accrétion et formation des disques

L'**accrétion** est l'un des processus fondamentaux régissant la croissance et l'évolution des objets compacts : l'accumulation graduelle de matière sur un corps astrophysique dû à l'attraction gravitationnelle. Dans la plupart des systèmes astrophysiques, l'accrétion implique la présence de matière dotée d'un moment angulaire, ce qui conduit à la formation d'une structure en forme de **disque** autour de l'objet central. La dynamique de ces disques d'accrétion dépend de l'interaction des forces gravitationnelles, du transfert de moment angulaire et des processus dissipatifs qui convertissent l'énergie potentielle en chaleur et en rayonnement.

Dans les systèmes stellaires binaires, l'accrétion peut se produire par deux mécanismes principaux : la capture des vents stellaires ou le débordement des lobes de Roche. Dans ce second cas, l'interaction gravitationnelle influence des objets orbitant un système à deux corps. Cela forme un paysage complexe, caractérisé notamment par les **lobes de Roche**, qui délimitent pour chaque étoile la région aux alentours où son influence gravitationnelle est prépondérante. La taille de ces lobes est principalement déterminée par le rapport de masse des étoiles et la distance qui les sépare. Lorsqu'un corps matériel, tel qu'une particule d'une étoile en expansion, dépasse le point de contact (L1) entre les deux lobes de Roche, elle passe dans une région dominée par l'attraction gravitationnelle de l'autre objet. La particule se retrouve alors en orbite autour de ce dernier, se déplaçant à une vitesse dictée par les lois de Kepler.

En pratique, dans un scénario plus réaliste, c'est un flux continu de gaz qui traverse le point L1, et forme tout d'abord une structure en anneau. Cette configuration s'étend ensuite en un disque d'accrétion, au fur et à mesure qu'un transfert de moment angulaire se produit, en raison de processus dissipatifs (comme la friction) au sein de la matière accrétée. La matière dans le disque dérive progressivement vers l'intérieur jusqu'à la surface de l'objet central, ce qui donne une structure dynamique qui maintient un transfert de masse continu vers l'accréteur, et joue un rôle central dans l'évolution des deux étoiles du système binaire.

L'accrétion sur des objets compacts, et notamment les Etoiles à Neutrons et les Trous Noirs, est reconnue comme l'un des processus de conversion d'énergie les plus efficaces dans l'univers. Cette efficacité est quantifiée par le **paramètre d'efficacité** de l'accrétion η, qui varie en fonction de la nature de l'objet compact, de 0.15 pour les Etoiles à Neutrons à 0.4 pour les Trous Noirs en rotation rapide. En guise de comparaison, même l'efficacité de la *fusion* nucléaire est inférieure à $\eta = 1\%$.

Pour plus de détails, voir les Sections 1.1.3 et 1.2.1.

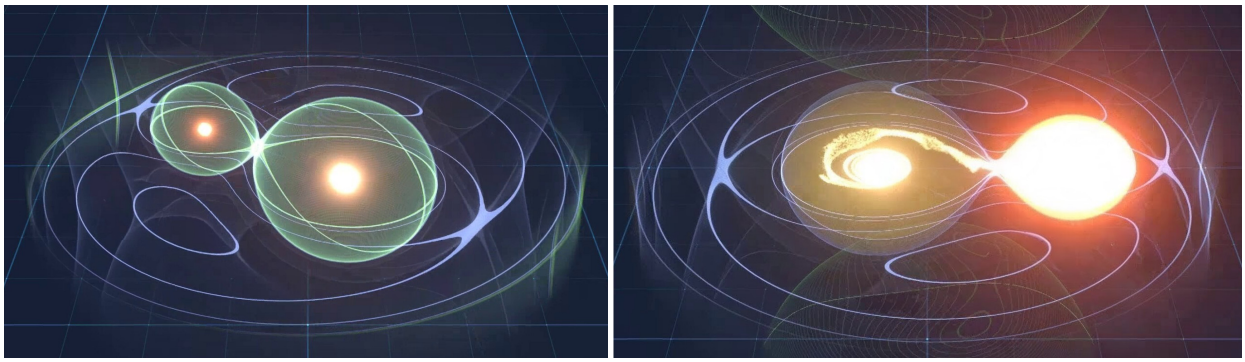

Figure 26: **(Gauche)** Équipotentielles gravitationnelles (bleu) et lobes de Roche (vert) dans un système stellaire binaire. **(Droite)** Système binaire avancé avec un débordement des lobes de Roche d'une étoile vers l'autre.
Source : https://www.artstation.com/artwork/v26KeO

Evolution et classification des systèmes binaires

L'évolution des systèmes binaires compacts est un processus complexe influencé par des facteurs tels que la masse et la nature de leurs composants. Si le cœur de l'étoile la plus avancée d'un tel système n'est pas assez massif, elle peut devenir une Naine Blanche, ce qui conduit souvent à la formation de **Variables Cataclysmiques** (CV). Ces dernières se caractérisent par le transfert de matière d'une étoile compagnon vers la Naine Blanche, ce qui entraîne diverses émissions de rayons X. Ces systèmes sont le type le plus courant de **Binaires X**, avec des milliers d'objets recensés dans un rayon de quelques centaines de parsecs (notre voisinage galactique). Les CV comprennent des sous-types tels que les Novae Naines, qui se caractérisent par des éruptions fréquentes dans leur disque, et les Novae classiques, connues pour des éruptions rares et bien plus brillantes, dues à la fusion nucléaire à la surface de la Naine Blanche.

Si le noyau de l'étoile avancée de la binaire est plus massif, il peut s'effondrer en Etoile à Neutrons (NS) ou en Trou Noir (BH) après une supernova, ce qui risque de perturber le système. Les Binaires X impliquant des objets compacts sont donc principalement situées dans le plan galactique, mais peuvent également se trouver à des latitudes plus élevées en raison d'éjections d'objets compacts après une supernova.

Les **Binaires X de Faible Masse** (LMXB) se forment lorsqu'une NS ou un BH accrète de la matière à partir d'une étoile de faible masse, via un débordement de lobe de Roche. Bien que plus lumineux que les CV, les LMXB sont moins fréquents, quelques centaines ayant été détectés dans la Voie lactée. Ces systèmes présentent souvent un comportement transitoire, avec de longues phases de repos (quiescence) ponctuées d'éruptions occasionnelles. Distinguer les accréteurs NS des accréteurs BH dans les LMXBs est un défi en raison des propriétés similaires de leur disque d'accrétion. La meilleure méthode pour les différencier reste l'estimation de masse, les NS étant limitées à environ 2.5 masses solaires ($M_\odot$) et les BH dépassant théoriquement ce seuil. En parallèle, de nombreux phénomènes restent spécifiques aux NS, notamment des sursauts de rayons X thermonucléaires, les pulsations magnétiques induites par l'accrétion, et l'émission thermique en provenance de leur surface.

Les **Binaires X de Forte Masse** (HMXB) diffèrent des LMXB par la présence d'étoiles compagnes massives, et un transfert de masse par l'intermédiaire de vents stellaires puissants. Ces systèmes sont persistants ou présentent des éruptions plus fréquentes. On compte plusieurs sous catégories comme les Be-HMXB, comprenant des étoiles de type Be, les HMXB avec supergéantes, et les HMXB Wolf-Rayet, où le compagnon évolue en une étoile à noyau d'hélium avec d'énormes vents et ne va pas tarder à s'effondrer en un objet compact.

Pour plus de détails voir les Sections 1.2.2 et 1.2.1.
Figure pertinente (pleine page): Fig. 1.3

Déclencher une éruption dans une Binaire X

Dans les Binaires X avec disque d'accrétion, le **modèle d'instabilité de disque** appelé DIM explique le cycle récurrent d'**éruptions** et de **quiescence** avec une **instabilité thermique** dans le disque. Cette instabilité résulte de l'équilibre entre le refroidissement radiatif (dépendant de la température) et le chauffage visqueux (dépendant de la densité de surface Σ et du paramètre de viscosité α). À des températures spécifiques (∼5000-6900 K), l'hydrogène s'ionise, et le taux de refroidissement devient négativement corrélé à la température. Cela rend le disque instable et conduit à un brusque saut de température vers un état plus chaud, initiant une éruption.

Lors d'une éruption, le disque entier devient ionisé, la viscosité augmente, et la matière est rapidement accrétée jusqu'à ce que le disque se refroidisse et retourne à son état quiescent. La dynamique de l'éruption dépend du rapport entre α dans les états "chaud" et "froid". La propagation de l'instabilité à travers le disque conduit à des fronts d'onde de chauffage et de refroidissement caractéristiques, qui dictent le comportement du disque au cours de la transition.

Le DIM décrit bien l'évolution des **Variables Cataclysmiques** et des **Binaires X de Faible Masse** observées, en particulier pour **distinguer les systèmes transitoires**. Cependant, l'irradiation des régions du disque interne joue un rôle très important dans les LMXBs, ce qui nécessite des ajustements du modèle. De plus, malgré ses succès, le DIM a des limites. Il repose sur de nombreuses hypothèses simplificatrices et ne fournit pas d'explication sur l'origine physique du transport du moment angulaire (la nature physique de la viscosité α). Ce rôle pourrait être joué par l'instabilité magnéto-rotationnelle (MRI), mais encore aujourd'hui, les simulations ne parviennent pas à reproduire l'évolution observée. La prise en compte des **éjections de matière** -qui transportent du moment angulaire- est prometteuse pour combler cette lacune, mais elles modifient fondamentalement la structure du disque, ce qui nécessite de nouveaux modèles.

En outre, le DIM ne peut à lui seul décrire l'évolution spectrale observée lors des éruptdans les LMXBs, en particulier les transitions entre les états spectraux, associés soit à des jets relativistes soit à l'émission thermique du disque (voir plus loin). Les modèles futurs doivent rendre compte de la complexité du champ magnétique et des éjections de matière en provenance du disque pour arriver à reproduire davantage d'éléments des vraies éruptions.

Pour plus de détails, voir Section 1.2.3.

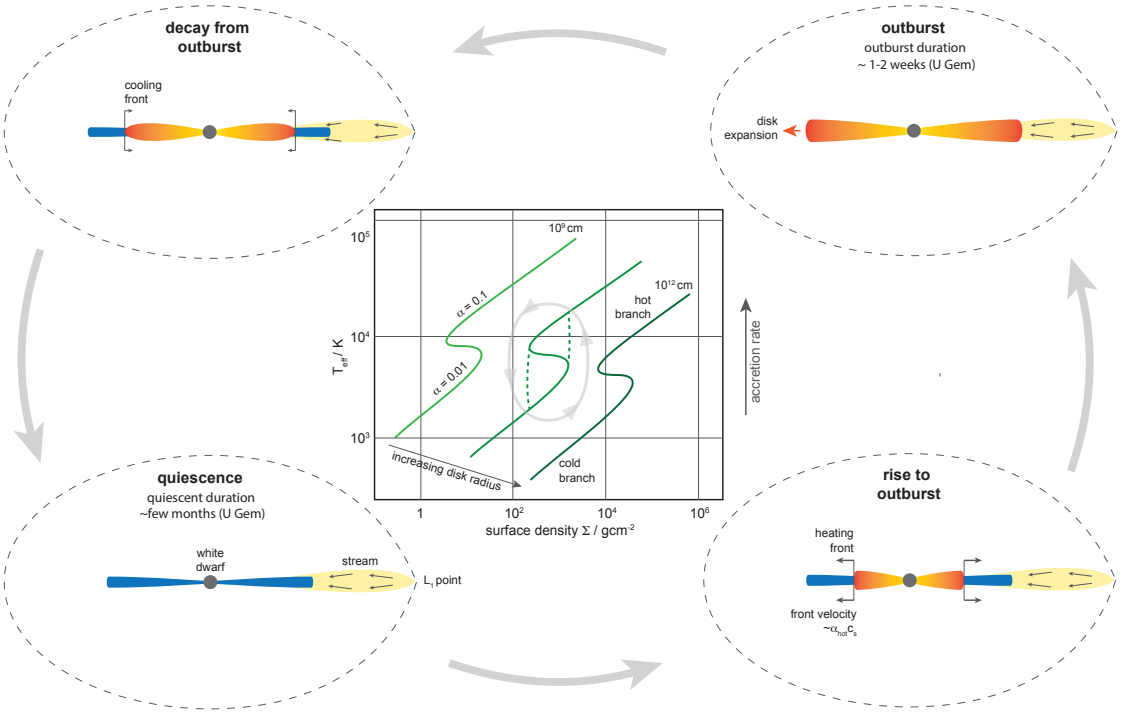

Figure 27: Evolution de la structure d'un disque d'accrétion au cours d'un cycle de DIM.
Source : Armitage (2022).

Propriétés spectrales des Binaires X de Faible Masse à Trou Noirs

Concentrons nous maintenant sur la catégorie des Binaires X de Faible Masse à Trou Noir (BHLMXB), qui sont le sujet de ce manuscrit. Même si ces objets émettent dans une large gamme de longueurs d'ondes, leur émission culmine en rayons X, et cette bande d'énergie est essentielle pour comprendre leur comportement. Les rayons X sont sujets à une forte évolution spectrale et temporelle, due à la variété des mécanismes physiques contribuant à l'émission dans cette bande. Les rayons X mous (0.1-10 keV[3]) sont particulièrement importants car ils sont ceux présentant la plus grande diversité spectrale, et la plupart des études sur les éruptions de Trous Noirs se concentrent sur cette bande.

Au cours d'une éruption, la luminosité X de la source augmente considérablement, souvent de plus de 5 ordres de grandeur, et s'accompagne de changements d'état spectraux et de variabilité à court terme. Ces transitions sont représentées dans un Diagramme Dureté-Intensité (HID), qui trace l'intensité (ou la luminosité) des rayons X en fonction d'un rapport de flux appelé "dureté" entre deux bandes d'énergie. L'évolution du Diagramme Dureté-Intensité suit généralement une forme distincte en "Q", reflétant les transitions entre les états durs et mous, dominés par des rayons X de haute (dur) ou basse (mou) énergie.

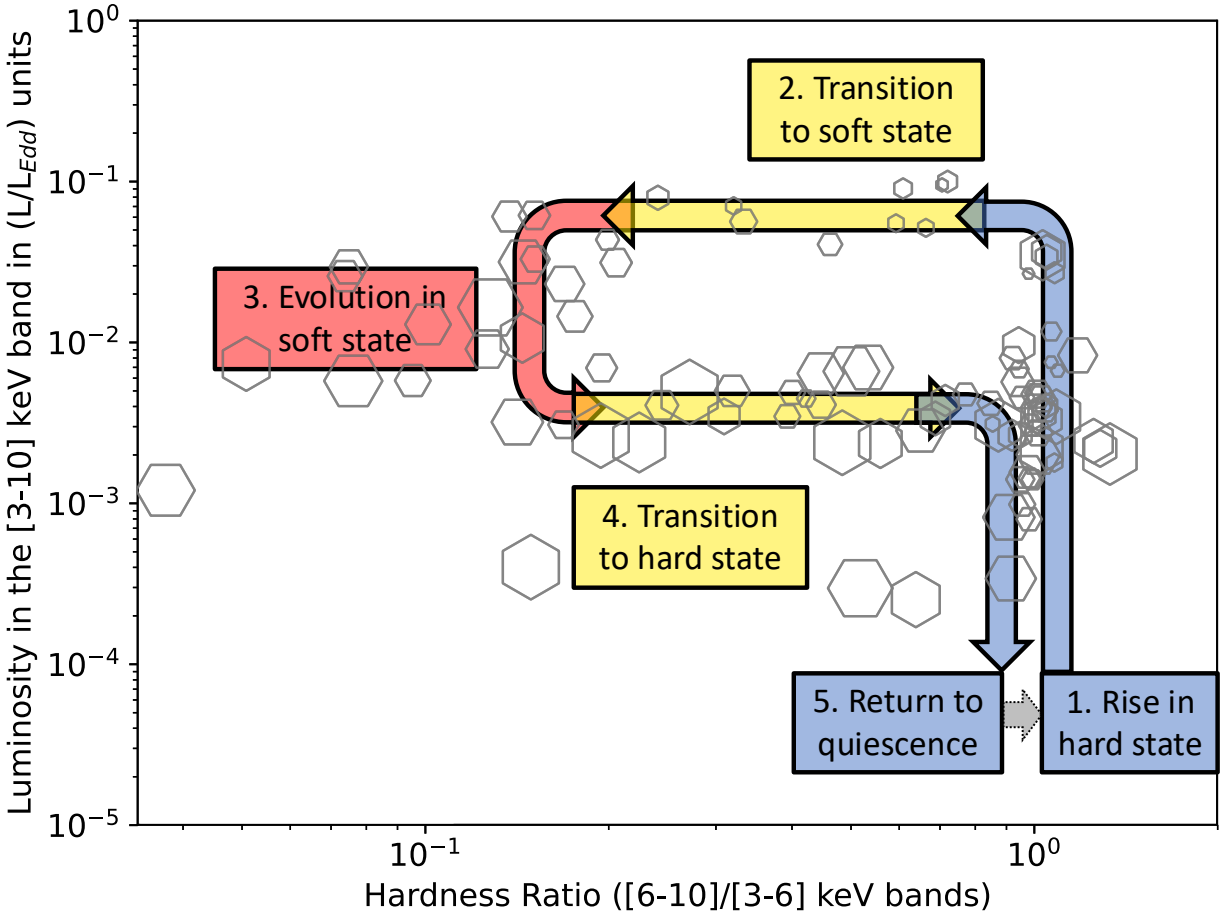

Figure 28: Evolution typique d'une éruption d'une Binaire X de Faible Masse à Trou Noir représentée dans un Diagramme Dureté-Luminosité. Normaliser la luminosité (axe des y) à la limite d'Eddington permet de supprimer la dépendance de cette dernière envers la masse du Trou Noir.

[3] en astrophysique, on caractérise souvent la lumière en unités d'énergie par photon, via $E = hc/\lambda$ où h est la constante de Planck et c la vitesse de la lumière. 0.1-10 keV correspond à une gamme de longueur d'onde λ de 0.12 à 12 nm.

Dans l'état dur, le spectre (ou SED) X est dominé par des processus de Comptonisation provenant d'un plasma chaud et optiquement mince près du BH. La réflexion de cette émission sur le disque d'accrétion ajoute notamment des raies de fluorescence du fer, et une signature de jet est observée en radio. Lorsque la luminosité augmente au-delà de ~10% de la limite d'Eddington (L_{Edd}, la luminosité maximale qui peut être émise avec de l'accrétion standard), une transition vers l'état mou se produit, et le spectre devient dominé par l'émission thermique d'un disque optiquement épais et géométriquement mince. Les jets sont supprimés pendant cette phase, et une composante supplémentaire apparaît aux hautes énergies. Au fur et à mesure que le système évolue dans l'état mou, la luminosité diminue, durant des semaines ou des mois, et la source finit par revenir à l'état dur lorsqu'elle atteint ~ 1 à 2% L_{Edd}, avant de retourner à l'état de quiescence et des émissions X négligeables.

Toutes les éruptions ne suivent pas ce schéma standard. Les 40% d'éruptions "ratées" ou "dures" atteignent ou s'approchent de la luminosité de transition mais ne parviennent pas à atteindre l'état mou, retournant directement à la quiescence. En revanche, certaines éruptions présentent des états mous très longs, ou des états très brillants (VHS) avec des spectres de rayons X distincts. Dans de rares cas, les systèmes dépassent la limite d'Eddington et entrent dans des états "ultra-lumineux", qui impliquent des configurations d'accrétion et des propriétés spectrales distinctes. Inversement, les éruptions obscurcies présentent des spectres opaques, souvent liés à des émissions massives de matière qui cachent l'émission centrale.

For plus de détails, voir Sec. 1.3.

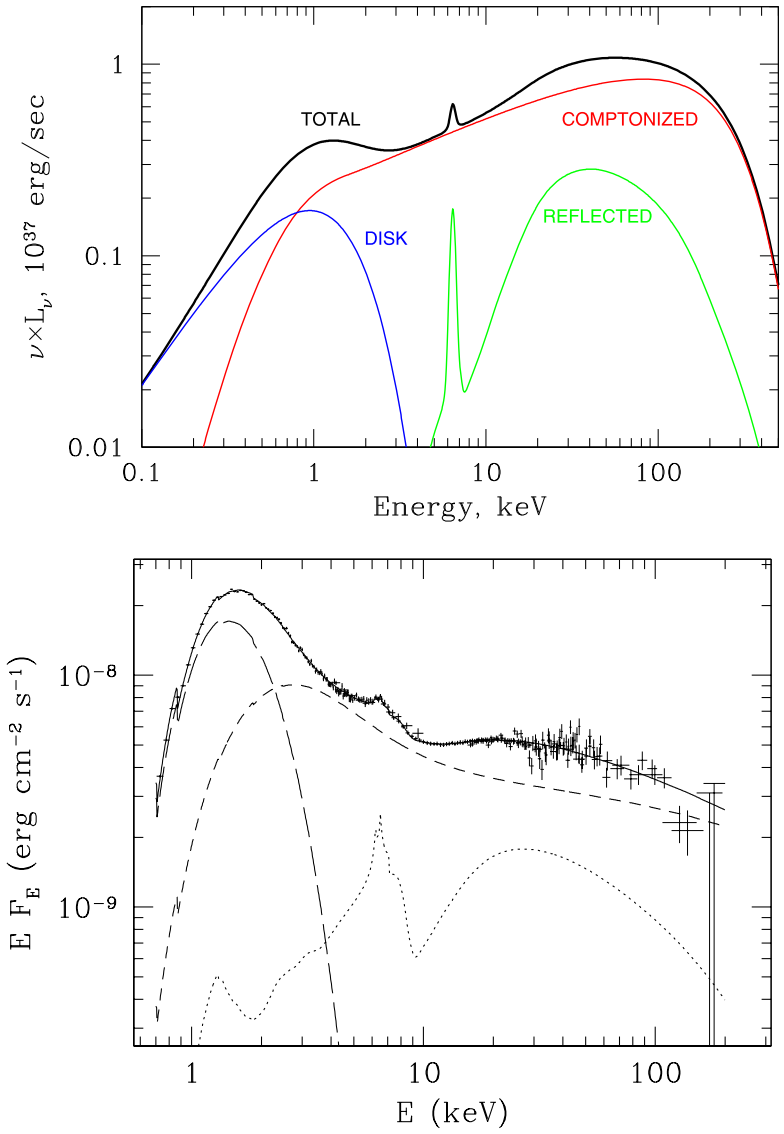

Figure 29: Spectres X typiques d'un état dur **(gauche)** et mou **(droite)** d'une BHLMXB. Sources: Gierliński et al. (1999); Gilfanov & Merloni (2014).

Vents

Signatures en rayons X

Le domaine de la **spectroscopie en rayons X** a considérablement fait progresser la compréhension d'un type d'éjection de matière appelée **vents** dans les Binaires X de Faible Masse à Trou Noir. La définition de ces vents reste cependant incomplète, et se précise au fur et à mesure que les instruments et les observations s'améliorent.

À la fin du XXe siècle, la compréhension des phénomènes stellaires a déjà considérablement progressé, grâce à la spectroscopie à haute résolution en optique et ultraviolet, qui permet d'étudier des composantes spectrales précises. Parmi elles, les raies d'absorption et d'émission, liées à la présence de matière dans la ligne de vue, permettent de sonder la densité, l'ionisation et la composition chimique des éjections de matière. En revanche, des contraintes technologiques limitent les astronomes X à des résolutions spectrales beaucoup plus faibles, ce qui a retardé leur capacité à identifier des processus similaires dans cette gamme d'énergie.

L'arrivée du satellite japonais ASCA en 1994 a marqué un tournant pour l'astronomie X. Équipé d'un spectromètre à haute résolution, ASCA a détecté pour la première fois des raies d'absorption en rayons X, traceurs d'éléments hautement ionisés tels que le fer. Puis, au début des années 2000, l'observatoire à rayons X *Chandra* montre que ces raies d'absorption sont décalées vers le bleu, ce qui signifie que la matière se déplace à des millions de kilomètres par heure dans notre direction. On est donc en présence d'un nouveau type d'éjection dans les Binaires X, qui prendra le nom d'éjections similairement "lentes" et massives déjà identifiées autour des étoiles et des disques protoplanétaires, les vents. Ces derniers, bien qu'encore mal compris, deviennent rapidement une composante importante du paradigme de l'accrétion-éjection des Binaires X.

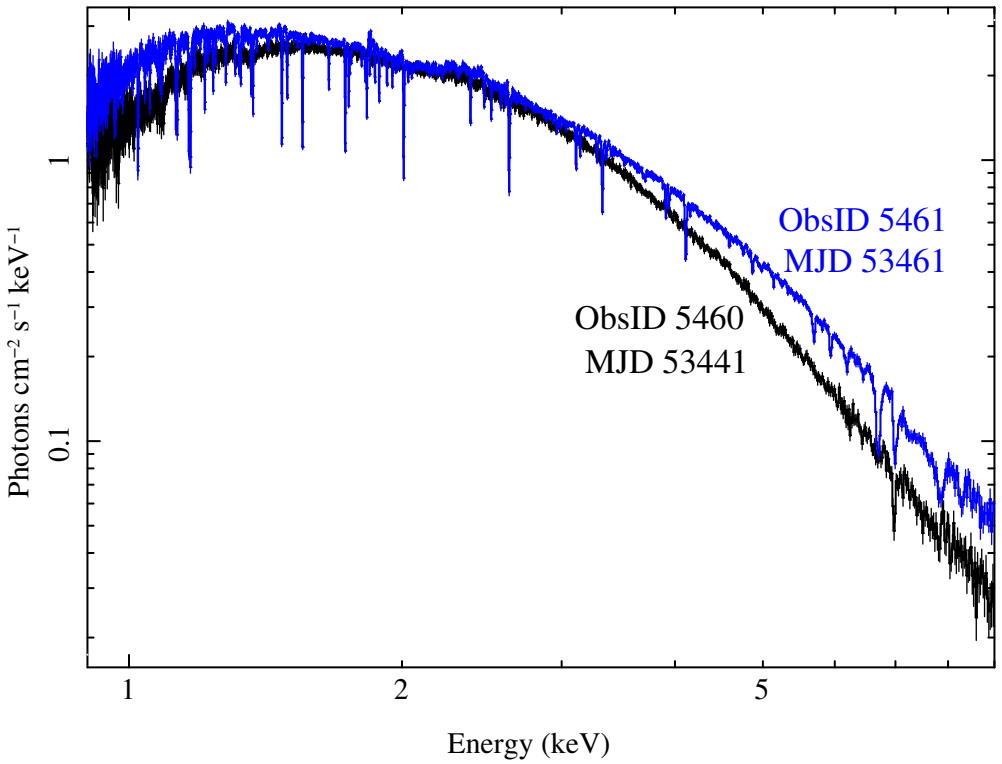

Figure 30: Exemples de spectres issus d'observations de BHLMXBs contenant des raies d'absorptions décalées vers le bleu. Les deux observations en bleu et noir sont seulement prises à 20 jours d'intervalle, mais leurs raies sont complètement différentes, montrant à quelle rapidité ce phénomène évolue dans une seule source. Source : Miller et al. (2008)

Au cours de la décennie suivante, davantage d'observations permettent de relier ces phénomènes à des états d'accrétion spécifiques, et des études montrent que les vents apparaissent principalement dans les états spectraux mous des sources à forte inclinaison (proches de l'axe du disque). Cela étaye fortement la thèse d'éjections équatoriales, en provenance du disque.

Néanmoins, malgré des progrès substantiels, de nombreux aspects des vents en rayons X restent non résolus. Par exemple, l'interaction entre les vents et les jets -l'autre type d'éjection, bien plus rapide mais moins massif, souvent observé dans les états spectraux durs- s'avère bien plus complexe que prévu. En parallèle, des détections récentes dans des états durs remettent en question les hypothèses initiales d'une dichotomie stricte. En outre, des limitations techniques empêchent de distinguer des structures dans les raies, ce qui permet difficilement de contraindre les modèles physiques de vents. Enfin, les observables actuelles s'appuient souvent sur des gammes d'ionisation relativement étroites, ce qui limite leur capacité à rendre compte de la dynamique des émissions de vents.

Pour plus de détails, voir Section 2.1.1.

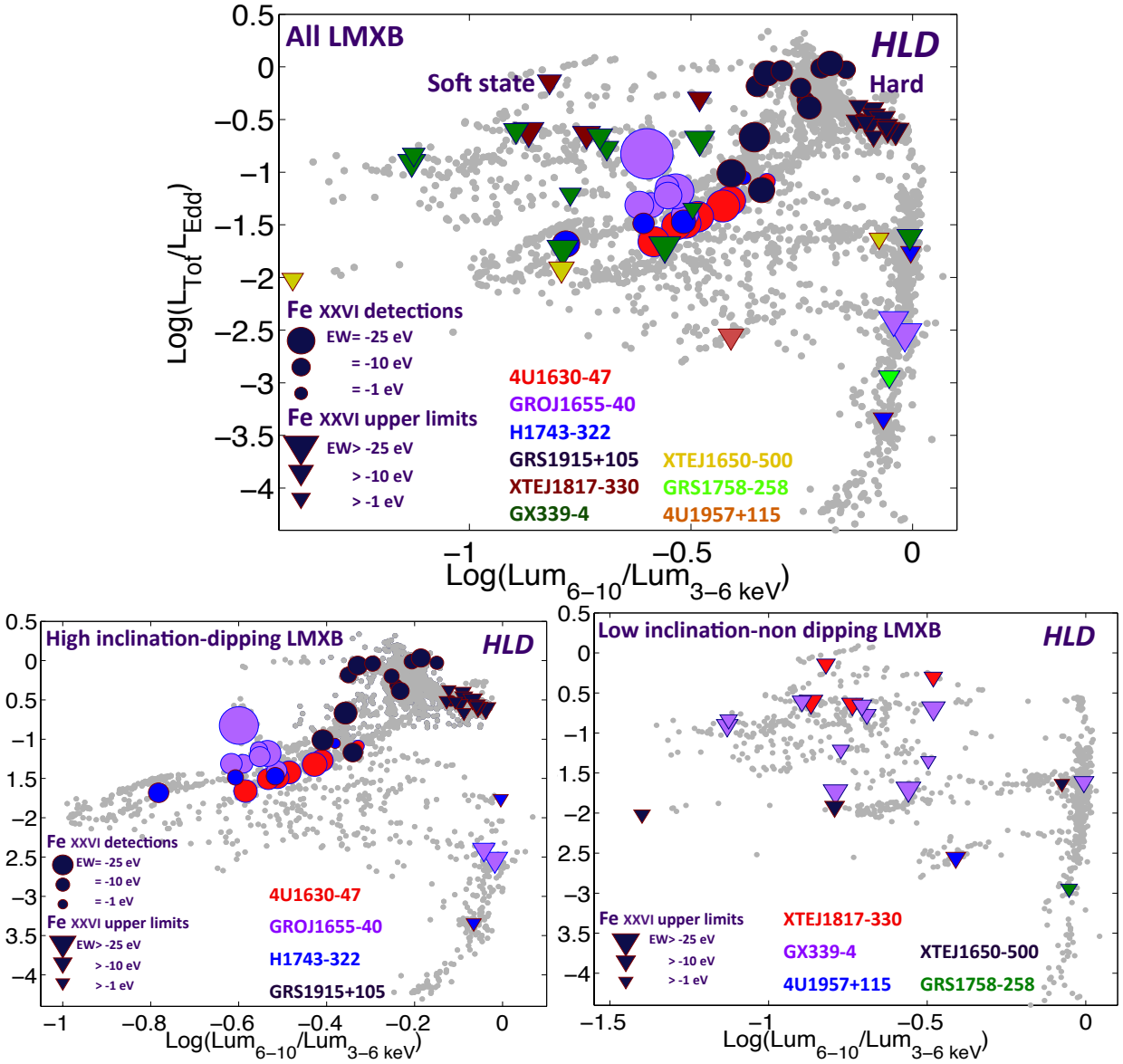

Figure 31: **(Gauche)**. Diagramme Dureté-Luminosité montrant les détections de vents et les contraintes dans un échantillon de BHLMXBs. Les points gris signalent les observations de basse qualité. A une exception notable près, toutes les détections proviennent d'observations dans l'état mou. **(Droite)** HLDs du même échantillon, mais restreint aux sources à forte et faible inclinaison respectivement. Seules les sources à forte inclinaison présentent les raies d'absorption caractéristiques des vents. Source : Ponti et al. (2012)

Contreparties en Optique-Infrarouge et vents froids

Au cours de la dernière décennie, de nouvelles études ont identifié des **signatures de vents optiques et infrarouges** (OIR) dans les Binaires X, mettant en évidence divers profils d'absorption et d'émission décalés vers le bleu, dont certaines propriétés tranchent avec ceux vus en rayons X. En effet, les raies d'absorption dans l'optique (longueurs d'onde visibles) caractéristiques de vents optiques apparaissent uniquement dans les **états durs** des BHLMXBs. Les signatures infrarouges sont également liées à l'état dur, bien que certaines persistent pendant toute la durée de l'éruption. Cette dichotomie suggère un passage de "vents chauds", vus à haute énergie dans l'état mou, à des "vents froids" à basse énergie dans l'état dur. Cependant, il n'est pas certain que ces vents aient la même origine physique ou géographique, au vu de l'absence de détections simultanées dans les états d'accrétion standard.

La géométrie de ces vents est débattue, et certains résultats suggèrent une distribution moins équatoriale pour les vents froids. Cela pourrait expliquer l'absence de détection de vents en rayons X dans certaines BHLMXBs qui présentent des signatures optiques et infrarouges, bien que l'échantillon de sources avec des détections dans l'une ou l'autre bande soit pour l'instant très limité. En parallèle, alors que les signatures de vent dans l'ultraviolet sont très communes dans les Trous Noirs SuperMassifs actifs, aucune détection de ce type n'a été confirmée dans les BHLMXBs. Néanmoins, des découvertes récentes dans des LMXBs à Etoiles à Neutrons -et à haute inclinaison- ont montré de faibles signatures de vent, suscitant l'espoir de futures découvertes dans des sources hors du plan galactique dont l'émission dans l'ultraviolet n'est pas absorbée par le milieu interstellaire.

Pour plus de détails, voir Section 2.1.2.

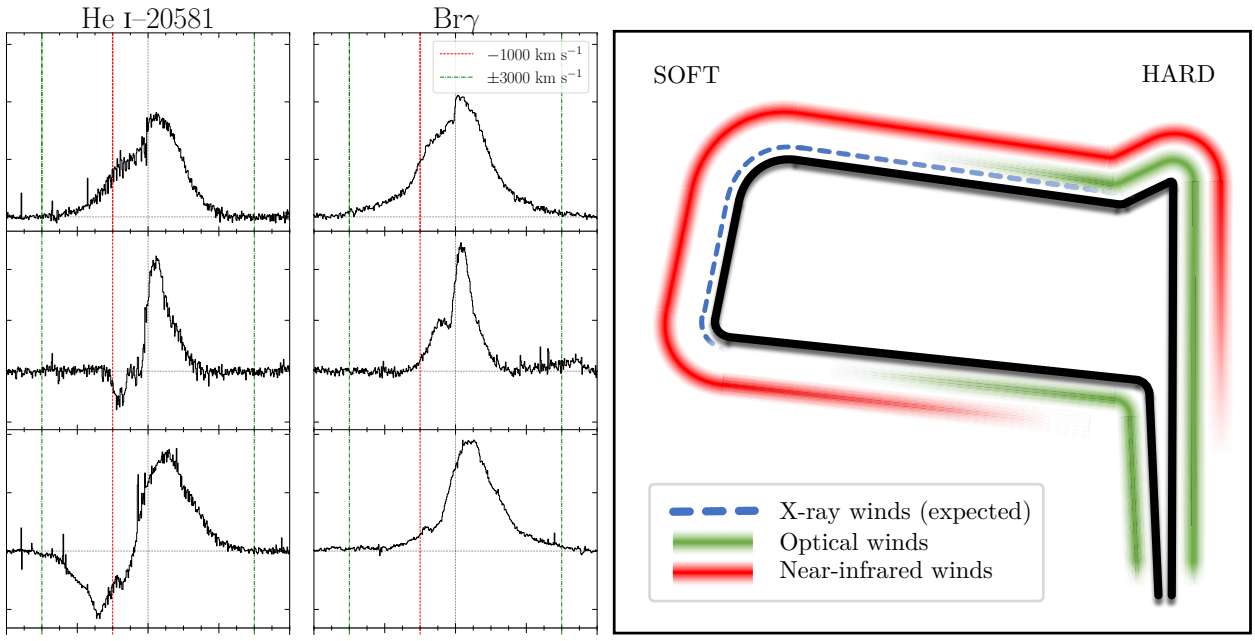

Figure 32: **(Gauche)** Exemple de profil P-Cygni (émission + absorption) décalé vers le bleu, en infrarouge. Source : Sanchez-Sierras et al. (2023b). **(Droite)** Répartition des détections de vents au cours d'une éruption de BHLMXB représentée dans un Diagramme Dureté-Luminosité. Source : Sanchez-Sierras & Munoz-Darias (2020).

Mécanismes de lancement

Plusieurs phénomènes physiques sont susceptibles de créer des vents dans les disques d'accrétion des Trous Noirs. Dans les Binaires X, les **vents thermiques** proviennent du **chauffage induit par l'irradiation du disque d'accrétion** externe par les rayons X provenant des régions internes. Ce chauffage crée une couche ionisée, où l'agitation thermique ($\sim$ 1000 km/s) peut dépasser la vitesse d'échappement, permettant ainsi des éjections à faible vitesse. Le rayon Compton R_{IC} définit le seuil où la matière passe de l'état lié à l'état non lié : la matière plus proche du BH reste liée, tandis que les régions au-delà peuvent supporter des vents facilement si la luminosité dépasse un seuil critique (L_{crit}). À des luminosités très élevées, le vent peut avoir une double origine thermique et radiative, de par l'influence non négligeable de la pression de radiation, qui augmente la vitesse de l'éjection et le taux de perte de masse.

Bien qu'ils soient limitées à de grands rayons et à des vitesses de quelques centaines de km/s, **les vents thermiques peuvent expliquer la grande majorité des détections actuelles** de vents en rayons X dans les BHLMXB. Les modèles actuels prédisent des **profils de raies symétriques**, qui ne pourront être confirmés ou infirmés qu'en comparant à des données à haute résolution. Néanmoins, certaines **observations de vents** soit **très rapides** soit à **faible luminosité** restent **incompatibles** et nécessitent une étude plus approfondie.

L'état spectral et la géométrie du système ont tous deux un impact important sur la dynamique de ce type de vent : les états durs réduisent le rayon de lancement du vent et les seuils de luminosité, élargissant ainsi l'espace des paramètres disponible. Néanmoins, dans cet état, une trop grande opacité de l'atmosphère du disque interne peut stopper toute éjection. En parallèle, les **instabilités thermiques** (voir plus loin) au sein du disque peuvent influencer le lancement des vents de manière plus complexe.

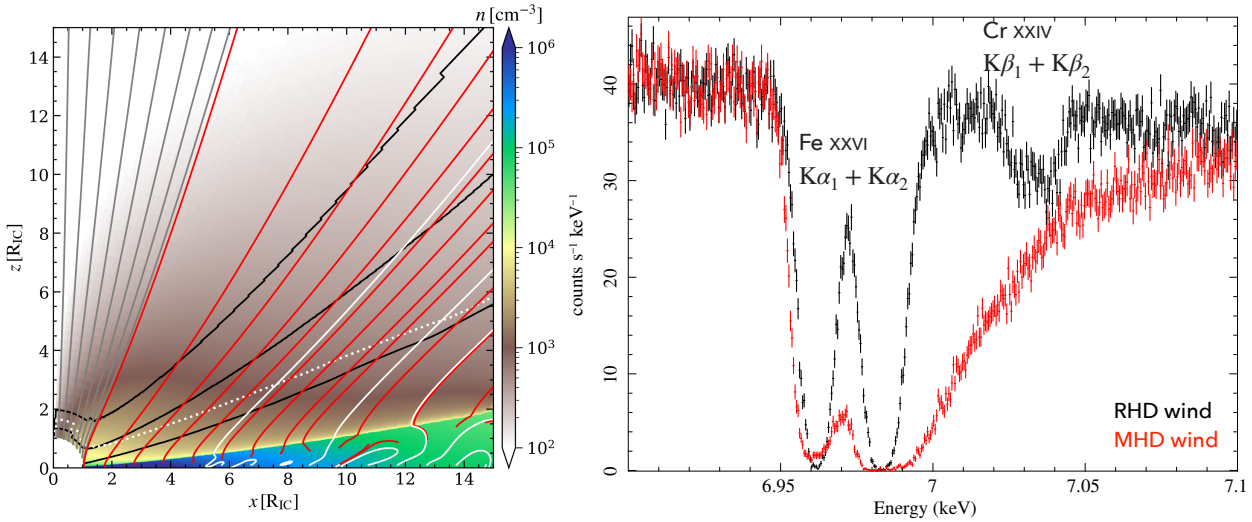

Figure 33: **(Gauche)** Vue en coupe d'une émission de vents thermiques, avec structure de densités et lignes d'écoulement. Source: Waters et al. (2021). **(Droite)** Comparaison des profils attendus de vents thermiques (RHD, noir) et magnétiques (MHD, rouge). Source: Tomaru et al. (2023)

Les **éjections magnétiques**, elles, ont été théorisées pour la première fois sous la forme de jets relativistes provenant de disques magnétisés, puis se sont étendues à des configurations plus diverses. Une **première gamme** de modèles se concentre **uniquement** sur les **éjections**, traitant le disque comme une condition limite. Des améliorations récentes de ce paradigme ont été **comparées avec succès** aux signatures de vents en rayons X observées **à la fois dans les BHLMXBs et les Trous Noirs SuperMassifs**, grâce à un espace de paramètres très étendu.

La **seconde approche** considère l'ensemble du **système d'accrétion et d'éjection**, ce qui permet d'obtenir des solutions plus cohérentes physiquement, au prix d'un espace de paramètres beaucoup plus restreint. Le modèle semi-analytique **Jet Emitting Disk (JED)**, développé à l'IPAG, intègre plusieurs paramètres de turbulence, et permet depuis longtemps de modéliser un **flux d'accrétion supersonique** couplé à des **éjections de jets**. En parallèle, une extension récente des solutions à une magnétisation plus faible, appelée **Wind Emitting Disk (WED)**, a permis d'obtenir des taux de **perte de masse** beaucoup **plus élevés** dans des disques plus conventionnels. La proportion de perte de masse **p** et la magnétisation μ, qui sont les principaux paramètres libres du modèle, influencent la transition entre les éjections de type jets (rapides et légers) et celles de type vents (denses et lents), donnant ainsi accès à des structures complémentaires.

Comme les vents magnétiques sont lancés à des vitesses différentes suivant leur point d'origine dans le disque, ils produisent des signatures en absorption spécifiques dans les rayons X, avec des **queues** caractéristiques **décalées vers le bleu**. Ces dernières sont aisément distinguables des vents thermiques dans les cas les plus extrêmes, mais peuvent se chevaucher dans les cas les plus faibles, et seules les données à haute résolution des télescopes nouvelle génération tels que XRISM et Athena, seront en mesure de les distinguer.

Pour plus de détails, voir Section 2.2.

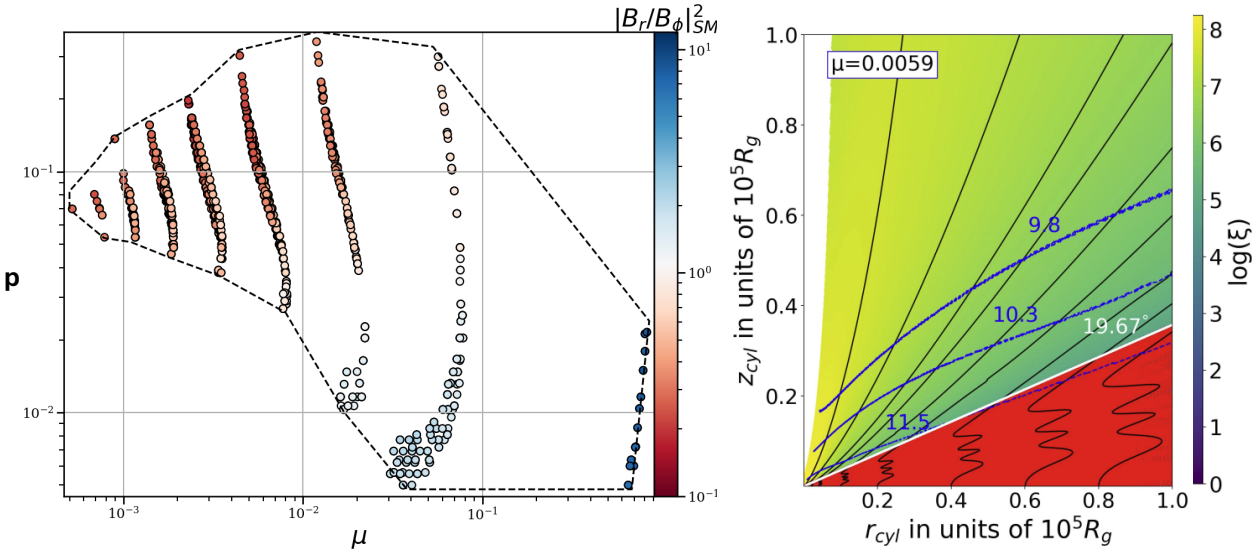

Figure 34: **(Gauche)** Espace des paramètres des solutions JED-WED, avec une échelle de couleur montrant le niveau de courbure des lignes de champ magnétique. Source : Jacquemin-Ide et al. (2019). **(Droite)** Contours de densité (bleu) et lignes de champ magnétique (noir) d'une solution de WED. Source: Datta et al. (2024).

Raies d'absorption et processus atomiques

La quantification des **niveaux d'énergie atomiques** explique l'origine des **raies d'émission et d'absorption** dans les spectres. Les atomes dans des états de basse énergie absorbent du rayonnement à des fréquences spécifiques, produisant des raies d'absorption, tandis que les atomes énergisés émettent un rayonnement lorsqu'ils retournent à des états plus faibles, formant des raies d'émission. Les caractéristiques de ces raies dépendent fortement des **niveaux d'ionisation** et de la **densité de colonne (NH, la densité intégrée le long de la ligne de visée)** du matériau. Les niveaux d'ionisation déterminent la force des transitions atomiques, tandis que la densité de colonne affecte à la fois la quantité d'ions et le trajet du rayonnement.

Les profils des raies sont influencés par **l'élargissement Doppler** et la **turbulence**, qui déterminent la **largeur équivalente (EW)**, quantité qui mesure la "profondeur" d'absorption des raies. Le profil des raies évolue de gaussien (faibles densités) à lorentzien à des densités élevées, en passant par des régimes de saturation. La turbulence est nécessaire pour expliquer les fortes valeurs d'EW observées, car l'élargissement thermique à lui seul est insuffisant. Les mesures d'EW dépendent de la densité ionique de colonne, de la fraction d'ionisation et de l'abondance des éléments. Le paramètre d'ionisation (ξ), qui représente le rapport flux/densité, aide à évaluer les états d'ionisation, mais son influence varie en fonction de la SED, ce qui complique les calculs directs.

La **profondeur optique** d'un matériau détermine son opacité au rayonnement. Dans la matière faiblement ionisée, les rayons X mous sont absorbés par l'**effet photoélectrique**, tandis que les rayons X durs sont diffusés principalement par l'**effet Compton**. Dans le cas des gaz très denses, la matière devient optiquement épaisse à cause de l'effet Compton, bloquant les rayons X au dessus de 10 keV. En parallèle, les transitions atomiques les plus importantes dans les rayons X se trouvent dans la "bande du fer" entre 6 et 9 keV, notamment Fe xxv Kα et Fe xxvi Kα à 6.7 et 7.0 keV. Leurs énergies, déterminées par les transitions des électrons vers ou depuis la couche K, sont cruciales pour les diagnostics de vitesse.

Poser un diagnostic précis nécessite souvent des **grilles de photoionisation** générées par des outils dédiés tels que **XSTAR**, **Cloudy** ou **SPEX**. Ces modèles supposent des géométries simplifiées à une dimension, mais des méthodes plus avancées prennent en compte la géométrie en 3 dimensions et la variabilité des sources d'irradiation. L'approche choisie doit équilibrer le coût de calcul et le réalisme physique. Les instruments à haute résolution permettront de clarifier davantage les ambiguïtés dans l'identification des raies et les diagnostics de vitesse.

Pour plus de détails, voir les Sections 2.3.1 et 2.3.2.

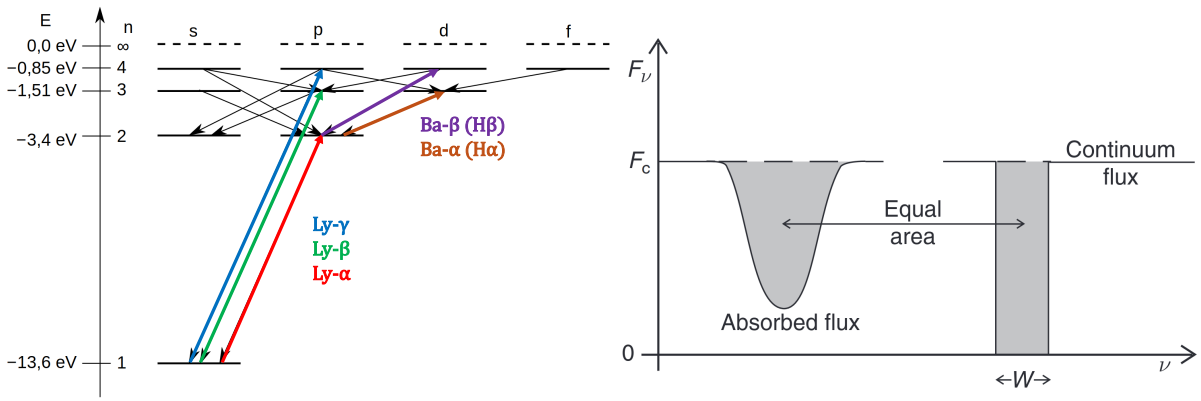

Figure 35:
(Gauche) Niveaux d'énergie, transitions et noms des premières raies pour l'atome d'Hydrogène. Pour l'ion Fe xxvi, dont la structure est similaire, les premières transitions utilisent souvent la lettre K. Adapté de wikimedia. **(Droite)** Représentation de la largeur équivalente d'une raie d'absorption. Source: Pradhan & Nahar (2011)

Stabilité thermique et visibilité des raies

L'apparition de raies d'absorption dans les vents astrophysiques est influencée par la **stabilité thermique** de la matière éjectée. Les courbes de stabilité, généralement tracées dans un plan log(ξ/T)-T, représentent l'équilibre entre les **pressions radiatives et gazeuses**. Ces courbes sont essentielles pour comprendre le comportement du vent en cas de perturbations, qui soit stabilisent soit déstabilisent le gaz. Dans les régions où la **pente** est **positive** ($d$logT/$d$log(ξ/T) > 0), les **perturbations** sont naturellement **compensées**, ce qui maintient la stabilité. Inversement, dans les régions où la **pente** est **négative**, un **emballement** du réchauffement ou du refroidissement se produit, entraînant des **instabilités**. Cette dynamique définit la migration de la matière entre les zones de stabilité délimitées par les branches stables les plus basses et les plus hautes. La température Compton marque la limite supérieure de ces branches.

Les **changements de spectre** entre les états durs et mous **altèrent** profondément **les zones de stabilité**. Dans l'**état mou**, la majeure partie de la courbe est **stable**, ce qui permet à certains états d'ionisation tels que Fe xxv et Fe xxvi de rester observables. En revanche, l'**état dur déstabilise** ces régions, **empêchant la formation des raies** d'absorption associées. Lors des transitions d'état, l'évolution de la matière est plus complexe, et des processus isobariques provoquent la condensation de la matière en amas denses au sein d'un milieu plus chaud et diffus. L'échelle de temps de ces transitions, dictée par des conditions locales telles que la vitesse du son et la dimension des amas de gaz instable, n'est accessible qu'avec la nouvelle génération d'instruments.

L'évolution de la SED sur une large bande joue un rôle essentiel dans la formation des courbes de stabilité. Les variations de l'énergie de coupure de la composante en rayons X durs affectent de manière significative la stabilité du gaz. En pratique, les contraintes sur la composante à haute énergie sont souvent incomplètes voire inexistantes, rendant toute modélisation délicate.

La compréhension de ces instabilités est essentielle pour dissocier la visibilité du vent, les mécanismes de lancement et la précipitation en amas. Cette dernière, confirmée par les observations dans les Trous Noirs SuperMassifs, augmente la densité du vent et peut expliquer des profils de raies d'absorption spécifiques. Dans les Binaires X à Trous Noirs, elle est étudiée pour son importance dans les vents froids à faible luminosité, inaccessibles aux vents thermiques ou magnétiques traditionnels.

Pour plus de détails, voir Section 2.3.3.

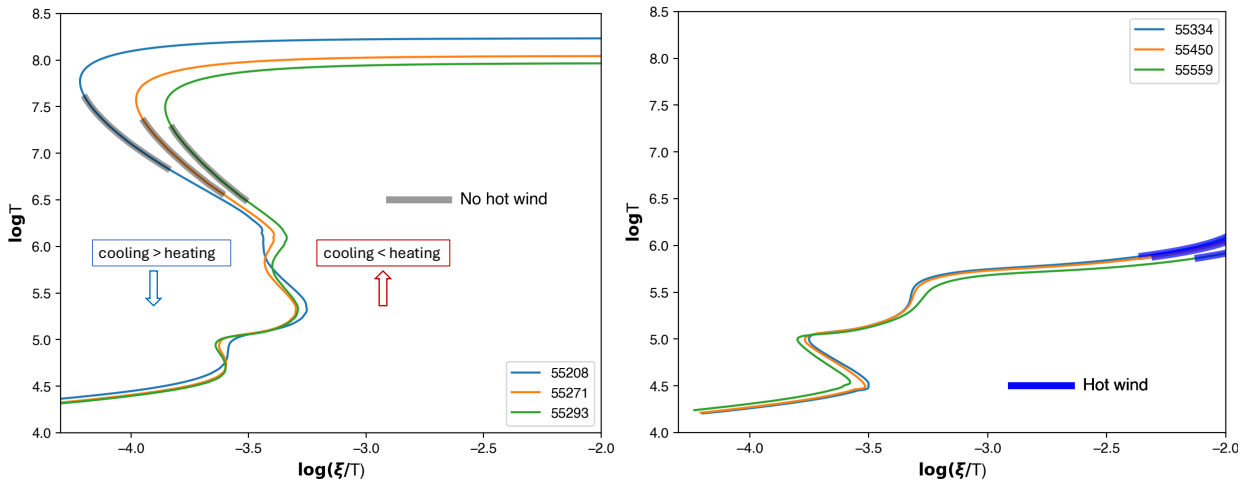

Figure 36: Evolution des courbes de stabilité pour un état dur **(gauche)** et mou **(droite)** d'une BHLMXB. Différentes courbes correspondent à différents jours d'observation. Adapté de Petrucci et al. (2021)

Etude globale des vents en rayons X dans les BHLMXBs

La nouvelle génération de télescopes à rayons X devrait permettre d'imposer des contraintes significatives sur les mécanismes de lancement des vents, et d'étudier plus en profondeur d'autres aspects comme l'évolution de la structure du vent au cours de l'éruption. Néanmoins, de nombreuses réponses peuvent être trouvées dans les observations existantes, et des contraintes supplémentaires peuvent être obtenues en utilisant de grands ensembles de données. En effet, les études observationnelles et les efforts de modélisation se concentrent souvent sur des observations uniques ou des échantillons spécifiques, avec une analyse ou une modélisation très précise des signatures de vents, et ils couvrent principalement les observations avec des raies très marquées. De plus, aucune étude détaillée d'un large échantillon de sources, avec une couverture exhaustive des données de plusieurs instruments, n'a été réalisée au cours de la dernière décennie, malgré une augmentation considérable du nombre d'observations et de sources, et une meilleure compréhension des vents en tant que processus physique.

L'un de mes premiers objectifs était donc d'obtenir une vue globale et à jour des signatures de vents X dans un large échantillon d'objets et d'observations. Cela permettrait non seulement de tirer de nouvelles conclusions sur les observations à partir d'un ensemble de données beaucoup plus important que celui étudié précédemment, mais aussi d'identifier les meilleures sources, les meilleures éruptions et les meilleurs ensembles de données dans lesquels les signatures de raies seraient susceptibles d'imposer des contraintes sur les mécanismes de lancement des vents.

Afin de maximiser le nombre de candidats BHLMXB, j'ai tiré mon échantillon des deux catalogues de Trous Noirs galactiques les plus récents, BlackCAT et WATCHDOG, pour un total de 88 sources. En parallèle, il existe de nombreux télescopes susceptibles de détecter des raies en rayons X mous : si l'on se limite à ceux dont les données d'archives sont facilement accessibles, il reste *Chandra*, *NICER*, *NuSTAR*, *Suzaku*, XMM-*Newton*,*Swift* et *HXMT* . Parmi ces instruments, XMM-*Newton* et *Chandra* présentent l'avantage d'être bien établis et (relativement) bien calibrés, de convenir à la détection de raies dans la bande du fer et de disposer d'études bien documentées sur la plupart des observations d'archive pour confronter mes résultats. En choisissant de plus de me limiter aux instruments les plus pertinents de chaque télescope, j'ai fini par analyser toutes les observations XMM-*Newton* EPIC-PN et *Chandra*-HETG des BHLMXBs actuellement connus, rendues publiques en Octobre 2022. Cela a d'ores et déjà limité l'échantillon à 42 sources.

Au moment de la rédaction de ce manuscrit, la littérature sur les BHLMXBs reste très fragmentaire, et aucun des catalogues de BHs n'est complètement à jour par rapport à la littérature. J'ai donc listé dans la Table 3.1 les propriétés physiques pertinentes et un aperçu des détections de raies d'absorption dans la bande du fer pour **l'échantillon complet des 88 sources** identifiées comme BHLMXBs dans la littérature à la mi-2024, et qui seront abordées à différents moments de l'étude.

Les procédures de réduction des données des télescopes concernés, ainsi que d'autres instruments utilisés pour le chapitre suivant, sont détaillées dans l'Annexe 6.1.

Pour plus de détails, voir Section 3.2.

Méthodologie pour la détection de raies

Pour détecter les raies d'absorption dans la bande du fer avec un rapport signal/bruit suffisant, un seuil de **5000 photons** dans la gamme d'énergie 4-10 keV a été appliqué aux spectres de XMM-*Newton* et de *Chandra*, équivalent à une limite de détectabilité à l'extrémité supérieure de la distribution en EW dans l'ensemble de données. Après cette étape, il restait **242 observations**, dont **137 spectres EPIC-pn** et **105 spectres HETG**. J'ai ensuite appliqué une procédure automatique pour chaque observation, dont les principales étapes sont résumées ci-dessous.

- **1. Modélisation globale**

  Le continuum est modélisé en utilisant une combinaison de composantes powerlaw, diskbb, et phabs (absorption neutre), pour représenter respectivement l'émission comptonisée dure, le disque, et l'absorption galactique. Ces composantes sont ajoutées de manière itérative et évaluées par des F-test, exigeant un seuil de confiance de 99% pour l'inclusion.

- **2. Recherche en aveugle**

  Pour identifier les caractéristiques des raies étroites dans la bande du fer, nous testons dans quelle mesure une composante de raie supplémentaire améliore ou détériore le *fit* (la comparaison entre le modèle et les données), pour une vaste gamme d'énergies et d'EWs. Cela produit une carte 2D de statistique (ici ΔC), où les régions présentant des changements statistiquement significatifs mettent en évidence de potentielles raies en absorption ou en émission.

- **3. Caractérisation des raies**

  Nous modélisons les éléments significatifs en détail, avec jusqu'à sept composantes de raies. Celles-ci comprennent les raies d'absorption du fer les plus fortes (notamment Fe xxv Kα et Fe xxvi Kα) et les raies d'émission du Fe Kα et Fe Kβ neutre. Les raies d'un même ion sont supposées avoir la même origine, avec des décalages de vitesse contraints pour éviter le chevauchement ou la dégénérescence. Après avoir calculé les erreurs sur les paramètres de chaque raie, qui seront nos principaux résultats, une deuxième recherche aveugle confirme l'absence de raies résiduelles.

- **4. Évaluation de la significativité des raies**

  Des simulations de Monte Carlo sont nécessaires pour évaluer correctement la significativité des raies détectées. Nous créons donc 1000 spectres synthétiques qui reproduisent l'observation en cours d'analyse, basés sur le modèle de continuum que nous avons obtenu, **sans les raies d'absorption**, et évaluons si le bruit de photons de l'instrument peut créer des résidus suffisamment significatifs pour être comparables à la statistique des raies, chacune dans sa gamme d'énergie. Seules les raies **dont le niveau de confiance dépasse 99.7%** (3σ) sont considérées comme des détections valides. Pour les observations sans raies significatives, nous calculons des limites supérieures de largeur équivalente dans l'observation initiale, à un niveau de confiance de 3σ.

Figure pertinente (pleine page): Fig. 3.1.
Pour plus de détails, voir Section 3.3.

Résultats globaux

Conditions favorables à la détection des raies d'absorption

Nos résultats sont en bon accord avec les dichotomies attendues: toutes les signatures du vent se trouvent dans des états mous ($HR_{[6-10]/[3-10]} < 0.8$) et lumineux ($L_X > 0.01 L_{Edd}$) de cinq sources très inclinées (dippeurs). L'absence de détection des raies d'absorption du Fe XXV et du Fe XXVI dans les états durs est en accord avec les études théoriques suggérant que la gamme d'ionisation compatible avec ces ions devrait être thermiquement instable lorsque le gaz est éclairé par une SED d'état dur. Ainsi, même si le vent lui-même était présent, il ne serait pas détectable à travers ces raies d'absorption.

Pour plus de détails, voir Section 3.4.2.

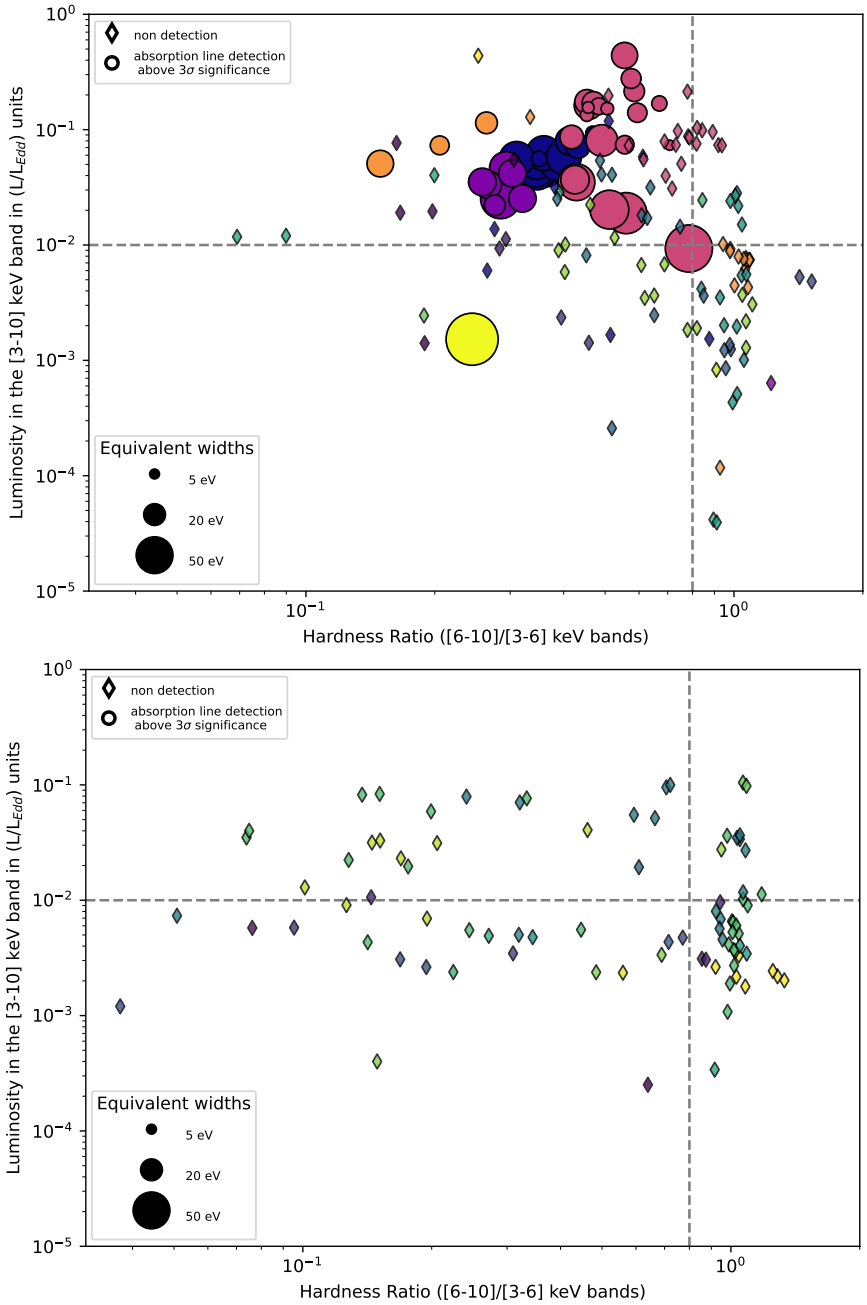

Figure 37: Diagramme Dureté-Luminosité avec la position de toutes les détections de raies (cercles) dans l'échantillon, séparé entre les sources à haute inclinaison **(gauche)** et à basse inclinaison ou inconnues **(droite)**. Le code couleur correspond aux sources.

Distribution des paramètres et corrélations

Grâce à l'instrument *Chandra*, des mesures précises des vitesses d'éjection révèlent une tendance globale à de légers décalages vers le bleu dans les signatures d'absorption, avec des vitesses de décalage en moyenne de -200 ± 60 km s^{-1} et jusqu'à -1000 km s^{-1} (une valeur négative indique un décalage vers le bleu). Ces résultats sont en accord avec des études antérieures sur les raies de basse énergie et mettent en évidence la précision des mesures malgré les limites instrumentales de *Chandra*.

Les quelques détections de largeur de raies, avec des largeurs à mi hauteur (FWHMs) atteignant quelques 1000 km s^{-1}, indiquent des vitesses de turbulence significatives dans les vents, qui sont estimées autour de 1000 km s^{-1} sur la base d'hypothèses géométriques simples.

En parallèle, nous trouvons un certain nombre de corrélations significatives entre les paramètres des raies et du continuum, dont une très forte anti-corrélation entre la luminosité en rayons X (en unités d'Eddington) et les largeurs équivalentes de Fe xxv Kα. Ceci suggère une structure de vent commune entre les sources, potentiellement influencée par des états d'ionisation au-dessus du pic de fraction ionique pour Fe xxv Kα.

Enfin, le manque notable de détections à des luminosités plus faibles peut refléter des changements d'ionisation, un échantillonnage insuffisant, ou la dépendance de l'écoulement à une illumination élevée, comme le proposent les modèles de vent thermique.

Pour plus de détails, voir la Sec. 3.4.1.

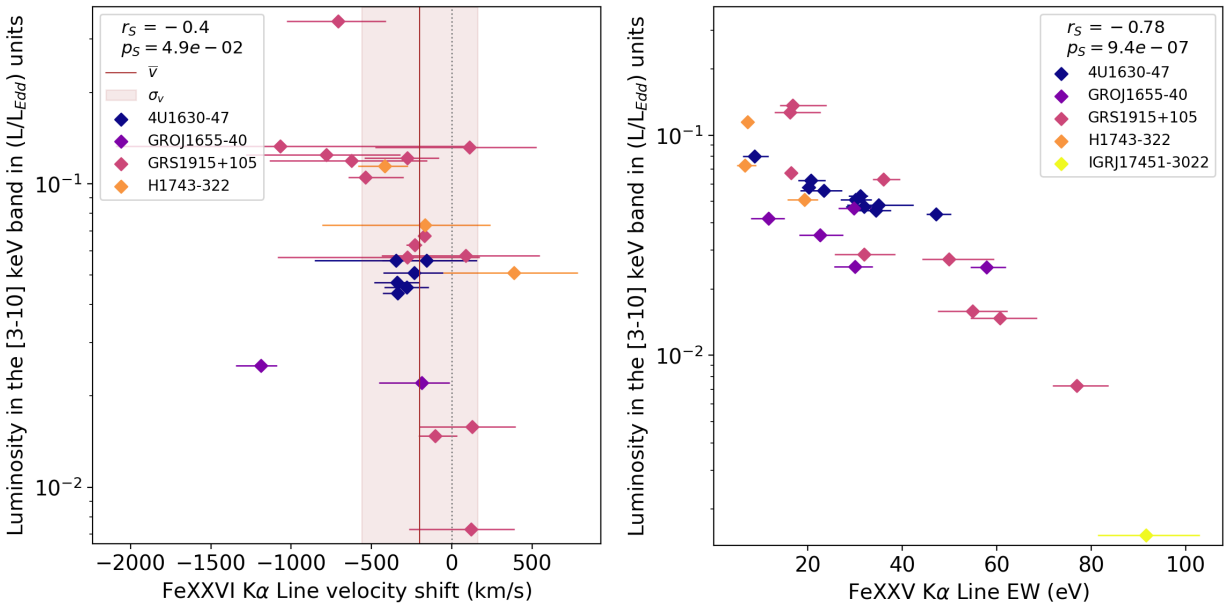

Figure 38: Evolution du décalage vers le bleu de la raie Fe xxvi Kα **(gauche)** et des EWs de la raie Fe xxv Kα **(droite)** en fonction de la luminosité, pour tout l'échantillon. Les valeurs r_S et p_S dans chaque graphe correspondent au score et à la p-value du test de Spearman, qui teste les relations monotoniques entre paramètres. La p-value correspond à la probabilité que la corrélation soit uniquement due au hasard. Ici, aucune corrélation n'est présente dans le graphe de gauche, et une corrélation très significative (p-value inférieure à 10^{-6} et score important) est présente dans le graphe de droite.

Mise en perspective avec le paysage observationnel global

Afin d'étudier les différences entre les résultats obtenus dans notre échantillon et le reste de la littérature, j'ai compilé dans la Table 3.3 les publications de raies d'absorption dans toutes les bandes d'énergie, les états d'accrétion associés, et les problèmes potentiels parmi tous les candidats BHLMXBs connus.

Dans la bande du fer, la majorité de la littérature est en accord avec nos résultats, à l'exception notable de signalements occasionnels de raies d'absorption à grande vitesse, dans des états durs, parfois pour des sources peu inclinées. En plus d'avoir des propriétés physiques qui ne correspondent en rien aux détections canoniques, ces détections proviennent principalement des spectres de *NuSTAR*, où le mélange avec les composantes de réflexion rend les évaluations de significativité difficiles. La résolution spectrale limitée de *NuSTAR* et le recours à des résidus dépendant du modèle posent aussi problème, car les résultats contradictoires entre les modèles de réflexion sont fréquents. De plus, d'importants problèmes d'étalonnage pouvant affecter les études de réflexion et d'absorption n'ont été considérés dans aucune de ces publications.

Bien que d'autres détections d'états durs aient été signalées dans les rayons X à des énergies plus basses, elles présentent des paramètres d'ionisation suffisamment faibles pour rester thermiquement stables, même avec des SED d'états durs, et s'alignent donc sur les prédictions théoriques. Cependant, les interprétations sont limitées par le manque de prise en compte des contributions multi-phases du milieu interstellaire, qui pourraient expliquer une partie des signatures. Pour distinguer les phases d'absorption statiques et dynamiques, des ensembles de données plus larges couvrant plusieurs états spectraux sont nécessaires.

Les raies d'absorption optiques et infrarouges offrent une perspective complémentaire sur les vents, car elles apparaissent souvent dans des états durs. Ces signatures sont observées dans des systèmes à forte inclinaison et s'alignent sur les détections de rayons X dans certaines sources, mais présentent des différences significatives (notamment en ce qui concerne les décalages de vitesse) dans d'autres. La rareté des détections simultanées empêche toute conclusion définitive, mais les ensembles de données actuels pointent vers un type d'éjection à plusieurs phases, avec des comportements différents pour les vents en rayons X et en OIR.

J'ai également utilisé ma vaste compilation de paramètres de sources pour étudier d'autres liens avec les propriétés des vents, notamment avec les périodes orbitales. Les vents froids, liés aux régions extérieures du disque, peuvent être influencés par la taille maximale du disque, mais aucun schéma clair n'émerge des données actuelles en raison des mesures limitées d'inclinaison et de période orbitale. Cependant, certains des systèmes ayant les périodes les plus courtes ont déjà montré des éjections importantes, ce qui pourrait déjà contraindre les mécanismes de lancement des vents.

Pour plus de détails, voir Section 3.6.

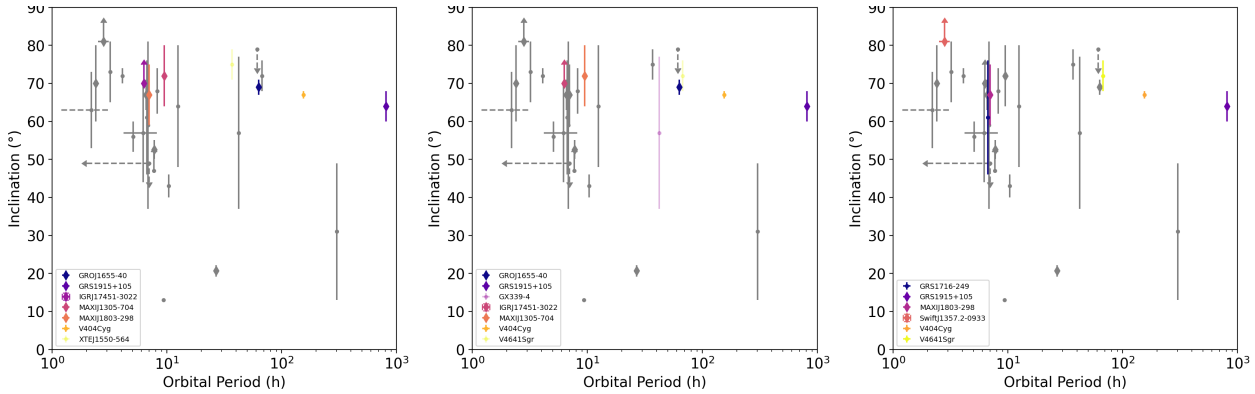

Figure 39: Distribution de la période orbitale et mesures d'inclinaison des candidats BHLMXBs avec des détections de vents claires dans la bande du fer **(gauche)**, en rayons X mous à plus basse énergie **(milieu)**, et en OIR **(droite)**, comparé au reste de l'échantillon en gris. Les diamants indique les dippeurs, et les tirets les mesures de période orbitale approximatives.

20 années de vents dans 4U 1630-47

L'étude globale décrite précédemment avait deux applications directes : soit réaliser une étude détaillée visant à combler certaines des lacunes identifiées dans le paysage observationnel, soit se concentrer sur les modèles et les comparaisons avec les données. Contrairement à ce que suggère la structure de ce document, j'ai d'abord terminé un travail préliminaire sur le projet de modélisation (sur lequel nous reviendrons plus tard), je suis retourné aux observations et me suis concentré sur l'une des sources dont les données d'archives avaient le plus grand potentiel : 4U 1630-47.

4U 1630-47, une source transitoire en rayons X avec des éruptions récurrentes tous les 600-700 jours, a été classée comme une BHLMXB sur la base de ses propriétés spectrales et temporelles. Malgré certaines similitudes avec d'autres sources du même type, son comportement s'écarte considérablement de la norme, avec des "super-éruptions" rares et de longue durée, une évolution spectrale atypique et de rares occurrences d'états durs canoniques. A la place, la source alterne de manière irrégulière entre des états spectraux mou/thermiques, intermédiaires, lumineux, et un état de "loi de puissance raide" (SPL), chacun ayant des composantes à haute énergie et des propriétés temporelles distinctes. Elle a également un historique d'éruptions entièrement dans l'état mou. Ces propriétés, combinées à une inclinaison très élevée, ont fait de la source l'un des émetteurs de vents les plus observés.

Les détections de vents ont commencé par des observations *Suzaku* en 2006, même si des indices étaient déjà présents précédemment dans des données *Chandra*-HETG. Ensuite, pendant l'éruption de 2012-2013, de nombreuses campagnes observationnelles ont été menées avec XMM-*Newton*, *Chandra*, *Suzaku*, et *NuSTAR*, révélant des raies d'absorption et de possibles raies d'émission relativistes, bien que ce dernier point reste débattu. Plus récemment, une surveillance continue par *NICER* tout au long de l'année 2018 et pendant la super-éruption prolongée de 2022-2024 a confirmé les signatures de vents et complémenté des études de polarisation en rayons X. Ces observations soulignent une récurrence quasi-décennale des éruptions sur trois décennies.

Les données d'archive comptent plus de 200 époques de "haute qualité" où des raies peuvent être détectées, réparties sur neuf éruptions, combinant de nombreux instruments différents (*Chandra*, *NICER*, *NuSTAR*, *Suzaku* et XMM-*Newton*), ainsi qu'une couverture importante en haute énergie (notamment via *Swift*-BAT et *INTEGRAL*). Ces données ont un potentiel inégalé pour comprendre l'évolution du vent dans une BHLMXB en éruption, mais jusqu'à présent, les travaux se sont concentrés sur des éruptions ou des instruments uniques. Afin de comprendre l'évolution à long terme de cette source, j'ai donc analysé toutes les observations réalisées jusqu'à la fin de l'année 2023.

Pour plus de détails, voir Section 4.1.

Note : Les procédures de réduction des données sont détaillées en Annexe 6.1.2, et les détails de l'analyse spectrale sont présentés dans Section 4.2. La procédure de détection des raies reste identique à celle utilisée pour l'étude précédente.

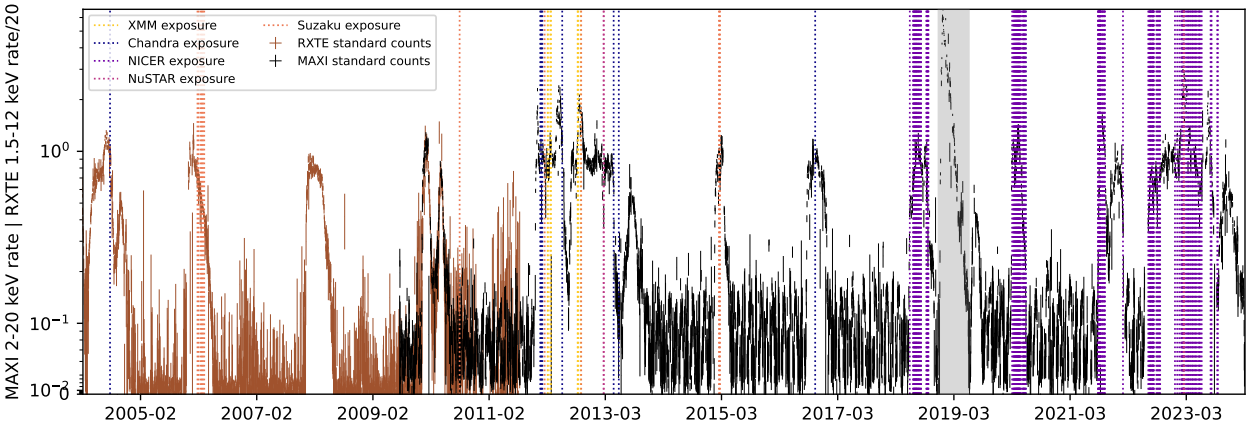

Figure 40: Courbe de lumière à long-terme de 4U 1630-47, montrant les observations utilisées dans cette étude avec des lignes verticales. La période grisée est contaminée par une source proche.

Résultats globaux

Evolution dans les Diagramme Luminosité-Dureté à basse et haute énergie
J'ai d'abord construit le diagramme standard de Dureté-Luminosité de 4U 1630-47, où la dureté est calculée avec les luminosités dans les bandes [6-10] et [3-6] keV, et la luminosité utilise la bande [3-10] keV en unités d'Eddington. Grâce à un ensemble de données couvrant de nombreuses éruptions, onous obtenons une couverture quasi-complète de l'évolution de la source à des luminosités élevées (au-dessus de $\sim 10^{-2} L_{Edd}$). La majorité des observations dans l'état mou s'alignent le long d'une diagonale étroite, conformément aux attentes pour les binaires très inclinées. L'ensemble des observations *NICER* corroborent les résultats précédents, notamment la décroissance puis disparition des raies d'absorption au-dessus des valeurs de HR de ∼0.4–0.45 et $L_{3-10} \sim 10^{-1}\ L_{Edd}$. Cependant, de nombreuses observations *NICER* dans des états mous sont des non-détections, avec des limites supérieures incompatibles avec des détections à des valeurs de HR et de luminosité identiques.

L'influence des rayons X durs au-dessus de 10 keV étant le principal suspect, j'ai implémenté un nouveau Diagramme Dureté-Luminosité "dur", qui remplace le HR en [6-10]/[3-6] keV (HR_{soft}) par un HR en [15-50]/[3-6] keV (HR_{hard}), accessible grâce à la couverture à haute énergie. Le diagramme résultant, où des marqueurs translucides indiquent les époques avec une limite supérieure sur HR_{hard}, fournit une bien meilleure distinction entre les états avec et raie d'absorption détectables. En effet, la largeur équivalente des raies est très clairement anti-corrélée avec HR_{hard}, ce qui est confirmé par une probabilité au rang de Spearman inférieure de 10^{-9}. Au-dessus de $HR_{hard} \sim 0.1$, les largeurs équivalentes attendues descendent sous le seuil de détectabilité avec les instruments actuels dans la plupart des observations, ce qui explique la rareté des détections.

Pour davantage de détails, voir Section 4.3.1.

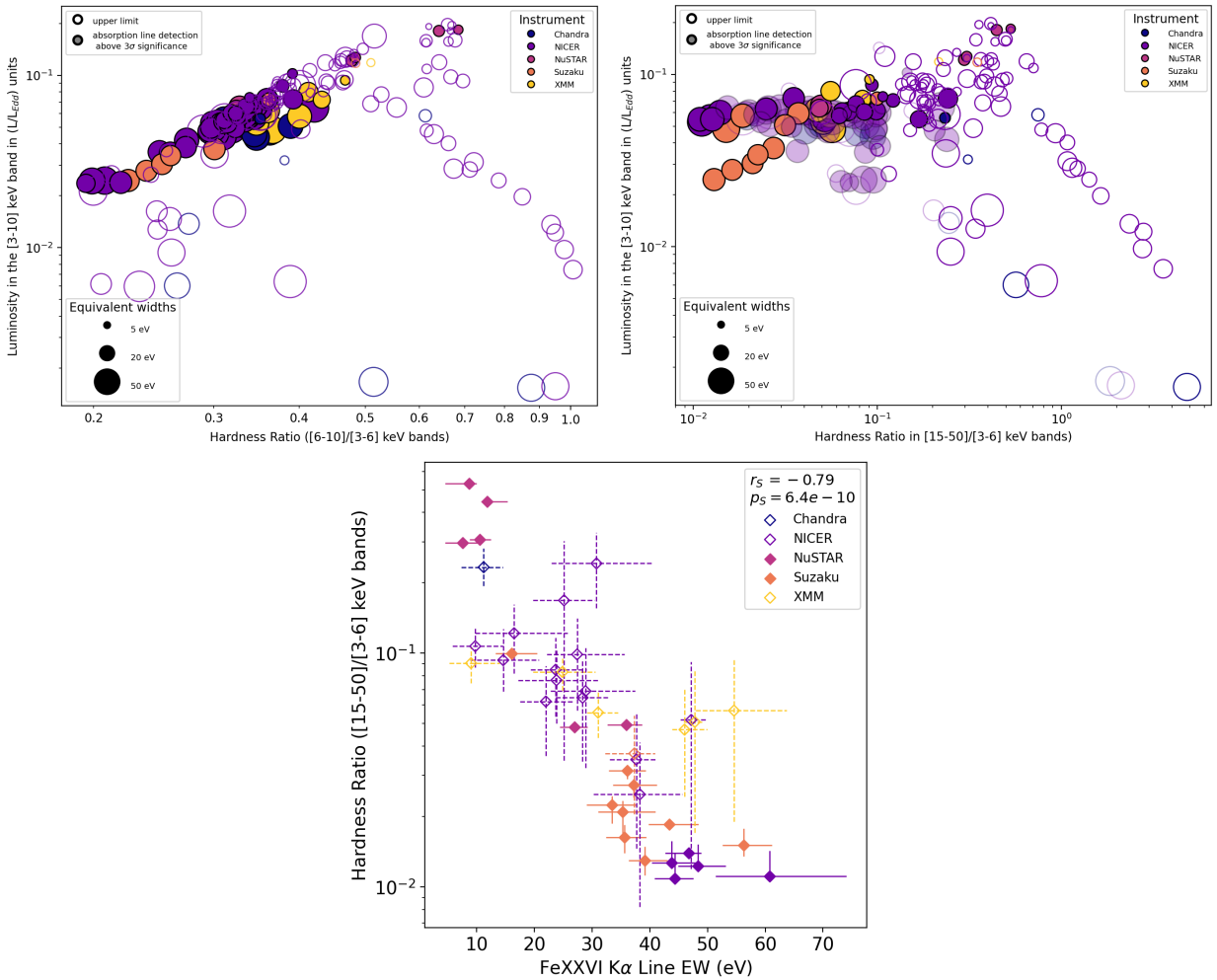

Figure 41: **(Haut)** Diagrammes Dureté-Luminosité "mou" **(gauche)** et "dur" **(droite)** pour 4U 1630-47, coloriés en fonction de l'instrument. **(Bas)** Corrélation entre les EWs de la raie Fe xxvi Kα et HR_{hard}.

Corrélations et structures

Les distributions et les propriétés des raies détectées avec *NICER*, *Suzaku* et *NuSTAR* restent pour l'essentiel cohérentes avec l'ensemble plus restreint d'observations XMM-*Newton* et *Chandra* de la source déjà analysée dans l'étude précédente. La distribution des décalages vers le bleu avec les satellites les plus précis reste significativement distincte de zéro, avec $\overline{v_{out}} \sim -560 \pm 60$ km/s.

En examinant les corrélations entre les paramètres des raies et les propriétés du continuum, la luminosité en rayons X mous ($L_{[3-10]}$) a une grande influence sur les EWs de Fe xxv Kα, dans une moindre mesure Fe xxvi Kα, et leur rapport. Ces corrélations sont significatives (p-value inférieure à 10^{-5}) et s'alignent sur les résultats précédents pour l'échantillon de plusieurs sources. En parallèle, le rapport de dureté mou n'est corrélé à aucun paramètre de raie, contrairement à HR_{hard}.

La différence notable avec l'étude précédente est l'apparition de déviations significatives aux luminosités les plus élevées et les plus faibles, très probablement en raison de la bien plus grande quantité de détections. En effet, l'exclusion des observations sous $L/L_{Edd} \sim 4{\cdot}10^{-2}$ et au-dessus de $L/L_{Edd} \sim 10^{-1}$ augmente considérablement les corrélations entre raies et luminosité. Plus particulièrement, la région à faible luminosité s'écarte de manière significative des tendances principales. Une régression confirme que les observations dans cette sous-structure se situent bien en dehors de l'intervalle de confiance de la structure principale, et montrent également un comportement distinct dans les Diagrammes Dureté-Luminosité. Les observations dans cette sous-structure font typiquement partie des hausses initiales ou des baisses finales de luminosité dans chaque éruption, contrastant avec les parties plus lumineuses de la diagonale de l'état mou.

Enfin, mettre en évidence l'évolution temporelle permet de mieux distinguer les types d'éruptions, car les super-éruptions semblent avoir des corrélations plus structurées que les éruptions standard. Toutefois, des observations plus uniformes et plus systématiques sont nécessaires pour déterminer si ce phénomène est simplement la conséquence d'un échantillonnage inégal.

Pour plus de détails, voir les Sections 4.3.2 et 4.3.3.

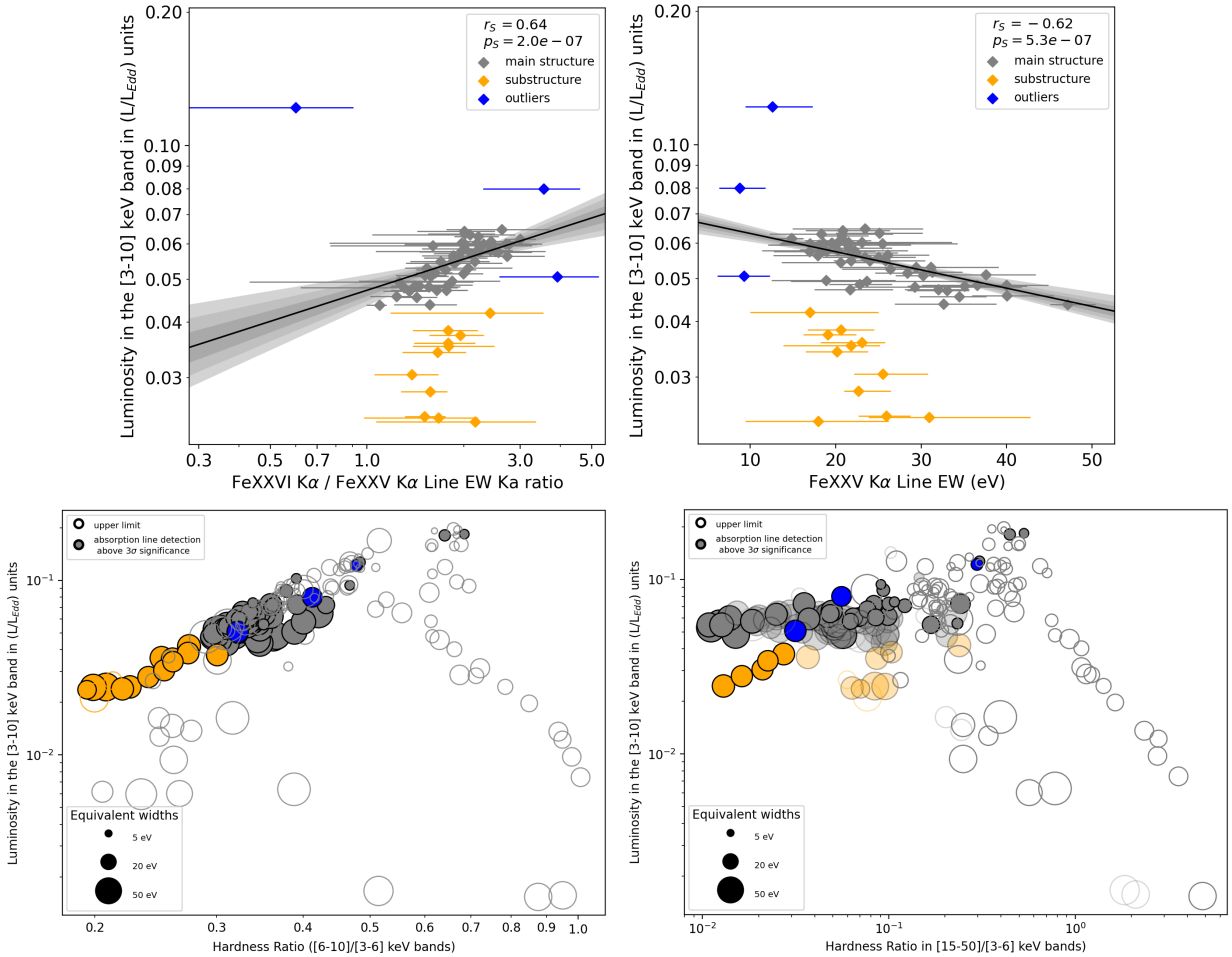

Figure 42: **(Haut)** Comparaison entre les EWs des raies et leur luminosité, indiquant les sous-structures et anomalies. **(Bas)** HLD mou **(gauche)** et dur **(droite)** de 4U 1630-47, avec le même code couleur.

Evolution du vent en fonction des états spectraux

L'évolution des raies d'absorption observées peut être le signe de changements intrinsèques dans les propriétés des éjections, mais aussi la conséquence des changements dans le spectre. Pour distinguer l'un de l'autre, deux effets principaux doivent être considérés : la stabilité du plasma, et l'évolution de son ionisation. Nous avons donc regroupé le comportement de la source en cinq états spectraux (mou, intermédiaire, SPL, QRM, dur) avant de tester comment la SED de chaque état affecte l'apparition des raies. Pour plus de détails, voir Section 4.4.

Influence de la stabilité du plasma

En dérivant les courbes de stabilité avec CLOUDY, nous avons identifié les régions thermiquement stables à différents paramètres d'ionisation dans une gamme d'observations de chaque état, en nous concentrant sur celles avec des données robustes à haute énergie. Nos résultats montrent que les plages d'ionisation du Fer XXV et XXVI ($\log \xi \sim 3.5-4$) restent thermiquement stables dans tous les états spectraux à l'exception de l'état canonique "dur".

La diminution observée des EWs des raies d'absorption du Fe XXV et du Fe XXVI lors de la transition vers les états intermédiaires et SPL ne peut donc être due à une déstabilisation du gaz. Étonnamment, même certains états totalement durs conservent une région thermiquement stable pour le Fe XXV. C'est la première fois qu'une telle stabilité dans les états durs de BHXRB est mesurée, ce qui tranche avec les états durs systématiquement thermiquement instables observés dans d'autres sources.

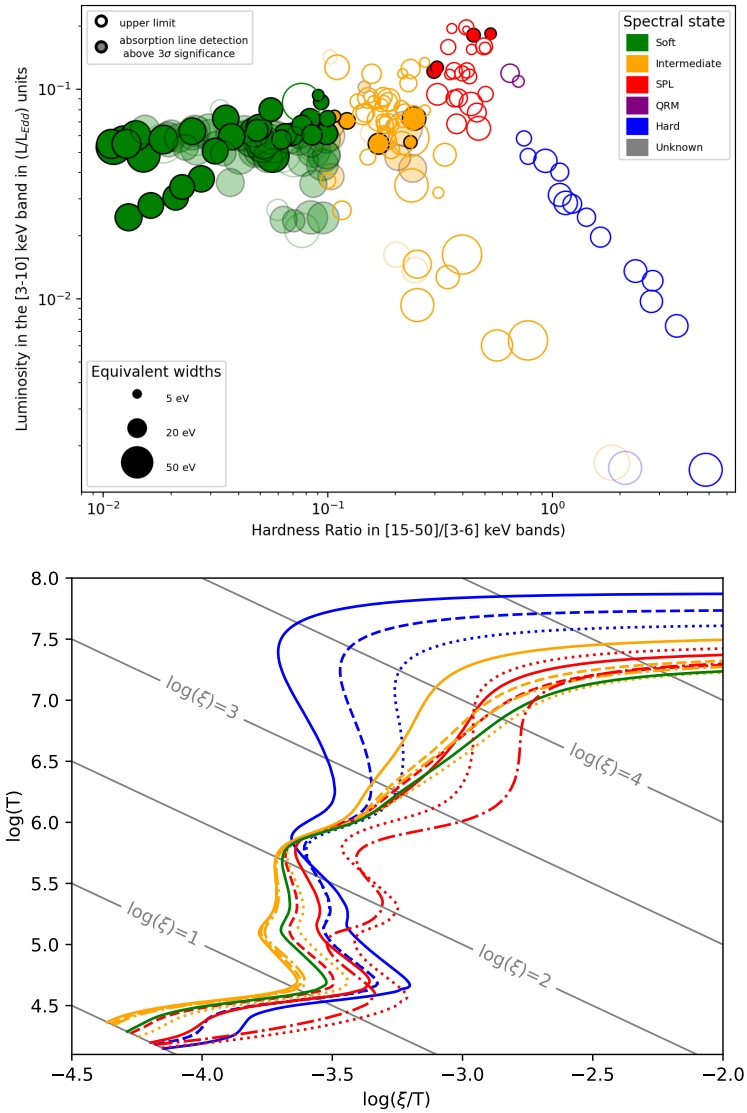

Figure 43: Diagrammes Dureté-Luminosité **(haut)** et courbes de stabilité des SEDs de chaque état spectral **(bas)** de 4U 1630-47, coloriés en fonction de ces derniers.

Influence des changements d'ionisation

Pour isoler davantage les paramètres du vent indépendamment des SEDs, nous avons calculé pour plusieurs observations la courbe de croissance de la largeur équivalente de chaque raie d'absorption, pour un N_H et une turbulence fixes, en les mettant à l'échelle des paramètres d'ionisation et des luminosités. Cette approche a été appliquée aux données dont les propriétés des raies et la position dans les HLD variaient le plus. Les résultats montrent qu'un changement significatif des paramètres du vent est nécessaire pour expliquer les divergences entre les observations de luminosité différentes ou de HR_{hard} différents.

Figure pertinente (pleine page): Fig. 4.11

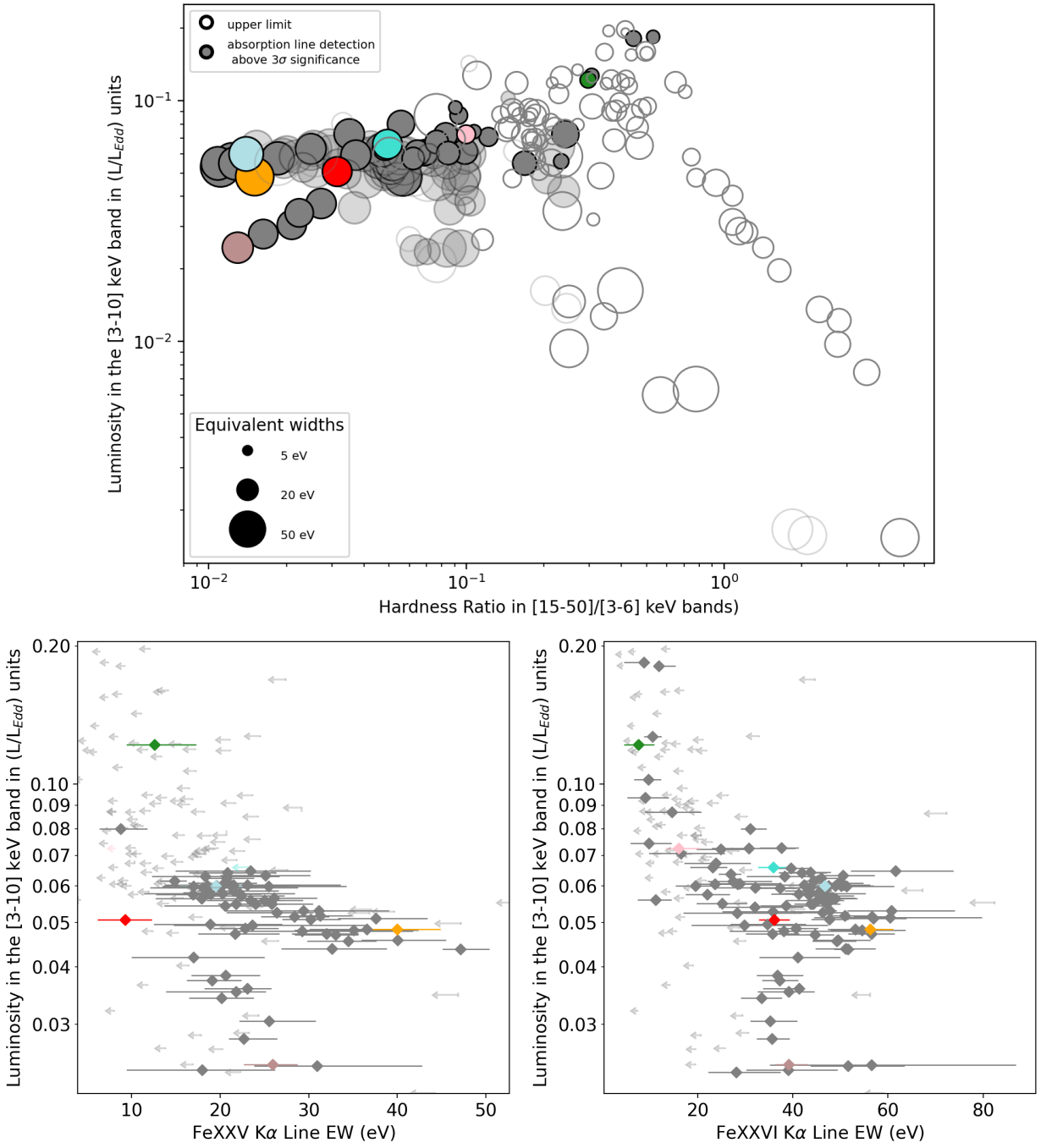

Figure 44: Diagramme Dureté-Luminosité **(haut)** et graphes de corrélation EW-luminosité de 4U 1630-47 **(bas)**, indiquant en couleur les observations testées pour comparer les différences de paramètres du vent.

Variabilité anormale des raies dans les éruptions récentes

Jusqu'à présent, nous nous sommes limités à la variabilité de la source à l'échelle d'observations moyennées à la journée. Cependant, un examen plus détaillé des orbites individuelles de *NICER* révèle un certain nombre d'évolutions spectrales sur de courtes périodes liées à la présence de raies. L'une d'entre elles est détaillée ci-dessous.

Pour plus de détails, voir Section 4.5.

Février 2023: Obscurcissement à haute variabilité

Le 23 février 2023, *NICER* a observé 4U 1630-47 au cours de 6 intervalles distincts (orbites). Si les 3 derniers ont un spectre mou standard sans raies d'absorption détectables, suggérant un état intermédiaire ou SPL, les 3 premiers montrent de très fortes raies d'absorption couplées à une variabilité erratique du flux sur des échelles de temps inférieures à la minute. Les spectres intégrés par orbite révèlent une diminution progressive de la luminosité jusqu'à 10% du flux initial dans la gamme 3-10 keV, accompagnée de raies d'absorption profondes et d'une large raie d'émission du fer. Cependant, une spectroscopie à des échelles de temps encore plus courtes montre que les baisses de flux elles-mêmes sont systématiquement plus molles, malgré des propriétés de raies d'absorption similaires. Ceci n'est pas compatible avec un obscurcissement standard dû à l'absorption de matériau très dense entrant dans la ligne de visée. L'autre scénario, à savoir un changement dans le continuum dû à des variations du flux d'accrétion, nécessiterait des changements très rapides dans la structure du disque, un événement extrêmement rare dans les sources non pulsantes.

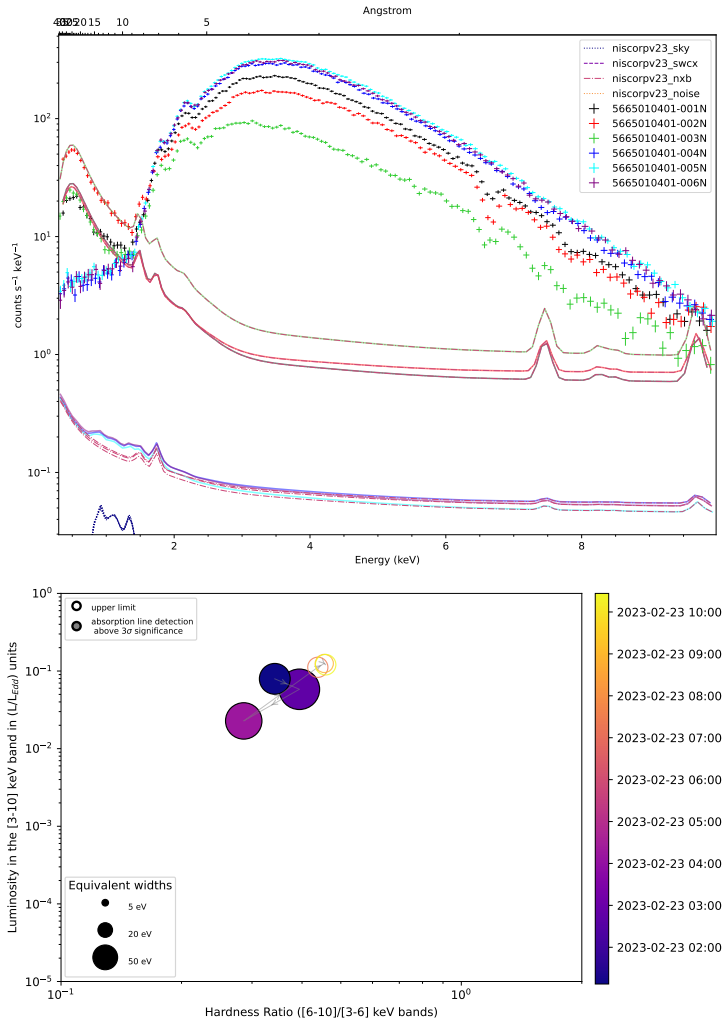

Figure 45: **(Haut)** Spectres intégrés par orbite des observations de 4U 1630-47 de Février 2023. **(Bas)** HLD mou des orbites individuelles et des EWs des raies Fe xxv Kα, colorié en fonction du temps..

Signatures observationnelles des Wind Emitting Disks

Les solutions Wind Emitting Disks développées à l'IPAG font partie des très rares modèles physiques de vents obtenus par éjection magnétique, et leur description auto-similaire fournit un moyen très prometteur d'accéder aux paramètres physiques clés de la structure d'accrétion-éjection par le biais des signatures observationnelles de l'éjection. Cependant, malgré quelques études pilotes au cours de la dernière décennie, les signatures observationnelles de l'espace des paramètres des WED n'ont pas encore été complètement caractérisées, et les comparaisons avec les données existantes n'ont pas encore été effectuées. L'un des principaux objectifs de mon doctorat était de poursuivre ce projet.

J'ai fini par me limiter à préparer le terrain, à savoir créer les outils nécessaires pour produire des tableaux de spectres synthétiques à haute résolution, afin de les comparer aux ensembles de données pertinents. L'étude des signatures de vent disponibles avec la version actuelle de l'espace des paramètres WED, ainsi que les comparaisons avec les ensembles de données actuels et futurs, sont deux projets en cours qui feront l'objet de ma prochaine bourse JSPS, en collaboration avec l'IPAG et les membres de l'équipe XRISM.

Observations synthétiques de WED: améliorations et dimensionnement

Le calcul des signatures spectrales synthétiques des Wind Emitting Disks nécessite un code de transfert radiatif avec des données atomiques précises, afin d'évaluer l'impact de la matière en éjection sur les spectres émis. Les solutions WED axisymétriques fournissent une structure autosimilaire en 3D pour les disques et les éjections, qui devraient idéalement être analysés avec des codes de transfert radiatif entièrement en 3D. Cependant, ces codes sont beaucoup trop coûteux en termes de temps de calcul, ce qui interdit de les utiliser pour l'exploration de l'espace des paramètres et les comparaisons directes avec des ensembles de données. Une approche plus simple développée par mes prédécesseurs utilise une méthode 1D discrétisée. Les spectres synthétiques sont calculés par itérations successives le long de chaque ligne de visée (LoS), divisées en une série de zones radiales ou "boites". Le spectre transmis après chaque étape est utilisé comme base pour les calculs suivants, jusqu'à ce que le spectre transmis final soit obtenu.

Notre approche présente plusieurs inconvénients. Tout d'abord, elle ignore la matière hors de la ligne de vue, une limitation dont l'importance ne peut être évaluée que par des comparaisons avec des modèles 3D (qui sont actuellement en cours). De plus, les solutions actuelles sont totalement "froides", c'est-à-dire qu'elles ne considèrent pas le chauffage dû à l'émission centrale sur les structures du disque ou du vent. L'une des conséquences principales est que la hauteur d'échelle du disque devient un paramètre libre au lieu d'être résolue physiquement. De plus, les SEDs instables devraient modifier les structures d'ionisation du gaz, mais la méthode de résolution actuelle ne tient pas compte de ces instabilités, qui doivent être implémentées ultérieurement.

L'algorithme WED initial, développé comme une surcouche autour du code de transfert radiatif XSTAR, souffrait d'une évolutivité et d'une portabilité limitées, que ce soit entre les versions XSTAR ou pour passer sur des codes alternatifs. La nouvelle implémentation est beaucoup plus flexible, prend en charge les ensembles de solutions à plusieurs dimensions, et peut être couplée avec n'importe quel code de transfert radiatif. Elle intègre également des effets supplémentaires, notamment des corrections relativistes, et un échantillonnage radial et spectral optimisé.

Pour plus de détails, voir Section 5.1.

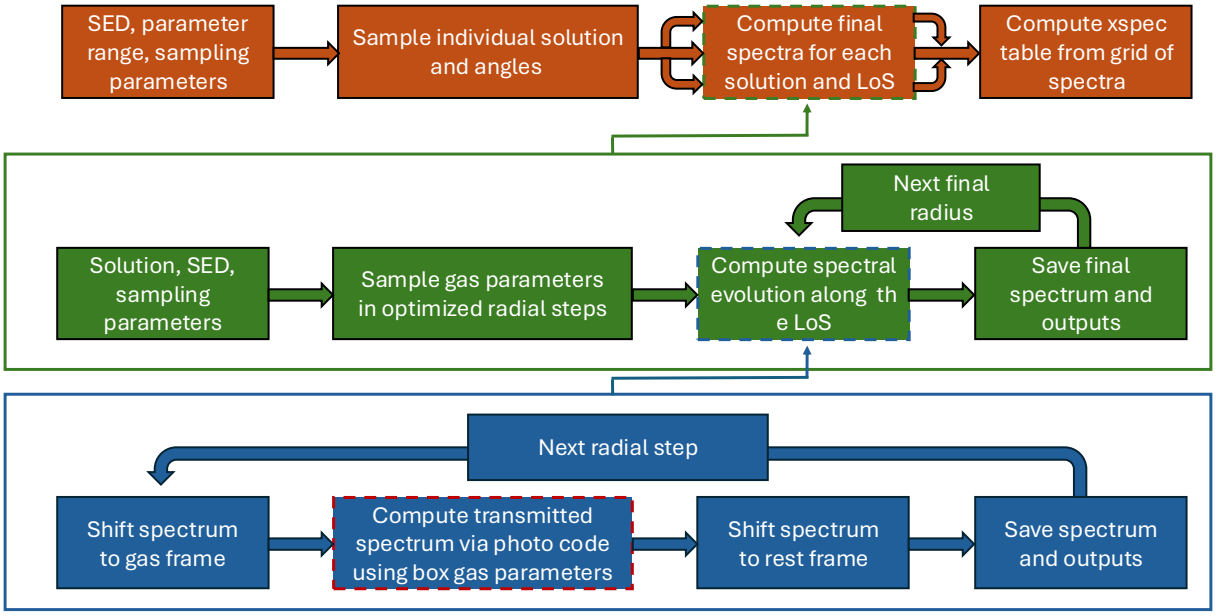

Figure 46: Aperçu de la logique de création des grilles de spectres synthétiques de WED. Le cycle en bleu représente les calculs successifs le long d'une ligne de visée, le cycle en vert le calcul d'une solution unique, et celui en marron le calcul d'une grille de spectres synthétiques. L'étape fondamentale qui nécessite un code de photoionisation externe, pour l'instant assurée par XSTAR, est indiquée en rouge.

Exploration de l'espace des paramètres du WED

Distribution radiale pour les solutions uniques

L'une des approches que j'ai utilisées pour caractériser la structure 3D du vent a été d'échantillonner différents angles au sein d'une solution unique et de comparer les distributions radiales des paramètres pertinents pour les calculs de vent.

Premièrement, la structure d'ionisation reste indépendante de la luminosité en raison de la dépendance linéaire entre la densité et le taux d'accrétion de masse. En pratique, une structure d'ionisation constante dans chaque solution WED permet de cartographier les vitesses maximales disponibles dans l'espace des paramètres WED pour une SED donnée sans avoir recours à des calculs spectraux approfondis. La combinaison de ces calculs avec ceux de l'ionisation pourrait révéler si les vitesses observées dans la littérature pour les BHLMXBs sont compatibles avec l'espace des paramètres WED actuel, sans avoir à directement comparer les modèles aux spectres.

Dans une solution unique, la densité de colonne s'échelonne linéairement avec le taux d'accrétion, ce qui signifie qu'entre plusieurs observations où la SED n'évolue qu'en flux, l'intensité des raies d'absorption devrait être corrélée de manière prévisible avec la luminosité. Cependant, l'évolution de la luminosité des BHLMXBs dans l'état mou implique souvent des changements spectraux importants (comme pour 4U 1630-47). En parallèle, l'influence de l'inclinaison est très prononcée, à la fois en termes de densité de colonne et de vitesse. La diminution importante de la densité pour des angles inférieurs à $\sim 50°$ limite les observations avec des caractéristiques d'absorption significatives à des angles d'inclinaison très élevés. Parallèlement, la gamme de vitesses disponibles pour la matière non complètement ionisée reste inférieure à quelques 1000 km/s, quel que soit l'angle d'inclinaison.

Pour davantage de détails, voir Section 5.2.2.

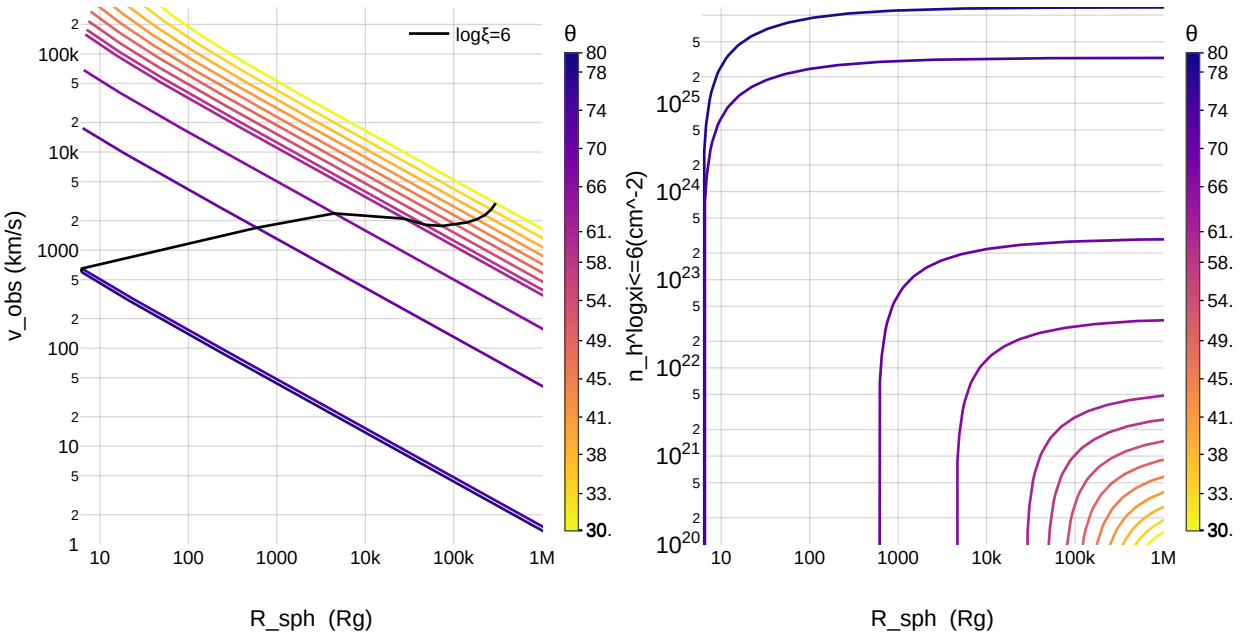

Figure 47: Aperçu de la dépendance radiale de la vitesse du vent dans la ligne de visée **(gauche)** et de la partie de la densité de colonne qui n'est pas entièrement ionisée **(droite)**, avec un échantillonnage linéaire des angles, pour une solution WED unique. Ici, la région dense au dessus du disque monte jusqu'aux environs de $\sim 75°$, ce qui explique les changements importants entre les deuxièmes et troisièmes valeurs d'angle.

Structure thermique

La hauteur d'échelle du disque ϵ est l'un des paramètres physiquement vérifiable du WED. Comme les modèles théoriques de structures des disques d'accrétion excluent généralement les régions extérieures où le vent crée les raies d'absorption, en raison de leur quantité négligeable d'émission, j'ai développé des outils pour calculer analytiquement un premier ordre de la structure thermique des solutions de WED.

Après avoir fait le calcul pour une gamme de solutions, l'évolution de ϵ avec le rayon dans la région typique d'émission de vent visible dans les rayons X ($\sim 10^3 - 10^5$ Rg, avec Rg le rayon du Trou Noir) est relativement faible, et donc l'hypothèse d'une hauteur d'échelle constante utilisée pour les calculs de grilles de spectres est une approximation décente. Cependant, elle reste significativement plus faible que les valeurs canoniques de $\epsilon = 0.1$ généralement admises dans la littérature.

Nous évaluons aussi l'influence de différents paramètres sur ces conclusions en échantillonnant l'effet des changements de taux d'accrétion (à travers la fraction d'Eddington) et l'évolution des principaux paramètres des solutions WED, l'indice d'éjection **p** et la magnétisation μ. Bien que l'influence de chaque paramètre soit fondamentalement différente, individuellement, aucun des changements n'est très significatif, et le rapport d'aspect du disque reste typiquement dans une fourchette de $\epsilon \sim$0.01-0.03. Toutefois, il convient d'être particulièrement prudent lors de la comparaison de solutions présentant les combinaisons les plus distinctes de paramètres, telles qu'une luminosité élevée, un indice d'éjection élevé et une faible magnétisation, ou une luminosité faible, un indice d'éjection faible et une magnétisation élevée, car la différence entre la valeur supposée de ϵ et les valeurs réelles dans le disque externe peut devenir problématique.

Pour plus de détails, voir Section 5.2.3.

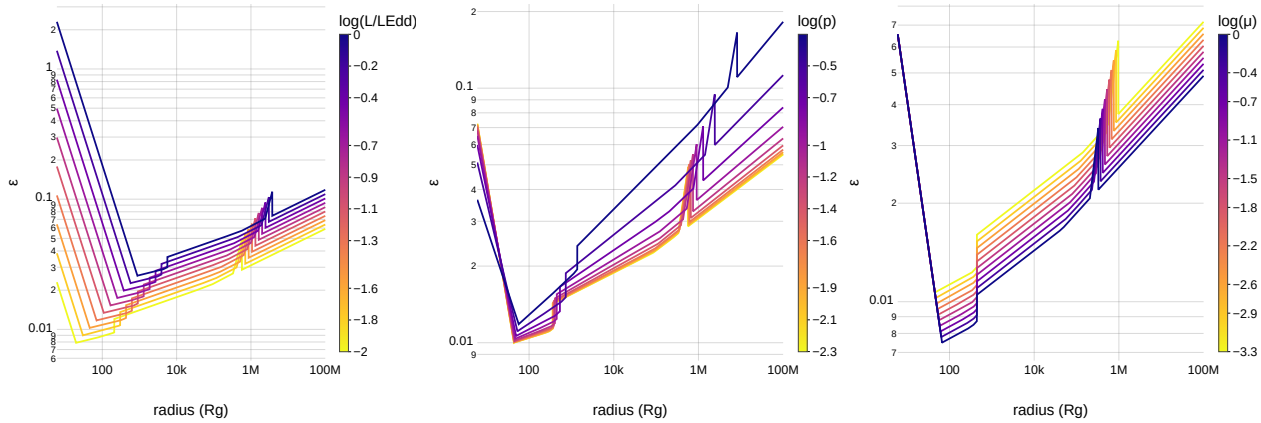

Figure 48: Evolution radiale de la hauteur d'échelle en fonction des variations d'un des paramètres de la solution. Les variations de L/L_{Edd} sont converties en taux d'accrétion pour refléter les gammes typiques de luminosité des états mous d'une BHLMXB en éruption.

Important note: The last few months have seen increasing concerns for a decrease in quality of scientific publications with the growing use of AI (see e.g. Guo et al. 2024). In the wake of a rapidly growing amount of scandals, several works have started to analyze the evolution of vocabulary in scientific publications (Astarita et al. 2024; Gray 2024; Kobak et al. 2024), finding few specific words with an extremely suspicious increase in frequency after the advent of large language models.

It is thus important to clarify my approach: for the sake of efficiency, the english and french overviews of my own work, required by my institution, **ARE** in part based on AI made summaries. However, the rest of this document results **IN ITS ENTIRETY** from the blood, sweat and chalk of its author. Any excessively weird vocabulary is solely the consequence of the writer's poor mastery of English, combined with a disgusting amount of review paper readings, and a very debatable sleep schedule.

In the same vein, the overwhelming majority of the results and plots presented in this work, as well as the codes used to derive them, were obtained and developed entirely by me. The only exceptions are the Suzaku (done by M. Shidatsu) and INTEGRAL (done by T. Bouchet) data reduction, as well as the photoionization results obtained with CLOUDY modeling (done by S. Bianchi), which notably led to the bottom panel of Fig. 4.11. Of course, the codes themselves use many libraries and existing data reduction softwares, which are cited whenever relevant in the appendix.

’ fu it , pur , « -fou ».
os , stance , jus
bi le , jus ’ vivant, ’ .
, le mme lié, poussi e r e .

I

Astrophysical context

1

Black Hole growth in disk-driven systems

1.1 Introduction

1.1.1 Compact Objects

Definitions

- **Compactness**: a dimensionless number, lower than 1, computed from the Mass and Radius of an object, to express the importance of its gravitational effects. Unrelated to density.
- **Compact Objects** (CO): A type of astrophysical object with high Compactness, typically causing significant relativistic effects in their surroundings. Among the final products of the stellar evolution, the White Dwarf (WD), Neutron Star (NS), and Black Hole (BH) are all members of this category.

The term “Compact Object" (CO) refers to a subcategory of astrophysical bodies characterized by the importance of their gravitational effects. A more quantitative definition involves the compactness parameter Ξ, a dimensionless quantity proportional to the ratio of the gravitational energy E_{grav} of a spherical object of mass M and radius R, to its mass energy E_{mass}:

$$\frac{E_{grav}}{E_{mass}} = \frac{-\frac{3}{5}\frac{GM^2}{R}}{Mc^2} \overset{\text{def}}{=} -\frac{3}{5}\Xi \Longrightarrow \Xi = \frac{R_s}{2R} \text{ with } R_s = \frac{2GM}{c^2} \tag{1.1}$$

While the proportionality factor in the definition above can vary, especially according to the conventions used to define the Schwarzschild radius R_s (Schwarzschild 1916), Ξ remains a simple parameter used to give an idea of the intensity of the gravitational field around the body of interest. We notably define $\Xi = 1$ in the case of maximally spinning Black Holes.

The commonly accepted lower limit for compact objects, $\Xi \gtrsim 10^{-4}$, is conveniently placed to include the 3 different astrophysical bodies who require a relativistic treatment, namely the White Dwarf (WD, $\Xi \sim 10^{-4}$), Neutron Star (NS, $\Xi \sim 0.2-0.4$) and Black Hole (BH, $\Xi = 1$). Those astrophysical objects can either be created at the endpoint of stellar evolution, which explains their other appellation as stellar remnants, or through accretion processes. BHs are also known to be created with different scenarios, such as the merger of other COs with high enough masses (see Sec.1.4.2).

1.1.2 Stellar Remnants

The field of stellar evolution (see Lamers & Levesque 2017a for a review) is a vast and rich topic, whose intricacies go way beyond what is necessary to introduce the objects relevant to this work. We shall thus restrict ourselves to a simplified overview of the creation of stellar remnants.

The existence of stars is enabled by a fragile balance between an outward pressure, resulting from nuclear fusion, and gravitational attraction. This process leads to embedded shells of more complex elements towards the core, with more diversity for more massive stars, where the conditions are sufficient to allow the fusion of more elements (Lamers & Levesque 2017b).

In the case of stars with **masses below** $\sim 8-10\,M_\odot$, the fusion process ends between Helium and Neon (Calcaferro et al. 2018; De Loore & Doom 1992; Gerónimo et al. 2022). When the star has attained its final structure and no more elements can fusion, the shells undergo a series of contraction and

Definitions

- **White Dwarf** (WD): A degenerate body of $\lesssim 1$ Solar Mass, sustained by the quantum pressure of its electrons. The end point of stellar evolution for stars of few solar Masses.
- **Neutron Star** (NS): A mostly neutronic body of $\sim$ 1-2 Solar Masses, sustained by the strong nuclear force and the quantum pressure of its neutrons. The end point of stellar evolution for stars of $\sim$ 10-20 Solar Masses.
- **Black Hole** (BH): A region of space(-time) with enough mass to prevent anything escaping from it, due to relativistic effects. The end point of stellar evolution for most stars above $\sim$20 Solar Masses.

expansions until the star finally expels its outer layers, leaving the core exposed. The remaining matter is in a quantum degenerate state, and thus the Pauli exclusion principle, which keeps nearby **electrons** from being in the same quantum state, leads to a **degeneracy pressure** sufficient to **balance out the gravitation**. This object, with temperature, density (and thus magnetic fields) orders of magnitudes above stellar values, a radius near $\sim 1-2\%\ R_\odot$ and Ξ between $\sim 10^{-4}$ and 10^{-3}, is called a **White Dwarf** (Anderson 1929; Chandrasekhar 1931).

For more **massive stars**, the fusion culminates in iron, the most stable of all elements. As such, a similar process happens with the iron core, but the energy needed to counteract gravity is much more important (Fowler 1926). For initial masses of $\mathbf{M} \lesssim 20\,\mathbf{M}_\odot$, when the core goes beyond the Chandrasekhar mass (Chandrasekhar 1931), the electron degeneracy pressure is no longer sufficient. The iron core was already affected by a neutronisation process, in which protons capture electrons and form neutrons and neutrinos, but the collapse greatly facilitates this reaction, up until nuclear density. At this point, the **strong force** becomes prevalent and, assisted by the **neutron degeneracy pressure** on the edges of the now mostly neutronic core, is able to oppose gravity, **interrupting the collapse** (Tolman 1939).

The brutal stop of the contraction initiates a shockwave, which ejects the external parts of the star, after a complex process involving the apparition of convection instabilities between the core and the shock wave. During this process, the tremendous amount of neutrinos generated by the neutronisation bombard the elements in the external layers, creating radioactive isotopes of the heaviest elements in the Universe in what is called explosive nucleosynthesis (Truran 1977). The gamma emission created by their prompt decay is then progressively reprocessed by the opaque matter, leading to a first thermal emission. However, the ambient medium rapidly becomes optically thin, due to the expansion of the shock front, and allows the emission of the extreme amount of electromagnetic radiation hitherto blocked, in what is called a **Supernova** (Baade & Zwicky 1934), although most of the energy is dissipated in the form of neutrino emission and Gravitational Waves (GW) (Ott et al. 2013). Behind stays a **Neutron Star** with a compactness of $\Xi \sim 0.2$, a radius of a few tens of kilometers, and a magnetic field increased to extreme values in the range of $10^8 - 10^{15}$ G by the shrinking of the remnant.

In the most extreme cases however, with **stars** of initial masses **above** $\sim 20\,\mathbf{M}_\odot$ (although the limit also depends on other parameters, such as angular momentum and metallicity), the strong force will not be able to even out gravity (Tolman 1939). In the resulting collapse, the matter condenses in a **region** where **space time** is so **bent** not even light can escape, and effectively decoupled from the rest of the Universe: a **Black Hole**. The limit, called an event horizon, marks the radius beyond which all information within becomes unavailable. In the case of a non-rotating Black Hole, the event horizon is located at the Schwarzschild radius R_S defined in Sec. 1.1.1. It is worth noting that there are other, more exotic scenarios depending on the mass and kinetic momentum of the initial star (Pons et al. 1998), involving a Supernova or not, and sometimes even the destruction of the star before a Black Hole can be created (see Sec. 1.4.2), but the endpoint is, in most cases, the same.

1.1.3 Accretion Disks

Definitions

- **Accretion**: A progressive growth of mass of an astrophysical object due to attraction of surrounding matter, dominated by gravitational forces. Among the most influential processes at many scales of the universe.

Accretion is one of the most common processes in our Universe, and is prevalent in the formation and evolution of a number of celestial bodies, from planetary systems, to stars, to stellar remnants and, at a larger scale, even galaxies themselves. Putting aside specific cases like Bondi-Hoyle accretion (Edgar 2004), the vast majority of physical configurations involve matter with pre-existing angular momentum, which naturally leads to the formation of a disk. To understand why, let us consider a classical scenario, involving mass transfer in a binary system, composed of a donor, usually a star or a stellar remnant, and an accretor.

The most common mechanisms of accretion in binaries are the capture of a significant amount of stellar wind emitted by the donor (namely, stellar wind accretion), and so-called Roche Lobe overflow. We will come back on the differences between the two in Sec.1.2, and a more complete derivation each can be found in e.g. Frank et al. (2002).

In the simplest case, we can consider the trajectories of a test particle in the gravitational field of the two bodies orbiting together, whose equipotentials delimit the so-called Roche Lobes, i.e. the positions at which the attraction generated by both members of the binary are equal. We show a simple example with orbits around point-like masses in Fig. 1.1, accompanied by a side view to highlight the 3D shape of the surface. The dimensions of the Roche lobe are mostly dependent on the separation between the members of the binaries and the mass ratios of the two components (Eggleton 1983, see also Pourmand & Ivanova 2023 for an up-to-date derivation).

A particle originating from the donor, whenever crossing the so-called "L1" point, ends up in a region dominated by the gravitational field of the accretor, and, disregarding any initial momentum, will settle in a uniform circular motion around the second body. This is a stable configuration where the particle revolves at the Keplerian velocity:

$$v_\phi(R) = \left(\frac{GM_{ac}}{R}\right)^{1/2} \tag{1.2}$$

Where R is the distance to the center of the accretor. Now, if instead of a single particle, a flow of gas crosses the L1 point, it will first settle into a ring. From then on, if, and only if a process allows for angular momentum transfer within the accreted matter (typically due to energy dissipation), the ring will progressively diffuse both inwards and outwards, "naturally" leading to the creation of a disk. Finally, the matter feeding the accretion disk invariably spreads closer and further from the object, the material neighboring the accretor eventually falls onto it, completing the mass transfer.

In practice, the processes which can be at the origin of this dissipation are few, and lead to vastly different types of disks depending on the central object and accretion rates. The issue is that most rely on instabilities which are both impossible to resolve analytically and challenging to simulate, due to the extreme differences in scales (time, space) between the microphysics governing the behavior and the astrophysical system itself. For Black Holes, the first notable successful approximation was derived in the seminal work of Shakura & Sunyaev (1973), with a parametric description of the dissipation via the so-called α viscosity prescription. Later developments with more realistic cases of magnetized disks highlight the importance of specific processes, such as the Magneto-Rotational Instability (Balbus et al. 1991), but their full description remains an open subject. Since the literature on this topic is as unstable as what it hopes to describe, we encourage the reader to search for the latest developments in the matter[4].

[4] e.g. at https://arxiv.org/search/?query=GRMHD+disk&searchtype=all

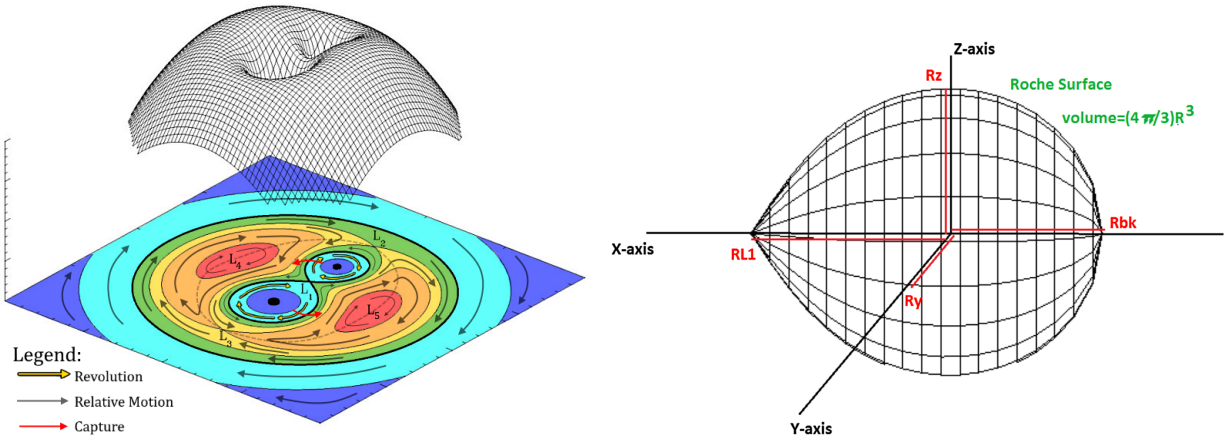

Figure 1.1: **(Left)** Equipotentials for a simplified binary system, with the Roche Lobe in bold, from wikimedia. The arrows show the upcoming trajectories of a test particle and highlight how only the L1 point at the center allows for direct mass transfer. The mesh above the projection represents the gravitational field.**(Right)** Side view of a Roche Lobe surface. While the total volume can be linked to that of a sphere of equivalent Radius R_{eq}, the individual dimensions are highly non-symmetric. From Leahy & Leahy (2015).

We shall come back to the intricacies of this topic in Sec. 1.2.3, 1.3.3 and 2.2.2). In the meantime, let us rejoice that a wide range of observational factors, from the direct observation of protoplanetary systems (see Fig. 1.2) to the high energy emission of Compact Objects (see Sec. **??**) confirm the existence of accretion disks.

Indeed, it is commonly accepted that the infalling material is greatly heated by viscous dissipation along the entire drift in the accretion disk, and thus must radiate a fraction of its energy. At first order, the potential (gravitational) energy E_p and kinetic energy E_k of a particle in the region disk can be expressed as:

$$E_p = -\frac{G m \mathrm{M_{ac}}}{R} \mid E_k = \frac{1}{2} m \big(v_\phi(R)\big)^2 = \frac{1}{2} m \frac{G \mathrm{M_{ac}}}{R} \text{ if Keplerian motion} \tag{1.3}$$

From an energy balance perspective, when the particle loses angular momentum and drifts towards the center, its potential energy decreases and its kinetic energy correspondingly increase, but not at the same rate: if we assume that the particles remain in Keplerian motion, E_k only increases half as fast as E_p decreases, and so the remaining half of energy must be dissipated in another way, namely heat[5]. Assuming that a **constant** fraction η of the liberated energy is liberated as radiation, we can express the output luminosity once the particle orbit reaches the surface of the accretor R_{ac} as:

$$L_{out} = \frac{\partial(\eta E_{out})}{\partial t} = \frac{\partial(\eta E_k)}{\partial t} = \eta \dot{m} \frac{G \mathrm{M_{ac}}}{2 R_{\mathrm{ac}}} = \frac{1}{2} \Xi \mathrm{c}^2 \eta \dot{m} \tag{1.4}$$

with $\dot{m}$ the accretion rate. The dependency in Ξ hints at how the nature of compact objects makes this process much more efficient. In reality, other elements also have to be considered, such as the remaining half of kinetic energy liberated by the collision between the accreted material and the surface of the compact object, which, combined to the differential rotation of the surface and the disk, adds another layer of heating -and thus emission- to the innermost parts of the disk (Popham & Sunyaev 2001). Black Holes, having no tangible surface, are exempt of this, and the existence of an Innermost Stable Circular Orbit (ISCO) for BHs, beyond which the distortion of space-time forces the matter to approach the object, adds another layer of complexity (Mummery & Balbus 2023). Intense magnetic fields can

[5]This highlights the difficult requirement for a high efficiency of the underlying dissipative process

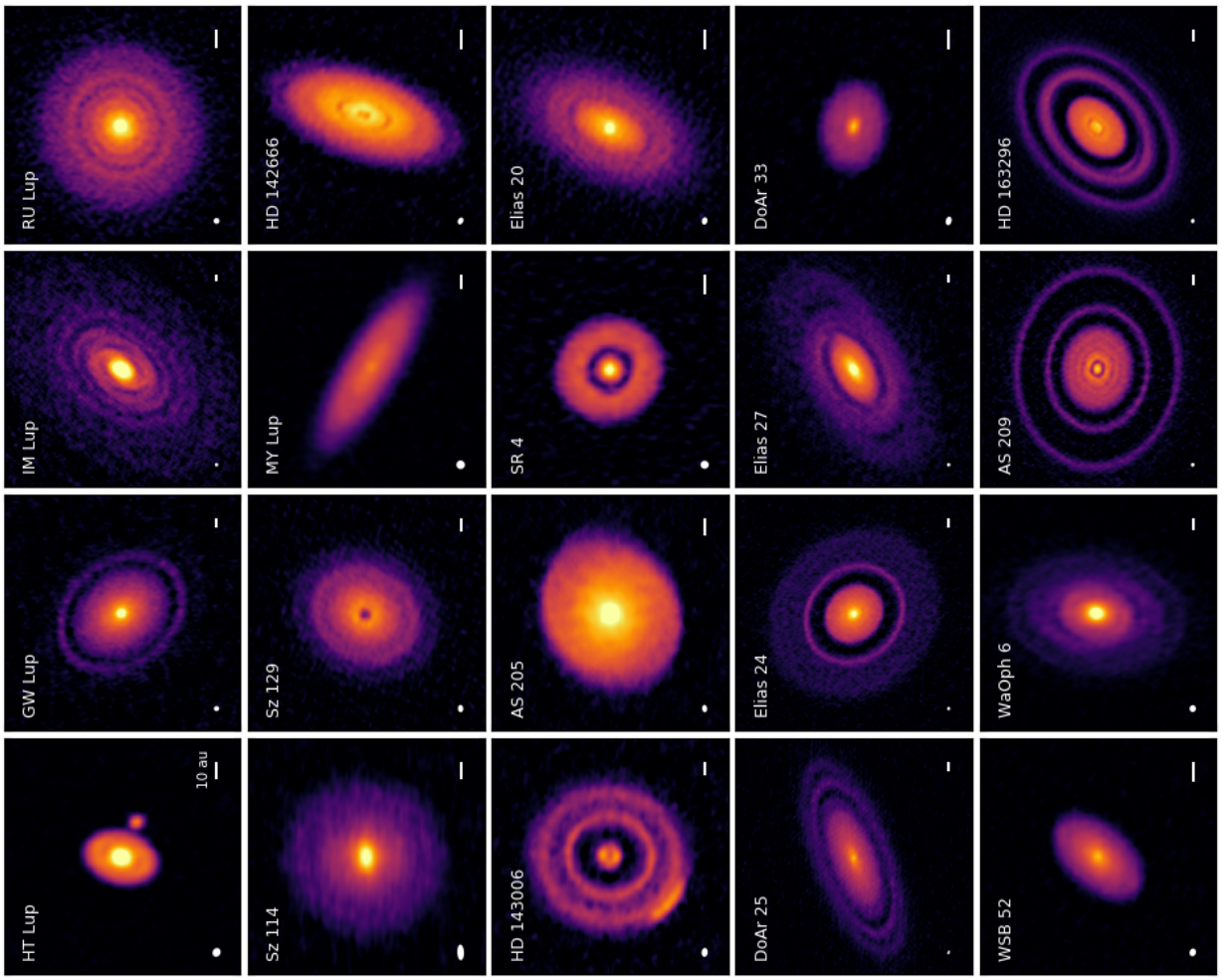

Figure 1.2: Radio observations of the DSHARP sample of protoplanetary disks, from Andrews et al. (2018). In these advanced systems, the rings and cavities indicate the presence of local stable orbits and planets, and thus accretion must rely on more complex structures (see e.g. Martel & Lesur 2022)

also distort the shape of the accretion disk to the point where it becomes unable to reach the surface of the most magnetized accretors (notably Neutron Stars). In this case, the material is constrained to follow the magnetic field lines and, as such, is accreted onto the magnetic poles of the compact object (Pringle & Rees 1972).

Because of this large taxonomy of accreting scenarios, the total emission resulting from the accretion is often the combination of several radiative processes (e.g. multiple thermal emissions, synchrotron emission, inverse compton scattering,...) originating from various positions within the disk (see e.g. Siemiginowska 2007 for a review of the emission processes). Yet, in total, with e.g. $\eta \sim 0.15$ for NS and up to $\eta \sim 0.4$ for Kerr Black Holes, accretion by COs is among the most efficient energy conversion processes in the universe, to the point where the liberated energy becomes a non-neglibile fraction of the rest mass energy of the particles $E_m = mc^2$ for $\Xi \rightarrow 1$, well above the meager $\eta \leq 0.01$ of nuclear fusion.

We note that in the more advanced theories of accretion disks, supported by multiple observational detections across a range of accreting systems, the accretion is systematically accompanied by ejections of matter coming from a range of regions in the disks. Thus, nowadays, it seems that instead of an "accretion disk", it is more relevant and less misleading to speak of an "accretion-ejection structure".

These ejections can be ambiguously called "outflows", "winds" or "jets" depending on their properties. For now, we will refer to these phenomena as "outflows" unless they are unambiguously defined in

a specific context. We will give a short description of "jets" in Sec. 1.3.3, before focusing on "winds" primarily from the start of Sec. 2 onward.

Before narrowing down on the descriptions of outflows and their origin, which will be the main focus of this work, it is useful to make a brief overview of the physical systems in which accretion disks are involved, and their evolution, to highlight the most relevant unknowns. For the sake of brevity, we will restrict ourselves to a biased overview of the ones most relevant to our case, namely Black Holes, particularly in X-ray Binaries.

Remember me

- The most standard form of mass transfer via accretion is the **accretion disk**, where rotating matter, either coming from the environment or unbound from a donor, progressively drifts inwards towards the accretor.
- Accretion in Compact Objects is among the most efficient energy conversion processes in the universe.

1.2 X-ray Binaries

1.2.1 Formation channels

Although it is hard to put precise numbers on the fraction of binary systems among stars, the proportion is known to be significant, varying between ~ 0.2 and ~ 0.8 depending on the system considered (see e.g. (Duchêne & Kraus 2013) for a review). There is a vast range of possible outcomes for these systems, depending on their mass, composition, and orbital separation, from a single star to two separated Compact Objects, (see e.g. Belloni & Schreiber 2023 for a review). Fig. 1.3 provides an overview of the main evolutionary paths and endpoints, which we shall briefly present in the following sections.

In stellar binaries, multiple scenarios can lead to the mass transfer mechanism discussed in Sec. 1.1.3, and thus affect the evolution both the donor and the accretor. As the delimitation of the Roche Lobes is mainly dependent on the mass of each component and their angular momentum (i.e., orbital separation/period), whenever low and intermediate mass stars expand significantly in the later phases of their evolution, they tend to become bigger than their Roche Lobe. In parallel, all binary systems see their orbital periods (and thus Roche Lobes) progressively shrink due to Angular Momentum Loss (AML). One systematic cause for this effect is the emission of gravitational wave radiation from the system, on top of several other possible mechanisms depending on the nature of the stars, such as magnetic wind braking.

In both cases, the resulting **Roche Lobe Overflow** leads to significant amounts of mass loss from the outer regions of the donor, some of which will be accreted by the remaining star in the form of a disk. This directly affects the masses and chemical compositions of both members of the binary. Once this happens, depending on how the Roche Lobe evolves with the mass loss, the mass transfer can become unstable and lead to a **Common-Envelope** evolution, where the donor's outer region expands far enough to cover its companion (see (Ivanova et al. 2013) for a review). Both of these processes end once the donor star is stripped of enough of its envelope to fall back inside its Roche Lobe, where it may continue to evolve and repeat the process. The final stages of evolution are highly dependent on the masses of both resulting stars, as we will detail in the next subsection.

1.2.2 Classification

If the core is too light, it remains as a White Dwarf and the system will typically evolve into a close binary, involving Roche Lobe overflow from another main sequence star onto a WD and thus forming a **Cataclysmic Variable**. With several thousands of detections, this is by far the most common type of

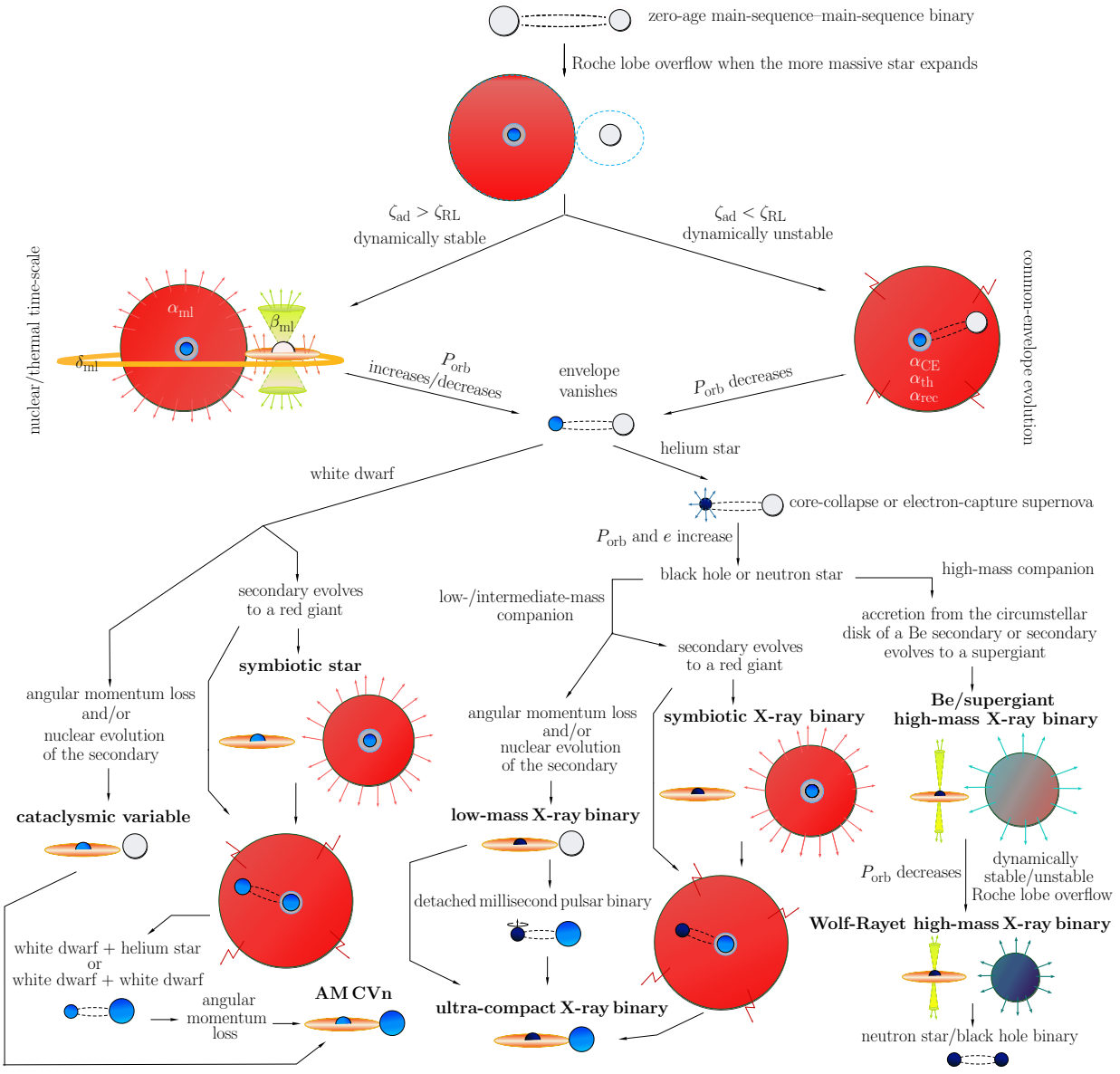

Figure 1.3: Formation channels leading to the formation of different types of X-ray Binaries in so-called "primordial" systems, namely without the involvement of additional bodies. From Belloni & Schreiber (2023).

X-ray Binaries, and the only one where the capabilities of current instruments are approaching complete samples in our neighboring Galactic environment, namely the detection of all existing CVs at less that few hundred parsecs (Inight et al. 2021). They are subdivided in different types, historically subtypes of "Novae" (an observational term for transient bright sources). First, and most commonly, Dwarf Novae, with recurrent, ∼ monthly disk driven brightening events or outbursts (see e.g. Lasota 2001 for a review, and Sec. 1.2.3). In parallel, (classical) Novae exhibit much rarer, brighter outbursting events due to the nuclear fusion of matter accumulating on the WD surface (see e.g. Chomiuk et al. 2021 for a review). In the even more elusive "recurrent" Novae, this process occurs periodically, although over several decades.

Aside from the nuclear fusion, which produces a thermal component in the soft X-rays, the emission process resulting from the accretion of CVs extends up to the hard X-rays, and depends on the intensity of their magnetic field. This will determine whether the matter in the innermost regions of the disk will be driven by the magnetic field onto the WD poles, or decelerated in a boundary layer around the NS surface. These two accretion modes lead to predominantly Bremsstrahlung emission for magnetic WDs,

Definitions

- **X-ray Binaries** (XRB): subclass of binary stellar systems where accretion onto one of the astrophysical bodies emits significant amounts of X-rays. The X-ray emission is mainly due to accretion onto the compact object, which weighs up to few solar masses, and results from the latest stages of evolution of progressively denser stars.

  The behavior and evolution of the system is very dependent on the nature of the accretors: systems with a primary White Dwarf can form a range of different subtypes, most commonly Novae and Cataclysmic Variables. Systems with Neutron Stars or Black Holes are divided in two main categories:

  - **Low-Mass X-ray Binaries** (LMXB) are X-ray Binaries with a small secondary star ($\lesssim 1 M_\odot$), often less massive than the Compact Object. In these systems, the latter often **accretes** the matter of the former when the star expands beyond the limits of its gravitational potential, called the **Roche Lobe**.
  - **High-Mass X-ray Binaries** (HMXB) are X-ray Binaries with a heavy secondary star ($\gtrsim 10 M_\odot$), often more massive than the Compact Object. The stars in these systems behave very differently, and naturally lose significant amounts of mass through dense **stellar winds**, which directly feeds the Compact Object. Although a disk can also form around the accretor, the dynamics are governed by the ejections of the companion star.

and thermal emission for non-magnetic WDs (Mukai 2017).

A number of more specific configurations exist, such as Super-Soft X-ray Binaries, where restrained mass ratios enable stable, long-term hydrogen fusion burning (Galiullin & Gilfanov 2021), Symbiotic Stars, referring to CVs with a low-mass evolved red giant (Munari 2019), and AM Canum Venaticorum stars (AM CVn stars) with very short periods and specific accretion and emission patterns (Ramsay et al. 2018) . The list goes on, but these systems are not the focus of this work.

Coming back to the previous step in binary evolution, if the donor core stripped of its envelope is too heavy, it will eventually collapse and create a Supernova, forming a Neutron Star. Similarly, an even more massive core would lead to the creation of a Black Hole. However, supernovas often imply strong natal kicks during the creation of the Compact Object. This can lead to a much wider orbit for a significant period of time, or a complete separation of the Binaries. From here on, it can be important to distinguish the Binaries resulting of so-called "primordial" systems, namely the initial binary in which the accretor was born, from other systems resulting from the dynamical interaction of an ejected CO with other stellar systems (often in dense environments). The main consequence of that effect is that while X-ray Binaries involving compact objects are typically discovered in the Galactic plane, and proportionally more common in globular clusters (Van Den Berg 2019), they are also (rarely) found at much more extreme latitudes (Bahramian & Degenaar 2023; Fortin et al. 2024; Jonker & Nelemans 2004), where they are more likely to have been ejected outwards from the Galactic plane.

NS and BH X-ray Binaries exhibit quite similar properties, and as such, are distinguished according to the stellar type of their companions, which has the most incidence on the accretion processes.

In **Low-Mass X-ray Binaries** (LMXBs, see Bahramian & Degenaar 2023 for a review), the Compact Object accretes the matter from a low-mass star ($\lesssim 1 M_\odot$) typically via Roche-Lobe overflow. Although orders of magnitude brighter than CVs, they are also significantly less common, with around $\sim$ 300-400 systems currently detected in the whole Galaxy (Avakyan et al. 2023; Fortin et al. 2024). The majority of

LMXBs are transients, exhibiting rare, erratically repeating outburst patterns lasting several months to years, in between $\sim 1-10+$ years periods of quiescence. The origin of this phenomenon is thought to be similar to the mechanism powering outbursts in Dwarf Novae (see Sec. 1.2.3). Because of the very long life span of the low-mass companion ($\gtrsim 10$ Gy), the LMXB configurations are expected to remain stable for similarly long timescales, and can thus become completely uncorrelated from their original stellar environment (Repetto et al. 2012).

For this category of accretors, uncovering the nature of the Compact Object can prove very difficult, due to the many similarities of the accretion disks surrounding BH and NS LMXBs. Among firmly identified objects, NS outnumber BH accretors by a factor ~ 2 (in accordance with theoretical predictions for primordial systems, see e.g. Kalogera & Webbink 1998). However, only two methods can unambiguously identify BH and NS in LMXBs, and the nature of most LMXB candidates remains unclear (Fortin et al. 2024).

- **Mass estimates:** The most straightforward way to distinguish the two categories of objects are direct mass estimates: since both observations and theoretical predictions agree on an upper limit of $\sim 2.5 M_\odot$ for NS masses, measurements above $\sim 3 M_\odot$ ensure the presence of a BH accretor. In practice, the issue is often the validity of the methodology: "dynamical" measurements, computed from radial velocities using optical spectroscopy of the companion (Casares & Jonker 2014), are by far the most reliable method, but are limited to systems in which the secondary is identified and bright enough for detailed spectroscopy. Unfortunately, many LMXBs in the Galactic plane are found in dense regions with very strong interstellar absorption, preventing good optical measurements. Less standard methods, such as using the properties of the Hα line (Casares 2016), are both less precise and more restrictive in terms of physical systems.
- **Surface properties:** While the X-ray spectral properties specific to BHs, such as the emission from the plunging region (Mummery & Balbus 2023), remain very difficult to disentangle with the current generation of X-ray telescopes, NS exhibit three unique (but not ubiquitous) signatures, consequences of the presence of a solid surface. First, thermonuclear (type-I) X-ray bursts, a rare type of flaring event in X-rays with very recognizable properties, consequence of runaway fusion of matter accumulating on the NS surface (Strohmayer & Bildsten 2003). Secondly, coherent pulsations from the rotation of the hotspots created by magnetic accretion onto some of the NS, in this case acting as X-ray pulsars (Bildsten et al. 1997). Thirdly, the thermal emission of the NS surface itself, which can be observed as a X-ray blackbody component even in quiescence, provided the emission is not at lower energy and/or absorbed due to insufficient temperature, and that there are no residual accretion or magnetic processes to reprocess that component (Guillot et al. 2013; Steiner et al. 2018).

To complete the picture, a range of other spectral diagnostics can provide less decisive arguments in favor of one type of accretor. Both types of sources are known for emitting radio jets, and in NS, the proportion of radio to X-ray flux is typically an order of magnitude lower (Gallo et al. 2018), although with too much spread and exceptions for a clear cut conclusion. The spectral properties of the sources in optical and infrared (Russell et al. 2007), or at low accretion rates (Wijnands et al. 2015) can also exhibit specific properties for some type of NS sources.

For sources in which the nature of the accretor is known, it is possible to refine the classification depending on the properties of the central objects. Black Holes are inherently limited to 2 physical parameters, namely mass and intrinsic angular momentum/spin (the electric charge is effectively zero for astrophysical BHs). The mass, being restricted to $\sim 3-15\ M_\odot$ from observations (Corral-Santana et al. 2016), has limited influence on the accretion processes beside changes in maximum luminosity but strong implications on the evolution of the sources (see Sec.1.4.2). As we will see in Sec. 1.3.3, the spin has a more diverse impact on the accretion properties, including the disk inner radius (due to changes in innermost circular orbit), and possibly the jet, but currently, spin measurements in Black Hole are

very tentative and mostly in disagreement with other BH populations (see Sec.1.4.2), so it is difficult to draw any conclusion.

On the other hand, NSLMXBs exhibit much more distinct properties. A significant fraction are X-ray pulsars and thus involve magnetic accretion, and about 20% are identified as Accreting Millisecond X-ray Pulsars (AMXPs, see Campana & Salvo 2018 for a review). A very small fraction, called transitional millisecond radio pulsars (tMSRPs), exhibit pulsations in radio during restricted intervals, hinting at a link between the AXMP population and the broader class of radio pulsars in NS systems.

The binary system itself can also lead to the creation of subgroups with different properties, which are illustrated in Fig. 1.4. First, Ultra-compact X-ray Binaries (UCXBs, see Bahramian & Degenaar 2023 for a review), identified by orbital periods below ~ 1.2h, and consequently restricted to systems with a sub-dwarf or white dwarf donors. Interestingly, for now, no BH UCXB has been clearly identified, and this expands to a more general lack of low orbital periods in BHs compared to NS LMXBs. This may be a byproduct of lower accretion efficieny in BHs for short orbital period systems (Knevitt et al. 2014). Among more exotic combinations, Symbiotic Stars with WDs have an analogue among LMXBs, called Symbiotic X-ray Binaries (SyXBs, see Bahramian & Degenaar 2023 for a review), and referring to a binary with a BH or NS wind fed by a low-mass giant companion. These systems are typically fainter than standard LMXBs, and remain overwhelmingly transients. For now, no BH SyXB has been confirmed.

Another parameter used to categorize the sources is the inclination. Besides being paramount to disentangle the physical properties and accretion state of the source, it can be used to infer the presence of several spectral-timing features[6] depending on whether the systems are "high" or "low" inclined, but these definitions vary depending on the physical mechanism considered. However, two precise classes exist for very high inclined sources:

- **Dipping** sources, or "dippers", refer to all types of XRBs exhibiting rare, erratic flux drops in their lightcurves, interpreted as obscuration by dense material at the surface of the disk, or flaring of the disk itself. In XRBs, this phenomenon remains very elusive and poorly understood, and no review has yet been made on the subject, although one is in preparation (D. Altamirano, priv. communication, see also Sec. 3.2, Sec. 3.6 and Sec. 4.5 and references therein). Dipping is nevertheless considered as a very strong argument in favor of inclinations $\gtrsim 55°$ (see Appendix A in Motta et al. 2015).
- **Eclipsing** X-ray Binaries are systems at even higher ($\gtrsim 80°$) inclination angle, in which the companion periodically obscures parts or all of the disk. Besides providing a very direct way to identify the orbital periods and their evolution (and the only direct way in the absence of optical companion), they also allow to study the disk properties through eclipse mapping (see Baptista 2007 for a review).

We also note the existence of a specific group of Very-Faint X-ray Binaries (VFXBs, see Bahramian & Degenaar 2023 for a review), referring to LMXBs with peak luminosities below 10^{36} ergs/s, recently discovered due to the telescope sensitivity required for their detection. They mimic the persistent/transient dichotomy of different subgroups of the main population, but their very low accretion rate remain puzzling, and is naturally more difficult to investigate with their low luminosities. Most VFXB with identified accretors are NS, but this may be a byproduct of the help of X-ray bursts in detecting the sources, and a handful of BHs have been dynamically confirmed. Several scenarios have been proposed to explain their peculiar properties, including obscuration due to very high inclination angles, but this should only account for a part of the existing population (Wijnands et al. 2006). It is worth noting that with such an arbitrary selection criteria, VFXBs may also gather the tail ends of several different populations.

[6] one of which has led to the writing of this thesis

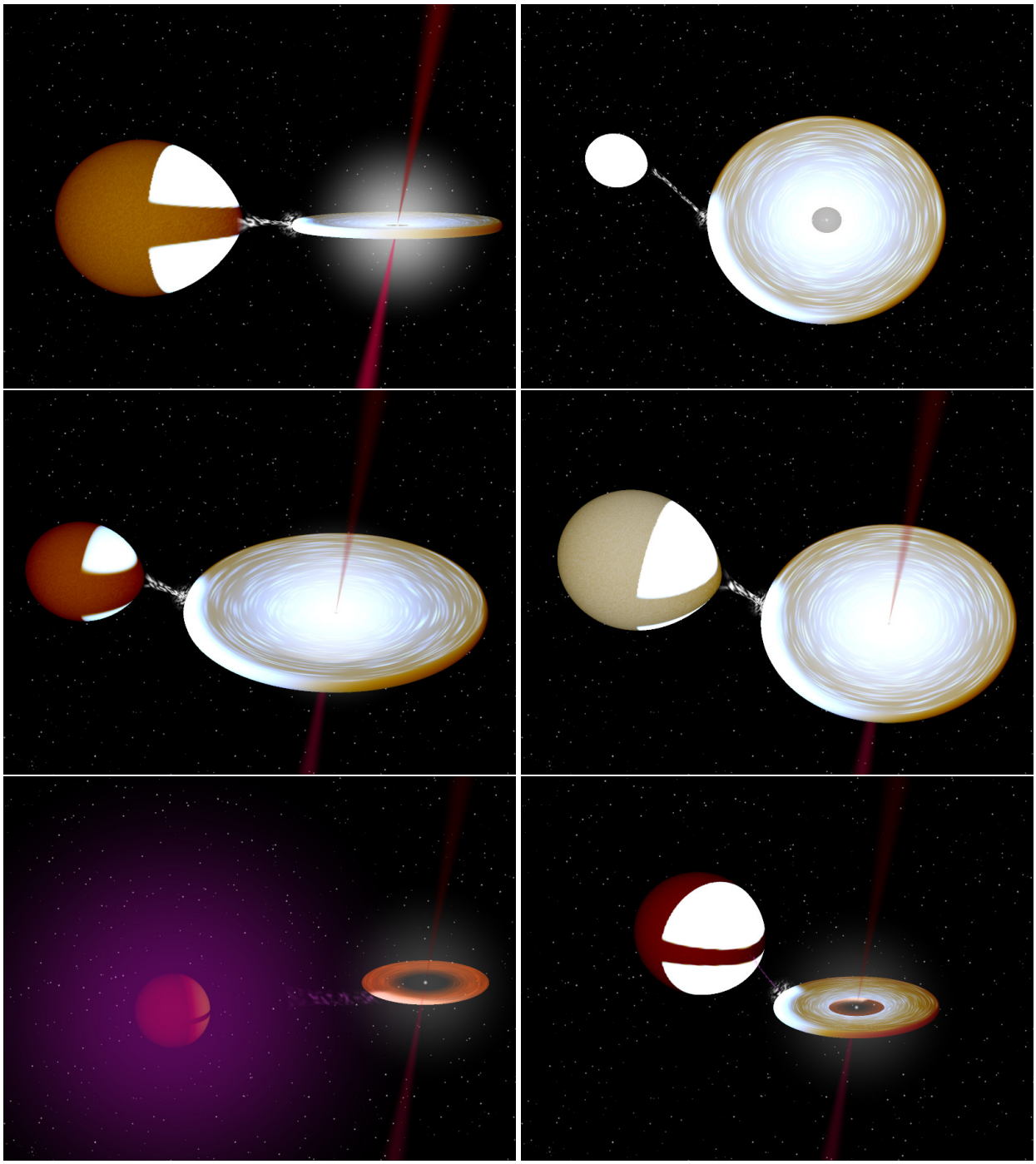

Figure 1.4: Illustrations of several configurations of LMXBs, from Bahramian & Degenaar 2023, using the BINSIM code (Hynes 2002). These images are at scale and provide an idea of the brightness and extension of the donor and accretion disk in different scenarios. From top left to bottom right: eclipsing LMXB in outbust, low-inclined Ultra Compact XRB, outbursting BHLMXB, persistent Z-source NSLMXB, symbiotic XRB, Very Faint XRB.

Finally, the pendant of LMXBs for high mass companions are the **High-Mass X-ray Binaries** (HMXB, see Fornasini et al. 2023 for a review), in which a NS or BH accretes from a high-mass ($\gtrsim 10\ M_\odot$) companion. In this scenario, the companion is either a massive Be giant (a B-type star with emission lines) or a supergiant, and naturally expels a significant ($\gtrsim 10^6\ M_\odot\ y^{-1}$) amount of matter via stellar winds (Smith 2014). This is typically the main mechanism powering accretion, although transient disks have been detected in several sources (Kretschmar et al. 2019), and recent simulations have shown that a persistent disk may form under certain conditions (El Mellah et al. 2019). Because of this specificity in accretion process, most HMXBs are either persistent or outbursting at a high cadence, and are bright not only in X-rays but also in optical and UV, due to the companion's intrinsic emission. Although only ~ 150 systems have been directly detected in our galaxy (Neumann et al. 2023), many have also been detected in neighboring galaxies (Mineo et al. 2012) thanks to their accretion patterns. Due to the short lifespan of massive stars and more important Angular Momentum Loss, the HMXB configuration is expected to begin few $10^6 - 10^7$ years after the birth of the initial binary system, and last for few 10^4 years (Postnov & Yungelson 2014). They are thus very correlated to their initial stellar forming regions, and are expected to play a role in Star Forming Galaxies and even the Reionization (Jeon et al. 2014). Moreover, since one of their natural evolutionary path is the creation of a double Compact Object, they are one of the main formation channels for stellar mass Gravitationnal Wave mergers (Belczynski et al. 2002).

Similarly to other XRBs, HMXBs are also divided into several subgroups, mainly depending on their companion and emission properties. The $\sim 60\%$ of detected HMXBs containing a Be-type star are Be-HMXBs, with very high orbital periods ($\sim$ 10d–y) and thus very wide Roche Lobes. They exhibit regular bright outbursts when the CO accretor reaches the "decretion disk" (a specific type of disk formed by the matter expelled in the winds of the companion, see Ziolkowski et al. 2002), which biases the detected distribution in their favor. They are completed by $\sim 32\%$ of SuperGiant HMXBs (sg-HMXBs), involving more general early type supergiant stars.

The lower end ($\lesssim 10$ d) of the orbital period distribution in these systems are persistent sources, which can be much fainter and thus significantly more difficult to detect than Be-XRBs. The higher end of the orbital period distribution form transient systems exhibiting distinct flaring characteristics, called Supergiant Fast X-ray Transients (SFXT). The last category, Wolf-Rayet HMXBs (WR-HMXBs), includes the direct descendant of the two main subgroups, in which the companion has lost most of its Hydrogen due to stellar winds. The donor thus turn into a massive Helium core Star, and enters a phase called the Wolf-Rayet (van den Heuvel et al. 2017) where it reapidly most of its outer layers in the form of stellar winds, causing the binary orbit to shrink to very low ($\sim$ h $-$ $\sim$ d) orbital periods due to AML. This is the last step before the companion implodes into a supernova (McClelland & Eldridge 2016) and the binary either breaks or turn into a pair of Compact Objects.

The perceptive reader has surely realized that none of the former categories include systems with a BH or NS accretor and a $1-10 M_\odot$ stellar companion. This portion of the companion mass distribution is sometimes split into the distinct Intermediate-mass X-ray Binary category (IMXBs, see e.g. (Tauris et al. 2006)), but most of their properties are reminiscent of LMXBs, as the companions do not expel significant winds, and thus the compact objects still accretes through Roche Lobe overflow and an accretion disk. In addition, in systems with NS, the high mass ratio in favor of the companion leads to either Common-Enveloppe evolution or unstable Roche-Lobe accretion, limiting the life expectancy of the systems to few ~ 1000 y, and thus significantly biases against their detection. Black Holes, being more massive, are typically exempt of this issue and allow for more stable systems.

Because of their similar behavior, in the rest of this work, we adopt the more broader distinction effectively used in the literature: any BH or NS Binary in which the mass transfer mainly happens through Roche-Lobe overflow and an accretion disk, without significant wind of the companion, is considered an LMXB.

1.2.3 Outbursting mechanism

In X-ray Binaries powered by accretion disks, the presence and recurrence of outbursts have been historically explained with the Disk Instability Model (DIM, see Hameury 2020; Lasota 2001 for reviews).

Remember me

- Most Low-Mass X-ray Binaries are **transient** systems, alternating between long periods of quiescence, where the primary accretes at a very small rate and emits negligible amounts of radiation, and **outbursts**, short (months to years) periods of very high accretion where their luminosity increases dramatically.

This model proposes a duty-cycle of repeating outbursts and quiescence periods, consequence of a region of thermal instability in the parameter space of the classical α prescription of accretion disks, combined with a significant change in disk viscosity between the different periods. It relies on the appearance of thermal instabilities (Field 1965) to brutally change the structure of the disk.

The thermal equilibrium of accretion disks typically results from the balance of radiative cooling, which is a function of temperature, and viscous heating, which is a function of the surface density Σ and of the viscosity parameter α. To illustrate the parameter space of the solutions, we show in the upper left panel of Fig.1.5 a surface density - effective temperature diagram. In this graph, the red-orange and cyan-blue lines show two distinct α disk solutions, in between which the disk will alternate depending on its configuration.

Indeed, in any solution, the thermal equilibrium of the disk depends on its opacity, which itself is a function of Temperature and (surface) density. In the bottom (red or cyan) portions of the S-curves, the opacity is dominated by hydrogen scattering, the cooling rate is a positive function of the temperature, and thus the disk is **stable**. Similarly, at high temperatures (orange or blue), the opacity is dominated by the Bound-Free/Free-Free interaction (following the so-called Kramer's Law), with a similar behavior. Both regions are materialized by **positive slopes** in the $\Sigma - T_{eff}$ diagram. However, in the $\sim 5000 - 6900$ K region, the hydrogen atoms start to become ionized, and the opacity dependence on temperature drastically changes for a small temperature interval. The cooling rate becomes a negative function of the temperature, and the disk becomes **unstable**. This is materialized by a switch to a **negative slope** in the $\Sigma - T_{eff}$ diagram. As we will detail in Sec. 2.3.3, in the latter case, any perturbation will trigger the instability, and (under a few assumptions) a temperature jump to another stable branch. We note that this framework is very general, and thermal instability is found in a wide range of astrophysical systems. Within the bounds of this work, it will also have notable consequences for the launching of outflows (see Sec.2.2.1) and their visibility (see Sec.2.3.3, where we give more details about the process itself).

The outburst mechanism specifically revolves around a clockwise evolution: cold, non-ionized matter slowly heats up to the point of instability, then jumps to a much hotter ionized phase, starting the outburst. When it eventually cools down to the second point of instability, it jumps once again to the lower temperature region, marking the end of the outburst. Although the most simple case is to simply switch to a higher branch of the same α disk solution, comparisons with observations constrain the α value to be an order of magnitude higher in outburst, no matter the type of source (Martin et al. 2019). Most of the outburst dynamics are thus dominated by the ratio between the α values in the "hot" and "cold" branches. The switch between the two phases is not instantaneous: since in actual accretion disks, the surface densities and temperatures are a function of the radius, the instability will propagate along the disk. This leads to the behavior modeled for a WD in the bottom left panel of Fig. 1.5, and summarized in the right panel.

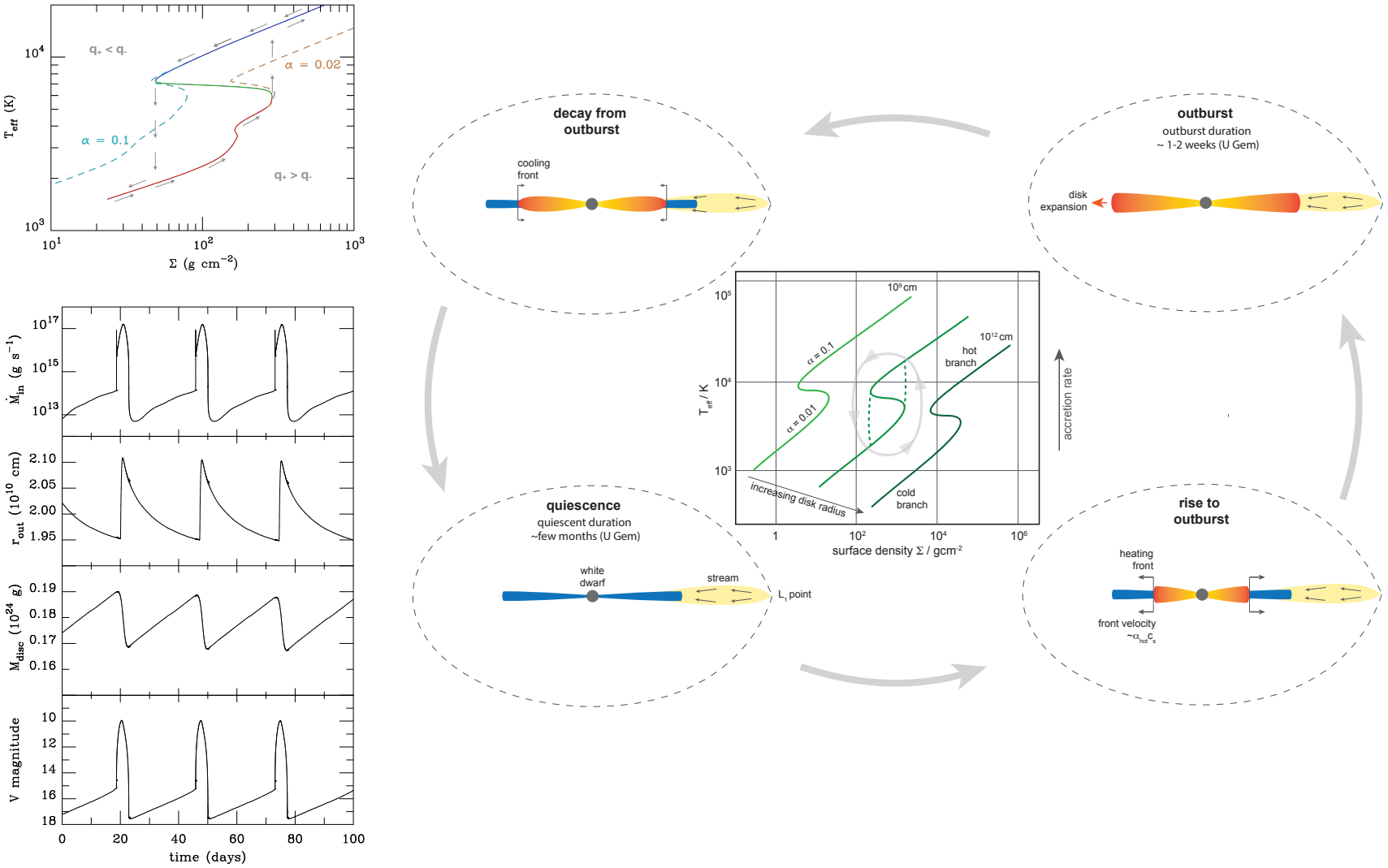

Figure 1.5: **(Top left)** Thermal stability curve of the DIM model for a DIM with a standard parametrized α disk prescription. From Marcel (2018), adapted from Lasota (2001). **(Bottom left)** Evolution of the mass inflow rate, outer disk size, mass of the disk, and lightcurves for a White Dwarf following a parametric DIM model. The peaks of all quantities indicate each outburst, and the more stable periods the quiescence in between. From Hameury et al. (1998). **(Right)** Evolution of the accretion disk structure along a DIM cycle, from Armitage (2022).

In quiescence, the entire disk is cold, accreting at very small rates, accumulating matter, and slowly heating up. This continues until the local accretion rate (and thus temperature/surface density) reaches the critical point of instability somewhere in the disk (which is often but not always, close to the inner boundary). The temperature jump then creates two heat fronts (inwards and outwards) which ionize the entirety of the disk on very short timescales. The temperature increases along with accretion and the matter available in the disk is quickly depleted, which then results in a progressive decrease of temperature until another temperature jump happens somewhere in the disk. This time, a slower cooling front progressively shifts back the disk into its first configuration, and the systems returns to accumulating mass in quiescence.

This mechanism implies that the disk can remain stable if it stays at sufficiently high or low accretion rates. This can be tested against observations of sources of different natures in order to explain transient and permanent sources, but requires a different treatment depending on the source. Indeed, while irradiation from the inner regions of the disk is usually negligible in Cataclysmic Variables, it is much more significant for X-ray Binaries and must be taken into account. This is a very difficult (and currently unsolved) problem that is very dependent on the geometry of the disk, especially in its inner regions, which remains widely debated (see Sec. 1.3.3). The current approach assumes that only a small fraction of the X-ray luminosity is absorbed by the outer disk (Dubus et al. 1999), which nevertheless lowers the threshold for persistent sources (Lasota et al. 2008).

This assumption matches very well against the properties of most known NS and BHLMXBs (Coriat et al. 2012), as we show in Fig. 1.6, with an updated version including all types of Roche Lobe accreting XRBs. The DIM threshold without irradiation is compatible with the position of the vast majority of CVs and UCXBs, outside of few specific cases currently under study. The same conclusion can be made for LMXBS and the limit with irradiation, with the notable exception of the NSLMXB Cygnus X-2, although this system could be a transient system ongoing a very long outburst, as is expected for the quasi-persistent source GRS1915+105 (Coriat et al. 2012). On the other hand, the specific evolutionary models cited in the figure, which assume a given type of stellar companion and mass transfer rate, struggle to explain the distribution of orbital period and accretion rate (with the notable exception of UCXBs), so the picture is still unclear.

Despite these successes, the DIM remains a very basic model with a number of simplifying assumptions. This leads to a number of shortcomings, among which we can highlight those most relevant to LMXBs. First, the question of angular momentum transport (the physical mechanism process behind the α prescription) remains open. The Magneto-Rotational-Instability (Balbus et al. 1991) is currently the most likely candidate to explain the viscous transport in magnetized disks. Its physical origin is illustrated in the upper panel of Fig. 1.7, and can be summarized in is simplest form as such: in a Keplerian disk threaded by a vertical magnetic field, any radial perturbation of such field links particles (or fluid elements) at different radii. However, the differential rotation progressively furthers them from one another, which creates a magnetic tension as feedback, increasing the momentum of the outer element and slowing down the inner element. This furthers increases the radial distance between the two, increasing the differential rotation, and so on.

MRI has rapidly imposed itself as the main driver of viscosity in accretion disks, because of its very easily accessible triggering conditions (see e.g. Balbus & Hawley 1998 for a review). Nevertheless, MRI simulations struggled to reach the values of $\alpha \gtrsim 0.1$ compatible with the observations of CV disks in the hot branch, until convection was properly implemented, and it remains difficult to reproduce the variations of α alongside the S-curve (Scepi et al. 2018b). We show an example of a recent results in the lower right panel of Fig. 1.7, with individual MRI shearing box simulations represented with points, and superposed to parametric alpha-disk computations. While the upper branch corresponds to quantitatively higher α, configurations with and without vertical magnetic flux in the disk both lead to highest α values restricted to the leftmost region of the upper branch (where convection enhances the MRI). The behavior even shifts to unrealistically higher α values in the lower branch for high enough magnetic field.

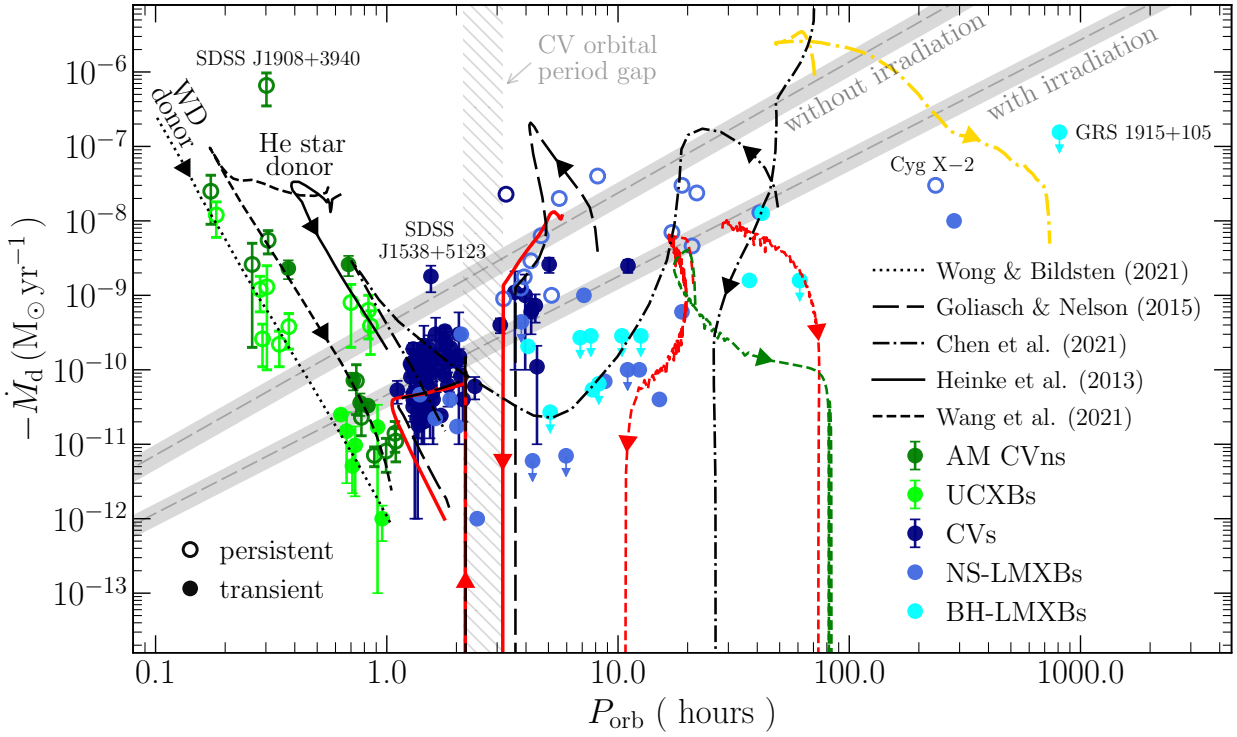

Figure 1.6: Distribution of accretion rates and orbital periods for X-ray Binaries, put in perspective with the DIM model. The grey regions highlight the limit below (above) which theoretical models predict transient (persistent) sources for a DIM with or without irradiation. Black lines represent several theoretical evolutionary models for specific donors. From Belloni & Schreiber (2023)

To make matters worse, outburst evolutions based on MRI α alone struggle to reproduce the observed evolution of Dwarf Novae (Coleman et al. 2016), with a notable lack of reflares, and insufficient angular momentum transport in quiescence (Scepi et al. 2018a). The saving grace might be the inclusion of outflows, which add another mechanism for angular momentum transport. Indeed, simple disk outflow prescriptions already show promising results when combined with dipolar magnetic fields, as seen in the lower right panel of Fig. 1.7, where the combination of both allows, for sufficiently high dipolar magnetic fields, to retrieve a good approximation of the results obtained in the fully empirical DIM shown in Fig. 1.5. However, in this configuration, the outflow dominates the angular momentum transport in some regions, fundamentally changing the disk structure, and thus new disk models need to be considered (Scepi et al. 2019, see also Sec. 2.2.2).

To conclude, although we've highlighted the applicability of the DIM to the general triggering of XRB outbursts, a more detailed study of the evolution during the outburst itself requires in any case a different description. One of the fundamental missing elements is the spectral evolution during the outburst, which cannot be directly estimated from simulations, as combining thermodynamics (and especially thermal instability) with complex magnetized structures is unrealistic with present day computer power. For CVs, it is long known that their spectral evolution during outburst follows a loop in a U-B,B-V color-color diagram[7] (Bailey 1980). Yet comparisons with a DIM evolution were only attempted very recently (Hameury et al. 2020), and with limited success, because of the number of elements which are known to be missing (Hameury 2020).

[7] a 2D-diagram where the two axes represent the intensity or luminosity in different spectral bands

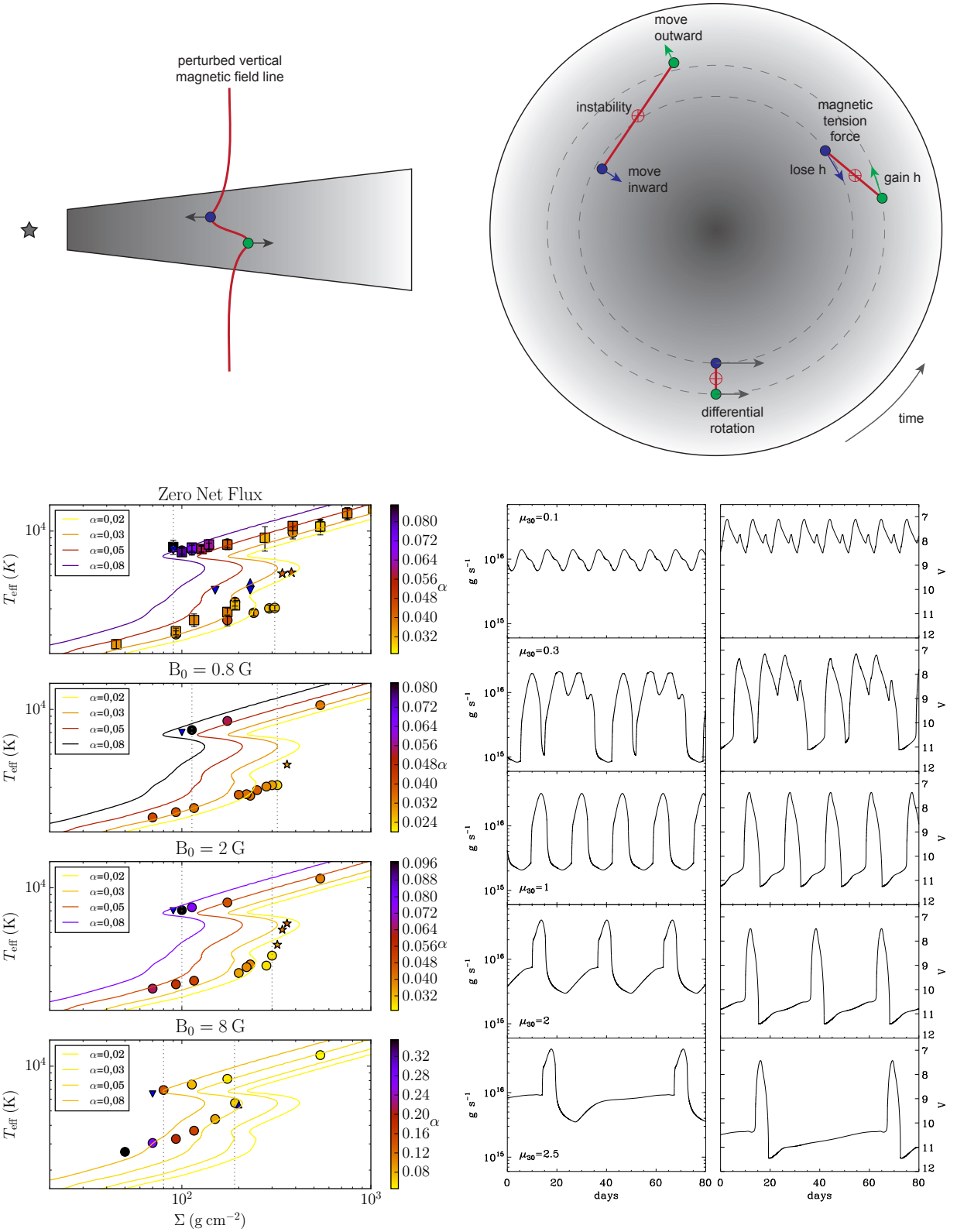

Figure 1.7: **(Top)** Illustration of the behavior leading to the Magneto-Rotational Instability, from Armitage (2022). See main text for details. **(Bottom left)** Attempts of reproducing the S-curve of the DIM model using MRI in sheraring box simulations (points) with increasing amounts of poloidal magnetic field B_0, with parametric alpha curves over-plotted. From Scepi et al. (2018b). **(Bottom right)** Mass inflow rate (left) and lighcurves (right) simulated from a modified DIM model including a wind torque, using an alpha prescription derived from the results on the left, and assuming an and increasingly dipolar magnetic field (with μ_{30} the dipole moment in units of 10^{30} G cm^3). From Scepi et al. (2019).

LMXBs, on the other hand, exhibit a far richer (and more complex) behavior in outburst, based on sharp evolution between distinct spectral and timing states, which we will detail in Sec. 1.3. The important point is that virtually all transient LMXBs rise and return to/from quiescence in a "hard" state, where the X-ray emission is completely different from a thermal disk, and accompanied by the radio signature of powerful jets. They only switch to a "soft", thermal disk dominated state in the middle of the outburst. The description of this hard state and of the spectral state transition require a completely different treatment, which is one of the main challenges of modern accretion physics (see Sec. 1.3.3).

One of the remaining barriers to achieve this description is the consideration of outflows. They have been largely observed in virtually all accreting systems (Díaz Trigo & Boirin 2016; Frank et al. 2014; Gianolli et al. 2024; Matthews et al. 2015), yet have long since proven a struggle to incorporate in disk models, and only recently did we see a first push in that direction for different objects (Jacquemin-Ide et al. 2019; Lesur 2021; Verhamme et al. 2024, although see Ferreira et al. 2006 for specifically jet-like solutions).

In the meantime, preliminary descriptions of outflows in LMXBs have been to shown to influence tremendously the global outburst and binary evolution (Dubus et al. 2019; Gallegos-Garcia et al. 2023; Tetarenko et al. 2018), similarly to what we previously discussed for CVs.

1.3 Taxonomy of Black Hole Binary Outbursts

The purpose of this section is thus to highlight the main properties of one of the most well-observed, yet more diverse category of sources where outflows have been detected : outbursting BHLMXBs. The projects subsequently tackled in this manuscript will focus on this specific category of sources.

We note that the following description is in part applicable to persistent HMXBs with strong disk components, such as Cygnus X-1, which exhibits similar spectral evolution, although without the evolution in luminosity.

1.3.1 Spectral Evolution

While it may seem obvious for X-ray Binaries to be primarily studied in the X-rays, the reality is a mix of scientific and practical interests. Firstly, although the spectra of galactic Black Hole transients can extend from the radio up to the gamma rays, their emission typically peaks in the X-ray band. In parallel, this specific range of energy combines very strong spectral evolution and extremely minute changes, due to the incredible amount of physical mechanisms which contribute to the emission in this specific energy range. The combinations of these two elements would already make the X-rays the prime target for understanding X-ray Binaries, but this is supported by a a range of observational effects, which can be highlighted by the caveats of different wavebands.

Indeed, radio telescopes are by design incapable of procuring detailed spectral and timing coverage, the emission from the infrared is typically obscured by dust along the line of sight, and the optical, while very well resolved, suffers from contamination of a number of different processes, including stars and notably the stellar companion. To finish, almost the entirety of the UV band (and a part of the soft X-rays) are completely absorbed by the interstellar medium. On the other hand, when looking at higher energies, it becomes increasingly difficult to properly detect and characterize the radiation, and thus the observation of anything above hard X-rays (starting from ~ 100 keV) and notably the gamma rays requires instruments with very poor spectral and angular resolution. Meanwhile, the soft to mildly hard X-rays ($\sim 0.1-100$ keV) is the hardest band in which focusing telescopes and cameras can be used, allowing for better spectral and angular resolution[8], although with the requirement of building satellites to avoid complete absorption by earth's atmosphere. For this reason, the X-rays are also one of the most practical bands to study the evolution of Black Hole outbursts.

[8] and a very low amount of competition with other domains of astrophysics

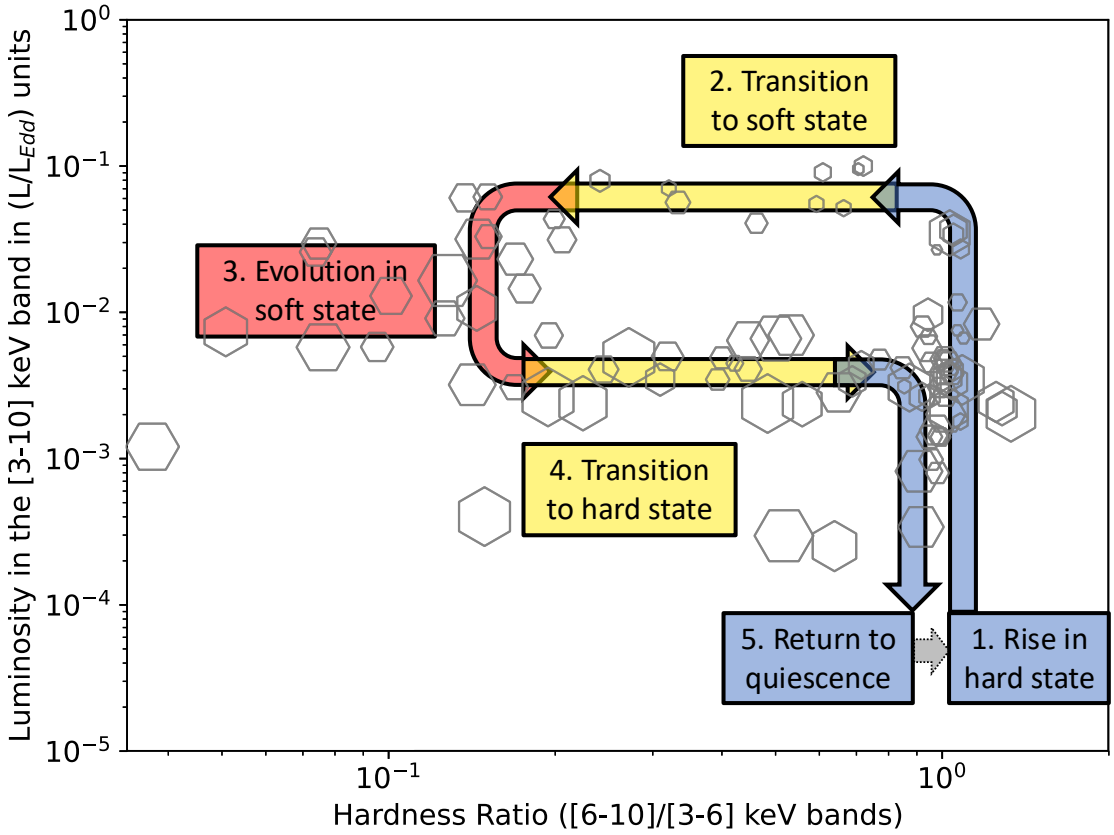

Figure 1.8: Typical evolution of a "standard" Black Hole Low-Mass X-ray Binary outburst represented in a soft X-ray Hardness Luminosity Diagram.

The X-ray themselves can also be subdivided into bands of varying relevance. It has been historically much simpler to create X-ray telescopes focusing on the soft X-ray band ($\sim 0.1-10$ keV), which also happens to be the part of the X-rays with the richest diversity in spectral features.

For all of these reasons, the coverage and representation of the evolution of Black Hole outbursts has been, and continues to be, mainly focused on the soft X-rays. In this band, Black Hole outbursts are typically characterized by a very high increase in luminosity (typically ≥ 5 orders of magnitude), and very distinct spectral(-timing) state changes that affect the hardness of the spectrum, namely the proportion of higher to lower energy radiation. Consequently, the main tool used to represent the spectral evolution of Black Hole outburst is the X-ray Hardness Intensity Diagram (HID), a 2D graph plotting the evolution of intensity (or luminosity) in the soft X-rays against a Hardness Ratio (HR) of different bands in the X-rays. For the reasons highlighted above, the HID is often restricted to the soft X-rays. The evolution of LMXB outbursts in the HID typically follows a distinct pattern, commonly referred as the "Q-shape" or "turtlehead", which we represent in a simplified version in Fig. 1.8 (see Belloni & Motta 2016 for a review). In parallel, a significant fraction of X-ray outbursts are preceded by a rebrightening in the visible band (Goodwin et al. 2020; Russell et al. 2019a), matching predictions of DIM outburst models. While outbursts can exhibit very different long-term intensity and spectral evolution, the most common type remains the Fast Rise Exponential Decay (FRED) (Chen et al. 1997), which also has the most simple spectral state evolution.

The beginning of these "canonical" outbursts is marked by a rise of the X-ray luminosity of several orders of magnitude, from X-ay luminosities below $\sim 10^{-5} L_{Edd}$ and thus inaccessible to current instruments. In this phase, the X-ray spectrum is dominated by a hard ($\Gamma \sim 1.5$) power law with an exponential cutoff around 100 kev(Done et al. 2007; Remillard & McClintock 2006), typical of Comptonization processes. This so-called *hard* spectral state is associated to non-thermal processes in

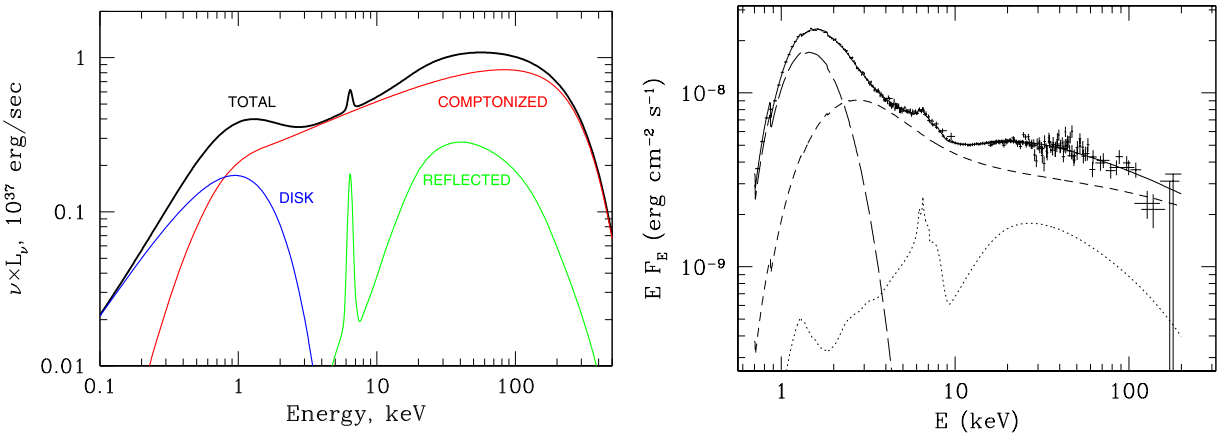

Figure 1.9: **(Left)** X-ray spectral components of a typical hard state of a Black Hole Transient, from Gilfanov & Merloni (2014). **(Right)** X-ray spectrum and spectral components of a soft state observation of the Black Hole Transient Cygnus X-1 in X-rays, from Gierliński et al. (1999). The long dashed, dashed and dotted lines refer respectively to the disk, comptonized and reflected components.

an extremely hot and optically thin plasma close to the BH (the 'corona'). Meanwhile, at much lower energies, the Spectral Energy Distribution (SED) is dominated by a synchrotron component associated with jets, which extends from the radio to the infrared. The last main element, restricted to bright hard states, is the tendency to show an additional component in the X-rays, interpreted as the reflection of the coronal emission on the outer accretion disk (see e.g. Fabian & Ross 2010). This can produce both an additional continuum component (the so-called Compton hump, peaking at 30-40keV) and a fluorescent $K\alpha$ iron line at $\sim$6.4 keV, whose shape can be distorted by gravitational effects and thus depends heavily on the properties and geometry of the inner accreting region. We show an example of the typical spectral components seen in the hard state in the left panel of Fig. 1.9.

When the source reaches luminosities of $\sim 10\% L_{Edd}$ (Tetarenko et al. 2016), a state transition occurs in the span of a few dayss. The X-ray powerlaw index raises to $\Gamma \geq 2.5$, and the spectrum transitions to being largely dominated by a bump appearing at around $\sim 1-2$kev. This is commonly modeled as a multi-temperature blackbody and interpreted as the thermal emission of an optically thick and geometrically thin accretion disk, extending close to the innermost stable circular orbit (ISCO) of the BH. Concurrently, the radio emission becomes strongly suppressed (see e.g. Corbel et al. 2001; Coriat et al. 2009; Fender et al. 1999b; Fender et al. 2004; Gallo et al. 2003), pointing towards a partial or complete quenching of the jet component. An additional "hard tail" of unknown origin, interpreted as a thermal or hybrid comptonization of a part of the disk emission (Del Santo et al. 2008, 2013), can also be seen at high energies (Motta et al. 2021), sometimes accompanied by its own reflection (see e.g. (Connors et al. 2021). We show an example of a soft state spectrum and its corresponding components in the right panel of Fig. 1.9. One element not included in this specific description is the tendency for some high-inclined sources to show absorption features in specific portion of their soft states. We will come back to this behavior in 2.1.

While the source evolves in the soft state, its luminosity typically decreases over the span of few weeks to months. Once it reaches few percents of L_{Edd} (Vahdat Motlagh et al. 2019; Wang et al. 2023), the inverse transition happens, bringing the source back to the hard state, before a final descent to quiescence. Interestingly, an analog of this state transition has been found at very similar Eddington fraction in AGNS (Hagen et al. 2024).

This template nevertheless remains a very simplistic scenarios of the evolution of BH XRB outbursts, and most sources tend to exhibit a number of more exotic outbursts, with more diverse properties. First, the transition to the soft state is only achieved in $\sim$60% of outbursts(Tetarenko et al. 2016). The remaining portion, called "failed" or "hard-only" outbursts, rise up to the transition luminosity or a

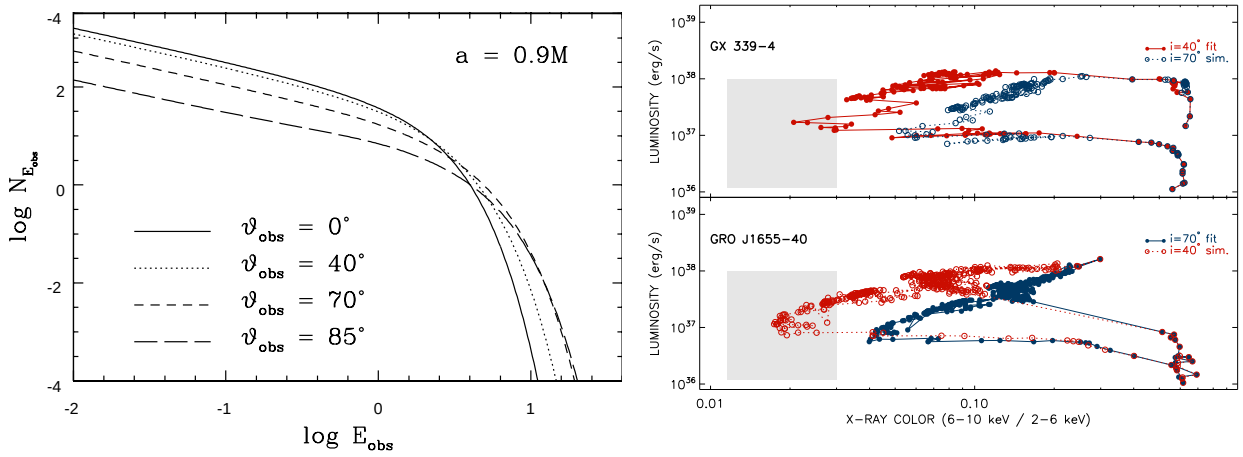

Figure 1.10: **(Left)** Influence of the viewing angle on the flux density of a relativistic thing accretion disk (x-axis in keV), from Li et al. (2005).**(Right)** Influence of the inclination on the HID evolution a low (GX 339-4) and high (GRO J1655-40) inclined sources, from Muñoz-Darias et al. (2013).

fraction of it before immediately fainting back to quiescence (Capitanio et al. 2009; Ferrigno et al. 2012). Although the physical differences at the origin of this different behavior is unknown, some sources are notably more prone to it than others (see e.g. Stiele & Kong 2021). In addition, while the X-ray spectral (and timing) properties during the rise of "standard" and "failed" outbursts are indistinguishable, the latter category is typically brighter in the optical band (Alabarta et al. 2021).

On the other end of the spectrum, other sources have a much shorter stay in canonical hard states and spend the vast majority of their outbursts in soft, intermediates or sometimes bright states with soft X-rays dominated by a comptonized component, but much steeper spectra in hard X-rays ($\Gamma \gtrsim 2.5$) than canonical hard states. These are often called "Very-High states" (VHS) or "Steep PowerLaw states" (SPL) (see Sec. 4 and references therein). These additional states, as well as various types of flares in hard (radio loud) states, are typical of much longer outbursts lasting several times longer than FRED type outbursts, including plateaus in either hard or soft states, and a significant amount of "back and forth" between different states while maintaining high Eddington fractions (Tetarenko et al. 2016), sometimes with a very characteristic evolution (Chen et al. 1997).

Even more rarely, sources may exhibit more exotic accretion states, completely leaving the standard paradigm. One of the main example is the small fraction of sources which approach or surpass the Eddington limit and enter so-called "Ultra-Luminous" states during parts of their outbursts. This leads to a different accretion configuration and thus spectral properties (Prabhakar et al. 2023, see also 3.5.2). On the opposite scale of spectral properties are obscured outbursts, during which few sources exhibit strongly absorbed spectra reminiscing of compton thick AGNs (Muñoz-Darias et al. 2016; Negoro et al. 2018; Shaw et al. 2022). Such sources are also expected to have gone through a Super-Eddington phase, expelling high amounts of matter via outflows, which eventually obscures the main emission of the source (Muñoz-Darias & Ponti 2022).

However, even with similar accretion properties, one must be careful about interpreting the evolution in the HID at face value. Indeed, the vast majority of BHXRBs lack either distance or mass estimates, and thus retain a significant degree of freedom for their luminosity when expressed in Eddington fraction (which is the only way to reliably compare different sources). In addition, the spin and inclination angle are known to significantly affect the disk component due to relativistic effects (Li et al. 2005; Mummery & Balbus 2023). While the first is an actual physical parameter that influences the entire spectrum, the second is the consequence of the anisotropy of the received radiation, with projection effects influencing the hardness of the disk thermal component,as we show in the left panel of Fig. 1.10. This has a strong effect on the path taken in the HID, artificially making the evolution in the soft state of high-inclined sources follow a diagonal, instead of a straight luminosity decrease for low-inclined

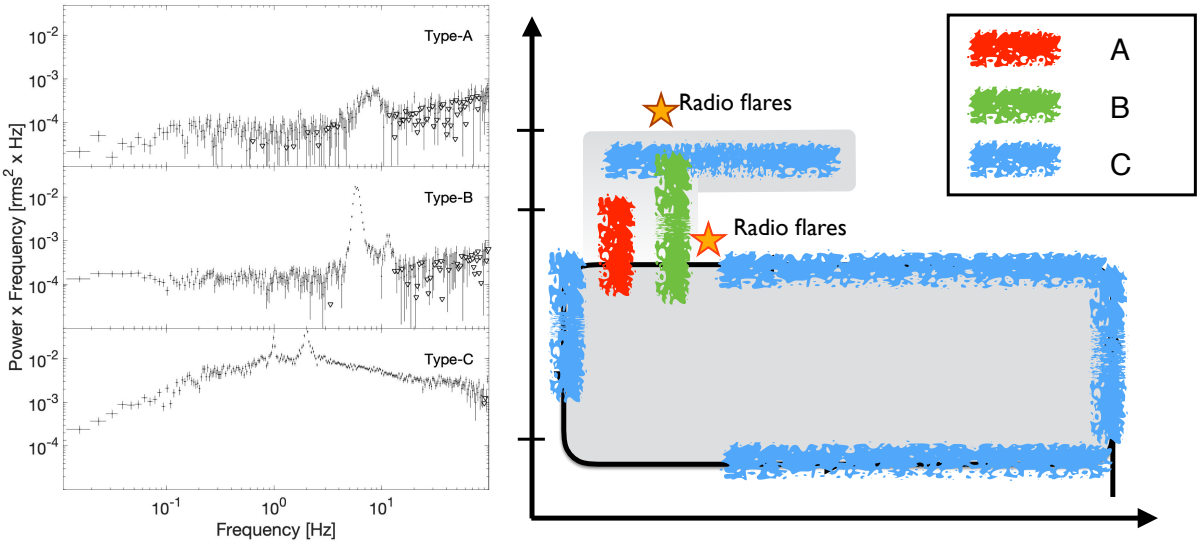

Figure 1.11: **(Left)** Power spectra of Black Hole Transients exhibiting the three main types of Quasi-Periodic-Oscillations. **(Right)** Repartition of type A, B and C QPOs along the Q-shape of BHT outbursts. Both panels from Ingram & Motta (2019)

sources (Muñoz-Darias et al. 2013). We show an example of such behavior in the right panel of Fig. 1.10.

While the spectral evolution provides a number of information about the accretion state of the source, it is becoming more and more apparent that a much better definition is achieved when considering the timing properties and spectral evolution together. This echoes the few existing sources which, instead of the standard evolution in the HID, evolve between distinct spectral-variability patterns(Altamirano et al. 2011; Belloni et al. 2000) whose origin remain for now completely out of reach. Although the focus on this work is not timing analysis, we highlight in the subsection below **some** of the main timing properties which vary during Black Hole outbursts, and their links with spectral properties and accretion states.

1.3.2 Timing Evolution

Studies of variability and periodicity in time series are typically performed in the Fourier domain. In Black Hole observations, which are (usually) continuous time series, the most common representation is the power spectrum, namely the squared modulus of the fourier transform of a given lightcurve. The study of power spectra allows to characterize peaks, related to periodicity at a specific frequency, or the continuum, which will relate to the amount of variability of the spectrum in a given frequency range. The power spectrum is commonly re-normalized to the fractional root mean square deviation (rms) of the lightcurve, which then shifts the normalization of its components to similar units.

First, Black Hole outbursts can exhibit a number of narrow periodic features in their lightcurves, called Quasi-Periodic Oscillations (QPO, see Ingram & Motta 2019 for a review). In the power spectrum, QPOs are typically modeled by a lorentzian functions (Belloni et al. 2002), and thus parametrized by a cendroid frequency μ_0, a width Δ, and a normalization A (which is the rms of the lorentzian when in rms normalization). In order to obtain a frequency independent measurement of the width, which will relate more to physical processes, Δ is often replaced by a quality factor $Q = \mu_0/2\Delta$. Since QPOs can appear as a series of harmonics, with frequencies being multiple integers of a given value, the QPO frequency usually refers to the frequency of the fundamental.

In BHLMXBs, a distinction is often made between periodic behavior at high frequency ($\gtrsim 60$ Hz) and low frequency ($\lesssim 30$ Hz), as high frequency QPOs relate more to particle motion close to the ISCO, and are both very rare and very weak. They can be used to constrain both the mass and spin of the central object via relativistic precession models (RPM, see e.g. Stella et al. 1999), and, despite the scarcity of

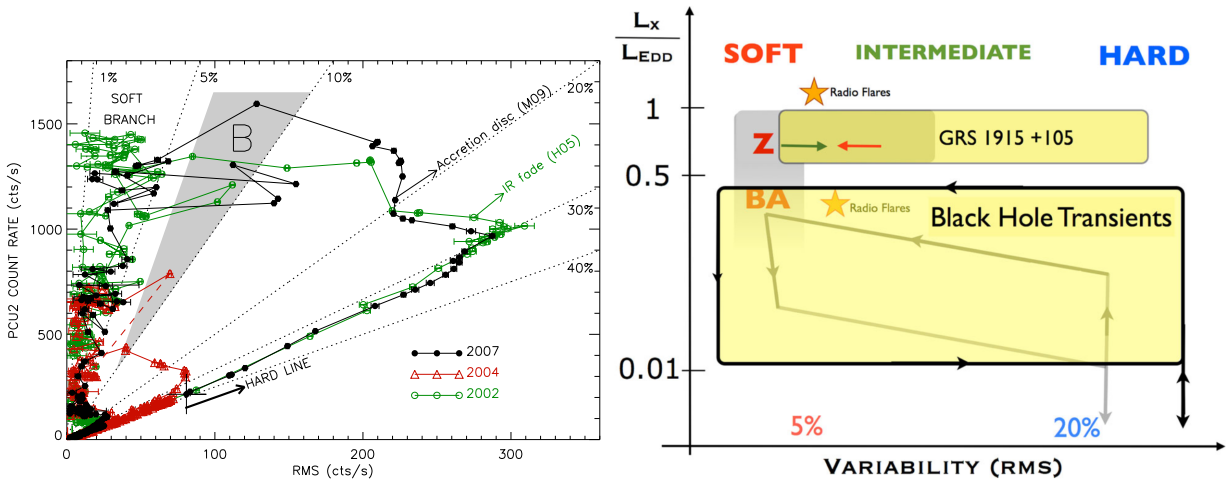

Figure 1.12: **(Left)** Evolution of several outbursts of the BHLMXB GX 339-4 in a absolute rms-intensity diagram using the absolute rms. The grey area highlights the position of type-B QPOs and the dashed lines given fractional rms values. From Muñoz-Darias et al. (2011). **(Right)** Typical evolution of BH (yellow) and NS (grey) outbursts in a fractional rms-intensity diagram. GRS1915+105 is highlighted due to remaining at higher Eddington fraction than other BHs. From Muñoz-Darias et al. (2014).

detections, have provided measurements completely independent from the spectral properties for a few sources (see Motta & Belloni 2024 and references therein). On the other hand, Low Frequency QPOs are much more common, and can be separated between three non-exclusive categories, with different properties and relation to the accretion states. We show their typical power spectra and repartition in the HID in Fig. 1.11.

Type-C QPOs represent the overwhelming majority of detections. They can be seen in virtually any state, although with a strong preference for harder spectra, and their peak frequency is correlated with the spectral state, varying from $\lesssim 1$ Hz in low hard states up to ~ 30 Hz for the rare detections in soft or ultra-luminous states (Motta et al. 2012). They exhibit high amplitude (up to $\sim 20\%$ rms), highly peaked profiles ($Q \gtrsim 8$), and can sometimes be observed in other wavelengths from the infrared to the ultraviolet (Gandhi et al. 2010; Hynes et al. 2003; Kalamkar et al. 2016), either at the X-ray fundamental frequency or half of it. In addition, a radio QPO with features reminiscing of type-C was recently detected in GRS 1915+105 (Tian et al. 2023), but the erratic variability of this source, combined with a strong X-ray obscuration, complicates the interpretation of the detection.

Type-B QPOs are restricted to a much more narrow portion of the HID, namely the Soft Intermediate State, which is entirely defined by their apparition (Belloni & Motta 2016). They have smaller amplitude ($\sim 5\%$ rms) than type-C QPOs, narrow profiles ($Q \sim 6$), and often exhibit a weak first harmonic. Their frequency range is also much more narrow, typically around $\sim 5-6$ Hz, and rarely down to $\sim 1-3$ Hz (Motta et al. 2011). Their also exhibit highly variable behavior, with appearances and disappearances on time scales of less than few seconds. Most importantly, they have been associated to transient radio flares, from both transient jets (Corbel et al. 2005) and discrete radio ejecta (Fender et al. 2004), indicating a possible association with the jet ejection process (see Fender et al. 2009 for a more detailed discussion).

Type-A QPOs are the most rare among the main categories, with very few detections exclusively in the soft state, immediately following the hard-soft transition. They exhibit both weak amplitude (few % rms) and broad peaks ($Q \lesssim 3$), with a narrow range of frequencies of $\sim 6-8$ Hz. While harmonics have yet to be detected in this category, this may be simply due to a limited SNR.

Finally, even rarer than Type-As and High Frequency QPOs are mHz QPOs, an extremely rare occurrence with frequencies in the range of $\sim 0.01-0.1$ Hz, with amplitudes of $\sim 10-20\%$ and quality factors of $Q \sim 3-8$, slightly lower than those of type-C QPOs (**?**). They are detected at very specific HID positions for their respective sources, and notably before the hard-soft transition (Altamirano & Strohmayer 2012), and may have a link with the radio jet, although no simultaneous radio observation has ever been

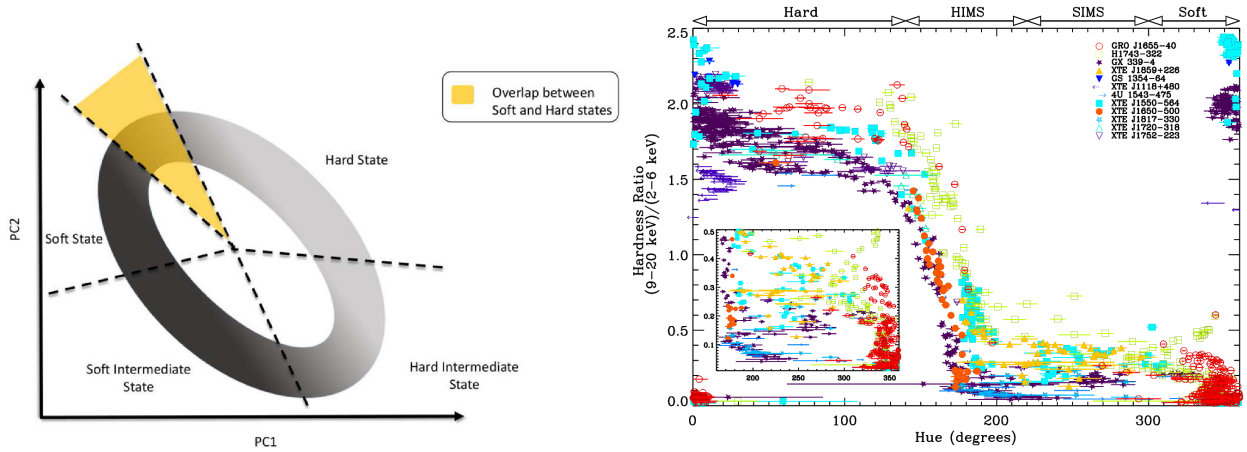

Figure 1.13: **(Left)** Repartition of sectral states of BHLMXBs in a power colour-colour diagram, from Heil et al. (2015b). **(Right)** Repartition of spectral states of BHLMXBs in a Power Hue-Hardness Ratio diagram. The delimitation above the graph highlights the different spectral states. From Heil et al. (2015a).

obtained. We discuss the few detections in more details in Sec.4.

It is worth noting that the QPOs are not an isotropic phenomenon: several studies have shown that the amplitude of type-B/type-C QPOs are respectively anti-correlated/correlated with the inclination (Motta et al. 2015), among other correlations with the noise at the QPO position, and even the QPO phase-lag between different spectral bands (van den Eijnden et al. 2017). This once again hints at type-Bs being linked to the jet emitting structure (which is supposedly face-on), while type-Cs would be more linked to the disk structure or a horizontally extended corona (see Sec. 1.3.1).

While the QPOs are suspected to match the appearance of specific processes, the continuum variability is an even better indicator of the global outburst evolution. First, the broad band variability, often expressed as the rms in a specific band, directly relates to the spectral changes along the outburst. This allows to create a rms-intensity diagram, where specific spectral states and different types of QPOs occupy well-defined regions (Heil et al. 2012; Muñoz-Darias et al. 2011). We show in Fig 1.12 two possible representations, using either the absolute rms or the (more common) fractional rms, defined as the ratio of the rms to the total count rate of a given energy band. While the absolute rms produces a diagram where the separation between accretion states follow an evolution in angles, in the fractional rms - Intensity (or luminosity) diagram (RID), the evolution forms a Q-shape very similar to the canonical HID. In addition, the fractional RID has the strong advantage of allowing to describe both BH and NS LMXBs outbursts (Muñoz-Darias et al. 2014), hinting at a more fundamental link to the evolution of accretion properties in both.

However, this diagram still relies on the intensity or luminosity, which, despite being useful for determining the evolution in and out of outbursts, might not always be as relevant to understand the evolution of the accretion state. One solution is thus to describe the outburst evolution entirely from timing properties, with the so-called "power-colour diagram" (PCC), which uses the ratios of two variances restricted to specific frequency ranges in each of its axis (Heil et al. 2015a). In this new diagram, shown in the left panel of Fig. 1.13, the outburst evolution forms an oval around an arbitrary center, which can be split into different angular sections matching continuous spectral evolution. The hard and soft states notably join in one section, while the spectral transition occurs close to $\sim 180°$ from this region. This diagram also shows a common evolution pattern for the outburst of BH and NSLMXBs (Gardenier & Uttley 2018), and can be decomposed to include another parameter.

Indeed, one can take a reference angle and an arbitrary center point and summarize the position in the PCC as a hue (rotation angle) parameter from that reference direction (which is arbitrary, but must stay common in the analysis). This hue value can then be combined to another independent parameter, such as the Hardness Ratio. As we show in the right panel of Fig 1.13, this Power Hue-Hardness Ratio

diagram allows for a much more visual representation of how well a specific angle region of the hue relates to the spectral transition, namely $\sim 160-200°$ if the origin of the Hue is taken in the soft-hard overlap region in the PCC. However, the hue value of the state transition still depends on the inclination of the source. This is because, as we've established previously, the Hardness Ratio itself depends on the inclination due to the anisotropy of (at least) the disk component, and the QPO themselves, which can account for a non-negligible fraction of the rms used to compute both power colour ratios of the PCC, are also inclination dependent. This issue can be resolved by using the fractional rms instead of the Hardness Ratio, and by removing the QPOs from the computation of the PCC. This creates the first inclination independent (and thus unbiased) accretion state diagram for XRB outbursts Gardenier & Uttley (2018); Heil et al. (2015a).

While these diagram can surely be used as a new inclination indicator in the future, several applications have already been found. Analysis comparing normal and failed outbursts have showed that these timing representations can act as "predictor" of state transitions, if only in a fraction of sources (Lucchini et al. 2023). Indeed, in some objects, the power spectral hue changes between 10 and 40 days before the spectral transition occurs, while the hue stays constant for the entire duration of failed outbursts.

Since we do not aim for an exhaustive coverage of timing properties, we simply highlight that other, more complicated timing/spectral-timing diagnostics exist. The studies of reverberation lags, tracing the delay between different spectral components in a spectrum, can be linked to the evolution of the accretion geometry during state transition (Wang et al. 2022b). Other studies using e.g. the Minimal Time Scale show a promising ability to separate BH from NS accretors, opening the door to new identification techniques (Sonbas et al. 2022).

1.3.3 Modeling accretion structures

Switching from phenomenological models to a more physical representation of the accretion-ejection structures would be a big step towards understanding the evolution of the spectral-timing states along the outburst. However, our current understanding remains very limited. The state transitions can be linked to a shift in geometry of the disk, from a (potentially) truncated accretion flow, a hot corona and a jet perpendicular to the accretion plane in the hard state, to a disk extending to the ISCO and no jets in the soft state (Gallo et al. 2003). However, the details of the geometry and structure of each state are difficult to distinguish with spectral information alone, and very few physical models allow direct comparisons with the data. Several timing properties can also be linked to the accretion flow. The most notable is the presence of type-C QPOs, which are commonly related to the corona due to their prevalence in the hard state, but have also been detected in the soft state (Motta et al. 2012) and may thus require a disk origin. However, since physically self-consistent timing evolution requires much more complicated models than spectral properties (because they have, by essence, to be time-dependent), only few tentative propositions have been made to explain the presence of QPOs (Ferreira et al. 2022; Ingram & Motta 2019; Stella et al. 1999) and the variability (Uttley & Malzac 2023), and even fewer are able to produce observable quantities. As they remain mostly independent of any spectral prescriptions, our understanding of the geometry was until recently limited to spectral evolution, which is notably degenerate. However, the advent of polarization measurements in the X-rays, with the launch of the *IXPE* telescope, now provide additional constrain on accretion geometries.

In the hard state, the X-ray emission is dominated by the presence of the corona, but its configuration and that of the disk are hard to distinguish and remain heavily debated. We show few examples of simplified coronal geometries in Fig. 1.14. Historically, the "lamp post" prescription, with the corona gathered in a sphere above the Black Hole, has been used as a toy model to compute tables of reflection models (Dauser et al. 2014; García et al. 2014), and provides good fits to reflection features. However, this geometry was initially chosen for its simplicity, with no physical justification. Nevertheless, reflection fits have routinely been used in the last decade to constrain various parameters, and notably the truncation radius of the accretion disk, since that information was not available via the (often undetected) disk component. Although it was measured to match the ISCO in multiple occasions (see e.g. Buisson et al.

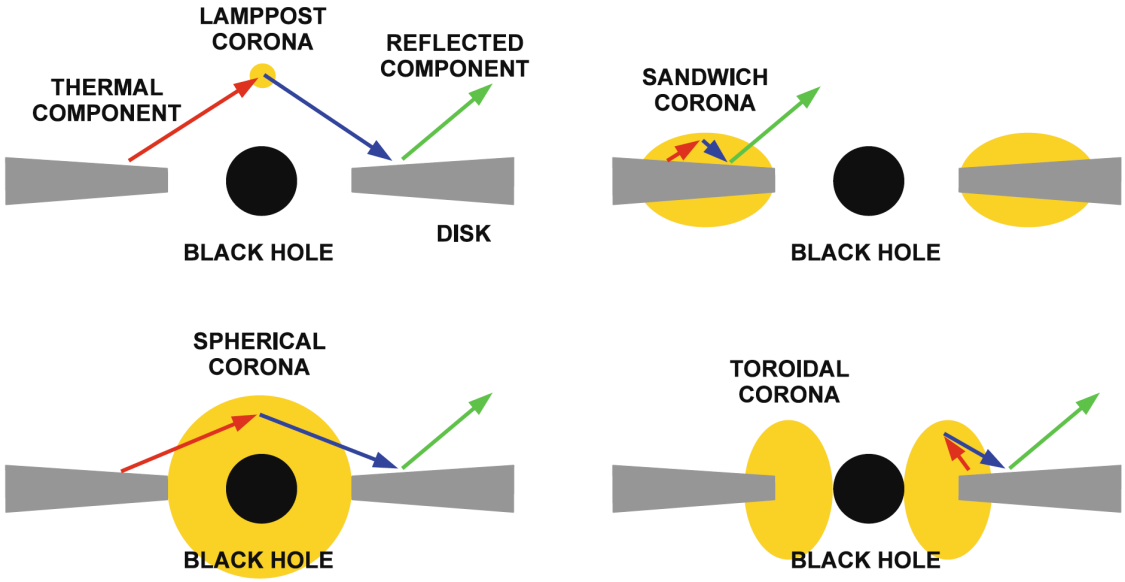

Figure 1.14: Example of simplistic coronal geometries, from Bambi et al. (2021)

2019), subsequent studies have shown than very good results can also be obtained at significantly higher values (Zdziarski et al. 2021b). This opens the door for more varied geometries in which the corona covers a part of the inner region around the Black Hole, which is especially relevant regarding recent discoveries made with polarization. Indeed, soft X-ray Polarization Degree and most notably Polarization Angle measurements are much more sensitive to the configuration of the corona (Podgorný et al. 2024; Schnittman & Krolik 2010; Zhang et al. 2022), and the first observations of BHs in the hard state heavily favor horizontally elongated geometries (either sandwich or inner flows) (Krawczynski et al. 2022).

Such constrains match very well more physical expectations of the inner most regions of the accretion flow. Indeed, before any consideration for coronal geometries were considered, specific solutions of radiatively inefficient, Advection Dominated Accretion Flows (ADAFs, see Esin et al. 1997) were already proposed to explain the hard state of X-ray Binaries. However, besides difficult application to observations and notably luminous hard states (Oda et al. 2012), ADAFS and other flavours of thermal-advection flows remain unable to produce one of the most important element of the hard state: the jet.

It is now well admitted that a poloidal magnetic field is needed to produce large scale jets (e.g. Beckwith et al. 2008), and that they can be powered by two mechanisms. These two processes, namely Blandford & Znajek (Blandford & Znajek 1977) and Blandford & Payne (Blandford & Payne 1982), extract rotational energy from the black hole or its accretion disk respectively. However, the relative importance of each in the formation of the global accretion-ejection structure remains largely unknown.

In an effort to tackle this fundamental question, numerical simulations of Black Hole accretion structures threaded by a large scale magnetic field have now become quite common, with computations recently rising to macroscopic dynamical time scales (e.g., Liska et al. 2018, 2022; McKinney & Blandford 2009; Narayan et al. 2003; Ohsuga et al. 2009; Tchekhovskoy et al. 2011). In their current state, they are divided in two very loosely defined categories: weakly magnetized flows, akin to magnetized ADAFS, called Standard And Normal Evolution (SANE, see Narayan et al. 2012 for the historical definition), and Magnetically Arrested Accretion Disks (MAD, see Fragile & Liska 2024 for a partial review), which, unlike what their name suggests, are accretion disks where saturation of the magnetic field in the inner regions slows down (but doesn't stop) the accretion flow. Both seem applicable to different portions of hard states of BHXRBs and AGNs alike, and can produce many of the desired properties for those objects, such as jets and broader outflows, while potentially remaining stable in a large range of accretion rates/luminosities.

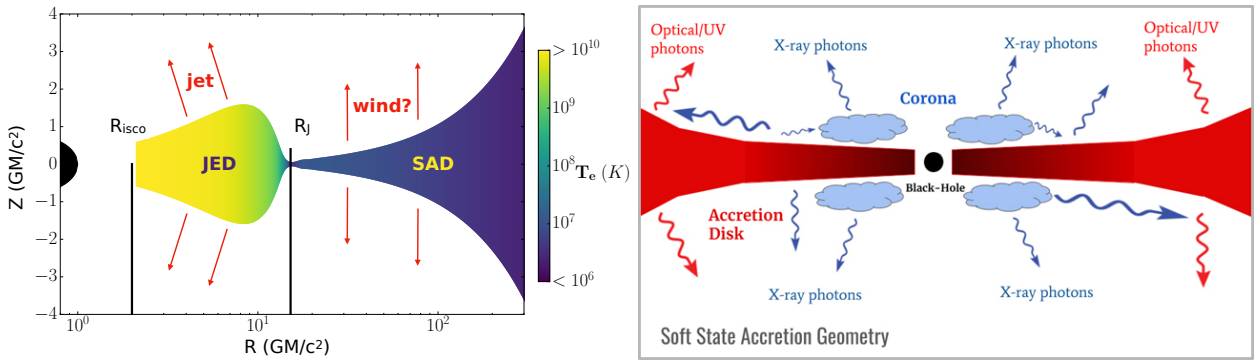

Figure 1.15: **(Left)** Physical solution of a JED-SAD hard state configuration, from Marcel et al. (2022). The temperature colormap highlights an optically thin inner flow (JED), and optically thick outer flow (SAD). **(Right)** Illustration of a possible soft state disk-corona geometry. Credit: ISRO.

However, these promising configurations are expanding in many directions, and are thus in dire need of a proper classification. Moreover, including realistic radiative processes remains a difficult task (see e.g. Liska et al. 2022; Scepi et al. 2024 for recent results). Direct comparison of these numerical simulations to observational data is thus far from being achieved, and recent efforts are turning towards converting MADs into analytic models (Hopkins et al. 2024, although see Ziminiak et al. -in prep- for a different perspective). It is worth noting that simulations tailored to AGNs have progressed at a similarly rapid pace in the last decade, and tend to highlight the importance of similar mechanisms, while suffering from the same limitations (see Davis & Tchekhovskoy 2020 for a review).

In parallel, the first jet emitting solutions have progressively evolved into self-similar models of magnetized "accretion-ejection" structures, which have shown promising developments in the last decades due to their analytical nature enabling simple comparisons with the data. An example of such efforts is the JED-SAD paradigm (Ferreira et al. 2006; Marcel et al. 2018a), which has shown impressive abilities to reproduce the general properties of the hard (and soft) states of Black Hole outbursts (Marcel et al. 2018b; Marino et al. 2021). We show an example of JED-SAD geometry in the left panel of Fig. 1.15, and leave a more precise description of JEDs for Sec. 2.2.2.

Meanwhile, in the soft state, even the description of "simple" geometrically thin, optically thick disks retains a very high amount of degenerate parameters (see Middleton 2016 for a review). The model most commonly used for relativistic thin disks, `kerrbb` (Li et al. 2005), makes use of several poorly constrained (if at all) source parameters, such as the mass, distance, and inclination, and others whose values are generally assumed from simulations or (outdated) theoretical models, like the torque at the inner disk boundary and the spectral hardening factor. This results in very high systematic uncertainties that, when considered properly, greatly limit the constrains on the most sought after parameters (such as the spin) even in the best observations currently available (Yorgancioglu et al. 2023). Moreover, such models rely on a number of simplifying assumptions, among which a disk that systematically extends at the ISCO (which would otherwise ruin any spin estimates), no consideration for natural changes in structure when switching to higher Eddington regimes (Abramowicz et al. 1988), and no intra-ISCO radiation (although see Mummery et al. 2024a for a recent development in that matter).

This is combined with a complete lack of understanding of the geometry beyond the disk: the presence of a weak but firmly detected hard tail up to very high energies indicates that there must be some semblance of a corona, as illustrated in the right panel of Fig. 1.15, but its physical origin remains a mystery. Unfortunately, unlike in the hard state, the polarization measurements in the soft X-rays are disk dominated and thus are not expected to provide information in that regard (Marcel, Ferreira, Petrucci, Barnier, Malzac, Marino, Coriat, Clavel, Reynolds, Neilsen, Belmont & Corbel Rat). More specifically, the lack of radio signature makes any vertically extended corona above the BH even less likely, and both an inner flow and a sandwich-type corona imply vastly different disk solutions compared to what is

currently used today. The saving grace may come in the form of non-thermal intra-ISCO emission, but this remains very hypothetical (Hankla et al. 2022b). In addition, this geometry must be able to create both standard reflection features and returning radiation (Connors et al. 2021), as well as the outflows detected in X-rays, whose launching mechanism is currently unconstrained (see Sec. 2.2).

To end this discussion, we note that no matter the numerical approach, and even if a few scenarii have been proposed (e.g. Begelman & Armitage 2014; Cao 2016; Kylafis & Belloni 2015; Meyer et al. 2000; Petrucci et al. 2008), none of the current simulations or models are able to reproduce the hard-to-soft and soft-to-hard transitions observed during the outbursts, as well as its relation with the jet appearance and disappearance. This is notably because the current solutions in both hard and soft states remain stable far beyond the luminosities at which the spectral transitions invariably occur. One significant development might come in the understanding of the timing properties of such solutions, but this description is far from being achievable at the moment. Among particularly sought after behaviors, we highlight the limit-cycles seen in few BHs (Neilsen et al. 2011; Wang et al. 2024a) and recently NS (Vincentelli et al. 2023), which are suspected to stem from disk instabilities affecting the entire accretion-ejection structure.

In parallel, one of the most promising directions to understand the evolution of different accretion flow structures is to focus on the description of their byproducts, and notably the signatures of jets and outflows. However, the description of the jet in itself is a notably difficult and rarely tackled task, combined with very difficult spectral measurements. On the other hand, significant progress in observations, theoretical modelings, and simulations of the broader types of outflow signatures have been achieved in the last decades, once again making outflows a prime candidate for improving our understanding of Black Holes. We shall focus on these elements in more details in the following section.

1.4 The broader scale of Black Hole evolution

1.4.1 AGNs

Definitions

- **SuperMassive Black Hole** (SMBH): Second main category of observed Black Holes, weighing $\gtrsim 10^6$ solar masses, and inhabiting the center of the vast majority of galaxies. Very few galaxies host more than one.
- **Active Galactic Nuclei** (AGN): Observational term, referring to the bright central part of the most luminous galaxies. This emission is the result of accretion on the central SMBH(s) at their center. Because this radiation is much more powerful than what is emitted by the rest of the galaxy, the term is also **used interchangeably** for the **galaxies** with this type of emission, and the "active" **Black Holes** they host.
- **Quasar, Blazar, Seyfert I, Seyfert II**: More specialized terms referring to different types of AGNs of varying physical properties, seen at different angles.

If the Black Holes detected in X-ray Binaries in our Galaxy and elsewhere are categorized as "Stellar-Mass" Black Holes, is it to emphasize the difference with the second main categories of astrophysical Black Holes. Indeed, **SuperMassive Black Holes** (SMBHs) refer to BHs with a Mass of $\gtrsim 10^6$ $M_\odot$, dynamically detected in the center of galaxies for more than 40 years (see Kormendy & Richstone 1995 and references therein), hinted at by the detection of unexpectedly powerful radio emission in some galaxies decades prior (Salpeter & E. 1964), and recently directly imaged (EHT Collaboration et al. 2019, 2022) thanks to interferometry[9]. These Black Holes refer to the same type of physical regions than

[9]The two EHT images of M87 and Sgr A* are by far the most unequivocal proofs of the existence of Black Holes

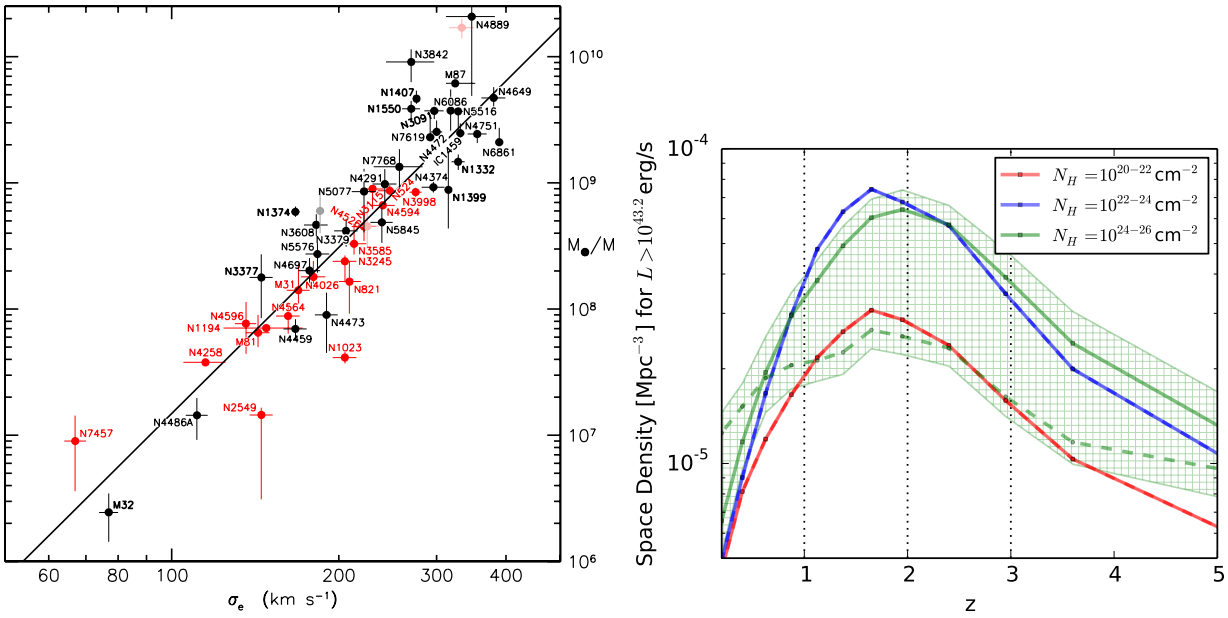

Figure 1.16: **(Left)** Correlation between dynamically measured SMBH masses and velocity dispersion in spiral (red) and elliptical (black) galaxies, from Kormendy & Ho (2013). **(Right)** Evolution of the spatial density of AGNs with redshift for different levels of obscuration, from Buchner et al. (2015)

their stellar mas counterpart, albeit in a significantly scaled up version, and are thought to inhabit the center of the vast majority of galaxies, growing along with them since their creation. Among a wide range of correlations (see Kormendy & Ho 2013 for a review), the most notable example of this co-evolution is the M–σ relation, which we show in the left panel of Fig. 1.16, linking the mass of a SMBH to the velocity dispersion of its host galaxy (Ferrarese & Merritt 2000; Gebhardt et al. 2000).

In the current universe, the majority of galaxies are in a low-activity regime, and the same can be said about the Black Holes at their center. Nevertheless, a portion of those SMBHs accrete matter at a high rate and become bright enough to dominate the emission of their entire galaxy in different wavebands. Such bright objects are nicknamed **Active Galactic Nuclei** (AGNs, see Padovani et al. 2017 for a review). The proportion of AGNs changes in the more distant (older) universe (Aird et al. 2015; Buchner et al. 2015), matching the peak of star formation of galaxies across cosmic time around $z \sim 2$, as we show in the right panel of Fig. 1.16).

Accretion in AGNs is also the result of an accretion disk. Since the Szchwarschild radius of a Black Hole scales linearly with its mass, AGN disks are necessarily millions to billion times bigger than those of Stellar Mass Black Holes. This has two **fundamental** consequences. First, the **accretion** region becomes much **more stratified** than a "simple" accretion disk, with a combination of a central disk, an obscuring torus, and (multiple) clumpier dusty regions with specific temperatures, chemical compositions and kinematics. Secondly, under Keplerian assumption, the **timescale** of evolution in an accretion disk scales linearly with its radius. For **AGNs**, this equals to **millions of years**, and thus forbids any comprehensive evolution study on single objects in human timescales.

The main practical outcome is that contrarily to XRBs, the classification of AGNs is mainly based on statistical studies, with large samples of virtually static objects being assumed as snapshots of a common evolution. Among the main differences in AGN behavior, some of the most important are the luminosity (or accretion rate) and the presence of a jet. The last parameter is the inclination angle, which can considerably modulate the detected properties of otherwise similar objects, i.e. due to obscuration (for high inclined sources) or doppler beaming (for face-on sources). The combination of all 3 leads to a "unification" scheme of all AGNs at first order, according to their detected properties

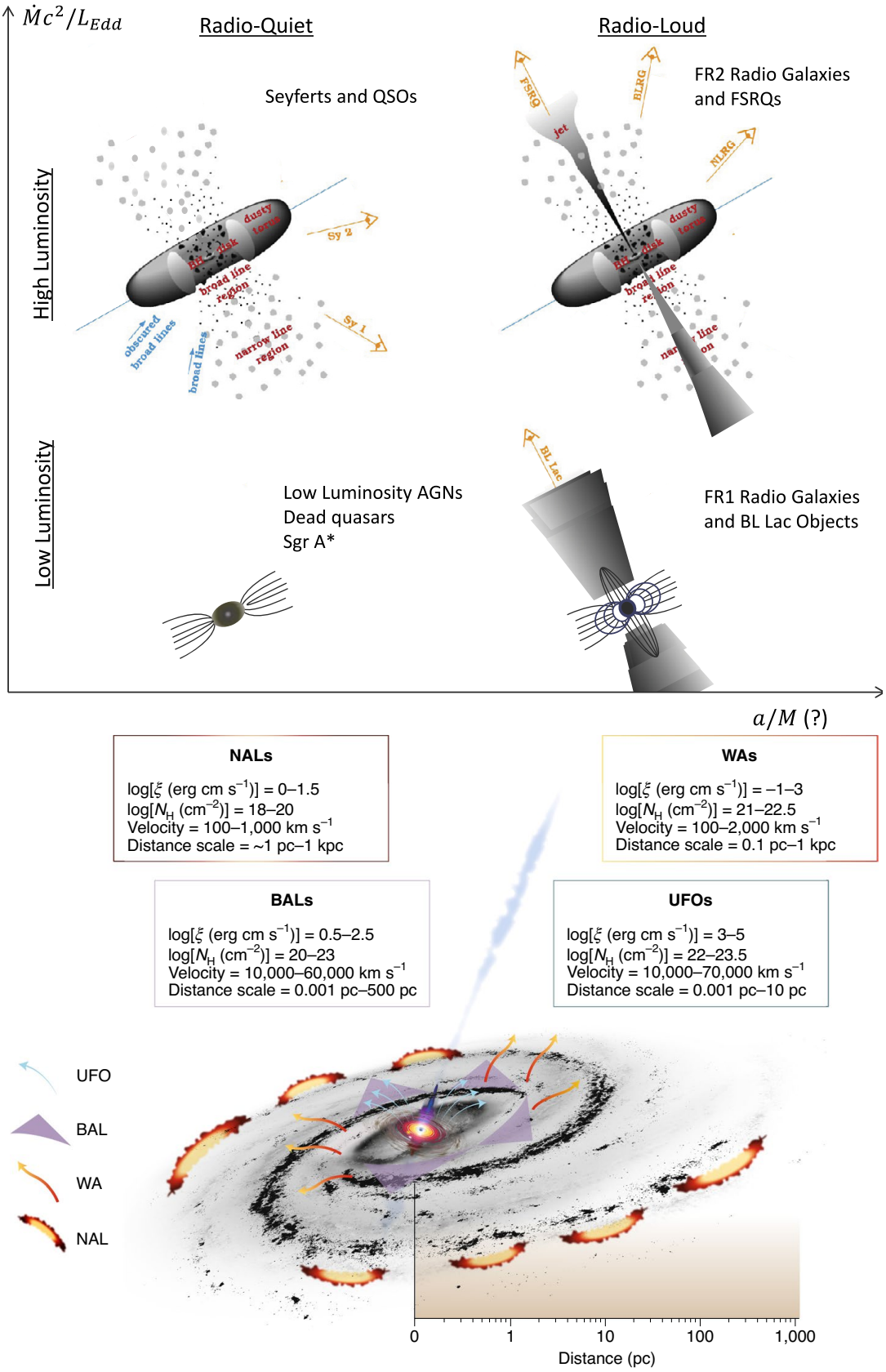

Figure 1.17: **(Top)** Illustration of a tentative AGN classification in a spin-luminosity plane, combined with inclination angle, from Dermer & Giebels (2016). **(Bottom)** Parameters and scales of the main ionized outflow types in AGNs, from Laha et al. (2020)

(Urry & Padovani 1995), of which an updated version is presented in the upper panel of Fig. 1.17.

It is important to highlight that in XRBs, dynamical measurements and jet properties allow for good inclination estimates in a significant portion of the population. On the contrary, direct inclination estimates of the SMBH are impossible in all but the closest (resolved) galaxies and jets. Instead, indirect properties, such as the ones we detail below, are correlated to assumptions of a geometry and give an approximate inclination ranges for each object.

Among the notable subtypes in this classification are quasars, a historical term referring to sources dubbed "quasi-stellar" for their optical emission, later revealed as very distant, unresolved bright AGNs. Nowadays, it refers to more face-on sources, and can be further distinguished depending on the presence of a jet and/or different types of emission lines. The brightest quasars with a notable jet contribution at high energies (and notably in γ) are often dubbed Blazars. Similarly, Seyfert galaxies are another term referring to radio-quiet (jet-less) AGNs, with either narrow (Seyfert I) or both narrow and broad (Seyfert II) emission line detections. A word of caution: in the illustration, the presence of jets is related to the spin of the Black Hole a. However, the mechanism at the origin of jets in Black Holes (and notably AGNs) remains debated (see Blandford et al. 2019 for a review). Among the competing (but potentially combining) hypothesis are processes involving extraction of the rotational energy from the Black Hole itself (Blandford & Znajek 1977), extremely reliant on high spins, but also from its disk (Blandford & Payne 1982), much less reliant on the spin.

Aside from collimated jets, the complex accretion structure in AGNs also leads to a number of different outflow types (see Laha et al. 2020 for a review and Fig. 1.17 for an illustration). Depending on their properties, they are commonly separated between Ultra-Fast Outflows (UFOs, see Gianolli et al. 2024 for an up-to-date overview), Warm Absorbers (WAs), Broad Absorption Lines (BALs) and Narrow Absorption Lines (NALs). We will come back to the different categories in Sec. 2.1.

Remember me

- in AGNs, the accretion onto SMBHs also takes the form of an accretion disk, although more stratified and orders of magnitude bigger than in XRBs.
- Since the timescale of the disk evolution is proportional to the BH mass, AGNs are expected to evolve over millions of years.
- The studies of X-ray Binaries and Active Galactic Nuclei are complementary:
  - Individual XRBs can be seen evolving significantly on human timescales, but because of their luminosities, only the few hosted in our galaxy can be studied.
  - AGN evolution happens way too slowly to be quantified, but the millions of potential sources allow to draw conclusions from population synthesis.

The combination of direct irradiation with the kinetic power and mass rate provided by jets and outflows are expected to be the cause of some, if not all, of the many links detected between SMBH and galactic properties. Similarly to XRBs, a definitive answer requires good theoretical models of the accretion flows and, especially here, of the corresponding outflows. Yet the task at hand is quite formidable, and for now no self-consistent physical model comparable to the data exists for the continuum properties themselves, nor the outflows, nor the jets.

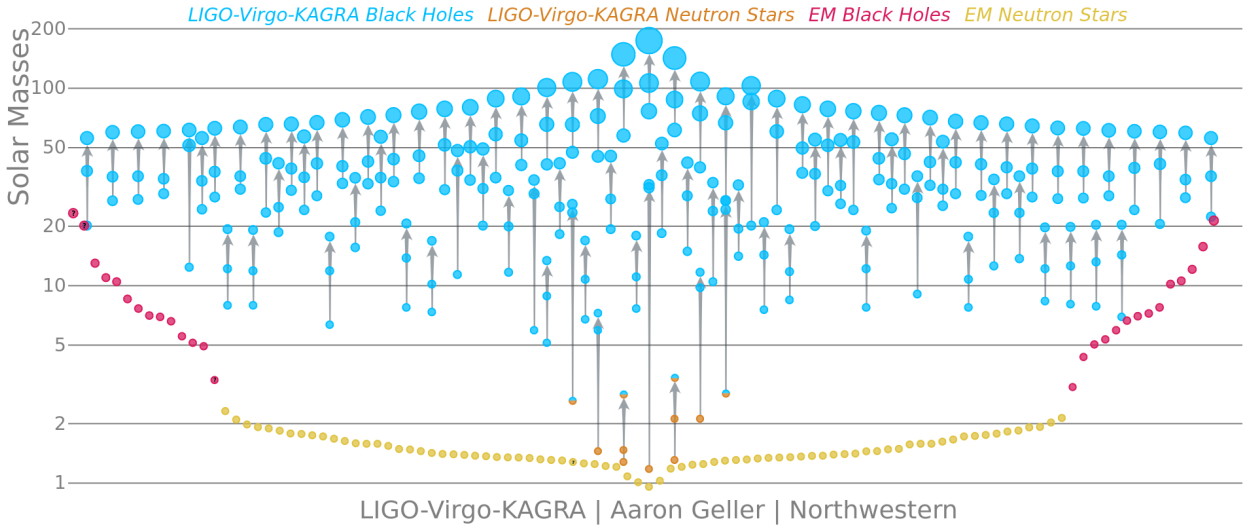

Figure 1.18: Comparison between the electromagnetic (EM) and Gravitational Wave (LIGO-Virgo-KAGRA) mass detections of Stellar Mass Black Holes and Neutron Stars, from https://media.ligo.northwestern.edu/gallery/mass-plot

1.4.2 Bridging the gaps

The Black hole parameter distribution

The advent of Gravitational waves and the detection of Black Hole binary mergers have opened an entirely new prospect, to compare the properties of an independent Black Hole population to the historical measurements from X-ray Binaries. It has quickly become apparent that both of the parameters that describe astrophysical Black Holes (namely mass and angular momentum, also called spin) have very different distributions in both populations. Despite being heavily unexpected, this is proving very useful to test the methodology of X-ray measurements and understand the evolution of Black Holes in and out of binary systems.

The most well constrained parameters in GW and electromagnetic radiation alike is the Black Hole Mass. When plotting the measurements of both populations in Fig. 1.18, it becomes apparent that the GW population is significantly more massive than the measurements of Black Holes in Binaries. In addition, the only values reported here for XRBs are the result of reliable dynamical measurements (see Sec.1.2.2), and thus their uncertainties are very low. This begs the question on how to explain a difference in populations leading to a ~ 5 factor in mass between the two. While Black Hole binaries are in a later stage of evolution compared to X-ray Binaries, this is far from sufficient to expect the discrepancy.

Several arguments have been proposed to resolve the tension (see Mapelli 2020 for a review), among which more metal poor (potentially older) stars collapsing into already higher mass BHs to create the GW population. The very recent discovery of a dormant 33 $M_\odot$ BH from Gaia (Panuzzo et al. 2024), in a binary with a metal-poor companion, provides a very strong argument in favor of the first scenario, and more are suspected to follow considering that the dataset from this detection, Gaia DR4, is still under preparation. Nevertheless, this cannot account for the entirety of the discrepancy, as the components of higher mass mergers, and notably the famous GW190521, are very unlikely to result directly from core-collapse Supernovae. Indeed, this event had both initial BH masses above $\sim 60 M_\odot$, incompatible with pair instability processes, which prevent the creation of BHs in the $\sim 60-140 M_\odot$ range (Abbott et al. 2020). Instead, these progenitors are more likely to result from progressive (hierarchical) BH mergers, which can create BH with much higher masses in dense environments.

The second parameter with tension is the spin, which is commonly expressed as a dimensionless parameter a between -1 (maximally retrograde spin) and +1 (maximally prograde spin). For single stars,

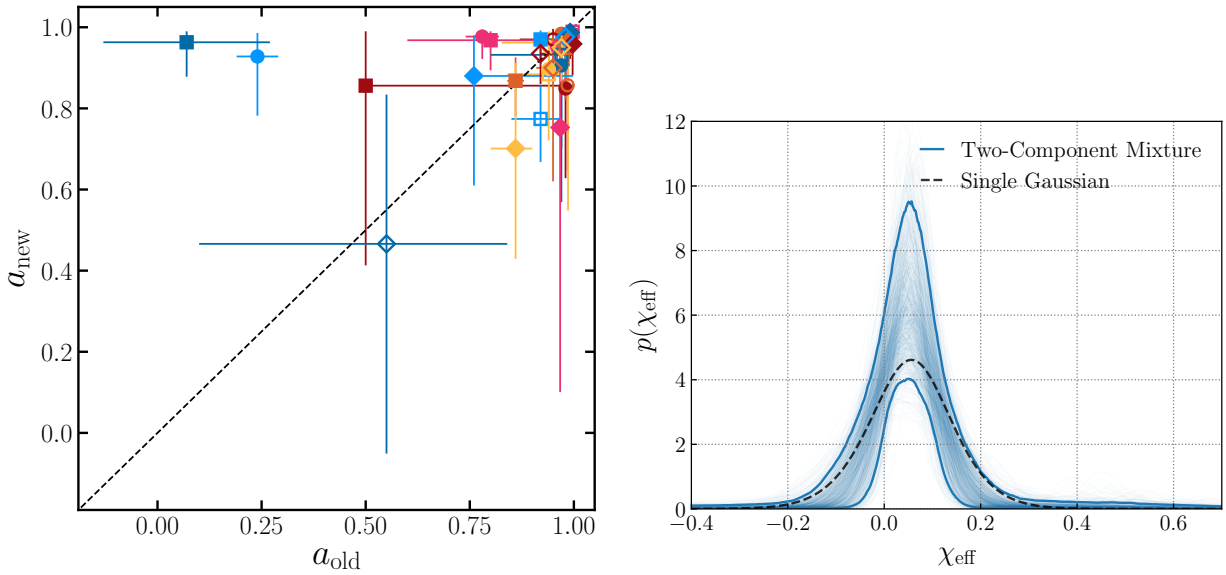

Figure 1.19: **(Left)** Distribution of the spin estimates from reflection measurements in a sample of 36 BH XRBs, from the literature (x-axis) and from a global study by Draghis et al. (2024) (y-axis). **(Right)** Distribution of the effective spin parameter (an almost conserved quantity in BH binary mergers) measured from GW mergers, from Callister et al. (2022)

theoretical estimates from stellar evolution models unequivocally points towards low spin values (Fuller & Ma 2019), but a much higher diversity of scenarios can expand the possible outcomes in binary systems. X-Ray Binaries allow for estimates of the spin notably from modeling of the relativistic iron line and reflection features seen in X-rays (see Sec. 1.3.1), which overwhelmingly result in high spin values, as seen in the left panel of Fig. 1.19). On the other hand, Gravitational Waves allow for a more direct estimation from the signal waveform, but are restricted to the effective spin parameter (namely, a combination of the spins of both components). Nevertheless, as we show in the right panel of Fig. 1.19, this effective spin clearly peaks around very low values (see Abbott et al. 2023 for a review), much more compatible with stellar evolution results, and the community is debating whether the distribution includes a 0 spin component (Callister et al. 2022). Such a starking difference in distributions may imply that the BH sources probed by mergers and XRBs may be coming from different populations, as the difference in mass distribution suggests. In this case, most BH could be sped up during specific accretion phases of LMXBs, which show typically higher spins than HMXBs (Fishbach & Kalogera 2022). However, recent simulations show than magnetized disks including outflows are more likely to significantly lower the spin instead (Lowell et al. 2023).

But the most simple solution may be an issue with the esimates of spins in BHXRBs. Indeed, one of the issues with reflection measurements, besides strong degeneracy between parameters, is how much they depend on the modeling of the continuum. Recent studies have shown that for HMXBs such as Cygnus X-1, spin measurements down to ~ 0.1 could be obtained under different assumptions (Belczynski et al. 2023; Zdziarski et al. 2024), and thus a global re-evaluation of spin measurement is required before comparing with GW estimates. In addition, tentative XRB spin estimates from purely timing properties (see Sec.1.3.2) provide much lower values, more in line with the GW measurements.

Extremal Black Hole growth in the old and recent Universe

Until this point, we've voluntarily omitted one of the most important elements influencing accretion, namely the feedback of the emission on the accretion process itself. Since the electromagnetic radiation will be at the origin of a certain amount of radiation pressure, above a certain threshold, it will be enough to overtake the gravitational attraction at the position at which it is emitted, disturbing the accretion process. This limit can, at first order, be estimated with a few simple assumptions, among which supposing the accreted material to be essentially composed of ionized hydrogen. In this case, the

Definitions

- **Eddington Limit** (L_{Edd},$\dot{m}_{Edd}$): Theoretical upper limit of standard spherical accretion, due to radiation pressure overpowering gravity. Because of the interplay between accreted matter and emitted radiation, this is both a luminosity and accretion rate limit. Sources or processes surpassing this limit are called **Super-Eddington**.
- **Ultra-Luminous X-ray Source** (ULX): Observational Term referring to sources above the Eddington Limit of stellar mass objects, yet not SuperMassive Black Holes. A peculiar type of X-ray Binary, thought to harbor Compact Objects accreting in Super-Eddington regimes.
- **Intermediate Mass Black Holes** (IMBH): Black Hole in a Mass Range between $\sim$ 100 and $\sim 10^5$ solar masses. The necessary link between Stellar Mass Black Holes and SuperMassive Black Holes, and the probable origin of the brightest Ultra-Luminous X-ray Sources. Only a handful of such objects have been discovered.

energy transfer from radiation pressure occurs through Thomson scattering, whose efficiency depends on the cross-section of the interaction, itself scaling with inverse square of the particle's mass. Thus, with $m_e/m_p << 1$, the photons transfer their energy mainly to the electrons. On the other hand, electrons themselves are barely affected by the gravitational attraction, but the Coulomb interaction still affects the protons as they are drawn to the electrons, so both masses need to be considered for the gravitational attraction. The point of balance between both forces happens at the so-called "Eddington Luminosity", defined for a steady accretion onto a spherical object as :

$$F_{rad} = F_G \iff \frac{L_{Edd}\sigma_T}{4\pi r^2 c} = \frac{G\mathrm{M}_{CO} m_p}{r^2} \iff L_{Edd} = \frac{4\pi G \mathrm{M}_{CO} m_p c}{\sigma_T} \sim 1.3 \cdot 10^{38} \left(\frac{\mathrm{M}_{CO}}{\mathrm{M}_\odot}\right) \mathrm{erg/s} \tag{1.5}$$

With σ_T the Thomson scattering cross-section, M_{CO} the mass of the accretor, m_p the mass of the proton, G the gravitational constant and c the speed of light. This estimation extends the local nature of the phenomenon to a global limit, and although this means that this specific approximation of L_{Edd} can be slightly exceeded in more complex geometries, it still acts as a decent approximation for the maximal attainable luminosity of an accretor in a classical configuration.

Another way to characterize the accretion flow is to consider the mass accretion rate. Using the relation between emitted luminosity and accreted matter defined in Sec.1.1.3, we can define the Eddington mass accretion rate as :

$$\dot{m_{Edd}} = \frac{4\pi G \mathrm{M}_{CO} m_p}{\eta c \sigma_T} \tag{1.6}$$

Which turns out especially problematic for the growth of SMBHs. As a simple example, for a BH seed of $\sim 100\ \mathrm{M}_\odot$ to reach $10^9\ \mathrm{M}_\odot$ through constant accretion at the Eddington limit with reasonable radiative efficiency, the process would take ~ 0.77 Gy (Pacucci et al. 2015). On the other hand, recent observations are making constant discoveries of Black Holes in the very young universe, with a number of AGN discoveries at z$\sim$ 7 (< 800 My after the big-bang with standard cosmological parameters), among which a recent detection at 7.642 (or < 700 My after the Big-bang, see Wang et al. 2021a). Matching the two is thus very unlikely, especially considering the stability of the accretion required and the constant reservoir of matter necessary, since the maximal accretion rate directly scales on the BH mass. Similarly, a recent discovery of a z= 10 SMBH of $10^7 - 10^8 \mathrm{M}_\odot$ (Bogdán et al. 2023) revealed a notably high mass ratio compared to the stellar mass in the galaxy, of $M_{BH}/M_\star \gtrsim 0.1$ (Goulding et al. 2023). This value, being several orders of magnitudes higher than local values, adds a new parameter to the tension. The assumption than one (or several) elements are missing in the global picture is thus becoming more and

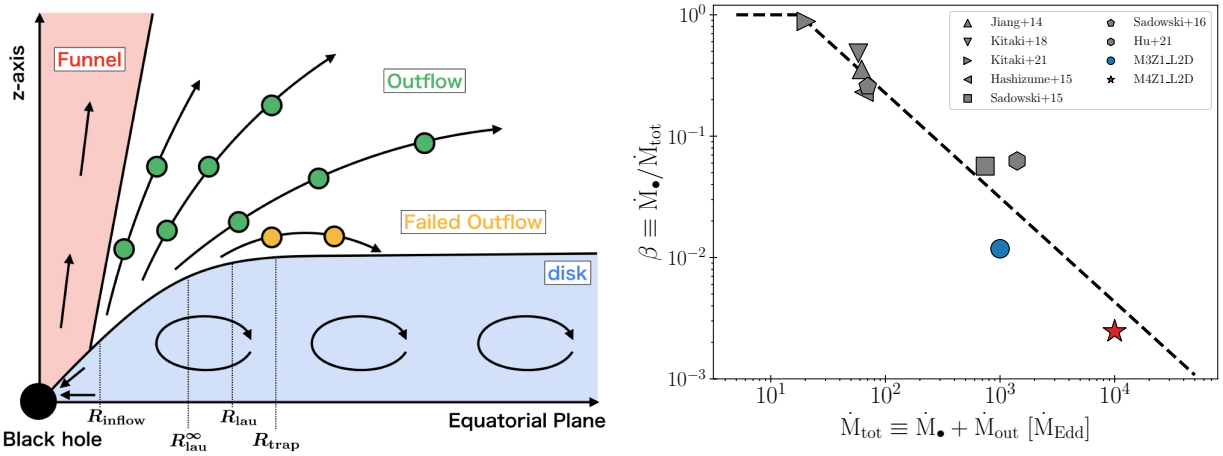

Figure 1.20: **(Left)** Illustration of the geometry of an accretion disk onto a Black Hole in a Super-Eddington Regime, from Kitaki et al. (2021). **(Right)** Evolution of the ratio of "final" accreted rate at the inner disk boundary β, for a range of total mass transfer rate $\dot{M}_{tot}$, combining a range of recent studies of S-E BH accretion disks. From Toyouchi et al. (2024)

more reasonable.

The most straightforward approach is to reconsider the masses of the initial Black Hole "seed". 100 solar Masses is considered a very generous upper limit for Stellar Mass Black Holes in our neighboring universe, and is already an overestimate when compared to the distribution of Black Hole masses from X-ray Binaries and from theoretical evolution models (see Sec.1.4.2). However, this is only when considering the neighboring recent stellar populations, and several more exotic formation channels are considered for the primordial universe (see Volonteri et al. 2021 for a review). It is theorized that at early cosmological times, metal free stars (the so-called population III) of several hundred $M_\odot$ could directly collapse into BHs of few $\sim 10^2$ $M_\odot$, which could then rapidly merge in dense stellar clusters. Another possibility is for heavy dense gas clouds, which could collapse into even bigger BHs weighing up to $\sim 10^4 M_\odot$. Nevertheless, no proofs of the existence of these objects will become available, for as long as no instrument can probe up to $z \sim 50$.

The second approach, which had already gained significant traction over the last decades, is to focus on accretion beyond the Eddington limit, namely, **Super-Eddington** accretion (S-E, see (King et al. 2023) for a review), which may also be the only way to explain the many detections of AGNs with significantly Super-Eddington luminosities (see e.g. (Suh et al. 2024) for a recent $40 \times L_{Edd}$ detection at $z \sim 4$).

Understanding Super-Eddington accretions requires a more careful treatment of the many processes known to affect the radiation of the disk. First, when the accretion rate surpasses $\sim 0.3\, \dot{m}_{Edd}$, radiation pressure tends to extend the height of the -hitherto thin- disk Shakura & Sunyaev (1973). This greatly reduces the efficiency of the emission process, since a part of the radiation now remains blocked in the disk, allowing for higher accretion rates. This idea is at the basis of a lot of the current Super-Eddington models, considered as “thick disk", where the H_{disk}/R_{disk} ratio can even go beyond 1, surpassing 5 for accretion rates 15 times above $\dot{m}_{Edd}$ Kaaret et al. (2017). Nevertheless, such scenarios also require massive, fast $v \geq 0.1c$ outflows which effectively eject the majority of the accreted matter before it reaches the BH.

In addition, when considering super-Eddington accretion for a BH, some photons could be lost by advection beyond the event horizon when trapped (i.e. continuously scattered) in this optically thick disk. Including this photon-trapping effect can lead to even more inefficient models for which the disk can remain geometrically thinner, with $H_{disk}/R_{disk} \leq 1$, hence called “slim disk" models Abramowicz et al. (1988). In all cases, the resulting models end up with very low radiative efficiencies, converging to

$L_{out} \sim 1 + ln(\dot{m})$ for highly S-E accretion, and making it virtually impossible to surpass few tens of L_{Edd} (see e.g. Sakurai et al. 2016). We show an illustration of a proposed geometry considering these effects in the left panel of Fig. 1.20.

In parallel, numerical simulations of BH Super-Eddington accretion tend to provide very different results in terms of outflow rates, with (notably) ratios of the outflow mass rate over the inflow rate at the inner radius varying between ~ 0.15 (Kitaki et al. 2021) and ~ 20 (Hu et al. 2022). Nevertheless, the common picture as slowly emerged in the last decade, in which the fraction of the total accreted matter in the outer disk (which effectively reaches the Black Hole) strongly decreasing with the accretion rate (Toyouchi et al. 2024), as shown in the right panel of Fig. 1.20. However, it is worth noting that none of these simulations consider the effect of large scale magnetic fields on the evolution of the disk, despite it being shown to affect significantly the accretion structure for sub-Eddington sources (see Sec. 1.3.3 and SEc. 2.2.2), despite some specific solutions of i.e. magnetically choked disks remaining viable well beyond the Eddington limit (Lowell et al. 2023).

Constrains on such extreme accretion flows may then be provided from S-E observational signatures, which are in fact not limited to SMBHs. Starting back from Equation **(1.5)**, the Eddington luminosity for a 20 $M_\odot$ BH is roughly $L_{Edd} \sim 3 \cdot 10^{39}$erg/s. This value is historical and matches the heaviest Stellar Mass BHs detected before the advent of GW astronomy, see 1.4.2. and can be considered as a decent order of magnitude of the maximal (isotropic) luminosity that can be emitted by stellar remnants. Thus, objects beyond this limit and located outside of the nucleus of their host galaxies (to rule out the presence of AGNs[10]) are considered **Ultra-Luminous X-ray Sources** (ULXs, see King et al. 2023 for a review). More than 1800 ULX candidates have been identified (Walton et al. 2022) in the neighboring galaxies, thanks to their high luminosities. As the population of ULXs originates from an entirely energetic dichotomy, it is (expectedly) heterogeneous, and a sub group seems to display remarkable spectral properties, at odds with those observed in galactic X-ray binaries in the classical regimes.

ULXs were initially supposed to simply be BHs accreting through accretion disks, and were thus modeled following the same principle (which we will detail in Sec. 1.3.1). However their thermal component tends to be better described with lower disk temperatures, and at first order, the disk temperature scales linearly with the mass of the BH. This was interpreted as the indicator of more massive objects (c.f. Mezcua & Mar 2017 and references therein), with a “classic" Sub-Eddington accretion pattern. However, ULXs also maintain a high energy component despite a much softer thermal component, meaning that their corona has to be much cooler and thus in a different configuration than standard X-ray binaries. This makes temperature parallels for mass estimates became much more questionable (Roberts et al. 2005). Moreover, broad band observations show that several ULXs exhibit a cutoff in their spectrum at $\sim 2-7$ keV (Bachetti et al. 2014; Stobbart et al. 2006), a much lower values than what is typically found in XRBs (see 1.3.1. Coincidentally, the spectral variability of ULXs greatly differs from the usual XRBs patterns (Roberts et al. 2005), as instead of DIM powered outburst with a standard cycle of state transitions, they tend to show more complex state evolution on timescales of days to weeks (Gúrpide et al. 2021; Roberts et al. 2005), but on much smaller ratios outside of a few outliers (see e.g. Bachetti et al. 2014).

Nowadays, the majority of ULXs are assumed to be either NS or stellar-mass BHs, with much higher accretion rates, in a so-called “ultra-luminous" states Gladstone et al. (2009) rarely seen in X-ray Binaries. The strongest argument in favor of stellar mass objects comes from a small but steadily increasing amount of ULXs found to exhibit notable pulsations in their light-curves (see e.g. Quintin et al. 2021 and references therein), with the added element of high positive $\dot{P}$ values (the period derivative). These Pulsating ULXs (PULXs) must thus be powered by an a accreting NS, progressively accelerated due to a transfer of momentum originating in the accretion disk Bachetti et al. (2014). The recent discovery of a

[10]While it is theoretically possible that off-center SMBHs could be at the origin of such emissions, the radial drift for such massive objects, due to gravitational friction with the contents of the galaxy, is very likely to bring them close to the galactic center in very short timescales (a few 10^6 years)

Be-HMXB with a Neutron Star in our galaxy, alternating between standard HMXB behavior and Ultra Luminous states (Wilson-Hodge et al. 2018), also points towards ULXs being simply a specific phase of accretion in otherwise standard X-ray Binaries. In this case, the (highly uncertain) proposition that most ULXs are Neutron Stars would match the standard distribution of NS and BHs in XRBs.

Meanwhile, some of the most luminous ULXs show properties differing vastly from the norm. ESO 243-49 HLX-1, discovered in 2009 (Farrell et al. 2009), is not only remarkable in terms of luminosity (with $L > 10^{42}$ erg/s recorded during flarings), but also for its spectral variability, much closer to standard XRBs than other ULXs. Indeed, its distinct state transitions match very well their LMXBs equivalents (Godet et al. 2009, 2012; Servillat et al. 2011), although at luminosities three orders of magnitude higher. This source is thus assumed to be a rare case of Black Hole of few 10^4 $M_\odot$, possibly a former SMBH at the low-end of the mass distribution, in a small galaxy that would have been tidally stripped by its current host (Mapelli et al. 2013). Despite the lack of similarly luminous objects until recently (Lin et al. 2018), the term “HLX" has emerged to distinguish the “standard" ULX population ($3 \cdot 10^{39}$ erg/s $\lesssim L \lesssim 10^{41}$ erg/s) from Hyper-Luminous X-ray Sources, with $L \gtrsim 10^{41}$ erg/s. An other element in favor of this distinction is the beginning of a cutoff appearing at 10^{41} erg/s in the luminosity function of ULXs (Mineo et al. 2012). However, the heavy fraction of contaminants remaining in current ULX catalogs and the lack of a reliable HLX sample makes any interpretation difficult.

Although its distance might complicate the detection of notable features in its environment, HLX-1 is devoid of influence on the surrounding medium, once more hinting to classical, Sub-Eddington accretion. However, this is not the case in at least a part of the standard ULX population, around which strongly ionized shock bubbles have detected in the optical and radio (Abolmasov et al. 2007; Gúrpide et al. 2022; Pakull & Mirioni 2002; Soria et al. 2021). The energy required to create these bubbles is several orders of magnitude above standard Supernova Remnants. This requires a very high mechanical power output from the central object, and thus strongly hints at the presence of powerful, long-lasting outflows emitted by the central ULXs. This interpretation is supported by an increasing amount of direct ionized outflow detections in the X-rays (Kosec et al. 2021) at relativistic velocities ($v \sim 0.1-0.3c$), notably in sources where ULX bubbles have been detected.

These multiple signs of outflows are perfectly compatible with typical Super-Eddington accretion models, but also have a very important consequence on the interpretation of the detected luminosities. Since even extremely Super-Eddington accretion disks can hardly produce luminosities of a few 10s of L_{Edd}, two interpretations have been advanced to explain the most luminous ($L \sim 100 L_{Edd}$) NS ULXs discovered. The first interpretation proposed after the discoveries of PULXs was that these NS-ULX are magnetars with magnetic fields beyond $B \gtrsim 10^{14} G$ (Dall’Osso et al. 2015; Ekşi et al. 2015). These extreme magnetic fields would be able to affect the electron scattering opacity (which defines the Eddington luminosity) in their vicinity, and thus "artificially" raise their Eddington limit, allowing them to accrete very high amounts of matter while maintaining subcritical rates (Mushtukov et al. 2015). However, this interpretation is severely criticized (Lasota & King 2023), in favor of the other scenario, namely an anisotropic, beamed emission (King et al. 2001), due to a powerful disk wind restricting the solid angle of the initial radiation. With sufficiently high degrees of beaming, the observed emission would be compatible with BHs and even NS sub-Eddington accretion.

While this scenario has yet to be directly validated, it is very compatible with the appearance of a low-density, narrow "funnel" around the spin axis seen in several existing Super-Eddington simulations (see e.g. Kitaki et al. 2021), and the increasing amount of direct and indirect outflow detections previously mentioned. Most importantly, it predicts that a much higher number of sources accreting in similar regimes should be seen, although at lower luminosities if from the inside of the wind funnel. While problematic in other galaxies due to the difficulty of detecting distant sub-Eddington sources, few promising candidates have been found, notably thanks to ULX bubbles associated with a significantly fainter, sub-Eddington X-ray sources (Pakull et al. 2010; Soria et al. 2010) that could be seen edge-on. In addition, the highly unusual galactic X-ray Binary SS433, also enveloped by a large Nebula, is expected to

match this accretion scenario. The most recent development is the recent discovery of a very high degree of linear polarization ($\sim 25\%$) orthogonal to the jet in the galactic BH HMXB Cygnus X-3, which has been interpreted as the signature of reflected radiation from the inside of a narrow funnel (Veledina et al. 2023). In this scenario, Cygnus X-3 would be detected as an ULX from an observer along the emission axis.

This discovery has very strong implications beyond ULXs: King (2024) have recently proposed that the high-redshift AGNs could present the same accretion configuration. In this case, the standard methods used to derive mass estimates would be strongly biased by the presence of high velocity ouflows, and the detected AGNS at very high luminosities would instead correspond to a much lower mass interval. This would be due to the beaming factor's dependence on the square of the accretion rate, making less massive objects accreting at high rates appear much brighter than more massive sources at lower accetion rates. Only more direct mass measurements, coupled to a much better description of the outflow properties, will provide a certain answer to this proposition, but it is worth noting that smaller SMBH masses at high redshifts would significantly reduce the tension on Super-Eddington sources.

Another problem in that regard is the sustainability of high accretion rates: while the discovery of ULXs shows that Super-Eddington accretion rates are possible, simplified models of strong outflows from S-E accretion regimes have a tendency to quickly limit the accretion rate to the Eddington limit in AGN simulations, due to the influence of outflows on the environment at bigger scales (Massonneau et al. 2023).

Remember me

- Our current understanding of accretion cannot explain the growth rates necessary to create the SuperMassive Black Holes already present in the early Universe. This is **problematic** because SuperMassive Black Holes and their evolution are the cornerstone of many elements of astrophysics.
- Several of the underlying solutions rely on powerful outflows, whose description is for now very preliminary.

2

Massive outflows: theories and signatures

A complete description of outflows can only be reached by combining three different approaches. An outflow is first and foremost an ejection of matter from a source, and thus there must a physical process enabling this ejection: a launching mechanism. In parallel, ejections have observational signatures that need to be detected, studied and interpreted. By combining the predictions of the former with the constrains of the latter, the passionate astrophysicist aims for two kinds of answers: the possible configurations that the outflow can take in realistic scenarios, and the actual configurations that do express in our Universe.

Nevertheless, performing the comparison requires an intermediate step. The main observational signatures of massive outflows, absorption lines, are not a direct and permanent imprint of the outflow behavior, as they are influenced by several elements aside from the wind itself.

In the following sections, we will progressively introduce each aspect of the description of outflows, focusing on the "massive" outflows colloquially known as winds. There is no "correct" ordering, as the different approaches are heavily interlinked. We thus choose to begin with an introduction of the outflow signatures, before diving into the physical processes generating outflows. Finally, describing the creation of absorption lines will feel much less disconnected after having introduced the ins and outs of outflows.

2.1 Observational evidence in Black Hole spectra

We first aim to introduce the context of winds through its historical definition, and the way it was progressively refined through observations, focusing on detections in Black Hole Low-Mass X-ray Binaries. We leave an exhaustive inventory and a review of up-to-date measurements to the results and discussion of Section 3, and refer to (Díaz Trigo & Boirin 2016; Neilsen & Degenaar 2023; Ponti et al. 2016) for reviews.

2.1.1 Wind signatures in X-rays

X-ray astronomy is a very young science, which has always been, and will continue to be very data limited. By the end of the 20th century, the understanding of many types of stellar objects had skyrocketed, thanks to easy access to high-resolution spectroscopy in the optical and uv band. Among the many processes already observed were absorption or emission lines with various flavors of asymmetry and velocity shifts. These profiles were well understood as the signature of moving gas or plasma, either absorbing or re-emitting radiation at defined energies (see Sec.2.3). For now, it is enough to know that these lines match the medium's ionization level ,often expressed through a so-called "ionization parameter" (which we will introduce properly in Sec. 2.3.2), as well as its density, and chemical abundances (Morton 1991).

The profiles that were blueshifted were explained by different type of **out**flows, including many different flavors of stellar winds (Ebbets et al. 1979; Morton et al. 1979), outflows around young stellar objects (Lada 1985), and even in accreting white dwarfs (Cordova & Mason 1982). The field was already sufficiently advanced to distinguish different categories of outflows for sources with complicated ejection structures: "**jets**" would unanimously refer to fast, narrow and highly collimated ejections, and slower ejections at a broader range of inclinations would be deemed "**winds**", "bipolar outflows" or other terms depending on the source.

However, the observables linked to these phenomena were beyond the craziest dreams of X-ray astronomers at the time: as a matter of fact, the spectral resolution of optical spectrographs commonly used in the 1970s (Tull et al. 1975) was already matching the goal of the X-ray community for the 2040s (Barret et al. 2023). Thus, even if a wide range of theoretical models already predicted the presence of

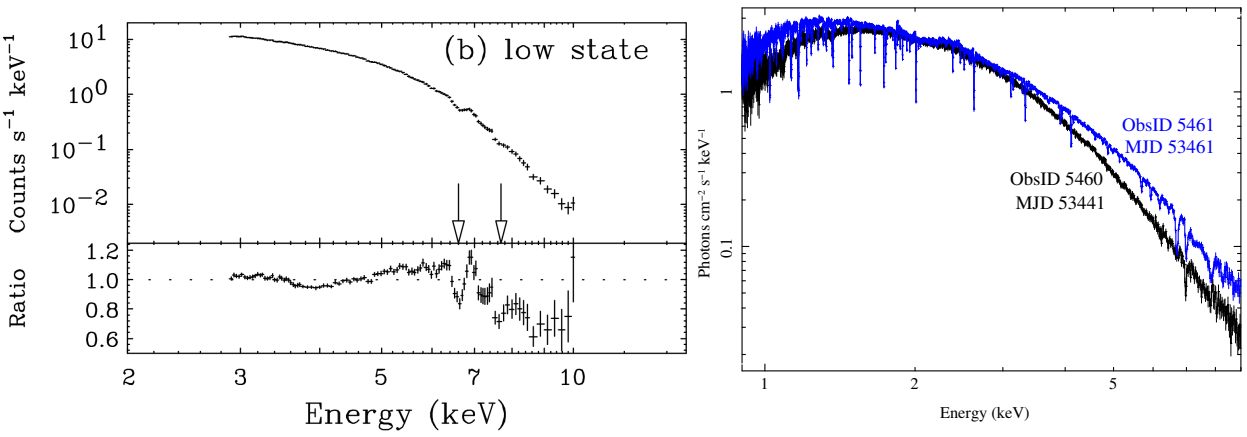

Figure 2.1: **(Left)** ASCA spectra of the BH GRO J1655-40 taken during its 1996 outburst. In the ratio plot between the spectrum and a continuum model, the arrows highlight the first report of ionized absorption lines from a Black Hole Binary. Adapted from (Ueda et al. 1998). **(Right)** *Chandra* spectra of the same source taken during its 2005 outbursts. The observation in blue exhibits the richest diversity of X-ray absorption lines ever seen as of the writing of this manuscript. From Miller et al. (2008).

outflows in X-ray Binaries (as we will see in more details in Sec. 2.2), observational validation would have to wait for the advent of instruments capable of detecting lines in the X-ray band. The first one with high enough capabilities would be the Japanese Advanced Satellite for Cosmology and Astrophysics (ASCA, Tanaka et al. 1994), which included a telescope with unprecedented effective area in the $\sim 0.3-10$ keV band, combined with a spectrometer with resolving power of ~ 50 at 6 keV, where the energy of many of the strongest soft X-ray transitions are gathered (see Sec. 2.3).

During its lifetime, ASCA would indeed make the first observations of absorption lines in X-rays (Kotani et al. 2000; Ueda et al. 1998), from Fe xxv Kα and Fe xxvi Kα transitions at ~ 6.7 and ~ 7 keV. We highlight one of such detections in the left panel of Fig. 2.1. Nowadays, these are regarded as the first ever X-ray wind detections, but at the time, the absolute calibration of the instrument was not sufficient to assess the velocity of the absorbing material, and the detections were conservatively reported as ionized absorbers. The matter was finally settled with the next generation of instruments, and notably the *Chandra* X-ray observatory (Weisskopf et al. 2000), embarking the first high-resolution X-ray instrument, HETG. This led to multiple detections of clearly blueshifted absorption lines in the following years (Lee et al. 2002; **?**), culminating in a spurious observation of an extremely rich structure in the BHLMXB GROJ1655-40 (Miller et al. 2006a), shown in the right panel of Fig. 2.1, which even now remains by far the most detailed X-ray outflow observation ever made.

A steadily growing number of signatures were found in the next few years, including with other recent telescopes (at the time) such as XMM-*Newton* and *Suzaku*, but only in very restricted categories of sources and observations, with high densities, and very low but significant velocities of few 100 km/s, matching the canonical definitions for "winds" in other wavelengths. In addition, these detections were overwhelmingly obtained through the lines of highly ionized ions (mainly Fe XXV and FeXXVI), implying that the outflowing material itself was highly ionized. As the dichotomy between absorption lines and the detections of radio jets was becoming more and more obvious, it was rapidly proposed that the two mechanisms were anti-correlated (Neilsen & Lee 2009).

The first true push in terms of global understanding of the properties of winds came from the seminal work of (Ponti et al. 2012), which linked the presence of absorption lines both to the accretion state and the geometry of the accretor. As we show in Fig. 2.2, this study showed that the detection of these "wind" signatures was restricted to the soft states of high-inclined BHLMXBs. This had strong implications on the accretion-ejection structure, leading them to propose a geometry (Fig. 2.3) in which the winds (the physical outflows) are primarily equatorial, and only launched from the fully thermalized disk of the soft state. They also derived orders of magnitudes of the mass outflow rate, which was found to be comparable or higher to the accretion rate over two orders of magnitude of luminosities. This gave the

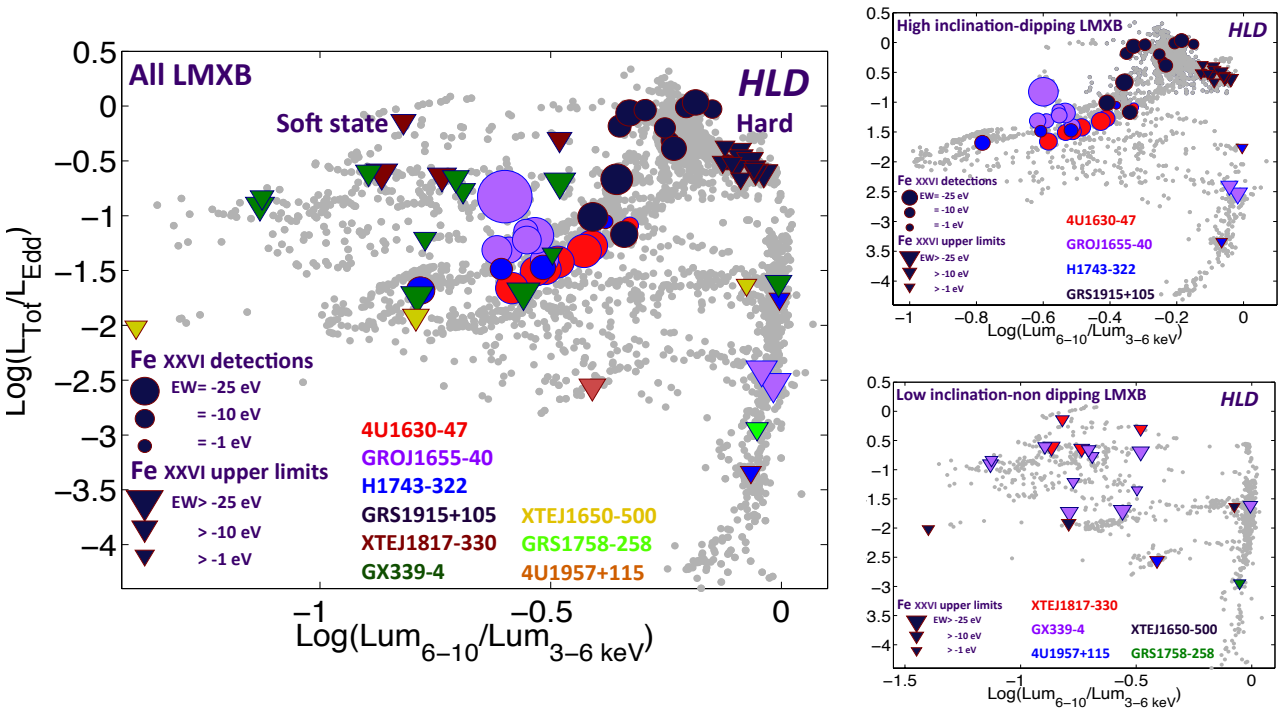

Figure 2.2: **(Left)** Hardness-Luminosity Diagram with wind detections and upper limits in a sample of BHLMXBs. The grey points highlight low quality observations. **(Right)** HLD from the same sample, but restricted to high and low inclination sources respectively. From Ponti et al. (2012)

observational confirmation that winds were a very important part of the accretion process, and would eventually need to be included into accretion models.

Now, more than a decade later, a flock of new detections and theoretical improvements have nuanced and contextualized these results. Among the two main conclusions on the wind geometry, the first assumption of equatorial outflows still holds, but the restriction to the soft states has been significantly weakened. Firstly, the discovery of cold wind signatures much more ubiquitous during the outburst (which we will detail in Sec. 2.1.2) limits this conclusion to X-ray winds, and secondly, the thermal stability of the gas itself is very likely to prevent any absorption line detection in the hard state, no matter the evolution of the outflow (Bianchi et al. 2017; Petrucci et al. 2021, see also Sec. 2.3.3). These new results, as well as several detections during more exotic high-luminosity hard states of BH and NSLMXBs (Homan et al. 2016), point to a more complex relationship between wind and jets than a simple dichotomy (see also Rogantini et al. 2024). In parallel,in the last ten years, X-ray absorption lines have been increasingly reported in more "standard" BHLMXB hard states (see e.g. Shidatsu et al. 2013; Xu et al. 2018a), sometimes for potentially low-inclined sources (see e.g. Chakraborty et al. 2021a; Wang et al. 2018). However, these detections are systematically mixed with strong reflection components, making the two very complex to disentangle, and their interpretation remains debated.

Meanwhile, it is becoming more and more evident that the estimates on the mass outflow rate are significantly oversimplified. As we will see in Sec. 2.2, all wind launching models predict complex evolutions of densities and velocity both with the radius from the central object and along the line of sight. Unfortunately, the inclination usually cannot be probed for single objects (unless they are significantly precessing, see e.g. Kosec et al. 2023), and in the overwhelming majority of observations, the only absorption lines detected are Fe xxv Kα and Fe xxvi Kα lines. As we detail in 2.3.2, this means that state of the wind has to be extrapolated from a single snapshot of a small part of the wind structure, barely bringing constrains to wind models. Only the detection of detailed outflow structures with a wide range of ionization parameters (preferentially combining hot and cold winds) can thus give real

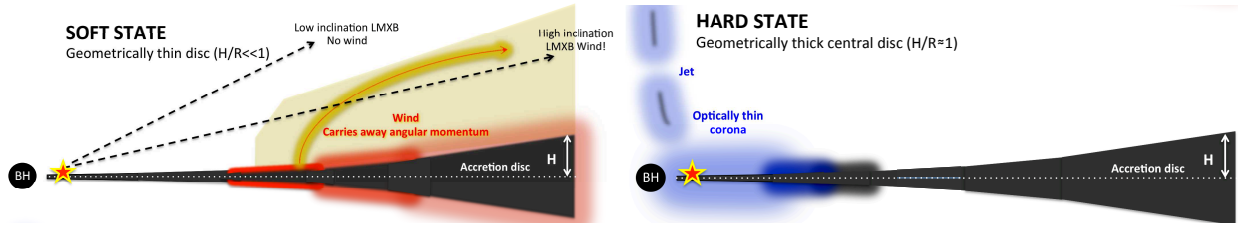

Figure 2.3: **Outdated** geometry proposed to explain the wind dichotomies of Fig. 2.2. From Ponti et al. (2012)

constrains on the actual amount of outflowing material.

For now, the most precise and diverse detections have been compared to simpler photoionization models, which in several cases have revealed additional faster components, with velocities up to ~ 10000 km/s (Miller et al. 2015). For now, it remains unsure if these are indicative of multi-phase outflows, the results of imperfect considerations for specific transitions (see e.g. Tomaru et al. 2023) or hints of specific launching mechanisms. Nevertheless, the overwhelming majority of standard absorption detections remains at $\lesssim 1000$ km/s, once again clashing with the view offered by reflection embedded lines, whose velocities are typically an order of magnitude higher.

However, the previous results only apply to standard XRBs. In recent years, a number of wind detections have also been reported in ULXs (see Pinto & Kosec 2023 for a review). Interestingly, due to the combination of the very low fluxes and (often) soft SEDs of ULXs, the signal to noise ratio in the iron band is insufficient to probe for wind signatures. Instead, a number of lines were found in the $0.5-2$ keV band with the Reflection Grating Spectrometers (RGS) aboard XMM-*Newton*, which is typically not used in most LMXBs due to being entirely absorbed for many galactic sources. These winds are seen in a proportionally much higher fraction of ULXs (Kosec et al. 2021), and with relativistic velocities of the order of 0.1-0.2c, they must thus come from much more powerful, less equatorial outflows. Another difference with standard LMXBs is that a fraction of these outflows are detected in hard states, at typically higher velocities, which can be linked either to the evolution of the S-E structure, or to the viewing angle (which is suspected to affect the Hardness Ratio in these sources). They are also thought to be powered by radiation pressure, due to the extreme intrinsic luminosity of the accretor.

Finally, as we briefly mentioned before, the progress of X-ray astronomy has also led to a number of wind detections in Active Galactic Nuclei (see e.g. (Laha et al. 2020) for a review). They are divided in two loosely defined categories: Ultra Fast Outflows (UFO, Tombesi et al. 2010), detected via very high velocity ($v \sim 0.03-0.3$c) lines at high ionization parameter (typically in the iron band), and Warm Absorbers (WA), found at lower ionization parameter in RGS spectra, with substantially lower velocities ($v \sim 100-2000$ km/s) and a possibly different origin (Yamada et al. 2024). The properties of both categories are significantly correlated with a number of accretion-related parameters (Gianolli et al. 2024), among which the luminosity of the AGN, hinting at a very complex relationship with the central accretion region and the radiation itself. Although these winds are expected to have a very high impact on their environment up to the galactic scales, very low SNRs, poor velocity measurements in most detections, and a much bigger parameter space in both sources and outflows make it very difficult to draw a global picture (Tombesi 2016).

In all cases, our current understanding of X-rays remains strongly limited by the capabilities of current instruments. The launch of the japanese X-Ray Imaging and Spectroscopy Mission (*XRISM*, Team 2020) in 2023, which includes the first true high-resolution X-ray instrument[11], is expected to revolutionize our understanding of winds, notably by allowing direct constrains on the different wind launching mechanisms, via the measurement of absorption line profiles (see Sec.2.2).

[11] to survive the curse of microcalorimeters

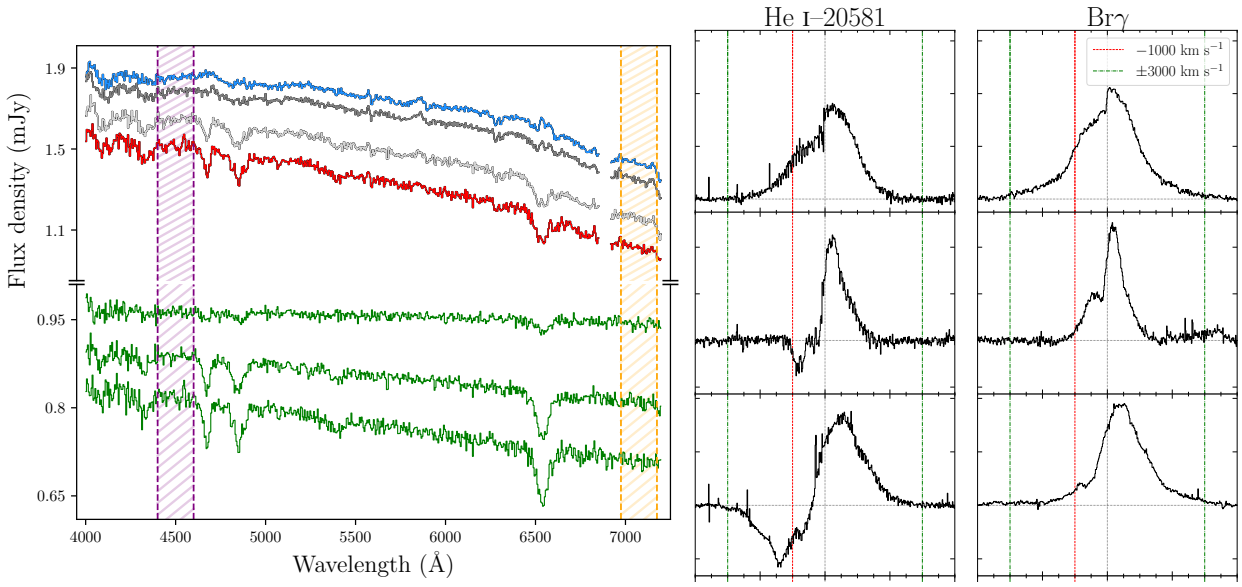

Figure 2.4: **(Left)** Evolution of optical spectral of the eclipsing BH binary Swift J1357.2-0933 during its 2017 outburst, from Jiménez-Ibarra et al. (2019). **(Right)** VLT spectra of the BH binary GRS1915+105 taken during a hard radio loud state in 2019, zoomed on two infrared lines to highlight absorption lines and asymmetric emission lines. From Sanchez-Sierras et al. (2023b).

2.1.2 Cold winds

Despite very high resolution instruments in the visible band, the first unambiguous discoveries of optical wind features in X-ray binaries are very recent (Muñoz-Darias et al. 2016), and probably stem from a renewed interest in high-resolution spectroscopy for LMXBs following the discovery of X-ray winds, combined with an abnormally bright outburst from the well known BH V404 Cyg (Casares et al. 2019; Motta et al. 2017). Since then, commendable efforts to catch up on the many sources with identified optical counterparts have led to a wealth of detections in both the optical and infrared band (see 3.6 for an up-to-date list), with a much broader panels of blueshifted absorption and/or emission profiles, and surprisingly different properties from their X-ray counterparts. We show two examples of the line profiles in Fig. 2.4, with both asymmetric emission and clear blueshifted absorption lines unequivocally signaling outflowing material. The velocity shifts measured for these lines are approximately an order of magnitude higher in cold winds (Panizo-Espinar et al. 2022), but this could stem from the way the observations are interpreted, since for OIR winds, the value generally reported is the terminal velocity, which could either not be detected or match the rarer high velocity secondary components in X-ray winds.

Optical wind signatures are seen exclusively in the hard state (Panizo-Espinar et al. 2022), and although direct near infrared absorptions features are for now also restricted to hard states (Sanchez-Sierras et al. 2023b), other wind signatures in this band have been detected along the entire outburst. These findings imply that the wind is an ubiquitous component of the outburst, preferentially seen at high energies ("hot winds", in the X-rays) in the soft state, and at larger wavelengths ("cold winds") in the hard state. We show a representation of the proposed dichotomy and its application in a wind-emitting BH source in Fig. 2.5. For now, it is unclear whether the high and low energy winds stem from a common phase, due to a (possibly intrinsic) lack of common wind detections except in very non-standard accretion states (Muñoz-Darias & Ponti 2022).

In addition, since several sources with good coverage of the X-ray band in the soft state have no reports of X-ray absorption lines despite a clear OIR detections (see e.g. Mata Sánchez et al. 2024 for a recent example), the "cold" wind phase is expected to have a different distribution, possibly less equatorial. This would also explain the detections in few "low-inclined" NSLMXBs (Panizo-Espinar et al. 2022), although the geometry may not be the same for different objects.

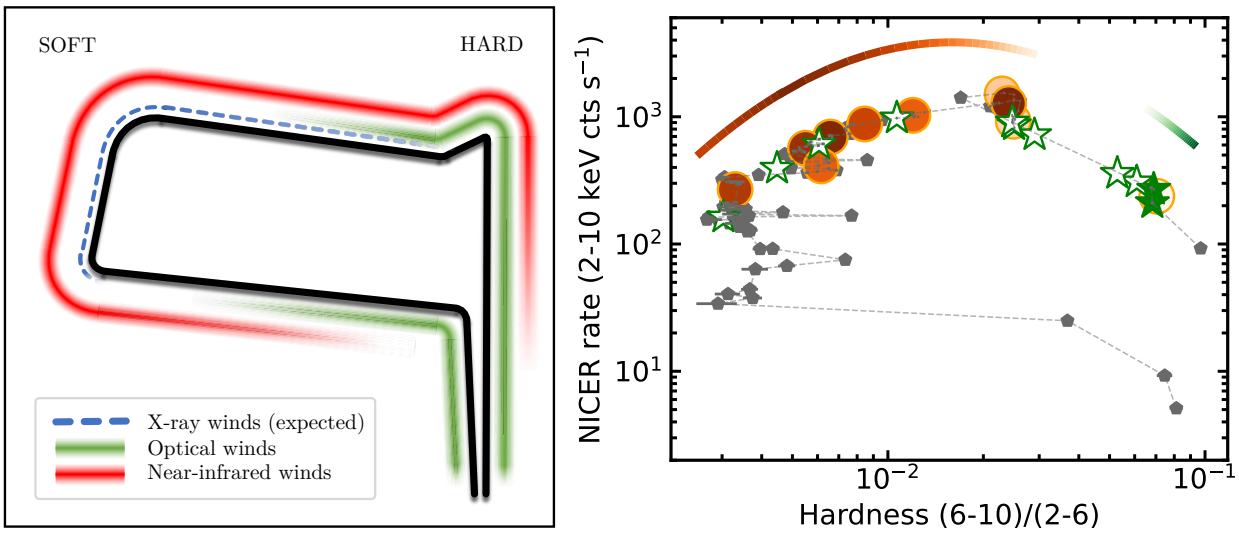

Figure 2.5: **(Left)** Illustration of the (supposed) evolution of the wind visibility along BH outbursts, visualized in a HID. From Sanchez-Sierras & Munoz-Darias (2020).**(Right)** Evolution of X-ray (brown circles) and Optical (green stars) wind detections along an outburst of the BHLMXB MAXI J1803-298. The circles are shaded according to the density of the X-ray wind, and empty stars indicate optical non-detections. No X-ray wind is seen in the hardest X-ray observation (simultaneous to optical wind detections). From Zhang et al. (2024a).

It is tempting to draw parallel with the behavior of AGNs, in which UFOs do not appear correlated to to radio loudness (Mestici et al. 2024). However, this has very different implications depending on whether the radio loudness is considered mainly as an indicator of inclination (implying more spherical outflows) or of the evolution of the accretion state (implying state dependend outflows).

Although this is not the focus of this work, we note that a wide variety of Ultra Violet wind signatures have been reported in AGNs, way before the first detections of winds in BHXRBs. They are mainly distinguished between Broad Absorption Lines (BALS) and Narrow Absorption Lines (NALs) depending on their width. BALs typically exhibit high velocities ($\sim 10000-60000$ km/s) (Weymann et al. 1981), while NALs are restricted to v$\lesssim 4000$ km/s(Chen & Pan 2017). Although no UV wind signatures have for now been reported in BHLMXBs, a few high-inclined NSLMXBs were recently found to exhibit clear P-Cygni (combination of blueshifted absorption and emission) profiles (Castro Segura et al. 2022; Fijma et al. 2023), and thus even if interstellar absorption prevents detection for the vast majority of BHLMXBs, there may be hope for sources out of the galactic plane.

2.2 An inventory of wind launching mechanisms

One of the biggest unknowns in our current understanding of winds is their physical origin. With the current lack of constrain on many aspects of the accretion-ejection structure, several processes can be the driver of the outflows depending on the system considered, with very different effects on the rest of the accretion structure and the outburst evolution itself. Here, we give a brief overview of the main launching mechanisms expected to play a role in BHXRBs, as well as the imprint they leave in the spectra and the current state of modeling efforts in each of them.

2.2.1 Thermal and Thermal-Radiative Launch

It is long known that the irradiation of the inner regions of the accretion disk is able to create mass loss in the outer regions (Begelman et al. 1983). In so-called thermal winds (see e.g. Done et al. 2018 for a review), the X-ray flux from the inner regions heats up the accretion flow, forming an ionized outer

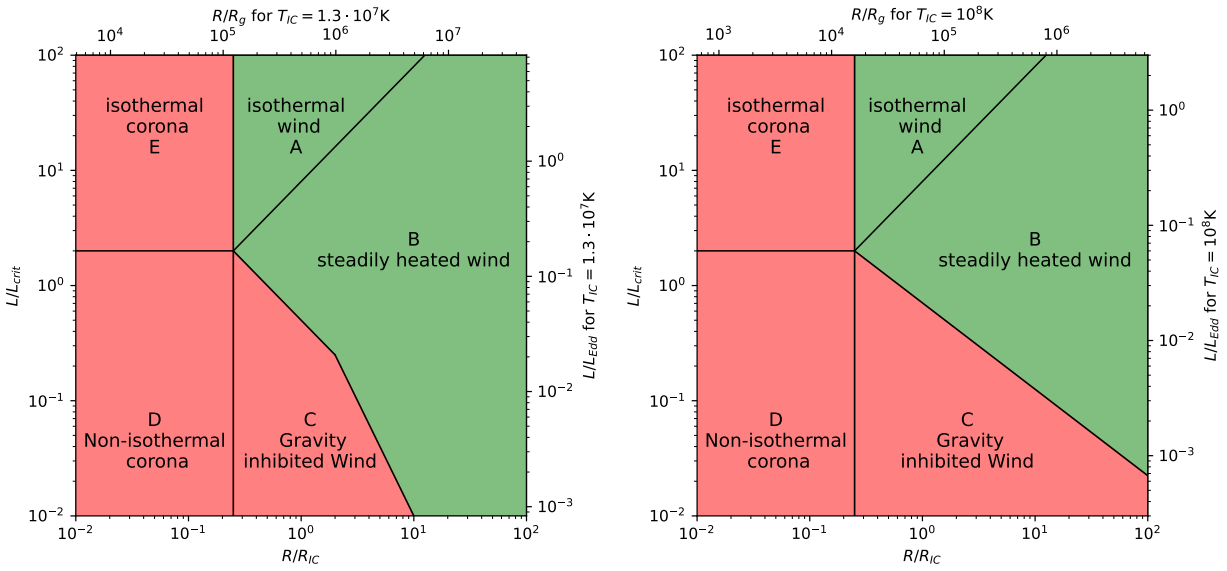

Figure 2.6: Different thermal wind/no-wind regions in a R-L diagram, with a soft state **(left)** and hard state **(right)** T_{IC} value. Adapted from Woods et al. 1996.

layer at the surface of the disk. At first approximation, this layer is in a steady state due to the balance of compton cooling and heating, and reaches a temperature T_{IC}, defined as:

$$T_{IC} = \frac{1}{4kL} \int h\nu L_\nu d\nu \tag{2.1}$$

With k the boltzmann constant and L the bolometric luminosity. T_{IC} does not depend on the luminosity, and instead varies according to the SED itself, with values of the order of $10^7 - 10^8 K$ for XRBs. At such a high temperature, the thermal motion of the particles can easily reach up to $\sim$ 1000km/s, which begs the question of whether this can be enough to unbind the disk material.

The most straightforward limit to for this to happen is the Compton radius R_{IC}, defined from the radius at which the sound speed of the material becomes higher than the escape velocity from the accretor. For a Keplerian disk, this can be expressed as:

$$c_{s,IC} = \sqrt{kT_{IC}/\mu} \;\rightarrow\; R_{IC} \equiv \frac{GM}{c_{IC}^2} = \frac{GM\mu}{kT_{IC}} \sim 6.4 \cdot 10^4 T_{IC,8}^{-1} R_g \tag{2.2}$$

with μ, the mean particle mass being taken at solar abundances in the numerical formula, and $T_{IC,8} = T_{IC}/10^8 K$. This limit can be reached in most XRBs since their typical disk extension is of the order of few $10^5 - 10^6 R_g$ (see e.g. Tetarenko et al. 2016 for BHs). At first approximation, below R_{IC}, the materials remains bound in an ionized atmosphere (Jimenez-Garate et al. 2002), and above R_{IC}, it is able to escape as a wind.

More realistic computations show that the wind can escape starting from a fraction of R_{IC}, and provide a more nuanced delimitation depending on both radius and luminosity (Begelman et al. 1983). Indeed, the compton heating rate depends on the received flux, and thus for a given luminosity, it will be fast enough to heat the material up to T_{IC} only up to a certain radius. The Luminosity limit L_{crit} at which this radius is exactly R_{IC} can be expressed as:

$$L_{crit} = \frac{1}{8}(m_e/\mu)^{1/2}(m_e c^2/kT_{IC})^{1/2} L_{Edd} \sim 0.03 T_{IC,8}^{-1/2} L_{Edd} \tag{2.3}$$

It thus becomes relevant to represent the behavior of the material in a R-L plane: we show two examples in Fig. 2.6, adapted from the simulations of Woods et al. 1996. If the radius is below $\sim 0.25 R_{IC}$,

the material cannot escape and will remain as a static corona, which may (region E) or may not (region D) be heated to T_{IC} depending on the luminosity, with a threshold of approximately ~ 2 times the theoretical L_{crit} value in simulations. Above R_{IC} and at $L > L_{crit}$, the wind is launched in all cases, but remains isothermal only up to a certain radius/luminosity threshold (region A). Beyond this threshold, the gas is only heated up to a characteristic temperature T_{ch} (region B), which is nevertheless enough for the wind to escape. On the other hand, below L_{crit}, T_{ch} becomes insufficient at R_{IC}, and the material can only escape at larger radii. Below this last separation, the corona is locked in the so-called "gravity-inhibited" wind region (region C, which does NOT emit wind).

As we show in the different panels of Fig. 2.6, the SED, via the change in compton temperature, has a very mild effect on L_{crit} and R_{IC}, but a much stronger influence on the physical scales of the system. With a typical change of a factor ~ 10 between $T_{IC,soft}$ and $T_{IC,hard}$, the threshold in radius in physical units for an isothermal wind is reduced by a factor 10 smaller in hard states compared to soft states, and the luminosity threshold becomes several times lower. Both of these make the allowed "parameter space" for the wind much wider in hard states, although stability effects may prevent observational signatures in the X-rays (see Sec.2.3.3).

We stress that these results do not give much constrain on the structure of the wind, but rather on the limits of its existence. Detailed derivations of the wind structure are out of scope of this brief summary, and we simply highlight that they result in much more nuanced behavior, such as the one highlighted in the left panel of Fig. 2.7 for a case of high luminosity wind, with progessive evolution between a cold and warm "corona" and a wind, which itself can be distinguished between a low-density radial component, consequence of streamlines originating from the below the Compton limit (grey) and the denser standard evolution taking its base in the disk atmosphere.

Still, these simple dichotomies are important to establish that thermal winds are restricted to **large radii** and **high luminosities**, which is very useful to understand when they become relevant in different systems. Indeed, one of the direct consequences of thermal wind is that the material has a **restricted velocity range**, of the order of the escape velocity at R_{IC} and thus "only" **few** $\sim$ 100 **km/s**. These elements match the vast majority of X-ray wind detections in BHLMXBS (see Sec.3), and explain the non-outflowing atmospheres found in NSLMXBs, preferentially at low disk extension (Díaz Trigo & Boirin 2016) (regions E and D in Fig. 2.6). However, several notable exceptions exist. In the X-rays, few very high SNR measurements have been made at high luminosities and low Eddington fraction (most notably Miller et al. 2006a, although see Tomaru et al. 2023), but the wind coverage with current datasets is very insufficient to give any global conclusion, both in terms of disk extension (due to the very few sources with this information available), and low luminosities (due to the intrinsic lower SNR of fainter observations), as we will see in Sec.3. On the other hand, the fast "cold" winds seen down to very low Eddington ratios (see Sec.2.1.2) are completely at odds with this view, but the behavior at such low ionization parameter requires a more careful treatment that hasn't been tackled at the moment.

In the meantime, more direct comparisons, and especially direct computations of the absorption line behavior, is a very important first step. Promising attempts have been made in the last few years (see e.g. Higginbottom et al. 2018, 2020; Tomaru et al. 2019, 2023), but increasing the level of fidelity requires departing from this purely theoretical prescription, and thus introduces several major differences.

- First, a more attentive look at the cooling and heating effects has very important effects, introducing a much more complex interplay between the SED and the launching region of the wind (Higginbottom et al. 2017). Indeed, the material at the surface of the disk can be subject to thermal instabilities as its temperature increases due to irradiation from the central source, with stable and unstable states similar to what we saw previously for the disk in the DIM (see Sec.1.2.3 and Sec. 2.3.3). Here, a material heated beyond the end of a "cold" stable branch will experience significant additional heating in order to reaches the next "hot" stable branch. This process may allow to reach the escape velocity much earlier than R_{IC}, but is very dependent on

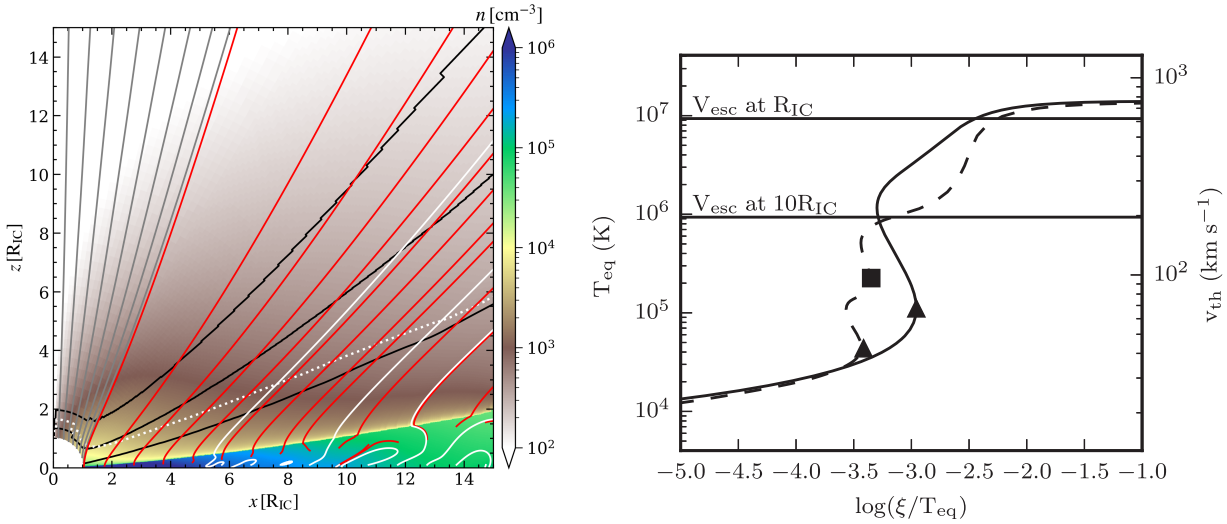

Figure 2.7: **(Left)** Detailed radial structure of a thermal wind solution outside of the compton radius R_{IC}, treating the disk as a z=0 boundary condition. The colormap distinguishes a cold atmosphere (green, blue) from a warmer "corona" (yellow) and the outflow itself (brown). The grey, white and red lines highlight streamlines of various origins, and the black contours the limits for poloidal wind velocities of 500, 1000 and 15000 km/s (from lowest to highest). From Waters et al. (2021). **(Right)** Influence of the stability curve on the thermal wind launching radius, using a parametric cooling rate (full line) and the radiative transfer code CLOUDY (dashed). The triangle show the last position in the first cold branch, but instead of an instability until v_{esc} for $10R_{IC}$, the CLOUDY computation has an intermediate stable branch, with a second threshold materialized by a square symbol. From Higginbottom et al. (2017).

the shape of the curve itself. As we show in the right panel of Fig. 2.7, detailed radiative transfer computations provide many more individual regions than the single unstable branch predicted by simple theoretical models, with different thresholds for increased disk heating due to instability.

- Secondly, the choice of geometry has a large impact on the launching region. One of the remaining uncertainties is the existence of the outflows in hard states, which cannot be probed directly in X-rays due to the lack of visibility (see Sec. 2.3.3). It has been proposed that the inner disk atmosphere could form an optically thick region at sufficiently low inclination angles, and thus shield a part of the outer disk from the X-ray irradiation, following the geometry proposed in the right panel of Fig. 2.8 (Tomaru et al. 2019). Using a purely theoretical prescription, Tomaru et al. (2023) derived that in a high luminosity soft state, the low T_{IC} creates an inner atmosphere with small vertical extension, only shadowing a fraction of the disk and thus with a limited effect on the wind. On the other hand, in a low luminosity hard state, the scale height of the atmosphere would be much bigger, and would thus shield the entirety of the disk from the X-ray radiation, completely preventing any outflow. This scenario could help understand a problematic lack of lines for some intermediate state observations, which cannot be explained by standard thermal wind geometries (Shidatsu & Done 2019).

  Nevertheless, computations of luminous hard states without this shadow zone show weak absorption lines for very high-inclined sources (Higginbottom et al. 2020), and the existence of this region is debated. Indeed, since its radial extension is very small compared to that of the wind, it has not yet been possible to include it directly in the computation, and it remains an 'ad-hoc' (if relevant) addition. The vertical extension of the inner atmosphere also needs to be compared to that of the inner flow, whose geometry is very debated (see Sec.1.3.3) and may be much more geometrically thick than a "simple" thin disk, which could affect the geometry of the atmosphere and/or prevent the formation of a shadow, if it does not already replace the disk at the radii where the atmosphere is expected to arise.

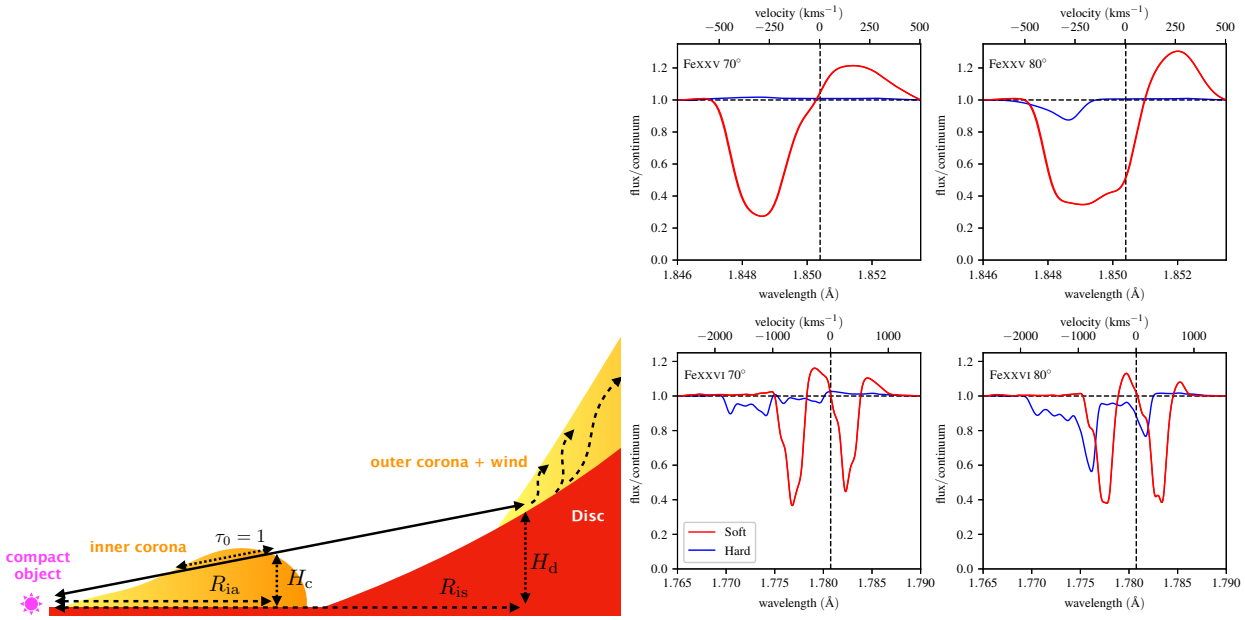

Figure 2.8: **(Left)** Geometry of a disk structure including an optically thick "corona" created by the thermal expansion of the atmosphere in the inner regions, which becomes optically thick at certain angles and thus shadows a part of the outer disk. From Tomaru et al. (2019). **(Right)** Inclination and SED dependence of the Fe xxv Kα and Fe xxvi Kα line profiles with a thermal-radiative wind, from Higginbottom et al. (2020).

- Thirdly, at high luminosities, the radiation pressure of the central object adds an additional force on the irradiated material due to electron scattering (see Sec.1.4.2). Taking this effect into consideration significantly changes the wind structure, and the outflow switches from a purely thermal to a "thermal-radiative" origin[12], with first studies showing that the launching radius is multiplied by a factor $1-L/L_{Edd}$ (Proga & Kallman 2002). More recent works considering this effect (Done et al. 2018; Higginbottom et al. 2020; Tomaru et al. 2019) confirm that its effect becomes particularly relevant at $L \gtrsim 0.2L_{Edd}$, not only reducing the launching radius, but increasing significantly the speed of the material, and thus the outflow rate. However, virtually no wind detection exist in such a high luminosity range for standard XRBs, preventing direct comparisons.

We note that one element that has yet to be considered is the dependence of the illuminating SED on the inclination angle. Indeed, all existing works involving thermal winds adopt an isotropic central SED, despite even "standard" thermal disks showing a very strong dependency on angles see (Muñoz-Darias et al. 2013).

One of the main predictions of current thermal-radiative wind models is a relatively constant wind efficiency, with $\dot{M}_{out}/\dot{M}_{in} \sim 2$, independently from the luminosity (Higginbottom et al. 2019). In addition, in models where the wind is present in the hard state, the wind efficiency is also independent of the spectral evolution, but the hard state wind are faster and thus produce a kinetic energy output an order of magnitude higher (Higginbottom et al. 2020). These should strongly affect the evolution of outburst (Dubus et al. 2019), but direct comparisons show that they may not be sufficient to reproduce some observational properties (Tetarenko et al. 2020).

While inaccessible with the current generation of instruments, the main "observable" remains the line profile, as all current thermal winds prescriptions, whether fully thermal of with radiation, and independently of the inclination angle, agree for symmetric (at first order) line shapes, of which we show few examples in the right panel of Fig. 2.8. Since the line profile, along with precise velocity

[12]Note: the extreme end of this evolution is the Super-Eddington radiation-driven outflows discussed in Sec. 1.4.2

measurements, will finally become directly accessible with the next generation of telescopes, such as *XRISM*, this will finally allow for a more direct constrain of the existence of thermal-radiative winds. In parallel, the evolution of the atmosphere/wind density with radius is a complex function, with a notable break at the wind launching radius (Tomaru et al. 2020), and is thus difficult to compare with current datasets (although see Tomaru et al. 2023, with a number of assumptions).

In parallel, recent efforts following the launch of the X-ray polarization satellite *IXPE* have led to few observations with puzzling polarization properties in high-inclined sources (Rodriguez Cavero et al. 2023; **?**), which are expected to be the affected by the wind. Although modeling efforts of wind polarization properties are very preliminary, it is possible that thermal winds could significantly depolarize the initial X-ray continuum (Tomaru et al. 2024).

Finally, although this is not the focus of this work, we note that the presence of thermal winds is not limited to (BH)XRBs alone. In AGNs, it is one of the most promising scenarios to explain the multiphase nature of Warm Absorbers and obscurers in X-rays (Dannen et al. 2020), due to thermal instabilities naturally developing in the outer regions of AGNs disks ($R \gtrsim 15 R_{IC}$, Waters et al. 2021). On the other hand, such conditions remain inaccessible in X-ray binaries due to their much smaller disk extension. Meanwhile, a complementary type of instabilities has been shown to affect the Ultra Fast Outflows (Waters et al. 2022), which could explain the link between the parameter regimes of these two categories of outflows (see e.g. Laha et al. 2020).

2.2.2 Magnetic Driving

Similarly to thermal winds, theoretical computations of magnetic outflows have long preceded X-ray observations. After the seminal work of Blandford & Payne (1982) (hereafter BP), who established that jet solutions could arise from magnetically threaded disks, this result has been generalized to progressively broader classes of solutions, following two separate approaches.

The first one has been to focus entirely on the wind solution and to treat the disk as a boundary condition. With this simplification, the BP solutions were generalized to a broader class of self-similar wind-only outflows (Contopoulos & Lovelace 1994; Safier 1993), whose properties were quickly found compatible with e.g. AGN torii (Konigl et al. 1994). Following this, theoretical advancements stalled until X-ray detections allowed for direct comparisons with predictions of magnetic models in the 2000s, prompting Fukumura et al. (2010) to revisit the generalized BP solutions in order to apply them to detections of Warm Absorbers, UFOS, and later BHLMXBs (Fukumura et al. 2017). The derivation of their self-similar model, detailed in (Fukumura et al. 2014), involves a density distribution of the form:

$$n(r) = n_0 \left(\frac{r}{r_0} \right)^{-\alpha_e} \quad | \quad \alpha_e = 3 - 2q \tag{2.4}$$

Where n_0 and α_e (or q) are free parameters that together define the structure of the wind. $\alpha_e = 1$ (or $q = 1$, high mass load, "wind-like"), matches the initial solutions of Contopoulos & Lovelace (1994), and $\alpha_e = 3/2$ ($q = 3/4$, low mass load, "jet-like") matches the canonical solutions of (Blandford & Payne 1982). The values of α_e can be (tentatively) extrapolated from X-ray observations with lines sampling a wide range of ionization parameters (see Sec. 2.3.2), with a resulting parameter space of $\alpha_e \sim 1-1.25$ for AGNs (Holczer et al. 2007; Laha et al. 2016), and few values of $\alpha_e \sim 1.3-1.4$ for XRBs (see e.g. Trueba et al. 2019). Meanwhile, direct fits with magnetic launch models have shown good first order agreements with observations, confirming this trend for AGNs (Fukumura et al. 2018a), with recent developments towards the characterization of UFOs (Fukumura et al. 2015, 2018b, 2022), and expanding the XRB mass load range measurements to $\alpha_e \sim 1.2-1.45$ (Fukumura et al. 2021; Ratheesh et al. 2021).

Besides imperfect comparisons with the data, the large parameter space of this model allows to get good global constrains on the wind **structure**, which we show via examples of radial distributions of typical solutions and an illustration of the wind region probed by X-ray signature, in the different panels of Fig. 2.9. However, the lack of direct link with underlying physics of the accretion-ejection structures

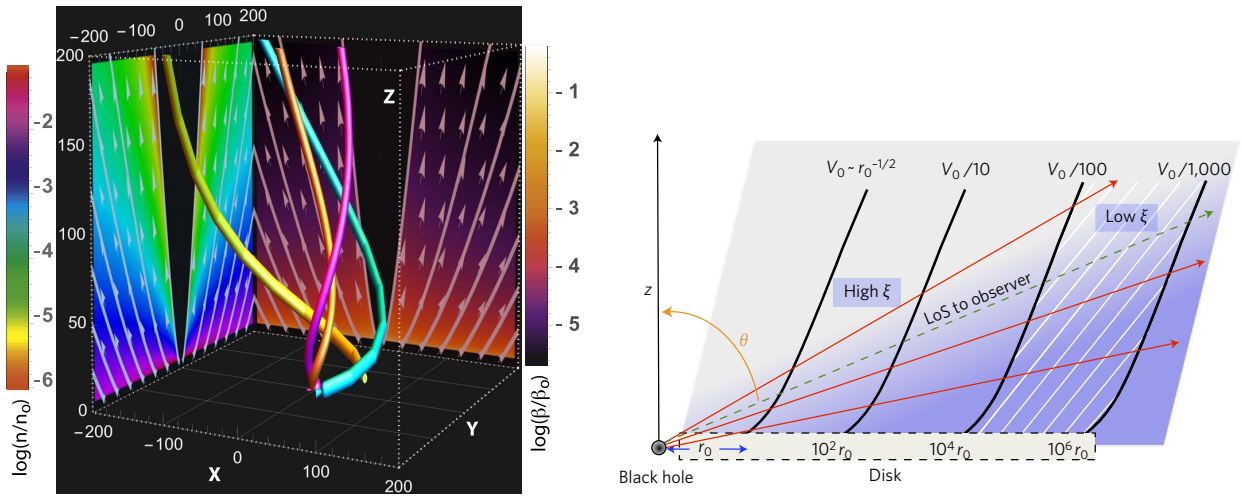

Figure 2.9: **(Left)** Density structure, magnetic field structure, wind velocity direction (white) and example field lines (colored tube) for a wind solution of the Fukumura et al. (2014) model. From Fukumura et al. (2021). **(Right)** Line of sight (green) and physical region (white hashes) probed by a typical X-ray wind signature in a BHLMXB, assuming a similar magnetic wind solution to the left panel. From Fukumura et al. (2017)

prevents direct conclusions on the **state** of the accretion flow, and the assumption of a completely thin disk allows for viable solutions well below what would be possible with a non-negligible aspect ratio (see Sec. 1.3.3).

The second approach, more accurate but more restrictive, consists in computing solutions encompassing the entire accretion (disk) and ejections (wind/jet/etc.) structure. Efforts to obtain self-similar steady state solutions using a parametric description of the MHD turbulence first led to the discovery of highly magnetized jet-emitting structures (Ferreira 1997; Ferreira & Pelletier 1993, 1995), now called Jet Emitting Disks (JED, Ferreira et al. 2006). More recently, new results by numerical simulations, showing the importance of winds in angular momentum transfer (Scepi et al. 2018b) AND the existence of oscillations in the magnetic fields within the disk (Zhu & Stone 2018), prompted for a generalization of JEDs into a broader class of solutions (Jacquemin-Ide et al. 2019), including both jet-like and wind-like solutions.

As self-similar solutions, these prescriptions also provide powerlaw evolutions of their main quantities, and notably the density, but contrarily to the previous model, here the values of α_e and the normalization are much more constrained, depending on physical parameters. Indeed, the governing MHD equations[13] (Casse & Ferreira 2000) notably incorporate 3 separate diffusivity prescriptions, which together depend on three parametrized (and assumed radially constant in a solution) turbulence parameters: the magnetic diffusivity α_m, the anisotropy parameter χ_m, and the Prandtl number P_m.

As these parameters have a considerable influence on the behavior of the solutions, it is important to consider realistic values backed by numerical studies of turbulence. α_m and P_m notably intervene in the description of the disk viscosity, with the "canonical" turbulence parameter of alpha-disks (which we dub here α_v to avoid confusion) expressed as:

$$\alpha_v = \alpha_m P_m \mu^{1/2} \tag{2.5}$$

With $\mu = B^2/\mu_0 P$ the disk magnetization (also expressed as $2/\beta$, with β being the plasma parameter in gas pressure dominated disks). This prescription matches the results found in MRI studies, where $\alpha_v = \alpha_0 \mu^{1/2}$ (Hawley et al. 1995) and $\alpha_0 \sim 8$ (Salvesen et al. 2016). This, together with local and global

[13] which we shall not detail here for the sake of the reader's sanity

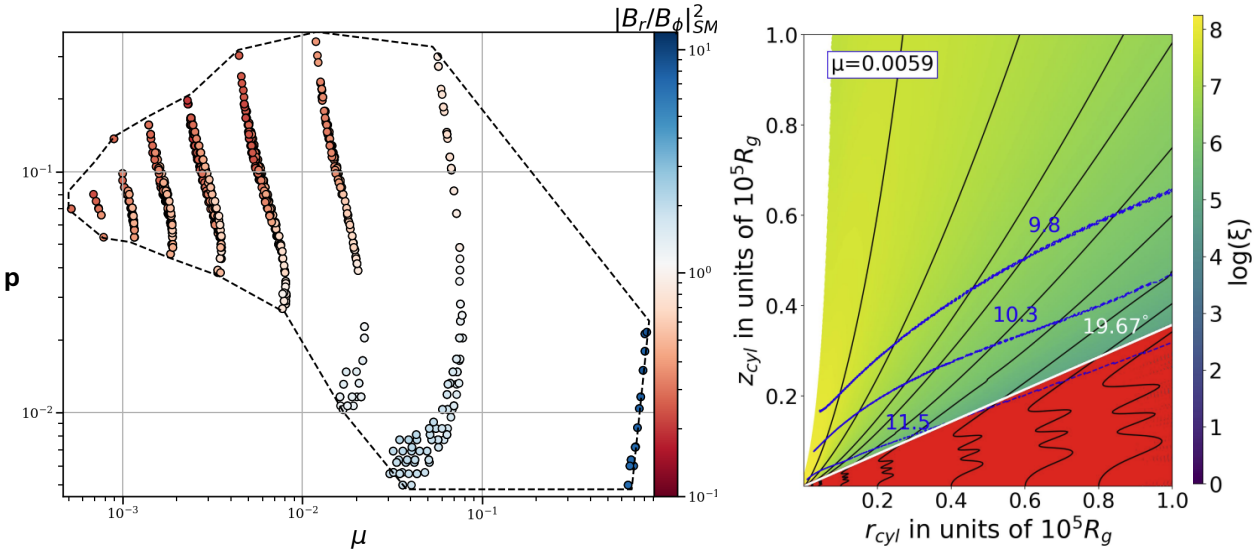

Figure 2.10: **(Left)** Parameter space of the JED-WED solutions, with all turbulence parameters set to 1 and an aspect ratio of 0.1, colored according a quantity highlighting the bending of the magnetic field lines. Adapted from Jacquemin-Ide et al. (2019). **(Right)** Density contours (blue) of a WED solution of the n=3 island, with the background colored according to the ionization parameter, and magnetic field lines (black) highlighting the 3 oscillations in the disk region. The red region highlights the compton thick region, which is ~ 2 times larger than the disk aspect ratio (taken at 0.1 in this solution). From Datta et al. (2024).

estimates of P_m and χ_m pointing to values $\gtrsim 1$ (Lesur & Longaretti 2009; Zhu & Stone 2018), hints at values of the order of unity for all three turbulence parameters.

For a given set of turbulence parameters, and after assuming an aspect ratio (as the energy equation is not yet self-consistently solved in this solutions, see Ferreira & Pelletier 1995), the remaining parameter space can be expressed in a two dimensional ejection index (p)- disk magnetization (μ) plane[14], with $\mathrm{p} = \mathrm{d}\ln\dot{M}_{in}/\mathrm{d}\ln r$ (which translates to $\mathrm{p} = 3/2 - \alpha_e$ from equation 2.2.2). However, a couple of parameters (p, μ) will only lead to a viable solution if the flow satisfies two additional conditions, namely crossing the super slow-magnetosonic Ferreira & Pelletier 1995 and super-Alfvenic Ferreira 1997 points. With this additional tension, the resulting parameter space has two fundamental differences with the previously mentioned outflow-only solutions, illustrated by the fiducial example we provide in the left panel of Fig. 2.10 :

- First, the parameter space is much more restricted: the bounds (represented by the black dashes) greatly limit the possible solutions. In the configuration of Fig. 2.10, the requirement of $5{\cdot}10^{-3} \leq p \leq 0.35$ translates to $1.15 \leq \alpha_e \leq 1.5$ in the density distribution, which remains compatible with the results obtained for both AGNs and BHXRBs. However, these bounds are extremely dependent on the turbulence parameters. For an aspect ratio of 0.1, the $\alpha_m = \chi_m = P_m = 1$ configuration of Fig. 2.10 provides the most extended bounds, and taking higher values of i.e. α_m and χ_m considerably reduces the parameter space in both dimensions. Consequently, if winds in BHs are identified as magnetically driven, their density evolution would provide a new way to constrain the turbulence levels of their accretion flows, which would be immensely useful to improve our understanding of accretion. It is worth noting that the $\mu \geq 5 \cdot 10^{-4}$ limit is artificially enforced to ensure solutions relatively free of the influence of MRI dynamo (Scepi et al. 2018b), which is not considered in the resolution.

[14] p is actually called ξ in the series of theoretical WED papers. We replace this symbol with p in order to avoid confusion with the ionization parameter, commonly noted as ξ, for which we will use ξ_i for clarity

- Secondly, the "allowed" solutions inside of the allowed parameter space are clustered around specific positions, each corresponding to a given number n of oscillations of the magnetic field in the disk. The rightmost "island" corresponds to the initial JED solutions with no oscillations (n=0), and each subsequent island to a higher number of oscillations, with its own restricted set of solutions within the bounds of the parameter space. We show an example of the field lines of a n=3 solution in the right panel of Fig. 2.10. Solutions at lower magnetization are able to access higher ejection indexes (and thus higher mass loads), which match the definition of "winds" from an observational perspective. Nevertheless, a more refined definition between "winds" and "jets", involving the ratio of Poynting flux to the thermal energy flux, is presented in (Jacquemin-Ide et al. 2019).

For our purposes, the definition of "Wind Emitting Disks" can also be linked to the nature of the accretion flow: the mach number of the flow can be expressed as $m_S = p\alpha_m\mu^{1/2}$, with $p \sim 1-6$ the toroïdal current, which is one of pthe free parameters explored to find valid p$-\mu$ solutions. In the current set of solutions, the high-magnetization ($\mu \gtrsim 0.1$) of the $n = 0$ island are the only ones resulting in supersonic ($m_s > 1$) accretion, which changes completely the nature of the flow to a geometrically thick, optically thin disk, and thus allows for the "corona" emission of the Jet Emitting Disks spectra (see Sec. 1.3.3). Thus, as long as X-ray winds are overwhelmingly detected in disk-dominated (and thus optically thick) accretion disks, comparisons with X-ray absorption features should be restricted to subsonic "WED" type solutions. On the other hand, the cold winds detected preferentially in hard state may instead require supersonic, "JED" type solutions, provided they are able to reach sufficiently high mass loads to reproduce absorption lines. The other possibility, quite reasonable (Ferreira et al. 2006) but difficult to prove, is to consider that μ is not radially constant but decreasing with the radius. With the previous set of solutions, it is already the base of the JED-SAD paradigm (Ferreira et al. 2006; Marcel et al. 2018a), and the addition of Wind Emitting Disks at low magnetization opens the way to a much wider variety of solutions to combine jets and winds.

Nevertheless, these models are still in development and reliant or a number of simplifications. Since the discovery of WED models, new sets of numerical simulations (Jacquemin-Ide et al. 2021; Scepi et al. 2024) have highlighted several missing elements in the current prescription. One of most notable is the lack of consideration for the turbulent magnetic pressure. This additional term introduces a new turbulence parameter α_p, estimated to be of the order of unity in the previously mentioned simulations, which has a very significant impact on the accretion structure, notably resulting in a puffier disk and a significantly reduced parameter space (Ziminiak et al. 2024, submitted). Yet for now, the study of this new behavior has been purposely restricted to JED-like solutions. This is because of the assumption, shared by all current MHD solutions, that the vertical stratification for each viscosity coefficient is gaussian. However, the results from recent simulations reveal a much more complex vertical stratification of the disk, which calls for a more realistic description, particularly for WED-like solutions and their vertical oscillations of the magnetic field in the disk.

In parallel to these ongoing theoretical advances, the observational signatures of different types of WED models are under investigation. The behavior of the pure JED (no oscillations) solutions was first studied in (Chakravorty et al. 2016), which showed that such type of disks could only reproduce the observations when considering an additional heating term (a "warm" wind, with which may thus require an hybrid magneto-thermal configuration). Subsequent studies considering the full range of the WED-JED regimes have shown much more promise (Chakravorty et al. 2023; Datta et al. 2024), but comparisons with real spectra are yet to be achieved, and are paramount to highlight the limits of the model. **This is one of the main motivation for this PhD project, and the modeling efforts that will follow.**

For now, existing studies of the line signatures of all flavors of MHD models (with or without the disk included) have shown a common specificity, namely that the absorption lines includes a blueshifted (high-energy) tail. This is because of the assumption that the outflow is launched at all disk radii. The

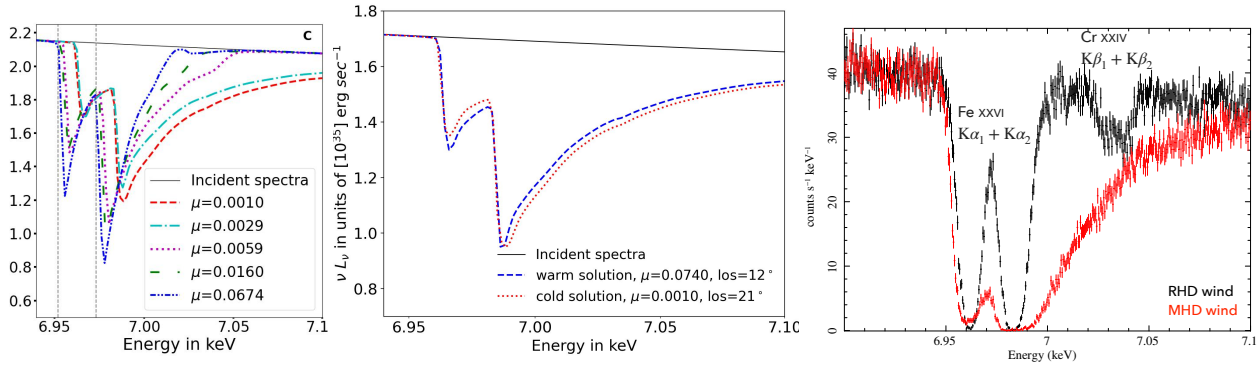

Figure 2.11: **(Left)** Evolution of WED spectral signatures for a range of magnetization, from Datta et al. (2024). **(Middle)** Comparisons of the spectral signatures of a warm high-magnetization solution and a cold high-magnetization solution, with two different inclination angle, from the same study. **(Right)** Simulations of observations of thermal radiative (black) and MHD (red) wind solutions with a short (30ks) *XRISM* exposure of a bright source, from Tomaru et al. (2023)

ionization parameter ξ_i of the gas, which dictates which atomic lines are absorbed in the transmitted spectra, is a linear function of n, and thus α_e (see Sec. 2.3.2). On the other hand, the velocity of MHD winds always decreases as $r^{-1/2}$, and thus the ionization range affecting a given line will include a distribution of different speeds, and notably a portion at higher velocity from regions closer to the Black Hole.

More specifically, in the WED parameter space, it has already been identified that the spectral signatures of solutions at lower magnetization show more pronounced blueshifted tails (Datta et al. 2024), as we show in the left panel of Fig. 2.11. This is because lower magnetized solutions have more bent magnetic field lines, leading to a higher projection fraction of the outflow velocity for equatorial lines of sight (where the density of the material is high). The magnetization also affects the shape of the high-energy tail, but in a much more subtle manner. However, several degeneracies between cold and warm wind models have been identified: as we show in the middle panel of Fig. 2.11, the same study has also shown that cold and warm solutions with very different magnetization, seen at different inclinations, can lead to very similar profiles. Since the inclination is poorly constrained in the vast majority of objects, it might not be possible to distinguish the two from the line shape alone. This may be solved by adding the thermal contribution of the irradiating source in a self-consistent (and thus mandatory) manner, but the geometry of the inner disk remains largely unknown, even in the soft state (see Sec. 1.3.3), and thermal wind models themselves are subject to very uncertain structures (see Sec. 2.2.1). On the other hand, the magnetization also has a fundamental effect on the density of the wind. This effect has been studied for the main iron lines (Datta et al. 2024), but a more global comparison is needed to understand whether the magnetization also affects the density diagnostics which, in the magnetic wind mode of (Fukumura et al. 2014), are only a function of the wind's ejection index (see Sec. 2.3.2).

Yet for now, the most pressing issue remains to distinguish magnetic and thermal driving. Thankfully, the very different profiles predicted by both models can be distinguished by the new *XRISM* mission (Chakravorty et al. 2023; Tomaru et al. 2023). However, this may only be the case for a specific type of signatures: as we show in the right panel of Fig. 2.11, a highly asymmetric, blueshifted profile can only be produced by MHD winds. However, more symetric, less blueshifted profiles can be obtained with both launching models, and a weak MHD tail may be impossible to detected with *XRISM* alone.

In this scenario, while waiting for the capabilities of Athena (Chakravorty et al. 2023), more answers may be found from more indirect measurements, such as the much more diverse amount of lines (and thus ionization parameters) that the spectral resolution of *XRISM* will allow to detect, the ability or not to reproduce the absorption signatures in the OIR band, and a better look at the outburst evolution.

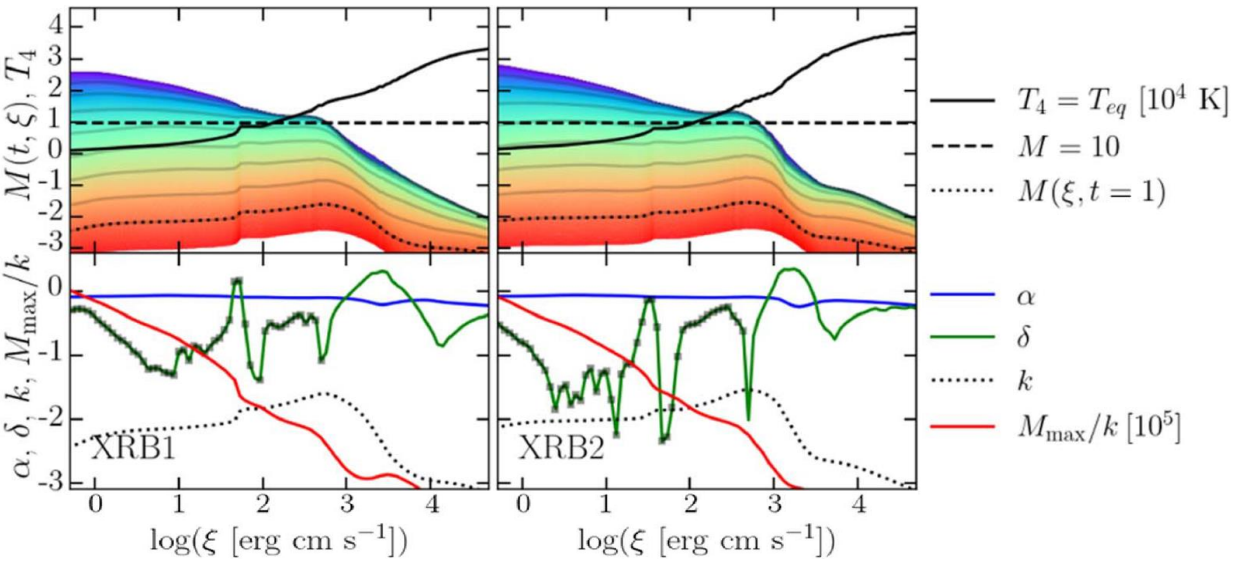

Figure 2.12: Evolution of several parameters characterizing the force multiplier for a hard **(left)** and soft **(right)** XRB SEDs. In the upper panels, the colormap highlights the strength of the force multiplier $M(t)$ for higher (red) and lower (blue) optical depths (the parameter t), as a function of the ionization parameter ξ_i . An approximate threshold for potentially dominant line-driving ($M = 10$) is highlighted in black dashes. Adapted from Dannen et al. (2024)

For this last point, few preliminary studies have favored a magnetic wind origin (Tetarenko et al. 2018) or at least point it as a possible solution to provide additional scattering compared to thermal winds (Tetarenko et al. 2020).

2.2.3 Towards a diverse view

In BHLMXBs, the vast majority of modeling efforts until now have been focusing exclusively on either pure thermal-radiative or pure magnetic driving. Nevertheless, it is important to provide some nuance in regard to more realistic expectations.

The first important point to address is the potential relevance of other wind launching mechanisms. The third canonical launching mechanism, line driving, extends the "standard" radiation pressure due to electron scattering (see Sec.1.4.2) to the interactions between photons and bound electrons in a partially ionized plasma. The ratio of this pressure to the standard electron scattering pressure, the so-called force multiplier M (Castor et al. 1975), can reach few 10^3 in ideal conditions, but is heavily dependent on the irradiating SED, the ionization state of the plasma and its optical depth. Since the value of M significantly decreases beyond low ionization parameters ($\xi_i \sim 1-10$), line driving is primarily expected to affect AGNs and CVs (although see Higginbottom et al. 2024 for a recent update on that matter), and has traditionally been considered negligible for the very highly ionized X-ray outflows (see e.g. Neilsen & Degenaar 2023). However, the recent detections of cold outflows, with much lower ionization parameters, could be the indicator of line-driven winds in the outer disk regions. Although very few studies have delved into this matter, we show in Fig. 2.12 an extract of a recent global work by Dannen et al. (2024), who tested typical hard and soft state SEDs of a BHXRB and found that although the force multiplier is systematically negligible at high ξ_i, this is not necessarily the case in the OIR wind range (below $\log\xi_i \sim 1$). Finally, recent studies show that introducing more position dependent can reduce the over-ionization issue (Smith et al. 2024), but this effects has yet to be properly quantified.

It is also possible that other, more exotic wind driving mechanisms may play a role (see e.g. Hankla et al. 2022a), but their relevance will have to wait for more comprehensive studies on their possible applications.

More importantly, the reality is mostly likely to combine the effects of several different driving mechanisms. For now, very few studies have focused on the direct interactions between thermal and magnetic driving, and the commonly accepted picture is that the inclusion of a thermal component should increase the potency of a magnetically driven wind. This has been considered for self-similar solutions with a limited prescription (Casse & Ferreira 2000), and subsequent applications have shown, as discussed in the previous subsection, that an empirical heating term does significantly increases the mass load of otherwise "JED-like" solutions (Chakravorty et al. 2016). For now, the combination of different phases is only favored to explain the evolution of the wind in the most exotic scenarii (see e.g. (Keshet et al. 2024; Muñoz-Darias & Ponti 2022; Neilsen & Homan 2012)), but this is probably the result of a lack of sufficiently detailed data in the overwhelming majority of cases.

However, the picture is certainly more complex: recent numerical simulations have shown that while an isothermal resolution does underestimate the power of magnetic driving, a more correct treatment of the radiative balance also changes significantly the accretion-ejection structure (Wang et al. 2022a). On the other hand, other studies have shown that a poloidal magnetic structure may completely inhibit thermal driving (Waters & Proga 2018). The picture is even more unclear for possible combinations of thermal/magnetic winds in the inner regions and line driving in outer regions. It is thus important to stress that any of the current wind descriptions, should they perfectly reproduce the data in different configurations, remain very preliminary, and are likely incomplete.

2.3 From wind to lines

For now, we've introduced the observables interpreted as the consequences of outflows, and the physical mechanisms able to create these outflows. However, we've voluntarily glossed over the mechanisms by which the material in the outflow is able to imprint the spectrum with absorption lines. The reality is that the creation of absorption lines is far from trivial: it results from the combination of several atomic processes with a plasma in very specific density and temperature conditions.

A comprehensive treatment of such effects would turn this work into an treaty of quantum mechanics and radiative transfer. This is not our goal, and instead we shall restrict ourselves to a brief introduction of the most important concepts, which govern both existence of the lines and the part of their evolution independent from the outflow itself. For a more exhaustive approach, we refer to e.g. Pradhan & Nahar (2011).

2.3.1 Overview of the underlying atomic physics

The existence of emission and absorption lines in a spectrum is caused by the quantization of the energy levels of atomic matter. Indeed, in quantum mechanisms, different possible configurations of the constituents of atoms (and notably electrons) have different **fixed levels of energy**. For astrophysical plasmas (which constitute the overwhelming majority of the *baryonic* matter in the universe), this has two relevant consequences. First, a gas in low-energy states irradiated by a continuous spectrum will absorb the specific frequencies of its atomic transitions, producing **absorption** lines. On the other hand, a gas with atoms previously energized by either radiation or its own thermal energy will progressively come back to ground (lowest energy) states, and de facto emit radiation at the energy of these transitions, producing **emission** lines.

Both of these phenomena are heavily dependent on specific properties of the irradiated matter. One of the most important is its ionization level, as different proportions of specific ions will lead to different strengths for the transitions associated to these materials (as we will see in Sec. 2.3.2). The second fundamental property is the column density N_H[15] of the material, as it will not only influence the amount of ions available for creating lines, but also limit the path of radiation.

Indeed, even outside of the atomic transitions, any material has a probability of interacting with (and absorbing) the radiation it receives. This is typically measured via the optical depth, namely the length

[15] the total density integrated along the line of sight, factoring the width of the absorbing material

Table 2.1: Atomic transitions, energies and oscillator strengths resulting in the five main iron absorption lines commonly studied in the 6-9 keV band, and in this work. The uncertainties on the energies of the Fe XXVI lines are negligible. Adapted from NIST 5.11 (Kramida & NIST ASD Team 2023)

Ion	Line group	Colloquial name	Transitions	Wavelength Å	Energy eV	Oscillator Strength
Fe XXV (He-like)	K α	Fe xxv Kα	$2^3S \rightarrow 1^1S$ (z)	1.868 ±0.001	6 637±4	3.3e-7*
			$2^3P_1 \rightarrow 1^1S$ (y)	1.860 ±0.001	6 668 ±4	0.069*
			$2^3P_2 \rightarrow 1^1S$ (x)	1.855 ±0.001	6 682 ±4	1.7e-5*
			$2^1P \rightarrow 1^1S$ (w)	1.850±0.001	6700 ±4	0.704*
	K β	Fe xxv Kβ	$3^2P^{1/2} \rightarrow 1^2S^{1/2}$	1.575 ±0.001	7872 ±5	0.017
			$3^2P^{3/2} \rightarrow 1^2S^{1/2}$	1.573 ±0.001	7881 ±5	0.138
Fe XXVI (H-like)	Ly α	Fe xxvi Kα	$2^2P^{1/2} \rightarrow 1^2S^{1/2}$	1.7834	6 952.0	0.137
			$2^2P^{3/2} \rightarrow 1^2S^{1/2}$	1.7780	6 973.2	0.269
	Ly β	Fe xxvi Kβ	$3^2P^{1/2} \rightarrow 1^2S^{1/2}$	1.5035	8 246.4	0.026
			$3^2P^{3/2} \rightarrow 1^2S^{1/2}$	1.5023	8 252.7	0.052
	Ly γ	Fe xxvi Kγ	$4^2P^{1/2} \rightarrow 1^2S^{1/2}$	1.4253	8 698.6	9.4e-3
			$4^2P^{3/2} \rightarrow 1^2S^{1/2}$	1.4249	8 701.2	0.019

of material necessary for a material to become (mostly) opaque, due to scattering or absorption of the radiation. In soft X-rays and for low-ionized matter, optical thickness is dominated by the photoelectric effect, while hard X-rays and highly ionized matter are primarily affected by Compton scattering. While the effect of the former depends heavily on the abundances of the gas and the energies considered (see e.g. Balucinska-Church & McCammon 1992), for the latter, above a certain column density threshold ($N_H \sim 1.5 \cdot 10^{24} \mathrm{cm}^{-2}$ for neutral hydrogen), the gas becomes "Compton Thick" and thus completely opaque to X-ray irradiation above 10 keV. Hereafter, we shall focus on the configuration most relevant to our work, namely irradiation of purely photoionized, optically thin material, and the resulting influence on soft X-rays.

Although a wide variety of lines exist in this band, they do not imprint the spectra equally. This is due to a combination of the differences in abundances (as we will see further down) and of the probability of each transitions. One of the main quantities to visualize the latter is the oscillator strength, a dimensionless number between 0 and 1, which directly translates to the intensity of a line.

In practice, two additional effects skew heavily the scales in favor of few transitions. First, the dense interstellar medium in the line of sight along the galactic plane completely absorbs the soft X-ray band (below $\sim 1-2$keV) of most X-ray binaries (Fortin et al. 2024), preventing access to the vast majority of the strongest transitions (Wilms et al. 2000). Secondly, the effective area and spectral resolution of most instruments drop sharply after few keV. This results in the vast majority of detections being obtained from 5 low-level transitions of the Fe xxv Kα and Fe xxvi Kα ions, between 6 and 9 keV (see Sec. 3.6 for a detailed inventory).

We list the energies, names and oscillator strengths of these transitions in Tab. 2.1. Since the Fe xxvi Kα ion only has a single electron remaining, the structure of its energy levels and transitions is similar to that of Hydrogen, and the lines expressing in the $6-9$ keV band are the equivalent of the three first levels of the Lyman series. For visualization, we show the corresponding atomic transitions in the case of Hydrogen in the left panel of Fig. 2.13. Each line can be split into individual doublets at very close energy, due to the additional degree of freedom of the spin of the initial electron. For this type of ions

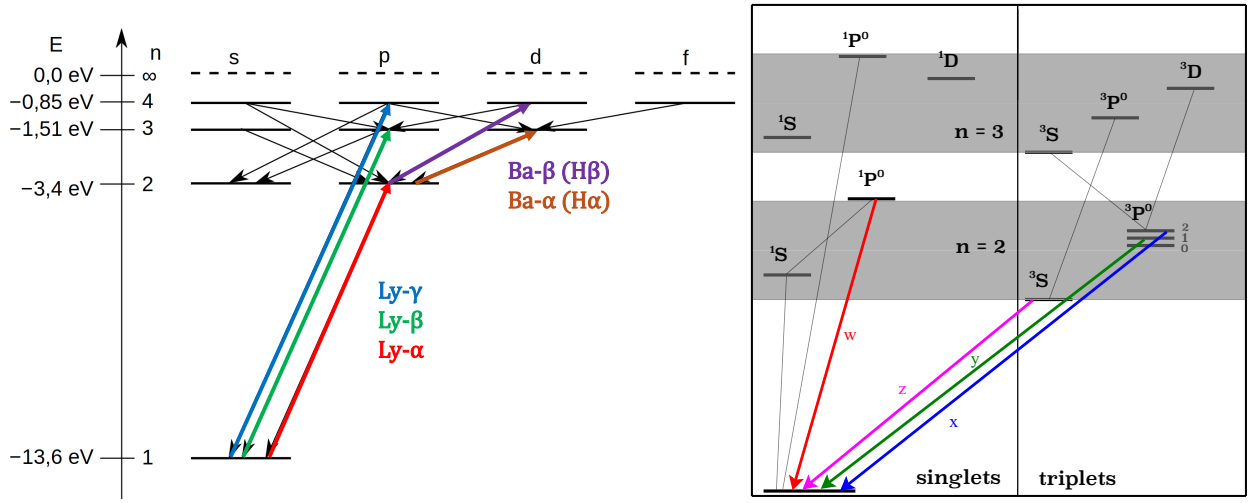

Figure 2.13: **(Left)** Grotrian diagrams showing the energy levels for the Hydrogen atom, highlighting the first Lyman and Balmer transitions. Adapted from wikimedia. **(Right)** Grotrian diagram highlighting the 4 transitions of high Z Helium-like atoms forming the K α line Chakraborty et al. (2020)

and transitions the higher energy individual transition having twice the oscillator strength (and thus intensity) of the low energy counterpart.

On the other hand, the Fe xxv Kα ion has two bound electrons, and its structure thus matches that of Helium, with a quadruplet of individual transitions at slightly different energies forming a line at $\sim$ 6.7 keV and a second doublet more similar to the Lyman series of Fe xxvi Kα at $\sim$ 7.88 keV. Because all of these lines result from the transition of an electron to the ground level on the innermost orbital (the so-called K-shell), they are called Kα, Kβ,...depending on the original position of the electron. We show an illustration of the more complex combination of energy transition forming the Kα line in the right panel of Fig. 2.13. The oscillator strengths for the (z) and (x) transitions are considerably lower than the two others, and most notably the z transition, whose optical depth (a more direct translation to the absorbing power) is 4 orders of magnitude lower than the second weakest transition (see Fig.6 in Chakraborty et al. 2021b). This line is thus considered a triplet, combining the x and y transitions.

In the rest of this work, since the Lyman transitions of Fe XXVI are also directed towards the K-shell, we will refer to them as Fe xxvi Kα, Fe xxvi Kβ and Fe xxvi Kγ.

Knowing the precise theoretical energies of the transitions **at rest** is fundamental to use them as a diagnostic of velocity: the absorption or emission of an atomic transition will occur in the referential of the receiving material, and thus, if the later is moving, interact with the doppler shifted radiation of the source. This means that the resulting lines will be blueshifted or redshifted depending on whether the material is outflowing or inflowing compared to the source of radiation. However, before any consideration on the profile of that velocity evolution and the precision of the instrument, diagnostics of velocities first and foremost depend on the identification of the line, which can be problematic for several transitions at very close energies. Among several lines with an history of ambiguous detection is notably a Cr xxiv Kβ doublet at 7.017-7.021 keV, which can be easily be misidentified as a mildly outflowing Fe xxvi Kα absorber with a speed of $\sim$ 2100 km/s. Another one is a Ni xxvii Kα quadruplet at $\sim$ 7.806 keV (for its main transition), which is completely indistinguishable from Fe xxv Kβ in most cases with the current generation of instrument. Although the increase resolution of new instruments will help in that matter, degeneracies between the velocity profile and the effect of non-standard abundances on secondary lines may remain difficult to solve.

The fundamental quantity to characterize the strength of absorption lines relative to the continuum is their "equivalent width" (EW), defined as the width of continuum whose integrated flux is equivalent

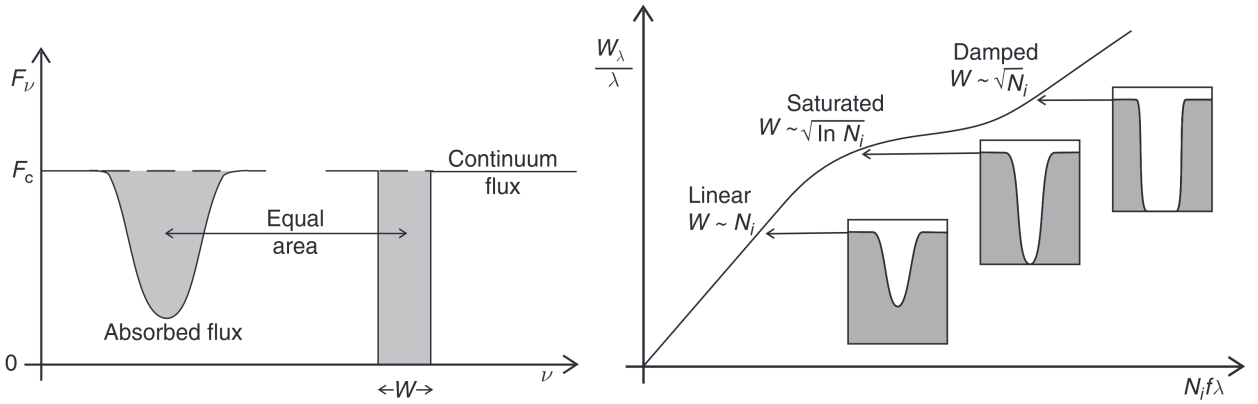

Figure 2.14: **(Left)** Illustration of the computation of the Equivalent width "W" of an absorption line. **(Right)** Different regimes of the evolution in equivalent width with density in a curve of growth, with W the EW and N_i the ionic column density (See 2.3.2). Both from Pradhan & Nahar (2011)

to that absorbed by the absorption line (see left panel of Fig. 2.14 for an illustration). The evolution of the EW of a line is a complex but monotonic function of its optical depth, itself a function of the **ionic** column density N_i. This evolution also dictates the shape of the line, which for astrophysical plasmas is a Voigt profile. It combines a gaussian profile, resulting from intrinsic Doppler broadening, and a Lorentzian profile, consequence of the intrinsic line width (due to the Heisenberg principle) and pressure broadening. The line profiles are thus very dependent on the temperature and density of the material, with each profile dominating in different column density regimes, as we show in the right panel of Fig. 2.14. At low column densities, the line is mostly gaussian and thus its EW increases linearly with the column density, until it starts becoming optically thick or "dark" (namely, absorbing the entirety of the continuum at the line center). This considerably slows down the growth of the line, which enters the so-called "saturated" regime. At even higher column densities, the lorentzian profile becomes dominant, due to a much higher EW evolution even after reaching large optical depths, consequence of much broader wings. The line is then in the "damped" regime.

In more realistic scenarios, another parameter needs to be considered: the turbulence. If the material has a **variable** velocity component along the line of sight, it will have a effect similar to thermal broadening, and thus increase the density threshold for saturation, allowing for much higher EWs at similar densities. The presence of significant turbulence is mandatory to explain existing observations: the highest EW values reported for Fe xxv Kα and Fe xxvi Kα are about $\sim$ 60 eV (see Sec. 3), which is completely inaccessible via thermal broadening alone at the typical temperatures of the plasma creating the lines (Bianchi et al. 2005). Turbulence values of the order of at least few $\sim$ 100 km/s are thus required, but this can be easily explained by thermal-radiative and magnetic launch models. Nevertheless, these profiles are for now impossible to distinguish in the data, due to insufficient spectral resolution, and the width of the line itself is only constrained in few observations (see Sec. 3.4).

2.3.2 Influence of the gas properties

We mentioned previously that the equivalent width of an absorption line is dependent on its ionic column density N_i. This quantity, which represents the total amount of absorbing ions along the line of sight, can be expressed globally as:

$$N_i = \frac{N_i}{N_Z} \times \frac{N_Z}{N_H} \times N_H \tag{2.6}$$

Here, each quantity defines a property of the gas: N_i/N_Z is the total ionization fraction of the specific i-th ion of the Z element,$N_Z/N_H = A_Z$ is the elemental abundance of Z and N_H the total hydrogen column density.

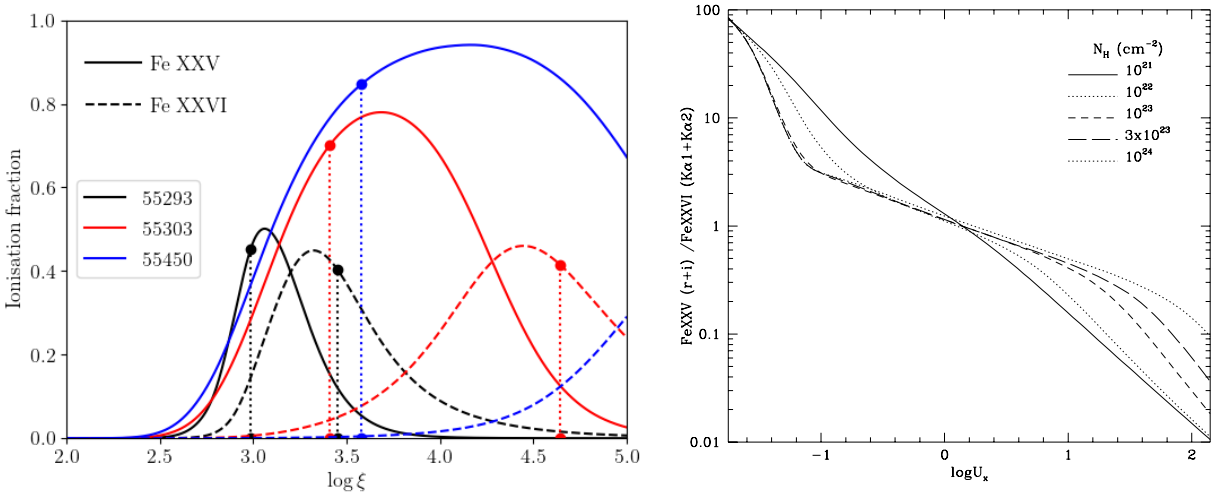

Figure 2.15: **(Left)** Evolution of the ionic fraction of Fe XXV and XXVI when illuminated by a hard (black), hard-intermediate(red) and soft (blue) SEDs. From Petrucci et al. (2021). **(Right)** Influence of the modified X-ray ionization parameter U_X on the ratio of the Fe xxv Kα and Fe xxvi Kα lines for a range of column densities, assuming zero turbulence. From Bianchi et al. (2005)

The abundance A_X is an intrinsic, constant property of the gas, which is the result of the composition of the accreted material. The secondary stars in galactic LMXBs consist of low mass companions in our own galaxy, and are thus expected to match (at first order) stellar abundances. More refined estimates can be derived for specific spectral types using stellar population studies (see e.g. Delgado Mena et al. 2021 and references therein for a recent sample), or, ideally, direct high-resolution spectroscopy of the companion (González Hernández et al. 2008). However such detailed approaches are only necessary in the rare cases where the absorption lines detected sample a high number of different elements (see e.g. Keshet et al. 2024 for independent measurements from the wind itself). However, such considerations are likely to become more important with the new generation of instruments.

The derivation of the other parameters is less straightforward, because they are not constant along the line of sight. A more local definition of N_i can be expressed as:

$$N_i = A_Z \int f_i n_H \, dR \tag{2.7}$$

With $f_i(R)$ the local ionic fraction and $n_H(R)$ the local hydrogen density (typically very close to the total density n). Collisional ionization notwithstanding, $f_i(R)$ results from the balance between photoionization, depending on the flux, and recombination, depending on the density (Tarter et al. 1969). This naturally leads to the definition of a ionization parameter ξ_i, which can be described as:

$$\xi_i = \frac{L}{n_H R^2} \tag{2.8}$$

Although other conventions exist, such as the "U" used in Cloudy (Ferland et al. 2000), using the hydrogen ionizing flux, we will adopt the formula above, following the Xstar definition (Kallman & Bautista 2001) where L is integrated between 1 and 1000 Rydberg.

However, ξ_i alone is not enough to encompass the effect of the SED, as each individual ion and transition is mainly influenced by a restricted energy range, whose individual fluxes can be widely different for a given total broadband luminosity. As an example, we show computations of the ionic fraction dependance on ξ_i with realistic BHXRB SEDs in the left panel of Fig. 2.15. The evolution of SED from the hard to the soft state completely changes the ionic fraction for a single ξ_i value, proving that

the ionization parameter alone is not sufficient to assess the state of the gas for such variable systems. A partial answer to that problem consists in restricting the range of luminosity considered in the ionization parameter to the band which most influences these atoms. For highly ionized iron, a modified X-ray ionization parameter computed from the $\sim 2-10$ keV band luminosity has been explored in Bianchi & Matt (2002); Bianchi et al. (2005), and proves to be much a much more direct, if still imperfect, measure of the ionization of the main transitions of Fe XXV and XXVI.

The link between the EW of each line and the ionization parameter is bimodal, following the evolution of the ionization fraction, and affected by many other parameters, meaning ξ_i can rarely be estimated directly from a single line. However, the ratio between lines with different properties, such as the Fe xxv Kα and Fe xxvi Kα, remains monotonic, and is even linear for small N_H, as we show in the right panel of Fig. 2.15. This allows for a good first order estimate of relative changes in ionization parameter between different observations from purely observational parameters, even without information about the value of $n_H R^2$.

Direct constrains on the density itself are much more elusive, and must rely on the detectable lines whose ratios are density dependent. The most commonly used diagnostics involve emission lines (see e.g. Porquet et al. 2010), which are quite common in AGNs but remain very rare in X-ray Binaries, and particularly alongside absorption features. In their absence, for XRBs, the only remaining solution is to use density sensitive metastable absorption lines (Mao et al. 2017; Mauche et al. 2003), but they remain very rare, and their interpretation requires a very careful treatment going beyond photoionization alone (Mitrani & Behar 2023). When none of these are available, only the integrated N_H can be derived. Here again, only emission lines allow from direct diagnostics from the ratios of specific emission lines, and column density estimates are otherwise derived to the combined effect of ξ and N_H on the line EWs, as well as global photo-electric absorption for high N_H values.

It is important to realize that computations of the evolution of the lines go way beyond the few elements highlighted here, with effects that cannot be fully encompassed by analytic models. It is common to compare the spectra to grids of pre-computed photoionization models resulting from dedicated codes, the three most notable being XSTAR[16] (Kallman & Bautista 2001; Kallman et al. 2021), Cloudy[17] (Chatzikos et al. 2023; Ferland et al. 2017), and SPEX [18] (Kaastra et al. 1996), which are all developed independently for the sake of cross-validating scientific results (see e.g. Mehdipour et al. 2016, although progress has been made since then). Such tables can provide a direct estimate of physical parameters, with reasonable computing times, but at the cost of some restrictions on the physical conditions of the material, which is assumed to be a one dimensional slab in thermal balance in these 3 codes. More complex considerations usually require dedicated tools, such as TEPID for the variability of the irradiating source (Luminari et al. 2023), or PYTHON[19] for 3D geometries (Long & Knigge 2002). However, these tools are much more computationally expensive, and the evolution of models with multidimensional parameters is usually probed with intermediate methods (see Sec. III).

Another example is the efforts towards disentangling the parameters affecting the famous Iron emission feature at $\sim 6-7$ keV (see 1.3.1). First, the influence of abundances and ionization will determine whether the profile will only result from the main (neutral) Fe Kα doublet at 6.391-6.404 keV, or from a more complex combination including other transitions. The result is then distorted by a mix of general relativistic effects depending on physical parameters (such as the spin of the Black Hole) and geometrical projections. This culminates in a wide range of degenerate scenarios, which have been extensively explored in hope of improving the reliability of spin measurements, notably in the last decade with the `relxill` models (Dauser et al. 2016; García et al. 2014). Ironically, while the geometry of the inner accretion flow is now by far the most limiting element (see Sec. 1.3.3), this family of models has become so complex that it is used in very contradictory ways in the community. This is particularly problematic for the detection of absorption lines, as the interplay between the reflection shape and the

[16] https://heasarc.gsfc.nasa.gov/xstar/xstar.html
[17] https://gitlab.nublado.org/cloudy/cloudy/-/wikis/home
[18] https://spex-xray.github.io/spex-help/theory/spexact/intro.html
[19] https://agnwinds.readthedocs.io/en/dev/input/wind_model_params.html

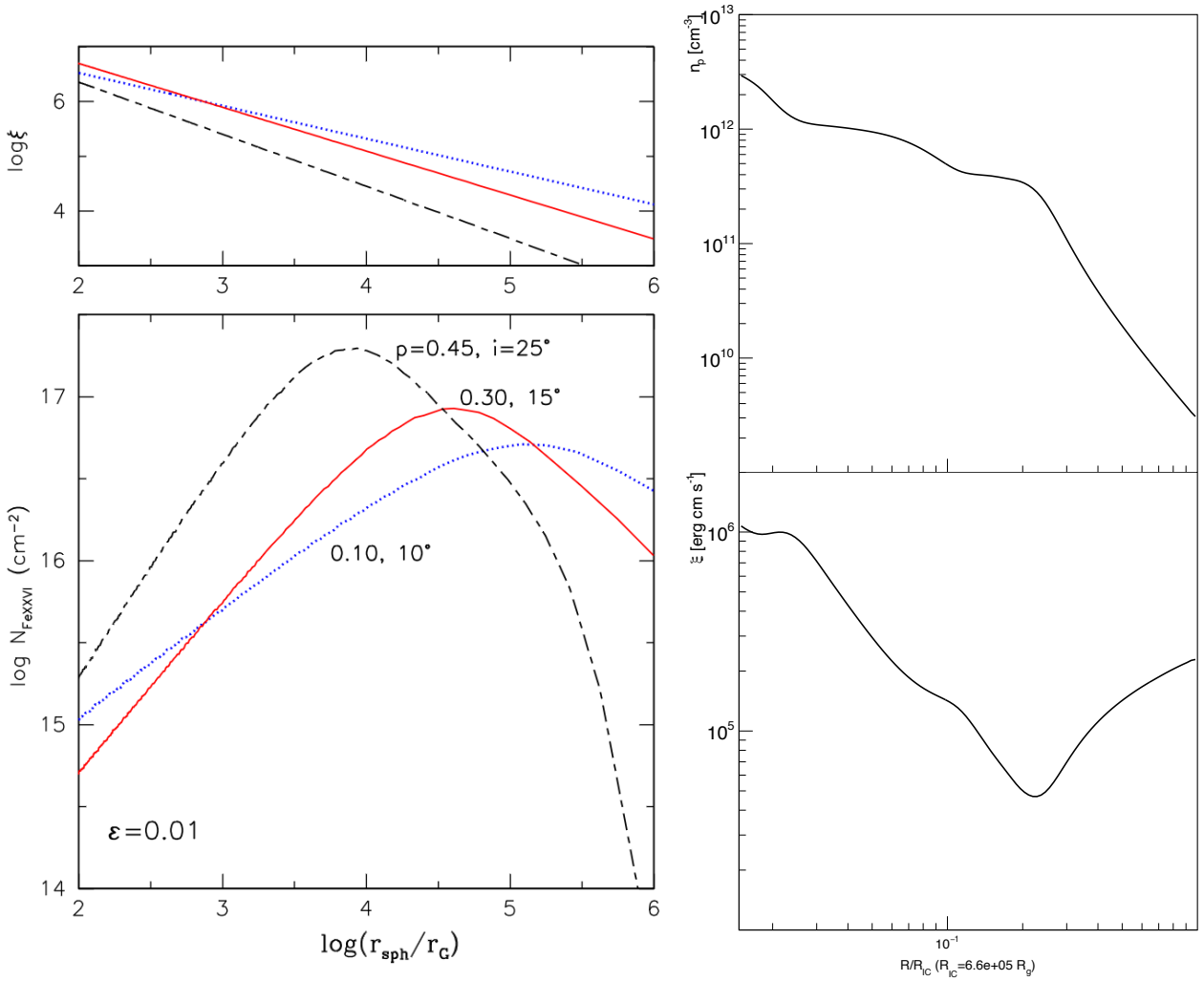

Figure 2.16: **(Left)** Evolution of the ionization parameter in magnetic and ionic density with the radius in WED models. Each color represents a different couples (p,θ) of ejection parameter and inclination angle. From Chakravorty et al. (2023). **(Right)** Evolution of the density and ionization parameter with radius in a thermal wind numerical simulation. Here, the strong decrease of n starting from $\sim 0.2 R_{IC}$ matches the launching radius of the wind, while the region a lower r is only a static atmosphere. From Tomaru et al. (2020).

absorption profile is often significant, and can prove very difficult to disentangle. We shall come back to this issue in Sec. 3.6.

To close out this section, we stress that with 1D photoionization models, a single absorber can only provide a single output of ξ_i, N_H, and velocity measurements, and thus cannot probe the radial evolution of the wind. However, whenever different absorbers are detected, it becomes possible to infer some information about the evolution of the material along the line of sight. The most sought after quantity is the evolution of the density with the radius, since it varies greatly between different launching mechanisms and defines the structure of the wind. Assuming an optically thin material, it can be derived even if no direct density diagnostics are available, as long the evolution of the ionization parameter with radius is known (by construction, see Eq. 2.8). We highlight different predictions in the different panels of Fig. 2.16, which show the typical evolution of several parameters for the main driving mechanisms. While the evolution of ξ_i with R is a powerlaw of index $-p-1/2$ in magnetic winds, for thermal winds, the evolution of n_H (and thus ξ_i) is much more complex, with a change in profile starting at the wind launching radius.

Unfortunately, the radius of the absorbers is not trivial to derive, and without direct density estimates, it is only weakly constrained by assumptions on the launching mechanisms, and direct comparisons remain mostly out of reach. Nevertheless, when only ξ_i and N_H are available, part of the evolution of the wind can still be quantified, even if a degeneracy between n and R will remain. We thus introduce the Absorption Measure Distribution (AMD) (Behar 2009; Holczer et al. 2007) as :

$$AMD = \xi_i \frac{dN_H}{d\xi_i} \tag{2.9}$$

Where the AMD is assumed to evolve as a ξ^a. The value of a is then derived from the parameters of different ionization zones, and provides a basic idea of the wind structure, which can be compared to the predictions of different launching mechanisms. Indeed, with current self-similar models of magnetic winds, the powerlaw assumption is always true at first order, and one can retrieve $\alpha_e = 3/2 - p = (2a+1)/(a+1)$, which allows to constrain the ejection index without direct fits of MHD line profiles. However, the structure can be more complex for thermal winds, notably when factoring the break between the atmosphere and wind zones. The AMD is particularly relevant to highlight complex (and for now unexplained) stratification of the wind structure, as seen in few sources (Keshet et al. 2024).

2.3.3 From plasma stability to visibility

The last element affecting the appearance of the absorption lines is the thermal stability of the outflowing material. Indeed, similarly to what we already mentioned in Sec. 1.2.3 and Sec. 2.2.1, the material in the wind itself is expected to remain thermally stable. Since for a given SED, the ionized gas is well represented by its ionization parameter, the stability curve for photoionized material is typically plotted in a $\log\xi_i/T$ - T plane. Since ξ_i/T is proportional to the ratio of radiative and gas pressures, an isobaric perturbation (assumed as such for simplicity), which only changes the temperature, corresponds to a vertical displacement in this plane. The material then enters a zone where cooling/heating dominates if it goes above/below the stability curve.

We then recover the standard instability behavior (Krolik et al. 1981), illustrated by the arrows shown in the upper left panel of Fig. 2.17: when leaving a part of the stability curve with $d\log T/d\log(\xi_i/T) > 0$ (a positive slope), the material will enter a zone that will counteract the perturbation and thus return to its original temperature. On the other hand, when leaving a part of the curve with a negative slope, the material enters a zone that amplifies the perturbation, leading to runaway heating or cooling, and thus instability. In the most simple case, the gas will maintain an isobaric track until the next stability zone, with the two final available boundaries being the lowest and highest stable branches. The asymptotic limit of the highest one is the maximal possible temperature accessible due to irradiation, namely the compton temperature T_{IC} previously defined for thermal winds.

As the stability curve is mostly determined by the irradiating SED, significant changes in spectral states have dramatic consequences on the existence of stable and unstable zones, as we show with examples of stability curves computed from hard and soft state BHLMXB SEDs in the left and right panels of Fig. 2.17. In the soft state, the vast majority of the curve is completely stable, unlike in the hard state, where the majority of the upper branches before the Compton temperature end up completely unstable. This has strong consequences on the **visibility** of the wind in the iron band (6-9 keV), as the range of ionization parameter with significant ionic fractions for Fe XXV and Fe XXVI, highlighted in Fig. 2.17, are completely stable in the soft state, but completely unstable in the soft state. Thus, in standard conditions, as the material in the wind is unable to remain at such ionizations, no absorption lines from these ions will be created in the hard state, independently of the column density of the outflow itself.

Nevertheless, the case covered previously only covers the extremes of the outburst evolution, and the behavior during the state transitions is expected to be much more nuanced, as analyzed by Petrucci et al. (2021). During the hard to soft state transition, it is for now unclear how the outflowing material reacts to the switch from unstable to stable SEDs, if it can directly retain the right structure as the irradiation becomes stable, and how this affects the creation of lines. The case of soft to hard state transition, while more difficult to probe due to a transition at much lower luminosity, is even more interesting. We

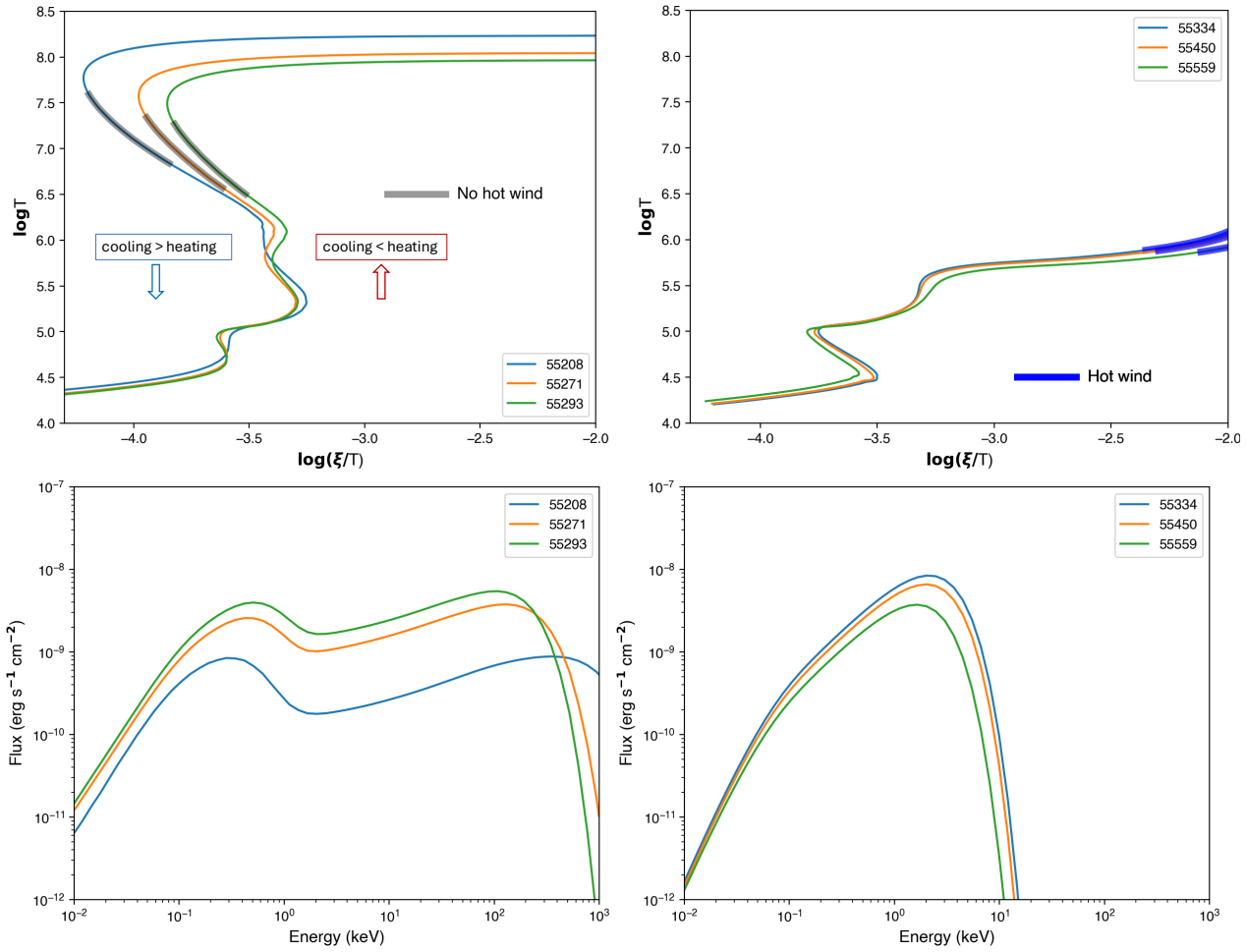

Figure 2.17: Evolution of the stability curves **(top)** and corresponding SEDs **(bottom)** for hard **(left)** and soft **(right)** states of the BHLXMB GX 339-4. Different curve highlight SEDs of different Julian days, derived from *RXTE* measurements, and the grey and blue bolded regions represent the range of ionization parameter covering 90% of the ionic fraction of Fe XXV and Fe XXVI. Adapted from Petrucci et al. (2021)

show in the left panel of Fig. 2.18 an example scenario from SEDs derived during such a state transition. The evolution of the material to the new hot and cold stable positions, here assumed to be isobaric, is materialized by the red arrows. This transition is not an instant process: assuming that the material condenses into cold, dense clumps (lower T and thus lower ξ_i for constant ξ_i/T) embedded into a hotter, more diffuse medium (higher T, higher ξ_i), the migration should occur on the dynamical time scale of the cold phase, of the order of $\Delta H/c_s$,with ΔH the thickness of the unstable region and c_s the local sound velocity (Gonçalves et al. 2007). For optically thin material, this translates to:

$$t_{dyn} \sim 2 \times 10^4 \frac{f_{multi}}{N_{H,23}} T_5 n_{12} \text{ (s)} \tag{2.10}$$

With f_{multi} the fraction of unstable gas thickness compared to that of the full absorber, and N_H, T and n normalized to different order of magnitudes in cgs units. For realistic values of each of them, and a non negligible unstable gas fraction, t_{dyn} can reach $10^3 - 10^4$ s, which makes this evolution accessible to the new generation of instruments, and in bright sources, potentially to the current one (see e.g. the results of Sec. 4.5).

In parallel, one must also carefully consider the many variables affecting the slope of the stability curve. Besides significant improvements in the photoionization codes used to derive the curve itself (see e.g.

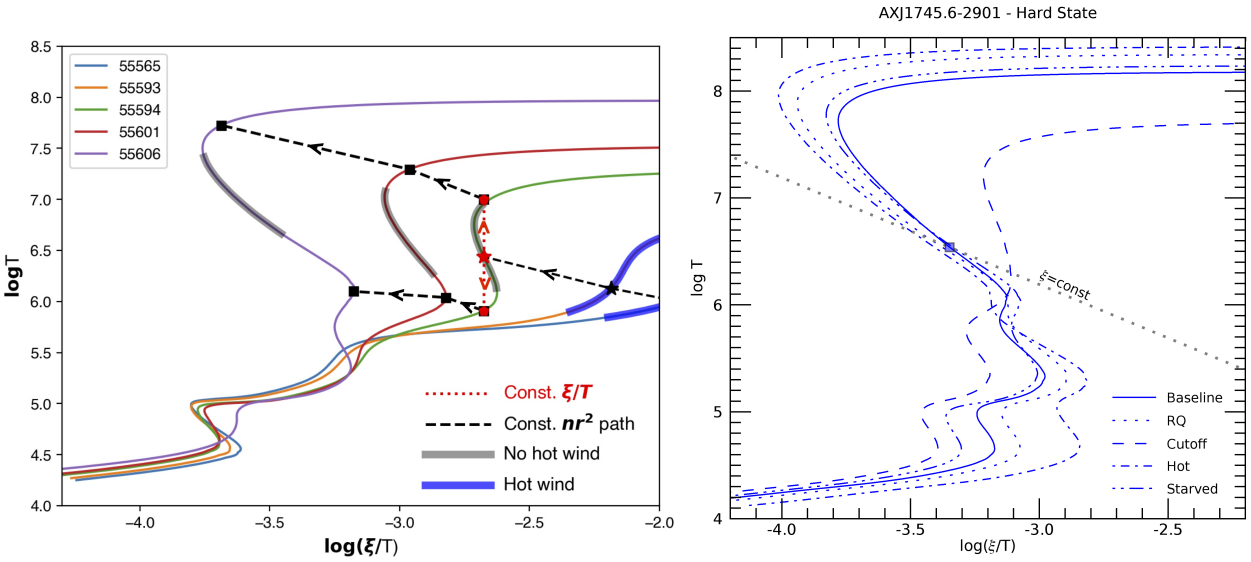

Figure 2.18: **(Left)** Evolution of the stability curves along the transition from soft to hard states of GX 339-4, similar to Fig. 2.17, and highlighting the two possible outcomes for an unstable material starting at the center of the unstable zone and maintaining an isobaric evolution. From Petrucci et al. (2021). **(Right)** Evolution of a set of hard NSLMXB stability curves with different assumptions on the broadband SED. See text from details. From Bianchi et al. (2017).

Chakravorty et al. 2008), several studies have studied the effects of density, abundances, and different broad band SEDs (Bianchi et al. 2017; Chakravorty et al. 2013; Petrucci et al. 2021). It turns out that the evolution of the broad band SED is by far the most impactful, due the lack of constrains on the hard X-rays component when only soft X-rays observations are available (which is a very common occurrence). We highlight tests for different broad band models of a hard state Neutron Star SED in the right panel of Fig. 2.18. The most notable contribution is that of the high-energy cutoff, which, expectedly, is the least constrained quantity, and can significantly stabilize an otherwise very unstable SED. Although the issue of the cutoff remains difficult to solve without very detailed hard energy coverage, we shall bring new insights to the matter in Sec. 4.

Other, more complex considerations require a more careful treatment. Indeed, the stability curve in its current form is a very simplified view, providing a single picture for the entire solution, without geometrical and radial considerations, while being restricted to optically thin solutions. Several of these limitations are the subject of ongoing efforts due to how restrictive these assumptions are compared to realistic systems. Recent developments including radial and more realistic radiative treatment of the stability criterion (Proga et al. 2022) highlight the need to consider a phase-space diagram, in which an "attenuation" curve will define less radially dependent instability criteria, which are particularly relevant when partial obscuration of the intrinsic luminosity in distant regions increases the Compton temperature (due to an predominant absorption in softer X-rays). Although this has yet to be considered, we highlight that the inclination dependence of the central SED, discussed in Sec. 1.3.1, should add an additional complexity to position dependent stability criteria. In parallel, the instability discussed here is restricted to the simplified case of static material in isobaric evolution, and more complete approaches removing these assumptions are progressively revealing an immensely more complex set of solutions (Waters & Proga 2023).

A more comprehensive understanding of instability is not only useful for understanding wind visibility, or specific driving mechanisms (Waters et al. 2021), but is also a fundamental process to help stratify the outflows and condense the material into clumps. This "clumping", which has strong observational backing in AGNs (Laha et al. 2016), is also proving immensely useful to aid in obtaining wind structures with sufficiently high densities to explain specific absorption line profiles in AGNs (Matthews et al. 2020,

2023), although this approach is for now limited to parametric models. In BHXRBs, a similar approach is being explored for cold outflows (Koljonen et al. 2023), and will be especially relevant for the signatures detected at very low luminosities, which are completely out of reach of thermal winds, and potentially of magnetic winds as well, due to their density scaling with $\dot{m}$.

l’or gi e fut vitesse, ve nt furtif, « vent-fou ».
le cosmos , prit s a forme, ’ lente
table , ’ vivant, jus ’ vous.
Bien à toi, homme lié, pouss e vite .

II
Observations

3

Global study of X-ray winds in BHLMXBs

3.1 Motivation and Approach

We established that the new generation of X-ray telescopes is expected to put significant constrains on launching mechanisms (Chakravorty et al. 2023; Gandhi et al. 2022) and probe deeper the influence of other parameters, such as the evolution of the wind structure along the outburst (Petrucci et al. 2021). Nevertheless, many answers can still be found in the existing observations, and more constraints can be put through with comparisons to much larger datasets. Indeed, observational studies and modeling efforts often focus on either single observations or select samples with very precise analysis or modeling of the existing features, but they mostly cover observations with the most prominent lines. Moreover, no detailed study of a large sample of sources, with exhaustive, multi-instrument data coverage, has been performed since the seminal work of Ponti et al. (2012), despite an extensive increase in the number of observations and sources, and a greater understanding of the winds.

One of my first objectives was thus to get a global, up-to-date view of the wind signatures in a large sample of objects and observations. This would not only allow to draw new conclusions on the observations from a much larger dataset than previously studied, but also to identify the best sources, outburst and datasets in which the line signatures would be susceptible to put constrains on wind launching mechanisms.

3.2 Data selection and Sample overview

In order to maximize the number of BHLMXB candidates, I drew my sample from both the BlackCAT (Corral-Santana et al. 2016) and WATCHDOG (Tetarenko et al. 2016) BH catalogs. The BlackCAT catalog has been continuously updated since its release but is voluntarily restricted to transient sources, which is why some archetypal binaries are missing from it. The WATCHDOG catalog, besides including the aforementioned persistent objects, also includes high-mass XRBs (HMXBs), and after its publication in 2016, some of its sources have been identified as NSs. Thus, the parent sample was initially composed of 79 sources: 67 from BlackCAT (in which we only excluded Cen X-2 due to a weak position determination and possible mismatch with GS 1354-64, according to Kitamoto et al. 1990) and 12 from WATCHDOG (as 11 of the 23 sources not overlapping with BlackCAT are either HMXBs or NSs).

There are many telescopes susceptible to see lines in the soft X-ray band: when restricting ourselves to the ones with easily accessible archival data, that leaves *Chandra*, *NICER*, *NuSTAR*, *Suzaku*, XMM-*Newton*, *Swift*, and *HXMT*. However, not all telescopes and data reduction softwares are created equal:

- *Swift* has an immense amount of data available, but its resolution, sensitivity and calibration are lacking to detect lines in all but the brightest sources. Some of the few line detections with this instruments will be discussed in Sec. 3.5.2.
- *HXMT*, being young and less confronted to other instruments, would require collaborations with members of the Chinese X-ray community to ensure up-to date data analysis. This issue was, to a lesser extent, also present for *Suzaku* (although we will incorporate its observations in Sec.4).
- When starting this project in 2021, *NICER* was also very young, and its calibration and data reduction methodology were still in improvement. The **significant** improvements in this regard

would later lead to the work presented in Chap. 3.

- Aside a much lower spectral resolution that mostly forbids precise velocity shift measurements, *NuSTAR* has, by design, fewer observations in soft states, since its high-energy capabilities are much less useful when there's no high-energies to observe.

The remaining telescopes, XMM-*Newton* and *Chandra*, had the advantages of being well established and (relatively) well calibrated, suited for line detections in the iron band, and having well documented studies of most archival line detections to confront my results. Further choosing to restrict myself to the most relevant instruments of each telescope, I ended up analyzing all XMM-*Newton* EPIC-PN and *Chandra*-HETG X-ray observations of currently known BHLMXBs, made public as of October 2022. This restricted the sample to 42 sources. Details about their physical properties, previous detections of iron K wind signatures in the literature, and number of exposures in our sample were highlighted in Parra et al. (2024) (see also Sec.7.1.1). We note that as of the writing of this manuscript, although additional observations have been made, there have been no reports of additional detections for HETG and EPIC-PN with these new datasets.

However, in the last two years, a number of updates on the physical properties of these sources were published, notably with a push towards systematic (if imperfect) analysis of Black Hole reflection features (Draghis et al. 2023, 2024), leading to significantly updated inclination measurements for a good portion of the sources. Moreover, several new binaries with wind features in different wavelengths were discovered.

As of the writing of this manuscript, the literature for BHLMXBs remains very fragmented, and none of the BH catalogs are fully up to date with the literature. We thus list in Tab. 3.1 the relevant physical properties and overview of iron band absorption line detections of the **full sample of 88 sources** identified as BHLMXBs in the literature as of mid-2024, which will be used at different point of the study. Besides the new BlackCAT sources, we also add several sources listed in Draghis et al. (2024), with reflection features strongly hinting at Black Hole accretors and no sign of High Mass companions. For a more complete review of the arguments in favor of individual sources hosting Black Hole, we refer the reader to previously mentioned catalogs and dedicated works such as Fortin et al. (2024).

The data reduction procedures of the relevant telescopes, which are summarized in (Parra et al. 2024), are listed along with other instruments used for subsequent analysis, in Appendix 6.1.

3.3 Line detection Methodology

To filter out spectra without sufficient S/N necessary to detect absorption lines in the iron band, we applied a predefined count threshold of 5000 counts in the $4-10$ keV band to both XMM-*Newton* and *Chandra* exposures. For XMM-*Newton*, simulations of template spectra from soft state SEDs of GRO J1655-40 in the soft state showed that observations fainter than the chosen threshold cannot detect Fe xxvi Kα EW upper limits below 75 eV, which coincides with the high-end tail of the equivalent width (EW) distribution in our sample and reports in the literature (see Sect. 3.4.1). While such simulations are less straightforward for *Chandra*-HETG, manual inspection of the excluded spectra confirmed that their S/N is always insufficient for detecting lines with EWs below 100 eV at 7 keV. After this final cut, 242 exposures remained: 137 EPIC-pn spectra and 105 HETG spectra.

Table 3.1: Sources included in our final sample, relevant physical parameters, and number of spectra of sufficient quality for our analysis.

Name	mass ($M_\odot$)	distance (kpc)	inclination (°)	dips	P_{orb} (h)	absorption lines reported in the iron band
1E 1740.7-2942	8	8	$31^{+29}_{-18}{}^{R}$ (1.)	X	303^{+1}_{-2} (2.)	X
4U 1543-475^{D} (3.)	8.4 ± 1 (4.)	7.5 ± 0.5 (5.)	20.7 ± 1.5^{D} (4.)/$67^{+7}_{-8}{}^{R}$ (1.)	✓ (6.)	26.8 (4.)	✓
4U 1630-47	8	8.1 ± 3.4 (7.)	$[60-75]^{D}$ (8.)/$55^{+8}_{-11}{}^{R}$ (1.)	✓ (8.)	X	✓
4U 1755-338	8	6.5 ± 2.5 (10.)	/	X	X	X
4U 1957+115	$3^{+2.5}_{-1}$ (9.)	8	$\sim13^{D}$ (9.)/$52^{+12}_{-13}{}^{R}$ (1.)	X	9.33 (9.)	X
A0620-00^{D} (13.)	6.6 ± 0.3 (13.)	1.06 ± 0.1 (13.)	52.6 ± 2.5^{D} (14.)	✓ (11.)	7.75 (12.)	X
A 1524-61^{D} (15.)	$5.8^{+3}_{-2.4}$ (15.)	8 ± 0.9 (15.)	57 ± 13^{D} (15.)	X	6.2 ± 2 (15.)	X
1A 1742-289	8	8	/	X (16.)	X (16.)	X
AT 2019wey	8	8	$14^{+12}_{-10}{}^{R}$ (1.)	X	X	X
CXOGC J174540.0-290031	8	8	X	✓ (17.)	7.8 (17.)	X
EXO 1846-031	8	~7 (18.)	40 ± 3^{R} (19.)/$62^{+9}_{-10}{}^{R}$ (1.)	X	X	✓
GRO J0422+32 (21.)	$2.7^{+0.7}_{-0.5}$ (14.)	2.5 ± 0.3 (21.)	56 ± 4^{D} (14.)	X	5.09 (21.)	X
GRO J1655-40^{D} (22.)	5.4 ± 0.3 (23.)	3.2 ± 0.2 (24.)	69 ± 2^{D} (23.)	✓ (25.)	62.9 (26.)	✓
GRS 1009-45^{D} (29.)	8	$3.8+0.3$ (27.)	59 ± 22^{D} (28.)	X	6.85 (29.)	X
GRS 1716-249	$6.4^{+3.2}_{-2}$ (30.)	6.9 ± 1.1 (30.)	61 ± 15^{D} (30.)/$59^{+7}_{-12}{}^{R}$ (1.)	X	6.67 (30.)	X
GRS 1739-278	8	7.3 ± 1.3 (31.)	$70^{+5}_{-11}{}^{R}$ (1.)	X	X	X
GRS 1730-312	8	8	/	X	X	X
GRS 1737-31	8	8	/	X	X	X
GRS 1758-258	8	8	$67^{+8}_{-13}{}^{R}$ (1.)	X	X	✓
GRS 1915+105^{D} (32.)	$11.2^{+2}_{-1.8}$ (33.)	$9.4^{+1.6}_{-1.6}$ (33.)	64 ± 4^{D} (33.)/ 60 ± 8^{R} (1.)	✓ (35.)	812 ± 4 (34.)	✓
GS 1354-64^{D} (36.)	8	~25 (36.)	$<79^{D}$ (36.)/ $47^{+11}_{-10}{}^{R}$ (1.)	X	61.1 (36.)	X
GS 1734-275	8	8	/	X	X	X
GS 2000+251^{D} (37.)	7.2 ± 1.7 (37.)	2.7 ± 0.7 (5.)	68 ± 6^{D} (14.)	X	8.26 (37.)	X

Table 3.1: Continued.

Name	mass ($M_\odot$)	distance (kpc)	inclination (°)	dips	P_{orb} (h)	absorption lines reported in the iron band
GX 339-4 ^{D} (38.)	5.9 ± 3.6 (38.)	8	$[37-78]^{D}$ (38.)/49 ± 14^{R} (1.)	X	42.2 (38.)	X
H 1705-250 ^{D} (41.)	5.4 ± 1.5 (40.)	8.6 ± 2.1 (5.)	64 ± 16^{D} (39.) (41.)	X	12.51 (41.)	X
H 1743-322	8	8.5 ± 0.8 (42.)	75 ± 3^{J} (42.)/$54^{+12}_{-13}{}^{R}$ (1.)	✓ (43.)	X	✓
IGR J17091-3624	8	8	$\sim 70^{H}$ (44.) (45.)/$47^{+10}_{-11}{}^{R}$ (1.)	✓ (35.)	X	✓
IGR J17098-3628	8	~ 10.5 (47.)	/	X	X	X
IGR J17285-2922	8	8	/	X	X	X
IGR J17451-3022	8	8	$> 70^{D}$ (48.)	✓ (48.)	6.3 (49.)	✓
IGR J17454-2919	8	8	$54^{+15}_{-14}{}^{R}$ (1.)	X	X	X
IGR J17497-2821	8	8	/	X	X	X
IGR J18175-1530	8	8	/	X	X	X
IGR J18539+0727	8	8	/	X	X	X
MAXI J0637-430	8	8	$63^{+9}_{-10}{}^{R}$ (1.)	X	$\approx 2.2 \pm 1$ (50.)	X
MAXI J1305-704 ^{D} (51.)	$8.9^{+1.6}_{-1.}$ (51.)	$7.5^{+1.8}_{-1.4}$ (51.)	$72^{+5}_{-8}{}^{D}$ (51.)	✓ (52.)	9.5 ± 0.1 (51.)	✓
MAXI J1348-630	8	$3.4^{+0.4}_{-0.4}$ (53.)	28 ± 3^{J} (54.)/65 ± 7 (55.)/ $52^{+8}_{-11}{}^{R}$ (1.)	X	X	✓
MAXI J1535-571	8	$4.1^{+0.6}_{-0.5}$ (56.)	$\leq 45^{J}$ (57.)/ $44^{+17}_{-19}{}^{R}$ (1.)	X	X	✓
MAXI J1543-564	8	8	/	X	X	X
MAXI J1631-479	8	8	$22^{+10}_{-12}{}^{R}$ (1.)	X	X	✓
MAXI J1659-152	8	8.6 ± 3.7 (58.)	70 ± 10^{D} (58.)	✓ (58.)	2.4 (59.)	X
MAXI J1727-203	8	8	$65^{+11}_{-14}{}^{R}$ (1.)	X	X	X
MAXI J1803-298	8	8	$\sim 67 \pm 8^{D}$ (60.)/$72^{+6}_{-9}{}^{R}$ (1.)	✓ (60.)	7 ± 0.2 (60.)	✓
MAXI J1810-222	8	8	/	X	X	X
MAXI J1813-095	8	8	$42^{+11}_{-13}{}^{R}$ (1.)	X	X	X
MAXI J1820+070 ^{D} (61.)	6.9 ± 1.2 (62.)	2.96 ± 0.33 (63.)	74 ± 7^{D} (62.)/$64^{+8}_{-9}{}^{R}$ (1.)	✓ (64.)	16.5 (61.)	✓

Table 3.1: Continued.

Name	mass ($M_\odot$)	distance (kpc)	inclination (°)	dips	P_{orb} (h)	absorption lines reported in the iron band
MAXI J1828-249	8	8	/	X	X	X
MAXI J1836-194	8	7 ± 3 (65.)	$9^{+6\,D}_{-5}$ (65.)	X	X	X
MAXI J1848-015	8	3.4 ± 0.3 (66.)	77 ± 2^{D} (66.)/$29^{+13\,R}_{-10}$ (1.)	X	X	X
Nova Muscae 1991^{D} (67.)	$11^{+2.1}_{-1.4}$ (67.)	5 ± 0.7 (67.)	$43^{+2\,D}_{-3}$ (67.)	X	10.4 (68.)	X
SAX J1711.6-3808	8	8	/	X	X	X
SLX 1746-331	8	8	/	X	X	X
Swift J1357.2-0933	$11.6^{+2.5}_{-1.9}$ (14.)	8	$81^{+9\,D}_{-12}$ (14.)	✓ (69.)	2.8 ± 0.3 (70.)	X
Swift J151857.0-572147	8	8	/	X	X	✓
Swift J1539.2-6227	8	8	/	X	X	X
Swift J1658.2-4242	8	8	$50^{+9\,R}_{-10}$ (1.)	✓ (71.)	X	✓
Swift J1713.4-4219	8	8	/	X	X	X
Swift J1727.8-1613	8	2.7 ± 0.3 (72.)	/	X	7.6 ± 0.2 (72.)	X
Swift J1728.9-3613	8	8.4 ± 0.8 (73.)	$7^{+8\,R}_{-3}$ (1.)	X	X	X
Swift J174510.8-262411	8	$\sim 3.7 \pm 1.1$ (74.)	/	X	< 11.3 (74.)	X
Swift J174540.2-290005	8	8	/	X	X	X
Swift J174540.2-290037 (T37)	8	8	$31^{+8\,R}_{-9}$ (1.)	X	X	X
Swift J174540.7-290015 (T15)	8	8	$63^{+10\,R}_{-8}$ (1.)	X	X	✓
Swift J1753.5-0127	8	$5.6^{+1.8}_{-2.8}$ (75.)	73 ± 8^{R} (1.)	X	3.2 (77.)	X
Swift J1753.7-2544	8	8	/	X	X	X
Swift J1842.5-1124	8	8	/	X	X	X
Swift J1910.2-0546	8	8	/	X	2.4 ± 0.1 (78.)	X
V404 Cyg^{D} (79.)	$9^{+0.2}_{-0.6}$ (79.)	2.4 ± 0.2 (80.)	$67^{+3\,D}_{-1}$ (79.)/$37^{+9\,R}_{-8}$ (1.)	X	155.3 (81.)	✓
V4641 Sgr^{D} (82.)	6.4 ± 0.6 (83.)	6.2 ± 0.7 (83.)	72 ± 4^{D} (83.)/$66^{+7\,R}_{-11}$ (1.)	X	67.6 (82.)	X

Table 3.1: Continued.

Name	mass ($M_\odot$)	distance (kpc)	inclination (°)	dips	P_{orb} (h)	absorption lines reported in the iron band
XMMSL1 J171900.4-353217	8	8	/	X	X	X
XTE J1118+480^D (86.)	7.1 ± 0.1 (86.)	1.7 ± 0.1 (84.)	72 ± 2^D (14.)	X	4.1 (85.)	X
XTE J1550-564^D (87.)	11.7 ± 3.9 (87.)	$4.4^{+0.6}_{-0.4}$ (87.)	75 ± 4^D (87.)/40 ± 10^R (88.)	X	37.0 (87.)	✓
XTE J1637-498	8	8	/	X	X	X
XTE J1650-500^D (89.)	8	2.6 ± 0.7 (90.)	$\geq 47^D$ (89.)	X	7.7 (89.)	X
XTE J1652-453	8	8	$\leq 32^R$ (91.)	X	X	✓
XTE J1720-318	8	6.5 ± 3.5 (92.)	/	X	X	X
XTE J1719-291	8	8	/	X	X	X
XTE J1726-476	8	8	/	X	X	X
XTE J1748-288	8	8	/	X	X	X
XTE J1752-223	8	$\sim 6 \pm 2$ (93.)	$< 49^J$ (94.)/35 ± 4^R (95.)	X	$\lesssim 7$ (93.)	X
XTE J1755-324	8	8	/	X	X	X
XTE J1817-330	8	5.5 ± 4.5 (96.)	/	✓ (97.)	X	X
XTE J1818-245	8	3.6 ± 0.8 (98.)	/	X	X	X
XTE J1856+053	8	8	/	X	X	X
XTE J1859+226 ^{D} (100.)	8 ± 2 (99.)	12.5 ± 1.5 (100.)	67 ± 4^D (99.)/71 ± 1^R (101.)	✓ (102.) (103.)	6.6 (99.)	X
XTE J1901+014	8	8	/	X	X	X
XTE J1908+094	8	6.5 ± 3.5 (104.)	28 ± 11^R (1.)	X	X	X
XTE J2012+381	8	8	46 ± 4^R (105.)/$68^{+6}_{-11}{}^R$ (1.)	X	X	X

Notes: The letter D in the object name column identifies dynamically confirmed BHs. A fiducial mass of 8 $M_\odot$ and distance of 8 kpc are used when not reliably known, including when dynamical constraints are only lower limits, according to the properties of the bulk of the Galactic BHLMXB population (see e.g. Corral-Santana et al. 2016). For inclination measurements letters D, J, H, R refer respectively to dynamical inclination measurements (dips/eclipses/modulations), jets, heartbeats, and reflection fits. Sources analyzed in (Parra et al. 2024) are highlighted in blue. Details and references for line

detection reports are provided in Tab. 3.3.

References: 1 (Draghis et al. 2024) 2 (Stecchini et al. 2017) 3 (Orosz et al. 1998) 4 (Orosz 2003) 5 (Jonker & Nelemans 2004) 6 (Park et al. 2004) 7 (Kalemci et al. 2018) 8 (Tomsick et al. 1998) 9 (Gomez et al. 2015) 10 (Angelini & White 2003) 11 (Haswell et al. 1993) 12 (Hernández et al. 2013) 13 (Cantrell et al. 2010) 14 (Casares et al. 2022) 15 (Yanes-Rizo et al. 2024) 16 (Kennea et al. 1996) 17 (Porquet et al. 2005) 18 (Parmar et al. 1993) 19 (Wang et al. 2020) 20 (Gelino & Harrison 2003) 21 (Webb et al. 2000) 22 (Van Der Hooft et al. 1998) 23 (Beer & Podsiadlowski 2002) 24 (Hjellming & Rupen 1995) 25 (Kuulkers et al. 1998) 26 (Petretti et al. 2023) 27 (Gelino & M. 2002) 28 (Shahbaz et al. 1996) 29 (Filippenko et al. 1999) 30 (Casares et al. 2023) 31 (Greiner et al. 1996) 32 (Reid et al. 2014) 33 (Reid & Miller-Jones 2023) 34 (Steeghs et al. 2013) 35 (Pahari et al. 2013a) 36 (Casares et al. 2009) 37 (Ioannou et al. 2004) 38 (Heida et al. 2017) 39 (Martin et al. 1995) 40 (Harlaftis et al. 1997) 41 (Remillard et al. 1996) 42 (Steiner et al. 2012) 43 (Miller et al. 2006b) 44 (Capitanio et al. 2012) 45 (Rao & Vadawale 2012) 46 (Xu et al. 2017) 47 (Grebenev et al. 2006) 48 (Jaisawal et al. 2015) 49 (Bozzo et al. 2016) 50 (Soria et al. 2022) 51 (Sánchez et al. 2021) 52 (Shidatsu et al. 2013) 53 (Lamer et al. 2021) 54 (Carotenuto et al. 2022) 55 (Titarchuk & Seifina 2023) 56 (Chauhan et al. 2019) 57 (Russell et al. 2019b) 58 (Kuulkers et al. 2013) 59 (Corral-Santana et al. 2018) 60 (Jana et al. 2022) 61 (Torres et al. 2019) 62 (Torres et al. 2020) 63 (Atri et al. 2020) 64 (Homan et al. 2018) 65 (Russell et al. 2014) 66 (Bahramian et al. 2023) 67 (Wu et al. 2016) 68 (González Hernández et al. 2017) 69 (Corral-Santana et al. 2013) 70 (Sánchez et al. 2015) 71 (Xu et al. 2018b) 72 (Mata Sánchez et al. 2024) 73 (Balakrishnan et al. 2023) 74 (Chaty et al. 2020) 75 (Arnason et al. 2021) 76 (Reis et al. 2009) 77 (Zurita et al. 2008) 78 (Saikia et al. 2023) 79 (Khargharia et al. 2010) 80 (Miller-Jones et al. 2009) 81 (Casares et al. 2019) 82 (Orosz et al. 2001) 83 (Macdonald et al. 2014) 84 (Gelino et al. 2006) 85 (González Hernández et al. 2014) 86 (Cherepashchuk et al. 2019) 87 (Orosz et al. 2011) 88 (Connors et al. 2020) 89 (Orosz et al. 2004) 90 (Homan et al. 2006) 91 (Chiang et al. 2012) 92 (Chaty & Bessolaz 2006) 93 (Ratti et al. 2012) 94 (Miller-Jones et al. 2011) 95 (García et al. 2018) 96 (Sala et al. 2007b) 97 (Sriram et al. 2012) 98 (Bel et al. 2009) 99 (Yanes-Rizo et al. 2022) 100 (Corral-Santana et al. 2011) 101 (Mall et al. 2024) 102 (Rodriguez & Varnière 2011) 103 (Sriram et al. 2013) 104 (Chaty et al. 2006) 105 (Kumar 2024)

The line detection process can be split into four main steps. First, a fit of the continuum with a broadband model (Sect. 3.3.1). Then, a blind search for line features in the high-energy (6-10 keV) band (Sect. 3.3.2), followed by an incremental fit of the line features in this energy range with the strongest absorption and emission lines expected in this band (Sect. 3.3.3). Once this is done, a second blind search from the best-fit model (including the lines) checks for the absence of the remaining line features, and finally the true significance of the absorption lines is assessed via Monte Carlo (MC) simulations (Sect. 3.3.4).

In the following, we used Xspec version 12.12.0 (Arnaud et al. 1996) via Pyxspec version 2.0.5 along with wilm abundances (Wilms et al. 2000) and the Cash statistic (Cash 1979). Uncertainties for all the reported parameters were estimated drawing an MC chain from the final fit using the internal Xspec `Chain` commands. Due to the great number of spectra to be analyzed and the use of multiple runs during the line detection process, for a given number of free parameters n_{free}, we only used $2 \cdot n_{free}$ parameters, for $4000 \cdot n_{free}$ steps, discarding the first $2000 \cdot n_{free}$ steps of each chain. Unless specified otherwise, all uncertainties are quoted at a 90% confidence level.

3.3.1 Broadband modeling

We used a simple fitting procedure in which a list of components is added recursively to converge to the best fit. Adding or choosing a component over its peers is deemed statistically significant through F-tests, with a threshold fixed at a 99% confidence level. For the broadband modelization of the continuum, three components can be combined: a `powerlaw`, a `diskbb`, and an absorption component `phabs`, which is applied to all of the additive components together. As the goal was to obtain a precise (although phenomenological) estimate of the continuum, we initially limited the contamination due to iron band features by ignoring the 6.7-7.1 and 7.8-8.3 keV bands in this step only.

To limit the effect of low energy spurious features, we restricted the broadband fit to 2-10 keV for XMM-*Newton*-pn and 1.5-10 keV for *Chandra*-HETG.[20] While the N_H value may not be estimated perfectly with this choice of energy band, notably for sources with low absorption, it still allows for a good measure of the intrinsic unabsorbed 3-10 keV luminosity and 6-10/3-6 keV hardness ratio (HR). Following this, we then fixed the neutral absorption column density in order to perform the blind search in the 4-10 keV range as a second step, which is described in the next section.

3.3.2 Blind search

Once the continuum was fixed, we carried out a standard blind search of narrow emission and absorption features in the 4-10 keV band. We measured the change in ΔC when adding a narrow (width fixed at zero)`gaussian` line with varying normalization and energy on the fit and mapped out the resulting 2D ΔC surface in the line normalization-energy plan. Regions of strong and relatively narrow (<1 keV) ΔC excess indicated the possible presence of lines. In contrast, broader regions (>1 keV) of ΔC excess could reflect the limit of our simple continuum fit process.

The Gaussian energy varies between 4 and 10 keV, with linear energy steps of 50 eV for XMM-*Newton*, which is around a third of the EPIC-pn spectral resolution at those energies,[21] and 20 eV for *Chandra*-HETG, which is slightly below HETG's energy resolution at 4 keV and half at 6 keV.[22] The line normalization was scaled in an interval of $[10^{-2}, 10^{1}]$ times the best-fit continuum flux in each energy step, split in 500 logarithmic steps for both positive and negative normalization.

We show in Fig. 3.1 an example of the result of the procedure for 4U 1630-47, a source well known for its absorption lines. Panels (A) and (B) show the spectrum and model after the first continuum fit in the 4-10 keV band and the ΔC map obtained with our blind search procedure. The contours over plotted in black highlight ΔC levels of 68%, 90%, and 99% confidence intervals with two parameters.

[20] In HETG exposures in timed mode, there can be issues with event resolution at high energy due to an overlap between the default HEG and MEG spatial masks. Thus, whenever necessary, we restrict the upper limit of all energy bands to 7.5 keV, so as to minimize the effect on the continuum while keeping the ability to at least analyze lines of the Kα complex.

[21] See https://xmm-tools.cosmos.esa.int/external/xmm_user_support/documentation/uhb/basics.html.

[22] See https://cxc.cfa.harvard.edu/proposer/POG/html/chap8.html.

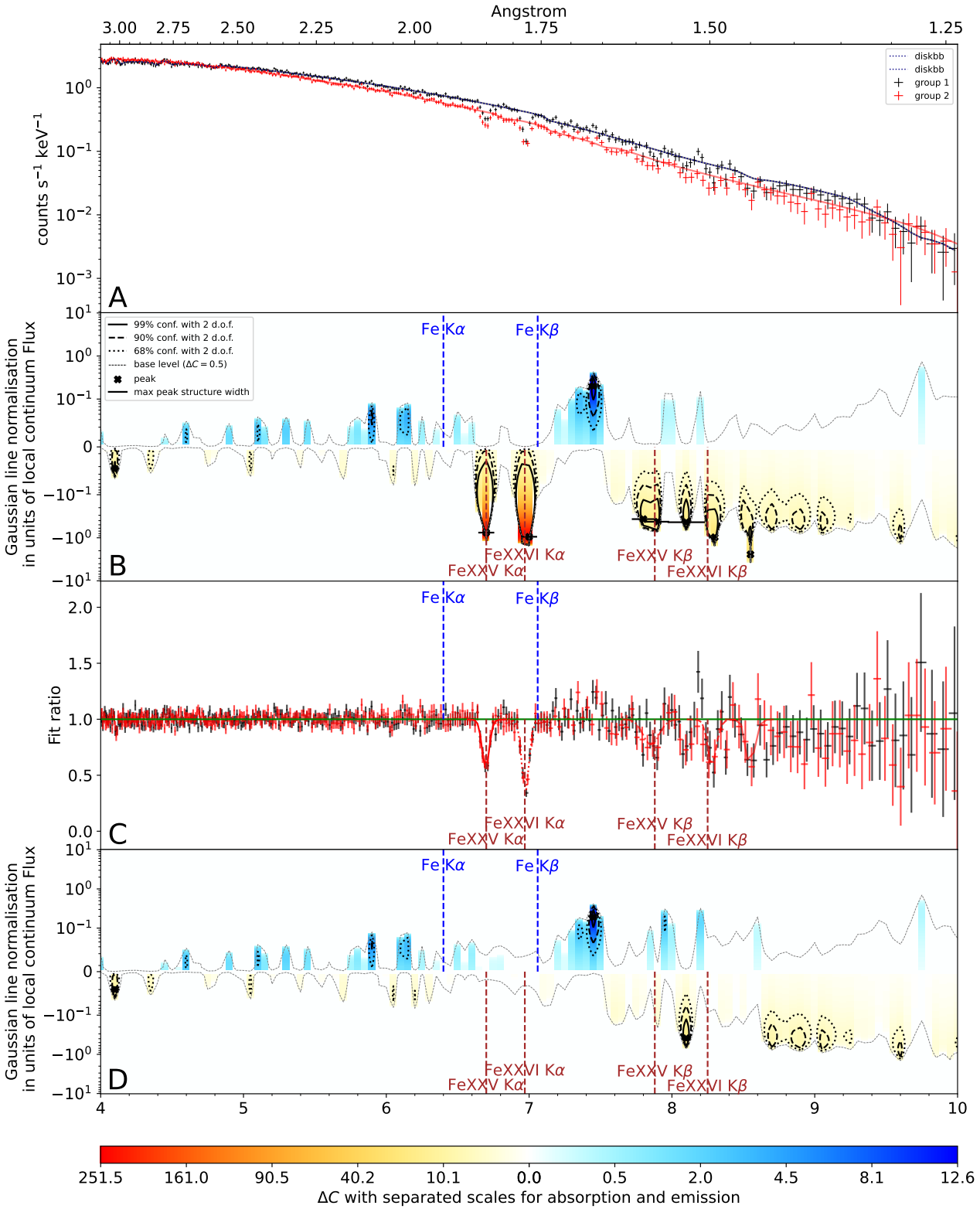

Figure 3.1: Steps of the line detection procedure for a standard 4U 1630-47 *Chandra* spectra. **Panel (A)**: Spectrum in the 4-10 keV band after the first continuum fit in this band. **Panel (B)**: Map of the line blind search restricted to positive ΔC regions (i.e., improvements of the fit). Standard confidence intervals are highlighted with different line styles, and the color map shows the ΔC improvements of emission and absorption lines. **Panel (C)**: Ratio plot of the best fit model once absorption lines are added. **Panel (D)**: Remaining residuals seen through a second blind search.

The position of the "maxima" in ΔC improvement are highlighted for visualization. In this example, the blind search clearly identifies two very significant (more than 99%) absorption features at $\sim$ 6.7 and $\sim$7 keV, compatible with the Fe xxv Kα and Fe xxvi Kα absorption lines, as well as fainter absorption features at higher energies, compatible with the Kβ complex. The significant emission residual identified at 7.5 keV does not seem to affect the absorption regions.

3.3.3 Line fitting procedure

While the blind search simply gives a semi-quantitative visualization of the possible presence of line-like features in the spectra, the goal of the next step was to identify the main individual absorption lines and to derive their physical parameters. Thus, we started from the continuum fit and added up to seven potential line features using the same F-test threshold as used for continuum components. Among these line features, five were the strongest absorption lines in the iron complex, namely, Fe xxv Kα (6.70 keV),[23] Fe xxvi Kα (6.97 keV), Fe xxv Kβ (7.88 keV), Fe xxvi Kβ (8.25 keV), and Fe xxvi Kγ (8.70 keV). The two remaining lines are fluorescent emission lines from neutral iron, Fe Kα (6.40 keV) and Fe Kβ (7.06 keV). We did not consider the Ni xxvii Kα and Fe xxv Kγ absorption lines, as they can be blended with the stronger Fe xxv Kβ and Fe xxvi Kβ, respectively, at our resolutions.

We modeled all lines with a simple `gaussian` component, convolved with `vashift` in order to allow for a shift of the lines, limited to $[-10000, 5000]$ km s^{-1}. Indeed, we did not expect significantly redshifted absorption lines nor speeds beyond 0.03c, as the vast majority of wind observations up until now have either shown wind speeds compatible with zero or a few thousands of kilometers per second at most (see references in Table 3.3). Moreover, allowing for higher blueshifts would produce degeneracy between neighboring lines (Fe xxv Kα reaches Fe xxvi Kα's energy at $v \sim$12000 km s^{-1}, and Fe xxv Kβ reaches Fe xxvi Kβ at v$\sim$ 14000 km s^{-1}). We assumed that all lines of a single ion are produced in the same region of the wind and consequently have the same velocity shift. All absorption lines were considered narrow, allowing their width to vary only up to $\sigma < 50$ eV. A line is considered resolved only if its width is larger than zero with a 3σ level of confidence.

While we are not interested in characterizing emission lines in detail, a good portion of observations show significant broad emission features in the iron region, which we modeled using up to two simple phenomenological neutral Fe Kα and Fe Kβ broad `gaussian` components, restricting their blueshift to the same interval taken for absorption lines and limiting their widths to $[0.2, 0.7]$ keV. The lower limit prevents overlapping between narrower emission and absorption features, while the upper limit prevents the broad emission features from modeling large parts of the continuum.

In very few XMM-*Newton* observations of GRS 1915+105 and GRO J1655-40, however, such as the exposures analyzed in Díaz Trigo et al. (2007), the presence of extreme emission features requires more complex modeling. For these spectra, we followed the same approach as Díaz Trigo et al. (2007), using a `laor` component with energy free in the range of [6.4 to 7.06] keV, inclination in the range of [50 to 90] degrees (consistent with the highly inclined sources), and R_{in} and R_{out} fixed at their default values.

We show in Panel (C) of Fig. 3.1 an example of the result of the procedure for a standard observation. In this case, all five Fe absorption components are sufficiently significant to be added in the model and reproduce the absorption features very well. Nevertheless, once the line fit was complete, we performed a second blind search to check the presence of the remaining line features in the residuals, following the procedure described in the previous section. We show in Panel (D) of Fig. 3.1 the result of this step for our example spectra. While all five main absorption features are indeed perfectly reproduced, a significant narrow feature at $\sim$ 8.1 keV remains, which can be identified with the Kα transition from Nixxviii. Similar residual features are only found in the highest S/N *Chandra* spectra, suggesting the presence of other weaker transitions not included in our five main components. However, these further absorption features are present only in combination with the much stronger lines considered in our analysis, but their detailed characterization is beyond the scopes of this paper.

[23] The energy of the Fe xxv Kα line was set equal to the resonant transition because the intercombination line is significantly weaker. Neither XMM-*Newton*-epic nor HETG were able to resolve the two lines without extremely high statistics.

For all the observations with no detected absorption lines, we computed the 3σ (99.7%) upper limit of each line's EW using the highest value in the line's range of velocity shift. All EW measurements and upper limits are reported in Tab. 7.1.1.

3.3.4 Line significance assessment

The goodness-of-fit and F-test methods have long been known to overestimate the detection significance of lines (Protassov et al. 2002). Reliable estimates can only be obtained through MC simulations (Porquet et al. 2004), which have been adopted as the standard since the last decade (Chartas et al. 2021; Gofford et al. 2013; Parker et al. 2020; Tombesi et al. 2010). We follow a similar procedure, adopting the same methodology as for the real data by putting similar constraints in energy and width as described in Sect. 3.3.3.

We thus generated 1000 distributions of parameters within the uncertainties of the final model from 1000 runs of the `simpars` xspec command. We then deleted all absorption line components from the models before repeating the following steps for 1000 iterations.

First, we loaded a set of model parameters from the simulated distribution. We then simulated a spectrum from the current model using the `fakeit` xspec command, retaining all of the observational parameters (exposure, response files, background) of the initial spectrum. After that, we fit the continuum plus emission lines model to the simulated spectrum in order to obtain a baseline C-stat. This allowed for the computation of the maximum possible ΔC gained from the addition of an absorption line in each line's allowed blueshift bands (exactly as done for the real data; described in Sect. 3.3.3).

The ΔC of the line detected in the real data can be compared to the distribution of the 1000 maximal ΔC_{sim} of the simulated spectra, and the statistical significance of the line is defined by $P = 1 - N/1000$, with N being the number of ΔC_{sim} larger than the real value. Only lines with a significance larger than 3 σ (99.7%) in their blueshift range, as derived from this procedure, are considered detections and are considered as such in the following sections, as well as reported in Tab. 7.1.1.

3.4 Global results

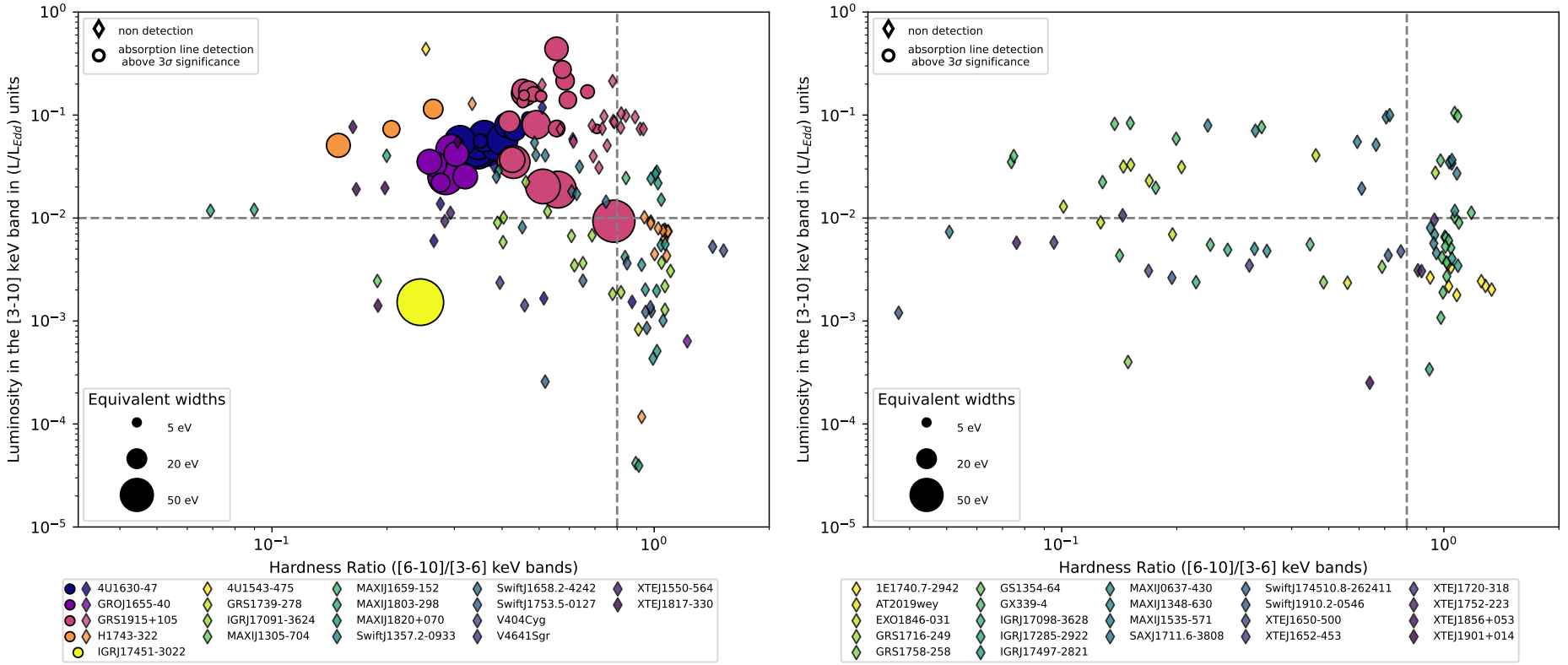

Figure 3.2: Hardness Luminosity diagram with the position of all line detections in the sample. The sample is split according to the viewing angle: the left panel is restricted to dippers, or sources, with $i > 55$, while the right panel shows all other sources. The vertical and horizontal lines highlight the luminosity and HR thresholds proposed in Sect. 3.4.2.

3.4.1 Parameter distribution and correlation

To study the behavior of the absorption lines and their interplay with the continuum SED in more detail, we analyzed the distribution of their main parameters and identified statistically significant correlations. To identify the correlations between individual parameters, we computed the Spearman coefficients, which trace general monotonic relations between two parameters. For that purpose, and in order to take into account the uncertainties of each parameter, we applied MC simulations to estimate the distribution of the correlation coefficients and associated p-values, following the perturbation method of Curran (2014). This was implemented through the python library *pymccorrelation* (Privon et al. 2020). In the following subsections, we focus on all correlations with $p < 0.001$ found in our sample.

Parameter distribution

We assessed the main properties of the absorption features in our sample with the detection of each line, their EWs, and the velocity shifts for the better constrained Kα complex. The distributions are presented in Fig. 3.3. The data in the left panels are split by source in order to show the properties of the absorption features in each object, but we stress that except for a few outliers, which are discussed below, the number of detections is too limited for the differences between the distributions to be significant. The data in the right panels, which are instead split by instrument, should exhibit mostly similar distributions, as XMM-*Newton* and *Chandra* observed similar portions of the HLD. This is clearly the case for the distribution of line detections: both instruments show the largest number of detections for Fe xxvi Kα, followed by Fe xxv Kα, Fe xxv Kβ, and Fe xxvi Kβ. Moreover, no Kβ or Kγ lines are detected without the corresponding Kα. In addition, as can be seen in the list of detections in Tab. 7.1.1, the Fe xxvi Kα line is present in nearly all observations where lines are detected, except one where only Fe xxv Kα was detected. Meanwhile, the single significant detection of Fe xxvi Kγ is found in a *Chandra* spectrum.

Although less apparent, the distribution of the EWs of both instruments are also broadly compatible, with a KS test p-value of 0.46. The whole sample spans a range of $\sim 5-100$ eV, with XMM-*Newton* detections expectedly dropping below 15 eV due to more limited energy resolution. The EW ratio between the Fe xxvi Kα and Fe xxv Kα line (hereafter called Kα EW ratio) provides a proxy of the ionization parameter ξ_i in our sample (e.g., Bianchi et al. 2005). As seen in the bottom-right panel in Fig. 3.3, in our sample, the majority of the Kα EW ratios are clustered between 1 and 2.5. This means that most exposures with line detections have sufficiently high ionization parameters for the Fe xxvi Kα line to be predominant. However, two objects (namely, GRS 1915+105 and GRO J1655-40) show Kα EW ratios also spread across the entire observed range, with a number of detections significantly below 1 associated with a lower ξ_i.

The velocity shift distributions for the strongest Kα lines are clearly different between the two instruments, with a KS test p-value of 1.7×10^{-7} (see bottom-right panel of Fig. 3.3). In particular, XMM-*Newton* showed a somewhat uniform distribution between -6500 and 2000 km s^{-1}, while the *Chandra* velocity shift distribution is much narrower and more symmetric around zero. The highest blueshift obtained with *Chandra* is around 1200 km s^{-1}, which is in accordance with the highest values previously reported in the literature for this observation (Miller et al. 2008).

This difference between the instruments can be at least partly attributed to the limits of the EPIC-pn camera. Indeed, in the timing mode used for the vast majority of EPIC-pn observations in our sample, even after recent updates in energy-scale calibration,[24] the energy accuracy remains limited, with a residual average shift of 18 eV ($\sim$ 800 km s^{-1} for Fe xxvi Kα) and a standard deviation of 80 eV ($\sim$ 3500 km s^{-1} for Fe xxvi Kα) at 12 keV. The standard deviation of our measured distribution is $\sim$ 2500 km s^{-1} and is thus compatible with the theoretical limits of the instrument's accuracy (which we can expect to be somewhat better at 7 keV). The mean value of our measured distribution is also $\sim$ 2500km s^{-1}, and it is significantly larger than the mean of post-calibration systematic energy accuracy. However, this may be the consequence of our choice to restrict the allowed blueshift fitting range to [-10000,5000] km s^{-1}, which would introduce a bias in a distribution with such a significant spread. In addition, this large average blueshift cannot be reconciled with the much smaller measurement of the more accurate

[24] See bottom-right panel of Fig. 3 in https://xmmweb.esac.esa.int/docs/documents/CAL-SRN-0369-0-0.pdf.

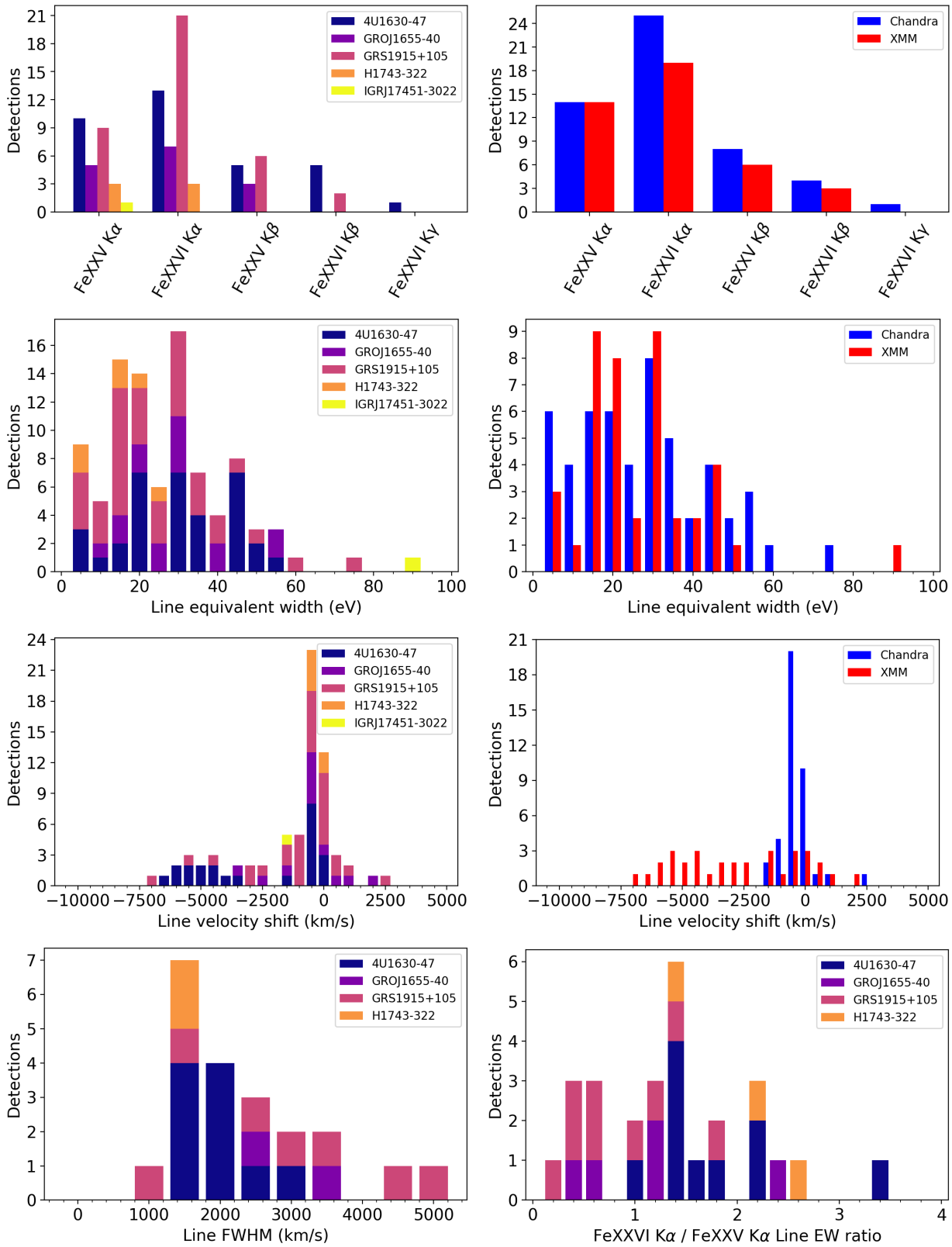

Figure 3.3: Distribution of intrinsic line parameters (detections of each line, EW, blueshift, widths, and Kα EW ratio) for the entire sample. The parameters are split by source and instrument whenever relevant. The blueshift distributions are restricted to the Kα complex.

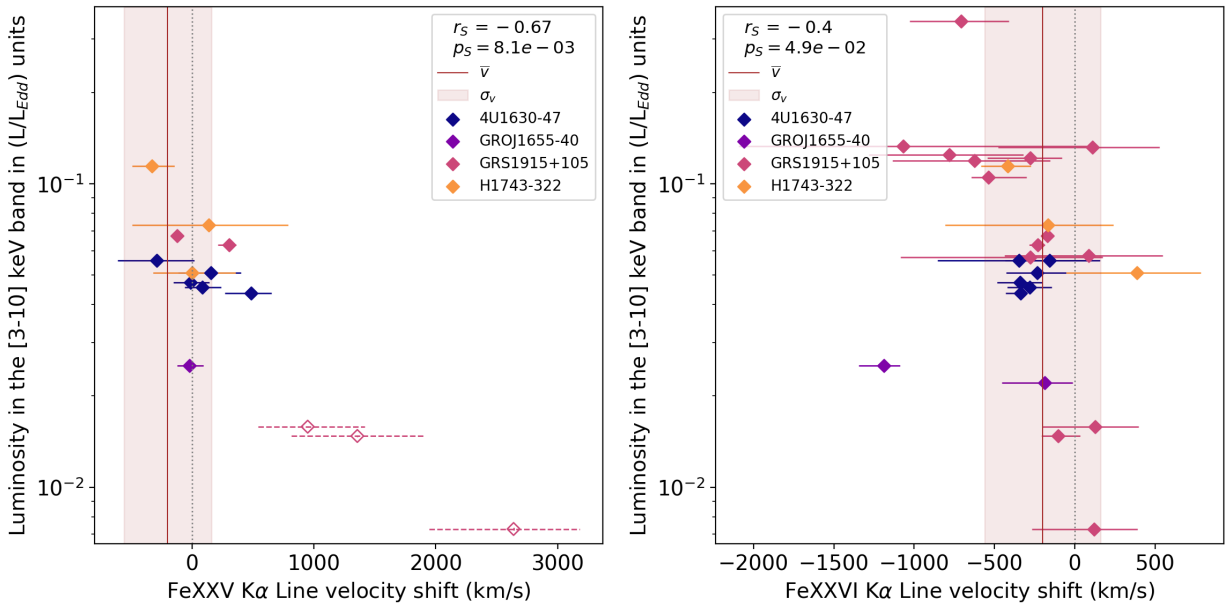

Figure 3.4: Scatter plot of the Fe xxv Kα (left) and Fe xxvi Kα (right) velocity shifts against luminosity in *Chandra* observations. The scatter plot is color coded according to the sources. The grey dotted line corresponds to zero velocity and the brown line to the mean of the curated Kα blueshift distribution, whose standard deviation is visualized by the brown region. The biased Fe xxv Kα blueshifts measured in the obscured GRS 1915+105 observations, which are excluded from this distribution, are marked in dashes.

Chandra-HETG instrument, so we only consider the *Chandra* blueshifts in the rest of the paper.

The observed *Chandra* velocity shift distribution is within the expectations from a sample of intrinsically zero-velocity absorption lines with an average value of $\mu \sim 60 \pm 100$ km s^{-1} and a standard deviation of $\sigma \sim 630$ km s^{-1}. However, few observations have significant velocity beyond 2 σ of the mean of this distribution. We report in Fig. 3.4 the scatter plots of the *Chandra* velocity shifts of the Fe xxv Kα (left panel) and Fe xxvi Kα (right panel) lines against the 3-10 keV luminosity in Eddington units, which highlights that the three faintest GRS 1915+105 exposures are the only ones to show significant Fe xxv Kα positive shifts (i.e., redshifts). However, the Fe xxv Kα absorption line profiles observed in these three cases exhibit unusually asymmetric and broad absorption features, while the Fe xxvi Kα lines energies are consistent with zero velocity. After confirming that these line features can be fit with more complex ionization structures that do not require redshifts (see 3.5.1), we excluded these three observations from the velocity shift distribution, changing the distribution average to $\mu \sim -200 \pm 60$ km s^{-1} and reducing the standard deviation to $\sigma \sim 360$ km s^{-1}, as highlighted in Fig. 3.4.

With this restriction, the only remaining outlier (more than 2σ away from the restricted mean) is found in the blueshifted Fe xxvi Kα line of the exceptional absorption signatures of GRO J1655-40's 2005 outburst (Miller et al. 2006a) and is in agreement with the extreme absorption features displayed in this observation (see Miller et al. 2008 for a detailed study). We note that one exposure of 4U 1630-47 (obsid 13716) remains at the tail end of the Fe xxv Kα velocity shift distribution, with a redshift of 500 km/s. This blueshift measurement is distinct from zero at more than 3σ as well as from the corresponding Fe xxvi Kα line (itself with a blueshift of $\sim$ 300 km/s). This result can once again be explained by contamination from a lower ionization component, in line with more in depth analysis, such as the work of Trueba et al. (2019), who modeled the outflow with two photoionization components. In this observation, both components show a significant decrease in the ionization parameter compared to rest of the coverage of the outburst while maintaining low, negative velocity shifts, in accordance with our results for the other exposures.

The mean value of -200 ± 60 km s^{-1} is very low compared to the standard *Chandra*-HETG absolute wavelength uncertainty of $\pm$ 0.006 Å[25], which translates to $\sim \pm 1000$ km s^{-1} at the Fe xxvi Kα energy (~ 300 km s^{-1} at 2 keV). However, empirical studies have shown that the "effective" absolute wavelength accuracy of HETG is significantly better and reaches ~ 25 km s^{-1} at energies below $\sim$2 keV (Bozzo et al. 2023; Ishibashi et al. 2006). This has been corroborated by other works making use of very precise spectral features (Ponti et al. 2018). The few existing BH wind studies that consider the effective HETG accuracy also estimate it to be up to 50-100 km s^{-1}, depending on the line considered (see Miller et al. 2020; Muñoz-Darias & Ponti 2022). Thus, our sample is likely to exhibit a significant global blueshift, in agreement with the common association of these absorption lines to outflowing winds, although the average velocity is very low.

It is also possible to measure the widths of the of Fe xxv Kα and Fe xxvi Kα lines in the *Chandra* observations with the highest S/N. The distribution of the full width at half maximum (FWHM) of the 21 lines with significant width measurements is reported in the lower-left panel of Fig. 3.3. While all significant line width measurements are in the 1500-5000 km s^{-1} range, the highest values, found in the three GRS 1915+105 exposures with contamination from other line complexes discussed above, are probably overestimated.

Significant correlations

The first significant correlation we found in our results is between the width and EW of the Fe xxv Kα line ($p \leq 0.0002$), which we show in Fig. 3.5 and contrast with the absence of correlation in the case of Fe xxvi Kα. Such a correlation may naturally arise because larger turbulence velocities delay the saturation at the line center, allowing the EW to grow to larger values (see e.g., the curve of growths presented in Bianchi et al. 2005). Moreover, the saturation itself at high column densities contributes to broadening the absorption lines. To test these effects, following the methodology detailed in Bianchi et al. (2005), we computed the curve of growths for Fe xxv Kα and Fe xxvi Kα lines as a function of the corresponding ionic column densities N_i and different turbulence velocities. Moreover, we estimated the FWHM of each computed profile relative to the given N_i (and therefore EW) and velocity. These computations allowed us to derive the theoretical curves superimposed on the data plotted in Fig. 3.5.

All measurements of the Fe xxv Kα and Fe xxvi Kα lines are compatible with the expectations because the lines appear in the allowed portion of the parameter space. Indeed, the lower-right corner of the plots in Fig. 3.5 are expected to be unpopulated since the EW saturates at large N_i and cannot grow further while the line width continues to rapidly increase. On the other hand, we would also expect observations to populate the upper-left corner, but there is likely a strong observational bias against broad lines with low EW. We find it is interesting to note that lower ionic column densities are needed for the majority of observed Fe xxv Kα lines with respect to Fe xxvi Kα, suggesting an average high ionization parameter, in accordance with the typical large Fe xxvi Kα/Fe xxv Kα EW ratio noted before in our sample. The few detections with the highest Fe xxv Kα EWs require higher Fexxv ionic column densities and thus a lower ξ_i, in accordance with their lower Fe xxvi Kα/Fe xxv Kα EW ratios.

We also observed a significant anti-correlation between the Fe xxv Kα EW versus the X-ray luminosity, as shown in the left panel of Fig. 3.6. We find it is worth noting that the p-value remains below 10^{-5} even without including the uncertain luminosity measurement of IGR J17451-3022. This anti-correlation may naturally arise if we take the luminosity as a proxy for the ionization parameter (i.e., assuming a universal nr^2 factor for the whole sample), and this is indeed what is expected if the average ionization parameter is just above the peak of the ionic fraction for Fexxv (e.g., Bianchi et al. 2005).

In comparison, no such correlation was observed for the Fe xxvi Kα line (see right panel of Fig. 3.6), as expected since its ionic fraction would instead be at its peak for the same ionization parameter. An equivalent way to show these different behaviors is via the significant correlation between the X-ray luminosity and the Fe xxvi Kα/Fe xxv Kα EW ratio for all the observations where both lines are detected (see Fig. 3.7). This ratio is expected to be a monotonic function of the ionization parameter (e.g., Bianchi et al. 2005) and should thus correlate with luminosity.

[25] See https://cxc.harvard.edu/proposer/POG/html/chap8.html.

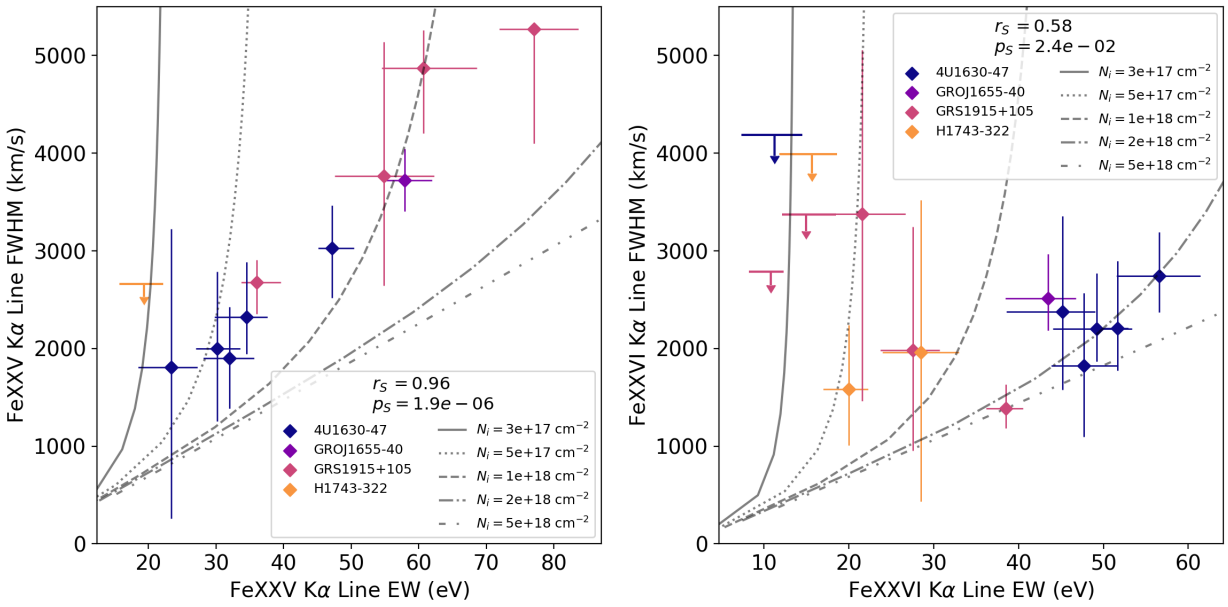

Figure 3.5: Scatter plots of the EW and width for the Fe xxv Kα (left) and Fe xxvi Kα (right) lines in *Chandra* observations. The curves highlight the theoretical evolution of these parameters for a range of ionic column densities of the respective ions.

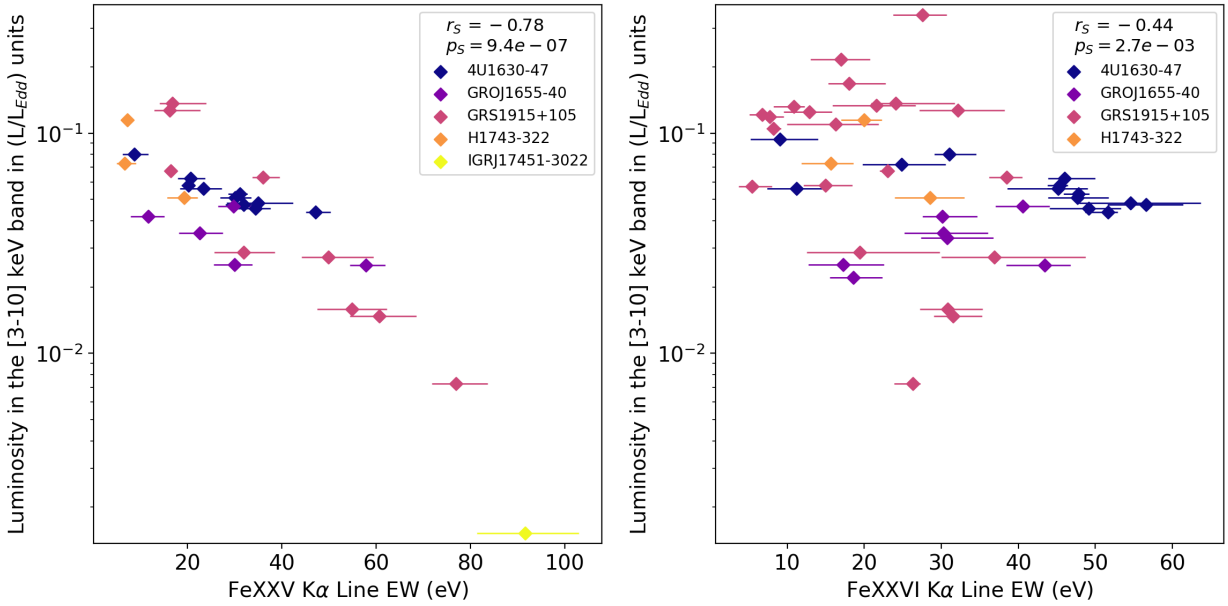

Figure 3.6: Scatter plot of the Fe xxv Kα (left) and Fe xxvi Kα (right) EW against luminosity for the entire sample. The scatter plot is color coded according to the sources.

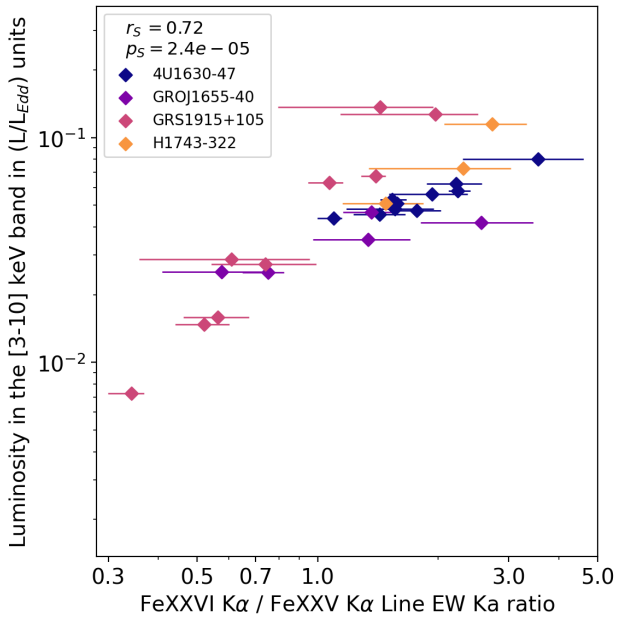

Figure 3.7: Scatter plot of the Fe xxvi Kα/Fe xxv Kα EW ratio against luminosity for the entire sample.

3.4.2 Favorable conditions for absorption line detection

Our HLDs in Fig. 3.2 show that absorption lines of He-like and H-like iron are mainly observed in luminous soft states of highly inclined sources. Indeed, we may further propose quantitative thresholds to define a "favorable" region for this type of wind detection based on the Hardness Ratio, inclination, and luminosity.

Our first observation is that all absorption line detections in our sample occur below an HR (computed using unabsorbed flux) of $HR_{[6-10]\,keV/[3-6]\,keV} = 0.8$. This cut nevertheless remains arbitrary[26]. because it depends on the black body temperature, which is affected by the mass and spin of the objects and, as such, is expected to differ for each source. This cut also does not restrict to pure soft states, as this threshold also includes observations in soft-intermediate and hard-intermediate states. The two most notable exceptions are the two hardest detections in our sample, and they are both exposures of the peculiar GRS 1915+105. One is in a bright, hard jet-emitting state Klein-Wolt et al. (2002), which is referred to as the χ state in Lee et al. 2002, whose wind signatures are normally undetected, although most χ state observations have a much higher HR (see Neilsen & Lee 2009). The other exposure occurred during a recent transition to a new obscured state in which the source has spent the majority of the past few years (Miller et al. 2020). In this second observation, the observed HR is not an intrinsic property of the SED but mostly an effect of absorption. A less conservative limit on the "soft" wind emitting states could be close to $HR_{[6-10]/[3-10]} = 0.7$ when these two observations are excluded. We note that the absorption line detections in sources other than GRS 1915+105 are generally softer ($HR_{[6-10]/[3-10]} < 0.5$), although this might simply be the result of a lack of both softer GRS 1915+105 exposures and harder (but still below the previously defined threshold) observations for other sources, at least with *Chandra* and XMM-*Newton*.

Focusing on the inclination, we note that the five objects with detections of absorption lines, 4U 1630-47, GRO J1655-40, GRS 1915+105, H 17432-322, and IGR J17451-3022, are all dippers (see Tab. 3.1), among which two, GRO J1655-40 and IGR J17451-3022, are eclipsing binaries (Bailyn et al. 1995; Bozzo et al. 2016). Dipping behavior is traditionally associated with high-inclination systems (Motta et al. 2015), and all independent inclination estimates for these five objects agree with values larger than 55 degrees. While estimates are too uncertain to propose this as a precise threshold, it suggests that the detection of X-ray wind signatures is restricted to the inclination range of dippers.

[26] however, because this HR is computed from counts, and not from luminosity, it remains instrument-independent

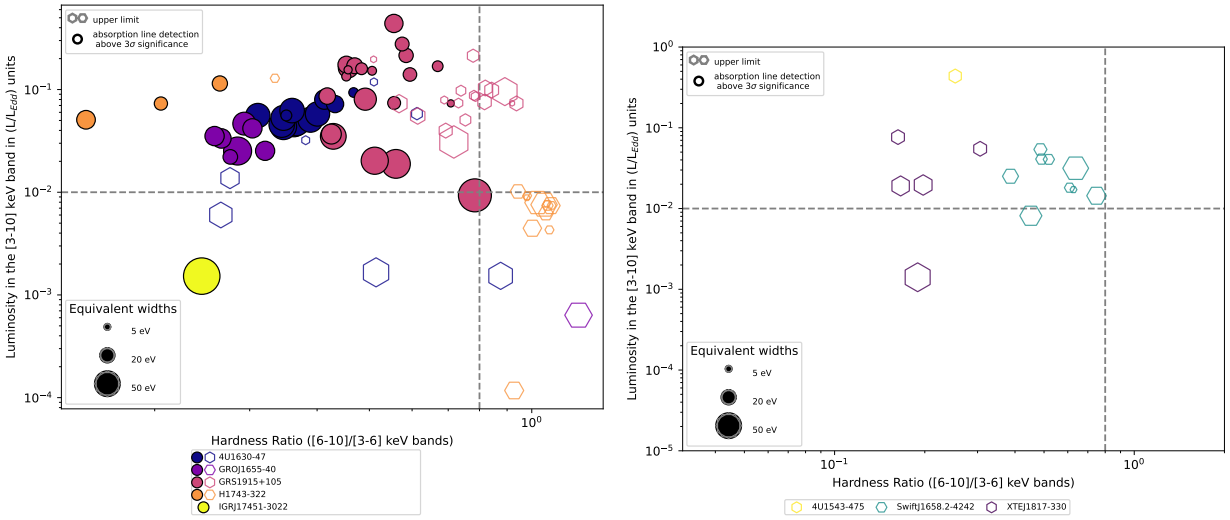

Figure 3.8: Hardness Luminosity Diagrams of subsamples with relevant non-detections. Left panel: Zoom on sources with detection and Fe xxvi Kα upper limits when no line was detected. Right panel: Sources with constraining upper limits in the favorable zone (discussed in Sect. 3.4.3).

Notably, none of the few non-dipping sources with inclination measurements below 55° show absorption lines (see right panel of Fig. 3.2). However, the coverage of the soft state is very limited in these objects, and few sources have stringent upper limits. More importantly, none of the remaining objects has a precise dynamical inclination measurement that does not conflict with reflection estimates. Thus, while dipping sources are definitely more prone to detection, better coverage of low-inclined sources (and consensus on inclination estimates) would be preferred in order to conclude whether they are truly exempt from detection.

Finally, there are only two detections below $L_X \sim 0.01 L_{Edd}$. One is from IGR J17451, whose true Eddington ratio is highly uncertain, as both its mass and distance are unknown, and the second is found in the faintest observation of GRS 1915+105, whose luminosity is probably underestimated, as it is in a semi-obscured state (Miller et al. 2020). This lack of detections below a certain luminosity threshold thus points to a certain Eddington ratio as a requirement to produce highly ionized iron absorption lines. However, our coverage of lower luminosity soft states is very limited, both in terms of number of sources and sampling. This, combined with the intrinsically worse S/N (and thus a lack of constraining upper limits), prevents any interpretation regarding the launching mechanism. We recall that the visibility of both thermal and magnetic wind is expected to decrease for lower luminosities, although more sharply for the former (reaching L_{crit}), while the density of the later is expected to scale with $\dot{m}$.

3.4.3 Non-detections in favorable conditions

The presence of non-detections and stringent EW upper limits (< 5 eV) in the wind-favorable region shown in the left panel of Fig. 3.9 indicate that luminous soft states of high-inclined sources do not necessarily show absorption lines. Among the sources with detections, 4U 1630-47, GRS 1915+105, and H 17432-322 have luminous soft state exposures without absorption lines, as can be seen in more detail in the left panel of Fig. 3.8.

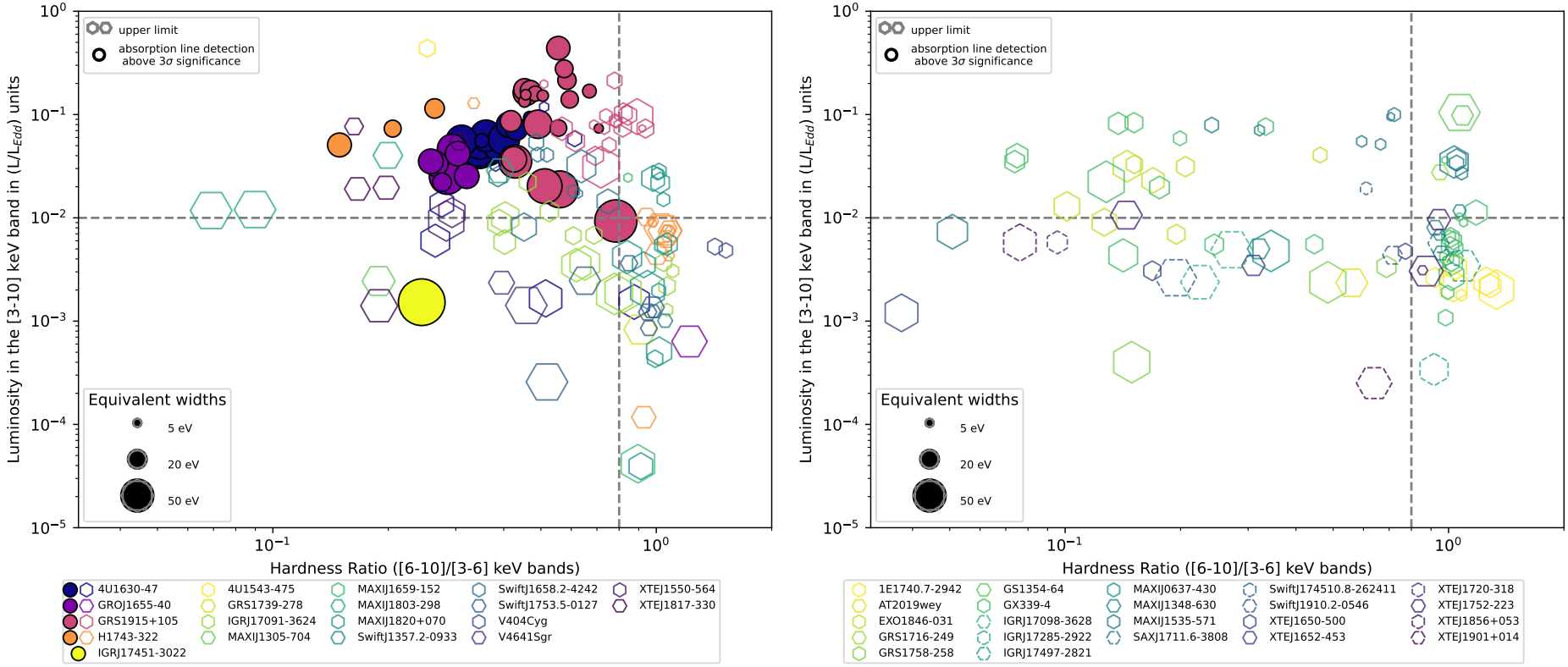

Figure 3.9: Hardness Luminosity Diagram with the position of all detections in the sample and 3σ Fe xxvi Kα upper limits when no line was detected. The diagram uses the same inclination split as in Fig.3.2. The vertical and horizontal lines highlight the luminosity and HR thresholds proposed in Sect. 3.4.2. Sources with no inclination measurements in the right panel are shown with dashed markers.

*

The source with the greatest number of observations, GRS 1915+105, does not follow the standard state evolution and instead evolves erratically in a limited part of the HLD. Most of the lower EW upper limits obtained for this source concern observations with larger HR and luminosity than observations with detection, but there is at least one observation, with HR ~ 0.5, with a very stringent absorption line EW upper limit. This limit, being even lower than the absorption line EWs observed in all neighboring detections, suggests different physical conditions for the wind between these observations, despite a similar SED. This behavior also reflects in the well known rapid variability of the lines themselves in this object (see e.g., Lee et al. (2002); Neilsen et al. (2011, 2020)).

In the case of 4U 1630-47, there are at least three observations, ObsIDs 14441, 0670673201, and 15511, with stringent upper limits of 14, 7, and 8 eV, respectively (see Table 7.1.1 for details). Only observation 14441 is harder than the cluster of exposures with detections in this source. We note the detection of a single, marginally significant (98.8% significance in the F-test) unidentified absorption feature at 7.8 keV in the third observation. Finally, H 17432-322 shows a single, very significant EW upper limit of 9 eV in ObsID 3804, which is relatively harder spectrally but remains both very soft and close (both in time and spectral distribution) to the three other detections in its 2004 outburst.

We also note that while GRO J1655-40 shows absorption lines in both of its soft state observations, the number of lines, parameters, and EWs are far more different than what could be explained by evolution in SED alone. This indicates extreme changes in the wind structure and possibly two distinct mechanisms (Neilsen & Homan 2012).

However, it is also important to assess whether non-detection in other dipper and high-inclined sources in the favorable zone are sufficiently significant. To aid readability, we highlight the three sources with no detection despite stringent upper limits in this zone, 4U 1543-47, Swift J1658-4242, and XTE J1817-330, in the right panel of Fig. 3.8. For 4U 1543-47, it is possible that the lack of lines is due to over-ionization stemming from the extreme luminosity of this source, which is the brightest observed in our sample at $L_X/L_{Edd} \sim 0.45$. We note that the bolometric luminosity of this source is expected to have surpassed the Eddington limit at the peak of its outburst, as seen by *NICER* and *NuSTAR* (Prabhakar et al. 2023). Another explanation could be that the peculiar dips detected in the source (Park et al. 2004) are not a consequence of high inclination. This would reconcile the geometry with the very low angle inferred from dynamical measurements (Orosz 2003; Orosz et al. 1998) and the optical features reminiscent of low inclination recently detected in this source (Sánchez-Sierras et al. 2023a). This would explain the lack of absorption lines.

The same could be said for XTE J1817-330, which has a few stringent absorption line EW upper limits but no inclination constraints and lacks an actual mass estimate. We find it is worth noting that this source was even reported as being low inclined in previous works (Ponti et al. 2012), but it lacks proper inclination measurements, and comparisons of its outburst evolution identify it with sources with mid- to high-inclination measurements (Muñoz-Darias et al. 2013), in agreement with reports of erratic dips (Sriram et al. 2012). Finally, Swift J1658-4242, the only source with clear dipping behavior and no contradictory inclination measurement, shows a range of exposures with stringent upper limits at HLD positions very close to detections in other sources. However, the lack of constraints on both its mass and distance prevents any definitive conclusion. Moreover, all constraining exposures are XMM-*Newton* observations with strong relativistic emission in the iron band, which are very complex to disentangle from possible absorption features and could completely hide a weak wind signature due to the limited spectral resolution of XMM-*Newton*.

3.5 Highlights on sources of interest

The 5 sources with absorption lines detected in our sample have already been extensively covered in the literature, including for most archival observations analyzed in this work. In the following subsections, we detail the history of wind detections and modeling efforts for each of them, except 4U 1630-47, which will be the subject of Sec. 4. Whenever relevant, we complete these overviews with some new results obtained with our sample and methodology.

3.5.1 GRS 1915+105

Initially discovered as a transient in 1992 (Castro-Tirado et al. 1992), GRS 1915+105 has remained in activity for more than 30 years, and is now considered a persistent source. Powerful, variable X-ray (Belloni et al. 1997) and radio (Fender et al. 1999a) emission, along with a K star as companion (Greiner et al. 2001), rapidly hinted at a BHLMXB candidate, and this was later confirmed with dynamical measurements (Reid et al. 2014), along with a mass, distance and inclination estimates. The last updates on these 3 parameters, reported in (Reid & Miller-Jones 2023), stand at $M_{BH} = 11.2^{+2}_{-1.8}\ M_{\odot}$, $d = 9.4^{+2.0}_{-1.6}$ kpc and $i = 64 \pm 4°$.

However, the source's behavior is completely at odds with other known BHLMXBs. Its persistent emission behaves according to a great number of very complex patterns, with at least 15 distinct spectral-variability patterns (Belloni et al. 2000; Hannikainen et al. 2005; Shi et al. 2023) that are still poorly understood. Among those, two have notably low variability, the soft ϕ and the hard χ, with the latter being the closest to the canonical "low-hard" state, while the wealth of other patterns are characterized by higher variability and, for some of them, very distinctive cycle patterns (i.e. the "heatbeat" ρ state). In spite of this complexity, the erratic behavior and multitude of remarkable features of GRS 1915+105 make it a prime candidate for studying accretion physics and the interplay between the disk, jets and winds. Recently, in 2018, the source has transitioned to a much fainter state (Negoro et al. 2018), interpreted as a combination of a dramatically increasing but very variable obscuration, often surpassing the Compton thick threshold, and a lower accretion rate (Balakrishnan et al. 2021; Miller et al. 2020). As of 2024, the source has settled in this state and only exhibits occasional flares (Homan et al. 2019) and re-brightening episodes (Athulya & Nandi 2023).

The extensive amount of X-ray observations of this source has led to a multitude of wind detections, and thus we follow the rich evolution of GRS1915+105's outflows in the paragraph below. After the initial detection of absorption lines in the source with ASCA observations from the late 1990s (Kotani et al. 2000), the first precise identification of the absorbers stemmed from a 2000 *Chandra*-HETG exposure in the hard χ class (Lee et al. 2002), with strong variability of the outflow's ionisation parameter in timescales of 10ks. Later, in 2004, wind signatures were claimed in two other observations in that same class (Martocchia et al. 2006). However, the combination of unexplained residuals in the lower energy bands of the spectra and strong mixing with reflection components and broad emission lines forbid definitive conclusion on these spectra. As time progressed, an increasing amount of observation in softer states highlighted the usefulness of phase/flux resolved spectroscopy to assert the behavior of the wind, even in the least variable soft state (ϕ class; Ueda et al. 2009).

Finally, in 2009, Neilsen & Lee (2009) compared the radio and X-ray signatures of all available *Chandra*-HETG data of the source (in $\phi, \gamma, \rho, \beta$ and χ states) and observed a strong anti-correlation between jets and wind signatures, with the 2000 exposure studied in Lee et al. (2002) as a notable exception. Shortly after, the study of a 2005 *Suzaku* observation during a class transition Ueda et al. (2010) showed that indeed, wind signatures were indeed appearing when switching from a hard χ to a soft θ class, supporting the previous claims. In 2011, Neilsen et al. (2011) performed for the first time a detailed, phase-resolved study of an 2001 HETG observation in the ρ class (in which the source exhibits so-called "heartbeats"), which showed that both the outflow structure and the hard x-rays (potentially the jet) varied jointly on very short timescales. Further studies of other variability classes, like β and γ, exhibited similar behaviors of interplay between the wind, the jet, and the ionizing continuum Neilsen et al. (2012), and highlighted the issue of spectra with longer integration times, where averaging of the strong wind variability led to an apparent reduction of the depth of the lines.

Few years later, joint *Chandra-NuSTAR* observations of a 2015 ρ state showed a significant change in the outflow parameters and their evolution with the heartbeat phase (Zoghbi et al. 2016), compared to what was observed in 2001. In parallel, a more detailed analysis of a soft 2007 observation, using third order HETG spectra, allowed for a very precise estimate of 4 different outflow zones, one of which with very high ionization parameter ($\log \xi_i$ / erg cm s^{-1} = 4.7) and blueshift ($v_{out} \sim 9000$ km/s) (Miller

et al. 2016). More recently, the source has been observed with the newer generation of instruments, such as the recent study of HMXT exposures in 2017, which, for the first time in the κ state, showed the interplay between the X-ray irradiation and the wind over multiple timescales (Liu et al. 2022). Meanwhile, extensive *NICER* monitoring in 2018 showed persistent wind signatures, mainly but not exclusively only in the λ state, which oscillates between brighter and fainter, softer periods (Neilsen et al. 2018a). In these observations, the EW of the absorption lines is once again anti-correlated with the hardness of the continuum.

The last *Chandra*-HETG observation before the source became Compton-thick, in 2019, revealed strong absorption signatures in a semi-obscured state, which maintains high degree of periodic variability (Miller et al. 2020). A phase-resolved analysis highlighted a range of outflow velocities, none of which reaching the escape velocity, prompting Miller et al. to argue that this dense, "failed" wind was at the origin of the obscured state of the source. Afterwards, a *Chandra* observation during the Compton-thick state showed very strong emission lines, significantly stronger than the fully absorbed continuum, and, expectedly, no absorption lines. However, a re-flaring period in 2019, in which a hard continuum reappeared, revealed extremely deep absorption features in the iron band, which were studied by HMXT (Kong et al. 2021), and *NICER* few months later (Neilsen et al. 2020). Here, beyond the highly variable and complex continuum, the lack of energy resolution forbids any definitive conclusion on the 'failed' nature of the wind. Meanwhile, although the *NICER* observations were not accompanied by simultaneous radio observations, the apparition of the wind during the higher and softer periods was suspected to the disappearance of the jet observed just after the X-ray observation (Koljonen et al. 2019).

More recent work on several re-brightening episodes between 2019 and 2021 (Athulya & Nandi 2023) showed very important wind variability during partially obscured variants of several variability classes, as well as new wind detections during the soft δ class, and the first clear report of a wind detection in a radio-quiet χ class (see Sanchez-Sierras et al. 2023b for an evolution of the radio flux of the source in this period). During this 2021 period, strong correlations have also been reported between the appearance of LFQPOs and absorption line detections (Kong et al. 2024). A new exhaustive analysis of *NuSTAR* spectra of the source (Draghis et al. 2024) also reported many detections of absorption lines, including in several *NuSTAR* χ spectra, although both overlapping with reflection, and with potentially over-simplistic modeling considering the atypical behavior of the source. Finally, a recent near-infrared study has found distinctive wind signatures in radio-loud states only (Sanchez-Sierras et al. 2023b).

In spite of the many recent studies, very few of the publications of this last decade actually focus on the evolution of the wind in the source (be it from an observation or modeling point of view), even with the new opportunities for modeling offered by recent multi-instrument observations, and our lack of understanding of the outflow evolution in most variability states. Most notably, the under-studied χ state, with its enigmatic wind-jet detection, remains very far from the classical "low-hard" states of BHXRBs (Van Oers et al. 2010), and can be further split into 4 sub-states (Belloni et al. 2000), with different spectral-timing properties (Pahari et al. 2013b; Van Oers et al. 2010), only two of which (nicknamed "plateau" states) are radio-loud. Fortunately, there are now sufficient amounts of high quality, broad band χ state observations, with and without wind signatures, to understand the evolution of the wind in this state. In parallel, the overwhelming majority of the 1.6 Ms of *NICER* coverage remains unpublished, with about 2 years of coverage, and several hundreds of high quality wind detections. This abundant X-ray wind coverage would also be very useful to correlate with the recent IR wind detections.

The most striking characteristics of the winds in GRS1915+105 are extrapolations of small launching radii, and a tendency to reach high outflow velocities, not to mention exceptional variability. As these are completely at odds with expected characteristics of thermal-radiative winds (although purely radiation driven wind could be possible if the source reaches S-E luminosities), the work done on modeling the wind signatures with physical components has been mostly restricted to MHD models, and the first attempts are very recent, probably due to the sheer complexity of the task at hand. Ratheesh et al. (2021) compared the results of MHD solutions similar to the work performed in Fukumura et al. (2017) for

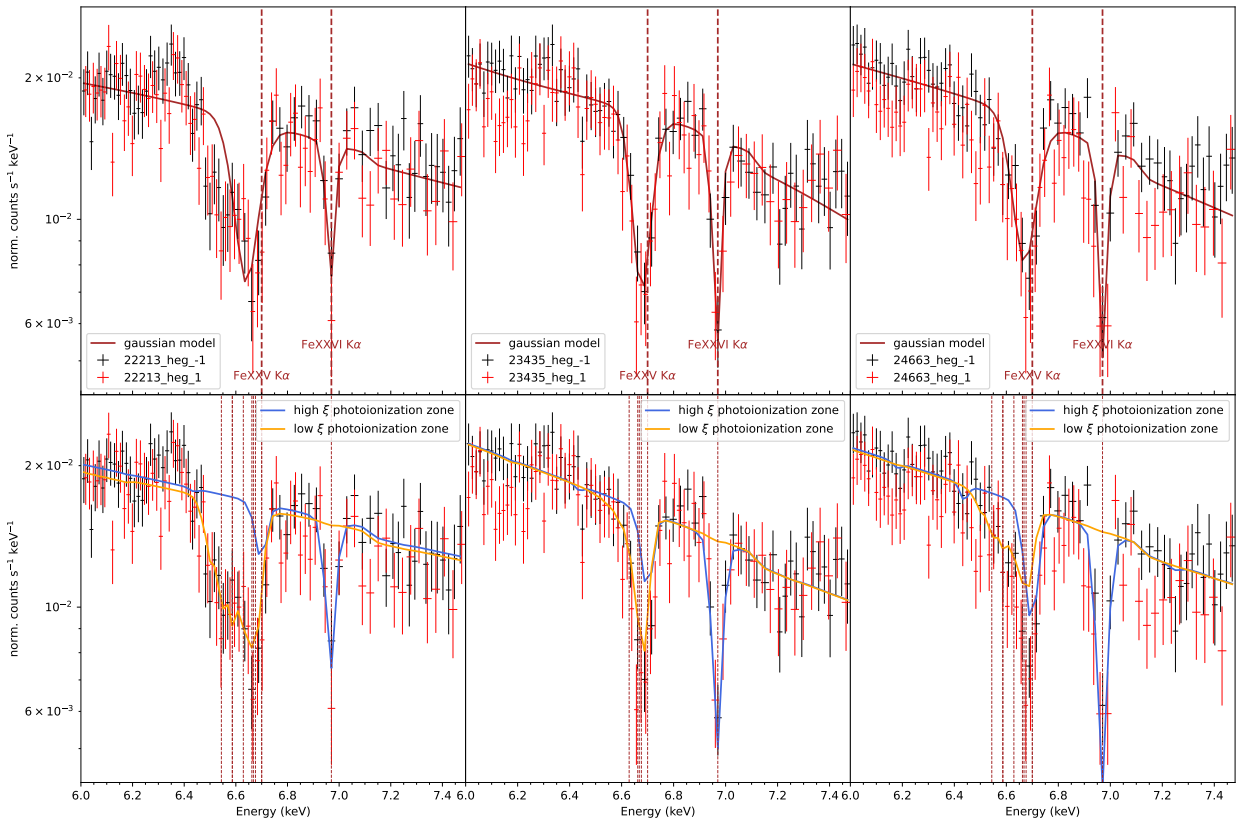

Figure 3.10: Zoom of the fit around the Kα lines for the three low-luminosity observations of GRS 195+105. The upper panels show the results of the autofit procedure with Gaussians, and the lower panels show the results of a fit with two photoionization zones; the lower ξ_i was fixed at zero velocity. The dashed lines show the energy of the main lines produced by the photoionization zones of each observation.

GROJ1655-40, selecting an observation with wind (in the soft ϕ class) and without wind (in the hard χ class). Finally, it is worth noting that, while the very high blueshifted outflows detected by Miller et al. (2016) would be almost impossible to create with thermal winds, Tomaru et al. (2023) recently argued that for a similar analysis on other sources (Miller et al. 2015), their interpretation of a marginal, high-speed outflow component could also be explained by a much more standard Cr xxiv Kβ feature, whose contribution is expected for thermal-radiative winds.

We note that these modeling efforts still have to properly consider the broad band continuum of the source, who is now accessible thanks to several *NuSTAR* observations, and is paramount for both ionization and stability considerations.

In subsection 3.4.1, we excluded 3 observations with asymmetric absorption features from the Fe xxv Kα velocity shift distribution. We show the automatic Gaussian fits of these 3 obsids in the upper panels of Fig. 3.10. They were taken during a pre-obscured state in 2019 (Obsid 22213) and a rebrightening state in 2021 (Obsids 23435,24663). According to the detailed analysis of the first observation of Miller et al. (2020), this apparent redshift might be caused by contributions from lines at lower energies blended with Fe xxv Kα. We verified this in the other observations with a simple fit with two photoionized slabs,[27] which we show in the lower panels of Fig. 3.10. We found that the highest ionization component ($\log(\xi_i) \sim 5-6$) models the Fe xxvi Kα and part of the Fe xxv Kα lines that show a blueshift ~ -250 km s^{-1}, while a lower ionization phase ($\log(\xi_i) \sim 2.5-3$) at zero velocity produces some of the Fe xxv Kα line but includes also strong absorption lines from Fe XXI to Fe XXIV, which reproduce the observed "redshifted" tail of the line profiles. However, these observations remain time-averaged, and the absorbers do show

[27] We used the same CLOUDY absorption tabular model described in **?**.

much more nuances when studied with time-resolved spectroscopy.

These recent observations are much more revealing when put in context with the complementary (and much more detailed) *NICER-NuSTAR-AstroSat* coverage of (Athulya & Nandi 2023). The two 2021 observations were taken close to the peak of the last 2021 rebrightening event (RBVi in that paper), in which the source was almost unobscured. However, other observations of RBVi show a progressive increase of this low-ξ_i phase, first similar to the 2019 *Chandra* observation (Fig. 3.10, left panel), then back to obscuration. This seems to indicate that the rebrightening events follow a similar pattern to what was seen in Miller et al. (2020) for the first obscuration, interpreted as a colder, "failed" wind progressively re-obscuring the source.

3.5.2 GRO J1655-40

Soon after its discovery as a transient X-ray source in 1994 (Zhang et al. 1994), the discovery of jets (Hjellming & Rupen 1995) and dynamical measurements of a low-mass star orbiting a compact object of mass 6−7 $M_\odot$(Van Der Hooft et al. 1998) catapulted GROJ1655-40 to the top of the list of BHLMXBs. In the following years, increasingly detailed studies led to inclination and mass measurements of $i = 69 \pm 2°$and $M_{BH} = 5.3 \pm 0.4\ M_\odot$(Beer & Podsiadlowski 2002) (although see Stuchlík & Kološ (2016) for a discussion on this value). The commonly accepted distance value is 3.2 ± 0.2 kpc from Hjellming & Rupen (1995).

Despite exhibiting a limited amount of outbursts since its discovery, the source hosts the richest wind features ever displayed in LMXBs. Indeed, even if the first wind detections trace back to the 1995 outburst (Ueda et al. 1998), GRO J1655-40 is widely known for the HETG exposures of the 2005 outburst, one of which revealed an extremely diverse outflow with 90 distinct absorption lines (Miller et al. 2006a). Two sets of XMM-*Newton* Observations during the same outburst also revealed abundant (although not as much as HETG) wind features (Díaz Trigo et al. 2007; Sala et al. 2007a), with RGS data allowing precise estimates of low (but significant) blueshift values in the outflow. This outburst had other notable properties, such as strong similarities to the so-called hypersoft state of the HMXB Cyg- X-3 (Uttley & Klein-Wolt 2015). The HETG wind signatures were analysed in detail by Kallman et al. (2009), which showed that the features required a broad range of ionization parameters, high abundances matching supernova enrichment, and column densities in excess of the Compton thick limit.

Later, Neilsen & Homan (2012) analyzed the evolution of the features between the HETG observations of the 2005 outburst, and demonstrated that the behavior of the absorber(s) was impossible to explain with changes in the ionizing spectrum alone. They proposed an evolving bi-component outflow -potentially hybrid between MHD and thermal- as an explanation for the sharp transition in absorption features observed between the two exposures, and would later argue in favor of a Compton-thick wind obscuring a Super-Eddington disk (Neilsen et al. 2016). Finally, more recent work, using high-quality *Swift* data taken during the 2005 outburst, allowed Balakrishnan et al. (2020) to probe in more detail the long-term variability of the outflow, with results compatible with MHD driving mechanisms. However, the absorption features they found were present during more than 70 days, which would require an unlikely scenario in which the source would sustain its Super-Eddington obscured state for extended periods of time.

The unique absorption features displayed in the source's 2005 outburst have been tested for a wide variety of outflow models. A preliminary analysis Miller et al. (2006a) attributed the wind to MHD launching due to its extreme characteristics, and notably a very high density implying a low launching radius. First claims of a possible thermal launch mechanism (Netzer 2006) have been heavily criticized (Miller et al. 2008), even more so when proper thermal wind modeling failed to reproduce the observations, corroborating the assumption of MHD winds (Luketic et al. 2010). Few years later, the first attempts at reproducing these extreme absorption features with magnetic processes (Fukumura et al. 2017) showed that a single component self-similar MHD wind solution resulting from the merge of different launching radii could recreate in part the absorption features of the extreme 2005 spectra. In the same manner, new solutions of thermal-radiative wind models were found to be able to quantitatively

reproduce GROJ1655-40's absorption features, both through analytical work (Done et al. 2018) and simulations (Higginbottom et al. 2018). Subsequent refinements of this launch mechanism have since then been quite effective at replicating even very minute absorption features in GROJ1655-40's spectrum (Tomaru et al. 2023), some of which may not be reproducible with current MHD wind models. However, the density values necessary to this recent derivation are still debated, with the latest developments in the matter (Keshet et al. 2024) retaining the high values initially associated to magnetic winds. Nevertheless, the position of the extremely dense absorber obscuring the source relative to that of the absorbing material remains mostly uncertain, leaving an additional degree of freedom which has yet to be solved.

Meanwhile, newer magnetic wind solutions are now able to reproduce the transition between "on" and "off"/weak absorption states of the source (Fukumura et al. 2021), without invoking a thermal component. In this framework, a strong evolution in the wind density is necessary to explain to difference between the Compton-thick wind and the observation with weaker lines beforehand, but the ejection parameter remains unchanged.

While our analysis is simpler than many of the other works published on this source, we get the benefit of directly comparing the *Chandra* and XMM-*Newton* observations, if only through their continuum and line parameters, which has not been done before. We plot the evolution of the source during its outburst, and of the Fe xxvi Kα and Fe xxv Kα line EWs, in the different panels of Fig. 3.11. At first order, the first XMM-*Newton* observations match the wind properties of the first *Chandra* observation, with compatible EW ratios, and increasing individual line EWs, in line with the progressive softening of the SEDs during the state transition. On the other hand, the EW ratio of the last XMM-*Newton* observation (27-03-2005) is much closer to the second *Chandra* observation in the hypersoft state, despite lower EWs. From a spectral-timing perspective in X-rays (Uttley & Klein-Wolt 2015) or when looking at the OIR flux evolution (Neilsen et al. 2016), this observation matches the very end of the transition to the hypersoft state, and can thus be used to test the different physical scenarios proposed. In addition, a more global study of the evolution of the wind properties could be used to to test different assumptions on which parameter in the wind was evolving, as done for the two *Chandra* observations in Neilsen & Homan (2012).

Combining our results with the literature, and notably the *Swift* coverage detailed in Balakrishnan et al. (2020) and the hypersoft state delimitations, we draw attention to missing elements, and propose new ways to gain insight on the behavior of the source:

1. The first *Chandra* exposure, the 4 XMM-*Newton* exposures in 03-2005, and the *Swift* exposures in this period are taken during a state transition from a hard/SPL state to the hypersoft state, as can be seen through the much decreasing but still significant BAT count rate in these periods in Fig. 3.11. So far, only Neilsen & Homan (2012) have considered the change in the broad band spectral properties in their modeling computations, and only between the two *Chandra* spectra. Applying photo-ionization models while considering the broadband SED evolution is required to know whether the wind was evolving at the beginning of the outburst, and if so, how it connects to the evolution seen during the hypersoft state (Balakrishnan et al. 2020).

2. The last 6 *Swift* exposures were all taken after the hypersoft state, in a much harder and highly variable flaring state (see middle panel of Fig. 3.11). Balakrishnan et al. (2020) noted significant wind evolution compared to the hypersoft state, but their photo-ionization modeling was based on the SED of the previous *Chandra* observation, which is completely different at high energies. The proper SEDs need to be considered to ensure the wind has changed during this flaring state. Moreover, with such high hard contribution, stability effects need to be studied to assess whether the absorbers seen in the hypersoft state remain stable (and thus visible) during the hard flare.

3. Several previously unnoticed elements support the idea that the outflow is strongly tied to the evolution of the hypersoft state. First, few *Swift* observation preceding the XMM-*Newton*

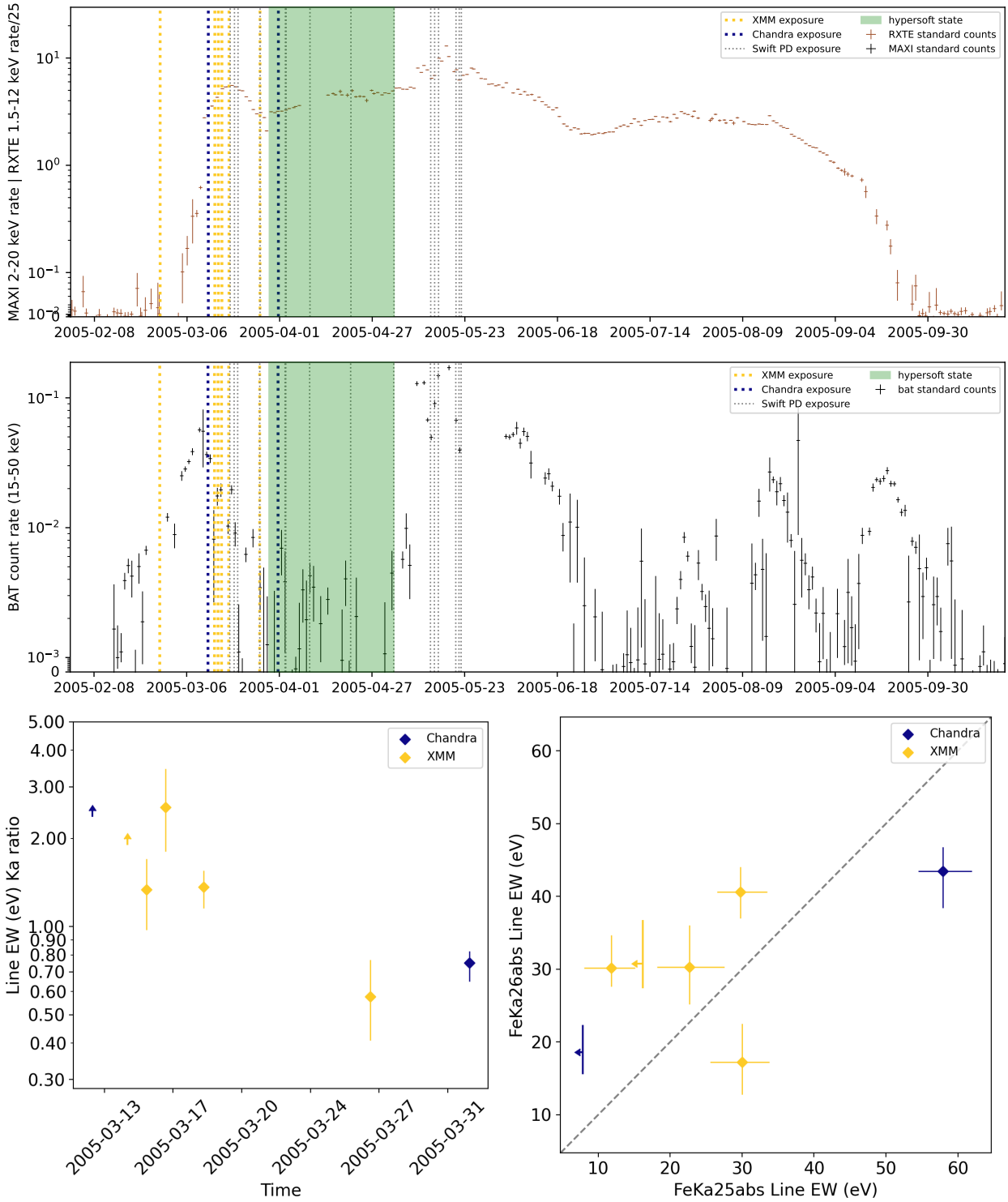

Figure 3.11:
Upper/Middle panels: Daily *RXTE*/BAT monitoring lightcurves of the 2005 outburst of GRO J1655-40, with exposures used for line detections highlighted by dashed vertical lines. The grey lines highlight the exposures used in Balakrishnan et al. (2020), and the green zone the long-lasting portion of the hypersoft state according to Uttley & Klein-Wolt (2015).
Bottom panels: In the XMM-*Newton* and *Chandra* observations highlighted above, **(Left)** Evolution of the Fe xxvi Kα/Fe xxv Kα EW ratio in time, and **(Right)** distribution of the EW of the two Kα lines.

observation of 27-03-2005 (see lower panels of Fig. 3.11) show column densities increasing up to being compatible with the most extreme *Chandra* observation, matching a first short-lived transition to the hyper soft state seen in several other indicators (Neilsen et al. 2016; Uttley & Klein-Wolt 2015). Secondly, the first of the *Swift* observations back to normal wind properties perfectly matches the end of the hypersoft state. However, as the transition in and out of the hypersoft state happens on very short timescales, a more precise comparison to the broadband spectral-timing properties is necessary to infer whether the wind changes precede or follow the state change.

4. The long-lived powerful wind seen in *Swift* (Balakrishnan et al. 2020) is one of the arguments against a short-lived Super-Eddington phase proposed in e.g. Neilsen et al. (2016). However, there is strong wind variability even within the hypersoft state, with several *Swift* observations at the middle of it showing column densities much closer to the more "standard" observations before and after it. The supposed wind duration of 70 days seen by *Swift* is also significantly overestimated, as both the hypersoft state and the extreme absorption line signatures are only seen for ~ 30 days.

3.5.3 H 1743-322

H1743-322 was discovered during an outburst in 1977 (Kaluzienski & Holt 1977), and despite spectral features reminiscing of a BH (White et al. 1983), it lacked more complete coverage for the next 25 years, until a second outburst in 2003 (Markwardt & Swank 2003), which exhibited a variety of BH features, such as X-ray jets (Corbel et al. 2005). Since then, other outbursts have been detected, with a frequency significantly higher than most other BH transients (Tetarenko et al. 2016), and clear distinction between two types: standard outbursts, very reminiscent of other sources, and "hard-only", so-called "failed" outbursts (Capitanio et al. 2009) during which the source rises but never leaves the hard state (see Stiele & Kong 2021; Stiele & Yu 2016, for a more detailed history of past outbursts). While the source has not been dynamically confirmed, and as such no direct estimates of its mass exist, strong dips observed during the 2003 outburst (Homan et al. 2005) indicate a high-inclination. This has since been corroborated by the modeling of the jet properties, leading to a jet inclination measurement of $i = 75 \pm 3°$, and a distance estimate of $d = 8.5 \pm 0.8$ kpc (Steiner et al. 2012).

The first and only wind detection in this source arises from 4 *Chandra* exposures in a very luminous soft state of the 2003 outburst, as seen in **?** (see Miller et al. (2015) for a detailed analysis of the absorption features in the first observation). Interestingly, no absorption lines were detected in the hardest exposure, more reminiscent of a "high-intermediate" state (see below for a discussion on this non-detection). Following this, all subsequent exposures with instruments sensitive enough to detect absorption features were performed during 'hard-only' outbursts, or hard portions of classic outbursts such as with *Suzaku* in 2008 (Blum et al. 2010) and 2012 (Shidatsu et al. 2014), and in 2010 (Miller et al. 2012). Expectedly, none did exhibit significant line features. In addition, a number of XMM-*Newton* exposures have been performed during very similar spectral states in subsequent outbursts, notably in 2014 (Stiele & Yu 2016) and 2018 (Stiele & Kong 2021).

There have been much less attempts to model the wind signatures in H1743-322 than its pairs, at least until recently. In 2018, preliminary work Done et al. (2018) indicated that thermal-radiative winds could potentially reproduce the changes in features seen between this source's soft and hard states, with their following study a year later confirming this hypothesis with thermal-radiative analytic solutions (Shidatsu & Done 2019). However, this model was completely unable to predict the lack of wind signature in the high-intermediate state observation, indicating that the picture was far from complete. Subsequent simulations confirmed the success for the high-soft state (Tomaru et al. 2019, 2020), but the hard state, and most importantly the high-intermediate state, are yet to be tackled. Finally, H1743-322's 2003 observations were also used as templates of 'wind-on' and 'wind-off' states in Fukumura et al. (2021), with strong expectations of changes in the wind structure.

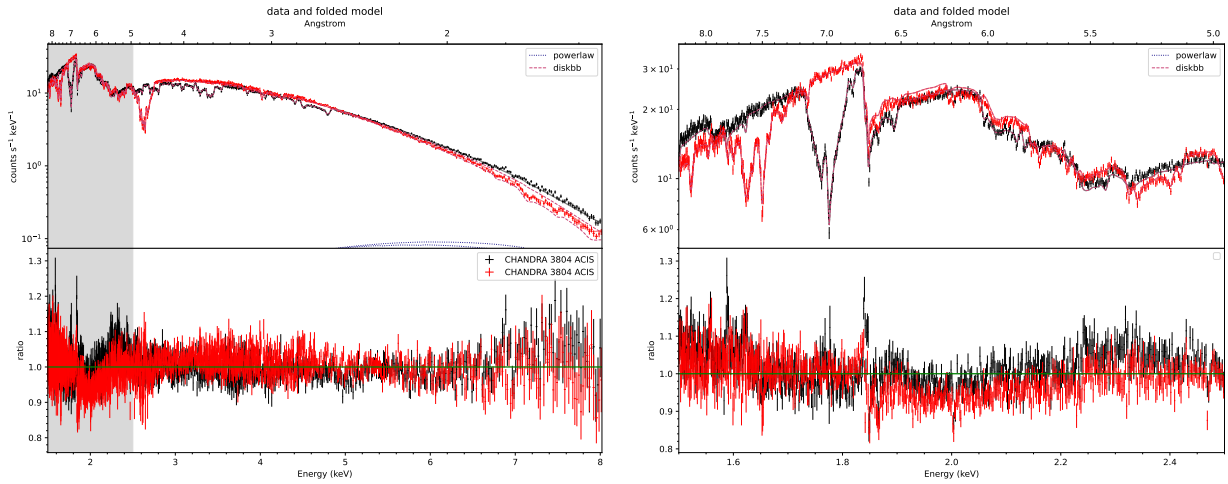

Figure 3.12: **(Left)** Residuals of a simple continuum fit in Obsid 3804. The grey area highlights the 1.5-2.5 keV range, with a significant portion below a ratio of 1. **(Right)** Residuals zoomed in the 1.5-2.5keV band.

This non-detection in the high-intermediate state of H1743-322 is thus a very important tool to test wind models, and an additional view on the structure of the wind when the iron lines are not detected would be very beneficial. We thus searched for additional absorption features in this spectrum. Unfortunately, this observation, along with all the observations of this outburst, is taken in CC-mode to mitigate pileup. This mode affects the calibration in a very complex, source dependent way, and as such, a number of residuals remain in these spectra [28]. In the left panel of Fig. 3.12, we show the residuals after a simple `tbabs(diskbb+powerlaw)` fit of the exposure where no lines are detected (Obsid 3804). In the right panel of Fig. 3.12, we zoom on one of the most affected regions, where many edges result in instrumental features in the spectra. However, even if the entire 1.8-2.2 keV range is globally below the model, there is also a clear absorption feature at $\sim$ 2.0 keV, present in both orders, not associated with an edge, nor with any calibration issues mentioned online. This energy matches very well the Si xiv Kα line detected as a wind signature in a number of BH and NS LMXBs (see e.g. Allen et al. 2018; Miller et al. 2008; Ponti et al. 2019; Ueda et al. 2009).

To assess whether this feature is significant or instrumental, we started by performing a blind search around the absorption line feature in different spectra of the source. Since the calibration residuals vary widely between observations, an ubiquitous line detection would greatly favor a real absorber. To limit the issues with a broad continuum fitting, we restrict ourselves to the 1.9-2.1 keV range, with a simple powerlaw model. The results for the 2003 spectra of H1743-322 are plotted in Fig. 3.13. A few absorption features potentially associated with edges appear around 1.975 and 2.03 keV, but they do not seem consistent between different observations and grating orders[29]. On the other hand, the Si xiv Kα feature is always clearly present in these soft to intermediate spectrum. In stark contrast, none of the hard state observations of the source (Obsids 110448,16738,16739,17679,17680) exhibit this feature, despite spanning several different observation modes. This once again points at an absorber whose properties either change or become unstable in the hard state. We further verified by searching in several other CC-mode observations of known BHXRB sources, but only found similar detections in soft states of high-inclined, canonical wind-emitters. This strongly points towards this feature being, indeed, the signature of a ionized absorber.

To constrain the evolution of the line between observations, we tested the addition to our empirical continuum of a `vashift*gaussian` line, centered at the Si xiv Kα doublet mean energy, 2.0055 keV (Kramida & NIST ASD Team 2023). The velocity shift interval is fixed to between -3000 and 3000 km/s, and the width of the line is fixed at 0, as it remains unconstrained in all observations. The results of the fits for the different observations are detailed in Tab. 3.2. Despite extremely low EWs, the line remains

[28] see https://space.mit.edu/ASC/calib/ccmode_final_doc.pdf

[29] The $\sim$ 2.03 keV feature seen in few spectra could match a NiXXVI line seen in e.g. (Ueda et al. 2009)

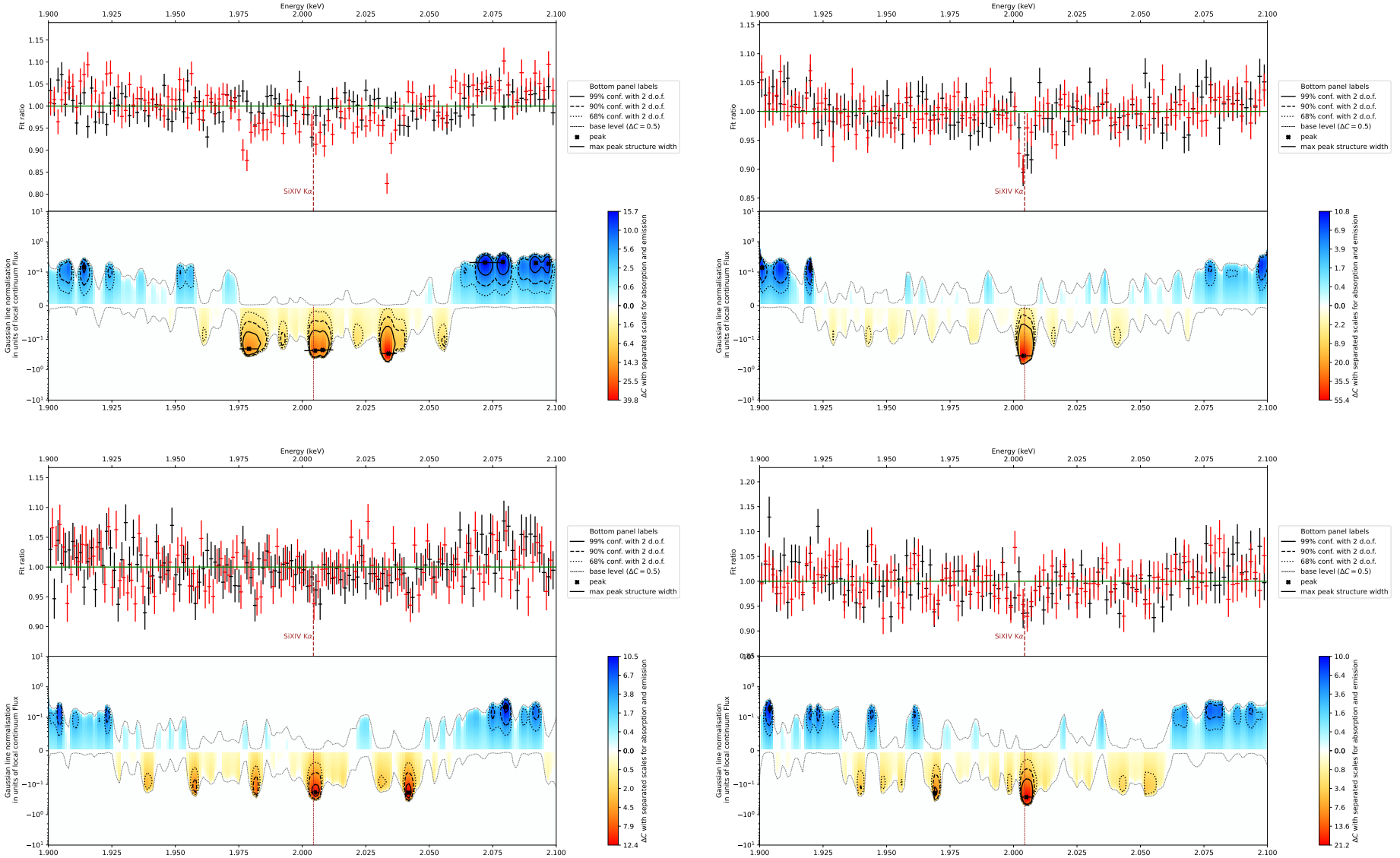

Figure 3.13: Results of a blind search in the 1.9-2.1 keV range of the 4 *Chandra* exposures of H 1743-322 (from upper left to down right: 3803, 3804, 3805, 3806) during its 2003 outburst, when fitted with an empirical powerlaw in this range. The rest energy of the Si xiv Kα line is highlighted in the bottom panels.

Line	Obsid	State	Iron lines	Order used	EW eV	velocity shift km/s	$\Delta\chi^2$	Sign.
Si xiv Kα	3803	soft	✓	**-1**,**+1**	0.24 ± 0.08	157^{+90}_{-87}	24.0	>99.9%
				-1†	0.22 ± 0.11	304 ± 136	11.2	99.9%
	3804	intermediate	X	**-1**,**+1**	0.37 ± 0.08	281^{+60}_{-87}	58.0	>99.9%
	3805	soft	✓	**-1**,**+1**	$0.18^{+0.10}_{-0.08}$	74^{+216}_{-179}	11.7	99.8%
	3806	soft	✓	**-1**,**+1**	$0.28^{+0.10}_{-0.09}$	71 ± 127	22.5	>99.9%
	11048	hard	X	**-1**,**+1**	<0.66	/	/	/
	all hard Obsids		X	**-1**,**+1**	<0.33	/	/	/

Table 3.2: Results of the fits for the Si xiv Kα absorption line in H 1743-322's *Chandra* obsids, after fitting the 1.9-2.1 keV range with an empirical powerlaw continuum. Negative values of velocity shifts indicate blueshifts. We compute the upper limit for Obsid 11048 as it is the brightest of the hard state observations (no Si xiv Kα are detected in any of the other hard state observations).† As the combination of two unidentified absorption features and an edge slightly below 2.000 keV in the +1 order (see upper left panel of Fig. 3.13) may affect the absorption line estimate, we also test fitting the absorption feature to the -1 order only. All errors are quoted at 90%.

clearly detected and significant in all 4 observations of the 2003 outburst, even when only considering the better calibrated -1 order for Obsid 3803 to avoid potential contamination. The equivalent width of the line is potentially stronger in the intermediate state, but all observations remain compatible within uncertainties. On the other hand, the very low velocity shifts hint at a redshifted line, especially in Obsid 3804 where the value is constrained to be positive at 3 σ. This is the most important difference compared to the lines of the same transition previously detected in BHXRBs, which were systematically outflowing (Allen et al. 2018; Miller et al. 2008; Ponti et al. 2019; Ueda et al. 2009).

Since the Si xiv Kα line is not detected in any of the hard *Chandra* observations of the source, we computed the 90% upper limit on its EW in the brightest and longest hard state observation, Obsid 11048, as well as when fitting a common line to all hard state observations (11048, 16738, 16739, 17679, 17680). Even with a common fit, the line is only marginally constrained to with an EW<0.33 eV, which remains compatible with the weak detected EWs in the soft state, and prevent any conclusion on the evolution of the line EW with the spectral state.

The question of whether this absorption feature is due to the source or an independant ISM absorber remains for now open. Proper photoionization and SED modeling will allow to distinguish between different phases, depending on whether the iron complex being significantly stronger in the intermediate state is incompatible with the Si xiv Kα line being stronger. In addition, while previous results indicate that this line should remain stable in typical hard states (Chakravorty et al. 2013), a detailed analysis using the proper SEDs of this source is needed for a definitive conclusion. It may also reveal other lines that were not previously detected, although we didn't notice any other significant feature that we could distinguish from the calibration.

3.5.4 IGR J17451-3022

IGR J17451-3022 is by far the least studied of all sources showing absorption features in our sample. After its discovery in 2014 with *INTEGRAL* Chenevez et al. (2014), its only outburst to date has been partially monitored by *Swift*, *INTEGRAL*, XMM-*Newton* (Bozzo et al. 2016) and *Suzaku* (Jaisawal et al. 2015). XMM-*Newton* and *Suzaku* both showed strong absorption line signatures, reminiscent of other high-inclination LMXBs, and most notably from the extreme wind states detected in few specific exposures (see subsections above). The presence of eclipses puts a second, independent constrain on its inclination (see e.g. Jaisawal et al. 2015). However, the source still lacks both a distance and mass

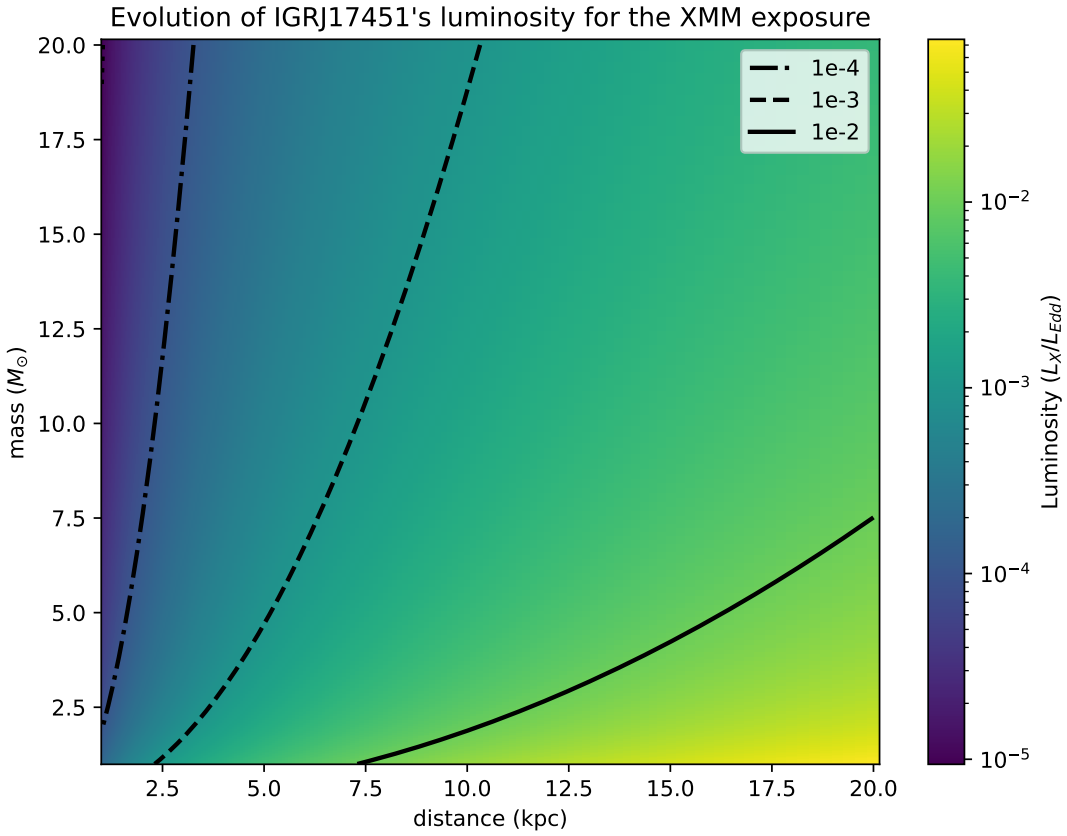

Figure 3.14: Eddington ratio evolution of the XMM-*Newton* exposure of IGR J17451-3022 as a function of its mass and distance

estimate, and as its potential counterpart (which might also be an interloper) is both faint and in a very crowed field (López et al. 2019), dynamical measurements remain complex. Consequently, suppositions on the source rely only on its X-ray spectral properties, which are also potentially in line with a NS. However, as the answer is not definitive, we keep this source in our sample.

The wind properties in the spectra of this source are particularly interesting: it exhibits a peculiar Fe xxvi Kα/Fe xxv Kα ratio (see Fig. 3.7) and a high number of spectral features (Bozzo et al. 2016) which are typically only seen in the most extreme wind states seen in LMXBs, and at an apparent Eddington ratio luminosity at least an order of magnitude below all other detections so far. However, the real Eddington ratio of the source remains unconstrained and can vary extremely depending on the assumptions on its mass and distance. We show in Fig. 3.14 the impact of a range of masses (between 1 and 20 $M_\odot$) and distances (between 1 and 20 kpc) on its Eddington ratio. It is clear that unless the source is beyond $\sim$ 10 kpc, its Eddington ratio remains quite low for wind detections, even for a Neutron Star.

However, a comprehensive analysis of the source's outflow evolution has yet to be done. Besides the intrinsic variability noted in **?**, the *Suzaku* exposure of the source was completely exempt of the rich warm absorber-like wind seen in the XMM-*Newton* observation, with a single Fe xxv Kα line remaining (G. K. Jaisawal, priv. communication) despite similar spectral properties. If properly modeled, this could put strong constrains on the changes in the outflow structure and whether they can be explained by changes in SEDs, or with different launching mechanisms. This, combined with a more physical modeling of the rare mix of dips and eclipses seen in XMM-*Newton* and *Suzaku*, could shed light on the nature of the source.

3.6 Contextualization in the global observational landscape

Our present study of Fexxv and Fexxvi absorption lines in all publicly available XMM-*Newton*-pn and *Chandra*-HETG observations of BHLMXB candidates yields results in good agreement with previous findings. All the wind signatures we found occur in luminous ($L_X > 0.01 L_{Edd}$) soft states ($HR_{[6-10]/[3-10]} < 0.8$) of five dippers: 4U 1630-472, GRO J1655-40, GRS 1915+105, H 1743-322 and IGR J17451-3022. Existing inclination measurements are consistent with this behavior, with i>55° in these five sources.

With the *Chandra* instrument, which proves to be the only instrument sufficiently precise to reliably measure the outflow velocity, the absorption signatures show a global trend of very small blueshifts. Indeed, the velocity shifts of our sample are negative and of the order of few hundreds of kilometers per second, with a mean of -200 ± 60 km s^{-1}. Moreover, only one detection (in GRO J1655-40) is significantly ($> 2\,\sigma$) below -1000 km s^{-1}. These values, although closer to the limits of HETG's absolute wavelength accuracy, remain consistent with past publications and in particular with velocity shift measurements in lower energy lines (compared to Fexxv and Fexxvi), where HETG's accuracy is more well studied (see e.g., Trueba et al. 2019; Ueda et al. 2009 and references therein). Other works claiming higher blueshift values employ more complex fits using several photoionization models (see e.g., Miller et al. 2015), and those works should not be directly compared to our results, although the main ionization zones generally remain in agreement with our findings.

We also obtained good constraints on a few line widths, with FWHMs on the order of a few thousands of kilometers per second for the broadest ones. The observed correlation between the line widths and Fe xxv Kα EW naturally arises in the presence of significant turbulence velocity in the wind, of the order of a thousand kilometers per second when assuming a simple slab geometry (see Sect. 3.4.1). Reality is expected to be more complex, possibly with a radial distribution of density and velocity. A more precise modeling is certainly needed to better characterize the amount of turbulence.

We detected a very significant anti-correlation between the X-ray luminosity (in Eddington units) and the line EW in the case of Fexxv, while no significant correlation was observed in the case of Fexxvi. This anti-correlation is present in single objects with multiple line detections but also in the entire set of sources showing absorption lines. Although already found in the past in more restricted datasets (Miller et al. 2020; Ponti et al. 2012), such a correlation observed in a sample of different sources would suggest a similar wind structure (i.e., a similar nR^2 factor) from source to source at a given L_X/L_{Edd}. This anti-correlation would then be expected if the wind ionization is on average above the peak of the ionic fraction for Fe xxv Kα. While it predicts quite large Fe xxv Kα EWs ($\sim$ 100 eV) below our threshold of $0.01 L_{Edd}$, the ionization at these luminosities could also go beyond the peak of the Fe xxv Kα ion fraction and shift to producing weaker lines from less-ionized ions. If this is not the case, the lack of detection at low flux may also be due to lower statistics or sparser coverage, but it could also be related to the physical processes producing the wind (e.g., thermal driven wind requiring high illuminating luminosity, Done et al. 2018; Tomaru et al. 2019).

The absence of Fexxv and Fexxvi absorption line detection in virtually all hard states in our sample agrees with recent theoretical studies, suggesting that the ionization range compatible with these ions could be thermally unstable when the gas is illuminated by a hard state SED (e.g., Bianchi et al. 2017; Chakravorty et al. 2013, 2016; Petrucci et al. 2021). Thus, even if the wind itself were present, it would not be detectable through Fexxv and Fexxvi absorption lines.

In Tab. 3.3, we list the reports of absorption lines in all wavebands, associated accretion states, and potential issues, among the known BHLMXBs listed in Tab. 3.1. There have been many recent reports in the literature of iron band absorption line detections in hard states. However, we must stress that the vast majority of these detections come from *NuSTAR* spectra, mostly blended with reflection. The limited spectral resolution of this instrument, combined with the model-dependent nature of the residuals of reflection components means that special care should be put into computing the significance of these lines, especially when different reflection models disagree on their existence (see e.g. Chakraborty et al. 2021a and Jia et al. 2022 for MAXI J1348-630). We note that this degeneracy between absorption lines and reflection features is also a well known problem in AGNs (Parker et al. 2022).

Table 3.3: Details of accretion states with reports of absorption line detection in both our work and the literature.

Source	accretion states with absorption lines reported		
	P24	other works	
	iron band	iron band	other energies
4U 1543-47	X	soft† (1.)	soft^{X} (2.)
4U 1630-47	soft	soft (3.) , SPL (4.)	soft^{X} (5.)
A 0620-00	X	X	outburst^{V} (6.)
EXO 1846-031	X	hard$^{\circledast}$ (7.) (54.)	X
GRO J0422+32	X	X	outburst^{V} (8.)
GRO J1655-40	soft	soft (9.)	soft^{X} (10.), soft^{V} (11.)
GRS 1009-45	X	X	outburst^{V} (12.)
GRS 1716-249	X	X	hard^{V} (13.)
GRS 1758-258	X	hard (14.)†	X
GRS 1915+105	soft,hard	soft:ϕ,γ,ρ,β (15.),θ (16.),κ (17.),λ (18.),ψ (19.),δ (23.) hard:χ_{loud} (20.),obscured* (22.), obscured* χ_{quiet} (23.)	soft^{X}:ϕ (21.) hard*:obscured^{IR} (24.)
GX 339-4	X	X	hard ^{X} (26.),soft^{V} (25.),hard^{V} (25.)
H 1743-322	soft	soft (27.)	soft (28.)
IGR J17091-3624	X	soft (29.),class-V (30.),class-X (30.), hard† (31.)	hard^{X} (32.)
IGR J17451-3022	soft	soft (33.)	soft^{X} (33.)
MAXI J1305-704	X	soft (34.) (35.)	soft^{X} (34.) (35.),hard^{X} (35.), soft^{V} (36.)
MAXI J1348-630	X	soft$^{\circledast}$ (37.), hard$^{\circledast}$ (37.)	hard^{X†} (38.),hard^{V,IR} (39.)
MAXI J1535-571	X	soft$^{\circledast}$ (54.), hard$^{\circledast}$ (54.)	X
MAXI J1631-479	X	soft$^{\circledast}$ (40.) (1.)	X
MAXI J1659-152		X	quiescence (41.)
MAXI J1803-298	X	soft (42.) (43.)	soft^{V} (44.),hard^{V} (44.)

Table 3.3: Continued.

Source	accretion states with absorption lines reported		
	P24	other works	
	iron band	iron band	other energies
MAXI J1810-222		X	soft^{X} (45.), hard^{X} (45.)
MAXI J1820+070	X	soft (46.)	hard^{V,IR} (47.), quiescence^{V} (48.)
Nova Muscae 1991	X	X	outburst^{V} (49.)
Swift J1727.8-1613		X	soft^{V†} (56.), hard^{V} (56.)
Swift J1357.2-0933	X	X	hard^{V} (50.) (51.), quiescence (52.)
Swift J151857.0-572147		soft*	X
Swift J1658.2-4242	X	soft$^{\circledast}$ (54.) (53.), hard$^{\circledast}$ (55.) (54.) (53.)	X
Swift J174540.7-290015 (T15)	X	soft$^{\circledast}$ (54.)	X
V404 Cyg	X	hard*:obscured (57.)	hard*:obscured^{X} (58.)^{V} (59.)
V4641 Sgr	X	X	soft^{X} (60.) (2.),hard*:obscured^{V} (61.)
XTE J1118+480	X	X	hard^{V} (62.)
XTE J1550-564	X	soft (63.)	X
XTE J1652-453	X	hard† (64.)	X
XTE J1859+226	X	X	soft^{V} (65.) (66.)

Legend:
Bold: dippers.
blue arc: X-ray absorption lines embedded in reflection components.
red arc: broad absorption line in optical, unclear origin (see Miceli et al. 2024 and the main text for details).
$^{\circledast}$: confirmed ($^{\circledast}$), suspected ($^{\circledast}$), or possible ($^{\circledast}$) edge mismatches in NuSTAR fits creating artificial absorption lines (see Bogensberger et al. 2020 and the main text for details).
$X/V/IR$: detection in soft X-rays / Visible / Infrared.
†: low significance or tentative detection.
$*$: The observed HR value of the obscured state might not reflect the actual HR of the source.

*: Source: IXPE collaboration.
The list of reference papers is not exhaustive for objects with many wind detections. Last update: 06-24.
References: 1 (Prabhakar et al. 2023) 2 (Draghis et al. 2023) 3 (Kubota et al. 2007) 4 (Parra et al. 2024a, in prep) 5 (Trueba et al. 2019) 6 (Whelan et al. 1977) 7 (Wang et al. 2020) 8 (Callanan et al. 1995) 9 (Miller et al. 2006a) 10 (Miller et al. 2008) 11 (Della Valle et al. 1998) 12 (Della Valle et al. 1997) 13 (Cúneo et al. 2020) 14 (Reynolds & al. 2018) 15 (Neilsen & Lee 2009) 16 (Ueda et al. 2010) 17 (Liu et al. 2022) 18 (Neilsen et al. 2018a) 19 (Shi et al. 2023) 20 (Lee et al. 2002) 21 (Ueda et al. 2009) 22 (Neilsen et al. 2020) 23 (Athulya & Nandi 2023) 24 (Sanchez-Sierras et al. 2023b) 25 (Rahoui et al. 2014) 26 (Miller et al. 2004) 27 (Miller et al. 2006b) 28 (Parra et al. 2024b, in prep. - PhD manuscript) 29 (King et al. 2012) 30 (Wang et al. 2024a) 31 (Wang et al. 2018) 32 (Gatuzz et al. 2020) 33 (Jaisawal et al. 2015) 34 (Miller et al. 2014) 35 (Shidatsu et al. 2013) 36 (Miceli et al. 2024) 37 (Chakraborty et al. 2021a) 38 (Saha et al. 2021) 39 (Panizo-Espinar et al. 2022) 40 (Xu et al. 2020) 41 (Torres et al. 2021) 42 (Coughenour et al. 2023) 43 (Zhang et al. 2024a) 44 (Mata Sánchez et al. 2022) 45 (Del Santo et al. 2023) 46 (Fabian et al. 2021) 47 (Muñoz-Darias et al. 2019) 48 (Yoshitake et al. 2024) 49 (Della Valle et al. 1998) 50 (Jiménez-Ibarra et al. 2019) 51 (Charles et al. 2019) 52 (Sánchez et al. 2015) 53 (Bogensberger et al. 2020) 54 (Draghis et al. 2024) 55 (Xu et al. 2018a) 56 (Mata Sánchez et al. 2024) 57 (Muñoz-Darias & Ponti 2022) 58 (King et al. 2015) 59 (Muñoz-Darias et al. 2016) 60 (Shaw et al. 2022) 61 (Muñoz-Darias et al. 2018) 62 (Dubus et al. 2001) 63 (Connors et al. 2020) 64 (Chiang et al. 2012) 65 (Welsh et al. 2002) 66 (Hynes et al. 2002)

In parallel, a recent study showed that XMM-*Newton* and *NuSTAR* can suffer from very important absolute energy calibration issues around the iron line. This has been shown to create artificial emission/absorption features in the case of very highly absorbed sources, due to incorrect fitting of a strong edge at 7.1 keV (Bogensberger et al. 2020). We thus highlight in our table several detections for sources with very high absorption that may suffer from similar issues. In addition, this effect can produce the same type of residuals in strong reflection features, where the asymmetric higher energy portion of the line acts like an edge. This has not been taken into account in any reflection study, and besides affecting the results of the reflection modeling (spin, inclination, etc.), it adds yet another potential issue to the *NuSTAR* absorption line reports with reflection. Finally, we stress that highest energy absorption line reports above ~ 9 keV (see e.g. Prabhakar et al. 2023) can also be simply the result of a Fe xxv Kα edge at 8.82 keV, instead of a very highly blueshifted Fe xxvi Kα line. While the edge itself can reveal the presence of a fast wind in a face-on geometry (Zhang et al. 2024b), such detailed profiles remain completely out of reach of the current generation of instruments.

The few remaining hard states absorption reports in the iron band are not well documented (Reynolds & al. 2018; Saha et al. 2021), and in the end, the only clear iron band hard state detections come from non-standard states of GRS 1915+105 and V404 Cyg (Lee et al. 2002; Muñoz-Darias & Ponti 2022), and for the former, the recent observations can help determined whether these detections are compatible with theoretical expectations (see sub 3.5.1).

In the soft X-ray band on the other hand, there have been few clear reports of detections in hard states (see references in Tab.3.3). However, these absorbers have different characteristics, systematically exhibiting much lower ionization parameters ($\xi_i \sim 1.5-2.5$) and negligible blueshifts. These ionization ranges match lower portions of the stability curve, which can remain stable even in hard states (Chakravorty et al. 2013), but a stability analysis on these specific datasets remain inconclusive, due to a lack of precise broad band coverage (Gatuzz et al. 2020). In addition, except for IGR J17091-3624, none of the studies consider the presence of a multiphase ISM absorber, which can contribute significantly to such transitions (Gatuzz & Churazov 2018), even if, at least in the case of IGR J17091, the ISM phase alone cannot reproduce the observed profiles. In order to distinguish whether the "static" (low ξ_i) and "dynamic" (high ξ_i) component trace different absorbing phases, they must be followed across the different spectral states, but no existing datasets allow for such a study.

Putting aside all of the unconfirmed or debatable reports, the (very restricted) population of sources with X-ray wind detections needs to be compared to the increasing number of optical and infrared absorption line detections (see Tab. 3.3), which suggest that the outflow persists independently of the spectral states (see Panizo-Espinar et al. 2022 and references therein). They arise from the same category of high-inclined (mostly dipping) sources, and provide different and complementary views of the outflow, namely, with visible and infrared absorption lines being restricted to hard states. We also note that other clear indicators of winds in emission (blueshifted emission line profiles and blueshifted absorption troughs) have been reported in infrared during the soft state, see (Panizo-Espinar et al. 2022; Sanchez-Sierras & Munoz-Darias 2020).

In addition, the "canonical" wind detections, with significantly blueshifted P-cygni profiles or absorption lines, must be distinguished from broad (FWHM of few 1000 km/s), typically symmetric absorption lines superposed on narrower emission profiles. This combination has been detected in a number of sources, and in virtually all states in and out of outburst. The origin of this specific profile remains unclear, and has yet to be associated with outflows (see Dubus et al. 2001 for a proposed explanation, and Miceli et al. 2024 for a recent discussion). In Tab. 3.3, we attempted to list all of the detections of this type in BHLMXBs, but as this feature is rarely the focus of the studies, we expect it to be present in other sources as well. Although this behavior has yet to be linked with outflows, several elements clash with the standard explanation of a uniform thick disk atmosphere: contrarily to what is seen in Novae (Han et al. 2020; Szkody et al. 1990), it remains restricted to mid to high inclined systems, and depending on the source, can either be ubiquitous (even in quiescence), or restricted to hard/soft states. Most importantly, a higher cadence of observations reveal that the "symmetric" line profile can

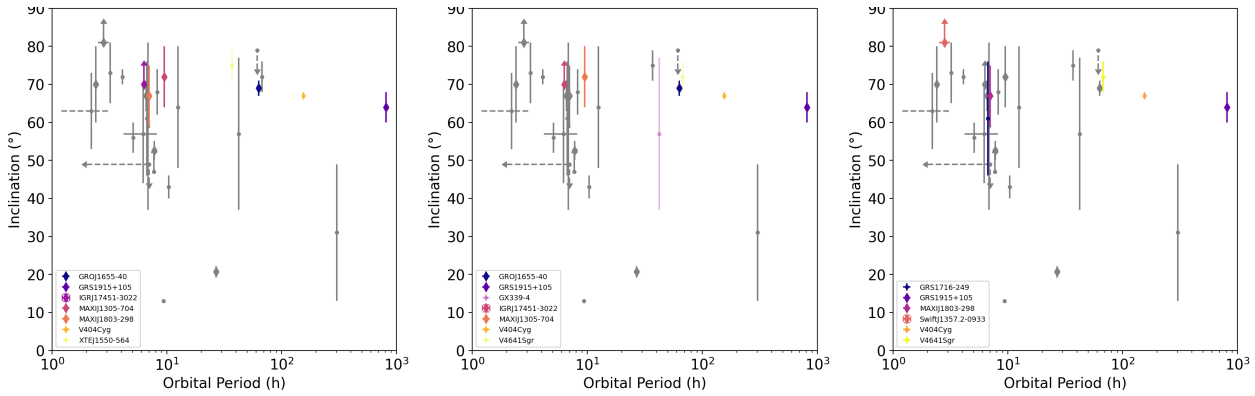

Figure 3.15: Distribution of the orbital period and inclination measurements of BHLMXB candidates with clear wind detections in the iron band **(left panel)**, soft X-rays **(middle panel)** and OIR **(right panel)**, compared to the rest of the sample (in grey). For the inclination, we consider in priority dynamical measurements, then jets, others, and finally reflection. For wind detections, we use transparency for observations with reflection, edge issues detections or generally tentative measurements, following Tab. 3.3. Diamond markers indicate dippers, and dashes tentative orbital period measurements.

sometimes be split between singular redshifted and blueshifted components, alternating on timescales from minutes to days (Miceli et al. 2024). This behavior, along with a significant velocity shift of the broad line centroid in some cases (Rahoui et al. 2014), hint at a much more complex geometry that could be associated with outflows. We note that similar behaviors have been -much more rarely- observed in UV (Haswell et al. 2002; Hynes et al. 2002), but are much harder to properly disentangle from interstellar absorption in this band.

When restricting our view to standard detections, the absorption lines exhibit terminal velocities in the range of a few -1000 km s^{-1} (blueshifted), which is significantly higher than in X-rays, but could be the result of observational constrains, as the terminal velocities may not be detectable in X-rays with the current generation of instruments. More critically, only V404 Cyg, MAXI J1803-298 and GRS 1915+105 have clear reports of detection in both X-rays and optical or infrared. In V404 Cyg, they are consistent with being produced by the same outflowing material (Muñoz-Darias & Ponti 2022), although in a non standard obscured state, with extremely strong emission lines dominating the spectra, and fast variability of absorption features in the iron band (which prevented their detection in our time-integrated spectra). In MAXI J1803-298, the visible and X-ray winds have been shown to be mutually exclusive (Zhang et al. 2024a), and thus no direct comparison is possible. In GRS 1915+105, the multi-wavelength wind connection has yet to be studied, although it may need to be considered differently due to the puzzling lack of infrared wind signatures in any of its radio quiet states.

It is difficult to assess whether the lack of X-ray and OIR absorption line detections in single sources is meaningful. In our study, the vast majority of objects with these features have very poor X-ray coverage in the favorable region. However, several objects have been extensively followed by other X-ray telescopes, such as MAXI J1820+070 with *NICER*, with only a single tentative report of X-ray absorption detections up to now (Fabian et al. 2021). On the other hand, most sources with X-ray detections in our sample lack either the optical counterpart or the high-quality optical data necessary to search for absorption lines. It is also possible that the physical conditions favoring X-ray and optical wind signatures do not perfectly match (see e.g., Koljonen et al. 2023), but more simultaneous optical and X-ray campaigns are required to draw conclusions.

One of the elements that may influence the detection of cold winds, expected to be launched in the outer regions of the disk, is the orbital period, being linked to the maximum disk size. To assess whether the "cold" (OIR), "warm" (soft X-rays) and "hot" (iron band) absorbers have different properties, we compare the orbital period and main inclination measurements of all BHXRB candidates with clear

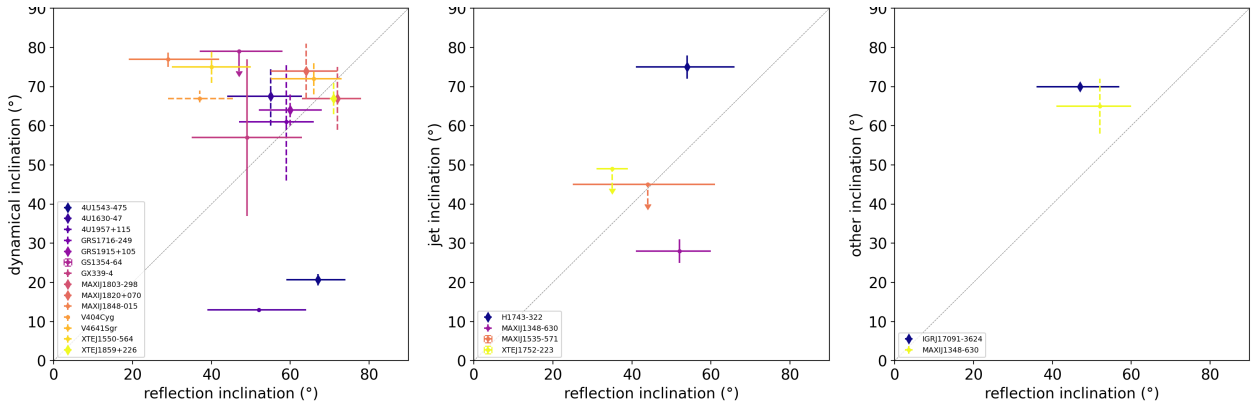

Figure 3.16: Comparisons of dynamical **(left panel)**, jet **(middle panel)** and other **(right panel)** inclination measurements against results obtained with reflections in known BHLMXB candidates. Diamond markers indicate dippers, and dashes tentative inclination measurements.

wind detections each of these bands in the different panels of Fig. 3.15, highlighting the remaining part of the sample. As the amount of sources in each population is very small, we do not see any difference between the distributions of each population: all confirmed wind emitters are seen at high-inclination, and do not seem to be restricted to a single part of the orbital periods sampled by the global BHXLMXB population. However, this lack of distinction might also be due to the very low number of sources with inclination measurements and low orbital periods.

Nevertheless, the optical wind detections seen in Swift J1357.2-0933 (Jiménez-Ibarra et al. 2019), which is the third smallest orbital period in the sample at 0.11 ± 4 d (Sánchez et al. 2015), should be very constraining for physical wind launch models. Indeed, while its dynamical parameters are not fully constrained, it is one of the most massive in the sample at $> 9.3 M_{\odot}$, and has thus one of the smallest disk extensions at $\lesssim 5.1 \cdot 10^4$ Rg (assuming Roche Lobe filling, $M_{BH} \geq 9.3 M_{\odot}$and $M_{\star}$=$0.4 M_{\odot}$, see Sánchez et al. 2015).

Finally, since conclusions about the physical interpretations of the outflows are extremely dependent on the inclination values, it is important to assess whether the current toolbox of inclination measurements is coherent. We thus take the advantage of having performed an exhaustive search of the different inclination reports in the literature for our sample of BH candidates. This notably allows to compare the measurements from reflection with other methods, and get an idea of whether they are generally biased, or incompatible due to potential misalignment between orbit and inner disk. We plot the comparisons with dynamical, jet and other measurements in Fig. 3.16. While reflection measurements may have previously been considered as biased towards high inclinations, the new measurements of Draghis et al. (2024), with several significantly lowered values, are now generally more compatible with other estimates. Nevertheless, they now tend to provide lower measurements compared to the other methods, with the notable exceptions of 4U 1957+115 and 4U1543-47's dynamical inclinations, and MAXI J1348-630's jet inclination.

For the first two, as the difference between the two methods appears unreasonably high for disk misalignment, it is possible that one of the previously mentioned issues with *NuSTAR* fitting may have affected the reflection estimates. In addition, in all three sources the claims of absorption line detections within reflection in this source may indicate an issue with the spectral modeling. Including an absorption line to the reflection measurements does not have a straightforward influence on the inclination, and as such, higher resolution instruments such as *XRISM* will be paramount to compute reflection properties and wind features self-consistently.

For the rest of the measurements, the lack of consideration for returning radiation has been shown to bias towards higher inclination in few cases (see e.g. Connors et al. 2020) and could explain the remainder of the discrepancies. Finally, we stress that current iterations of reflection models systematically provide extremely high spin values, which might indicate a bias in the modeling of

physical parameters, potentially affecting inclination values as well. One of the causes may also be the degeneracy between reflection and the plunging region in the soft state (Mummery et al. 2024a), the latter providing much lower spin values while being compatible with completely different inclination measurements (Mummery et al. 2024b).

4

20 years of disk winds in 4U 1630-47

The global study of Chap. 3 had two direct applications: either perform a detailed study aiming to fill some of the gaps identified in the observational landscape, or focus on the WED models and comparisons with the data. Unlike what the structure of this document suggests, I ended up leaning towards the second option first. However, in parallel, I took the opportunity of recent improvements (and simplification) in the software tools used to reduce *NICER* data to take a look at its public archive, which was (and still is) far and away the biggest and least published source of wind-constraining X-ray observations available for X-ray Binaries. Over the course of several months, I thus reduced and ran the line detection procedure on the entirety of the *NICER* archive for the most observed BHLMXBs at the time. After 7 sources and more than 2000 individual observations, it became glaringly obvious that formalizing even a fraction of these results would be more than enough to fill the remaining time of my PhD. Thus, after finishing the groundwork on the modeling project (which we will detail in Part. III), I returned to observations and focused on one of the sources whose archival data had the most potential: 4U 1630-47.

4.1 Introduction to the source

4U 1630-47 is one of the first identified transient X-ray sources (Jones et al. 1976), known for a pattern of recurring outbursts over a 600-700 days period (Kuulkers et al. 1997). Despite lacking dynamical mass measurements and a proper distance estimate (Kalemci et al. 2018), the source has been classified as a BH, mainly due to its spectral and timing properties (see e.g. Seifina et al. 2014, and references therein), and the detection of a K=16.1 mag infrared counterpart (Augusteijn et al. 2001) cements it as a solid candidate BHLMXB. Finally, recurring dips in the X-ray lightcurve constrain its inclination to $\sim 60-75°$ (Kuulkers et al. 1998; Tomsick et al. 1998).

Nevertheless, its spectral and timing behavior rarely match the standard outburst patterns seen in Black Hole Binaries. First, in addition of its recurring standard outbursts, the source occasionally enters "super-outbursts" of much longer duration (Kuulkers et al. 1997) and with varying spectral and timing evolution (Abe et al. 2005; Tomsick et al. 2005). Second, the source rarely exhibits proper hard states with very small disk contribution and standard $\Gamma < 2$ high-energy component. Instead, a large fraction of its outbursts are spent alternating between Soft/thermal dominated states, intermediate (sometimes flaring) states, and Steep Powerlaw (SPL) states, the latter 2 showing an increasing contribution of a $\Gamma \sim 2.5-3.5$ high-energy component and very distinct timing properties (Tomsick et al. 2005). Finally, 4U 1630-47 has both a history of mostly/completely soft outbursts (Capitanio et al. 2015), and of decays in the soft state down to extremely low luminosities ($< 10^{-4} L_{Edd}$) before transitioning back to hard states (Tomsick et al. 2014, see also Kalemci et al. 2018).

The unusual behavior of this source has prompted many observational campaigns and studies in the last decades, and it has rapidly become one of the archetypal wind-producing, high-inclined BHLMXBs. The first report of a wind detection stemmed from a set of *Suzaku* observations in 2006 (Kubota et al. 2007), although a 2004 *Chandra*-HETG observation already exhibited an absorption line feature, later reported in Trueba et al. (2019). Afterward, extensive monitoring campaigns were performed during the 2012-2013 outburst, using XMM-*Newton* (Diáz Trigo et al. 2014), *Chandra*-HETG (Neilsen et al. 2014), and *Suzaku* (Hori et al. 2014). In parallel, 3 *NuSTAR* observations were performed in this period due to a planned survey of the Norma Cluster (Fornasini et al. 2017), with one too off axis to be analyzed, and another studied in details in King et al. (2014). A single XMM-*Newton* detection of a relativistic emission line during this outburst has been interpreted as a baryonic jet (Díaz Trigo et al. 2013), but this conclusion remains debated (Neilsen et al. 2014).

In the following years, few individual observations with a variety of instruments kept exhibiting wind signatures, such as *Suzaku* and *NuSTAR* in 2015 (Connors et al. 2021; Hori et al. 2018), *AstroSat* and HETG in 2016 (Pahari et al. 2018; Trueba et al. 2019), and *NICER* in 2018 (Neilsen et al. 2018b). *NICER* coverage has continued during every subsequent outburst until now. We note that a serendipitous XMM-*Newton* pointing of a nearby source, performed during a bright portion of the 2018 outburst, provided a completely oversaturated and pile-uped spectrum, which could be analyzed but would require a very advanced and careful analysis.

The source's most recent and longest recorded outburst, which started in the second half of 2022 up until April 2024, has been extensively observed with multiple instruments in order to study the source's X-ray polarisation properties, and wind signatures have been reported in *IXPE*, *NuSTAR* and *NICER* (Ratheesh et al. 2024; Rodriguez Cavero et al. 2023). We note that this last outburst confirms a near-decadal recurrence of "super-outbursts" of this source in the last $\sim$ 30 years, as the very bright outburst of 2018-2019 seen in *MAXI* lightcurves (see Fig. 4.1) is in fact from the nearby binary MAXI J1631-479, as indicated in the *MAXI* webpage for this source [30].

The sampling of 4U 1630-47's outburst evolution is one of the best among BHLMXBs, and even more so for the (currently very limited) population of wind-emitting sources. However, the tens of high-quality exposures with multiple highly sensitive instruments have for now exclusively been studied for single outbursts (e.g. 2012-2013 in Gatuzz et al. 2019) or instruments (e.g. *Chandra* in Trueba et al. 2019), limiting potential interpretations. Moreover, they are now backed up by hundreds of *NICER* observations performed in the last few years, and other observations with e.g. *Suzaku* or *NuSTAR*, which provide additional understanding to previous outbursts, remained to be studied.

I thus performed an exhaustive study of archival observations of 4U 1630-47 until the end of 2023. The combination of the 5 main X-ray telescopes generally used for X-ray wind studies, namely *Chandra*, *NICER*, *NuSTAR*, *Suzaku* and XMM-*Newton*, totals more than 200 epochs spanned over 9 separate outbursts and two decades. The high-energy coverage is complemented by the daily *Swift*-BAT transient monitoring (Krimm et al. 2013), and for specific observations, the BAT survey spectra (Parsotan et al. 2023). These, together with the entirety of the *INTEGRAL* archives for this source, allow us to derive a first order of the high-energy flux behavior in a large fraction of the soft X-ray coverage. The data reduction procedures for the different telescopes used in this chapter are detailed in App. 6.1.2.

4.2 Spectral Analysis

Our spectral analysis, line detection and line significance methodology remain similar to the previous study (see Sec.3.3). In this work, I use Xspec version 12.13.1 (Arnaud et al. 1996), via Pyxspec version 2.1.2.

For 4U 1630-47, we choose a continuum composed of a `diskbb` convolved with a `thcomp` (Zdziarski et al. 2021a) component, multiplied by a `TBabs` for the ISM absorption. The high-energy cutoff of the Comptonized component is unconstrained with the available data and thus kept frozen at 100 keV. In most soft observations without high-energy coverage, the photon index cannot be constrained, and the covering fraction of the `thcomp` component is then fixed to 0. In addition, the procedure can add up to five absorption lines whose energy are tied to the main transitions in the iron complex (Fe xxv Kα, Fe xxvi Kα, Fe xxv Kβ, Fe xxvi Kβ and Fe xxvi Kγ), and two broad (width up to 0.7keV) emission lines for neutral Fe at 6.4 and 7.06 keV (similarly to Sec.3).

This list of components, while relatively basic, works well with 4U 1630-47's very simple evolution in the soft, SPL, and hard state, and allows for a sufficient estimate of the hard X-rays continuum of the source for the sake of photoionization and stability computations. We note that 4U 1630-47 only shows weak reflection features, which we found to be sufficiently well modeled with the two empirical emission line components, as a detailed reflection modeling remains beyond the scope of our analysis.

[30] http://maxi.riken.jp/star_data/J1634-473/J1634-473.html

In addition, 4U 1630-47 is surrounded by a well-known dust scattering halo (DSH, Kalemci et al. 2018), which has a non-negligible effect on the spectral shape (Gatuzz et al. 2019). However, the distance between 4U 1630-47 and the neighboring dust clouds is poorly constrained (Kalemci et al. 2018) and makes for a complicated modeling. We tried several dust scattering models, including `xscat` (Smith et al. 2016) and `dscor` (Jin et al. 2019) to quantify the effect of the correction, but none of the models were able to reconcile the discrepancies between different instruments (and notably between *NuSTAR* and *NICER*/*Suzaku*). Since the DSH is mostly affecting an annulus from 100" to $\sim$ 200" around the source (Kalemci et al. 2018), the bigger extracting region of *NICER* (180") is the least affected, which is why this instrument is considered as the main datagroup in simultaneous observations. In addition, the discrepancy with *NuSTAR* (see below) is the opposite to what the effect of the DSH predicts, as *NuSTAR* typically measures a higher flux in the 3-10 keV keV band compared to other instruments (an effect we also observed for several sources with very low absorption, and is thus not a byproduct of the DSH). *NuSTAR* aside, we do not detect significant flux differences between instruments, and none of the behaviors detailed in the following sections rely on a slight flux/hardness change with a single instrument. We thus choose not to include a DSH component in our analysis. We note that this might explain the marginally lower luminosities in the XMM-*Newton* + *Chandra* set of observations during the 2012-2014 soft states, compared to the behavior in other outbursts (mostly sampled by *NICER*), but we lack simultaneous data for a proper comparison.

The following paragraphs highlight the specifics of the procedure with each telescope not included in the previous study, and the specific case of simultaneous observations. For XMM-*Newton* and *Chandra*, aside from the change in continuum component, the spectral analysis is performed similarly to Sec. 3.

4.2.1 Individual satellites

In *NICER*-only epochs, we restrict the broadband fit to 0.3-10 keV for this instrument. We group individual orbit GTIs within a single MJD and analyze them together as daily "epochs". In each day, observations whose 6-10/3-6 counts HR or 3-10 count rate[31] differ by more than 20% are separated into different epochs. Similarly to XMM-*Newton* and *Chandra*, we use a predefined count threshold to restrict the analysis to *NICER* gtis with sufficient data quality. We use a threshold of 5000 net counts (subtracting the scorpeon model rate of each GTI with default parameters) in the 4-10kev band for the sum of all individual orbits, which results in a total of 172 (out of 189) *NICER* epochs after this quality cut. In order to account for small differences between individual GTIs, we let a `constant` multiplicative component free to vary in xspec for each GTI datagroup in a *NICER* epoch. We account for an instrumental Si Kα feature at 1.74 keV with an empirical `gaussian` fixed at this energy (see e.g. Wang et al. 2024a), which we restrict to emission considering our residuals, and for a known $\sim$ 2.4 keV feature (see e.g. Wang et al. 2021b) with an empirical edge at 2.42 keV.

The background `scorpeon` model of each *NICER* GTI is left free to vary independently during the broad band fits, and remains fixed during the remaining part of the spectral analysis. In order to avoid issues with the non-xray background parameters `saa_norm` and `prel_nom`, which have a very significant effect on the broadband continuum in case of flares, and are sometimes frozen to incorrect values by default, both are systematically thawed at the beginning of the analysis. Finally, we manually split a small number (9) of epochs due to significant variability in the spectral shape of the continuum between the different GTIs of a given day, preventing good absorption line estimates. Each daily epoch is then considered as an individual observation, up until Sec. 4.5.

For *Suzaku*, we analyze the spectra of the XIS and PIN detectors together, restricting their energy range to [1.9-9.0] keV and [12-40] keV respectively. In addition, we ignore the [2.1-2.3] keV and [3.0-3.4] keV intervals in XIS spectra, due to known calibration uncertainties (see e.g. Hori et al. 2018). We analyze the summed FI XIS, BI XIS and (when available) PIN spectra of individual observations together, and account for known discrepancies between the detectors (notably the FI and BI detectors of XIS, see e.g. Shidatsu et al. 2013 Hori et al. 2018), by applying a global `crabcorr` correction (Steiner et al. 2010) to

[31] normalized to the sum of the ARF weighing factors, see https://heasarc.gsfc.nasa.gov/docs/nicer/analysis_threads/arf-rmf/

each datagroup. This model multiplies the rest of the components by a powerlaw with two parameters, the normalization and a $\Delta\Gamma$ between datagroups. Here, we left the normalization free to vary except for the BI-XIS, which serves as a reference and is thus frozen at 1. The $\Delta\Gamma$ is only left free to vary for the FI-XIS datagroup, and kept frozen at 0 for the others. We also verified that all PIN spectra remain above the systematic uncertainty (3%) of the background modeling of the instrument. As the 2010 low-hard state *Suzaku* observation (ObsID 405051010) ends up with very poorly constrained upper limits for the presence of lines, due to a very low luminosity of $\sim 3 \cdot 10^{-5} L_{Edd}$, we discard this observation from the remainder of this study. he results of the line detection are still accessible in the Appendix tables and Sec. 4.7.

For *NuSTAR*, we analyze the data of each focal plane together, allowing a multiplicative `constant` to vary between the two components. We found no significant discrepancy between the FPMA and FPMB that would warrant the use of the MLI correction model[32] in any of the observations. We restrict the lower bound of our energy band to 4keV, as the residuals strongly deviate from the continuum below this value in every observation. For the upper bound, a dynamical restriction is preferable, since the spectral shape strongly affects at which energies the spectrum remains significantly above the background. The limit is fixed independantly for each focal plane, to the energy where the SNR of the source[33] passes below 3, up to a maximum of 79keV. We also add a common empirical 9.51keV `edge` component tied to both detectors to account for an instrumental feature, in accordance to previous studies of this source (Podgorný et al. 2023; Ratheesh et al. 2024; Rodriguez Cavero et al. 2023).

4.2.2 Simultaneous observations

In a number of bright epochs, the soft X-ray coverage provided by *NICER* or *Suzaku* is complemented by simultaneous *NuSTAR* coverage. While fitting the different instruments together is beneficial, the low-energies (below $\sim$ 10 keV) of *NuSTAR* remain typically very inconsistent with the spectra of the other instruments, and can only be broadly reconciled by applying a very significant $\Delta\Gamma$ (beyond 0.15) to the entire spectrum. Meanwhile, the high energies of *NuSTAR* agree well with the low energy continuum of other instruments without the need of a $\Delta\Gamma$ correction. Since the low-energy spectrum of *NuSTAR* barely provides additional constraints on the lines because of the better spectral resolution and already very high SNR of the spectra of other instruments, whenever there is good agreement between the characteristics of the lines measured by *NuSTAR* and other telescopes, we fit the different instruments together while ignoring *NuSTAR* energies below 8 keV, which allows us to reach good agreement without the need of a slope correction for the *NuSTAR* spectrum.

We make an exception for all observations between 09-03-2023 and 13-03-2023. During this period, several *NICER* and *NuSTAR* observations were triggered to complement the first SPL *IXPE* exposure of this source (Rodriguez Cavero et al. 2023). A Fe xxvi Kα line is detected with very high significance in all *NuSTAR* exposures but not in any of the partially simultaneous *NICER* exposures. This might be the consequence of high variability and lower SNR in the (much shorter) *NICER* exposures, or of the issues in *NuSTAR* absolute energy calibration (see Sec. 3.6). For now, the results of the line detection for these *NuSTAR* exposures are considered independent epochs, distinct from the *NICER* exposures. These epochs are analyzed in more detail in Sec. 4.5.2.

4.2.3 Secondary coverage from *Swift*-BAT and *INTEGRAL*

The coverage of the high-energy band with *Suzaku*-PIN and *NuSTAR* exposures remains limited to $\sim$ 20 daily epochs. While *INTEGRAL* has observed the source for a significant number of revolutions (93), the vast majority were performed before the recent increase in the monitoring of this source thanks to *NICER*, and are typically not simultaneous with soft X-ray instruments or made in conjunction with *Suzaku* and *NuSTAR* (and thus do not provide additional information for our purposes). In addition, a significant portion of *INTEGRAL* soft-state exposures are too short to derive a proper spectrum. On

[32] https://nustarsoc.caltech.edu/NuSTAR_Public/NuSTAROperationSite/mli.php

[33] computed according to
https://xmm-tools.cosmos.esa.int/external/sas/current/doc/specgroup.pdf

the other side, the *Swift*-BAT monitoring provides almost daily coverage of the source, but is lacking in sensitivity and provides very limited spectral information.

However, we can still compute flux estimates using the count rate of both instruments. For this, we take advantage of the very strong correlations between the high-energy flux of the source, its photon index, and the count rate of *Swift* and *INTEGRAL* observations. The full procedure is detailed in Appendix 6.1.2, and provides first order estimates of the [15-50] keV flux, or its upper limit when the source is observed but not detected with BAT and/or *INTEGRAL*.

In addition, the recently released Python library BatAnalysis[34] (Parsotan et al. 2023) allows to compute BAT survey spectra with 8 energy bands from 14 to 195 keV. We thus extracted mosaic spectra of all epochs with low-energy coverage since the launch of BAT, and are in the process of testing the calibration compared to *INTEGRAL* and *NuSTAR* data (extending what has been done in Appendix 6.1.2) to directly perform broad band fits.

4.3 Global behavior

In Table 4.1, we list the numbers of observations analyzed in each of the outbursts covered in this work, and how many of them use the BAT or *INTEGRAL* coverage. To highlight the long-term evolution of the source, we also show a long-term monitoring lightcurve of the last 20 years in Fig. 4.1. Due to the lack of precise measurements for the mass and distance of the source, for the luminosity estimates, we assume a fiducial mass of 8 $M_{\odot}$, and a distance of 8 kpc.

4.3.1 HLD evolution at low and high energies

We plot in the left panels of Fig. 4.1 the unabsorbed Hardness-Luminosity Diagram (HLD) of 4U 1630-47, using the ratio of the intrinsic luminosities in the [6-10] and [3-6] keV bands for the Hardness Ratio, and the [3-10] keV band luminosity in Eddington units. The full sample provides a near complete coverage of the typical evolution of the source above luminosities of $\sim 10^{-2} L_{Edd}$, although spread over different outbursts. The vast majority of soft state observations follow a very narrow diagonal, as expected for highly-inclined binaries (Muñoz-Darias et al. 2013), and the recent observations (notably from the high cadence *NICER* monitoring of the outbursts after 2017) confirm the already reported disappearance (or at least strong decrease) of the absorption lines above a HR value of ∼0.4-0.45 and $L_{3-10} \sim 10^{-1} L_{Edd}$ (see e.g. Diáz Trigo et al. 2014). Nevertheless, a significant part of the *NICER* observations in softer states are non-detections with upper limits far too low to be compatible with the detections seen in other observations at very similar HR and luminosity.

Since the standard HLD lacks information about the hard X-rays above 10 keV, which can affect the properties of the plasma producing the absorption lines, we construct a new "hard" HLD, replacing the 3-6 keV Hardness Ratio (hereafter HR_{soft}) by the [15-50]/[3-6] keV Hardness Ratio (hereafter $\mathrm{HR_{hard}}$). The [15-50] luminosity is the most direct way to use the BAT monitoring, and the [3-6] band matches the peak of the `diskbb` component, while remaining less affected by uncertainties in interstellar absorption, calibration issues and the DSH, compared to a wider, softer band. For the y axis, we keep the [3-10] keV Eddington ratio, for an easier comparison with the soft HLD. The hard HLD is presented in the right panel of Fig. 4.1, using shaded markers for epochs where the [15-50] keV estimates are not at least 2 σ significant.

This new diagram significantly improves the separation between the states with lines and the states without detections. The EW of the absorption lines is clearly anti-correlated with $\mathrm{HR_{hard}}$ (which we confirm quantitatively in Sec.4.3.2), which explains the lack of detections in harder states, as above $\mathrm{HR_{hard}} \sim 0.1$ the expected EWs of the lines becomes too low to be detected in most observations. Among the few detections with high EWs (≥ 20 eV) above $\mathrm{HR_{hard}} \sim 0.1$, most are associated to non-significant BAT detections, which are thus compatible with much lower $\mathrm{HR_{hard}}$ values, and the remaining 2 are still compatible with sufficiently low $\mathrm{HR_{hard}}$ values to match the rest of the observations within

[34] https://github.com/parsotat/BatAnalysis

Table 4.1: List of outbursts covered in our sample, number of observations suitable for line detection with each instrument, and number of observations with additional high-energy telescope from monitoring (see Sec. 4.2.3). ⋆ All the 2015 and 2022-2023 *NuSTAR* exposures are simultaneous to *Suzaku* and *NICER* observations, and only the 4 2023 observations are considered independently (see section 3.2) and highlighted in the figure below. † I am currently analyzing additional observations of this outburst, starting from the end of 2023.

Outburst period	Outburst type	Observations					High-E monitoring	
		Chandra	*NICER*	*NuSTAR*	*Suzaku*	XMM-*Newton*	*Swift*-BAT	*INTEGRAL*
2002-2004	super (triple)	**1**	0	0	0	0	0	1
2006	standard	0	0	0	**6**	0	/	/
2010	standard (double)	0	0	0	**1**	0	/	/
2012-2013	super (triple)	**7**	0	**2**	**2**	**8**	15	/
2015	standard	0	0	**2**⋆	**3**	0	1	/
2016-2017	standard	**1**	0	0	0	0	1	/
2018	standard	0	**33**	0	0	0	32	0
2020	standard	**3**	**39**	0	0	0	42	/
2021-2022	standard (double)	0	**29**	0	0	0	29	/
2022-2024	super (double)	0	**71**†	**7**⋆	0	0	61	1
Total		12	172	11	11	8	180	2

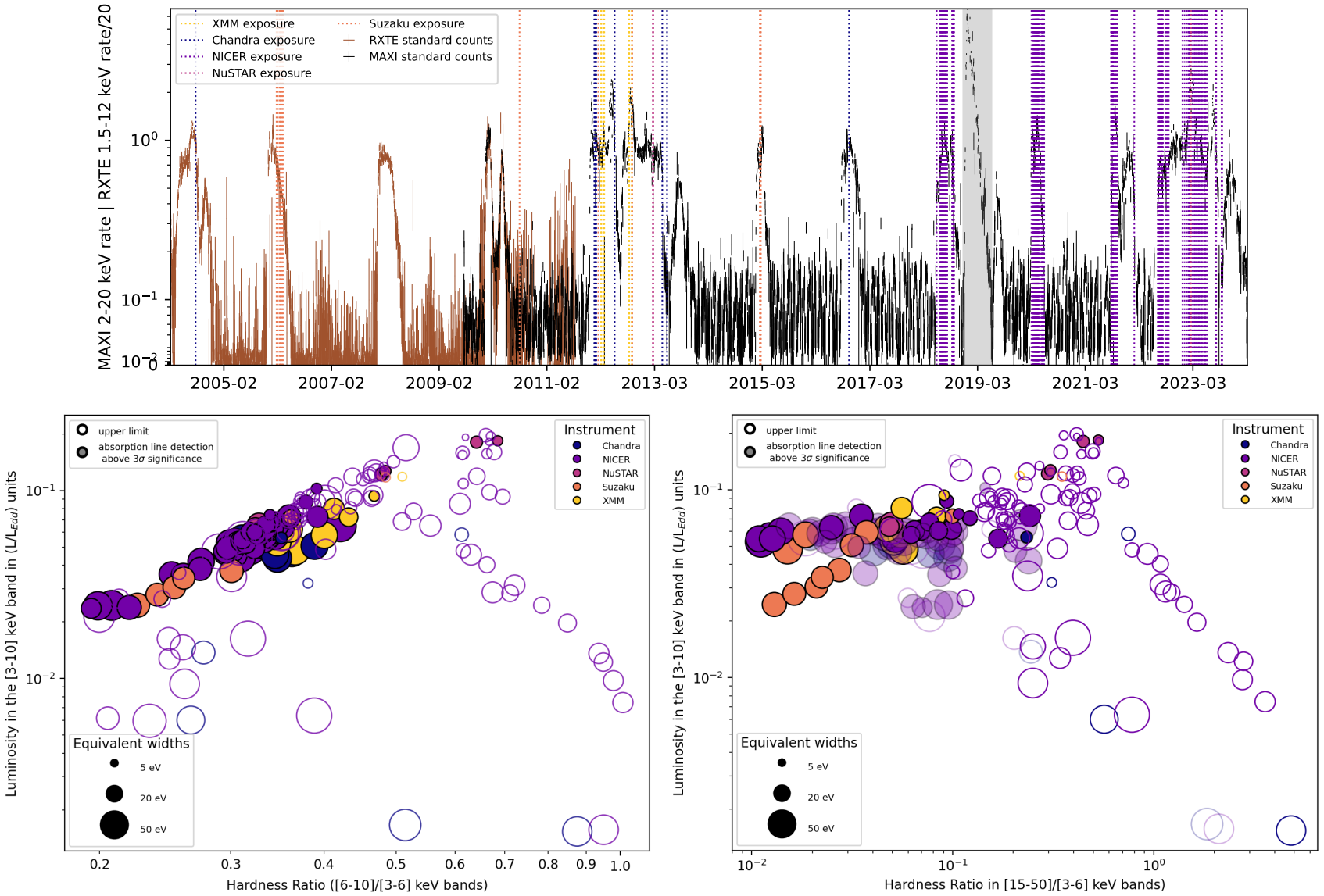

Figure 4.1: **(Top)** Long-term *RXTE*/*MAXI* Lightcurve of 4U 1630-47, with exposures used for line detections highlighted by dashed vertical lines. The greyed zone highlights contamination by the 2018 outburst of the nearby BHXRB MAXI J1631-479 (Miyasaka et al. 2018).
(Bottom) Multi instrument "soft" **(left)** and "hard" **(right)** HLDs of 4U 1630-47, colored according to instruments. In the right panel, transparent markers indicate the position of 1σ HR upper limits in non-significant detections (see Appendix 6.1.2). Similar plots for individual outbursts are presented in Sec. 4.7

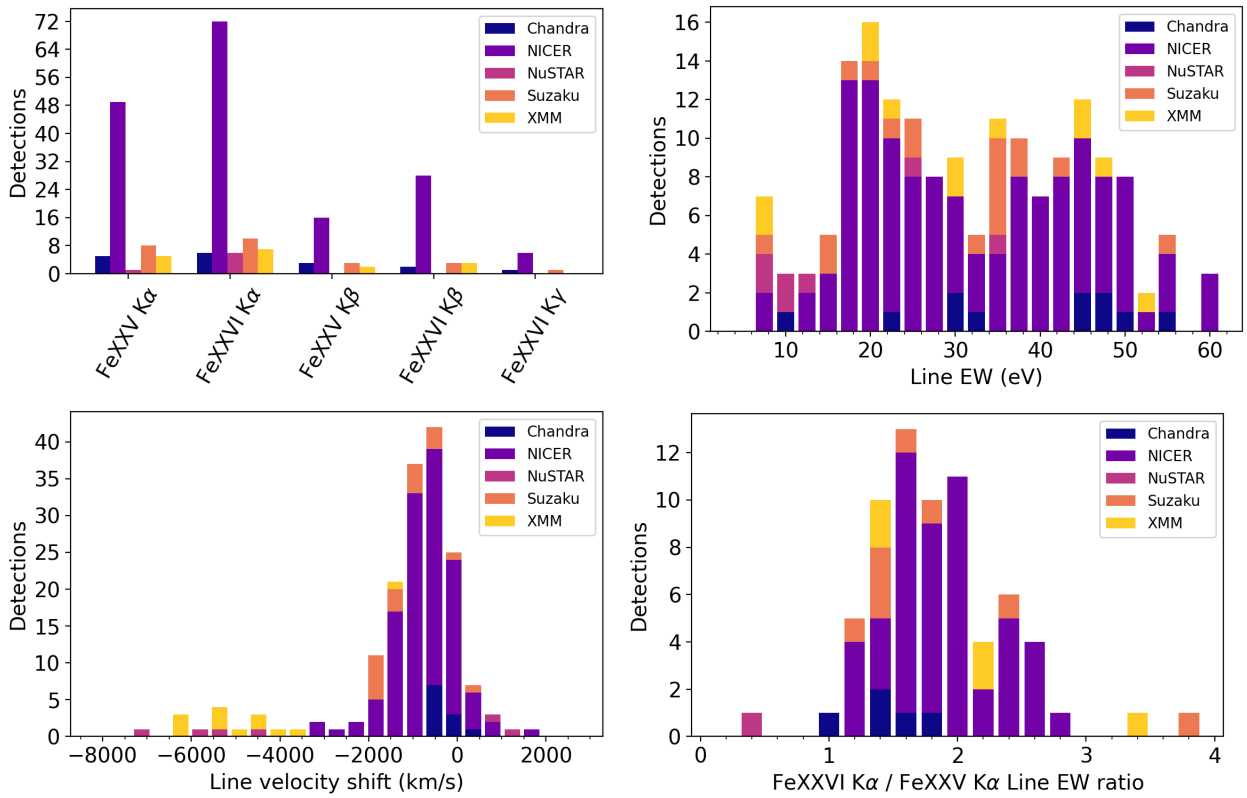

Figure 4.2: Distribution of intrinsic line parameters (detections of each line, EW, Kα complex blueshift and Kα EW ratio) for the entire sample, split by instrument.

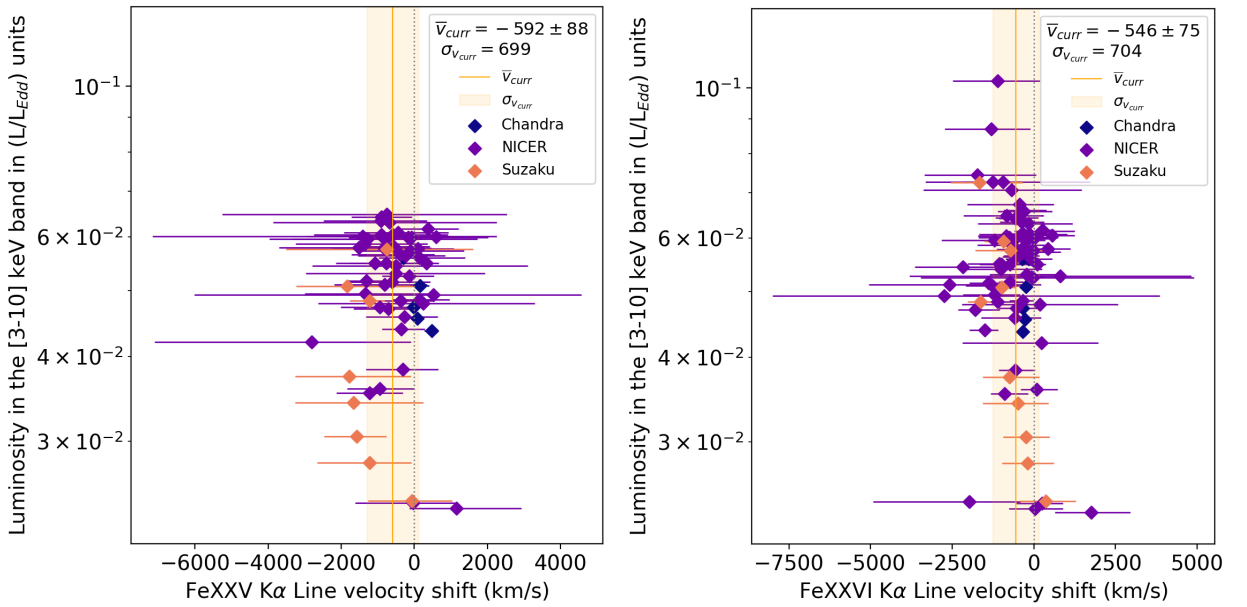

Figure 4.3: Global scatter plots of the velocity shifts of each of the K α lines for the three instruments with the best line calibration. In each plot, the orange line and region highlight the mean and variance of the current distribution

errors. Meanwhile, the few constraining upper limits with low HR_{hard} values systematically have high uncertainties and are compatible with $HR_{hard} \gtrsim 0.1$. In addition, the majority of these low HR_{hard} non-detections show hints of weak lines, although not significant enough to be reported.

4.3.2 Parameter distribution and correlations

We study the behavior of the absorption lines and quantify the influence of the continuum SED by computing the distribution of gaussian parameters, as well as statistically significant correlations between line parameters and continuum parameters at low and high energy. To compute the correlations, we use MC simulations of the Spearman coefficient and p-values, similarly to Chap. 3.

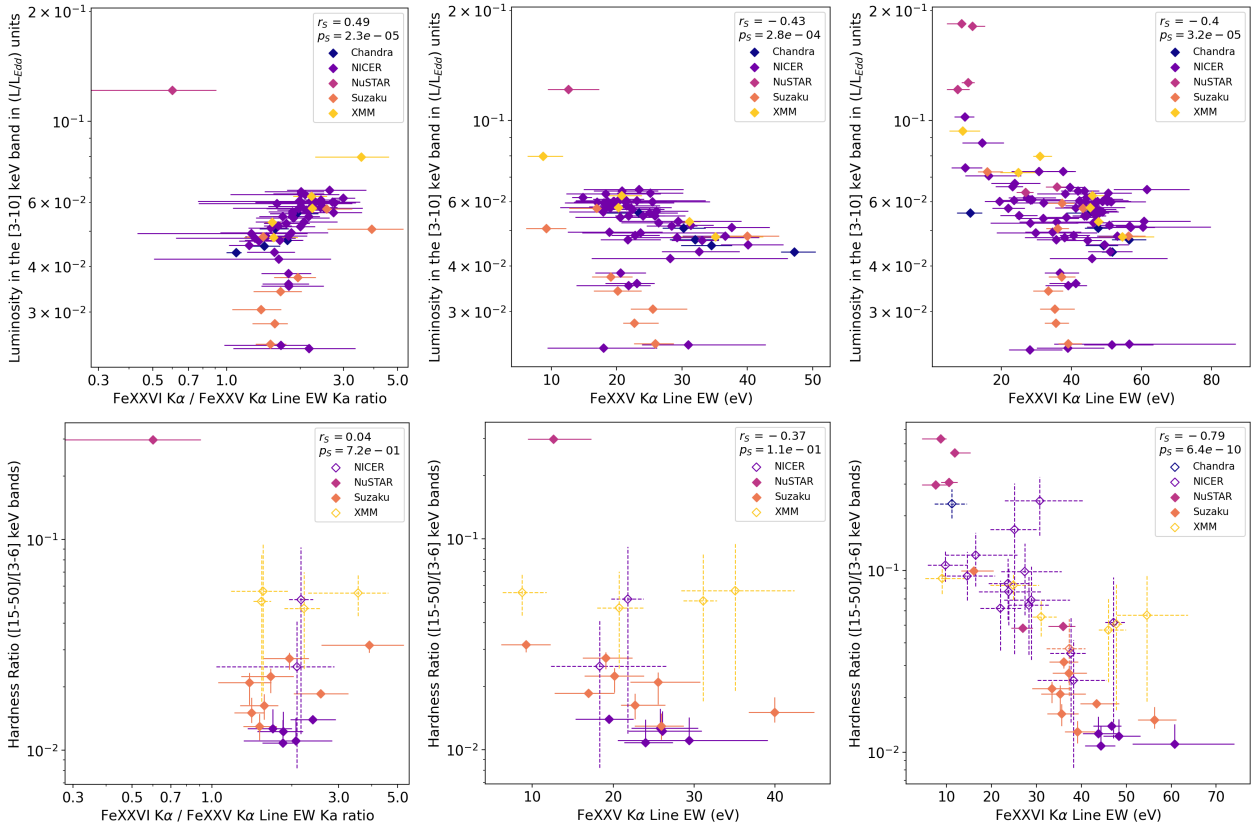

Figure 4.4: Global scatter plots of line parameters against soft X-ray luminosity (top) and the hard X-ray Hardness Ratios (bottom). In the bottom panels, the markers are dashed for epochs with a high-energy flux converted from BAT or *INTEGRAL*, and full markers observations with simultaneous high-energy coverage from *NuSTAR* or *Suzaku*-PIN.

Parameter distribution

The main properties of the absorption lines in our sample are the number of individual lines detected, their EWs, and in the case of the better constrained Kα complex, the line blueshifts and the ratio between the EW of the lines. We show the corresponding distributions in Fig. 4.2. We split them among the different instruments mainly for the sake of visualization, as except for the velocity shifts, the differences between individual distributions are too small to be significant, considering the limited number of detections for all instruments except *NICER*.

The distribution of main parameters follow both the trends previously established for wind-emitting sources in general, and the individual results obtained for 4U 1630-47 with *Chandra* and XMM-*Newton* specifically (see e.g. Diáz Trigo et al. 2014,Gatuzz et al. 2019, Chap. 3). The proportion of detections matches the differences in strength between the iron lines, and the sampling of *NICER* confirms that individual line EWs remain below $\sim$ 60 eV, pointing towards ionic column densities and FWHMs of the order of what was measured in Chap. 3 for the few lines resolved in *Chandra*-HETG. On the other side, the lines are being detected down to 8-10eVs depending on the instruments. The velocity shift distributions confirms the bias of XMM-*Newton* towards high blueshifts reported in Chap. 3, with *NuSTAR* showing similar behavior, at odds with the rest of the instruments.

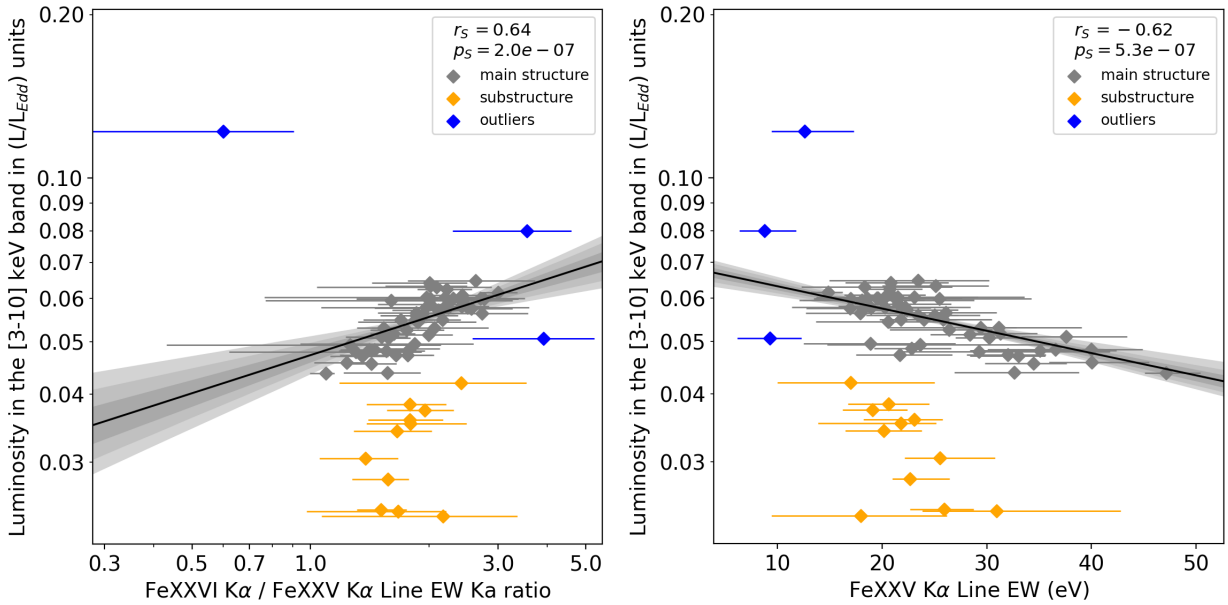

Figure 4.5: Global scatter plots of the Fe Kα EW ratio **(Left)** and Fe xxv Kα EW**(right)** against luminosity. In the left panel, EW ratio lower limits are plotted for observations with only Fe xxvi Kα detected, and the black line and grey region show the extent of the log-log linear correlation and its 1,2 and 3σ confidence intervals. Both these and the spearman rank are computed only from observations of the main structure (in grey).

When restricting the distribution to *Chandra*, *NICER* and *Suzaku*, the velocity shift distribution has an average of $\overline{v_{out}} \sim -560 \pm 60$ km/s, with a standard deviation of ~ 700 km/s. However, this result does not factor *NICER*'s absolute energy accuracy of 5 eV (Markwardt et al. 2023), or ~ 220 km/s at the Kα lines. Still, even adding this systematic, the average of the distribution remains very significantly distinct from 0, pointing at very low but systematic blueshifts in this source, fully compatible with the results obtained for *Chandra*-HETG only in standard wind-emitting sources in Chap. 3. The Fe xxv Kα and Fe xxvi Kα individual distributions, which we show in Fig. 4.3, remain extremely similar, with $\overline{v_{out\,K\alpha,25}} \sim -590 \pm 90$ km/s, $\overline{v_{out\,K\alpha,26}} \sim -550 \pm 75$ km/s, and standard deviations of ~ 700 km/s for both.

Finally, we show in the last panel of Fig. 4.2 the distribution of the EW ratio of the Fe Kα complex, defined as the ratio of the EWs of the Fe xxvi Kα and Fe xxv Kα lines and used as a proxy of the ionization parameter. The present sample confirms the trend previously seen in other standard wind-emitting sources: almost all common detections of the $K\alpha$ complex have an EW ratio above 1, with a single detection (*NuSTAR* in 2023) below as a possible outlier.

Significant correlations

We do not measure any significant correlation between the line parameters themselves, and notably no link between the EW of each line and their velocity. However, this may be due to the very high uncertainty of the velocity measurements with all instruments except *Chandra*. When restricting to *Chandra* only, we see a hint of correlation between the Fe xxv Kα velocity and EWs (higher EWs being associated to redshifts). However, this is a natural consequence of the contamination by lower-E satellite lines for lower ionization when using a single gaussian to model the line, as seen in Chap. 3 for GRS 1915+105. The number of observations with such line detections (6) remains too low for any other conclusion.

As there are no notable correlations between the line parameters themselves, we focus on their behavior compared with the continuum, both at low energy (HR_{soft},L_{3-10}) and at high-energy ($\mathrm{HR_{hard}}$,L_{15-50}, Γ_{thcomp}). We first note a lack of correlation between the EW of the lines and the soft Hardness Ratio, similarly to what we obtained for the global wind-emitting sample. This is however not the case for the luminosity: as we show in the upper panels of Fig.4.4, the Fe xxv Kα EW, Fe xxvi Kα and $K\alpha$ EW ratio are all significantly correlated with the soft X-ray luminosity, with $p_s \sim 2 \times 10^{-5}$, $r_s = 0.49$ for the EW ratio correlation, $p_s \sim 3 \times 10^{-4}$, $r_s = -0.43$ and $p_s \sim 3 \times 10^{-5}$, $r_s = -0.4$ for the Fe xxv Kα and Fe xxvi Kα EWs

respectively. These trends match both what was found for the global wind-emitting sample in Chap. 3 and the individual correlations which were already present using only XMM-*Newton* and *Chandra*, but not significant due to the low number of observations.

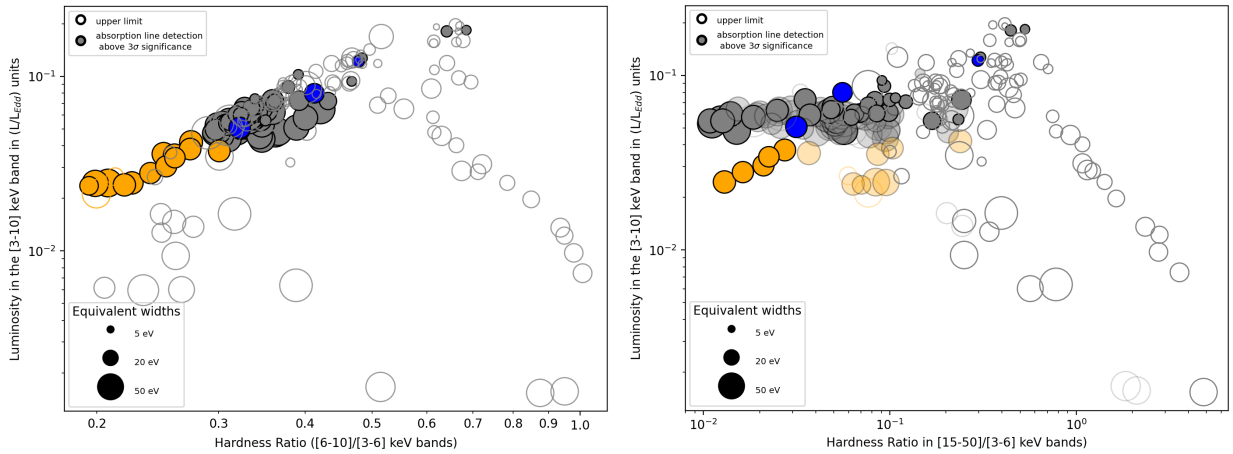

Figure 4.6: Multi instrument "soft" (left) and "hard" (right) HLDs of 4U 1630-47, colored according to the substructure and outliers defined in Sect. 4.3.3 and Fig. 4.5

The main difference from the global sample of Chap. 3 is the number of observations that clearly depart from this common structure, notably at the highest and lowest luminosities. A simple way to quantify their effect on the correlations is to compare the correlation coefficients with and without them: by removing all observations below $L/L_{Edd} \sim 4 \cdot 10^{-2}$ and above $L/L_{Edd} \sim 10^{-1}$, the spearman rank p-values drop from $p_S = 2.3 \cdot 10^{-5}$ to $p_S = 5 \cdot 10^{-7}$ for the Kα EW ratio, and from $p_S = 2.8 \cdot 10^{-4}$ to $p_S = 7.5 \cdot 10^{-7}$ for Fe xxv Kα. On the other hand, the p-value of Fe xxvi Kα only decreases by a factor ~ 2. Due to the very high significance of this evolution, we discuss these regions in more detail in Sect. 4.3.3.

When focusing on high energies, we first note a very strong correlation between $\mathrm{HR_{hard}}$ and the Fe xxvi Kα EW, with $p_s = 6.4 \cdot 10^{-10}$ and $r_s = -0.79$, contrasting with the lack of correlations of the individual line EWs. The other parameters still see hints of structured behavior, but the sample size remains too limited for any definitive conclusion. We plot the 3 different correlations in the lower panels of 4.4. On the other hand, the correlations of the line parameters with L_{15-50}, turn out mostly identical, although with more spread. All of these aspects strongly contrast with the behavior at low energy, as in the 3-10keV band, theFe xxvi Kα EW has significantly more spread than the other line parameters, which all correlate with the luminosity. In addition, none of the line parameters are correlated with HR_{soft}.

Finally, we do not see a single significant correlation between the thcomp Γ and the line EW parameters. This may be due to the few amount of observations with *NuSTAR* or *Suzaku*-PIN spectra, combined with the line detections largely favoring soft states, where the hard X-ray flux is too low for Γ to be well constrained.

4.3.3 Characterizing sub-structures

We now focus on the upper left and upper middle panels of Fig. 4.4, in which a portion of the detections with low luminosity and low EWs seems to detach from the main structure. These observations drive the Spearman rank and p-values down significantly (around than two orders of magnitudes for the latter, as discussed in the previous section). In Fig. 4.5, we visually identify in yellow the observations of this "sub-structure" , defined as below $L_{[3-10]}/L_{Edd} = 4.2 \cdot 10^{-2}$. To compare the behavior of both groups, we compute log-scale linear regressions for the observations in the main structures (in gray), along with their confidence intervals. All observations in the substructure end up very distant from the linear regression and its 3 σ envelope.

We also highlight three distinct outliers in blue, which, substructure aside, are the most distant observations from the regressions, being the only ones further than 3σ (all are beyond 7 σ) from the regression. The outlier at highest luminosity, above $L_{[3-10]}/L_{Edd} = 10^{-1}$, is the *NuSTAR* SPL observation with a Fe xxv Kα detection (ObsID 80902312002), from march 2023. The detailed behavior of this

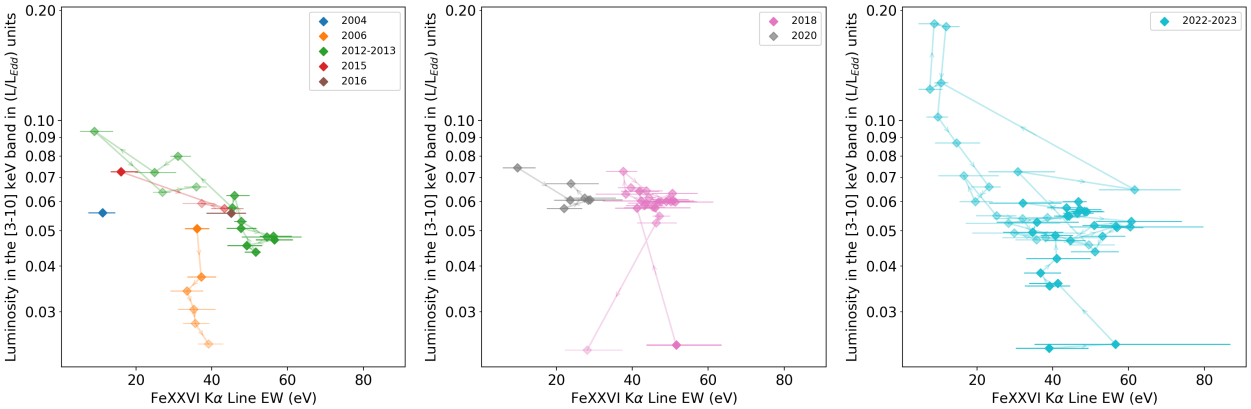

Figure 4.7: Global scatter plots of the Fe xxvi Kα EW and [3-10] keV band luminosity, color-coded according to their outburst and split for legibility. Arrows and increasing transparency highlight the time evolution in each outburst.

observation is left for a future work. The second observation, at $L_{[3-10]}/L_{Edd} \sim 8 \cdot 10^{-2}$, is a XMM-*Newton* observation from 2013 (ObsID 0670673001_S003), at the beginning of a state transition (Diáz Trigo et al. 2014). The third, at $L_{[3-10]}/L_{Edd} \sim 5 \cdot 10^{-2}$, is the first and brightest of the set of 2006 *Suzaku* observations (ObsID 400010010) during the source's declining soft state. Interestingly, the behavior of this observation in the scatter plots (higher EW ratio and lower Fe xxv Kα EW than the main structure) matches the line behavior of the low-luminosity substructure.

In parallel, we consider the disposition of these observations in the HLDs, which is plotted with the same color coding in Fig. 4.6. In the soft HLD, the substructure forms the lower end of the main soft state diagonal, which is much less populated than the higher luminosity ranges above $\sim 4 \cdot 10\text{—}2 L_{Edd}$. In the hard HLD, the observations in the substructure with good constrains on the high-energy flux(represented by fully colored circles, c.f. Fig.4.1) are much more distinct from the main group, with both a lower L_{3-10} for the same $\mathrm{HR_{hard}}$ and a clear correlation between the two. Meanwhile, the other substructure observations (without *Suzaku*) lack good simultaneous BAT measurements, resulting in very high $\mathrm{HR_{hard}}$ upper limits. However, neighboring days of monitoring strongly suggest that their $\mathrm{HR_{hard}}$ values are much lower than presently displayed upper limits, in line with the more constrained observations. It is also worth noting that the observations of the substructure are systematically part of either the very first raise or the final decay to quiescence of their respective outbursts, while the usual soft-state "back and forth" patterns often seen for 4U 1630-47 are generally restricted to the brighter portion of the diagonal.

Finally, we can look more in depth at the behavior of the third panel of Fig. 4.4, which is the correlation with the most spread in the bulk of the soft state. We focus on the evolution of this correlation with time, splitting different outbursts in the panels of Fig. 4.7. The different outbursts evolve very differently: only the 2012-2014 super outburst (left panel, green) and post 2023 part of the 2022-2024 super outburst outburst (right panel, transparent cyan) follow a clear, structured path, with both of these periods having individual Spearman p-values below 10^{-4}. These two are the main drivers of the low p-value for the global correlation in Fig. 4.4. On the other hand, the normal outbursts appear much more spread out in individual clusters, but they are sampled much more scarcely, both in terms of duration and HLDevolution. This is partly due to super outbursts remaining in the soft state for much longer periods than normal outbursts. Some differences between individual periods (such as 2018 and 2020 in the middle panel) remain clear, but could be imputable to other parameter changing, such as $\mathrm{HR_{hard}}$. A more complete sampling of normal outbursts in both soft and hard X-rays is thus necessary to disentangle potential wind evolution between outbursts from changes in SED of individual soft states, as we will confirm in Sec. 4.4.2.

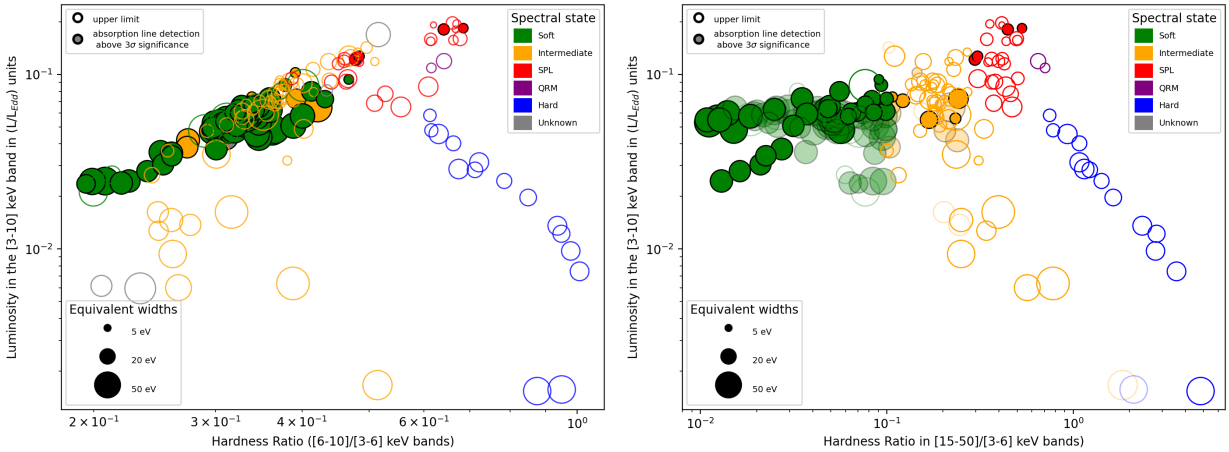

Figure 4.8: Soft **(left)** and Hard **(right)** HLDs of 4U 1630-47, colored according to the spectral states defined in Sec. 4.4.

4.4 Wind evolution along the spectral states

The evolution of the absorption lines seen in the observations can be the sign of intrinsic changes in the outflow properties, but also the consequence of the changes in the SED. To distinguish the two, two main effects need to be considered: the stability of the plasma, and the evolution of its ionization. Here, we assume that both the SEDs and the properties of the outflow themselves do not vary significantly on the timescale of the thermal equilibrium of the plasma.

4U 1630-47 evolves between complex accretion states, with a combination of specific spectral and timing properties, which time-integrated spectra and the HLDs alone does not fully encompass. However, when computing the products of each instrument, we also computed individual lightcurves in several bands. This allowed us to verify that the sources did not significantly vary on the timescale of the observation, in the overwhelming majority of cases. After discarding the very few exceptions to this rule (see Sec. 4.5), and the observations in which no good hard X-ray constrain is available, we can regroup the behavior of the source in five basic states. We display the different states in both HLDs in the upper panels of Fig. 4.8. Our distinction follows the following criteria:

- The "soft" state (green) is restricted to observations with $HR_{hard} < 0.1$, which is the limit below which virtually all observations with good constrains show absorption lines. It is characterized by a spectrum dominated by a thermal component, and a very small (if at all) amount of disk comptonization.
- The "hard" state (blue) is restricted to observations with a weak or negligible disk component, and dominated by a hard component with $\Gamma \lesssim 2.5$.
- The "intermediate" (orange) and SPL (red) states correspond to observations where there is still an important disk component, but the spectrum shows a noticeable contribution at high energies. In the canonical definitions of Tomsick et al. (2005), three different states (intermediate, flaring, and SPL) are distinguished by their disk contribution, flux, high energy Γ, and timing properties. Here, because we lack the temporal information to perform proper distinctions, we regroup together the intermediate and flaring states (which are very similar except for their variability) and define the SPL states as the hardest ($HR_{hard} \gtrsim 0.3$) and brightest ($L_{[3-10]}/L_{Edd} \gtrsim 0.05$) of the intermediate states, which matches the Tomsick et al. (2005) spectral definition.

Finally, we highlight in purple the observations in which the source exhibits Quasi-Regular Modulations (QRM), very low-frequency QPOs (also called mHZ QPOs) with high RMS ($\sim 10-20\%$). These timing properties have been previously seen in few other sources in hard states: in X-rays for BHLMXBs, GRO

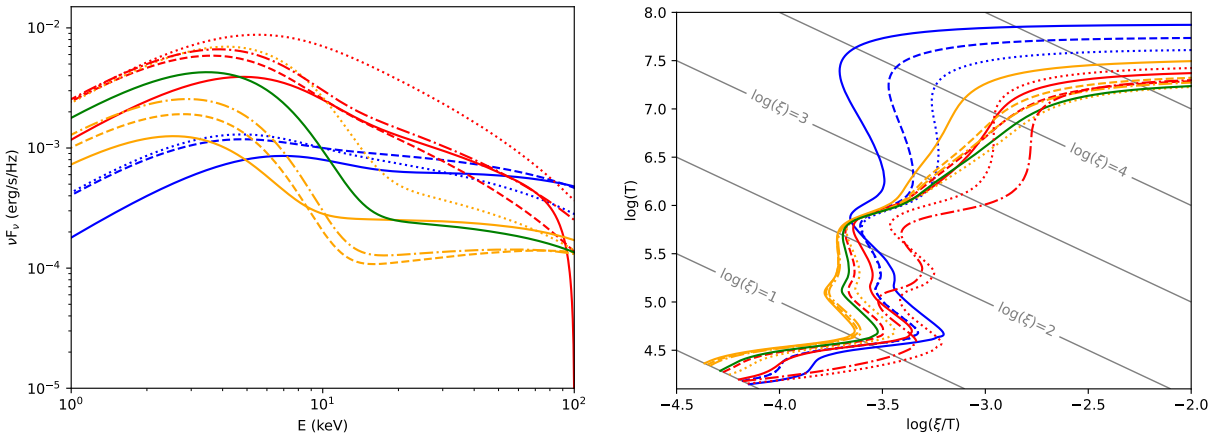

Figure 4.9: Unabsorbed SEDs **(left)** and corresponding stability curves **(right)** for few SEDs in each states, sampling observations from Fig. 4.8.

J1655-40 (Remillard et al. 1999), H 1743-322 (Altamirano & Strohmayer 2012), MAXI J1348-630 (Wang et al. 2024b), and previously in 4U 1630-47 in 1998 (Trudolyubov et al. 2001; Zhao et al. 2023) and 2021 (Yang et al. 2022). We distinguish these states from the so-called "heartbeat" states seen in IGR J17091-3624 (Altamirano et al. 2011; **?**) and GRS1915+105 (Neilsen et al. 2011; Zoghbi et al. 2016), which are soft, with systematic wind detections, and even higher RMS(up to $\geq 40\%$), and "flip-flops" which typically occur at the very end of a hard-soft spectral transition (Bogensberger et al. 2020). On the other hand, QRM states are hard, powerlaw dominated, with no signs of absorption lines. In 4U 1630-47, QRM states occupy a very well defined region of the HLD. We consider this as a "transition" state because the two previously reported detections in 4U 1630-47 signaled the transition from the canonical "hard" state into a SPL-like state. In several other sources, the QRMs are also seen just before or just after state transitions, e.g. H1743-322 (Altamirano & Strohmayer 2012) and MAXI J1348-630 (Wang et al. 2024b). We note that in our sample, beside the 2021 QRM-state seen with *NICER*, we discovered another observation with clear QRMs during the 2022-2024 outburst (obsid 6130010109), which this time occurred before the transition from SPL and soft states. A detailed analysis of this observation is out of scope of this study, but we note that its spectral properties match very well that of the 2021 QRM period. We shall come back to QRM observations in Sec. 4.5.3.

To complete, we highlight in gray in the soft HLD the observations without simultaneous hard X-ray coverage and thus no identification. We also remove from both HLDs two hard state observations during the 2021 outburst, where the *NICER* observation happened during very short hard flares. In both cases, the BAT daily average count rates are much lower than the peak seen in individual snapshots corresponding to the *NICER* period and thus the hard HLD value would be artificially softer.

4.4.1 Influence of plasma stability

The global hard X-ray coverage provided by *NuSTAR*, *Suzaku*, *Swift*-BAT and *INTEGRAL* allows, for the first time in an XRB, to compute the evolution of the plasma stability (Krolik et al. 1981) along the entire path of the source in the HID. We can then assess whether the correlation between the disappearance of the lines and the increase in HR_{hard} is the consequence of the favorable ionization states for Fe XXV and Fe XXVI becoming progressively unstable as we move to harder states and SEDs.

We thus computed stability curves using CLOUDY, from a range of observations in each of the previously defined accretion, prioritizing observations with good high energy coverage, from which we extracted broad band, unabsorbed SEDs in the 0.01-1000 keV band. We show the results in the lower panels of Fig. 4.9, highlighting different ionization parameters. Previous studies with detailed photoionization modeling of the absorption line features seen in *Chandra* spectra have led to estimates of $\log\xi_i \sim 3.5-4$ for the main absorption zone in soft and intermediate states (Gatuzz et al. 2019; Trueba et al. 2019). In this ionization range, all observations in the soft, intermediate, SPL and QRM

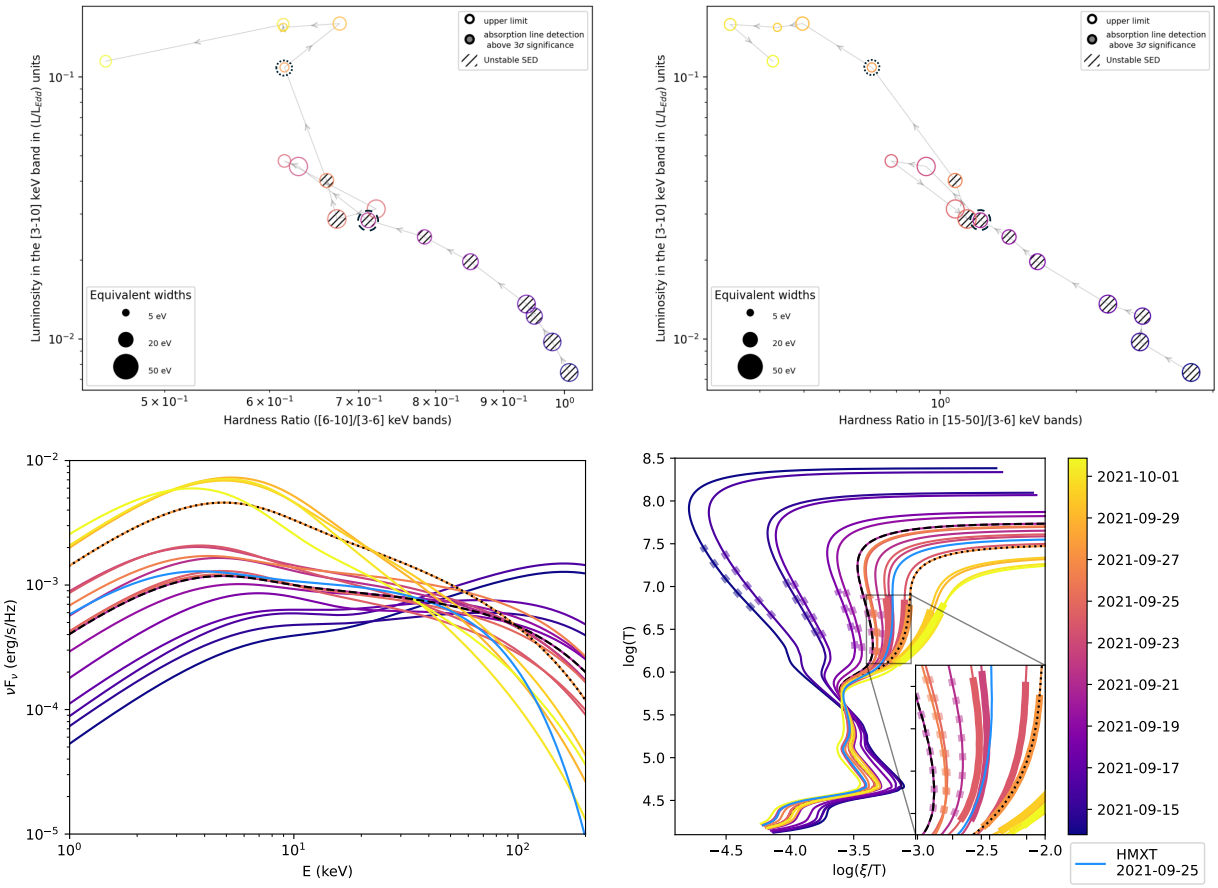

Figure 4.10: Evolution of the beginning of the 2021 outburst of 4U 1630-47, seen in the Soft (upper left) and Hard (upper right) HLDs, corresponding unabsorbed SEDs (lower left), and stability curves (lower right). The regions bolded in the stability curves shows the 90% ionization range of Fe XXV and Fe XXVI, and are dotted when mostly unstable. The black overplotted circles (top) and lines (bottom) highlight the observation simultaneous with a radio jet (dashed) and radio ejecta (dotted). The light blue SEDs and stability curves are derived from the fit parameters of Yang et al. (2022) in their last pre-transition observation.

states are completely thermally stable, in accordance with previous results for this source (Gatuzz et al. 2019). Stability effects thus cannot explain the decrease in absorption line EW between soft and intermediate/SPL states.

Unexpectedly, the hard states also retain a stable region around $\log\xi_i$ ~2.5-3., which corresponds to a non-negligible ionic fraction of (notably) Fe XXV for such SEDs (see e.g. (Chakravorty et al. 2013; Petrucci et al. 2021)). To the best of our knowledge, this is the first time that a stable region at this $\log\xi$ range is found in a BHLMXB hard state. Its existence stems from the unexpectedly steep comptonized component of 4U-1630-47: in most LMXBs, both NS and BHs, hard states typically show a $\Gamma \sim 1.5-2$. high-energy component, and are completely thermally unstable (see e.g. (Bianchi et al. 2017; Petrucci et al. 2021). Here, on the other hand, the "softer" hard states reach up to $\Gamma \gtrsim 2.3$ before the transitions to the QRM state. We stress that these high photon indexes are not a specificity of the recent outbursts, whose hard state was sampled by *NICER*, as our results remain in line with other hard state measurements obtained during previous outbursts of this source (Seifina et al. 2014).

This thermally stable ξ_i region has strong implications on the detectability of wind signatures via highly ionized absorption lines in hard states, which could give new constrains on the disk-wind geometry and allow for direct comparisons with the cold winds seen in OIR. We thus investigate the transition from unstable to stable SEDs in more details. For that, we take advantage of the detailed *NICER* coverage of the hard state rise at the beginning of the 2021 outburst, and compute the stability curves of the first 18

observations, sampling from very unstable hard states to the SPL, well after the SEDs have become stable. To maximize our constrain on the broad band SEDs, here, we directly fit the *NICER* spectra together with daily BAT survey spectra derived with BaTAnalysis, for a total energy coverage of 0.3 − 195 keV. In order to account for potential BAT calibration uncertainties, we allow for a variation of 30% in the constant factor of the BAT datagroup during the fit, and keep the `thcomp` cutoff frozen at 100 keV since it remains unconstrained even with BAT spectra.

We plot the HLDs, SEDs and stability curves of these observations in Fig. 4.10, highlighting stable SEDs in the HLDs for the ionization range dominated by Fe XXV and Fe XXVI. The first half of the hard state observations exhibit more standard (although relatively steep compared to other binaries) Γ values of ~ 2, and are all largely unstable. The latter observations before the QRM, with $\Gamma \sim 2.2-2.4$, are either very close to stability or barely stable, and after the QRM state, all observations in the SPL are much softer ($\gtrsim 2.7$) and completely stable down to much lower ionization parameters. This would indicate that there is a short period at the very end of the hard states (below $HR_{hard} \sim 0.1$, as seen in the HLDs) where the SEDs would not prevent the apparition of wind signatures from highly ionized iron.

There are nevertheless some caveats in our SED derivation, due to the large uncertainties of BAT measurements at high energies. In comparison, when analyzing *HXMT* observations during the same period (just before the transition to the QRM state), Yang et al. (2022) report high energy rollovers down to $kT_e \sim 20$ keV. A lower energy cutoff would tend to reduce the amount of hard photons, and thus stabilize the plasma, but this effect may be negligible as the physical cut-off happens at $E \gtrsim 2-3kT_e$ (see Miyakawa et al. 2008; Petrucci et al. 2001; Zdziarski et al. 2021a). As a sanity check, we thus compute the stability curve of the average "pre-QRM" epoch of (Yang et al. 2022), using their reported model parameters to reproduce the SED. The results, displayed in cyan in the lower panels of Fig. 4.10, are in very good agreement with our own SEDs for the last hard state periods, cutoff aside, and most notably result in almost identical (stable) stability curves.

We note that Yang et al. (2022) classify the "pre-QRM" observations as "intermediate states", notably from their position in the HLD. This raises an important point of whether such "soft" SEDs, although dominated by a comptonized component, should be interpreted as the signature of canonically "hard" accretion states. First, the timing properties they report for this period, such as the type-C QPO quality factor and important continuum RMS ($> 20\%$), are much more in line with the hard state than with the SPL state according to their definition in (Tomsick et al. 2005). Secondly, a weekly radio monitoring was performed during this period (Zhang et al. in prep), including observations on the 20-09, which corresponds to our seventh observation, and on the 27-09, during the QRM state. We highlight the corresponding X-ray observations in black in Fig. 4.10. The strong evolution in radio spectral index between the the radio detection signals a change from a compact jet on the 20-09 (black dashes), to a radio ejecta on the 27-09 (black dots). This provides a very strong argument to consider all of the observations before the 27-09 (which all show SEDs and timing properties similar to the 20-09 observation) as coming from a canonically "hard" accretion-ejection structure, and for the QRM state to be the consequence of a significant change in the accretion flow.

4.4.2 Influence of ionization changes

The second element affecting the ionization structure is the influence of the SED on the ionization range with high ionic fractions of Fe XXV and Fe XXVI. In order to correct for this effect, we compute the EW response of each line to an SED independent wind parameter. Since we are interested in any type of change in the wind, we assume a single fiducial N_H and turbulence value across all observations, then derive the EW response of each line to the ionization parameters with the SED of each observations, which are then divided by their respective luminosities. For now, we only apply this process to few observations with good high-energy coverage (including *NuSTAR* or *Suzaku*-PIN coverage) distributed along the HLD and EW plots, as we show in the upper and middle panels of Fig. 4.11.

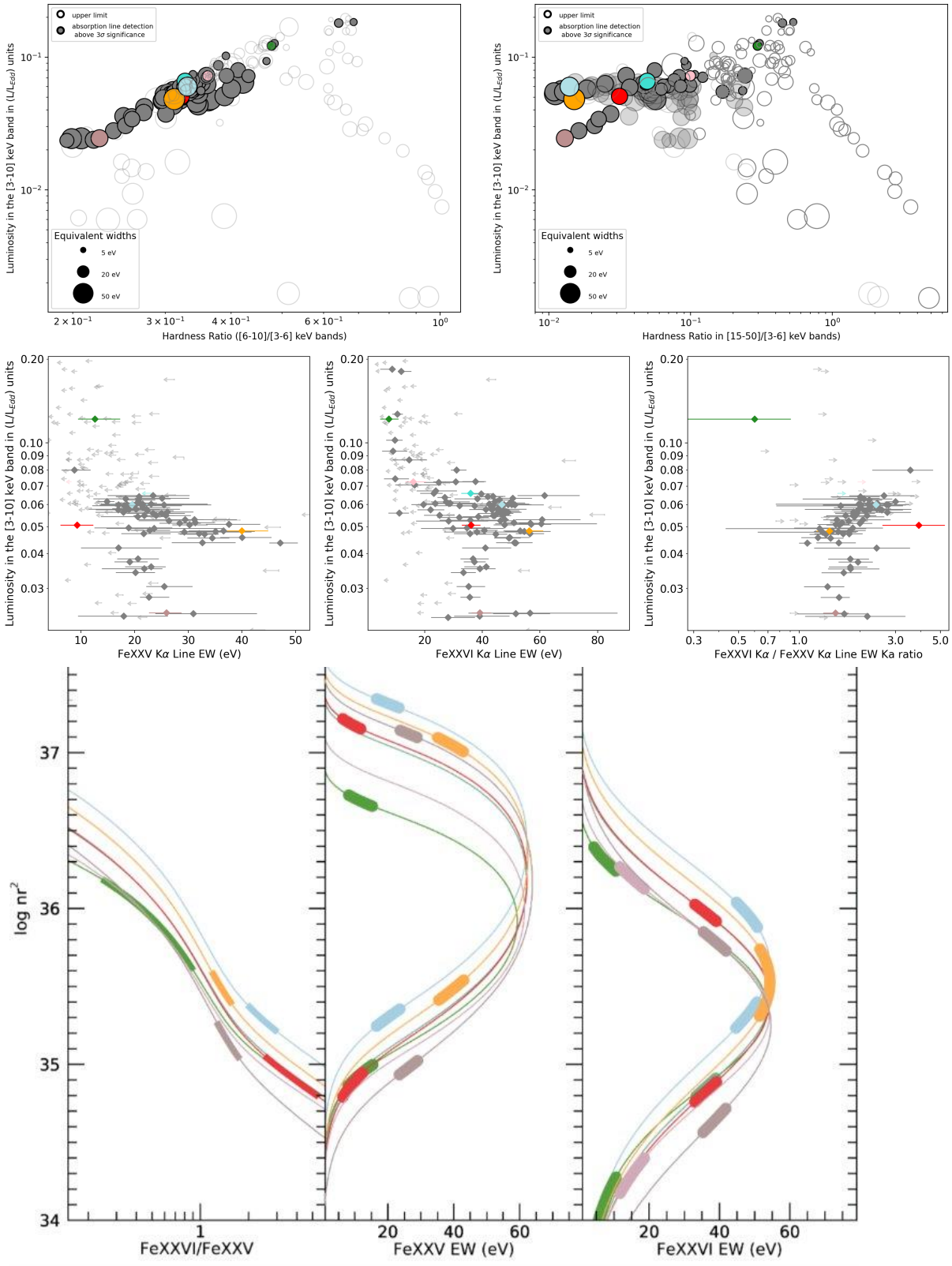

Figure 4.11: **(Top)** soft **(left)** and hard **(right)** HLDs highlighting specific observations sampling different portions of the wind structure. **(Middle)** Global scatter plots of the Kα line EWs and EW ratios, including upper limits and color-coded according to the observations highlighted above. **(Bottom)** Evolution of the EWs of each $K\alpha$ line and their EW ratio with the wind parameter nr^2, computed using the SED and luminosity of each observation separately, but assuming a common fiducial N_H and turbulence. The bolded regions highlight the 90% uncertainties of the detection in each observation. Note: the turquoise observation, which only appears in the Fe xxvi Kα plot, almost entirely overlaps with the red observation.

The individual observations highlighted are the following:

- The observation highlighted in red is taken at the beginning of the decay of the 2006 outburst, and previously highlighted as an outlier (blue, at $\sim 5 \cdot 10^{-2}$ L_{Edd}) in the EW plots of Fig. 4.6. The observation in brown-red is the latest observation taken during the same outburst, with much lower luminosity, and part of the potential substructure described in Sec. 4.3.3.
- The observations in orange and pale blue are from the main portion of the soft state diagonal above $\sim 4 \cdot 10^{-}2$ L_{Edd}, both at very low HR_{hard}, but with luminosities covering at the lower and upper parts of the so-called "main structure".
- The observations in turquoise and pink are chosen for their higher HR_{hard} but similar luminosities to previous observations.
- The green observation is from the *NuSTAR* SPL state where both a Fe xxv Kα and Fe xxvi Kα lines are detected

The SED independent plots are shown in the lower panels of Fig. 4.11, using nr^2 as a proxy of the wind structure. In these figures, the absorption features of a single observation can be described by a single wind structure if the bolded regions from all three panels have a compatible nr^2 value. Similarly, differences in wind parameters between observations will translate to different nr^2. Interpreting this change is however not straightforward, as it is degenerate with potential changes in N_H, which nevertheless signal a (different) change of the wind structure. We will thus only speak of relative change in "wind parameter", and detail the implications of the position of each observation below.

- First and foremost, the change in EWs and EW ratios between low HR_{hard} observations at both ends of the main structure (orange and light blue) are broadly compatible, showing that this structure can be explained by a single wind parameter, whose absorption lines vary due to the evolution in luminosity and HR_{soft}.
- This main structure is however incompatible with both the low luminosity substructure (red brown) and the *Suzaku* outlier (red), who are also broadly compatible with each other. We note some tension between the individual parameters derived from the different lines of the low luminosity observation, although the regions remain compatible at three sigma.
- The detections at higher HR_{hard} (pink and turquoise) also require a significant change in the wind structure. Interestingly, the parameter in the turquoise observation remains very similar to that of the *Suzaku* outlier (in red),despite different luminosities, soft and hard HRs. The pink observation, which is at the edge of the limit to "intermediate" states (as defined in Sec. 4.4.1), requires an even stronger change. This confirms that the correlation of the Fe xxvi Kα EW with HR_{hard} is the result of progressive changes in the wind structure. The lack of correlation between Fe xxv Kα and HR_{hard} may then be a natural consequences of higher HR_{hard} producing Fe xxv Kα too weak to be detected with the current generation of instruments.
- The *NuSTAR* SPL absorption features both cannot be described by a single parameter, and requires very different wind parameters compared to the soft state observations. We will discuss the implications more extensively in Sec. 4.5.
- There is no significant change in wind structure between most outbursts. Indeed, the behavior of the main structure (and e.g. the orange and light blue observations) combines observations from 2012 to 2023, and the low luminosity structure observations from 2006 to 2023. The changes highlighted above are only following the evolution of the SED, independently from time.

4.4.3 Interpretation

Several works have probed the evolution of the wind in 4U 1630-47 in more restricted datasets, either from absorption lines or using photoionization modeling. Analyzing *Suzaku* and *NuSTAR* data exclusively,

Hori et al. (2018) report a strong change in absorption line properties in the first of their three 2015 *Suzaku* epochs (epoch 8), which cannot be explained by the evolution of the illuminating SED. We highlighted this specific observation in pink in Sec.4.4.2. In this observation, the Fe xxv Kα line is not detected, and our estimates give an upper limit for its EW which restricts the observation to a ratio above ~ 2 (see middle right panel of Fig. 4.11), while the very weak Fe xxvi Kα lines is the main feature constraining the wind parameter to be different from both the main structure and the low-luminosity substructure. Hori et al. (2018) then probe a common evolution of the wind parameters with luminosity and T_{IC}, but they use a very heterogeneous population: two out of the three 2015 *Suzaku* observations are part of the "main structure" as defined in our study, the 2006 *Suzaku* observations all have different wind properties, and the latter are all distinct from the single harder 2015 outlier. Assuming all of these changes trace a common evolution is likely to be an oversimplification, as our study shows that the wind structure changes both with HR_{hard} and with the luminosity below a certain threshold.

More recently, Gatuzz et al. (2019) considered the evolution of the main absorber with the evolution of the continuum and radio properties, and also found that the evolution of the stability of the plasma or the changes in illumination alone could not explain the disappearance of the wind in their harder *Chandra* observations. These *Chandra* observations without lines (dubbed Obs 5, 6 and 7) all have high HR_{hard} values, and are thus all compatible with the continuous evolution of the wind with HR_{hard}, although the physical mechanism behind this change remains unknown. We note that their Obs 5 (Obsid 14441) was classified as a canonical hard state in our study due to its soft and hard HR properties, which perfectly matches the optically thick radio observation during this epoch (Neilsen et al. 2014). On the other hand, Obs 6 (Obsid 15511) and 7 (Obsid 15524) are classified as intermediate states, matching their lack of radio detection.

Finally, Trueba et al. (2019) performed a detailed two zone modeling of the wind properties using the *Chandra* observations, which goes beyond the simple derivations considered in our study. Our conclusions are mainly applicable to their outer zone, which dominates the absorption features of Fe xxv Kα and Fe xxvi Kα. To test whether we could extend our analysis to the second zone, we tested for the presence of low energy lines (such as from Ca XX and Ar XVIII) below ~ 4.5 keV in the spectra of different instruments, but they remain only detectable with *Chandra*. The study of their evolution along the outburst is thus left to future work.

4.4.4 Evolution of the high-energy component

Now that we've established that the wind structure evolves with HR_{hard}, testing correlations against the photon index of the high-energy component in our models could allow to break the degeneracy between the high-energy and low-energy behavior, and test whether the change in wind parameter is specifically tied to the slope of the high-energy component or its normalization. However, the slope of the high-energy component evolves along with its normalization in intermediate and harder states. When using a `nthcomp` component to obtain an additive measurement of the comptonized flux, this reflects in very significant correlations between the nthcomp Γ and [15-50] keV luminosities in the *NuSTAR* and *NuSTAR* observations, which we confirm with individual fits of all *INTEGRAL* revolutions (independently for any soft X-ray coverage) made with a powerlaw. Both of the correlations are shown in Fig. 4.12. This behavior was already reported for older outbursts in Seifina et al. (2014) and might be important to determine the nature of the coronal emission in this source, but indicate that we cannot isolate the effect of a change in the slope of the comptonization on the absorption lines. However, in our sample, the correlation with Γ visibly breaks down below a limit common to *NuSTAR*/*Suzaku*-PIN and *INTEGRAL*, namely $L_{[15-50]}/L_{Edd} \sim 3 \cdot 10^{-3}$ (which translates to $L_{[30-50]}/L_{Edd} \sim 10^{-3}$ for *INTEGRAL*, with a Γ of 2). In addition, with *NuSTAR* and *Suzaku*-PIN, the residuals to our simple `nthcomp` component increase significantly below that limit. This could either mean that this is the rough threshold below which secondary sources of high energy flux, such as reprocessing and reflection, become too important to be ignored (see e.g. Connors et al. 2021), or that a significant change happens in the comptonized emission itself.

This contrasts with the results obtained by Seifina et al. (2014), who see a monotonic evolution of the comptonized photon index in several outbursts between 1998 and 2004, down to very low accretion

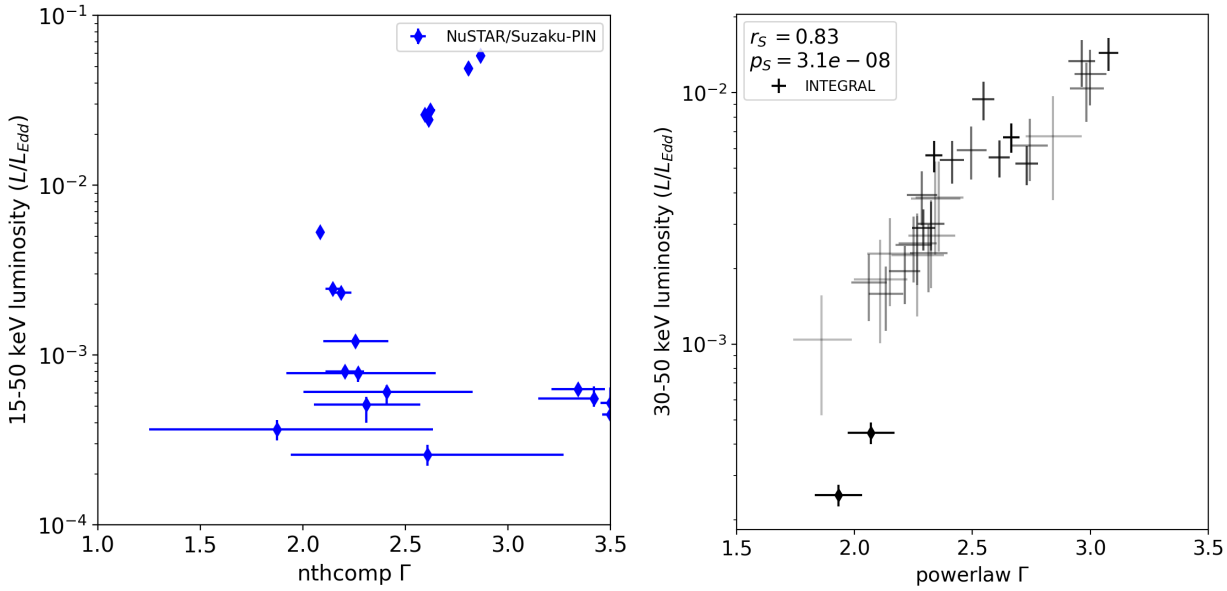

Figure 4.12: Intrinsic correlations of the luminosity and slope of the high-energy components in broad band fits with *Suzaku* and *NuSTAR* epochs **(left)** and for individual fits of *INTEGRAL* revolutions **(right)**. For *INTEGRAL* revolutions, we limit the luminosity measurement to the [30-50] keV band to avoid being affected by low-energy IBIS residuals, and use a transparency factor proportional to the errors.

rates and $\Gamma \sim 1$. However, this study was based on *BeppoSAX*, which is lacking in sensitivity and spectral resolution compared to *NuSTAR* and *Suzaku*, and wasn't making any distinction between spectral states (whereas the observations sampled here are predominantly soft). The discrepancy with this behavior is particularly apparent in the *Suzaku* observation at the very end of the 2010 outburst, which we put aside in the previous sections due to being too faint (ObsID 405051010). This observation is more than one order of magnitude fainter than all of the spectra analyzed in Seifina et al. (2014). When studying this observation and neighboring *Swift*-XRT exposures, Tomsick et al. (2014) found that the data was well reproduced by a $\Gamma \sim 1.5$ powerlaw, but without using the PIN camera, and thus without coverage above 12 keV. The 12-40 keV spectrum deviates from this component by more than 50%, even when adding a cutoff. Although the limits of the calibration of PIN might become significant at such low fluxes, we note that the PIN spectrum remains significantly above the $\sim 3\%$ of the NXB limit in its entire range.

4.5 Outstanding line variability in recent Outbursts

Until this point, we've limited ourselves to the variability of the source on the timescale of daily-averaged epochs. However, a more detailed look at the individual *NICER* orbits reveals of a number of peculiar short-lived spectral-timing properties related to the presence of lines. We stress that the detection of these features results both from the high cadence of the *NICER* monitoring, and our deliberate choice of separating individual *NICER* orbits (for individual observations of less than 30 minutes) before fitting. Although time-resolved spectroscopy of wind features is rarely attempted due to the limitations of current instruments, the large collective area of *NICER* gives us a glimpse of the short-term variability of these observations, and shows that the behavior of the ionized absorbers in this source is vastly more complex than what can be probed with time-average spectral products. We expect that many other objects host a similarly rich behavior. In the following subsections, we highlight our (ongoing) efforts to characterize these outlier periods.

4.5.1 February 2023: Highly variable dipping

NICER observed 4U 1630-47 during 6 individual orbits on 2023-02-23 (Obsid 5665010401) between 1:00 and 10:30 UTC. These observations were performed during a gap in *MAXI* and *Swift*-BAT visibility, and

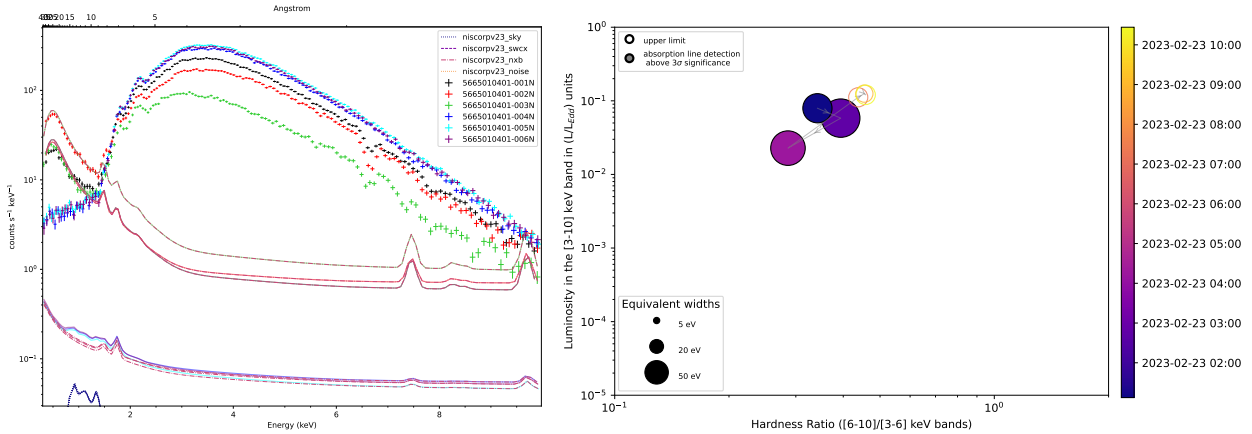

Figure 4.13: **(Left)** Time-integrated spectra of the individual orbits when removing the SAA filtering criteria, with manually adjusted `saa_norm` scorpeon values in the first 3 orbits to match the flare peak at low energies, and highlight the effect of the flares on the rest of the spectra. **(Right)** soft HLD of the individual orbits and corresponding EWs for Fe xxv Kα with the same axe limits as Fig. 4.1, color-coded with time.

NICER is thus the only instrument with coverage of the source during this period. Among these orbits, 3 (orbits 5665010401-004, 5665010401-005 and 5665010401-006, hereafter named 004, 005 and 006) show a very standard thermal state spectrum, but no trace of absorption line, hinting to the presence of a hard component (and HR_{hard}) invisible to *NICER* that would affect the wind structure. On the other hand, the orbits 5665010401-001 to 5665010401-003 (hereafter named 001, 002 and 003) show multiple dipping events with strong absorption features in the iron band and erratic variability on timescales of less than a minute. However, their identification is not straightforward due to the presence of very intense non-X-ray flares: orbits 002 and 003 are automatically discarded by the default *NICER* pipeline due to passage over the South Atlantic Anomaly (SAA). However, the associated SAA flares have a very characteristic spectral contribution, that can be well fitted from their low (2 keV) and high ($\gtrsim$ 8 keV) energy behavior, and a notable lack of features below 6 keV. We confirmed with the *NICER* team that this type of flare cannot create absorption features in our spectra, and that the lines that we will discuss below are not the result of incorrect background filtering. We thus started by regrouping the data in individual orbits, after removing the SAA passage criteria, and replacing the static flare threshold by a dynamic criteria, which only excludes events where the overshoots are 5 times above the 0.35-8keV count rate. The resulting diagnostic plots of this data treatment are shown in Fig. 4.14.

Since creating background corrected lightcurves with such variable flares is a very complex task, we will use these diagnostic plots to discuss the temporal evolution of the source. With our first selection criteria, the entire on-target gtis of orbits 001, 004, 005 and 006 are retained, and orbits 002 and 003 only lose a portion of their exposure. In orbit 002, the excised period includes a short dipping event. In orbit 003, the excised period is part of a "stable period where the source remains at dipping flux level.

The resulting orbit integrated spectra are shown in the left panel of Fig. 4.13. There are indeed significant flaring events in the first 3 orbits, but they can be very well considered by fitting the scorpeon model, and do not affect significantly the spectrum below $\sim$ 7 keV. Meanwhile, the part of the SED dominated by the source shows similarities with a thermal continuum identical to the last three orbits, absorbed by progressively more dense material. The very low energy of the Fe xxv Kα line indicates either a significant infalling outflow, or, more probably, a very high degree of contamination by lower energy lines, and thus a relatively low ξ_i. However, both partial covering absorbers and precomputed photoionization tables using soft 4U 1630-47 SEDs provide very poor fits, both to the continuum and the line features.

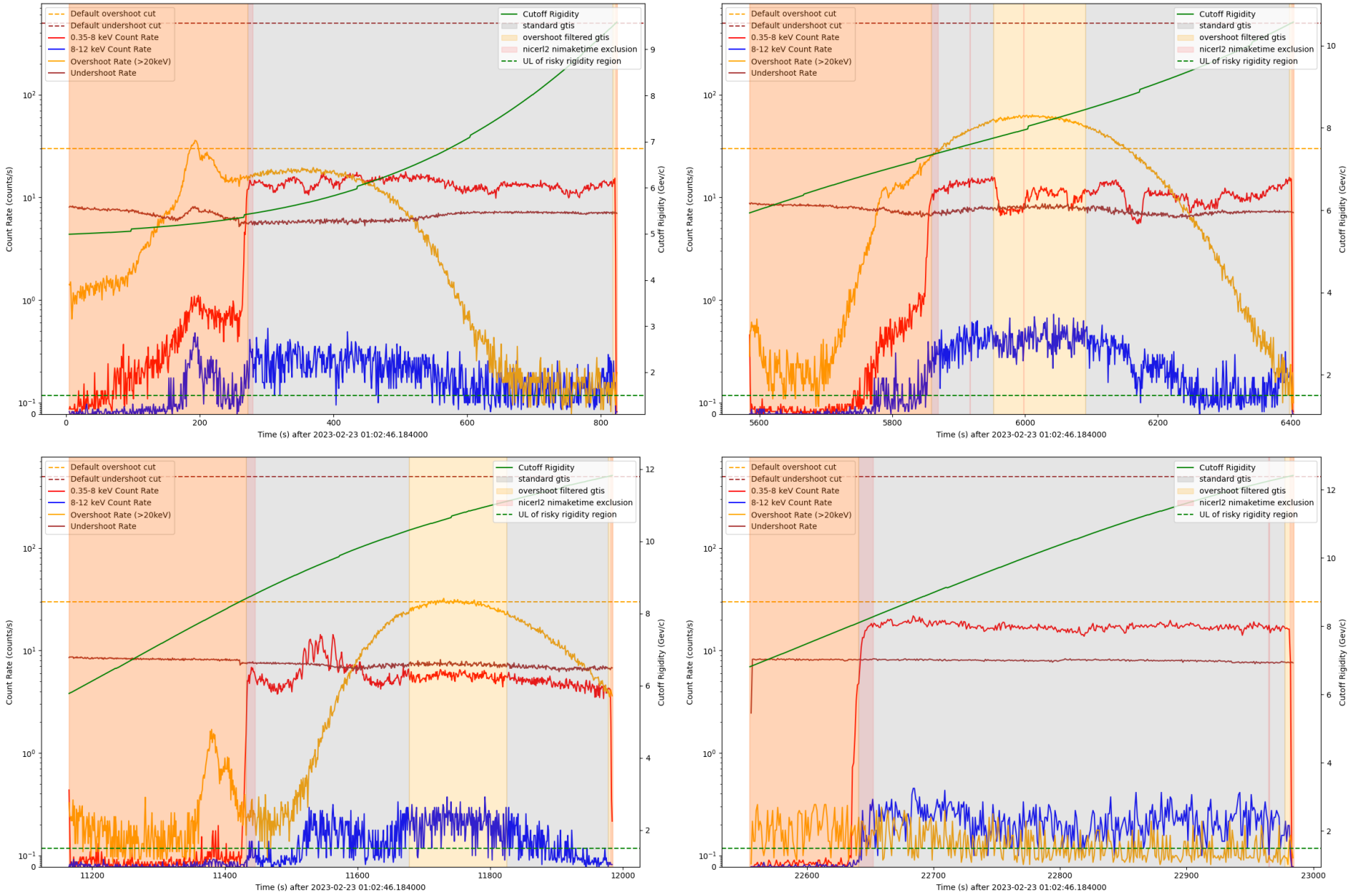

Figure 4.14: Diagnostic plots of the filtering of the 6 individual orbits of *NICER* Obsid 5665010401. Continued in the next page.

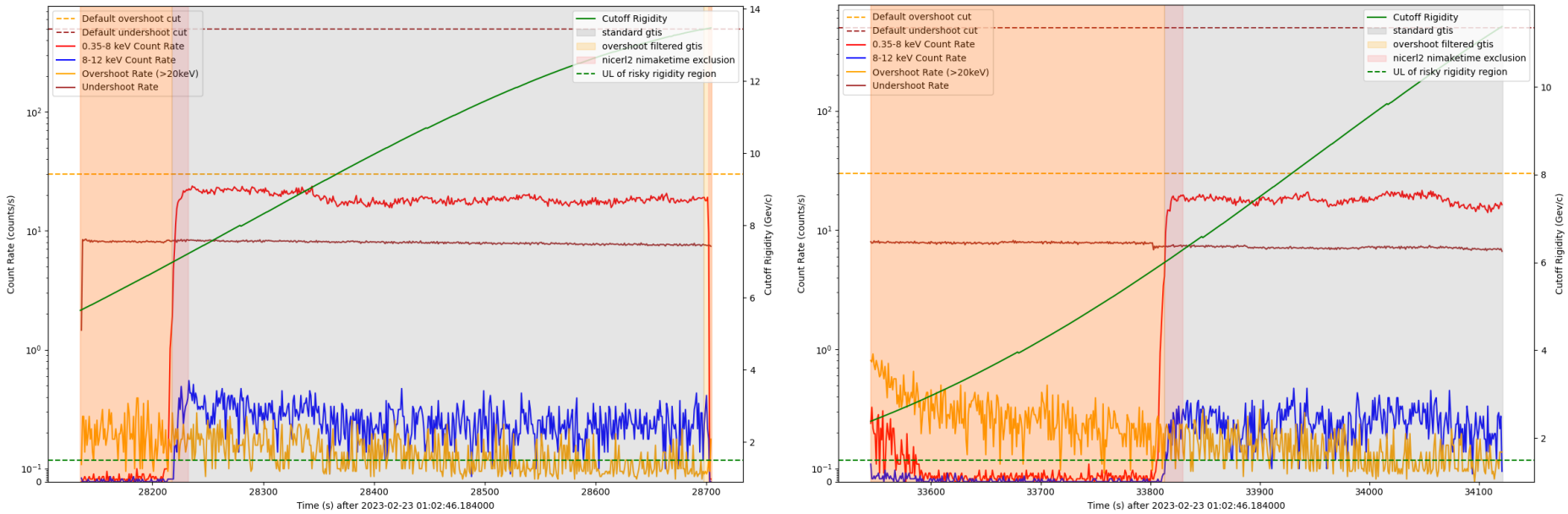

Figure 4.14: Diagnostic plots of the filtering of the 6 individual orbits of *NICER* Obsid 5665010401, highlighting the source count count rate below (red) and above (blue) 8 keV, as well as undershoots (brown) and overshoots (orange), which help characterize the presence of flares. The green curve is plotted according to the secondary axis, which highlights the Cutoff Rigidity, a quantity inversely related to the penetrating power of charged flaring particles and thus the presence of flares. The horizontal lines highlight the standard `nimaketime` filtering thresholds in NICERDAS, and the red regions the time intervals automatically excluded by nimaketime (which, among many other criteria, include these thresholds). In the first 3 obsids, the combination of a very high overshoot rate and a relatively low increase of the 8-12 keV count rate hints at the presence of strong SAA flares.

We thus start with a fully empirical modeling where we allow for a change in continuum and simply characterize the lines themselves, in order to measure their properties and the absorbed continuum luminosity. The resulting HLDis shown in the right panel of Fig. 4.13, and shows a progressive decrease down to 10% of the non-absorbed luminosity in the 3-10 keV flux, accompanied by extremely deep absorption lines centered around 6.5 keV, with EWs between 60 and $\sim$ 100 eV. In addition, a very significant broad iron emission line appears is present in the spectrum of orbit 003.

Although it would be tempting to propose physical interpretations or conduct more advanced modeling, these spectra remain time-integrated and thus blend the extremely variable evolution apparent in the diagnostic plots of Fig. 4.1. We thus further split individual orbits in different periods. Since orbit 001 has no structured evolution, we split it in even 100s individual bins. Orbits 002 and 003 are split manually to isolate the dipping and flaring events. For these new intervals, we do not excise the periods most affected by flares. We show the resulting splits, spectra, and line detection soft HLDs in the different panels of Fig. 4.15. During the first orbit, although the absorption lines become progressively stronger along the orbit, the different intervals can be well fitted with a single model and small variations in constant factor. This is not the case for the subequent two orbits.

In the second orbit, we manually discarded the very short transition periods between the normal and flaring periods, and end up with a total of seven spectra suitable for analysis. As shown in the residual plots and HLDs, the two most intense dipping periods (M003 and M008) are (expectedly) significantly fainter, but also significantly softer. This effect is not what is usually expected from a standard highly absorbed event (Bozzo et al. 2016; Church 2001; Díaz Trigo et al. 2006), and may indicate a more complex evolution. Although the spectra were fitted individually with a different continuum, an absorbed disk component remained sufficient to fit the data, aside from the iron absorption lines. These lines are also notably similar along the intervals, and a discrepancy within the dipping period is hard to assess due to limited statistics. This is also due to the non-detections displayed in the HLD: for $\sim 30s$ intervals, the MC significance tests, coupled with the very high background level, virtually prevent any line from being considered as significant. Of course, considering the situation, the absorption features we see in the residuals are very unlikely to result from photon noise, and a more in depth analysis will give more constrain on the evolution of the absorbing material.

Finally, the temporal behavior in the third epoch sharply contrasts with what is seen in the first two orbits: instead of occasional dipping events, the source remains in the lower state for the vast majority of the orbit, except for a very erratic flare soon after the start of the pointing. We stress that there is no reason to consider the flare as a background event: besides the lack of important increase in any of the flaring lightcurves, the spectrum during the flare remains compatible with the SEDs of BHXRBs. More precisely, although both of the "dipping" or "low-flux" periods require a very broad emission line in the iron region to reach a decent fit, this line is completely unnecessary in the higher flux observation (but is not constrained to having diminished either, due to the significant increase in continuum flux). Moreover, in this orbit as well, we once again see a puzzling softening of the spectrum during the low-flux period. The flaring period, on the other hand, is not only significantly harder than the low-flux periods, but also compared to the other "high" flux periods during the first two orbits.

In terms of line properties, with the better statistics of this observation, we can confirm that the EW of the absorption line itself remains notably similar for both flux levels. Although this may simply mean that the line is already completely saturated in the upper flux level, it can also be interpreted as a similar absorber remaining constant across all flux levels, in the case where the evolution of the continuum would be due to a change in the accretion flow However, we stress that the latter case would require a very significant change in disk structure (since the spectrum remains thermally dominated) within timescales of few seconds, which is suspiciously unheard of in the literature.

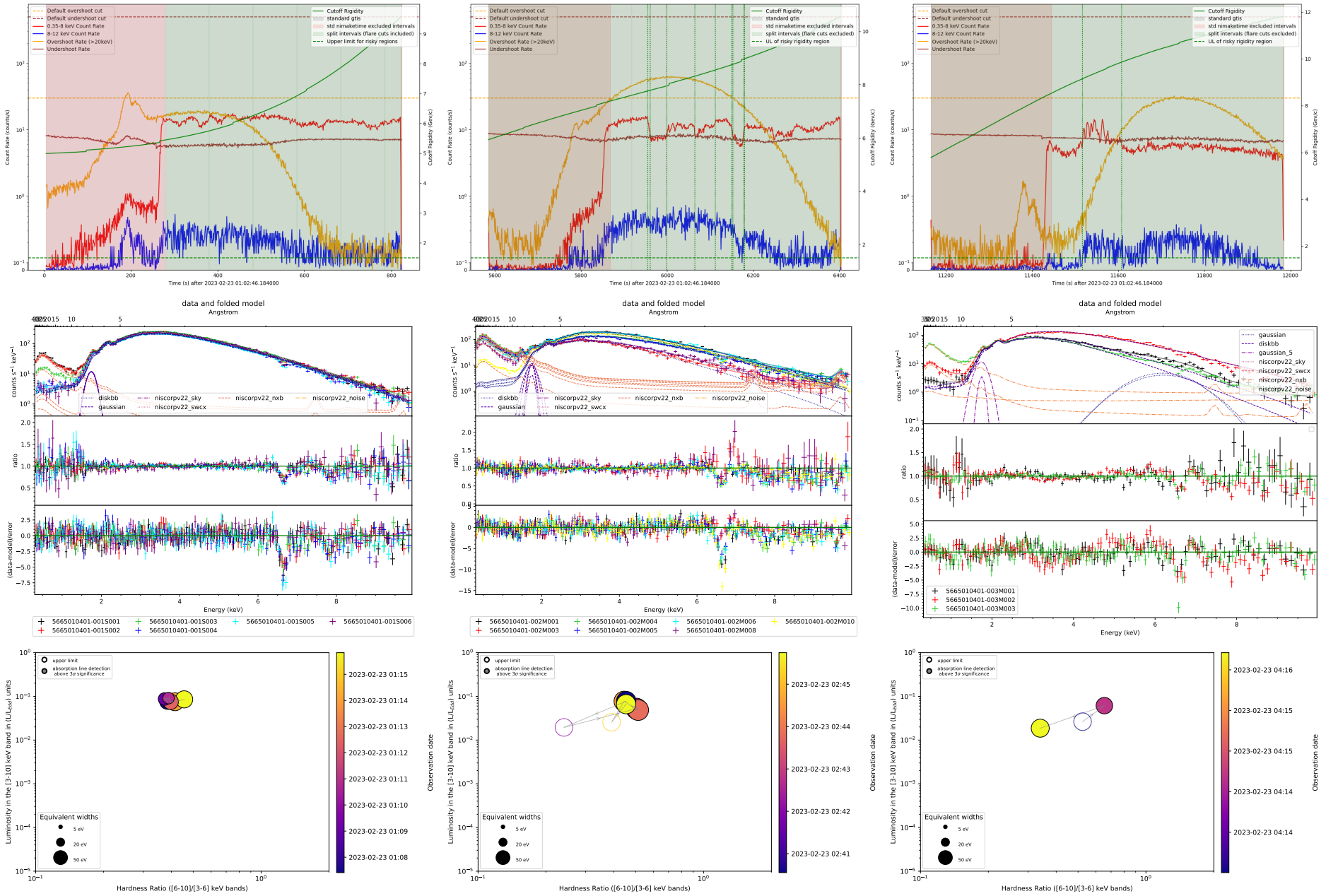

Figure 4.15: **(Top)** Diagnostic plots of orbits 001 (**(left)**, 002 **(middle)**and 003 **(right)**, highlighting the splitting procedure adopted for time-resolved spectroscopy. **(Middle)** Residuals obtained when fitting individual observations together with a variable continuum and while ignoring the iron region. **(Bottom)** Soft HLD after applying the line detection procedure to each splits of the orbit.

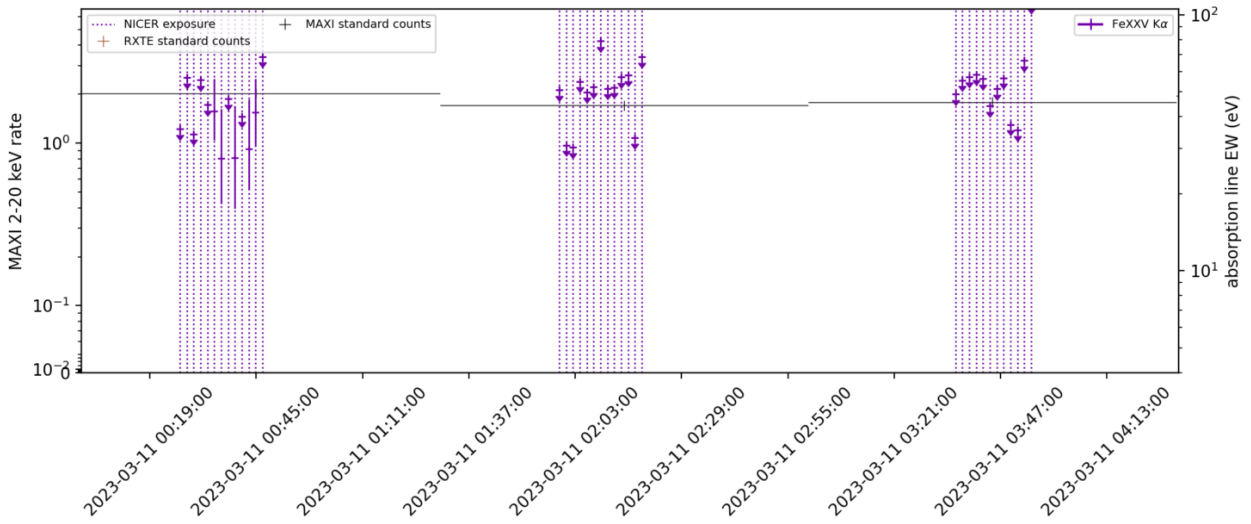

Figure 4.16: Temporal evolution of the Fe xxv Kα absorption line in individual 100s *NICER* intervals for the first 3 orbits of 11-03-2023.

4.5.2 March 2023: Short lived absorber and discrepancies

From March 10 to March 14 2023, 4U 1630-47 was observed by the *IXPE* telescope, for the first time in a SPL state. The source was subjected to a very significant complementary spectral coverage, as both *NICER* and *NuSTAR* observed the sources in several occasions during these 4 days. The evolution of the source during these 3 days is not straightforward, as a sudden hardening of the SPL was observed at around 14:00 on March 11. However, we are not interested in the continuum, but instead in the absorption line properties. As seen in the line measurements listed in Tab. 7.2.1, and the blind search for the spectra, which we show in Fig. 4.17, these are the only epochs for which *NICER* and *NuSTAR* significantly disagree: in *NICER*, no absorption line is systematically detected along the observations, with often very constraining upper limits (4eV at 3 sigma) due to the very high SNR of the observations. On the other hand, *NuSTAR* detected a weak ($\sim 8-12$ eV) but very significant line in every observation.

The discrepancy is actually more global: these *NuSTAR* observations are the only ones with absorption line detections along the entire SPL coverage, which samples tens of exposures with different instruments accross several outbursts. It is thus very likely to be an instrumental feature, which, considering the very neutral high absorption column in 4U 1630-47, is likely to arise from an incorrect fitting of the iron edge resulting from an energy calibration issue (as we've discussed in Sec. 3.6). However, in this situation, simply fitting a gainshift to the *NuSTAR* spectra in a common fit with *NICER* is not straightforward, as the discrepancy between both instruments remain very significant with or without the presence of an absorption line. A more complex correction of the instrument is thus left to future work.

However, Fig. 4.17 also highlights that in at least one observation, this is not the only line seen. Indeed, the *NuSTAR* observation of March 11 also detects an even more prominent Fe xxv Kα line, and while there is no direct detection in the *NICER* spectra, there is an obvious variation in the residuals between orbits. We thus investigated this further by fitting independently each *NICER* and *NuSTAR* orbit during the *IXPE* period. The resulting temporal and spectral evolution is shown in Fig. 4.18.

First, the Fe xxv Kα line is significantly detected in a single *NICER* orbit starting on 2023-03-11 at 00:26, and the following *NuSTAR* orbit, which covers the following hour. The next two *NICER* orbits and the next *NuSTAR* orbit provide very good upper limits, ensuring than the line has disappeared, before it reappears for the last time in the third *NuSTAR* orbit of that MJD, which starts at 4:10 am. Although the *NuSTAR* lightcurves reveal significant variability along these epochs, this is common to all observations in that period, including those where the line isn't detected. In parallel, there is no noticeable spectral change in any of the observation with the absorption line. We also show the HLD restricted to Fe xxvi Kα to highlight the difference between instruments, as for orbit-resolved spectroscopy, the vast majority

of individual *NuSTAR* orbits with a good enough exposure time also show a line detection, unlike the *NICER* epochs.

Since the absorber disappears on timescales of an hour, and does not exhibit a significant velocity shift, it is likely to be a single dense clump of gas rising above the disk, which comes in contact with the line of sight. If we assume that the second detection at 4 am comes from the same clump, its evolution is likely to arise from the rotation of the disk. This can directly constrain the location of the absorber: at Keplerian velocity, a rotation period of $\sim$ 3h, corresponds to a radial distance of $\sim 6 \cdot 10^4$ Rg for a 8 $M_\odot$ BH. This could then be combined with a measure of the ionization parameter, and determine the density of the clump. However, this hypothesis relies on several fragile assumptions, among which the fact that the clump seen in both *NuSTAR* orbits, which is contradicted by a much higher EW during the second *NuSTAR* orbit compared to *NICER*.

However, this can also be an unfortunate consequence of the sampling: if the first *NuSTAR* orbit covers a bigger fraction of the obscuration of the clump compared to the first, and furthermore the *NICER* orbit, their integrated spectrum will show a diluted line. Investigating this matter requires switching to time-resolved spectroscopy, and this data reduction is still an ongoing project: for now, we restrict ourselves to splitting the first 3 *NICER* orbits of 2023-03-11 in 100s periods. We show the time-evolution of the Fe xxv Kα line with such a sampling in Fig. 4.16. Despite reaching the limit of the capabilities of *NICER*, which prevents us from detecting an evolution in the EW of the line between individual detections, it is clear that the line is only detected during the second part of the observation. Moreover, the periods in which the line is detected all show a much higher EW, perfectly compatible with the second *NuSTAR* orbit. This would tend to confirm our hypothesis, but each *NuSTAR* orbit needs to be analyzed in depth to give a proper conclusion.

Finally, we investigated the possibility of a change in polarization during the period where the transient absorber is detected. Although the work of Rodriguez Cavero et al. (2023) doesn't show the short term evolution of the different polarization properties, we directly confirmed with N. Cavero that no significant change in polarization occurred during this period.

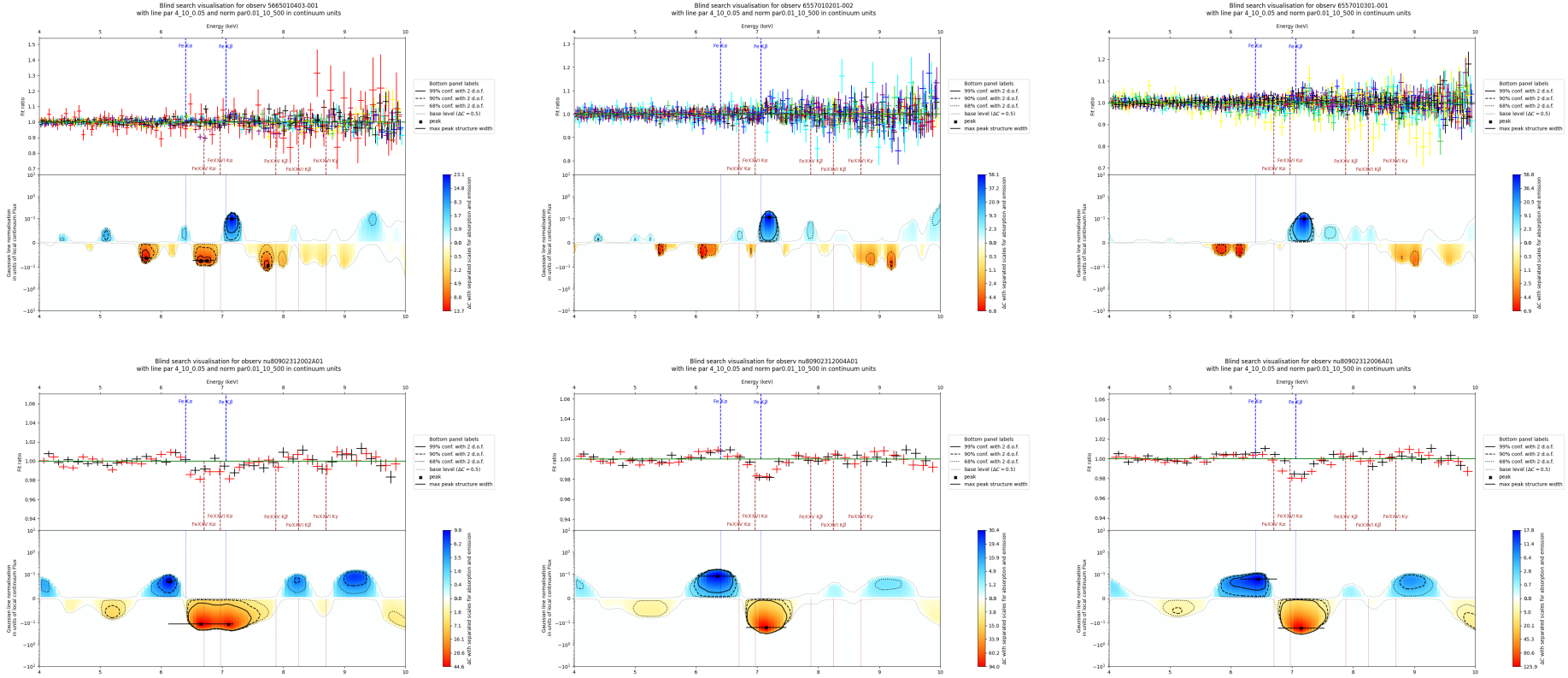

Figure 4.17: Results of a blind search for the *NICER* **(top)** and *NuSTAR* **(bottom)** observations simultaneous to the *IXPE* exposure. An additional *NuSTAR* exposure shortly before shows similar residuals to the other 3 epochs.

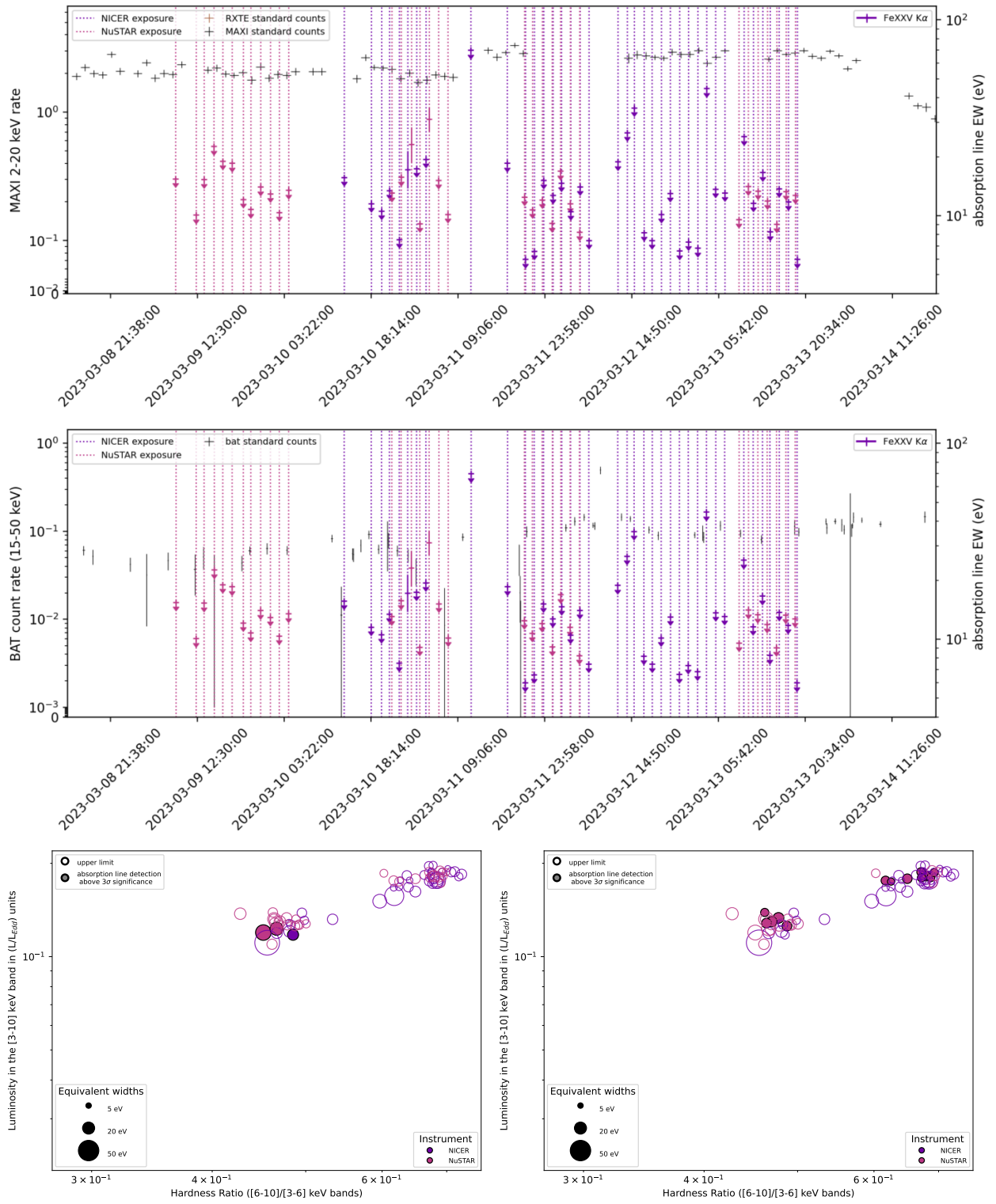

Figure 4.18: Upper panels: Temporal evolution of the Fe xxv Kα absorption line in individual orbit observations of *NuSTAR* and *NICER*, seen with *MAXI* **(Top)** and BAT **(middle)** monitoring. The spectral and flux transition during the middle of 2023-03-11 is obvious in the *MAXI* monitoring. Bottom panels: Soft HLD evolution of the Fe xxv Kα and Fe xxvi Kα lines in individual orbits during this period.

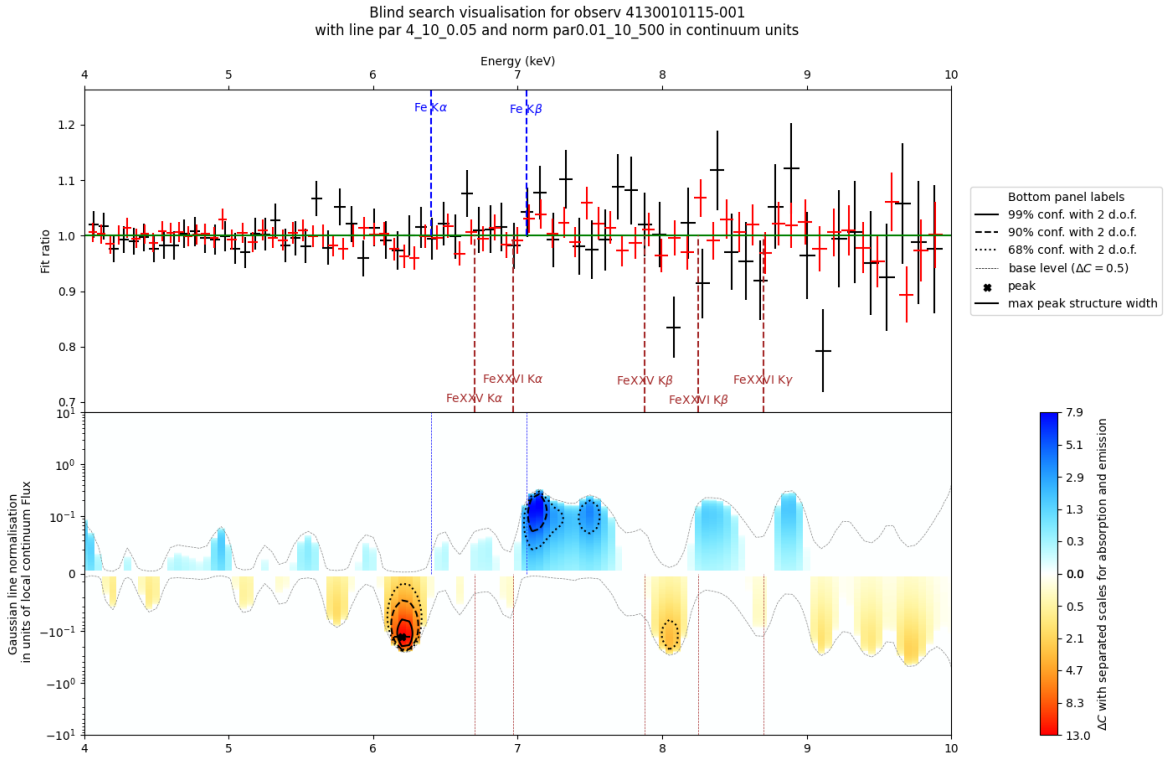

Figure 4.19: Results of a blind search for the two orbits of the 2021 mHZ QPO periods, highlighting a significant absorption feature around ∼ 6.2 keV

4.5.3 mHZ QPOs

Although a detailed study of the mHz QPO properties remain beyond the scope of our analysis, one particular element is worth investigating. Indeed, while no obvious absorption line is detected during the 2021 observations where the mHz QPOs are found, there remain a significant absorption feature of unknown origin at around 6.2 keV, which we show in Fig. 4.19. This feature has no obvious line equivalent that wouldn't require much stronger absorption lines at other energies, or an uncharacteristically high redshift. Nevertheless, it remains of high significance for a spurious photon noise feature. We thus investigated in more detail the evolution of this residual, by flux-resolving the 3 *NICER* orbits in which mHZ QPOs are detected.

To achieve this, we first compute a broad band lightcurve of the source for a given orbit at a 0.1s binning (which is negligible compared to the period of the QPO), then divide each observation in three linear flux intervals. The resulting separation is used to recompute different spectra, which are then analyzed separately and probed for the presence of lines. Unfortunately, as we show in the blind search plots of Fig. 4.20, we did not find any significant line feature in any of the flux resolved spectra. This does not necessarily invalidate the presence of the line, but since these QPOs are found in spectral states significantly harder than where the absorption lines are usually detected (see Fig. 4.8), it would be reasonable to expect a link with the QPO mechanism, and thus the flux (or phase).

We thus favor the hypothesis of a spurious detection, which, for a ΔC of 13 with 2 d.o.f., corresponds to a NHP of $\sim 1.5 \cdot 10^{-3}$. This value is low, but considering the hundreds of datasets analyzed, it is not significant enough to warrant further investigation.

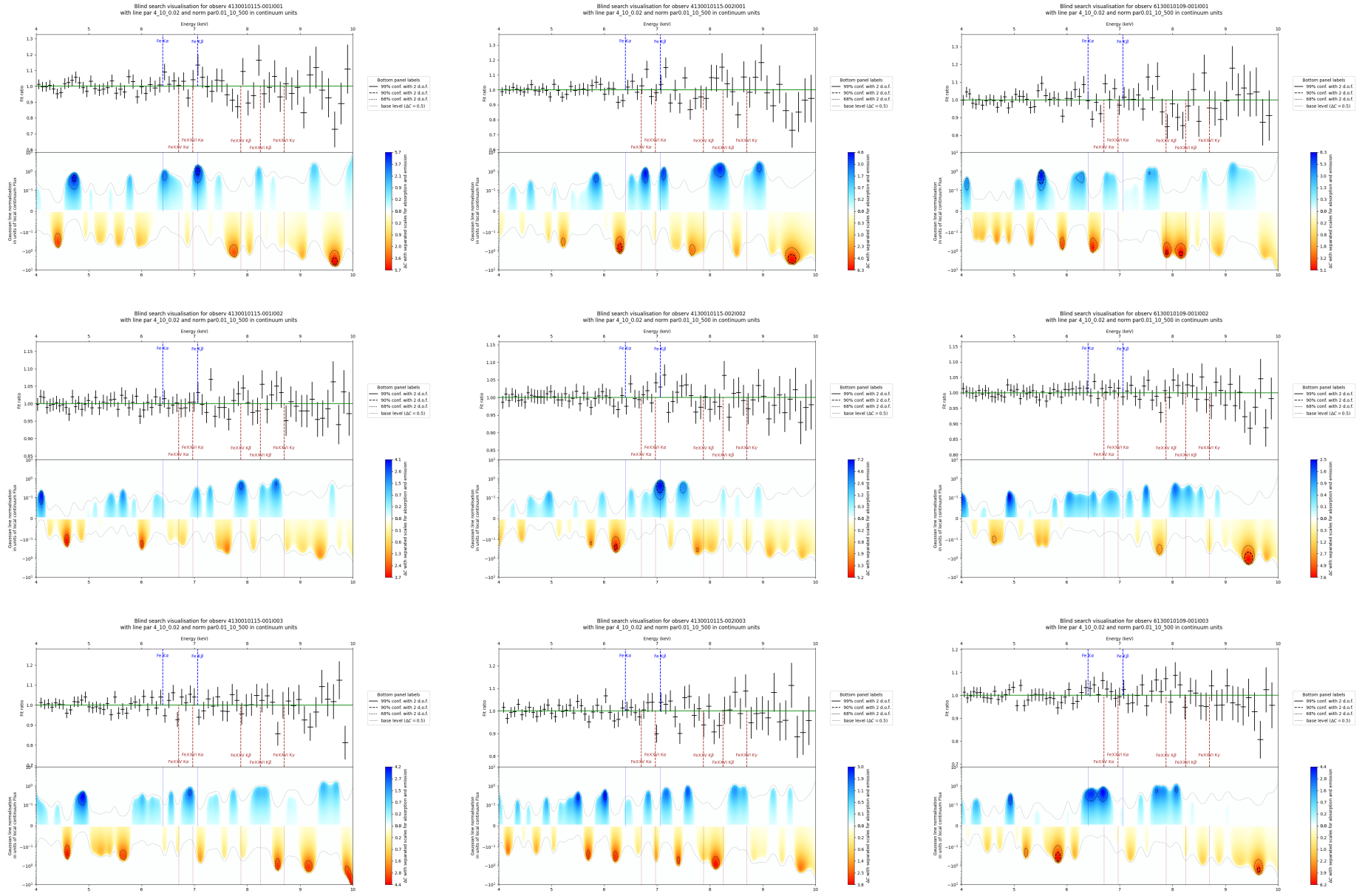

Figure 4.20: Results of a blind search for the low **(Top)**, middle **(Center)** and high **(Bottom)** flux-resolved periods of the three individual NICER orbits where mHZ QPOs are present.

4.6 Overview of individual outbursts

Revisiting the evolution of the line properties during each outburst and between different outbursts is out of scope of this study. For now, we simply provide an overview of the evolution of the absorption lines during each individual outburst, using the *RXTE*/*MAXI* and (whenever available) BAT monitoring, completed with soft and hard HLDs color-coded with instruments and time, and highlighting non-significant BAT detections with transparent colors. We only show the instruments used for line detection, which means that due to our choice of ignoring *NuSTAR* low-energy data in simultaneous epochs (see Sec.4.2.2), the only *NuSTAR* exposures that appear explicitly in the following graphs are the ones where no other soft X-ray instrument is available (such as in 2013) or when the discrepancy between the results justified separating the instruments (such as in 2023). In the following lines, we briefly summarize the source and line behavior covered within the sample for each outburst.

- 2004: only a single observation was performed with high-sensitivity instruments, at the end of a super-outburst. We note that the *Swift* satellite wasn't yet launched and thus the BAT monitoring is not available for the entirety of this outburst. However, the *Chandra* exposures benefits from a simultaneous *INTEGRAL* observation, which allows to pinpoint its HR_{hard} with very good accuracy. This observation, with $\sim HR_{hard} > 0.2$, is the second hardest line detection in the entire sample aside from the SPL detections, which must be considered differently from the normal line behavior (see Sec. 4.5.2). Due to *INTEGRAL*'s capabilities, it is by far the most precise measurement of HR_{hard} in this hardness range, and shows unequivocally that X-ray wind signatures are detected during intermediate states. Moreover, the *RXTE* lightcurves and HR show that the observation occurs at the beginning of a transition from a SPL (or hard) state towards a quickly dimming soft state.
- 2006: A series of 6 *Suzaku* exposures are performed during the soft state decay of a seemingly soft-only outburst (although BAT observations are missing during crucial periods at the beginning of the outburst). These observations, aside from their peculiar line properties (see Sec. 4.3.3 and Sec. 4.4), show a significant evolution of HR_{hard} with the luminosity, which is never seen outside of this outburst, but may be simply impossible to detect with the limited BAT sensitivity.
- 2008-2010: The only high-sensitivity observation is performed during an extremely faint state at the end of the 2010 outburst. Although line detection remains completely inaccessible, we note the puzzling hard tail in PIN that cannot be explained by a standard comptonized component.
- 2012-2013: Several observations with 4 different instruments are performed during many different states of a super (double, arguably triple) outburst. The combination of all available telescopes, coupled with the HR_{hard} consideration, allow to draw significantly more insight on the reason for which the lines evolved compared to previous studies like (Diáz Trigo et al. 2014; Trueba et al. 2019). We note that the 09-2012 XMM-*Newton* observations are performed during a swift state transition to a SPL, which naturally explains the disappearance of the lines from an outflow evolution (and not simply overionization) scenario. The HR values of both the XMM-*Newton* and *Suzaku* observations at the peak of the flare confirm the source does not settle into a pure hard state before returning to a softer state. The early 2013 *NuSTAR* observations show that the second long-term plateau is (as expected) a soft state with strong lines. Here, we note that the *Chandra* non-detections in both 2012 and 2013 match more "pure" hard states. They are performed before the source faints significantly (L_X of few 10^{-3} Eddington, according to the last *Chandra* observation) in the hard state before re-brightening.
- 2015: Three *Suzaku* observations are performed around a small flaring event in a soft to intermediate period during a single outburst. Two observations benefit from simultaneous *NuSTAR* coverage (where the lines are also detected). The evolution of the EW of the lines matches perfectly the link between the wind and HR_{hard}.

- 2016: a single *Chandra* observation is performed during a soft state plateau, at the beginning of a single outburst.
- 2018: a high-cadence *NICER* monitoring covers the majority of a single outburst. In the first period, the source evolves along the standard soft state diagonal, with constant line detections. In the second period, despite appearing on the same path in the soft HLD, the hard HLD shows that the source is transitioning from a SPL or hard state to a soft state, and the *NICER* observations are performed during intermediate states. The weak line detection in the penultimate observation is in line with an X-ray wind that is either weaker or with a different structure, and that could not be detectable during the harder observations that precede. Stacking the observations during the second period could allow to probe deeper into the *NICER* upper limits, but only up to the intrinsic limits of the instruments, which amount to ~ 5 eV for 3 σ detections.
- 2020: a high-cadence *NICER* monitoring and a few *Chandra* observations cover the majority of a single outburst, with a strong and almost permanent hard X-ray contribution, unlike the previous outburst. The majority of the observations are performed during an intermediate/flaring plateau entirety and do not show lines, except for the small group of observations with HR_{hard} values sufficiently dropping to soft states, at the beginning of the monitoring. Stacking observations would improve the constrains on the possible presence of a weak wind in the intermediate states.
- 2021-2022: a high-cadence *NICER* monitoring is performed at the beginning of a single outburst. There are no detections as the source remains in pure hard, SPL or intermediate states, but this is the only outburst with a detailed coverage of the hard state rise, which allows to test the evolution of the stability curves of the source with unprecedented precision.
- 2022-2024: several high-cadence *NICER* monitorings, some simultaneous with *NuSTAR*, *IXPE*, and *XRISM*, are performed during a super (double) outburst. The first period is performed during a soft plateau which directly follows the rise of the source from quiescence, with no apparent transition to a bright hard state beforehand. There, the source shows constant line detections. The second period covers a very complex evolution from SPL to intermediate and short periods in the soft state. The very high amount of long observation allows for few detections of "standard" weak lines during intermediate states, beyond the outliers discussed in Sec. 4.5. The third period, after a brief SPL or flaring decay, covers the last soft plateau of the source between 08-2023 and the first half of 2024. The vast majority of these observations were not yet public during the elaboration of this work, and will be discussed in more detail during future studies. The 08-2023 observations (the last two with the current dataset) are some of the only observations taken during a very stable period plateau that match the typical soft state "floor" that can be found in many outbursts in the *MAXI* lightcurves, at $\sim 1.5 \cdot 10^{-1}$ cts/s. Some of the early 2024 faint soft state observations are simultaneous to long *INTEGRAL* observations and allow for some of the most precise measurements of the broad band SED in the soft state to date, with a notable departure from the $\Gamma - L_{hard}$ correlation discussed in Sec. 4.4.4.

4.6.1 2004

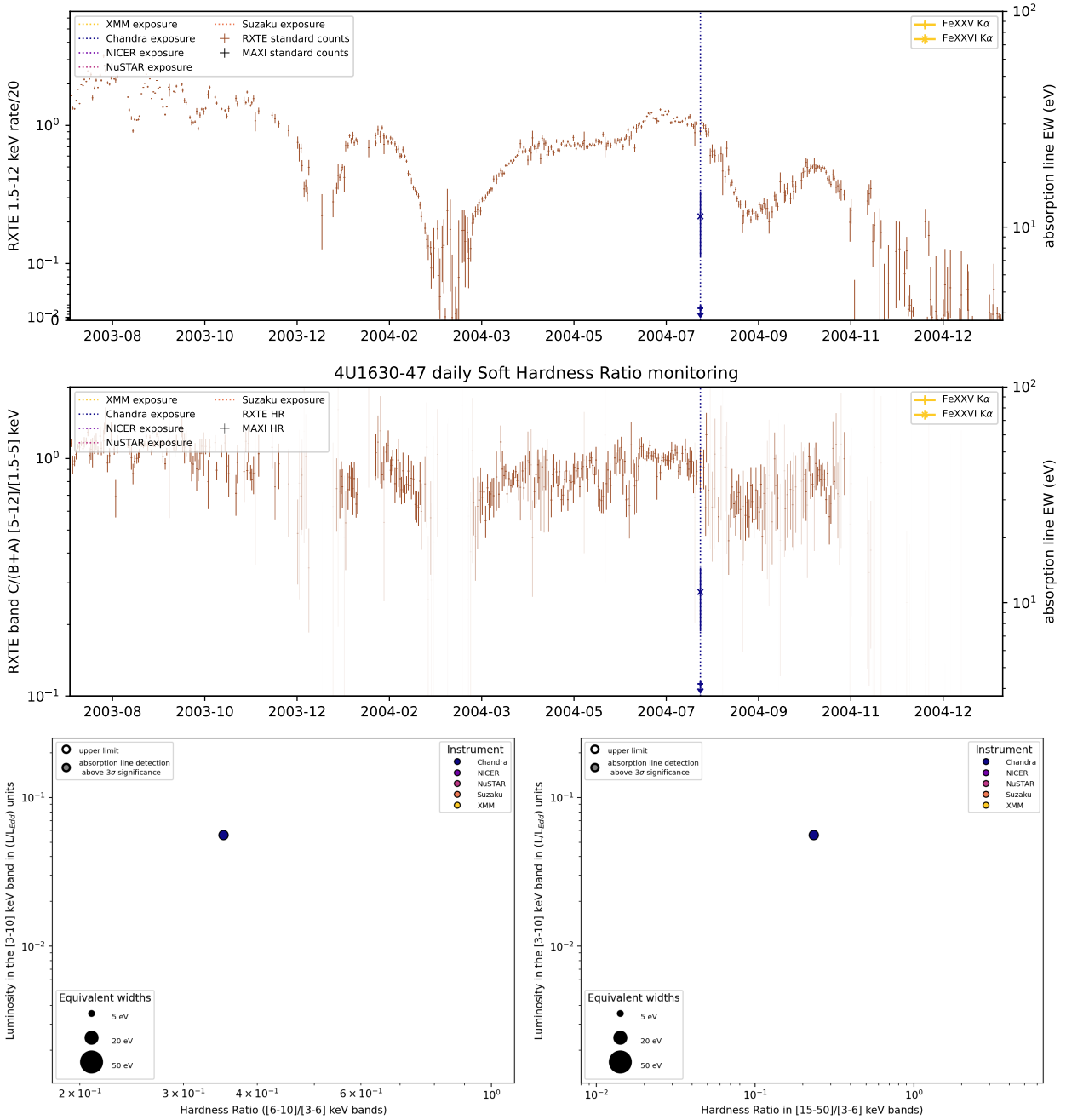

Figure 4.21: Overview of the evolution of the Kα absorption lines during the 2004 outburst

4.6.2 2006

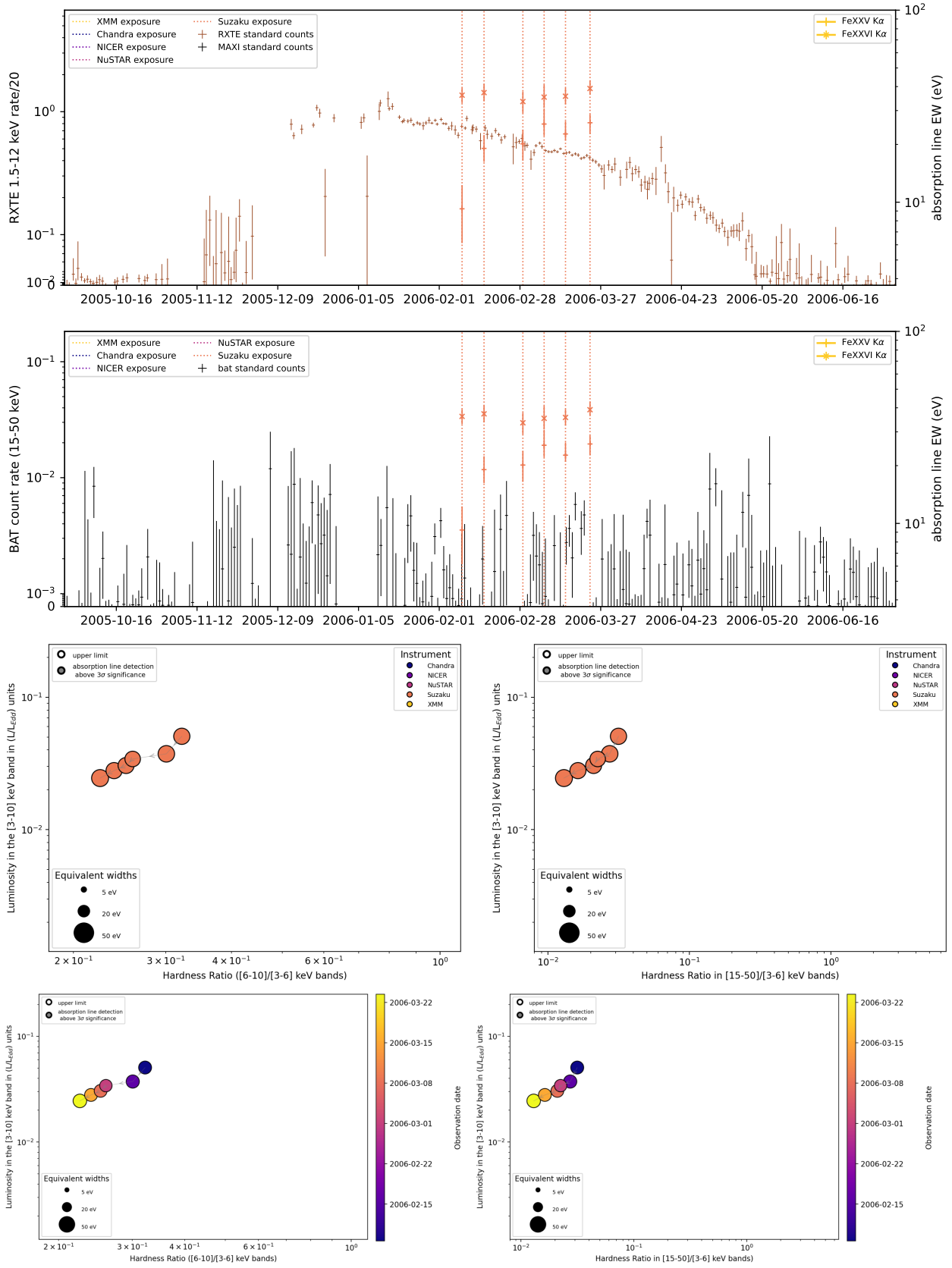

Figure 4.22: Overview of the evolution of the Kα absorption lines during the 2006 outburst

4.6.3 2008 & 2010

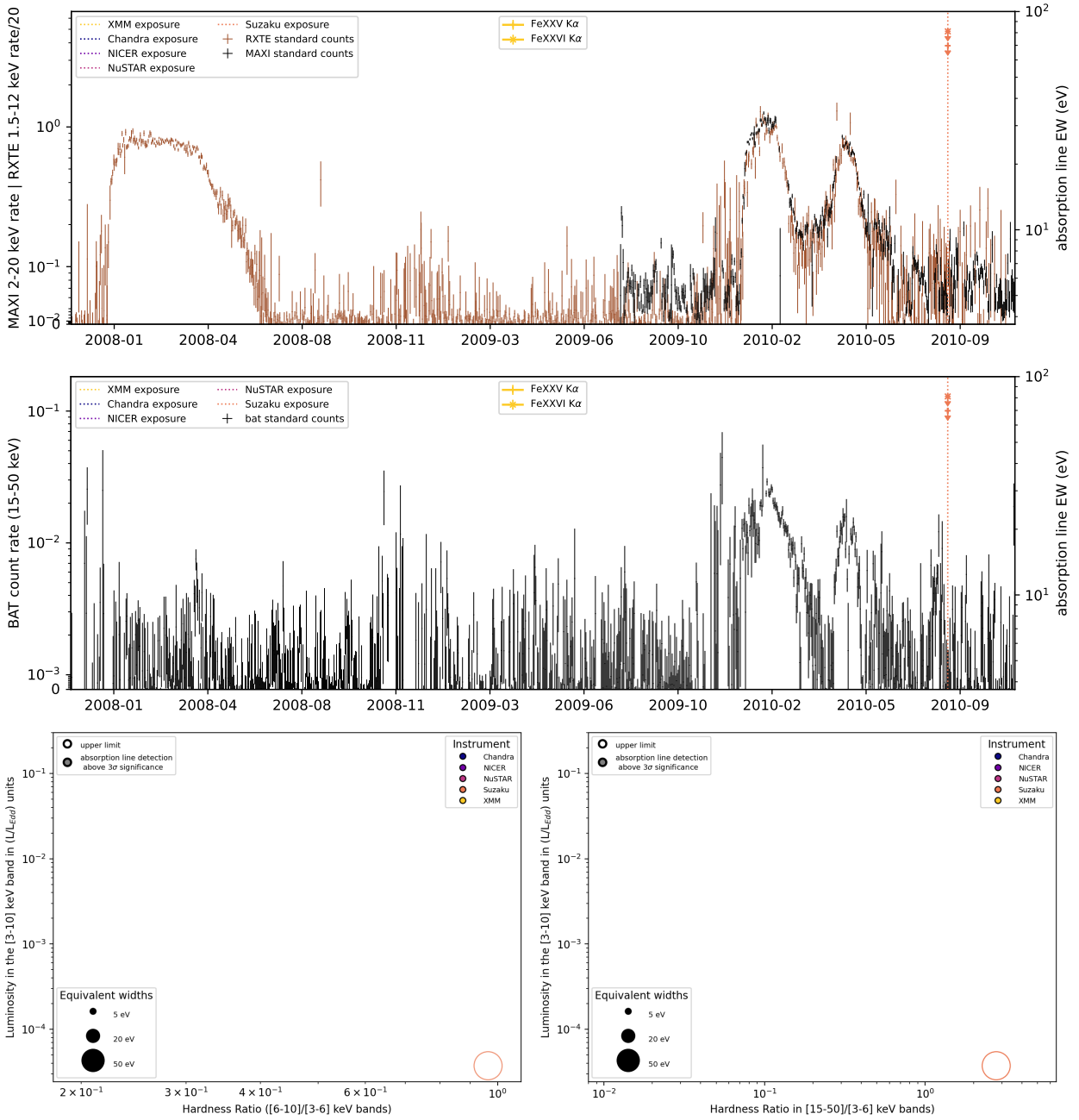

Figure 4.23: Overview of the evolution of the Kα absorption lines during the 2008 and 2010 outbursts

4.6.4 2012-2013

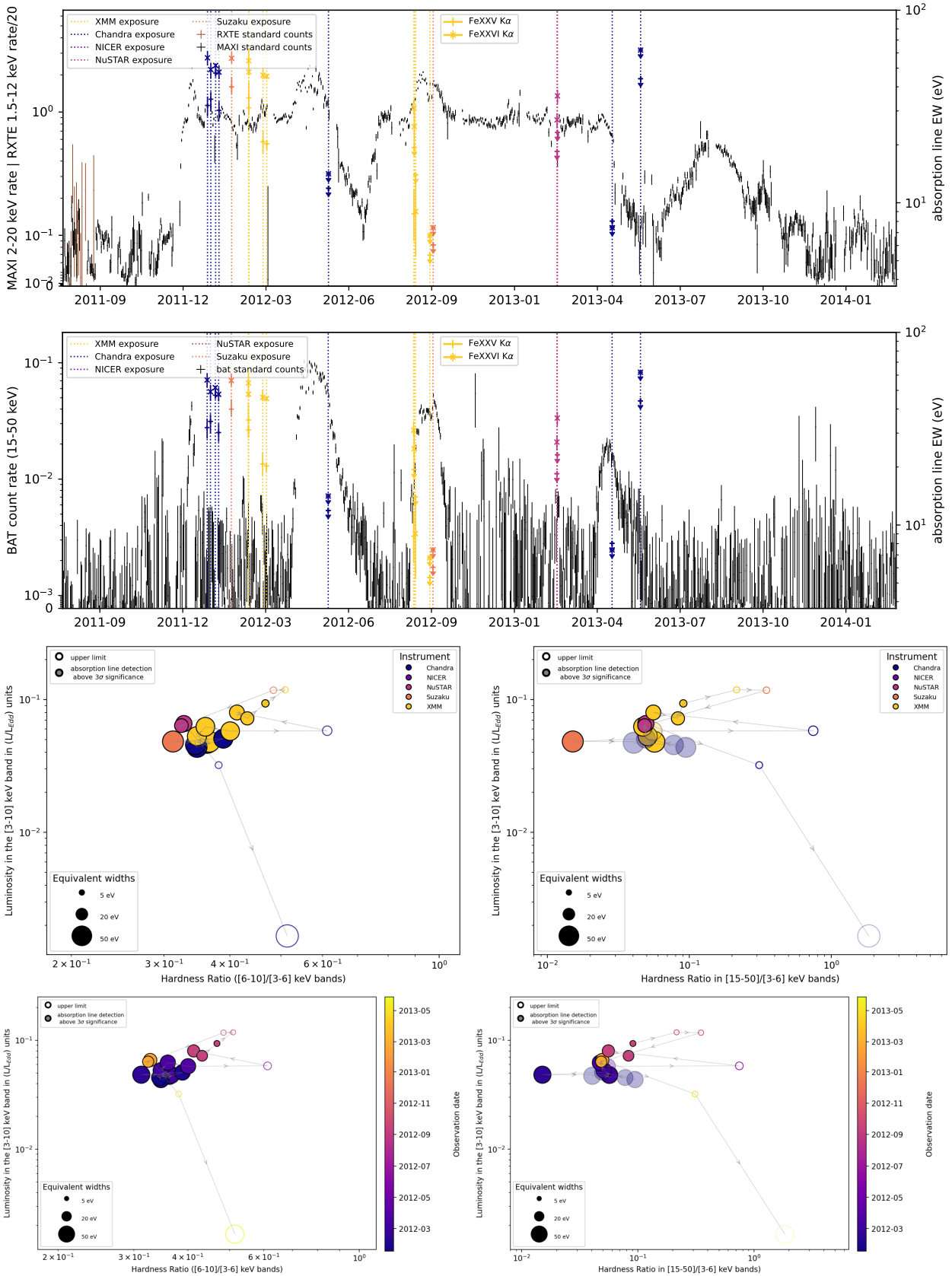

Figure 4.24: Overview of the evolution of the Kα absorption lines during the 2012-2013 outburst

4.6.5 2015

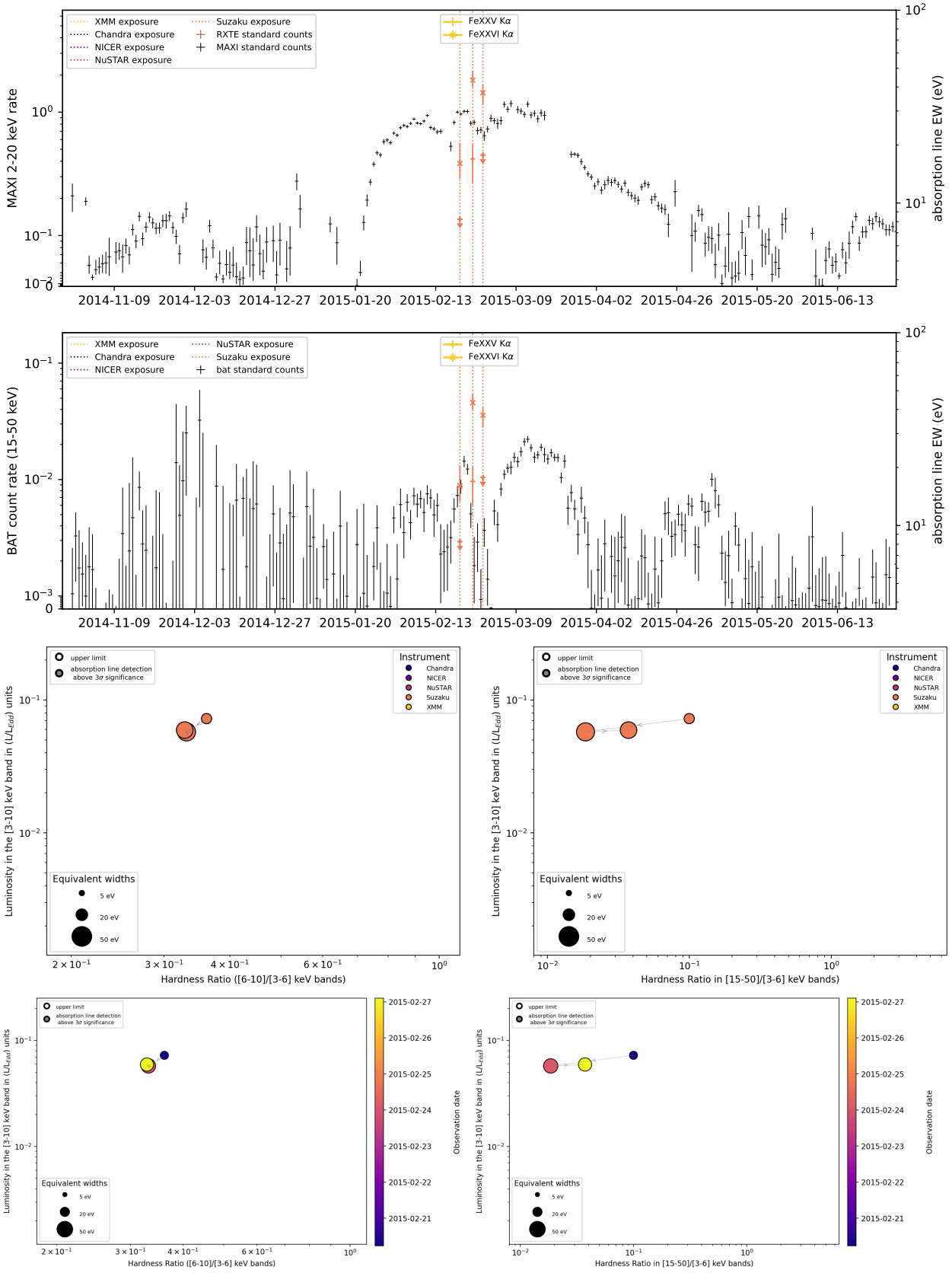

Figure 4.25: Overview of the evolution of the Kα absorption lines during the 2015 outburst

4.6.6 2016

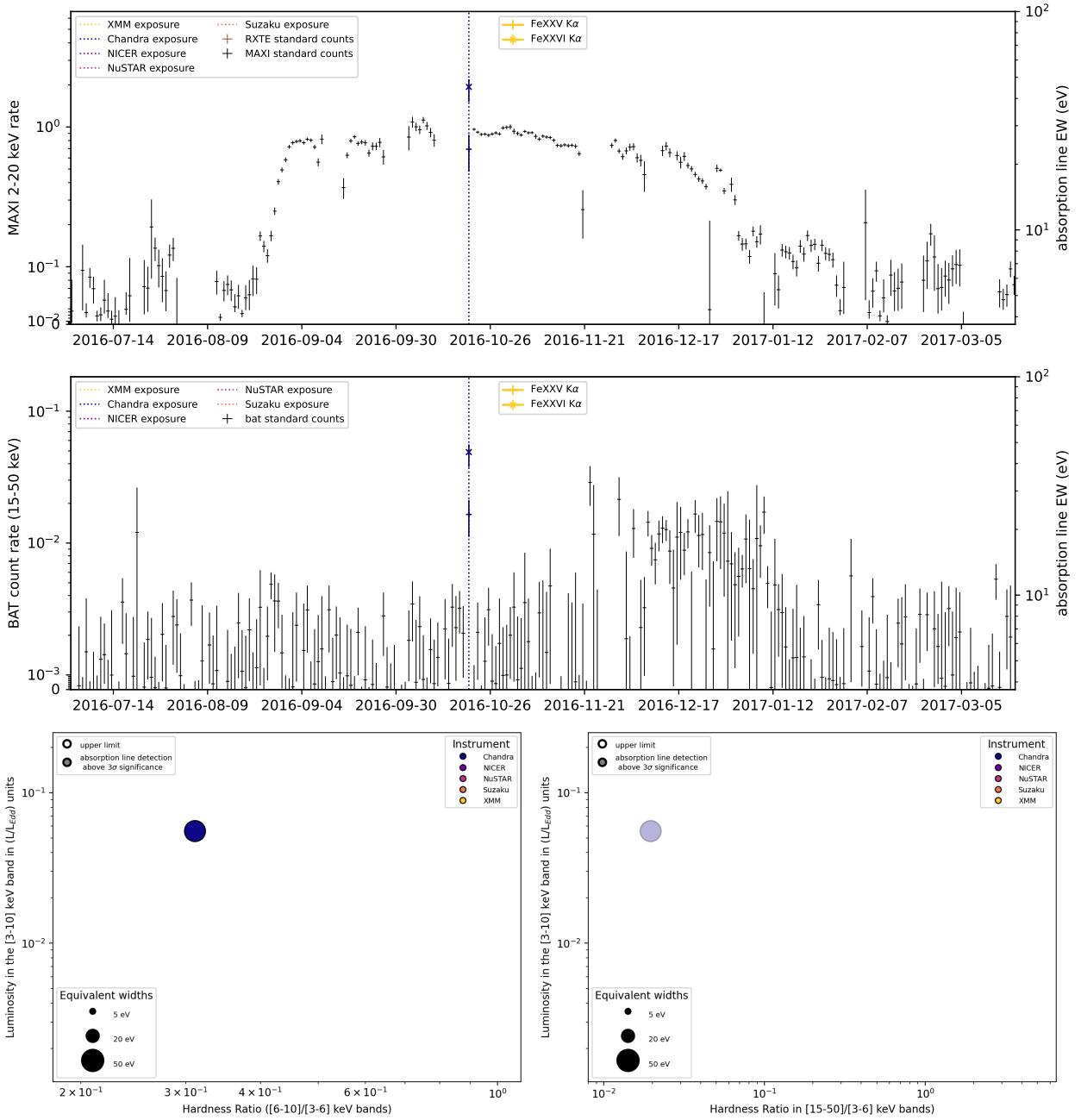

Figure 4.26: Overview of the evolution of the Kα absorption lines during the 2016 outburst

4.6.7 2018

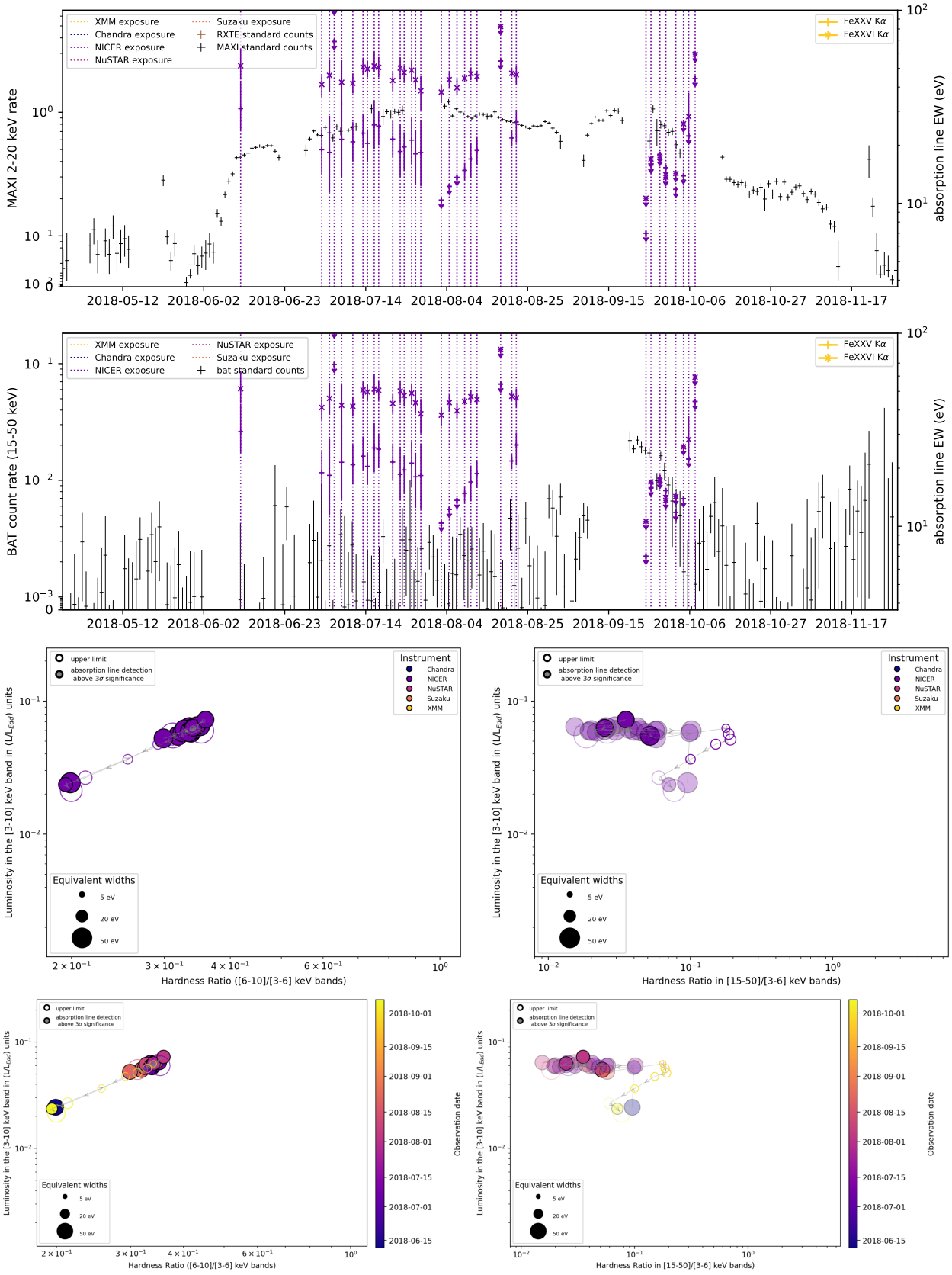

Figure 4.27: Overview of the evolution of the Kα absorption lines during the 2018 outburst

4.6.8 2020

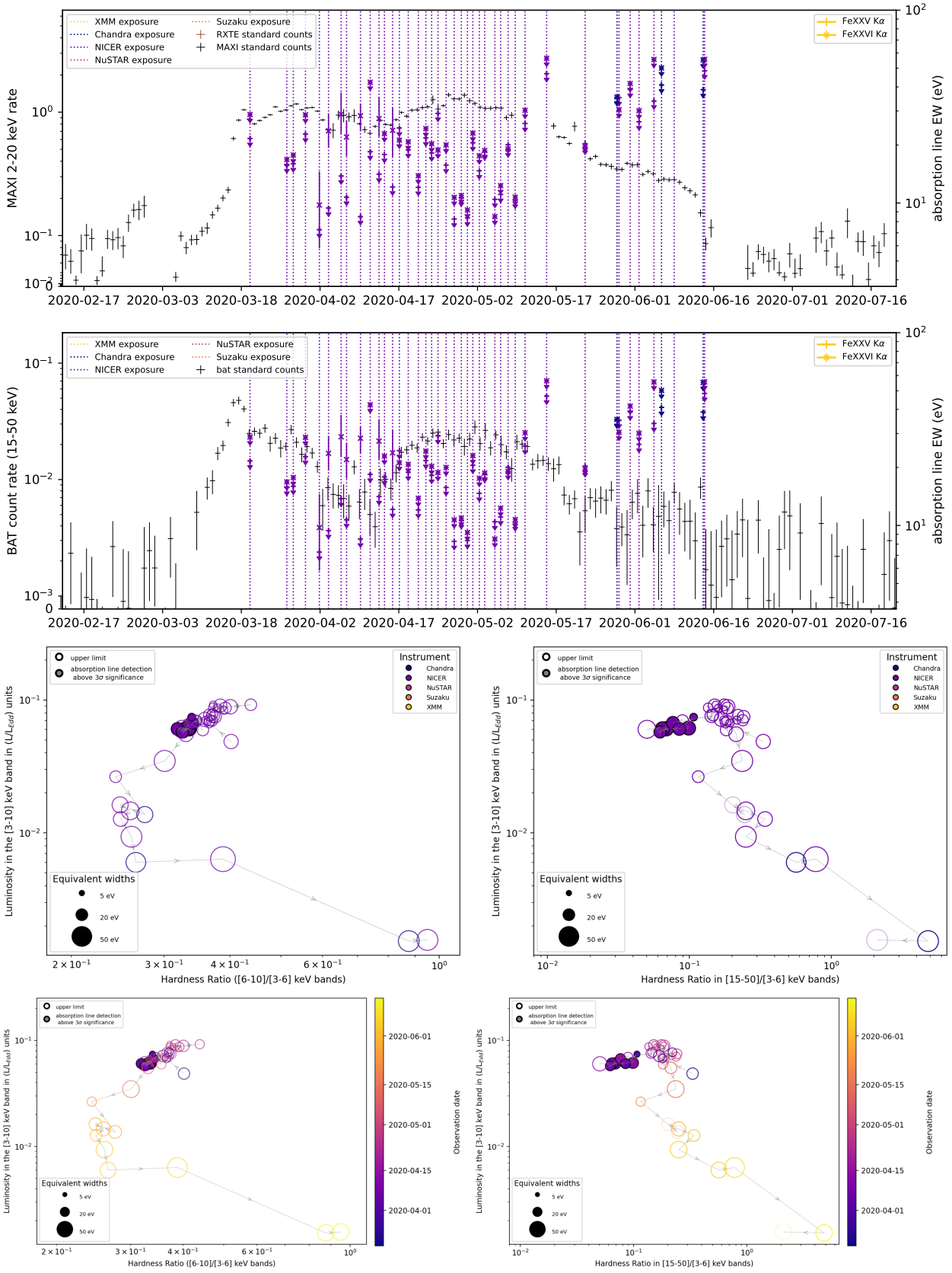

Figure 4.28: Overview of the evolution of the Kα absorption lines during the 2020 outburst

4.6.9 2021-2022

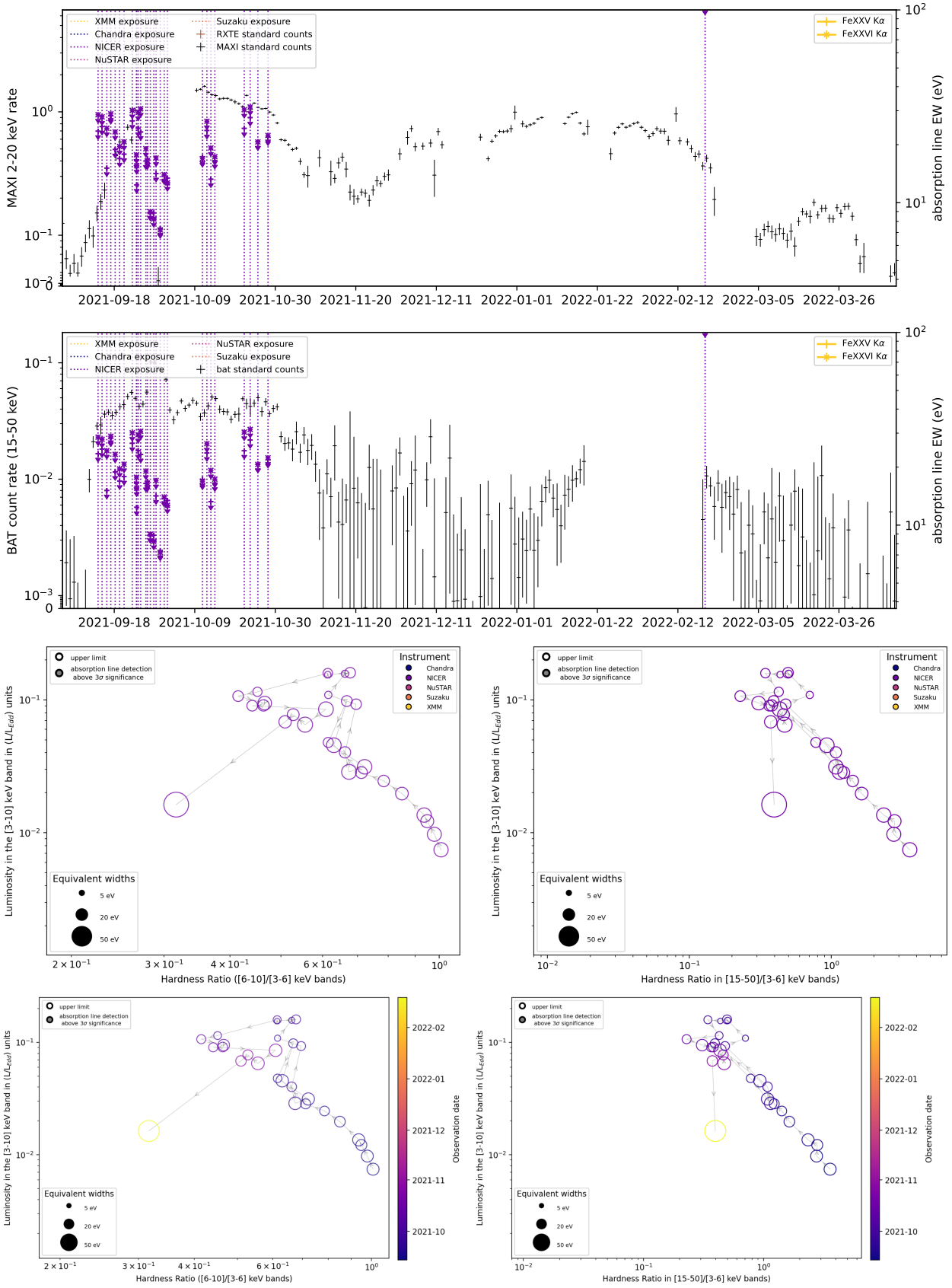

Figure 4.29: Overview of the evolution of the Kα absorption lines during the 2021-2022 outburst

4.6.10 2022-2024

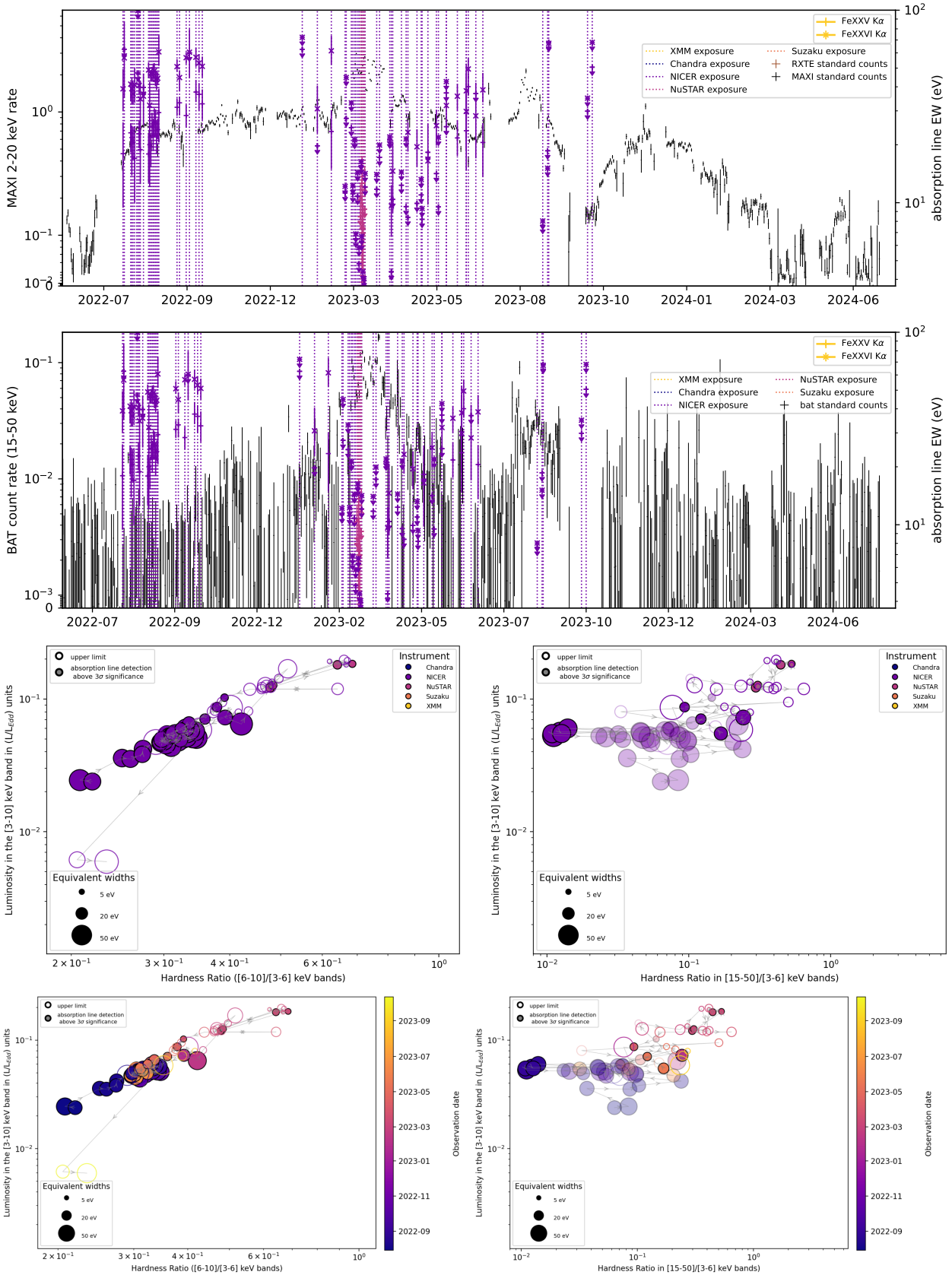

Figure 4.30: Overview of the evolution of the Kα absorption lines during the 2022-2024 outburst

4.7 Conclusion

Our exhaustive study of Fe xxv Kα and Fe xxvi Kα absorption lines in all publicly available *Chandra*, *NICER*, *NuSTAR*, *Suzaku* and XMM-*Newton* observations of 4U 1630-47 significantly expands our understanding of X-ray wind signatures in BHLMXBs.

First, the combination of more than 200 individual days of observation results in an unparalleled coverage of the HLD evolution of the source above $\sim 10^{-2} L_{Edd}$. This allows to clearly identify the limitations of the "soft" HR dichotomy for line detections, as tens of constraining non detections across several outbursts are observed with the same HLD position as significant detections. We thus refine the dichotomy by replacing the "soft" [6-10]/[3-6] keV Hardness Ratio by a "hard" [15-50]/[3-6] keV HR, built using *Swift*-BAT, , *NuSTAR*, and *Suzaku*-PIN. This new HR is much more efficient in distinguishing observations with and without line detections, as shown by the very strong ($p_S = 6.4 \cdot 10^{-10}$, $r_S = -0.79$) anti-correlation between HR_{hard} and the Fe xxvi Kα line EW.

On the other hand, the correlations with the soft X-rays remain similar to what was observed for more sources with XMM-*Newton* and *Chandra* in (Parra et al. 2024), with no correlation between HR_{soft} and the line EWs, a significant anti-correlation between Fe xxv Kα EW and the 3-10 keV luminosity, and a significant correlation between the Fe xxvi Kα/Fe xxv Kα EW ratio and the 3-10 keV luminosity. In parallel, The line properties of the source are similar to what was found in (Parra et al. 2024), with EWs between ~ 5 and ~ 60 eV, predominant Fe xxvi Kα and Fe xxv Kα detections. The small but significant blueshift found across most *Chandra* observations is also found in the much larger (but less precise) *NICER* and *Suzaku* measurements, while XMM-*Newton* and *NuSTAR* remain completely unable to access these low velocities due to instrumental limits.

Secondly, and for the first time in a XRB, the number of observations allows to grow past the simple on/off wind visibility dichotomy between soft and hard states, and attempt to characterize the evolution of the X-ray outflow along the HLD in a systematic manner. Two elements may indicate an intrinsic outflow evolution: the anti-correlation between HR_{hard} and the Fe xxvi Kα EWs, and the distinct groups (notably at low luminosities) and outliers found in the EW-$L_{[3-10]}$ correlations.

To assess whether the changes in illumination can explain the evolution in line properties without an intrinsic change in the outflow, we tested two different scenarios. First, the presence of thermal instabilities for harder SEDs, which could explain the global disappearance of the lines for high HR_{hard}. We thus split the source in 4 main spectral states and compute the stability curves using the best broad band SEDs available in each states. This clearly shows that the Fe xxv Kα and Fe xxvi Kα ionization range remains stable all the way through the hard states, and thus that instabilities cannot explain the disappearance of the lines. We investigate in more detail the possibility of stable stability curves for Fe xxv Kα and Fe xxvi Kα in the hard state, using a detailed monitoring of the rise in the 2021 outburst, and conclude that at the end of the canonical hard state, a very small HLD region is soft enough to be thermally stable in this ionization range. This is unprecedented for an XRB, and is likely to be the consequence of the unusually steep ($\sim \Gamma = 2.3$) comptonization component seen in this source at the end of the hard state.

We also directly disentangle the SED and luminosity's influence on the EW of the lines by using photoionization modeling. For this, we compute individually the curve of growths of select observations with strongly different HLD positions or line behaviors, assuming a given N_H and v_{turb} before renormalizing to a common scale of nR^2, which gives a single parameter to assess the wind evolution. With this, we obtain significant differences in "wind parameter" with evolution in both luminosities and HR_{hard}, but the lack of tests for more values of N_H and v_{turb} (something which is still ongoing) prevents any definitive conclusion as of now. Nevertheless, if the differences are confirmed, then the evolution of the outflow properties would be tied to that of the HLD position, and thus purely the accretion state, with no detected change between outbursts.

In parallel, we complement our long-term analysis with our first results in an ongoing study of the (only) observations with noticeable line variability on an orbit timescale. First, we focus on a series of observations performed in February 2023, in which the source dims and softens progressively to almost an order of magnitude less than its initial luminosity during erratic periods over several hours, before returning back to its initial state. This behavior, while accompanied by the appearance of extremely deep Fe xxv Kα lines, cannot solely be imputed to a neutral or ionized absorber along the line of sight, and is thus likely to arise from strong changes in the accretion flow. This type of strong soft dimming events with absorption features is, to the best of our knowledge, unheard of in XRBs, aside from the special cases of GRS 1915+105 and IGR J17091-3624.

We then focus on another fast line variability event in march 2023, during which the source shows strong Fe xxv Kα lines appearing and disappearing on the timescale of few hours, despite a complete lack of continuum evolution. We also confirms that the Fe xxvi Kα lines detected during all *NuSTAR* epochs around this period are very likely to result from calibration issues, considering their total incompatibilities with a great number of *NICER* observations. Finally, we test the presence of an absorption line in QRM states using flux-resolved spectroscopy, but do not detect any significant absorption lines.

Finally, we present an overview of the evolution of the source and the line behaviors for every single outburst probed in our study. Our exhaustive, multi-instrument approach can give new interpretations to outbursts already studied in the literature. This is left for future studies.

l’origine fu s e, le pur ou rt , « ent foudre ».
Puis le cosmos , consista , jusqu’aux s
tables, ’au viva t, jusqu’à vous.
Bienvenue , lent homme , ou tres des vi es .

III
Modeling

5 Observational signatures of Wind Emitting Disks

The Wind Emitting Disks solutions of Jacquemin-Ide et al. (2019), which we've introduced in Sec. 2.2.2, are among the very few physical models of magnetically launched winds, and their self-similar description provides a very promising way of accessing key physical parameters of the accretion-ejection structure via the outflow signatures. However, despite few pilot studies in the last decade (Chakravorty et al. 2016; Datta et al. 2024), the observational signatures of the WED parameter space have yet to be fully characterized. Furthermore, comparisons with existing data have yet to be performed, despite promising prospects with the new generation of instruments (Chakravorty et al. 2023). One of the main objectives of my PhD was to continue this project, build the tools allowing to compare WED signatures to the data, and take advantage of the launch of *XRISM*, as well as several extensive X-ray observation programs, to assess the ability of WED solutions to match high quality observations. However, several events have affected these prospects, among which delays on the launch and start of the observational phases of *XRISM*, the lack of suitable candidates to trigger our existing X-ray programs, improvements in the theoretical description of the WED models, and my own desire to take advantage of the goldmine of unpublished datasets in existing X-ray archives.

I have thus restricted myself to laying the groundwork, namely creating the tools necessary to produce tables of synthetic high-resolution spectra, to compare against relevant datasets. The study of the wind signatures available with the current version of the WED parameter space, as well as comparisons against present and future datasets, are both ongoing projects that will be the focus of my upcoming JSPS fellowship, in collaboration with IPAG and members of the *XRISM* team.

5.1 WED synthetic signatures: improvements and scaling

In order to compute the synthetic signatures of Wind Emitting Disc spectra, a radiative transfer code with highly precise atomic data must determine the influence of the outflowing material on the transmitted spectra. Because axisymmetric WED solutions provide a 3D self-similar structure for the disk and outflowing material at all radii, the spectral signatures of the wind should ideally be computed using a full 3D radiative transfer code. Although such codes exist (Long & Knigge 2002), they are (at least for now) too computationally expensive to allow for the exploration of multidimensional parameter spaces and direct fitting against datasets. Thus, the algorithm initially developed by S. Chakravorty and S. Datta for (Chakravorty et al. 2023) and (Datta et al. 2024) used a more simple resolution, in which the transmitted spectra are computed independently along each line of sight (LoS). In this scheme, a LoS is discretized into a sufficiently high amount of radial steps to justify the use of 1D slab photoionization codes, whose gas parameters are given by the radial distribution of the solution in this specific region. Starting from the source (or a given entry point), the transmitted spectra of each radial step is then used as input for the next radiative computation, and so on, until a final spectrum at a given final radial extension is computed, defining the total outwards transmitted spectrum. The main drawback of this technique is to completely ignore the influence of the material that is not directly along the line of sight. The validity of this assumption can be tested a posteriori with comparisons between the outputs of discretized 1D results and 3D codes. We are aware of current efforts in this direction, and an exhaustive study is left for future work.

Similarly, 1D codes do not consider the effect of the illumination on the disk or wind structure itself. Although the main advantage of cold wind solutions is to avoid the requirement of a heating function, the current solutions are nevertheless not solved in terms of energy, and thus the radial extension of the

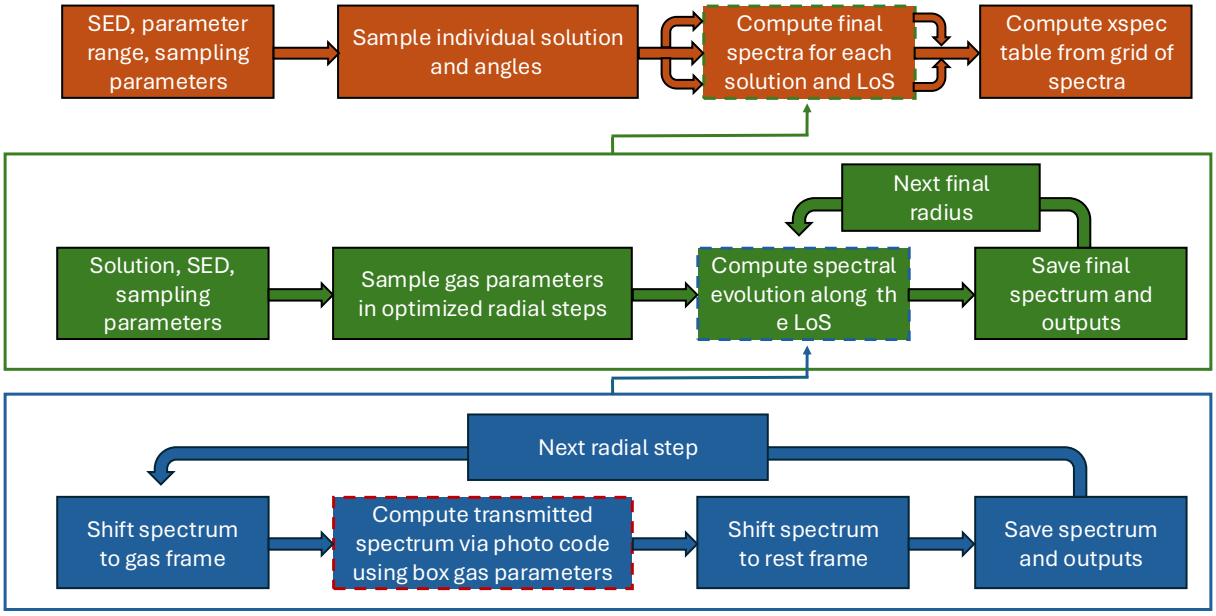

Figure 5.1: Overview of the logic of the grid creation framework. The cycle in blue represents individual radial computations along a line of sight, the cycle in green the computation of a single solution, and the one in brown the computation of a grid of synthetic spectra. We highlight in red dashes the fundamental step which involves an external photionization code, for now assured by XSTAR.

disk has to be assumed. We will come back to this matter in Sec. 5.2.3. Finally, the change in ionization structure of the gas in the advent of unstable SEDs is completely ignored. Although a first approximation may be obtained by artificially increasing or lowering the gas temperature in the solution to reach the next stable branches, this ignores several effects discussed in Sec. 2.3.3, among which the timescale necessary for the gas phase to evolve, the number of possible solutions, and the complexities introduced by the dynamical nature of the instability. Although we are aware of ongoing efforts to characterize the effect of unstable SEDs on the wind structure, for now, we will restrict ourselves to stable SEDs for the sake of reliability.

More practically, the algorithm used in previous works had been developed directly as an internal extension of the XSTAR fortran subroutine, with several hard coded parameters, for the sake of simplicity and with the idea of computing few single solutions. This had several drawbacks, including a lack of easy scalability and the issue of portability to future and different versions of XSTAR (due to progressive changes in the code structure), and to other radiative transfer codes. I thus rewrote entirely the code in python, with the same logic but significantly improved flexibility. This allowed me to include several additional effects and to build a more general set of tools tailored towards the computation of large multi-dimensional sets of solution. Finally, and most importantly, this allowed to completely detach the code itself from XSTAR, which allows to easily test differences between versions and for comparison with other codes (e.g. CLOUDY, SPEX) if desired.

Although the purpose of this chapter is not to provide an exhaustive code documentation, the computational scheme itself has never been formalized in previous works. In the following sections, I thus give an overview of the logic of the code in its new version, and highlight several of the changes and new functionalities I have implemented. An overview of the logic of the global framework is shown in Fig. 5.1

5.1.1 Necessary parameters

We list in Tab. 5.1 the fundamental parameters required to compute a synthetic spectrum. The different WED parameters (which we will discuss in Sec. 5.2) determine a single solution, and its radial distributions

Table 5.1: List of the parameters required for the computation of a single line of sight solution. Parameters listed with a † are restricted to the quantization of the WED parameter space. For comparisons with real datasets, free Object and Observation parameters are constrained by the spectra and dynamical information on the source.

Type	Name	Symbol	Available range
WED	Disc ejection index	p	$5{\cdot}10^{-3}-0.33$†
	Disc magnetization	μ	$5{\cdot}10^{-4}-0.7$†
	Disc aspect ratio	ϵ	$0.01-0.1$
	magnetic diffusivity	α_m	1-8
	Anisotropy of Turbulence	χ_m	1-8
	Magnetic Prandtl number	P_m	1
	Turbulent magnetic pressure	α_p	0-10
Object	Black Hole Mass	M_{BH}	free
	Inclination	θ	free
	Inner WED radius	r_{in}	$\geq 6R_g$
	Outer WED radius	r_{out}	$\geq r_{in}$
Observation	Spectral Energy Distribution	F_ν	stable
	Intrinsic luminosity	L_{bol}	free
Sampling	Velocity resolution	v_{resol}	free
	radial step	$\Delta r/r$	free

along a line of sight can be reconstructed using the Black Hole Mass, inclination angle, inner and outer disk radius, and the physical mass inflow rate at the inner disk boundary $\dot{m}_{acc}$. On the other hand, the incident spectrum from the central source, for now assumed isotropic, is determined by its SED and bolometric luminosity. Similarly to Chakravorty et al. (2016), the intrinsic luminosity also determines $\dot{m}_{acc}$ via:

$$\dot{m}_{acc} = \frac{1}{\eta_{acc}}\frac{\dot{m}_{obs}}{\eta_{rad}} \simeq 1.59\,\eta_{acc}^{-1}\eta_{rad}^{-1}\left(\frac{L_{bol}}{10^{38}\ \mathrm{erg.s.cm^{-2}}}\right)\cdot\left(\frac{M_{BH}}{M_\odot}\right)^{-1} \tag{5.1}$$

Since the density of the WED solution depends linearly on $\dot{m}_{acc}$ in the WED solutions, the choice of the values of the efficiencies deserves to be discussed. Chakravorty et al. (2016) assume a constant $\eta_{acc} = 1/12$ and $\eta_{rad} = 1$ following a radiatively efficient Schwarzschild solution. On the other hand, a Novikov-Thorne prescription (Novikov & Thorne 1973) for a perfectly radiating disk gives $\eta_{acc} \sim 0.057$, and more realistic derivations (see e.g. Noble et al. 2011) predict a non-negligible angular dependence of η_{acc}, especially in the assumption of an optically thick disk, for which $\eta_{acc,10^\circ} = 0.04$ and $\eta_{acc,70^\circ} = 0.12$.

Since the self-similar solutions assume a disk with a constant ejection parameter along the radius, the choice of r_{in} also affects the effective $\dot{m}_{acc}(r)$. Since the WED solutions are non-relativistic, we voluntarily restrain the inner WED radius to be bigger than the ISCO of a non-rotating BH. However, we do not yet have constrains on where the WED actually begins: typically, the JED-SAD paradigm includes an inner JED flow up to a transition radius r_J. In the new WED description, the JED and SAD are simply different classes of WED solutions, and thus the transition between the JED and the SAD corresponds to a change in (p,μ). It is entirely possible that several of such transitions exist along the radial structure, and that an "effective" WED with high ejection index only appears at high R. For now, we focus on solutions where r_{in} is fixed to 6 R_g, as this gives the maximum possible accretion rate (and thus density) along the

disk, and will thus provide an upper limit to the strength of the wind signatures.

Similar considerations may apply to the choice of r_{out}, although it does not affect the entirety of the disk structure. If we instead assume that the current WED solution persists for the entire disk extension, this gives an order of magnitude of $\sim 10^6$ Rg for XRBs. However, the density of the wind at these radii is typically too low to have a real influence on the absorption lines, and thus a strict determination of r_{out} will rarely affect the results of our computations, unless for specific cases with very small disk extensions as discussed in Sec. 3.6.

Aside from the influence of luminosity, the choice of using arbitrary SEDs is another approximation. Although the illuminating SEDs are typically derived from the data itself, a fully self-consistent approach should make use of the continuum SEDs derived from WED solutions. Such tables do not yet exist: their creation is possible using the same radiative solver DYPLO (Marcel et al. 2018a) used to create the initial JED-SAD tables used in (Marcel et al. 2018b) and afterwards, but it would require an exponentially higher computing time, as the derivation of the optically thin emission in the current version of DYPLO is interfaced with BELM tables (Belmont 2009; Belmont et al. 2008), and assumes fixed values of μ for the SAD, and no ejection parameter. Replacing a JED-SAD continuum by a JED-WED (where the new JED computation are also defined from the new version of highly magnetized WED solutions) would thus introduce several additional continuum parameters (notwithstanding the possible inclusion of turbulence) to an already undersampled set of models.

Finally, the velocity resolution and radial step size only affect the number of radial increments in which a photoionization code will be applied, and the precision of the derived spectra. These parameters are nevertheless the main drivers of the computing time of single solutions, and thus act as the main limitation for the computation of detailed tables and the exploration of the interplay between physical parameters. Unfortunately, comparisons with observations of the future generation of instruments requires the detailed profile of the lines, and thus a very detailed spectral resolution. For now, the XSTAR grid only accepts a constant logarithmic energy step, unlike the resolution of microcalorimeters, which is a constant value. We thus focus on their resolution at the iron lines: for *XRISM*-level tables, the resolution of Resolve[35] is 5 eV, which translate to $\Delta E/E = 7.14 \cdot 10^{-4}$ at 7 keV. After adding an oversampling factor of 3, we end up with an equivalent velocity resolution of $v_{resol} = 71.4$ km/s. This is the value that is passed to the code, as it also influences the determination of the radial steps, as we will see in Sec.5.1.2. We then translate the required spectral resolution to the number of bins in the XSTAR spectrum following:

$$\texttt{nbins} = \frac{\log(400\text{keV}/0.1\text{eV})}{\log(1+v_{resol}/c)}/0.98 \tag{5.2}$$

As the main grid wth a $\Delta E/E$ resolution ranges from 0.1eV to 400 keV[36], and a second coarse grid extends this range up to 1 MeV using 1/50 of the total number of bins. At such resolutions, for optically thin computations, the runtime of XSTAR is largely dominated by the time spent computing and writing the transmitted spectra. The computing time of a single XSTAR run is thus (at first order) proportional to the number of bins, and thus to the inverse of v_{resol}. We stress that this computing time is not spent equally on all bins, but instead mostly on those for which atomic transitions are relevant.

Nevertheless, the default XSTAR grid provides a very fine resolution in a vast range of energies irrelevant to X-ray absorption lines. I thus tested with T. Kallman the possibility of replacing the standard XSTAR grid with a custom grid where the "coarse" sampling covers from 0.1 eV to 0.1 keV, and from 10 keV to 1 MeV, which reduces the grid size by a factor 3.5. This improves the required computational time, but also introduces unexplained artifacts in the transmitted spectra. Thus, for now, I restrict myself to the default XSTAR grid.

[35] https://heasarc.gsfc.nasa.gov/docs/xrism/

[36] and not 40 keV as mentioned in the XSTAR manual https://heasarc.gsfc.nasa.gov/xstar/docs/xstarmanual.pdf

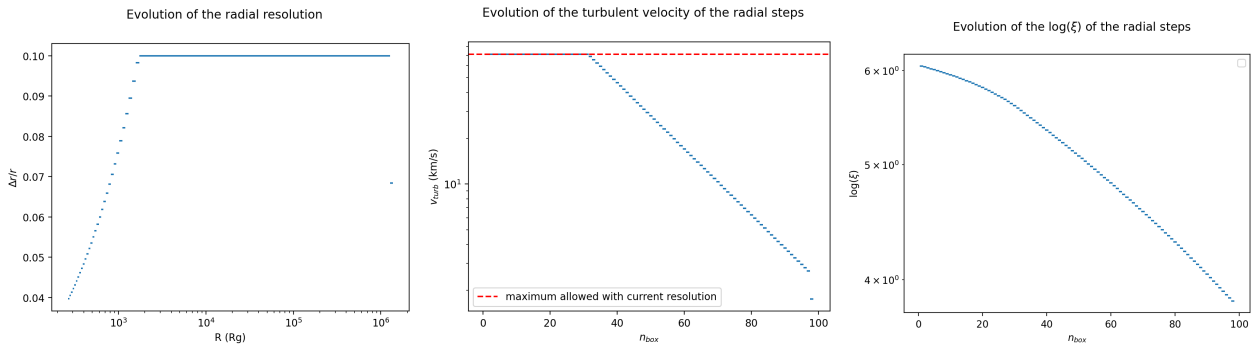

Figure 5.2: Overview of the evolution of different gas parameters along the line of sight with the current discretization method, for a solution with exaggerated parameters, $\Delta r/r = 0.1$ and $v_{resol} = 71.4$ km/s . The middle panel highlights the limit of turbulent velocity due to the spectral resolution. In all three graphs, the resolution of the last radial step is smaller because it is adjusted to match the desired value of r_{out}

5.1.2 Radial sampling

The objective of the discretization process is to reach a "sufficiently good" sampling of the evolution of the gas parameters to justify the use of 1D photoionization model. There is no obvious answer as to how this should be performed: for now, this is mainly achieved through a constant logarithmic step $\Delta r/r$, whose value ranges from 0.1 to 0.15 in the literature (Datta et al. 2024; Fukumura et al. 2017). We verified with S. Datta than values below 0.1 lead to insignificant changes in the resulting spectra, and thus retain this fiducial value. However, while this leads to a very straightfoward definition of the radial steps, the MHD solution parameters evolve differently. Among the most important is the speed of the outflow, which, besides blueshifting the lines, also defines the turbulent speed at each radial step from the difference of LoS velocity between the beginning and end of that step. Since this turbulence level affects the width of the absorption lines, the spectral resolution of the transmitted spectrum should always be kept sufficiently high so that this effect can be resolved (which we approximate by $v_{turb} \leq v_{resol}$). In previous work such as Datta et al. (2024), this criteria was manually verified to be valid for all radial steps of the computations, but it is more reasonable to include it directly as an additional sampling threshold: namely, any radial step whose v_{turb} is higher than the resolution of the spectra is reduced to a step size corresponding to $v_{turb} = v_{resol}$. We show an example of a typical result of the discretization process in Fig. 5.2. Since the outflow velocity evolves as $r^{-1/2}$, the first slabs are the ones subjected to the second criteria, and the rest evolves with a constant $\Delta r/r$. However, the right panel of this figure highlights that the sampling of other important parameters, such as $\log(\xi_i)$, remains arbitrary: this is because the radial evolution of n_H is a function of p. It would thus be worthwhile to ensure that the evolution of other gas parameters is kept below physically motivated thresholds. This is left to future work.

5.1.3 Computational scheme for a single solution

The computation of a single solution is summarized in green in Fig. 5.1. Once provided with the MHD solution for a specific ensemble of parameters (and notably the self-similar indexes of that solution), the code firsts derives the appropriate radial sampling of the line of sight between r_{in} and r_{out}, and the corresponding evolution of the gas parameters within this radial steps. The initial spectrum is then ready to follow the cycle of actions highlighted in blue in Fig. 5.1 for each radial step.

First, the illuminating spectrum is redshifted into the frame of the gas of the current radial step. This modified spectrum is then fed to the chosen photoionization code, along with the corresponding luminosity, and the gas parameters in that radial step. For XSTAR, this includes an initial temperature, ionization parameter, density, column density and turbulent velocity. For the first radial step, we let the initial temperature to its default value of $4{\cdot}10^6$ K, and its value is then taken from the thermal equilibrium obtained in the previous box. The other values are given by the discretized WED solutions. Those quantities should be defined using the parameters at the center of the radial step. However, XSTAR determines the radius of the slab from the input ionization parameter, luminosity and density. We

thus provide a modified ionization parameter computed from the central parameters and the radius of the start of the radial steps, to ensure self-consistent computations. In addition, to avoid issues with the obscure way by which XSTAR computes spatially resolved thermal equilibrium in different zones, we keep the radial decomposition of the slab `nsteps` to 1. On the other hand, the number of iterations `niter` allowed to reach the thermal equilibrium is fixed to its maximum value (100) to ensure convergence. Another important parameter of ionization codes is the abundances of different elements. This data, being typically completely unconstrained in most BHXRBs, is left to the XSTAR default, which assumes solar abundances. This may be refined to different values in the future, should the solutions be computed for galactic sources with notably non-stellar abundances, or AGNs.

Once the XSTAR computation has converged, and an output spectrum has been generated, the spectrum is then blueshifted back into the standard observer frame, which allows to store the evolution of several physical parameters, before switching to the next radial step. This process continues until reaching the final radial step(s), who are each considered as independent computations to keep a straightforward radial evolution.

5.1.4 Relativistic effects

In previous works deriving WED spectra, the Doppler shifting of the spectrum completely ignored relativistic effects. This approximation is mostly valid for X-ray Binaries, in which the distribution of the ionization parameter restricts the part of the outflows imprinting the spectra to reasonably high distances from the central source. However, this remains a very limiting approximation for both high column densities and AGNs. Thus, for a more correct approach and in hope of future comparisons with UFO signatures, I implemented the entire set of relativistic corrections described in Luminari et al. (2020), which include a deboosting factor on both the SED itself and the luminosity. In addition, a relativistic treatment of the gas modifies the influence of the different velocity components, which are very uneven in WED solutions, and affects both the terms depending on the total gas velocity, and the direction of the gas in the observer frame, due to relativistic aberration. For now, these considerations only solve half of the issue, as the WED solution themselves are currently computed in a fully non-relativistic manner. Although I correct the outflow speed distributions a posteriori to convert them to relativistic values, this remains a very adhoc correction, and the solutions themselves should eventually be computed using at least special relativity.

5.1.5 Grid computing

The most important addition compared to the previous methods is a framework allowing to compute grids of simulations in parallel. The basic idea, which we highlight in brown in Fig. 5.1, is relatively simple: starting with a multi-dimensional parameter space and sampling parameters, we define a list of individual solutions for which a synthetic spectrum should be derived. Each solution is then computed independently in a folder tree, with individual progress (or issues) along radial steps saved and reported to a watcher. Once all computations are complete, the final spectra are gathered and merged into an Xspec additive table, suitable for fitting.

The creation of grids warrants parallelization and the usage of clusters, which are rarely suited to the installation and maintenance of heavy software suites such as Heasoft (for XSTAR). To alleviate this issue, I interfaced the code with a modified version of the newly released PyXstar suite (Mendoza et al. 2024), in which the runs are performed in a containerized version of XSTAR, easily interchangeable and portable on clusters. The individual solutions along the grid, being fully independent, can then be parallelized and performed in independent cores via separate container instances, which allows for a very high degree of parallelization.

Of course, this process is greatly limited by the amount of computing time necessary to create the tables. Typically, a *XRISM*-resolution synthetic spectrum sampled with $\Delta r/r = 0.01$ takes few hours to compute, and this can hardly be sped up by parallel computing due to the limitations of XSTAR and the incremental nature of the computation. With the amount of physical parameters to sample, this rapidly leads to extremely high computing times: even a 10x10x10 grid with a hundred p-μ solutions, each sampled for 10 different angle values, already represents thousands of hours of computing time.

Aside from the issue of exploring turbulence parameters and different disk aspect ratios, this means that microcalorimeter-level tables are (for now) globally restricted to single SEDs, and should thus be computed on a case to case basis. On the other hand, CCD-level tables may be derived with a sufficiently high SED sampling to allow for global comparisons along varying spectral states, but at such resolutions, the spectra are likely to retain very high degeneracies between physical parameters.

Nevertheless, the structure of the solution computation has the advantage of being a great grid "filler". Indeed, the computation of a single radial step is only a matter of minutes, and, combined to an appropriate saving of the parameters, can be easily continued. I thus implemented a system of saves and reloads of the incremental steps of the computation, which can be used to fill out completely a cluster with "best-effort" level instances. When processes with a higher level of priority replace the instances, the only time loss is from the ongoing radial step. A watcher can then be used to monitor the unfinished computations, and reload them progressively as soon as cluster cores become available. When put on a sufficiently big (and not overbooked) shared structure, this can significantly increase the effective time spent dedicated to grid computing, with the added benefit of (almost) completely eliminating dead time in the cluster where it is applied.

The last important element to consider is the creation of the xspec model itself. Custom xspec tables require evenly sampled parameters, which is incompatible with the quantized nature of the WED solutions (see Fig. 2.10). The only solution is thus to parametrize the evolution accross the solution space: the p-μ solution space can be re-expressed with non-physical parameters such as the number of oscillations (an "island" of solutions) and an "island depth", which would characterize a parametric distance along an island from one of the edges of the parameter space. Since the turbulence parameters and aspect ratio fundamentally change the position of the islands, such a mathematic description is the only one to persist independently of the solution. Of course, this raises the issue of interpolation, as the evolution along an island is very unlikely to be linear, and the interpolation between island may only have a physical meaning if it can be interpreted as the sign of a missing element that would provide a continuous parameter space, such as the (for now ignored) heating term. The other option is to compute independent table for each island, but this makes the fitting procedure very tedious.

The issue of the validity and artifacts of the interpolation is however not limited to our model: one of the proposed solutions is the implementation of Machine Learning techniques (Matzeu et al. 2022), which take advantage of the ability of Neural Networks to emulate interpolated spectra with significantly more accuracy and speed than the standard methods, and to be trained using an uneven parameter space. On the other hand, generating an accurate Neural Network requires an extremely high amount of data, and thus this process can only be used to improve the precision of already existing tables.

5.2 Exploring the WED parameter space

In order to complement computations of synthetic spectra, and to study the behavior of WED solutions, I built an interactive tool to visualize and compare their properties. In the following subsections, I highlight some direct interpretations on the effect of the physical parameters of the WED, that can be derived from the tools themselves, using a limited sample of solutions for the sake of simplicity. However, the main strength of its tool its that all of the plots shown in the following subsections can be computed "on-the-fly" for any subsample of solutions, which will be extremely useful to perform a more exhaustive analysis in the future.

5.2.1 Evolution between solutions

The first main comparison involves the self similar constants used to define the radial dependencies of the each parameters between solutions, and thus provide an overview of the structural differences between different solutions. For now, we focus on a set of solutions with turbulence parameters maximizing the parameter space (namely $\alpha_m = P_m = \chi_m = 1$) and an aspect ratio of $\epsilon = 0.1$. In Fig. 5.3, we show the difference between a set of solutions within a single island (small variation in μ) and across islands (small variation in p). We note that due to computational limitations with low density values, the solutions at low ejection index are typically not computed up to $\theta = 90$. Since we are not particularly interested in low inclinations, this is not an issue. The aforementioned plots highlights several important global trends that hint at possible ways of distinguishing the parameters:

- In a single island, solutions with similar μ are denser for higher p. This behavior remains identical across angles. In parallel, across islands, solutions with a similar p are denser for higher μ. This behavior decreases when closing on on the disk, becoming negligible around 60. Nevertheless, as the powerlaw index of the density is a direct function of p, the change in density distribution between solutions remains largely driven by p.
- In a single island, solutions with similar μ are faster for smaller p (we can largely ignore the much smaller $v_{out,\varphi}$). The relative difference is weakly dependent on the angles, but the absolute values are significantly higher for low-inclined LoS. In parallel, across islands, solutions with a similar p are faster for smaller μ. The relative difference decreases at high inclinations, but remains significant: at 60°, we still have approximately a factor 1.3 between the u_r of each solution. Since the velocity always evolves as $r^{-1/2}$, the changes in these constant are the only drivers of the difference between the speed distributions in the outflow itself. However, this difference does not directly translate into a change in the absorption lines, as the evolution of the radial density affects the $\log\xi_i$ distribution, and the SED affects the $\log\xi_i$ regions where lines appear. In addition, the total evolution in velocity across the line of sight is an angle-dependent combination of u_r and u_z which can also be derived analytically, although the norm of the LoS velocity will be affected by relativistic aberration at low radii.
- For all solutions, a linear angle sampling provides a relatively even logarithmic sampling of the density, due to the regularity of the solutions below the compton thick threshold. This is also true for the evolution of velocities.
- In all solutions, the compton thick limit is systematically around 20, which translates to $\sim 3.5\epsilon$. Since several dynamical measurements of BHLMXBs show that permanent dips and eclipses occur for binary inclination of respectively $\sim 55-80$ and $\gtrsim 80$, this shows that $\epsilon \sim 0.1$ is a good first order upper limit of the disk thickness in permanent dipping sources, under the limit of a constant aspect ratio. However, high inclined systems showing sporadic dips (if any) and measured below ~ 80 are likely to host significantly thinner disks.

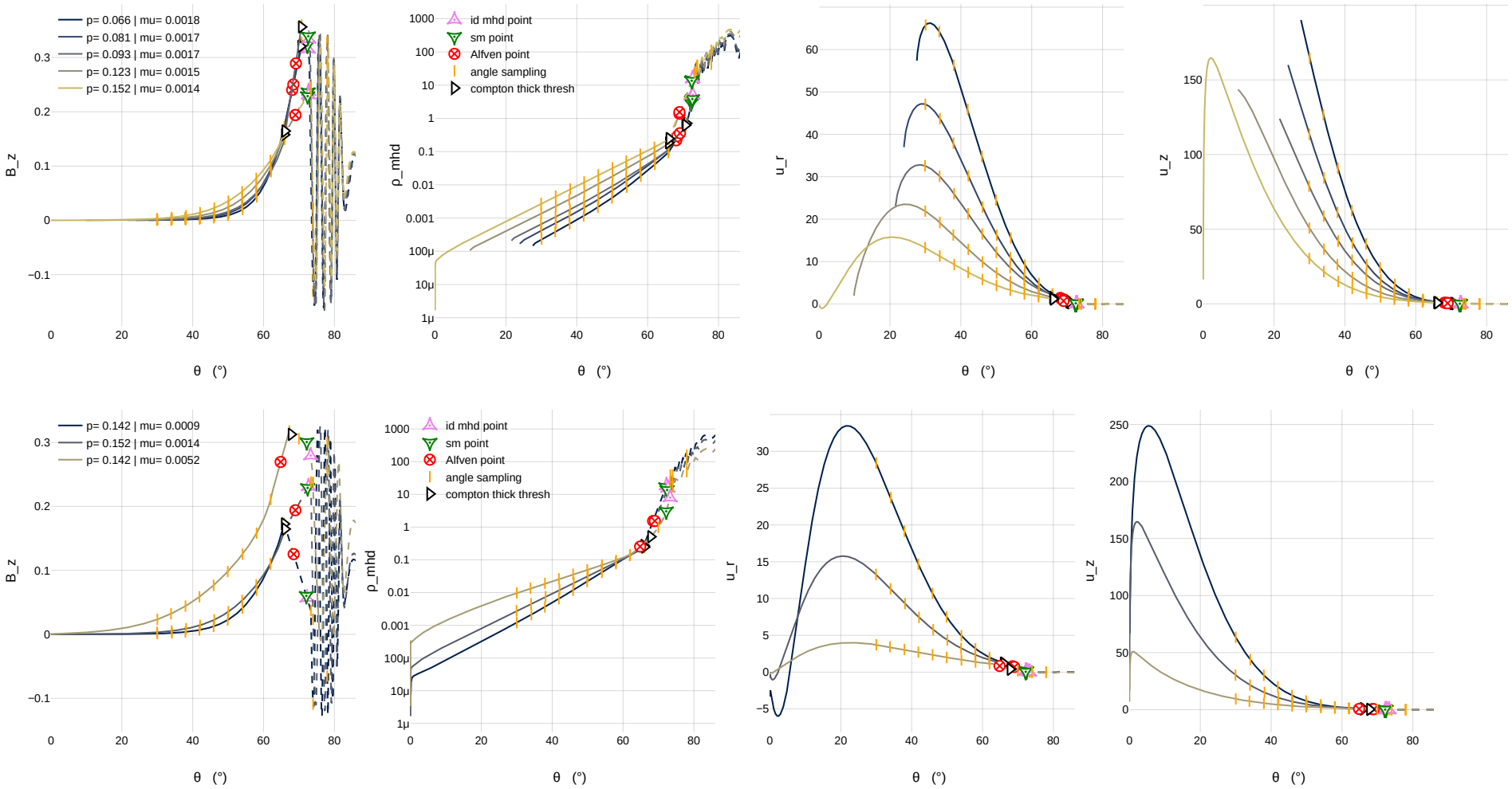

Figure 5.3: Overview of the angular dependence of the self-similar constants for B_z, n_H, $v_{out,r}$ and $v_{out,z}$, accross the n=5 island **(top)**, and for an approximately constant p between islands 5, 7 and 8 **(bottom)**, with $\theta = 0°$ being face-on, in a set of canonical solutions (all turbulence parameters fixed at 1 except α_p fixed at 0, $\epsilon = 0.1$). The plots highlight a linear angle sampling between 30°and 80°with steps of 4°, as well as several important thresholds for the MHD solution. The delimitation of the compton thick threshold, which assumes $\dot{m}_{obs} = 0.1$, is displayed among the values of the angle sampling, to highlight the last possible solution that can be computed safely (the difference between the analytical thresholds is not 4°).

5.2.2 Radial distribution for single solutions

Another useful way of characterizing the wind structure is to sample a set of angles in a single solution, and compare the corresponding radial distributions for several parameters relevant to the wind computation. We show several examples in Fig. 5.4. The study of these representations highlight key properties of the illuminated solutions:

- The most important is that the ionization structure remains independent of the luminosity, due to the linear dependence of the density on $\dot{m}_{obs}$ (potential changes in accretion efficiency aside). The first two panels of Fig. 5.4 are thus unique for each solution. This provides a unique opportunity to map out the maximal velocities available in the WED parameter space for a given SED, without performing extensive spectral computations. In our example, we highlight the limit of $\log\xi_i = 6$, which is a reasonable limit above which Fe XXV and Fe XXVI ionic fractions are typically negligible (se e.g. Chakravorty et al. 2013; Datta et al. 2024). Combined with a few ionization computations to determine the evolution of the ionic fraction with SEDs, this allows to test whether the current observational landscape of velocity measurements is accessible with the current iterations of WED. Although this is very likely to be the case for XRBs, it may not be such a trivial task for AGN UFOs.
- On the other hand, for a single solution, the column density of the gas depends linearly on $\dot{m}$. This means that in a single source with an SED evolving only in luminosity (such as a raise in hard state), the intensity of the absorption lines should increase in a very predictable manner with luminosity. Although the luminosity evolution of XRBs in the soft state is typically tied to a spectral evolution, and thus the influence of the later should be factored in, this is not necessarily true for the hard states, and can thus give strong constraints for the observations performed in low-luminosity states (notably as the OIR wind signatures). The current trends recently observed in several sources (see Sec. 3.6), and our recent results in Sec. 4.4.2, being much more nuanced than a simple luminosity evolution, seem to indicate that if magnetic winds are responsible for the signatures seen in XRBs, their physical parameters must evolve significantly along the outburst.
- The influence of different inclination angles on the absorption signatures is particularly brutal. In this solution, the strong change in N_H (or n_H, which we do not show here) between 78 and 74°is due to the switch to the very dense region above the disk with radial magnetic field fluctuations. Above this value, the column densities are extremely high and the system is fully obscured. However, for smaller inclinations, the column density quickly evolves to values of $N_H \lesssim 10^{22}$. In our example, when factoring the restriction to regions of sufficiently low ionization (bottom right panel), this happens for $\theta = 70°$, which indicates that this solution is unlikely to host significant wind signatures below this threshold (which is very high compared to most observations). This could be used to screen out the parts of the parameter space unable to create significant lines for a source whose inclination is known, and raises the issue of the possibility of fitting OIR wind signatures in mid-inclined ($\sim 45°$) systems.
- The bottom panels of Fig. 5.4 also highlight that an even angle sampling is very inadequate to provide a good sampling of N_H, which is the actual parameter affecting the wind structure. A more appropriate discretization of the LoS should instead be based on a good logarithmic resolution of the column density, combined with a good velocity resolution for the wind-absorbing regions. Although both can be computed beforehand, the former depends on $\dot{m}_{obs}$ and is thus degenerate with the luminosity, and the later is not trivial to assess. It may be derived from a suitable region of high ionic densities, but this would require preliminary ionization computations to describe the influence of the SED. Moreover, since the thresholds of N_H for physically relevant wind solutions are fixed values, the "appropriate" angle sampling is likely to differ between solutions, which once again raises the issue of the creation of tables and their interpolation. In this case, it may be more adequate to use the column density along the LoS as a model parameter inside the table, instead of the angle itself. This parameter would still define specific LoS and hold a physical meaning, and could be deprojected into an angle if need be when comparing with real data.

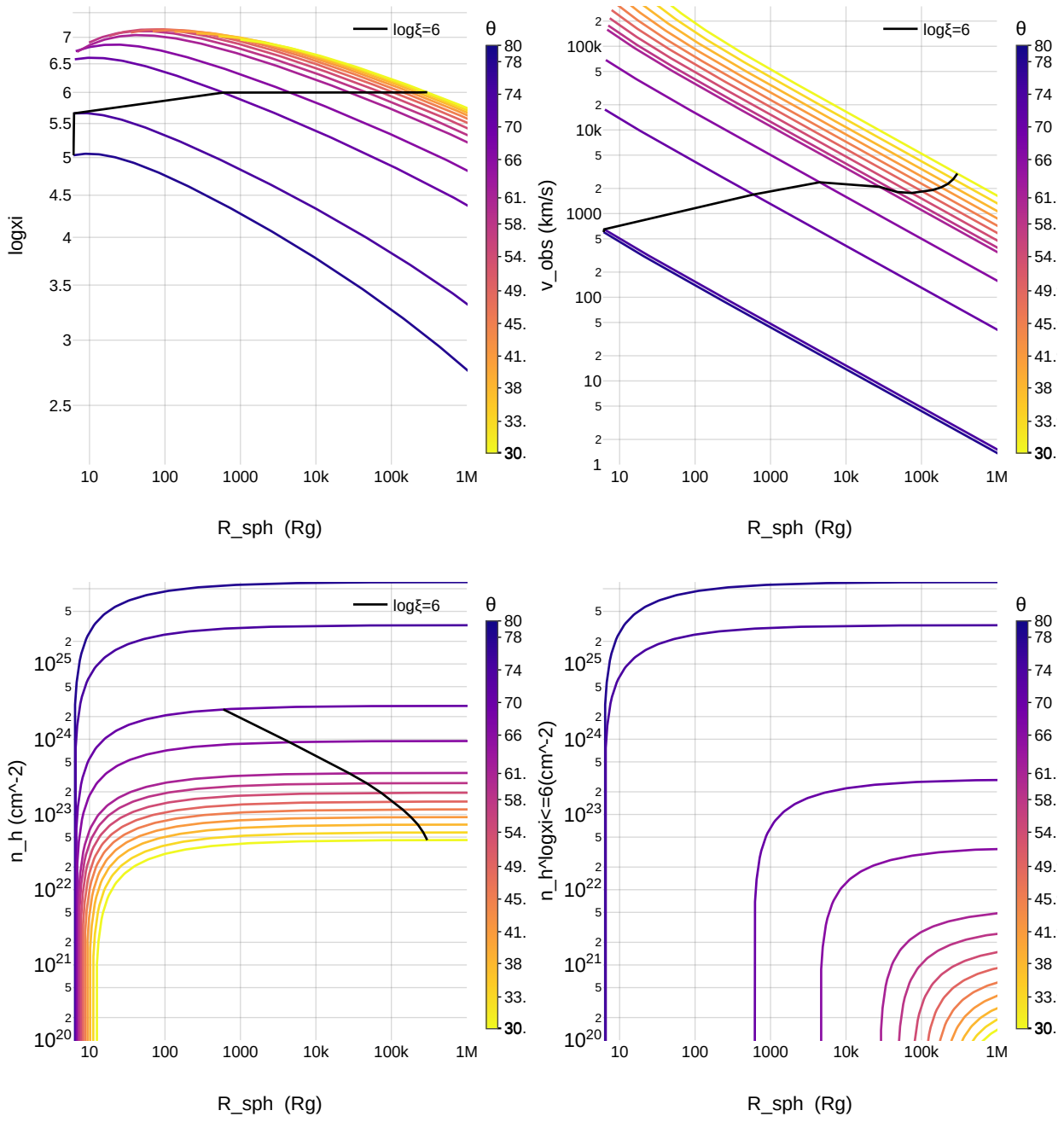

Figure 5.4: Overview of the radial dependence of several parameters, using the linear angle sampling highlighted in Fig. 5.3, in a canonical WED solution with p=0.201, $\mu = 0.0048$, $\dot{m}_{obs} = 0.111$, and the corresponding luminosity for a a $8M_{\odot}$ Black Hole. The black line highlights the minimal radii for a value of $\log\xi_i = 6$ across the angles.

5.2.3 Thermal structure

Finally, there is one WED parameter whose values may be verified physically: the aspect ratio of the disk. However, to the best of our knowledge, theoretical approaches to accretion disk structure never extend to the outer disk regions ($\gtrsim 10^3 Rg$) due to their negligible emissions. I thus implemented the tools to compute the thermal structure of a WED-like solution of thermal disks. For now, the resolution is analytical and relatively simple: it notably doesn't provide a realistic treatment to the regions where P_{rad} and P_{gaz} are comparable, nor to the optical depth when several opacity regimes become similar. In addition, the opacities themselves are determined following the canonical description of (Bell & Lin 1994), and would benefit from a more up-to-date treatment using e.g. data from the opacity project (Badnell et al. 2005). Nevertheless, our approach here is only quantitative, and even if the spikes and brutal gradients resulting from our limited computations are unrealistic, the zones where a single regime dominates are likely to be correct.

We show the evolution of the aspect ratio and other important parameters in the upper panels of Fig. 5.5. One one hand, the evolution of ϵ with radius in the typical wind-emitting region visible in X-rays $\sim 10^3 - 10^5 Rg$) is relatively small, and thus the assumption of a constant HR is a decent approximation. On the other hand, this value remains significantly lower than the canonical values of $\epsilon = 0.1$ assumed in previous works deriving WED solutions. We note that the spike in ϵ below $10^6 Rg$ should be validated with a more careful treatment, and is any case unlikely to have important consequences on the wind structure, due to the negligible contribution of this region of the disk.

We further asses the influence of different parameter on these conclusions by sampling the effect of changes in the Eddington fraction ($\dot{m}_{acc}$), p, and μ, as shown in the bottom panels of Fig. 5.5. The influence of each parameter is fundamentally different: higher luminosities/$\dot{m}_{acc}$ naturally lead to a thicker disk, and shift the opacity regime transitions to slightly higher radii. The effect of the ejection index is more complex: values of p below ~ 0.1 barely have any effect on the aspect ratio, while higher ejection indexes significantly increase the absolute value of the aspect ratio, its increase with radius, and increase the radii of the opacity regime transitions. Finally, the involution of μ is only noticeable in gas dominated regions, where higher magnetizations slightly decrease the aspect ratio.

Individually, none of the effects highlighted above are very significant, and the aspect ratio of the disk typically remains in a range of ϵ ∼0.01-0.03. However, special care should be put when comparing solutions with extreme combinations, such as high luminosity, high ejection index, and low magnetization, or low luminosity, low ejection index, and high magnetization, as the difference between the assumed value of ϵ and the real values in the outer disk may become the source of significant inaccuracies. We note that these conclusions are not fully self-consistent, as they ignore the influence that ϵ has on the available parameter space of WED solutions. Nevertheless, as long as no complete work on the matter (including a more accurate description of of the opacities, magnetic pressure, etc.) comes to nuance this view, the behavior of solutions at a lower aspect ratio should be studied with attention, if not prioritized.

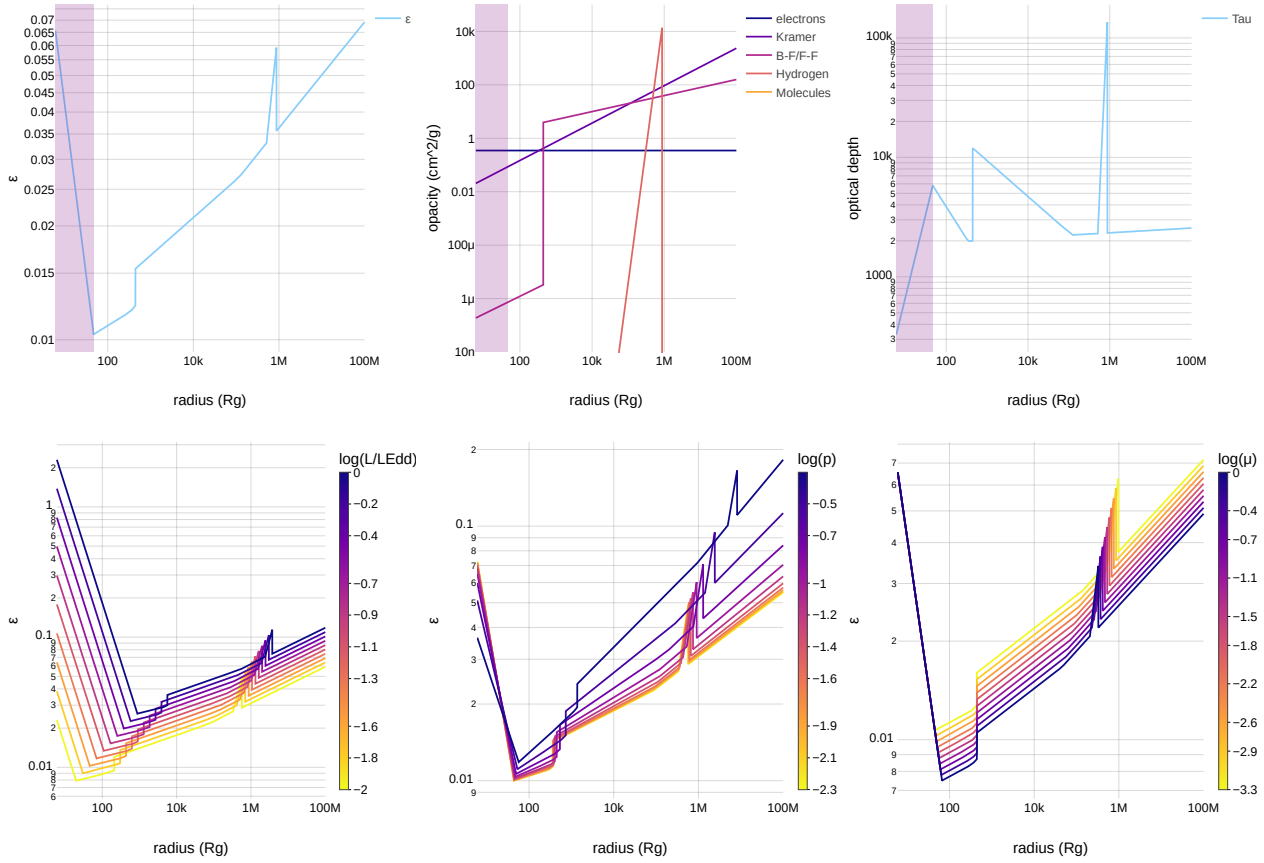

Figure 5.5: **(Top)**Radial evolution of the aspect ratio, opacities, and optical depth for an magnetized α disk solution solved for $r_{in} = 6$, $\dot{m}_{acc} = 1$, $\eta_{rad} = 0.057$, $\mu = 10^{-3}$, p=0.1, $\alpha_v = 8$, no jet power, and a $M_{BH} = 8\ M_{\odot}$. The purple region highlights the zone where $P_{rad} > P_{gaz}$.
(Bottom) Radial evolution of the aspect ratio when varying a single of the parameters of the solution. Variations of L/L_{Edd} are translated into a range of $\dot{m}_{acc}$ using the values of η_{rad} and M_{BH} highlighted above, to reflect the typical luminosity range of the soft states in a BHLMXB outburst. The intervals of p $(5 \cdot 10^{-3} - 0.5)$ and μ $(5 \cdot 10^{-4} - 1)$ reflect the WED parameter space for $\alpha_p = 0$ (see Fig.2.10 and Jacquemin-Ide et al. 2019)

À l'origine fut la vitesse, le pur mouvement furtif, le « vent-foudre ».

Puis le cosmos décéléra, prit consistance et forme, jusqu'aux lenteurs habitables, jusqu'au vivant, jusqu'à vous.

Bienvenue à toi, lent homme lié, poussif tresseur des vitesses.

ALAIN DAMASIO
La Horde du Contrevent

IV

Conclusions and Perspectives

Condensed results

In the last decade, the description of disk winds in Black Hole X-ray Binaries has become one of the fundamental goals of accretion theory and observational efforts. This is due to their fundamental influence on many aspects of the accretion ejection structure, their applicability to large scale feedback processes in similar systems such as AGNs, and their ubiquitous presence in accreting astrophysical systems. My work during the last three years has focused on improving our global understanding of the observational signatures of X-ray winds, and on preparing comparisons between the new generation of physical wind models and the next generation of instruments.

To these ends, I performed two complementary studies of archival wind signatures. The first (Chap. 3) consisted in an exhaustive analysis of the iron band wind signatures in all existing Black Hole Low Mass Binary candidates observed by XMM-*Newton* and *Chandra*-HETG. This allowed me to:

- refine the accretion state and inclination dichotomies associated with X-ray wind signatures in the last ten years (Ponti et al. 2012), and to identify their limits: X-ray absorption lines in the iron band are almost systematically found in soft states, and only in high-inclined sources. However, every wind-emitting source with sufficient sampling also shows constraining non-detections in the same range, hinting at a more complex interplay with the SED and/or intrinsic wind evolution during the soft state. Absorption line detections also seem restricted to high-luminosities, but the lack of constrains in low-luminosity observations prevents any conclusion.
- Confirm the systematic, weakly outflowing nature of the detected absorbers, with an average of $\sim$ 200 km/s obtained in the *Chandra* observations, combined with significant spread.
- Identify several trends hinting at similar wind structures across sources, with significant correlations between the 3-10 keV luminosity and both the EW of Fe xxv Kα and the ratio of Fe xxvi Kα and Fe xxv Kα EW, which is a common proxy of the ionization parameter.
- Provide a detailed description of the canonical wind emitters, supplemented by several new results and insights drawn from my own analysis, with new axes of study for GRS 1915+105 and GRO J1655-40, a new line detection at low energies in H 1743-322, and a discussion on how the nature and physical parameters of IGR J17451-3022 would impact the interpretation of its wind.

Finally, and perhaps most importantly, I extensively reviewed observational claims of wind signatures in all wavelengths, across the entirety of BHLMXB candidates. This allowed me to discuss the common grounds and discrepancies between different types of wind detections, and to highlight that absorption lines found within reflection components are not only at odds with every other line detection in terms of velocity, accretion state and inclination, but also that their existence is biased by several observational and modeling shortcomings, and thus should not be considered a valid result as of now. I also highlighted the gaps in our understanding that will need to be addressed in further studies, and notably the lack of simultaneous hot-cold wind detections, and the insufficient sampling of states and sources both with and without absorption lines.

The second observational project (Chap. 4) was a direct answer to one of the most significant limitations I had identified: the lack of in-depth studies for well-sampled sources with enough coverage to derive the evolution of the wind across entire outbursts. I thus focused on one of the most observed wind-emitting Black Hole X-ray Binary, 4U 1630-47, and combined the data of seven different X-ray telescopes to constrain the evolution of its absorption lines over 9 different outbursts, spread across twenty years. This unprecedented wind coverage in both soft and hard X-rays allowed me to:

- Derive a novel, much cleaner spectral dichotomy for the detection of iron band wind signatures, replacing the standard soft X-ray hardness ratio by one created using both soft and hard X-rays. This new HR_{hard} completely solves the issue of wind-less observations in soft states, at least in this source, and is generally much better to assess or predict the presence and absence of lines.

- Identify clear correlations between the evolution of the absorption lines and the spectral evolution along the outbursts. Besides confirming and refining correlation between lin and illuminating continuum properties found in the first project, I was able to identify outliers and groups of observation that seemed to detach from the main group, and detect a very strong anti-correlation between the presence of lines and the new HR_{hard}.
- Attempt to isolate the evolution of the outflow in the absorption lines, by studying potential degeneracies with the evolution of the stability of the plasma and the influence of the illuminating central source. For this, I:
  - Confirmed that the SEDs of the source remain fully stable all the way to (and surprisingly into) the hard state, for the ionization parameters that express in the iron band, and thus that this has no impact on the evolution of the lines.
  - Use photionization modeling to detect a probable change in intrinsic wind properties, both in low luminosity soft states, and with the evolution of the hard X-ray component.
- Perform an in depth (but still in progress) characterization of several outlier epochs, with an unexpectedly rich line variability down to sub-minute timescales, both correlated to unprecedented continuum variability and without any continuum evolution, depending on the case.
- Provide a more accessible overview of the wind evolution across each individual outburst observed in the sample, which I aim to shape up into a more detailed comparison in the future.

Finally, in Chap. 5, I continued a long-standing effort to characterize the spectral signatures of Wind Emitting Disks solutions of magnetically launched winds, building upon the results of Chakravorty et al. (2016, 2023); Jacquemin-Ide et al. (2019) and Datta et al. (2024). My main contributions consisted in:

- A significant overhaul and improvement of the radiative transfer framework used to derived synthetic spectra of WED solutions comparable with observations. It is now detached from the photo-ionized solver, uses much more flexible sampling criteria, and includes relativistic effects. Most importantly, this tool is now appropriately scaled to compute large numbers of synthetic spectra in parallel, and derive fitting tables ready for direct comparisons with observations.
- The creation a second set of tools to study and compare the behavior of the WED solutions, which I used to highlight the effect of physical parameters on the gas structure responsible for the absorption lines.
- Analytical computations of the thermal structure of WED solutions, to provide physically motivated values for the aspect ratio depending on the parameters.

Future endeavors

The dual approach of these projects open the door to numerous other studies. For observations, as I have taken great care in creating flexible and scalable data reduction and spectral analysis tools, and fostered collaborations to complete my instrumental coverage, I can now easily perform studies on the same level of depth as what has been done -but remains to be published- on 4U 1630-47. A preliminary study on the existing *NICER* archive has already revealed a virtually endless amount of potential results, which I aim to tackle in the following years, on a source by source basis. However, this is just the tip of the iceberg, as I hope to explore these (and the 4U 1630-47 datasets) in several new ways in the future. First, the empirical study on line properties should be complemented by a systematic photoionization modeling, which would give more direct constraints on the nature of the wind evolution, even in the case where a single absorber can be constrained. Moreover, the presence of wind signatures has for now only been compared to spectral properties. The many timing and spectral-timing diagnostics highlighted

in Sec.1.3.2 will certainly provide a completely new look on the mechanisms influencing the outflow properties, and a direct search of absorption features in spectrally-resolved timing properties could allow for an independent way to detect the lines themselves (Parker et al. 2020).

On a more general scale, my own impression of the X-ray Binary observational landscape, derived from my extensive research for wind signatures and inclination properties, is that of a very dispersed, often confusing, and largely misunderstood field. However, unlike many other domains of astrophysics, we are still in a situation of handling "human-scale" amounts of sources and datasets. It would thus be immensely beneficial to gather the entire outburst coverage (notably in X-rays) of these objects into a single place, both because global X-ray binary outburst studies are a good decade overdue, and to provide an easily accessible overview of the existing coverage, remarkable features and literature published on each source. While the data reduction, analysis and visualization tools I developed for my observational studies are all designated for this glorious purpose, this remains a very large scale project. I would thus be already satisfied to build its first bricks in the upcoming years, potentially as a complement to the increasing scope of my wind analysis.

The perspectives of model comparisons are equally prolific. Although I haven't mentioned the recent launch of *XRISM* in the previous paragraphs, as repeated extensively in this manuscript, its upcoming observations will revolutionize our understanding of outflows. This has already been confirmed by the first glimpses of AGNs results shown in this year's conferences, and thus bods very well for brighter sources like XRBs. The main objective of *XRISM* remains (in our field) to distinguish launching mechanisms via their line profiles. I am hoping to be at the forefront of this effort, now that the tools are ready to map out the signatures of WED tables, and I aim to keep developing the largely untouched potential of WED solutions. For this reason, I applied (and obtained) a fellowship from the Japanese Society for the Promotion of Science, which will allow me to work directly in Japan for the next two years, in close relationship with wind experts of the *XRISM* team and the theoretical group remaining at IPAG.

This will be the occasion to focus more largely on the development of WED models, with both an exhaustive characterization of the WED absorption line signatures across the full and up-to-date parameter space, and comparisons with observations that may either come from *XRISM* or from the archival data I've already analyzed. Here again, opening the scope of the comparisons is only a matter of time: the UFOs detected in both AGNs and Ultra-Luminous X-ray Sources provide a formidable opportunity to test a completely different parameter space of the magnetic models, and to provide a first realistic derivation of the outflow structure and power for these sources, both of which are direly needed to aliment feedback models at broader scales.

As both observational and modeling prospects would greatly benefit from new dedicated datasets, I have also spent a non-negligible part of the past few years applying for observational programs. This has led to several accepted programs, and notably a XMM-*Newton*-*NuSTAR*-*Swift* Target of Opportunity Large Program in AO23, an update from a previous accepted LP (PI Petrucci) in AO20, that will provide for the first time a well sampled broadband coverage of the Hard-Soft state transition in a wind-emitting BHLMXB. I have also obtained a set of 5 *XRISM* observations (for a total of 100ks) to accompany this program in AO1, which, combined to 80ks of additional JAXA time, will give us an opportunity to build an exceptional dataset in the year to come. I have also significantly contributed to a recent DDT request of the obscured source V4641Sgr, which ended up being the first accepted DDT of *XRISM*. Although the observation was performed after an unexpected drop of more than an order of magnitude in luminosity, the spectrum, which is currently being analyzed, remains rich in emission line components.

In addition, although the word polarization has barely made it in this manuscript, as a member of the *IXPE* collaboration, I have been a part of several recent studies that stemmed from the first X-ray polarization measurements in BHXRBs, and I am involved in modeling efforts to compute the polarization signatures of the JED-SAD suite of models. This is especially relevant as one of the most puzzling observations to date remains the high polarization degree measured for the wind-emitter 4U 1630-47, which is suspected to come from the outflow, and may provide a completely different avenue to

constrain the outflow structure. To improve our understanding of the polarization of wind-emitters, as part of the *IXPE* collaboration, I have led a ToO proposal to provide a new observation of a wind-emitting BHXRB in the soft state. Since it has yet to be triggered, I have resubmitted it for the next year, with a longer exposure, more soruces, simultaneous *NuSTAR* time, and the added benefit of coordinating with my other accepted programs, to create a spectro-polarimetric dataset of unprecedented precision. In parallel, once our understanding of the JED-SAD polarization signatures will have matured, via the new PhD project of R. Muhammad in IPAG, I hope to perform a similar analysis of the much more complex WED structure, and provide constrains on both polarization and the absorption signatures simultaneously.

It is certainly an exciting time to become an X-ray Astrophysicist, and my only worry for the years to come will be to choose what to focus on among the myriad of the interesting projects highlighted above.

I've had it worse.

V
Appendixes

6 Methodology

6.1 Data treatment

6.1.1 Global study

XMM

Data reduction for XMM-*Newton* observations was performed with the Science Analysis System (SAS[37]) version 19.1.0, following the standard analysis threads.[38] Observation data files (ODFs) were reduced with the $epproc$ task.

To optimize the absorption line detection, we maximized the signal-to-noise ratio of the final spectra through an automated procedure. We describe the main steps in the following paragraphs.

The automated procedure first extracts an image centered on the sky coordinates of the source from the event files in the 4-10 keV band. It then computes an initial source and background regions. In imaging, the image is fit with a point spread function (PSF) in order to optimize the source localization. The background region is then generated from the largest circular region not intersecting the brightest 2σ of the source PSF in the source and neighboring CCD, with an area between one and two times that of the source region. Whenever the background region rate exceeds 100 times the value of standard blank fields[39], its contribution is disregarded. In timing and burst mode, the source region is centered on the brightest column, and the background is always disregarded in order to avoid source contamination.

Following this, the procedure computes the size of the source region and the filtering of high background periods in a self-consistent way to reach the highest S/N. For this, it selects increasingly large circular (rectangular in timing) regions, each of which is independently filter ed for good time intervals (GTIs) in order to maximize its individual S/Ns against the background computed previously (following the method of Piconcelli et al. 2004).

The procedure then estimates the pile-up value with $epatplot$, and, if necessary, excises an increasingly larger circular portion of the source region until the pile-up value falls below 5%,[40] a level at which no significant effect on the line detection process is expected. We note that the majority of the spectra actually remain below 1%. After an excision, the first two steps are repeated, this time starting with the filtered GTIs and the excised image, in order to refine the region and filtering of the events.

The final step is the extraction of the source and background spectra from the final region files and GTIs, and the generation of response matrices and ancillary response files with the standard SAS tasks $arfgen$ and $rmfgen$. The source spectra are grouped using the heasoft task *ftgrouppha*, following the Kaastra & Bleeker (2016) optimized binning.

We note that although recent work has shown that dust scattering halos can significantly alter the broadband SEDs of XRBs (see e.g., Jin et al. 2017, 2019), this effect is smaller at high energies and is not expected to affect the detection of narrow absorption lines. We thus did not apply such corrections for simplicity.

Chandra

The reduced, science-ready spectra of the first order of all grating observations are publicly available on the *Chandra* Transmission Grating Data Archive and Catalog (TGCat;Huenemoerder et al. 2011), and observations of BHLMXBs have been recently updated according to recent improvements in data reduction. We only considered the first order spectra and regrouped the products according to the

[37] https://www.cosmos.esa.int/web/XMM-Newton/sas
[38] see https://www.cosmos.esa.int/web/XMM-Newton/sas-threads
[39] obtained from https://www.cosmos.esa.int/web/XMM-Newton/bs-countrate
[40] Up to 7% was accepted for four exposures, highlighted in Table. 7.1.1.

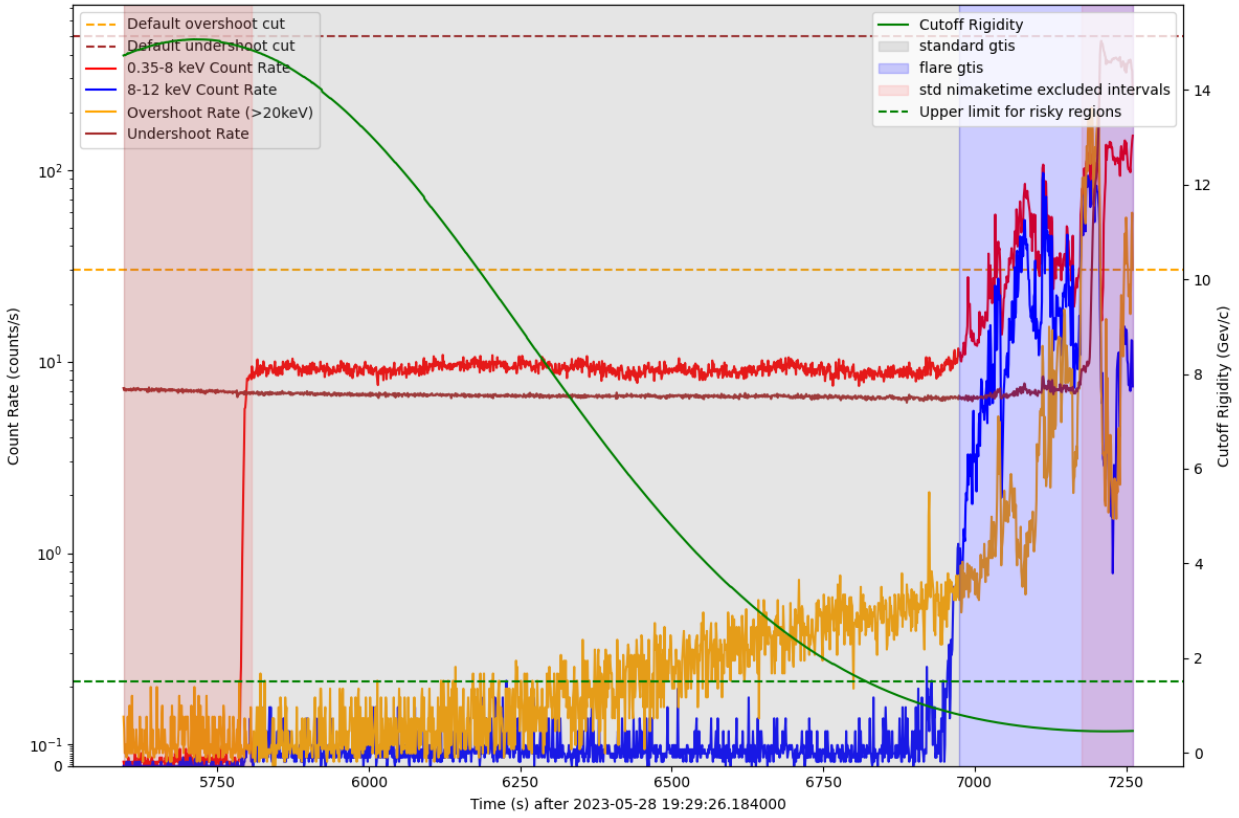

Figure 6.1: Diagnostic plot of several quantities stored in the *NICER* filter file for a single continuous GTI of ObsID 6130010118. A bright X-ray flare is easily visible at the end of the observation in the soft X-ray (bright red) and high-energy(blue) lightcurves. The automatic filtering (red regions) only removes a part of this flare, whereas the additional screening (blue region) removes it entirely

Kaastra & Bleeker (2016) optimized binning. Background spectra were not computed, as they are often contaminated by the PSF wings.[41]

6.1.2 4U 1630-47

NICER

The Neutron star Interior Composition Explorer (*NICER*, Gendreau et al. 2016) has observed extensively every single outburst of 4U 1630-47 since its launch in 2017. We analyze every observation listed in the *NICER* Master HEASARC catalog[42] as of 2023-12-01, for a total of 224 ObsIDs with non-zero exposure. Our data reduction procedure mainly relies on the simplified pipeline tasks of the NICERDAS software[43] version 11, and uses the CALDB calibration files xti20240206, the latest as of the writing of this manuscript. We downloaded up-to-date geomagnetic data, necessary for our choice of background model, using the `nigeodown` task of NICERDAS.

The Good Time Intervals (GTIs) are first split into continuous periods, but need to be filtered to remove background flares. *NICER* is sensitive to several different types which can contaminate the data and significantly change the shape of the continuum. As the standard screening criteria of `nicerl2` are not always sufficient to exclude entirely (if at all) these periods, we implement an additional screening, following the methodology proposed in the *NICER* threads[44] in order to recognize and

[41] See https://cxc.cfa.harvard.edu/ciao/threads/xspec_phabackground/.
[42] https://heasarc.gsfc.nasa.gov/db-perl/W3Browse/w3table.pl?tablehead=name%3Dnicermastr&Action=More+Options
[43] https://heasarc.gsfc.nasa.gov/docs/nicer/nicer_analysis.html
[44] https://heasarc.gsfc.nasa.gov/docs/nicer/analysis_threads/flares/

exclude precipitating electron flares. We use the information of the filter file of each observation, split independently for each continuous gti, basing on two complementary criteria. First, we exclude statistically distinct events, which we define as >100 times the median count rate of the 2 sigma clipped high energy (8-12keV) events. Secondly, we search and exclude significant peaks present in both the 8-12keV and 0.35-8keV event list, using the python library findpeaks[45].

The first of these two methods allows us to exclude long flare periods that do not register as peaks through a topological analysis, and the second to extend the exclusion to the "wings" of each flare's peak, in order to limit residual contamination. We show an example of the screening in figure 6.1, with a plot of several parameters stored in the filter file of a continuous GTI. The manual screening (blue region) is necessary to complement the automatic *NICER* screening (red regions), in order to remove the flare visible in all 3 lightcurves towards the end of the observation. These diagnostic plots, as well as the lightcurve products we create for the remaining "cleaned" GTIs, were then use to verify that the flares were adequately removed in all observations.

The resulting GTIs were then used as input for the `nicerl3-spect` and `nicerl3-lc` tasks, which respectively create all spectral and lightcurve products. We used the xspec-model version of the scorpeon background model, and created lightcurves with a 1s binning in different bands. This last choice allowed us to manually inspect the continuous GTIs remaining after the filtering procedure, to confirm that any flare had been correctly screened out. Finally, the spectra were grouped according to the Kaastra & Bleeker (2016) optimized binning.

The procedure resulted in 618 individual orbit spectra, covering 189 days. In the remaining 35 days, all the *NICER* orbits were completely discarded by the *NICER* data reduction pipeline.

NuSTAR

The *NuSTAR* telescope (Harrison et al. 2013) has observed 4U 1630-47 in several different outbursts since its launch in 2012. On top of its ability to detect iron lines, it provides the most precise view of the 10-80keV band of any flying instrument, which makes it particularly suited to model the broad band X-ray SED of the source. We analyzed every public observation in the *NuSTAR* Master HEASARC catalog [46] as of 2023-12-01. We discarded ObsID 40014006001, which was too off-axis to be usable, and ObsID 30001016002, which was performed in quiescence, and where the source is not detected. For the data reduction, we used the standard `NuSTARDAS` tasks and the latest CALDB available, and applied a fully automated procedure to compute spectral and temporal products.

For each ObsID, we first reprocess the data using the `nupipeline` task, using standard parameters and filter criteria. We extract an image in the [3-79] keV using `xselect`, then extract a background region from the largest circular region not intersecting with the brightest 2σ regions in the field of view, with a radius up to 120". In parallel, we fit a Point Spread Function (PSF) starting on the theoretical source position, in order to optimize its localisation, and compute the source region radius which optimizes the S/N of the source region (Piconcelli et al. 2004), considering the background, up to 120".

Once a suitable source and background regions have been defined, we extract a 1s binned lightcurve of the source in the [3-79] band using the `nuproducts` task. If any part of the lightcurve exceeds 100 counts/sec, following the recommendations of the standard threads[47], we re-run the previous steps of data analysis (both nupipeline and region definition), this time having added the `"(STATUS==b0000xxx00xxxx000)&&(SHIELD==0)"` keyword in `nupipeline`, in order to mitigate the mismatching of noise events.

We then extract the final spectral and temporal products of each focal plane independently, using the `nuproducts` task, and group the spectra according to the Kaastra & Bleeker (2016) optimized binning.

[45] https://github.com/erdogant/findpeaks

[46] https://heasarc.gsfc.nasa.gov/db-perl/W3Browse/w3table.pl?tablehead=name%3Dnumaster&Action=More+Options

[47] https://heasarc.gsfc.nasa.gov/docs/nustar/nustar_faq.html#bright

Suzaku

Suzaku (Mitsuda et al. 2007) observed the source 12 times in 2006, 2010, 2012, and 2015 at different luminosities. Among them, 11 observations were performed at bright phases in outbursts when the source was in the high/soft or intermediate state (Hori et al. 2018) and the other one was at the end of the 2010 outburst when the source was in the low/hard state (Tomsick et al. 2014).

The observations were made with two detectors: the X-ray Imaging Spectrometer (XIS) and Hard X-ray Detector (HXD). The HXD stopped its operation before the observations in 2015 (OBSID=409007010, 409007020, and 409007030) due to the power shortage of the spacecraft, and therefore only the XIS data are available in these epochs. The XIS are composed of three frontside-illuminated (FI) CCDs (XIS-0, XIS-2, and XIS-3) and a backside-illuminated (BI) CCD (XIS-1). The XIS-2 stopped working from the end of 2006 so the data of it are only available in 2006 observations (OBSID=400010010 through 400010060).

We adopted all the available XIS and HXD PIN data and conducted data reduction for the individual observations, using the latest *Suzaku* CALDB (version 20160607). We utilized the cleaned event files produced by the final version (v3.0.22.43 or v3.0.22.44) of pipeline processing. For the 2010 data (OBSID=405051010), which did not suffer from pile-up effects, we extracted the source spectra from circular regions of $1'.3$ radii centered at and $\sim 7'$ apart from the source position as the source and background regions, respectively. For the data taken in 2012 February (OBSID=906008010), we adopted an annular region with inner and outer radii of $0'.7$ and $1'.8$ respectively. The background subtraction was not conducted for this observation, because its contribution was negligible, less than 0.1% at all energies, and the inner radius is chosen to limit the pile-up fraction to below 1% , estimated in the same way as in Hori et al. (2018) using the tool `aepileupcheckup.py`[48]. For all other observations, which were already analyzed in Hori et al. (2018), we employed the same source and background regions as those in that work. The response matrix files and ancillary response files were made with the ftools `xisrmfgen` and `xissimarfgen`, respectively. We merged the FI CCD data taken in the same observations. For the HXD PIN, we created the background data by merging the "tuned" Non-X-ray background files provided by the *Suzaku* team[49] and the modeled cosmic X-ray background[50]. We used the appropriate versions of the PIN response files[51] included in the CALDB.

INTEGRAL

The INTErnational Gamma-Ray Astrophysical Laboratory (*INTEGRAL*) satellite was launched in 2002 and made observations for most outbursts of 4U 1630-47. We used data from the Imager on-Board the *INTEGRAL* Satellite (IBIS, Ubertini et al. (2003)), and more specifically from the IBIS Soft Gamma Ray Imager (ISGRI, Lebrun et al. (2003)) which is sensitive in the 30 - 500 keV range and has a 12' angular resolution thanks to its coded aperture. For data reduction we used the Off-line Scientific Analysis (OSA) v11.2 software [52] which allowed us to produce lightcurves and spectra on satellite revolution basis ($\sim$ 2.5 days).

We used 20 logarithmically spaced energy bins between 30-200 keV for every spectra, which we fitted with a simple powerlaw model, allowing us to derive fluxes.

***Swift*-BAT**

In order to assess the long-term evolution of the source, and to complement our high-energy coverage, we use the daily BAT lightcurve products available via the BAT Transient Monitor[53] (Krimm et al. 2013).

Extending the high energy coverage

With *Suzaku* and *NuSTAR*, the fits above $\sim$ 15 keV show that the source is at first order well described by a simple comptonized component, with a photon index varying between 2 and 3. Thus, we can draw

[48] `http://www-x.phys.se.tmu.ac.jp/~syamada/ana/suzaku/XISPileupDoc_20120221/XIS_PileupDoc_20120220_ver1.1.html`

[49] `https://darts.isas.jaxa.jp/astro/suzaku/analysis/hxd/pinnxb/tuned/`

[50] `https://heasarc.gsfc.nasa.gov/docs/suzaku/analysis/pin_cxb.html`

[51] `https://darts.isas.jaxa.jp/astro/suzaku/analysis/hxd/pinnxb/quick/`

[52] `https://www.isdc.unige.ch/integral/download/osa/doc/11.2/osa_um_ibis/man_html.html`

[53] https://swift.gsfc.nasa.gov/results/transients/weak/4U1630-472/

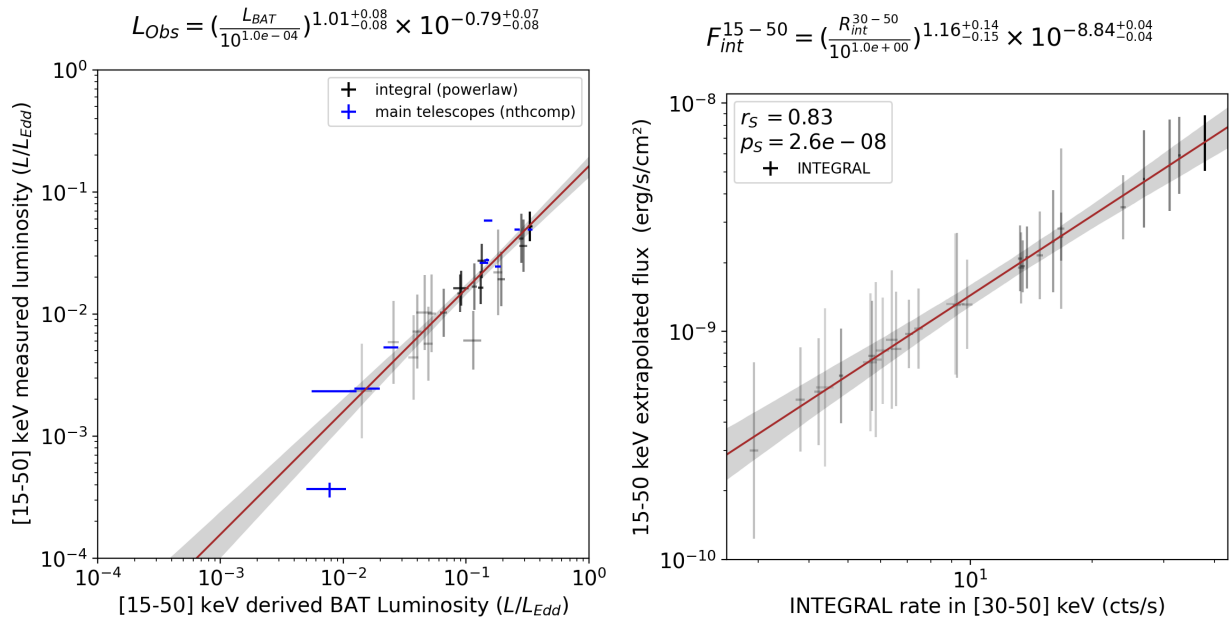

Figure 6.2:
(Left) Luminosity of the source in the [15-50] keV band in Eddington units, using BAT flux values estimated via WEBPIMMS, compared to actual measurements from *INTEGRAL*, *Suzaku* and *NuSTAR* datasets.
(Right) *INTEGRAL* 30-50 count rates versus 15-50 keV projected fluxes in observations of sufficiently high SNR to perform a fit. Uncertainties on both linear regression regions and coefficients are quoted at a 1 σ confidence level.

estimates of the daily source flux in a given band by estimating the SED of a given day, and computing the corresponding conversion factors from the source count rate, using WEBPIMMS. Surprisingly, for *Swift*-BAT, the photon index has a very limited effect on the resulting flux: a Γ varying from 2 to 3 only results in a flux variation of less than 5%, much lower than the BAT count rate uncertainties. Similarly, we verified with the existing multi-instrument coverage that the typical variations of both N_H and the typical disk parameters have negligible effects above 15 keV, except for states much too soft for BAT to detect. We thus choose a single SED template, using a typical nH value of $1.1 \cdot 10^{23}$ cm^{-2} and a fixed $\Gamma = 2.5$. Since the BAT lightcurves are computed in the [15-50] keV band, we compute the flux estimates in the same band.

In order to verify that this conversion was accurate, we compared it to the measurements from existing high-energy spectra of this source. In addition to the exposures listed in Tab. 4.1, we also used all of the *INTEGRAL* revolutions with good enough SNR to get a constrain on the spectral index in individual high-energy fits. For these, since the ISGRI instrument is only reliable above 30keV, we extrapolate flux measurements in the BAT band (15-50 keV) from the measurements in the individual *INTEGRAL* fits (obtained with a powerlaw). The result, which we show in the left panel of Fig. 6.2, is that the BAT webpimms conversion is significantly off, but individual *INTEGRAL* fits and our main analysis agree very well on the value of this error (about a factor ~6 for the majority of measurements). We thus apply a correction on the first conversion, using a linear regression derived from these measurements. This allows us to obtain good flux estimates down to the edge of the BAT sensitivity, which lies around $10^{-3} L_{Edd}$ for this source, and coincides with states where the [15-50] keV flux of the source departs from the standard powerlaw approximation, exemplified by the point with the lowest flux value (see Sec. 4.4.4).

INTEGRAL can also benefit from the same type of conversion, since only 29 of its 93 revolutions have a good enough SNR to create a spectrum and compute a flux directly. However, for ISGRI, the webpimms count rate-flux conversion is much more dependent on the SED's photon index. We thus directly test whether the ISGRI count rate is sufficiently well correlated with the flux measurements in the "high SNR" observations, once again extrapolating a flux measurement to the BAT band. The result, which we

show in the right panel of Fig. 6.2, shows once a gain a very significant and linear correlation, and we thus directly compute a linear regression to convert the *INTEGRAL* rates in fluxes in all the observations where the flux cannot be constrained from the fit. As seen in Tab. 4.1, this allows to add high-energy coverage to 2 observations without BAT coverage and with limited *INTEGRAL* coverage, notably in the 2004 outburst, with a very high HR_{hard} measurement.

6.2 Interactive visualisation tool: visual_line

One of the secondary goals of the work of Sec. 3 is to complement the current black hole candidate catalogs, which only list the physical parameters of the sources, with an inventory of the absorption feature properties accessible with X-ray telescopes. To enable ease of access and visualization of the data, we built an interactive webpage with the python library streamlit,[54] accessible at https://visual-line.streamlit.app/. The dataset is loaded internally and the options chosen in the sidebar allow the user to navigate and display different information of any subsamples of the data and download results. The figures presented in Sec. 3, except for Fig. 3.1 can be recreated using the online tool, as well as the two main tables, which will be updated according to new measurements and references. This tool itself is continuously updated to add more options, flexibility, and relevant information on the sources. The current main options of the tool as of the first study are described below. For now, improvements and datasets following the work on 4U 1630-47 are being implemented, and the next version of the tool will be made public once the first paper on this source will be published.

Sample selection: The first option in the sidebar allows the user to restrict the data selection to any part of the sample. This can be achieved by manually selecting a subset of sources or via global constraints on inclination properties using the values listed in Tab. 3.1. For a more precise control, it is also possible to manually exclude observations using their ObsIDs. Other options include restricting which absorption lines to consider, a time interval restriction, and the choice of significance threshold for features to be considered as detections (which uses the assessment of Sect. 3.3.4).

Hardness intensity diagram: The main visualization tool is the HID in which both detections and non-detections are displayed. Exposures can be colored coded according to several line parameters (in which case only extremal values are displayed for exposures with several lines) and several parameters specific to each observation or source. The fitting errors of both HID parameters can be displayed, and upper limits can be plotted for non-detection using different symbols in order to aid visibility for large subsamples. There are also a range of other visualization options.

Monitoring: Whenever the sample selection is restricted to a single source, long-term light curves and HR evolution can be displayed using *RXTE*-ASM, *MAXI* and *Swift*-BAT data with either one-day or single orbit binning. The *RXTE* data is taken from a copy of the definitive products available at http://xte.mit.edu/ASM_lc.html. The *RXTE* light curves use the sum of the intensity in all bands ([1.5−12] keV) corrected by a factor of 25 to match (visually) *MAXI* values, and the HR values are built as the ratio of bands C and B+A, that is, [5.5−12]/[1.5−5] keV. The *MAXI* data is loaded on the fly from the official website at http://maxi.riken.jp/top/slist.html in order to use the latest dataset available. The *MAXI* light curves use the full [2−20] keV band, and the HR is built from the [4−10]/[2−4] keV bands. For *MAXI*, a second HR using the [10−20]/[2−4] keV bands is also available. The *Swift*-BAT data is loaded on the fly from the official website at https://swift.gsfc.nasa.gov/results/transients/

A transparency factor proportional to the quality of the data (estimated from the ratio of the HR values to their uncertainties) is applied to both HRs to aid visibility, and the dates of exposures with instruments used in the line detection sample are highlighted. The date restriction selected in the sample selection can be both highlighted and used to zoom in on the light curve display, while EW values and upper limits can be displayed on a secondary axis at the date of each exposure.

Parameter analysis: The distribution and correlation of the line parameters can be computed on the fly from the chosen data selection. Distributions are restricted to the main line parameters and can be stacked or split according to the sources and instruments. Scatter plots between various intrinsic parameters as well as observation-level and source-level parameters can be displayed, with p-values computed according to the perturbation method discussed in Sect. 3.4.1. Similar to the HID, scatter

[54] https://streamlit.io/

plots can be color coded according to various information, and EW upper limits for currently selected sources can be included in the relevant plots, along with other secondary options.

Data display and download: The main tables of Sec. 3, Tab. 3.1 and Tab. 3.3, are displayed and will be updated in order to account for new sources, datasets, instruments, and updates in the literature. The complete data of sources, observations, and line parameters according to the current selection is also displayed in the form of dataframes and can be downloaded through separate csv files that can be loaded as multidimensional dataframes.

About: This final section summarizes the science case developed in this study, and details the behavior and logic of each option of the tool.

7 Line detection results

7.1 BHLMXB sample

7.1.1 Results of the line detection procedure

EW values for each line and each exposure analyzed in the sample. The sources are ordered alphabetically and with observations listed chronologically. The columns also report the exposure time after data reduction and either EW results for detections or EW upper limits for non-detections of the main lines. Line EWs are only provided for detections above 3 σ significance (see Sect. 3.3.4) along with 90% uncertainties. Upper limits above 100 eV are not reported. The ObsIDs marked with a dagger symbol (†) have pile-up values between 5 and 7% after the data reduction process.

Source	Date	Instrument	ObsID + identifier	exp. time (ks)	Fe line Equivalent Width / 3 σ upper limit (eV)				
					xxvKα	xxviKα	xxvKβ	xxviKβ	xxviKγ
1E1740.7-2942	2000-09-15	XMM	0112970901_S003	10.88	≤ 32	≤ 69	≤ 57	≤ 57	≤ 66
	2000-09-21	XMM	0112970801_S003	17.25	≤ 28	≤ 28	≤ 41	≤ 46	≤ 51
	2001-04-01	XMM	0112971801_S003	8.82	≤ 29	≤ 39	≤ 26	≤ 28	≤ 32
	2001-09-14	Chandra	2491	61.16	≤ 37	≤ 45	/	/	/
	2003-09-11	XMM	0144630101_S003	5.93	≤ 30	≤ 30	≤ 40	≤ 41	≤ 44
	2005-10-02	XMM	0303210201_S003	16.46	≤ 20	≤ 21	≤ 28	≤ 29	≤ 32
	2012-04-03	XMM	0673550201_S003	93.51	≤ 8	≤ 5	≤ 9	≤ 9	≤ 9
4U1543-475	2021-06-21	Chandra	25079	4.59	≤ 15	≤ 17	≤ 57	≤ 59	≤ 90
4U1630-47	2004-08-04	Chandra	4568	49.99	≤ 4	$\mathbf{11}^{+3}_{-4}$	≤ 19	≤ 76	/
	2012-01-17	Chandra	13714	28.92	$\mathbf{32} \pm 4$	$\mathbf{57} \pm 5$	/	/	/
	2012-01-20	Chandra	13715	29.28	$\mathbf{34}^{+3}_{-5}$	$\mathbf{49}^{+4}_{-5}$	$\mathbf{23}^{+7}_{-5}$	/	/
	2012-01-26	Chandra	13716	29.28	$\mathbf{47}^{+3}_{-2}$	$\mathbf{52}^{+1}_{-3}$	$\mathbf{32}^{+11}_{-2}$	$\mathbf{38}^{+9}_{-6}$	/
	2012-01-30	Chandra	13717	29.44	$\mathbf{30} \pm 3$	$\mathbf{48} \pm 4$	$\mathbf{32}^{+14}_{-7}$	$\mathbf{35}^{+10}_{-11}$	$\mathbf{36}^{+13}_{-8}$
	2012-03-04	XMM	0670671501_S003	2.54	$\mathbf{35} \pm 7$	$\mathbf{55}^{+9}_{-7}$	≤ 34	/	/
	2012-03-04	XMM	0670671501_U014	69.86	$\mathbf{31} \pm 2$	$\mathbf{48}^{+1}_{-2}$	$\mathbf{21}^{+3}_{-1}$	$\mathbf{22}^{+3}_{-0}$	/
	2012-03-20	XMM	0670671301_S003	22.26	$\mathbf{21} \pm 3$	$\mathbf{46}^{+4}_{-2}$	≤ 16	$\mathbf{18}^{+6}_{-5}$	/
	2012-03-25	XMM	0670672901_S003	62.81	$\mathbf{20} \pm 1$	$\mathbf{45}^{+1}_{-2}$	$\mathbf{9} \pm 2$	$\mathbf{19} \pm 2$	/
	2012-06-03	Chandra	14441	19.0	≤ 12	≤ 14	≤ 34	≤ 42	≤ 62
	2012-09-09	XMM	0670673001_S003†	22.48	$\mathbf{9}^{+3}_{-2}$	$\mathbf{31}^{+3}_{-2}$	≤ 10	≤ 10	≤ 10
	2012-09-10	XMM	0670673001_U002	0.8	≤ 19	$\mathbf{25}^{+6}_{-5}$	≤ 17	≤ 22	≤ 23
	2012-09-11	XMM	0670673101_S003	0.93	≤ 14	$\mathbf{9}^{+5}_{-4}$	≤ 19	≤ 16	≤ 19
	2012-09-28	XMM	0670673201_S003	1.56	≤ 5	≤ 7	≤ 9	≤ 11	≤ 19
	2013-04-25	Chandra	15511	49.39	≤ 8	≤ 7	≤ 26	≤ 32	≤ 35
	2013-05-27	Chandra	15524	48.91	≤ 44	≤ 62	/	/	/
	2016-10-21	Chandra	19904	30.93	$\mathbf{23}^{+4}_{-5}$	$\mathbf{45}^{+4}_{-7}$	/	/	/
	2020-05-28	Chandra	22376	24.5	≤ 35	≤ 35	≤ 75	/	/
	2020-06-06	Chandra	22377	24.5	≤ 41	≤ 50	/	/	/
	2020-06-13	Chandra	22378	23.54	≤ 39	≤ 55	/	/	/
	2004-09-07	Chandra	4552	65.6	≤ 14	≤ 16	/	/	/
	2004-10-16	XMM	0206320101_S003	34.15	≤ 5	≤ 9	≤ 10	≤ 10	≤ 15
	2008-12-07	Chandra	10659	9.87	≤ 41	≤ 58	/	/	/

Table 7.1: continued

Source	Date	Instrument	ObsID + identifier	exp. time (ks)	Fe line Equivalent Width / 3 σ upper limit (eV)				
					xxvKα	xxviKα	xxvKβ	xxviKβ	xxviKγ
4U1957+115	2008-12-07	Chandra	10660	13.44	≤ 44	≤ 48	/	/	/
	2008-12-08	Chandra	10661	9.82	≤ 26	≤ 42	/	/	/
	2013-11-17	XMM	0720940101_S003	36.89	≤ 12	≤ 15	≤ 20	≤ 27	≤ 36
AT2019wey	2020-09-20	Chandra	24651	24.51	≤ 26	≤ 47	≤ 85	/	/
EXO1846-031	2019-08-13	Chandra	21235	27.99	≤ 12	≤ 14	≤ 29	≤ 40	≤ 66
	2019-08-28	Chandra	21236	29.95	≤ 22	≤ 32	≤ 59	≤ 83	/
	2019-09-15	XMM	0851181101_S009	0.3	≤ 34	≤ 47	≤ 66	≤ 77	/
	2019-09-15	XMM	0851181101_S003	13.37	≤ 17	≤ 19	≤ 39	≤ 40	≤ 56
	2019-09-19	Chandra	21237	29.4	≤ 15	≤ 22	≤ 48	≤ 65	≤ 86
	2019-10-19	Chandra	21238	28.54	≤ 34	≤ 41	/	/	/
	2019-10-31	Chandra	20899	48.77	≤ 25	≤ 37	≤ 95	/	/
	2019-11-09	Chandra	20900	45.85	≤ 17	≤ 21	≤ 54	≤ 62	≤ 99
GROJ1655-40	2005-02-27	XMM	0112921301_S003	1.23	≤ 56	≤ 43	≤ 67	/	/
	2005-03-12	Chandra	5460	24.53	≤ 8	$\mathbf{19}^{+4}_{-3}$	≤ 65	/	/
	2005-03-14	XMM	0112921401_S003	0.44	≤ 16	$\mathbf{31}^{+6}_{-3}$	≤ 31	≤ 29	≤ 46
	2005-03-15	XMM	0112921501_S003	0.44	$\mathbf{23}^{+5}_{-4}$	$\mathbf{30}^{+6}_{-5}$	≤ 25	≤ 30	≤ 45
	2005-03-16	XMM	0112921601_S003	0.44	$\mathbf{12}^{+3}_{-4}$	$\mathbf{30}^{+4}_{-3}$	/	≤ 20	≤ 38
	2005-03-18	XMM	0155762501_S001	0.69	$\mathbf{30}^{+4}_{-3}$	$\mathbf{41}^{+3}_{-4}$	$\mathbf{23} \pm 6$	≤ 32	≤ 19
	2005-03-27	XMM	0155762601_S001	0.64	$\mathbf{30} \pm 4$	$\mathbf{17}^{+5}_{-4}$	$\mathbf{26}^{+7}_{-6}$	/	/
	2005-04-01	Chandra	5461	44.4	$\mathbf{58}^{+4}_{-3}$	$\mathbf{43}^{+3}_{-5}$	$\mathbf{58}^{+10}_{-4}$	/	/
GRS1716-249	2017-02-06	Chandra	20008	29.95	≤ 12	≤ 15	≤ 28	≤ 51	≤ 50
GRS1739-278	2016-09-24	Chandra	17791	29.39	≤ 47	≤ 51	/	/	/
GRS1758-258	2000-09-19	XMM	0112971301_S003	8.97	≤ 24	≤ 24	≤ 32	≤ 35	≤ 39
	2001-03-22	XMM	0136140201_S001	18.43	≤ 73	≤ 91	/	/	/
	2002-03-18	Chandra	2750	26.47	≤ 51	≤ 82	/	/	/
	2002-09-28	XMM	0144630201_S003	5.94	≤ 25	≤ 26	≤ 32	≤ 37	≤ 41
GRS1915+105	2000-04-24	Chandra	660	29.76	≤ 5	$\mathbf{5}^{+3}_{-2}$	/	/	/
	2001-03-24	Chandra	1944	30.42	≤ 7	≤ 5	≤ 17	≤ 17	≤ 24
	2001-05-23	Chandra	1945	30.04	≤ 3	$\mathbf{8}^{+2}_{-1}$	≤ 10	≤ 12	≤ 15
	2001-08-05	Chandra	1946	28.44	≤ 8	≤ 9	≤ 22	≤ 32	≤ 33
	2003-03-29	XMM	0112990101_U002	0.23	≤ 13	≤ 22	≤ 17	≤ 28	≤ 34
	2003-04-10	XMM	0112920701_S007	0.18	≤ 14	≤ 22	≤ 26	≤ 31	≤ 36
	2003-04-16	XMM	0112920801_U002	0.04	≤ 55	≤ 58	≤ 88	/	/
	2003-10-17	XMM	0112990501_S008	0.48	≤ 10	$\mathbf{18}^{+5}_{-3}$	≤ 10	≤ 13	≤ 12
	2003-10-22	XMM	0112920901_S003	0.28	≤ 13	$\mathbf{16} \pm 6$	≤ 15	≤ 23	≤ 20
	2004-03-20	Chandra	4587	30.04	≤ 5	≤ 11	≤ 18	≤ 18	≤ 22
	2004-03-30	Chandra	4588	27.17	≤ 8	≤ 10	≤ 18	≤ 36	≤ 39
	2004-04-06	Chandra	4589	30.02	≤ 8	≤ 9	≤ 21	≤ 28	≤ 37
	2004-04-17	XMM	0144090101_U002	14.1	≤ 4	≤ 4	≤ 6	≤ 6	≤ 10
	2004-04-21	XMM	0144090201_S003	0.62	≤ 18	≤ 19	≤ 27	≤ 26	≤ 32
	2004-05-03	XMM	0112921201_U002	0.56	≤ 19	≤ 21	≤ 28	≤ 30	≤ 34

Table 7.1: continued

Source	Date	Instrument	ObsID + identifier	exp. time (ks)	Fe line Equivalent Width / 3 σ upper limit (eV)				
					xxvKα	xxviKα	xxvKβ	xxviKβ	xxviKγ
GRS1915+105	2005-12-01	Chandra	6579	12.3	≤ 10	$\mathbf{13} \pm 3$	≤ 13	≤ 90	/
	2005-12-01	Chandra	6580	12.14	≤ 14	$\mathbf{22}^{+5}_{-6}$	≤ 22	/	/
	2005-12-03	Chandra	6581	9.73	≤ 10	$\mathbf{28}^{+3}_{-4}$	/	/	/
	2007-08-14	Chandra	7485	47.38	$\mathbf{36}^{+4}_{-2}$	$\mathbf{38} \pm 2$	$\mathbf{27}^{+8}_{-3}$	$\mathbf{24}^{+5}_{-6}$	/
	2007-09-24	XMM	0506160901_U002	0.53	$\mathbf{17}^{+7}_{-3}$	$\mathbf{24}^{+8}_{-3}$	≤ 18	≤ 16	≤ 15
	2007-09-26	XMM	0506161001_U002	0.53	$\mathbf{16}^{+6}_{-3}$	$\mathbf{32}^{+6}_{-5}$	≤ 12	≤ 17	≤ 21
	2007-09-28	XMM	0506161101_S001	0.52	$\mathbf{50}^{+10}_{-6}$	$\mathbf{37}^{+12}_{-7}$	$\mathbf{45}^{+14}_{-11}$	/	/
	2007-09-30	XMM	0506161201_U002	0.59	$\mathbf{32}^{+7}_{-6}$	$\mathbf{19}^{+10}_{-7}$	$\mathbf{31} \pm 12$	/	/
	2011-06-21	Chandra	12462	116.4	≤ 2	$\mathbf{8} \pm 1$	≤ 5	≤ 6	≤ 79
	2015-02-23	Chandra	16709	39.91	≤ 2	$\mathbf{7}^{+1}_{-2}$	≤ 7	≤ 10	≤ 11
	2015-03-19	Chandra	16710	38.04	≤ 4	≤ 5	≤ 7	≤ 10	≤ 19
	2015-06-09	Chandra	16711	118.65	$\mathbf{17} \pm 1$	$\mathbf{23} \pm 1$	$\mathbf{17}^{+1}_{-3}$	$\mathbf{16}^{+2}_{-1}$	/
	2017-02-22	Chandra	19717	24.96	≤ 13	≤ 14	≤ 29	≤ 36	≤ 60
	2017-03-27	Chandra	19718	25.01	≤ 13	≤ 20	≤ 31	≤ 59	≤ 68
	2017-05-02	XMM	0804640201_U002	0.06	/	≤ 100	/	/	/
	2017-06-24	Chandra	19719	25.03	≤ 5	$\mathbf{15}^{+4}_{-3}$	≤ 12	/	/
	2017-08-09	Chandra	19720	23.88	≤ 4	$\mathbf{11}^{+1}_{-3}$	≤ 10	≤ 18	≤ 99
	2017-09-22	XMM	0804640501_S003	0.4	≤ 14	≤ 16	≤ 20	≤ 22	≤ 30
	2017-10-12	XMM	0804640601_S003	0.43	≤ 10	$\mathbf{17} \pm 4$	≤ 10	≤ 12	≤ 16
	2018-04-10	XMM	0804640701_S003	0.45	≤ 27	≤ 28	≤ 39	≤ 43	≤ 47
	2018-04-19	XMM	0804640801_S003	0.51	≤ 13	≤ 23	≤ 20	≤ 30	≤ 38
	2019-04-30	Chandra	22213	29.08	$\mathbf{77}^{+7}_{-5}$	$\mathbf{26}^{+1}_{-2}$	/	/	/
	2021-07-14	Chandra	23435	24.5	$\mathbf{55} \pm 7$	$\mathbf{31}^{+5}_{-4}$	$\mathbf{34}^{+9}_{-5}$	/	/
	2021-07-15	Chandra	24663	23.5	$\mathbf{61}^{+8}_{-6}$	$\mathbf{32}^{+4}_{-3}$	$\mathbf{42}^{+23}_{-17}$	/	/
GS1354-64	2015-08-06	XMM	0727961501_S003	0.24	≤ 77	≤ 84	/	/	/
	2015-08-06	XMM	0727961501_S004	10.99	≤ 21	≤ 24	≤ 30	≤ 32	≤ 36
GX339-4	2002-08-24	XMM	0093562701_S005	1.28	≤ 24	≤ 25	≤ 36	≤ 49	≤ 59
	2002-09-29	XMM	0156760101_S001	2.25	≤ 10	≤ 12	≤ 15	≤ 18	≤ 22
	2003-03-08	XMM	0148220201_S001	12.75	≤ 16	≤ 20	≤ 34	≤ 39	≤ 49
	2003-03-17	Chandra	4420	74.05	≤ 45	≤ 50	/	/	/
	2003-03-20	XMM	0148220301_S001	3.98	≤ 23	≤ 22	≤ 34	≤ 44	≤ 47
	2004-03-16	XMM	0204730201_U002	101.25	≤ 5	≤ 5	≤ 8	≤ 8	≤ 8
	2004-03-18	XMM	0204730301_U002	88.92	≤ 5	≤ 5	≤ 7	≤ 5	≤ 8
	2004-03-20	XMM	0204730301_U003	5.07	≤ 31	≤ 31	≤ 38	≤ 43	≤ 33
	2004-08-22	Chandra	4569	49.9	≤ 25	≤ 26	/	/	/
	2004-10-04	Chandra	4570	44.53	≤ 24	≤ 25	/	/	/
	2004-10-28	Chandra	4571	43.36	≤ 13	≤ 30	/	/	/
	2007-02-19	XMM	0410581201_S001	0.45	≤ 18	≤ 21	≤ 48	≤ 50	≤ 62
	2007-03-05	XMM	0410581301_S001	0.48	≤ 17	≤ 17	≤ 28	≤ 29	≤ 45
	2007-03-30	XMM	0410581701_U002	0.26	/	/	/	/	/
	2009-03-26	XMM	0605610201_S003	31.75	≤ 15	≤ 14	≤ 17	≤ 22	≤ 28

Table 7.1: continued

Source	Date	Instrument	ObsID + identifier	exp. time (ks)	Fe line Equivalent Width / 3 σ upper limit (eV)				
					xxvKα	xxviKα	xxvKβ	xxviKβ	xxviKγ
	2010-03-28	XMM	0654130401_S001	25.29	≤ 4	≤ 4	≤ 6	≤ 5	≤ 6
	2013-09-29	XMM	0692341201_S003	8.54	≤ 9	≤ 10	≤ 14	≤ 14	≤ 17
	2013-09-30	XMM	0692341301_S003	9.43	≤ 19	≤ 21	≤ 29	≤ 30	≤ 31
	2013-10-01	XMM	0692341401_S003	15.04	≤ 18	≤ 18	≤ 21	≤ 22	≤ 24
	2015-08-28	XMM	0760646201_S003	14.73	≤ 21	≤ 18	≤ 27	≤ 33	≤ 38
	2015-09-02	XMM	0760646301_S003	15.74	≤ 13	≤ 14	≤ 17	≤ 19	≤ 33
	2015-09-07	XMM	0760646401_S003	20.18	≤ 16	≤ 18	≤ 20	≤ 22	≤ 27
	2015-09-12	XMM	0760646501_S003	18.62	≤ 37	≤ 38	≤ 46	≤ 55	≤ 62
	2015-09-17	XMM	0760646601_S003	36.53	≤ 10	≤ 12	≤ 12	≤ 13	≤ 23
	2015-09-30	XMM	0760646701_S003	33.42	≤ 13	≤ 15	≤ 16	≤ 17	≤ 23
	2003-05-01	Chandra	3803	48.26	$\mathbf{7} \pm 1$	$\mathbf{20}^{+2}_{-3}$	/	/	/
	2003-05-28	Chandra	3804	43.89	≤ 6	≤ 9	≤ 19	≤ 24	≤ 34
	2003-06-23	Chandra	3805	49.87	$\mathbf{7} \pm 2$	$\mathbf{16}^{+3}_{-4}$	/	/	/
	2003-07-30	Chandra	3806	50.0	$\mathbf{19}^{+3}_{-4}$	$\mathbf{29}^{+4}_{-5}$	/	/	/
	2008-09-29	XMM	0554110201_S005	20.56	≤ 18	≤ 19	≤ 25	≤ 24	≤ 30
	2010-08-08	Chandra	11048	60.29	≤ 16	≤ 21	≤ 46	≤ 49	≤ 69
	2010-10-09	XMM	0553950201_S003	59.96	≤ 24	≤ 30	≤ 51	≤ 51	≤ 49
	2014-09-21	XMM	0724400501_S001	135.08	≤ 5	≤ 6	≤ 6	≤ 6	≤ 10
	2014-09-23	XMM	0724401901_S001	77.74	≤ 10	≤ 11	≤ 15	≤ 14	≤ 18
	2014-09-24	XMM	0740980201_S003	48.61	≤ 8	≤ 8	≤ 8	≤ 9	≤ 15
H1743-322	2015-06-11	Chandra	16738	9.22	≤ 27	≤ 28	≤ 63	≤ 91	/
	2015-06-12	Chandra	17679	9.22	≤ 43	≤ 52	/	/	/
	2015-06-13	Chandra	17680	9.22	≤ 47	≤ 50	/	/	/
	2015-07-03	Chandra	16739	26.84	≤ 22	≤ 28	≤ 51	≤ 79	≤ 91
	2016-03-13	XMM	0783540201_S003	137.42	≤ 8	≤ 8	≤ 11	≤ 11	≤ 15
	2016-03-15	XMM	0783540301_U002	134.52	≤ 4	≤ 5	≤ 5	≤ 6	≤ 7
	2018-09-26	XMM	0783540401_S003	128.95	≤ 6	≤ 8	≤ 8	≤ 9	≤ 10
	2011-03-27	XMM	0677980201_S003	1.14	≤ 44	≤ 46	≤ 67	≤ 76	/
	2011-08-01	Chandra	12405	31.21	≤ 34	≤ 32	≤ 57	≤ 93	/
	2011-10-06	Chandra	12406	27.29	≤ 10	≤ 23	≤ 87	/	/
	2012-09-29	XMM	0700381301_S003	46.12	≤ 10	≤ 10	≤ 12	≤ 13	≤ 15
	2016-03-07	XMM	0743960201_S003	57.98	≤ 10	≤ 11	≤ 17	≤ 17	≤ 21
	2016-03-09	XMM	0744361501_S003	38.16	≤ 15	≤ 19	≤ 20	≤ 21	≤ 40
	2016-03-11	XMM	0744361801_S003	28.59	≤ 15	≤ 18	≤ 17	≤ 18	≤ 26
	2016-03-23	XMM	0744361701_S003	61.24	≤ 13	≤ 18	≤ 22	≤ 23	≤ 29
	2016-03-30	Chandra	17787	39.48	≤ 16	≤ 18	≤ 40	≤ 58	≤ 95
	2016-04-30	Chandra	17788	38.75	≤ 19	≤ 30	≤ 69	/	/
	2016-05-26	Chandra	17789	20.05	≤ 48	≤ 53	/	/	/
	2016-05-27	Chandra	18855	19.97	≤ 31	≤ 51	/	/	/
IGRJ17091-3624	2016-06-24	Chandra	17790	19.97	≤ 66	≤ 77	/	/	/
	2016-06-25	Chandra	18874	19.86	≤ 60	≤ 91	/	/	/

Table 7.1: continued

Source	Date	Instrument	ObsID + identifier	exp. time (ks)	Fe line Equivalent Width / 3 σ upper limit (eV)				
					xxvKα	xxviKα	xxvKβ	xxviKβ	xxviKγ
	2022-06-16	Chandra	26435	29.09	≤ 16	≤ 20	≤ 51	≤ 55	≤ 76
IGRJ17098-3628	2006-08-25	XMM	0406140101_U002	3.74	≤ 83	/	/	/	/
	2007-02-19	XMM	0406140401_S003	7.02	≤ 47	≤ 66	/	/	/
IGRJ17285-2922	2010-09-09	XMM	0405182701_S003	18.5	≤ 49	≤ 48	≤ 60	≤ 69	≤ 72
IGRJ17451-3022	2015-03-06	XMM	0748391201_S001[†]	36.45	$\mathbf{92}^{+11}_{-10}$	≤ 77	/	/	/
IGRJ17497-2821	2006-09-22	XMM	0410580401_S001	31.18	≤ 13	≤ 14	≤ 14	≤ 17	≤ 23
	2006-10-01	Chandra	6613	19.7	≤ 46	≤ 56	/	/	/
MAXIJ0637-430	2019-11-17	XMM	0853980801_S001	0.6	/	/	/	/	/
MAXIJ1305-704	2012-04-29	Chandra	14425	29.38	≤ 50	≤ 30	/	/	/
MAXIJ1348-630	2019-02-01	XMM	0831000101_S001	7.85	≤ 10	≤ 10	≤ 13	≤ 14	≤ 21
	2019-02-26	XMM	0831000301_S001	3.58	≤ 24	≤ 26	≤ 37	≤ 42	≤ 54
	2019-06-21	Chandra	21239	19.04	≤ 12	≤ 15	≤ 43	≤ 36	≤ 55
	2019-06-26	Chandra	21240	20.04	≤ 8	≤ 9	≤ 22	≤ 30	≤ 31
	2019-07-07	Chandra	21241	20.05	≤ 11	≤ 14	≤ 29	≤ 33	≤ 37
MAXIJ1535-571	2017-09-07	XMM	0795711801_S014	4.6	≤ 6	≤ 11	≤ 9	≤ 11	≤ 14
	2017-09-07	XMM	0795711801_S003	0.57	≤ 14	≤ 14	≤ 20	≤ 24	≤ 29
	2017-09-08	XMM	0795711801_U014	0.05	≤ 48	≤ 49	≤ 68	≤ 75	≤ 82
	2017-09-08	XMM	0795711801_U015	0.25	≤ 23	≤ 24	≤ 31	≤ 34	≤ 39
	2017-09-13	Chandra	20203	22.97	≤ 8	≤ 8	≤ 23	≤ 44	≤ 45
	2017-09-14	XMM	0795712001_S003	0.82	≤ 4	≤ 5	≤ 6	≤ 7	≤ 8
	2017-09-15	XMM	0795712101_S003	0.46	≤ 11	≤ 11	≤ 16	≤ 20	≤ 21
	2017-09-27	Chandra	20204	18.85	≤ 12	≤ 14	≤ 37	≤ 63	/
	2017-10-08	Chandra	20205	20.7	≤ 7	≤ 8	≤ 22	≤ 37	≤ 60
	2017-10-24	Chandra	20206	27.22	≤ 7	≤ 8	≤ 20	≤ 26	≤ 41
	2017-12-31	Chandra	20169	21.19	≤ 46	≤ 55	/	/	/
MAXIJ1659-152	2010-09-27	XMM	0656780601_S003	22.88	≤ 5	≤ 6	≤ 8	≤ 6	≤ 8
	2011-03-22	XMM	0677980101_U002	20.51	≤ 66	≤ 66	/	/	/
MAXIJ1803-298	2021-05-17	Chandra	25039	10.02	≤ 30	≤ 41	/	/	/
	2021-05-23	Chandra	25040	10.24	≤ 28	≤ 36	/	/	/
	2021-06-17	Chandra	25041	6.31	≤ 85	/	/	/	/
	2021-06-18	Chandra	25063	7.91	≤ 92	/	/	/	/
MAXIJ1820+070	2018-03-17	XMM	0830190201_S001	5.37	≤ 24	≤ 26	≤ 33	≤ 36	≤ 42
	2018-03-17	XMM	0830190201_S002	2.04	≤ 12	≤ 10	≤ 15	≤ 14	≤ 17
	2018-03-19	XMM	0820880201_S003	0.3	≤ 21	≤ 23	≤ 29	≤ 29	≤ 35
	2018-03-19	XMM	0820880201_S011	3.85	≤ 17	≤ 20	≤ 22	≤ 25	≤ 50
	2018-03-22	XMM	0820880301_S003	0.6	≤ 13	≤ 15	≤ 17	≤ 20	≤ 23
	2018-03-27	XMM	0820880401_S003	0.85	≤ 5	≤ 10	≤ 8	≤ 9	≤ 10
	2018-04-12	XMM	0820880501_S003	0.11	≤ 33	≤ 31	≤ 41	≤ 45	≤ 56
	2018-09-28	XMM	0820880601_S003	0.3	≤ 46	≤ 51	≤ 64	≤ 71	≤ 80
	2018-09-30	XMM	0820881101_S003	0.24	≤ 33	≤ 33	≤ 44	≤ 49	≤ 71
	2018-10-05	XMM	0830191901_S001	0.15	≤ 62	≤ 66	≤ 94	≤ 91	≤ 79

Table 7.1: continued

Source	Date	Instrument	ObsID + identifier	exp. time (ks)	Fe line Equivalent Width / 3 σ upper limit (eV)				
					xxvKα	xxviKα	xxvKβ	xxviKβ	xxviKγ
	2018-10-05	XMM	0830191901_S002	5.24	≤ 13	≤ 14	≤ 21	≤ 20	≤ 31
	2019-03-22	XMM	0844230201_S003	8.49	≤ 40	≤ 40	≤ 56	≤ 61	≤ 73
	2019-03-26	XMM	0844230301_S003	11.34	≤ 17	≤ 17	≤ 21	≤ 23	≤ 34
	2019-09-20	XMM	0851181301_S003	56.28	≤ 35	≤ 33	≤ 51	≤ 56	≤ 60
SAXJ1711.6-3808	2001-03-02	XMM	0135520401_S001	6.03	≤ 17	≤ 23	≤ 23	≤ 26	≤ 26
SwiftJ1357.2-0933	2011-02-05	XMM	0674580101_U014	33.48	≤ 13	≤ 11	≤ 22	≤ 19	≤ 21
	2018-02-25	XMM	0802300201_S003	41.06	≤ 13	≤ 10	≤ 17	≤ 18	≤ 26
	2018-02-27	XMM	0811213401_S003	28.58	≤ 15	≤ 15	≤ 25	≤ 26	≤ 30
	2018-03-04	XMM	0805200201_S007[†]	0.66	≤ 45	≤ 50	≤ 52	≤ 77	≤ 82
	2018-03-04	XMM	0805200201_S003[†]	30.96	≤ 11	≤ 12	≤ 21	≤ 21	≤ 27
SwiftJ1658.24242	2018-03-11	XMM	0805200301_S003	29.45	≤ 9	≤ 10	≤ 13	≤ 15	≤ 29
	2018-03-11	XMM	0805200301_S014	0.44	≤ 27	≤ 31	≤ 65	≤ 65	≤ 53
	2018-03-15	XMM	0805200401_S003	32.95	≤ 4	≤ 5	≤ 9	≤ 9	≤ 12
	2018-03-28	XMM	0805201301_S003	33.72	≤ 20	≤ 22	≤ 34	≤ 37	≤ 44
	2018-04-28	Chandra	21083	29.08	≤ 26	≤ 38	≤ 63	/	/
SwiftJ174510.8-262411	2012-09-28	XMM	0693020301_S003	1.11	≤ 9	≤ 10	≤ 10	≤ 12	≤ 13
	2006-03-24	XMM	0311590901_S001	40.11	≤ 13	≤ 15	≤ 20	≤ 23	≤ 26
	2009-09-29	XMM	0605610301_U002	25.19	≤ 15	≤ 16	≤ 18	≤ 19	≤ 24
	2012-05-03	Chandra	14428	19.63	≤ 46	≤ 45	/	/	/
	2012-09-10	XMM	0691740201_S001	37.42	≤ 9	≤ 11	≤ 13	≤ 14	≤ 25
SwiftJ1753.5-0127	2012-10-08	XMM	0694930501_S001	28.38	≤ 28	≤ 28	≤ 39	≤ 44	≤ 48
	2014-09-13	XMM	0744320201_S001	46.18	≤ 15	≤ 18	≤ 26	≤ 27	≤ 33
	2015-03-19	XMM	0770580201_S003	31.37	≤ 74	≤ 79	/	/	/
	2012-09-22	Chandra	14634	29.96	≤ 77	≤ 89	/	/	/
SwiftJ1910.2-0546	2012-10-17	XMM	0691271401_S001	40.49	≤ 19	≤ 21	≤ 27	≤ 32	≤ 37
	2015-06-22	Chandra	17696	20.76	≤ 10	≤ 16	≤ 25	≤ 31	≤ 37
V404Cyg	2015-06-23	Chandra	17697	25.25	≤ 12	≤ 13	≤ 33	≤ 48	≤ 59
	2020-02-14	Chandra	22389	44.0	≤ 20	≤ 33	/	/	/
V4641Sgr	2020-02-15	Chandra	23158	29.35	≤ 48	≤ 77	/	/	/
	2000-05-03	Chandra	680	2.14	≤ 33	≤ 43	≤ 99	/	/
XTEJ1550-564	2000-05-06	Chandra	681	2.13	≤ 63	≤ 72	/	/	/
	2001-09-13	XMM	0136140301_S001	0.69	≤ 10	≤ 14	≤ 16	≤ 17	≤ 18
	2001-10-05	Chandra	2699	22.51	≤ 16	≤ 20	/	/	/
XTEJ1650-500	2001-10-29	Chandra	2700	26.36	≤ 47	≤ 63	/	/	/
XTEJ1652-453	2009-08-22	XMM	0610000701_U002	38.22	≤ 22	≤ 27	≤ 40	≤ 39	≤ 43
XTEJ1720-318	2003-02-20	XMM	0154750501_S001	7.73	≤ 24	≤ 27	≤ 42	≤ 50	≤ 67
	2009-11-01	Chandra	10069	30.55	≤ 15	≤ 27	≤ 42	≤ 51	≤ 73
	2010-02-08	Chandra	10070	21.31	≤ 40	≤ 47	/	/	/
XTEJ1752-223	2010-04-06	XMM	0653110101_S003	18.17	≤ 6	≤ 6	≤ 11	≤ 11	≤ 12
	2010-04-07	XMM	0653110101_S008	0.57	≤ 36	≤ 53	≤ 58	≤ 59	≤ 73
	2006-02-13	Chandra	6615	29.07	≤ 15	≤ 19	≤ 38	≤ 66	≤ 97

Table 7.1: continued

Source	Date	Instrument	ObsID + identifier	exp. time (ks)	Fe line Equivalent Width / 3 σ upper limit (eV)				
					xxvKα	xxviKα	xxvKβ	xxviKβ	xxviKγ
XTEJ1817-330	2006-02-24	Chandra	6616	38.96	≤ 19	≤ 19	≤ 48	≤ 75	≤ 91
	2006-03-13	XMM	0311590501_S003	0.6	≤ 30	≤ 32	≤ 59	≤ 56	≤ 68
	2006-03-15	Chandra	6617	46.53	≤ 27	≤ 34	≤ 57	≤ 92	/
	2006-05-22	Chandra	6618	50.77	≤ 60	≤ 61	/	/	/
XTEJ1856+053	2007-03-14	XMM	0510010101_U002	1.5	≤ 53	≤ 62	/	/	/
XTEJ1901+014	2006-10-14	XMM	0402470401_S003	8.73	≤ 56	≤ 57	≤ 88	≤ 81	/

7.1.2 Parameters of Kα detections

Main characteristics of significant Kα line detections from the sample. Uncertainties regarding luminosity are not quoted, as they were negligible.

Source	Date	ObsID	$HR_{[6-10]/[3-10]}$	$L_{[3-10]}/L_{Edd}$ $\times 10^{-2}$	Fe xxv Kα			Fe xxvi Kα		
					EW	blueshift	width	EW	blueshift	width
			Bands in keV		eV	km/s	km/s	eV	km/s	km/s
4U1630-47	2004-08-04	4568	$0.351^{+0.003}_{-0.003}$	5.6	/	/	/	$\mathbf{11}^{+3}_{-4}$	$\mathbf{-300}^{+500}_{-500}$	$\mathbf{0}^{+4200}$
	2012-01-17	13714	$0.362^{+0.003}_{-0.003}$	4.7	$\mathbf{32}\pm4$	$\mathbf{0}^{+200}_{-100}$	$\mathbf{1900}^{+500}_{-500}$	$\mathbf{57}\pm5$	$\mathbf{-300}^{+100}_{-100}$	$\mathbf{2700}^{+400}_{-400}$
	2012-01-20	13715	$0.344^{+0.002}_{-0.002}$	4.6	$\mathbf{34}^{+3}_{-5}$	$\mathbf{100}^{+200}_{-100}$	$\mathbf{2300}^{+600}_{-400}$	$\mathbf{49}^{+4}_{-5}$	$\mathbf{-300}^{+100}_{-100}$	$\mathbf{2200}^{+600}_{-300}$
	2012-01-26	13716	$0.347^{+0.002}_{-0.003}$	4.4	$\mathbf{47}^{+3}_{-2}$	$\mathbf{500}^{+200}_{-200}$	$\mathbf{3000}^{+400}_{-500}$	$\mathbf{52}^{+1}_{-3}$	$\mathbf{-300}^{+0}_{-100}$	$\mathbf{2200}^{+700}_{-400}$
	2012-01-30	13717	$0.389^{+0.003}_{-0.003}$	5.1	$\mathbf{30}\pm3$	$\mathbf{200}^{+200}_{-300}$	$\mathbf{2000}^{+800}_{-700}$	$\mathbf{48}\pm4$	$\mathbf{-200}^{+200}_{-200}$	$\mathbf{1800}^{+700}_{-700}$
	2012-03-04	0670671501_S003	$0.366^{+0.002}_{-0.002}$	4.8	$\mathbf{35}\pm7$	$\mathbf{-5000}^{+2200}_{-1900}$	/	$\mathbf{55}^{+9}_{-7}$	$\mathbf{-5800}^{+1600}_{-1200}$	/
	2012-03-04	0670671501_U014	$0.347^{+0.0}_{-0.0}$	5.3	$\mathbf{31}\pm2$	$\mathbf{-5200}^{+200}_{-300}$	/	$\mathbf{48}^{+1}_{-2}$	$\mathbf{-5200}^{+100}_{-200}$	/
	2012-03-20	0670671301_S003	$0.36^{+0.001}_{-0.001}$	6.2	$\mathbf{21}\pm3$	$\mathbf{-3900}^{+900}_{-800}$	/	$\mathbf{46}^{+4}_{-2}$	$\mathbf{-4300}^{+400}_{-400}$	/
	2012-03-25	0670672901_S003	$0.401^{+0.0}_{-0.0}$	5.8	$\mathbf{20}\pm1$	$\mathbf{-6000}^{+500}_{-500}$	/	$\mathbf{45}^{+1}_{-2}$	$\mathbf{-5900}^{+200}_{-300}$	/
	2012-09-09	0670673001_S003	$0.413^{+0.001}_{-0.001}$	8.0	$\mathbf{9}^{+3}_{-2}$	$\mathbf{-4600}^{+2600}_{-3000}$	/	$\mathbf{31}^{+3}_{-2}$	$\mathbf{-4300}^{+1000}_{-800}$	/
	2012-09-10	0670673001_U002	$0.432^{+0.002}_{-0.002}$	7.2	/	/	/	$\mathbf{25}^{+6}_{-5}$	$\mathbf{-3500}^{+2700}_{-3000}$	/
	2012-09-11	0670673101_S003	$0.467^{+0.002}_{-0.002}$	9.4	/	/	/	$\mathbf{9}^{+5}_{-4}$	$\mathbf{-1200}^{+5800}_{-6400}$	/
	2016-10-21	19904	$0.311^{+0.002}_{-0.002}$	5.6	$\mathbf{23}^{+4}_{-5}$	$\mathbf{-300}^{+300}_{-300}$	$\mathbf{1800}^{+1400}_{-1500}$	$\mathbf{45}^{+4}_{-7}$	$\mathbf{-200}^{+300}_{-300}$	$\mathbf{2400}^{+1000}_{-800}$
GROJ1655-40	2005-03-12	5460	$0.276^{+0.003}_{-0.004}$	2.2	/	/	/	$\mathbf{19}^{+4}_{-3}$	$\mathbf{-200}^{+200}_{-300}$	/
	2005-03-14	0112921401_S003	$0.266^{+0.002}_{-0.001}$	3.3	/	/	/	$\mathbf{31}^{+6}_{-3}$	$\mathbf{900}^{+700}_{-1200}$	/
	2005-03-15	0112921501_S003	$0.258^{+0.002}_{-0.001}$	3.5	$\mathbf{23}^{+5}_{-4}$	$\mathbf{-2400}^{+1500}_{-1500}$	/	$\mathbf{30}^{+6}_{-5}$	$\mathbf{-500}^{+1200}_{-1100}$	/
	2005-03-16	0112921601_S003	$0.304^{+0.002}_{-0.002}$	4.2	$\mathbf{12}^{+3}_{-4}$	$\mathbf{2300}^{+900}_{-2300}$	/	$\mathbf{30}^{+4}_{-3}$	$\mathbf{1100}^{+600}_{-500}$	/
	2005-03-18	0155762501_S001	$0.293^{+0.001}_{-0.001}$	4.7	$\mathbf{30}^{+4}_{-3}$	$\mathbf{-100}^{+800}_{-600}$	/	$\mathbf{41}^{+3}_{-4}$	$\mathbf{300}^{+600}_{-500}$	/
	2005-03-27	0155762601_S001	$0.32^{+0.002}_{-0.002}$	2.5	$\mathbf{30}\pm4$	$\mathbf{-200}^{+600}_{-600}$	/	$\mathbf{17}^{+5}_{-4}$	$\mathbf{-3500}^{+1400}_{-1600}$	/
	2005-04-01	5461	$0.285^{+0.001}_{-0.001}$	2.5	$\mathbf{58}^{+4}_{-3}$	$\mathbf{0}^{+100}_{-100}$	$\mathbf{3700}^{+300}_{-300}$	$\mathbf{43}^{+3}_{-5}$	$\mathbf{-1200}^{+100}_{-200}$	$\mathbf{2500}^{+500}_{-300}$
	2000-04-24	660	$0.708^{+0.008}_{-0.005}$	5.7	/	/	/	$\mathbf{5}^{+3}_{-2}$	$\mathbf{-300}^{+500}_{-800}$	/

Table 7.2: continued

Source	Date	ObsID	$HR_{[6-10]/[3-10]}$	$L_{[3-10]}/L_{Edd}$ $\times 10^{-2}$	Fe xxv Kα			Fe xxvi Kα		
					EW	blueshift	width	EW	blueshift	width
			Bands in keV		eV	km/s	km/s	eV	km/s	km/s
GRS1915+105	2001-05-23	1945	$0.506^{+0.003}_{-0.003}$	11.9	/	/	/	$\mathbf{8}^{+2}_{-1}$	$\mathbf{-600}^{+500}_{-500}$	/
	2003-10-17	0112990501_S008	$0.585^{+0.002}_{-0.002}$	16.8	/	/	/	$\mathbf{18}^{+5}_{-3}$	$\mathbf{-2900}^{+1100}_{-1100}$	/
	2003-10-22	0112920901_S003	$0.595^{+0.004}_{-0.004}$	11.0	/	/	/	$\mathbf{16 \pm 6}$	$\mathbf{500}^{+1700}_{-2400}$	/
	2005-12-01	6579	$0.484^{+0.005}_{-0.007}$	$12.5_{-0.1}$	/	/	/	$\mathbf{13 \pm 3}$	$\mathbf{-800}^{+500}_{-500}$	/
	2005-12-01	6580	$0.47^{+0.005}_{-0.006}$	$13.3^{+0.1}_{-0.1}$	/	/	/	$\mathbf{22}^{+5}_{-6}$	$\mathbf{-1100}^{+1100}_{-1000}$	$\mathbf{3400}^{+1700}_{-1900}$
	2005-12-03	6581	$0.555^{+0.003}_{-0.003}$	$34.4^{+0.1}_{-0.1}$	/	/	/	$\mathbf{28}^{+3}_{-4}$	$\mathbf{-700}^{+300}_{-300}$	$\mathbf{2000}^{+1300}_{-1000}$
	2007-08-14	7485	$0.491^{+0.003}_{-0.003}$	6.3	$\mathbf{36}^{+4}_{-2}$	$\mathbf{300}^{+100}_{-100}$	$\mathbf{2700}^{+200}_{-300}$	$\mathbf{38 \pm 2}$	$\mathbf{-200}^{+0}_{-100}$	$\mathbf{1400}^{+200}_{-200}$
	2007-09-24	0506160901_U002	$0.453^{+0.002}_{-0.002}$	13.7	$\mathbf{17}^{+7}_{-3}$	$\mathbf{-600}^{+1700}_{-1300}$	/	$\mathbf{24}^{+8}_{-3}$	$\mathbf{-1400}^{+1500}_{-700}$	/
	2007-09-26	0506161001_U002	$0.457^{+0.002}_{-0.002}$	12.7	$\mathbf{16}^{+6}_{-3}$	$\mathbf{-4100}^{+1900}_{-1700}$	/	$\mathbf{32}^{+6}_{-5}$	$\mathbf{-2900}^{+1100}_{-500}$	/
	2007-09-28	0506161101_S001	$0.429^{+0.004}_{-0.004}$	2.7	$\mathbf{50}^{+10}_{-6}$	$\mathbf{300}^{+900}_{-900}$	/	$\mathbf{37}^{+12}_{-7}$	$\mathbf{-2000}^{+1700}_{-1400}$	/
	2007-09-30	0506161201_U002	$0.425^{+0.004}_{-0.004}$	2.9	$\mathbf{32}^{+7}_{-6}$	$\mathbf{700}^{+1100}_{-1600}$	/	$\mathbf{19}^{+10}_{-7}$	$\mathbf{-6600}^{+3700}_{-2300}$	/
	2011-06-21	12462	$0.453^{+0.001}_{-0.002}$	10.5	/	/	/	$\mathbf{8 \pm 1}$	$\mathbf{-500}^{+200}_{-100}$	/
	2015-02-23	16709	$0.457^{+0.002}_{-0.002}$	12.2	/	/	/	$\mathbf{7}^{+1}_{-2}$	$\mathbf{-300}^{+200}_{-300}$	/
	2015-06-09	16711	$0.418^{+0.002}_{-0.002}$	6.7	$\mathbf{17 \pm 1}$	$\mathbf{-100}^{+0}_{-0}$	/	$\mathbf{23 \pm 1}$	$\mathbf{-200}^{+0}_{-0}$	/
	2017-06-24	19719	$0.556^{+0.006}_{-0.006}$	5.8	/	/	/	$\mathbf{15}^{+4}_{-3}$	$\mathbf{100}^{+500}_{-500}$	$\mathbf{0}^{+3400}$
	2017-08-09	19720	$0.669^{+0.005}_{-0.004}$	13.2	/	/	/	$\mathbf{11}^{+1}_{-3}$	$\mathbf{100}^{+400}_{-600}$	$\mathbf{0}^{+2800}$
	2017-10-12	0804640601_S003	$0.575^{+0.002}_{-0.002}$	21.7	/	/	/	$\mathbf{17 \pm 4}$	$\mathbf{-5000}^{+1400}_{-1400}$	/
	2019-04-30	22213	$0.784^{+0.013}_{-0.013}$	0.7	$\mathbf{77}^{+7}_{-5}$	$\mathbf{2600}^{+500}_{-700}$	$\mathbf{5300}_{-1200}$	$\mathbf{26}^{+1}_{-2}$	$\mathbf{100}^{+300}_{-400}$	/
	2021-07-14	23435	$0.512^{+0.007}_{-0.006}$	1.6	$\mathbf{55 \pm 7}$	$\mathbf{900}^{+500}_{-400}$	$\mathbf{3800}^{+1400}_{-1100}$	$\mathbf{31}^{+5}_{-4}$	$\mathbf{100}^{+300}_{-300}$	/
	2021-07-15	24663	$0.56^{+0.007}_{-0.007}$	1.5	$\mathbf{61}^{+8}_{-6}$	$\mathbf{1400}^{+600}_{-500}$	$\mathbf{4900}^{+400}_{-700}$	$\mathbf{32}^{+4}_{-3}$	$\mathbf{-100}^{+100}_{-100}$	/
H1743-322	2003-05-01	3803	$0.264^{+0.002}_{-0.002}$	11.5	$\mathbf{7 \pm 1}$	$\mathbf{-300}^{+200}_{-200}$	/	$\mathbf{20}^{+2}_{-3}$	$\mathbf{-400}^{+100}_{-200}$	$\mathbf{1600}^{+700}_{-600}$
	2003-06-23	3805	$0.205^{+0.002}_{-0.002}$	7.3	$\mathbf{7 \pm 2}$	$\mathbf{100}^{+600}_{-600}$	/	$\mathbf{16}^{+3}_{-4}$	$\mathbf{-200}^{+400}_{-600}$	$\mathbf{0}^{+4000}$

Table 7.2: continued

Source	Date	ObsID	$HR_{[6-10]/[3-10]}$	$L_{[3-10]}/L_{Edd}$ $\times 10^{-2}$	Fe xxv Kα			Fe xxvi Kα		
					EW	blueshift	width	EW	blueshift	width
			Bands in keV		eV	km/s	km/s	eV	km/s	km/s
	2003-07-30	3806	$0.149^{+0.002}_{-0.002}$	5.1	$\mathbf{19}^{+3}_{-4}$	$\mathbf{0}^{+400}_{-300}$	$\mathbf{0}^{+2700}$	$\mathbf{29}^{+4}_{-5}$	$\mathbf{400}^{+400}_{-400}$	$\mathbf{2000}^{+1600}_{-1500}$
IGRJ17451-3022	2015-03-06	0748391201_S001	$0.244^{+0.003}_{-0.003}$	0.2	$\mathbf{92}^{+11}_{-10}$	$\mathbf{-1200}^{+800}_{-1100}$	/	/	/	/

7.2 4U 1630-47

7.2.1 Results of the line detection procedure

EW values for each line and each exposure analyzed in the sample, with observations listed chronologically. We report EW results for detections or EW upper limits for non-detections of the main lines. Line EWs are only provided for detections above 3 σ significance along with 90% uncertainties. Upper limits above 100 eV are not reported. For NICER, the exposure time refers to the total exposure time of all the individual orbits selected in the epoch, and the ObsID marks the main ObsID of that epoch (see Sect. 4.2).

Outburst	Date	Instrument	ObsID + identifier	exp. time (ks)	Fe line Equivalent Width / 3 σ upper limit (eV)				
					xxvKα	xxviKα	xxvKβ	xxviKβ	xxviKγ
2002/2004	2004-08-04	Chandra	4568	49.99	≤ 4	$\mathbf{11}^{+3}_{-4}$	≤ 19	≤ 76	/
2005/2006	2006-02-08	Suzaku	400010010	11.06	$\mathbf{9} \pm 3$	$\mathbf{36} \pm 3$	≤ 17	$\mathbf{17}^{+7}_{-5}$	≤ 22
	2006-02-15	Suzaku	400010020	10.7	$\mathbf{19}^{+3}_{-4}$	$\mathbf{37}^{+4}_{-3}$	≤ 25	$\mathbf{22}^{+8}_{-7}$	≤ 27
	2006-02-28	Suzaku	400010030	10.72	$\mathbf{20} \pm 4$	$\mathbf{34} \pm 4$	≤ 24	≤ 36	≤ 27
	2006-03-08	Suzaku	400010040	10.66	$\mathbf{25}^{+4}_{-5}$	$\mathbf{36}^{+5}_{-4}$	$\mathbf{32}^{+9}_{-6}$	≤ 41	≤ 39
	2006-03-15	Suzaku	400010050	23.18	$\mathbf{22} \pm 3$	$\mathbf{36} \pm 3$	≤ 17	≤ 20	≤ 19
	2006-03-23	Suzaku	400010060	21.65	$\mathbf{25}^{+4}_{-3}$	$\mathbf{38} \pm 4$	≤ 23	≤ 31	≤ 22
Out of outburst	2010-08-24	Suzaku	405051010	99.92	≤ 66	≤ 77	≤ 79	/	/
2011/2013	2012-01-17	Chandra	13714	28.92	$\mathbf{32} \pm 4$	$\mathbf{57} \pm 5$	/	/	/
	2012-01-20	Chandra	13715	29.28	$\mathbf{34}^{+3}_{-5}$	$\mathbf{49}^{+4}_{-5}$	$\mathbf{23}^{+7}_{-5}$	/	/
	2012-01-26	Chandra	13716	29.28	$\mathbf{47}^{+3}_{-2}$	$\mathbf{52}^{+1}_{-3}$	$\mathbf{32}^{+11}_{-2}$	$\mathbf{38}^{+9}_{-6}$	/
	2012-01-30	Chandra	13717	29.44	$\mathbf{30} \pm 3$	$\mathbf{48} \pm 4$	$\mathbf{32}^{+14}_{-7}$	$\mathbf{35}^{+10}_{-11}$	$\mathbf{36}^{+13}_{-8}$
	2012-02-13	Suzaku	906008010	7.71	$\mathbf{39}^{+3}_{-4}$	$\mathbf{56} \pm 4$	$\mathbf{50}^{+9}_{-6}$	$\mathbf{57}^{+7}_{-9}$	$\mathbf{33}^{+8}_{-7}$
	2012-03-04	XMM	0670671501_S003	2.54	$\mathbf{35} \pm 7$	$\mathbf{55}^{+9}_{-7}$	≤ 34	/	/
	2012-03-04	XMM	0670671501_U014	69.86	$\mathbf{31} \pm 2$	$\mathbf{48}^{+1}_{-2}$	$\mathbf{21}^{+3}_{-1}$	$\mathbf{22}^{+3}_{-0}$	/
	2012-03-20	XMM	0670671301_S003	22.26	$\mathbf{21} \pm 3$	$\mathbf{46}^{+4}_{-2}$	≤ 16	$\mathbf{18}^{+6}_{-5}$	/
	2012-03-25	XMM	0670672901_S003	62.81	$\mathbf{20} \pm 1$	$\mathbf{45}^{+1}_{-2}$	$\mathbf{9} \pm 2$	$\mathbf{19} \pm 2$	/
	2012-06-03	Chandra	14441	19.0	≤ 12	≤ 14	≤ 34	≤ 42	≤ 62
	2012-09-09	XMM	0670673001_S003	22.48	$\mathbf{9}^{+3}_{-2}$	$\mathbf{31}^{+3}_{-2}$	≤ 10	≤ 10	≤ 10
	2012-09-10	XMM	0670673001_U002	0.8	≤ 19	$\mathbf{25}^{+6}_{-5}$	≤ 17	≤ 22	≤ 23
	2012-09-11	XMM	0670673101_S003	0.93	≤ 14	$\mathbf{9}^{+5}_{-4}$	≤ 19	≤ 16	≤ 19
	2012-09-28	XMM	0670673201_S003	1.56	≤ 5	≤ 7	≤ 9	≤ 11	≤ 19
	2012-10-02	Suzaku	907003010	2.88	≤ 8	≤ 9	≤ 15	≤ 14	≤ 48
	2013-02-20	NuSTAR	40014008002	16.57	≤ 21	$\mathbf{30}^{+3}_{-2}$	$\mathbf{13}^{+4}_{-3}$	≤ 18	≤ 8
	2013-02-21	NuSTAR	40014009001	14.65	≤ 24	$\mathbf{37}^{+0}_{-1}$	≤ 6	≤ 8	≤ 7
	2013-04-25	Chandra	15511	49.39	≤ 8	≤ 7	≤ 26	≤ 32	≤ 35
	2013-05-27	Chandra	15524	48.91	≤ 44	≤ 62	/	/	/
2015	2015-02-20	Suzaku	409007010	6.04	≤ 9	$\mathbf{17}^{+4}_{-3}$	≤ 12	≤ 18	≤ 18
	2015-02-24	Suzaku	409007020	5.57	$\mathbf{18} \pm 3$	$\mathbf{44} \pm 5$	≤ 27	$\mathbf{21}^{+9}_{-6}$	≤ 19
	2015-02-27	Suzaku	409007030	5.15	≤ 19	$\mathbf{38}^{+4}_{-3}$	≤ 23	≤ 24	≤ 19
2016/2017	2016-10-21	Chandra	19904	30.93	$\mathbf{23}^{+4}_{-5}$	$\mathbf{45}^{+4}_{-7}$	/	/	/
	2018-06-11	NICER	1130010104	1.96	$\mathbf{31}^{+12}_{-7}$	$\mathbf{52}^{+12}_{-8}$	/	/	/
	2018-07-02	NICER	1130010105	1.48	$\mathbf{19}^{+6}_{-5}$	$\mathbf{41}^{+5}_{-6}$	≤ 35	/	/
	2018-07-04	NICER	1130010106	0.64	$\mathbf{18}^{+10}_{-7}$	$\mathbf{46}^{+9}_{-8}$	/	$\mathbf{37}^{+16}_{-12}$	/
	2018-07-05	NICER	1130010107	0.09	≤ 69	/	/	/	/

Table 7.3: continued

Outburst	Date	Instrument	ObsID + identifier	exp. time (ks)	Fe line Equivalent Width / 3 σ upper limit (eV)				
					xxvKα	xxviKα	xxvKβ	xxviKβ	xxviKγ
	2018-07-07	NICER	1130010109	0.41	$\mathbf{21}^{+12}_{-8}$	$\mathbf{42}^{+13}_{-10}$	≤ 54	/	/
	2018-07-10	NICER	1130010111	1.79	$\mathbf{21}^{+6}_{-4}$	$\mathbf{42}\pm 5$	/	/	/
	2018-07-13	NICER	1130010113	1.36	$\mathbf{23}^{+6}_{-4}$	$\mathbf{51}^{+6}_{-5}$	$\mathbf{24}^{+11}_{-9}$	/	/
	2018-07-14	NICER	1130010114	2.07	$\mathbf{20}\pm 4$	$\mathbf{50}\pm 5$	$\mathbf{19}^{+9}_{-6}$	$\mathbf{37}\pm 10$	/
	2018-07-16	NICER	1130010116	0.94	$\mathbf{25}^{+9}_{-6}$	$\mathbf{51}^{+10}_{-3}$	/	/	/
	2018-07-17	NICER	1130010117	1.52	$\mathbf{25}\pm 5$	$\mathbf{51}^{+7}_{-6}$	/	/	/
	2018-07-21	NICER	1130010119	1.63	$\mathbf{22}^{+5}_{-4}$	$\mathbf{43}\pm 5$	/	$\mathbf{28}^{+14}_{-8}$	/
	2018-07-22	NICER	1130010120	1.01	$\mathbf{19}^{+7}_{-5}$	$\mathbf{50}^{+7}_{-6}$	/	/	/
	2018-07-23	NICER	1130010121	2.84	$\mathbf{20}^{+4}_{-5}$	$\mathbf{48}^{+4}_{-5}$	/	$\mathbf{28}^{+10}_{-8}$	/
	2018-07-25	NICER	1130010123	1.19	$\mathbf{21}^{+6}_{-5}$	$\mathbf{49}\pm 6$	/	/	/
2018/2019	2018-07-26	NICER	1130010124	1.14	$\mathbf{18}\pm 6$	$\mathbf{44}^{+7}_{-5}$	/	/	/
	2018-07-28	NICER	1130010125	0.79	$\mathbf{18}^{+8}_{-6}$	$\mathbf{38}^{+7}_{-8}$	≤ 41	/	/
	2018-08-02	NICER	1130010126	2.02	≤ 10	$\mathbf{38}^{+4}_{-5}$	≤ 17	$\mathbf{18}^{+9}_{-7}$	/
	2018-08-04	NICER	1130010128	2.34	≤ 12	$\mathbf{44}^{+4}_{-5}$	≤ 25	$\mathbf{23}^{+10}_{-8}$	/
	2018-08-06	NICER	1130010130	2.04	≤ 14	$\mathbf{40}^{+4}_{-3}$	≤ 17	≤ 25	/
	2018-08-08	NICER	1130010132	12.06	$\mathbf{15}^{+1}_{-2}$	$\mathbf{44}\pm 2$	/	$\mathbf{18}\pm 3$	/
	2018-08-10	NICER	1130010134	3.36	$\mathbf{17}\pm 4$	$\mathbf{47}^{+4}_{-3}$	$\mathbf{19}\pm 5$	$\mathbf{20}^{+10}_{-7}$	/
	2018-08-11	NICER	1130010135	4.82	$\mathbf{19}\pm 3$	$\mathbf{45}^{+3}_{-2}$	/	$\mathbf{22}^{+8}_{-7}$	/
	2018-08-17	NICER	1130010137	0.12	≤ 55	≤ 82	/	/	/
	2018-08-20	NICER	1130010139	7.75	$\mathbf{22}\pm 2$	$\mathbf{47}^{+3}_{-2}$	/	$\mathbf{22}^{+5}_{-6}$	/
	2018-08-22	NICER	1130010141	2.32	$\mathbf{26}^{+4}_{-6}$	$\mathbf{46}\pm 5$	/	$\mathbf{26}\pm 10$	/
	2018-09-24	NICER	1130010142	3.64	≤ 7	≤ 11	≤ 15	≤ 22	≤ 29
	2018-09-25	NICER	1130010143	0.94	≤ 16	≤ 17	≤ 32	≤ 41	≤ 57
	2018-09-28	NICER	1130010144	2.23	≤ 18	≤ 17	≤ 32	≤ 33	≤ 52
	2018-09-29	NICER	1130010145	1.99	≤ 15	≤ 14	≤ 23	≤ 38	≤ 53
	2018-10-02	NICER	1130010146	2.65	≤ 12	≤ 14	≤ 32	≤ 34	≤ 56
	2018-10-04	NICER	1130010147	4.16	≤ 14	≤ 26	≤ 29	≤ 34	≤ 39
	2018-10-05	NICER	1130010148	3.06	≤ 22	$\mathbf{28}^{+9}_{-6}$	≤ 47	≤ 44	/
	2018-10-07	NICER	1130010150	0.9	≤ 44	≤ 59	≤ 74	≤ 70	/
	2020-03-19	NICER	3130010101	0.57	≤ 22	≤ 29	≤ 36	≤ 59	≤ 65
	2020-03-26	NICER	3130010102	0.88	≤ 16	≤ 17	≤ 25	/	≤ 43
	2020-03-27	NICER	3130010103	2.18	≤ 16	≤ 18	≤ 26	≤ 33	≤ 43
	2020-03-30	NICER	3130010105	0.43	≤ 23	≤ 29	≤ 46	≤ 45	≤ 74
	2020-04-01	NICER	3130010106	2.51	≤ 7	$\mathbf{10}^{+5}_{-4}$	≤ 14	≤ 16	≤ 25
	2020-04-03	NICER	3130010108	2.47	≤ 9	$\mathbf{24}^{+5}_{-4}$	≤ 15	≤ 19	≤ 32
	2020-04-06	NICER	3130010110	0.76	≤ 14	$\mathbf{29}^{+9}_{-6}$	≤ 25	≤ 43	≤ 42
	2020-04-07	NICER	3130010111	2.56	≤ 11	$\mathbf{22}^{+5}_{-4}$	≤ 15	≤ 25	≤ 27
	2020-04-09	NICER	3130010112	1.98	≤ 8	$\mathbf{28}^{+4}_{-5}$	≤ 16	≤ 23	≤ 26
	2020-04-11	NICER	3130010114	0.39	≤ 18	≤ 42	≤ 54	≤ 71	≤ 75
	2020-04-13	NICER	3130010116	1.06	≤ 14	$\mathbf{27}^{+8}_{-5}$	≤ 22	≤ 40	≤ 49
	2020-04-14	NICER	3130010117	0.83	≤ 18	≤ 23	≤ 36	≤ 42	≤ 52

Table 7.3: continued

Outburst	Date	Instrument	ObsID + identifier	exp. time (ks)	Fe line Equivalent Width / 3 σ upper limit (eV)				
					xxvKα	xxviKα	xxvKβ	xxviKβ	xxviKγ
	2020-04-15	NICER	3130010118	0.97	≤ 12	**24** ± 7	≤ 32	≤ 34	≤ 45
	2020-04-17	NICER	3130010119	0.4	≤ 24	≤ 21	≤ 39	≤ 66	≤ 72
	2020-04-18	NICER	3130010120	1.47	≤ 19	≤ 21	≤ 37	≤ 43	≤ 56
	2020-04-20	NICER	3130010122	1.05	≤ 12	≤ 14	≤ 22	≤ 33	≤ 54
	2020-04-22	NICER	3130010124	0.62	≤ 22	≤ 24	≤ 26	≤ 38	≤ 48
	2020-04-23	NICER	3130010125	0.95	≤ 18	≤ 20	≤ 22	≤ 35	≤ 41
	2020-04-24	NICER	3130010126	0.6	≤ 29	≤ 19	≤ 46	≤ 58	≤ 55
	2020-04-26	NICER	3130010127	1.49	≤ 16	≤ 20	≤ 30	≤ 31	≤ 43
	2020-04-27	NICER	3130010128	2.64	≤ 8	≤ 11	≤ 14	≤ 15	≤ 29
	2020-04-28	NICER	3130010129	2.04	≤ 11	≤ 11	≤ 15	≤ 26	≤ 38
	2020-04-30	NICER	3130010131	3.15	≤ 8	≤ 9	≤ 13	≤ 16	≤ 23
	2020-05-01	NICER	3130010132	1.4	≤ 21	≤ 23	≤ 35	≤ 35	≤ 57
	2020-05-02	NICER	3130010133	2.61	≤ 15	≤ 18	≤ 26	≤ 33	≤ 42
	2020-05-03	NICER	3130010134	2.04	≤ 18	≤ 19	≤ 30	≤ 38	≤ 43
2020	2020-05-05	NICER	3130010136	2.6	≤ 10	≤ 9	≤ 16	≤ 18	≤ 32
	2020-05-06	NICER	3130010137	2.25	≤ 11	≤ 12	≤ 26	≤ 22	≤ 35
	2020-05-07	NICER	3130010138	1.87	≤ 20	≤ 19	≤ 34	≤ 43	≤ 51
	2020-05-09	NICER	3130010140	1.99	≤ 10	≤ 11	≤ 18	≤ 30	≤ 33
	2020-05-11	NICER	3130010141	1.04	≤ 26	≤ 30	≤ 51	≤ 60	≤ 79
	2020-05-15	NICER	3130010143	0.17	≤ 47	≤ 56	/	/	/
	2020-05-22	NICER	3130010144	2.92	≤ 20	≤ 20	≤ 42	≤ 45	≤ 52
	2020-05-28	Chandra	22376	24.5	≤ 35	≤ 35	≤ 75	/	/
	2020-05-28	NICER	3130010145	1.23	≤ 35	≤ 30	≤ 54	≤ 70	≤ 78
	2020-05-31	NICER	3130010146	0.76	≤ 39	≤ 42	/	/	/
	2020-06-01	NICER	3130010147	1.63	≤ 26	≤ 30	≤ 63	≤ 97	/
	2020-06-04	NICER	3130010148	1.51	≤ 34	≤ 56	≤ 73	≤ 97	/
	2020-06-06	Chandra	22377	24.5	≤ 41	≤ 50	/	/	/
	2020-06-08	NICER	3130010149	0.61	/	/	/	/	/
	2020-06-13	Chandra	22378	23.54	≤ 39	≤ 55	/	/	/
	2020-06-14	NICER	3130010151	2.05	≤ 48	≤ 56	/	/	/
	2021-09-13	NICER	4130010101	5.88	≤ 23	≤ 29	≤ 31	≤ 42	≤ 58
	2021-09-14	NICER	4130010102	5.01	≤ 25	≤ 28	≤ 38	≤ 36	≤ 53
	2021-09-16	NICER	4130010104	3.96	≤ 15	≤ 24	≤ 20	≤ 25	≤ 29
	2021-09-17	NICER	4130010105	3.27	≤ 28	≤ 29	≤ 42	≤ 48	≤ 45
	2021-09-18	NICER	4130010106	4.42	≤ 19	≤ 23	≤ 32	≤ 35	≤ 44
	2021-09-19	NICER	4130010107	5.5	≤ 17	≤ 20	≤ 25	≤ 29	≤ 36
	2021-09-20	NICER	4130010108	3.21	≤ 18	≤ 21	≤ 29	≤ 33	≤ 45
	2021-09-22	NICER	4130010110	1.37	≤ 27	≤ 30	≤ 44	≤ 48	≤ 57
	2021-09-23	NICER	4130010111	0.61	≤ 17	≤ 18	≤ 20	≤ 34	≤ 33
	2021-09-23	NICER	4130010111	2.09	≤ 12	≤ 16	≤ 24	≤ 24	≤ 37
	2021-09-24	NICER	4130010112	2.03	≤ 24	≤ 29	≤ 38	≤ 46	≤ 55

Table 7.3: continued

Outburst	Date	Instrument	ObsID + identifier	exp. time (ks)	Fe line Equivalent Width / 3 σ upper limit (eV)				
					xxvKα	xxviKα	xxvKβ	xxviKβ	xxviKγ
	2021-09-24	NICER	4130010112	1.87	≤ 23	≤ 31	≤ 38	≤ 43	≤ 62
	2021-09-26	NICER	4130010114	1.48	≤ 16	≤ 19	≤ 27	≤ 25	≤ 44
	2021-09-26	NICER	4130010114	0.55	≤ 17	≤ 16	≤ 32	≤ 33	≤ 32
	2021-09-27	NICER	4130010115	1.48	≤ 9	≤ 9	≤ 20	≤ 19	≤ 18
	2021-09-28	NICER	4130010116	1.1	≤ 9	≤ 8	≤ 19	≤ 18	≤ 22
	2021-09-28	NICER	4130010116	1.18	≤ 14	≤ 17	≤ 24	≤ 27	≤ 32
	2021-09-29	NICER	4130010118	3.08	≤ 7	≤ 7	≤ 9	≤ 10	≤ 17
	2021-10-01	NICER	4130010119	1.5	≤ 14	≤ 14	≤ 23	≤ 23	≤ 34
2021/2022	2021-10-01	NICER	4130010119	2.73	≤ 13	≤ 13	≤ 22	≤ 23	≤ 30
	2021-10-11	NICER	4130010121	1.58	≤ 17	≤ 17	≤ 31	≤ 32	≤ 42
	2021-10-12	NICER	4130010122	0.79	≤ 24	≤ 26	≤ 40	≤ 44	≤ 61
	2021-10-13	NICER	4130010123	0.69	≤ 13	≤ 19	≤ 23	≤ 34	≤ 36
	2021-10-14	NICER	4130010124	1.86	≤ 17	≤ 17	≤ 31	≤ 37	≤ 35
	2021-10-21	NICER	4130010126	0.76	≤ 24	≤ 30	≤ 42	≤ 52	≤ 44
	2021-10-23	NICER	4130010127	0.91	≤ 28	≤ 31	≤ 50	≤ 55	≤ 64
	2021-10-25	NICER	4130010128	1.32	≤ 21	≤ 21	≤ 20	≤ 29	≤ 52
	2021-10-28	NICER	4130010130	1.01	≤ 22	≤ 22	≤ 26	≤ 49	≤ 53
	2022-02-19	NICER	4130010131	0.3	/	/	/	/	/
	2022-07-30	NICER	5130010101	2.14	$\mathbf{18}^{+8}_{-9}$	$\mathbf{39}^{+10}_{-9}$	≤ 58	≤ 76	/
	2022-07-31	NICER	5130010102	0.35	≤ 63	$\mathbf{57}^{+30}_{-21}$	/	/	/
	2022-08-06	NICER	5130010103	3.32	$\mathbf{23}^{+3}_{-5}$	$\mathbf{41}^{+1}_{-8}$	/	/	/
	2022-08-07	NICER	5130010104	3.55	$\mathbf{22}^{+3}_{-8}$	$\mathbf{39}^{+5}_{-6}$	/	/	/
	2022-08-08	NICER	5130010105	3.48	$\mathbf{21} \pm 4$	$\mathbf{37}^{+5}_{-4}$	≤ 25	/	/
	2022-08-09	NICER	5130010106	0.35	$\mathbf{28}^{+18}_{-12}$	$\mathbf{46}^{+21}_{-12}$	/	/	/
	2022-08-11	NICER	5130010108	0.06	/	/	/	/	/
	2022-08-13	NICER	5130010109	0.21	≤ 47	≤ 100	/	/	/
	2022-08-14	NICER	5130010110	3.36	$\mathbf{23} \pm 4$	$\mathbf{41}^{+5}_{-4}$	/	/	/
	2022-08-15	NICER	5130010111	0.95	$\mathbf{19}^{+8}_{-6}$	$\mathbf{35} \pm 8$	/	$\mathbf{41}^{+17}_{-15}$	/
	2022-08-18	NICER	5130010112	0.4	≤ 40	$\mathbf{36} \pm 11$	≤ 64	≤ 76	/
	2022-08-22	NICER	5501010101	1.91	$\mathbf{18} \pm 5$	$\mathbf{49} \pm 5$	$\mathbf{26} \pm 8$	/	/
	2022-08-23	NICER	5501010102	0.58	$\mathbf{20}^{+9}_{-8}$	$\mathbf{32}^{+10}_{-9}$	≤ 59	/	/
	2022-08-25	NICER	5501010104	3.92	$\mathbf{19}^{+3}_{-4}$	$\mathbf{47}^{+2}_{-4}$	/	$\mathbf{18} \pm 7$	/
	2022-08-26	NICER	5501010105	3.06	$\mathbf{25}^{+4}_{-3}$	$\mathbf{47} \pm 4$	$\mathbf{25}^{+8}_{-5}$	$\mathbf{28}^{+9}_{-7}$	$\mathbf{27}^{+10}_{-11}$
	2022-08-27	NICER	5501010106	2.02	$\mathbf{22}^{+5}_{-4}$	$\mathbf{47}^{+6}_{-4}$	$\mathbf{20}^{+7}_{-8}$	$\mathbf{35}^{+12}_{-8}$	$\mathbf{29}^{+16}_{-13}$
	2022-08-28	NICER	5501010107	2.8	$\mathbf{26}^{+5}_{-4}$	$\mathbf{48}^{+5}_{-3}$	$\mathbf{21} \pm 7$	$\mathbf{20} \pm 9$	/
	2022-08-29	NICER	5501010108	2.31	$\mathbf{26}^{+5}_{-4}$	$\mathbf{44}^{+5}_{-3}$	$\mathbf{19}^{+10}_{-5}$	$\mathbf{36}^{+9}_{-8}$	/
	2022-08-30	NICER	5501010109	2.27	$\mathbf{22}^{+5}_{-4}$	$\mathbf{44} \pm 5$	$\mathbf{20}^{+8}_{-7}$	$\mathbf{32}^{+10}_{-7}$	$\mathbf{31}^{+15}_{-9}$
	2022-08-31	NICER	5501010110	4.45	$\mathbf{24} \pm 3$	$\mathbf{44} \pm 3$	$\mathbf{27} \pm 7$	$\mathbf{34}^{+8}_{-6}$	$\mathbf{25}^{+11}_{-9}$
	2022-09-01	NICER	5501010111	0.48	$\mathbf{29}^{+10}_{-9}$	$\mathbf{61}^{+13}_{-9}$	/	$\mathbf{62}^{+23}_{-18}$	/
	2022-09-18	NICER	5130010114	3.78	$\mathbf{31}^{+4}_{-3}$	$\mathbf{51}^{+5}_{-3}$	$\mathbf{23}^{+6}_{-7}$	$\mathbf{24}^{+10}_{-11}$	/
	2022-09-20	NICER	5130010116	3.32	$\mathbf{33}^{+3}_{-5}$	$\mathbf{45}^{+4}_{-7}$	/	/	/

Table 7.3: continued

Outburst	Date	Instrument	ObsID + identifier	exp. time (ks)	Fe line Equivalent Width / 3 σ upper limit (eV)				
					xxvKα	xxviKα	xxvKβ	xxviKβ	xxviKγ
	2022-09-27	NICER	5130010118	3.87	$\mathbf{28}\pm4$	$\mathbf{57}\pm4$	$\mathbf{37}^{+8}_{-7}$	$\mathbf{36}^{+10}_{-9}$	$\mathbf{31}^{+15}_{-11}$
	2022-09-30	NICER	5130010119	0.23	≤ 60	$\mathbf{60}^{+19}_{-16}$	≤ 90	/	/
	2022-10-06	NICER	5130010120	1.38	$\mathbf{38}^{+6}_{-4}$	$\mathbf{57}^{+7}_{-6}$	$\mathbf{38}^{+12}_{-11}$	$\mathbf{34}^{+16}_{-12}$	/
	2022-10-09	NICER	5130010121	2.18	$\mathbf{37}^{+5}_{-6}$	$\mathbf{53}\pm6$	$\mathbf{28}^{+10}_{-8}$	$\mathbf{31}^{+12}_{-10}$	/
	2022-10-12	NICER	5130010123	2.1	$\mathbf{33}\pm6$	$\mathbf{51}\pm6$	$\mathbf{46}^{+10}_{-7}$	$\mathbf{38}^{+17}_{-10}$	$\mathbf{44}^{+23}_{-16}$
	2023-01-13	NICER	5665010101	0.49	≤ 63	≤ 72	/	/	/
	2023-01-28	NICER	5665010201	0.92	≤ 20	$\mathbf{31}^{+10}_{-8}$	≤ 31	≤ 56	≤ 49
	2023-02-10	NICER	5665010301	0.48	$\mathbf{23}^{+7}_{-9}$	$\mathbf{62}^{+12}_{-9}$	/	$\mathbf{42}^{+22}_{-14}$	/
	2023-02-23	NICER	5665010401	1.44	≤ 11	≤ 12	≤ 14	≤ 17	≤ 26
	2023-02-24	NICER	5665010402	0.07	≤ 27	≤ 45	≤ 51	≤ 88	≤ 87
	2023-02-28	NICER	5130010124	0.37	≤ 25	≤ 33	≤ 51	≤ 50	≤ 78
	2023-03-02	NICER	6130010101	0.58	≤ 11	≤ 12	≤ 32	≤ 30	≤ 28
	2023-03-03	NICER	6130010102	1.18	≤ 21	≤ 21	≤ 30	≤ 34	≤ 40
	2023-03-05	NICER	6130010103	1.37	≤ 6	≤ 7	≤ 12	≤ 15	≤ 17
	2023-03-06	NICER	6130010104	2.92	≤ 11	≤ 14	≤ 19	≤ 21	≤ 20
	2023-03-08	NICER	6130010106	3.19	≤ 5	≤ 6	≤ 10	≤ 11	≤ 16
	2023-03-09	NuSTAR	80801327002	12.16	≤ 8	$\mathbf{11}\pm2$	≤ 4	≤ 5	≤ 4
	2023-03-10	NICER	6130010107	0.95	≤ 16	≤ 16	≤ 16	≤ 28	≤ 34
	2023-03-10	NICER	5665010403	9.45	≤ 6	≤ 7	≤ 11	≤ 12	≤ 17
	2023-03-10	NuSTAR	80902312002	10.8	$\mathbf{13}^{+5}_{-3}$	$\mathbf{8}\pm3$	≤ 6	≤ 5	≤ 6
2022/2024	2023-03-11	NICER	6557010201	12.67	≤ 4	≤ 4	≤ 6	/	≤ 12
	2023-03-11	NuSTAR	80902312004	7.94	≤ 7	$\mathbf{9}^{+1}_{-4}$	≤ 3	≤ 4	≤ 4
	2023-03-12	NICER	6557010301	14.97	≤ 4	≤ 4	/	≤ 7	≤ 12
	2023-03-13	NuSTAR	80902312006	9.62	≤ 9	$\mathbf{12}^{+4}_{-1}$	≤ 3	≤ 4	≤ 3
	2023-03-13	NICER	6557010302	1.28	≤ 12	≤ 14	≤ 19	≤ 22	≤ 27
	2023-03-24	NICER	5665010404	2.61	≤ 12	≤ 14	≤ 17	≤ 20	≤ 29
	2023-03-27	NICER	6130010109	1.11	≤ 17	≤ 20	≤ 27	≤ 31	≤ 37
	2023-04-05	NICER	5665010406	0.87	≤ 21	≤ 22	≤ 34	≤ 40	≤ 50
	2023-04-07	NICER	5665010407	4.34	≤ 4	$\mathbf{10}\pm3$	≤ 13	≤ 12	≤ 17
	2023-04-08	NICER	5665010408	0.97	≤ 10	$\mathbf{15}\pm6$	≤ 19	≤ 26	≤ 33
	2023-04-16	NICER	6130010110	0.73	≤ 12	≤ 14	≤ 33	≤ 37	≤ 47
	2023-04-21	NICER	5665010409	1.33	≤ 10	≤ 21	≤ 18	≤ 20	≤ 38
	2023-04-22	NICER	6130010111	3.51	≤ 8	$\mathbf{23}^{+3}_{-5}$	≤ 12	≤ 22	≤ 20
	2023-05-01	NICER	6130010113	2.92	≤ 10	$\mathbf{20}^{+5}_{-4}$	≤ 23	≤ 37	≤ 28
	2023-05-05	NICER	5665010410	1.95	≤ 11	≤ 13	≤ 23	≤ 33	≤ 27
	2023-05-06	NICER	6130010114	1.98	≤ 8	≤ 9	≤ 18	≤ 27	≤ 30
	2023-05-11	NICER	6130010115	0.72	≤ 18	$\mathbf{16}^{+9}_{-7}$	≤ 25	≤ 38	≤ 41
	2023-05-19	NICER	5665010411	2.0	≤ 14	$\mathbf{25}\pm5$	≤ 18	≤ 42	/
	2023-05-21	NICER	6130010117	1.63	≤ 10	≤ 22	≤ 19	≤ 24	≤ 35
	2023-05-28	NICER	6130010118	1.18	≤ 37	≤ 43	/	/	/
	2023-05-28	NICER	6130010118	1.17	≤ 25	$\mathbf{32}^{+10}_{-8}$	≤ 41	≤ 45	/

Table 7.3: continued

Outburst	Date	Instrument	ObsID + identifier	exp. time (ks)	Fe line Equivalent Width / 3 σ upper limit (eV)				
					xxvKα	xxviKα	xxvKβ	xxviKβ	xxviKγ
	2023-06-08	NICER	6130010119	2.21	$\mathbf{22}^{+5}_{-4}$	$\mathbf{36}\pm6$	/	$\mathbf{31}^{+11}_{-9}$	/
	2023-06-16	NICER	6130010120	0.47	$\mathbf{24}^{+13}_{-9}$	$\mathbf{30}^{+18}_{-11}$	≤ 68	≤ 73	/
	2023-06-16	NICER	6130010120	0.47	$\mathbf{29}^{+13}_{-8}$	$\mathbf{38}^{+15}_{-11}$	≤ 62	/	/
	2023-06-18	NICER	6130010121	2.0	$\mathbf{40}^{+5}_{-4}$	$\mathbf{50}^{+7}_{-5}$	$\mathbf{32}\pm9$	$\mathbf{30}^{+13}_{-11}$	/
	2023-06-25	NICER	6130010122	0.59	≤ 37	$\mathbf{28}^{+14}_{-11}$	≤ 60	≤ 69	/
	2023-07-02	NICER	6130010123	1.27	$\mathbf{21}^{+5}_{-7}$	$\mathbf{39}^{+9}_{-5}$	/	/	/
	2023-08-27	NICER	6588010111	2.94	≤ 8	≤ 8	≤ 13	≤ 17	≤ 22
	2023-08-31	NICER	6588010112	2.46	≤ 19	≤ 15	≤ 28	≤ 33	≤ 44
	2023-09-01	NICER	6588010113	0.08	≤ 68	≤ 67	/	/	/
	2023-10-08	NICER	6588010116	3.57	≤ 30	≤ 35	≤ 61	≤ 89	/
	2023-10-12	NICER	6588010117	3.79	≤ 51	≤ 68	/	/	/

7.2.2 Parameters of Kα detections

Main characteristics of significant Kα line detections from the sample. Uncertainties regarding luminosity are not quoted, as they were negligible.

Source	Date	ObsID	$HR_{[6-10]/[3-10]}$	$L_{[3-10]}/L_{Edd}$ $\times 10^{-2}$	Fe xxv Kα			Fe xxvi Kα		
					EW	blueshift	width	EW	blueshift	width
			Bands in keV		eV	km/s	km/s	eV	km/s	km/s
2002/2004	2004-08-04	4568	$0.351^{+0.003}_{-0.003}$	5.6	/	/	/	$\mathbf{11}^{+3}_{-4}$	$\mathbf{-300}^{+500}_{-500}$	$\mathbf{0}^{+4200}$
2005/2006	2006-02-08	400010010	$0.306^{+0.001}_{-0.002}$	5.1	$\mathbf{9}\pm3$	$\mathbf{-1600}^{+1500}_{-2000}$	/	$\mathbf{36}\pm3$	$\mathbf{-1200}^{+400}_{-500}$	/
	2006-02-15	400010020	$0.287^{+0.001}_{-0.002}$	3.7	$\mathbf{19}^{+3}_{-4}$	$\mathbf{-1400}^{+1500}_{-1400}$	/	$\mathbf{37}^{+4}_{-3}$	$\mathbf{-1000}^{+700}_{-900}$	/
	2006-02-28	400010030	$0.249^{+0.001}_{-0.002}$	3.4	$\mathbf{20}\pm4$	$\mathbf{-1200}^{+1400}_{-1500}$	/	$\mathbf{34}\pm4$	$\mathbf{-700}^{+900}_{-900}$	/
	2006-03-08	400010040	$0.239^{+0.001}_{-0.002}$	3.0	$\mathbf{25}^{+4}_{-5}$	$\mathbf{-1300}^{+1800}_{-1600}$	/	$\mathbf{36}^{+5}_{-4}$	$\mathbf{-400}^{+1100}_{-1300}$	/
	2006-03-15	400010050	$0.229^{+0.001}_{-0.001}$	2.8	$\mathbf{22}\pm3$	$\mathbf{-800}^{+1200}_{-1200}$	/	$\mathbf{36}\pm3$	$\mathbf{-300}^{+800}_{-700}$	/
	2006-03-23	400010060	$0.213^{+0.001}_{-0.001}$	2.5	$\mathbf{25}^{+4}_{-3}$	$\mathbf{300}^{+1100}_{-1300}$	/	$\mathbf{38}\pm4$	$\mathbf{200}^{+800}_{-700}$	/
2011/2013	2012-01-17	13714	$0.362^{+0.003}_{-0.003}$	4.7	$\mathbf{32}\pm4$	$\mathbf{0}^{+200}_{-100}$	$\mathbf{1900}^{+500}_{-500}$	$\mathbf{57}\pm5$	$\mathbf{-300}^{+100}_{-100}$	$\mathbf{2700}^{+400}_{-400}$
	2012-01-20	13715	$0.344^{+0.002}_{-0.002}$	4.6	$\mathbf{34}^{+3}_{-5}$	$\mathbf{100}^{+200}_{-100}$	$\mathbf{2300}^{+600}_{-400}$	$\mathbf{49}^{+4}_{-5}$	$\mathbf{-300}^{+100}_{-100}$	$\mathbf{2200}^{+600}_{-300}$
	2012-01-26	13716	$0.347^{+0.002}_{-0.003}$	4.4	$\mathbf{47}^{+3}_{-2}$	$\mathbf{500}^{+200}_{-200}$	$\mathbf{3000}^{+400}_{-500}$	$\mathbf{52}^{+1}_{-3}$	$\mathbf{-300}^{+0}_{-100}$	$\mathbf{2200}^{+700}_{-400}$
	2012-01-30	13717	$0.389^{+0.003}_{-0.003}$	5.1	$\mathbf{30}\pm3$	$\mathbf{200}^{+200}_{-300}$	$\mathbf{2000}^{+800}_{-700}$	$\mathbf{48}\pm4$	$\mathbf{-200}^{+200}_{-200}$	$\mathbf{1800}^{+700}_{-700}$
	2012-02-13	906008010	$0.292^{+0.001}_{-0.001}$	4.8	$\mathbf{39}^{+3}_{-4}$	$\mathbf{-800}^{+800}_{-900}$	/	$\mathbf{56}\pm4$	$\mathbf{-1700}^{+700}_{-500}$	/
	2012-03-04	0670671501_S003	$0.366^{+0.002}_{-0.002}$	4.8	$\mathbf{35}\pm7$	$\mathbf{-5000}^{+2200}_{-1900}$	/	$\mathbf{55}^{+9}_{-7}$	$\mathbf{-5800}^{+1600}_{-1200}$	/
	2012-03-04	0670671501_U014	$0.347^{+0.0}_{-0.0}$	5.3	$\mathbf{31}\pm2$	$\mathbf{-5200}^{+200}_{-300}$	/	$\mathbf{48}^{+1}_{-2}$	$\mathbf{-5200}^{+100}_{-200}$	/
	2012-03-20	0670671301_S003	$0.36^{+0.001}_{-0.001}$	6.2	$\mathbf{21}\pm3$	$\mathbf{-3900}^{+900}_{-800}$	/	$\mathbf{46}^{+4}_{-2}$	$\mathbf{-4300}^{+400}_{-400}$	/
	2012-03-25	0670672901_S003	$0.401^{+0.0}_{-0.0}$	5.8	$\mathbf{20}\pm1$	$\mathbf{-6000}^{+500}_{-500}$	/	$\mathbf{45}^{+1}_{-2}$	$\mathbf{-5900}^{+200}_{-300}$	/
	2012-09-09	0670673001_S003	$0.413^{+0.001}_{-0.001}$	8.0	$\mathbf{9}^{+3}_{-2}$	$\mathbf{-4600}^{+2600}_{-3000}$	/	$\mathbf{31}^{+3}_{-2}$	$\mathbf{-4300}^{+1000}_{-800}$	/
	2012-09-10	0670673001_U002	$0.432^{+0.002}_{-0.002}$	7.2	/	/	/	$\mathbf{25}^{+6}_{-5}$	$\mathbf{-3500}^{+2700}_{-3000}$	/
	2012-09-11	0670673101_S003	$0.467^{+0.002}_{-0.002}$	9.4	/	/	/	$\mathbf{9}^{+5}_{-4}$	$\mathbf{-1200}^{+5800}_{-6400}$	/
	2013-02-20	40014008002	$0.33^{+0.001}_{-0.001}$	6.2	/	/	/	$\mathbf{30}^{+3}_{-2}$	$\mathbf{500}^{+700}_{-800}$	/
	2013-02-21	40014009001	$0.331^{+0.001}_{-0.001}$	6.4	/	/	/	$\mathbf{37}^{+0}_{-1}$	$\mathbf{900}^{+400}_{-600}$	/
2015	2015-02-20	409007010	$0.363^{+0.002}_{-0.002}$	7.3	/	/	/	$\mathbf{17}^{+4}_{-3}$	$\mathbf{-1600}^{+1200}_{-900}$	/

Table 7.4: continued

Source	Date	ObsID	$HR_{[6-10]/[3-10]}$	$L_{[3-10]}/L_{Edd}$ $\times 10^{-2}$	Fe xxv Kα			Fe xxvi Kα		
			Bands in keV		EW	blueshift	width	EW	blueshift	width
					eV	km/s	km/s	eV	km/s	km/s
	2015-02-24	409007020	$0.327^{+0.002}_{-0.002}$	5.8	$\mathbf{18 \pm 3}$	$\mathbf{-600}^{+1200}_{-1100}$	/	$\mathbf{44 \pm 5}$	$\mathbf{-1000}^{+600}_{-500}$	/
	2015-02-27	409007030	$0.33^{+0.002}_{-0.002}$	6.0	/	/	/	$\mathbf{38}^{+4}_{-3}$	$\mathbf{-1200}^{+1100}_{-1000}$	/
2016/2017	2016-10-21	19904	$0.311^{+0.002}_{-0.002}$	5.6	$\mathbf{23}^{+4}_{-5}$	$\mathbf{-300}^{+300}_{-300}$	$\mathbf{1800}^{+1400}_{-1500}$	$\mathbf{45}^{+4}_{-7}$	$\mathbf{-200}^{+300}_{-300}$	$\mathbf{2400}^{+1000}_{-800}$
	2018-06-11	1130010104	$0.199^{+0.002}_{-0.002}$	2.4	$\mathbf{31}^{+12}_{-7}$	$\mathbf{0}^{+1200}_{-1600}$	/	$\mathbf{52}^{+12}_{-8}$	$\mathbf{200}^{+600}_{-800}$	/
	2018-07-02	1130010105	$0.334^{+0.002}_{-0.002}$	5.8	$\mathbf{19}^{+6}_{-5}$	$\mathbf{100}^{+1000}_{-1100}$	/	$\mathbf{41}^{+5}_{-6}$	$\mathbf{0}^{+600}_{-600}$	/
	2018-07-04	1130010106	$0.337^{+0.003}_{-0.003}$	5.8	$\mathbf{18}^{+10}_{-7}$	$\mathbf{-1500}^{+1800}_{-2200}$	/	$\mathbf{46}^{+9}_{-8}$	$\mathbf{400}^{+700}_{-800}$	/
	2018-07-07	1130010109	$0.341^{+0.004}_{-0.005}$	6.0	$\mathbf{21}^{+12}_{-8}$	$\mathbf{-600}^{+1500}_{-2200}$	/	$\mathbf{42}^{+13}_{-10}$	$\mathbf{-800}^{+1000}_{-900}$	/
	2018-07-10	1130010111	$0.351^{+0.002}_{-0.002}$	6.4	$\mathbf{21}^{+6}_{-4}$	$\mathbf{-900}^{+800}_{-800}$	/	$\mathbf{42 \pm 5}$	$\mathbf{-600}^{+500}_{-500}$	/
	2018-07-13	1130010113	$0.335^{+0.002}_{-0.002}$	6.0	$\mathbf{23}^{+6}_{-4}$	$\mathbf{-900}^{+900}_{-900}$	/	$\mathbf{51}^{+6}_{-5}$	$\mathbf{-300}^{+500}_{-400}$	/
	2018-07-14	1130010114	$0.335^{+0.002}_{-0.002}$	6.1	$\mathbf{20 \pm 4}$	$\mathbf{-500}^{+1400}_{-1500}$	/	$\mathbf{50 \pm 5}$	$\mathbf{-100}^{+600}_{-600}$	/
	2018-07-16	1130010116	$0.328^{+0.002}_{-0.003}$	6.0	$\mathbf{25}^{+9}_{-6}$	$\mathbf{-200}^{+2200}_{-1600}$	/	$\mathbf{51}^{+10}_{-3}$	$\mathbf{-200}^{+800}_{-800}$	/
	2018-07-17	1130010117	$0.335^{+0.002}_{-0.002}$	6.3	$\mathbf{25 \pm 5}$	$\mathbf{-900}^{+1300}_{-1600}$	/	$\mathbf{51}^{+7}_{-6}$	$\mathbf{-400}^{+700}_{-700}$	/
2018/2019	2018-07-21	1130010119	$0.335^{+0.002}_{-0.002}$	5.9	$\mathbf{22}^{+5}_{-4}$	$\mathbf{-1400}^{+1700}_{-1900}$	/	$\mathbf{43 \pm 5}$	$\mathbf{-700}^{+1000}_{-1100}$	/
	2018-07-22	1130010120	$0.333^{+0.002}_{-0.002}$	6.0	$\mathbf{19}^{+7}_{-5}$	$\mathbf{-1400}^{+3700}_{-5800}$	/	$\mathbf{50}^{+7}_{-6}$	$\mathbf{-700}^{+900}_{-1000}$	/
	2018-07-23	1130010121	$0.338^{+0.002}_{-0.001}$	6.0	$\mathbf{20}^{+4}_{-5}$	$\mathbf{-900}^{+600}_{-800}$	/	$\mathbf{48}^{+4}_{-5}$	$\mathbf{-300}^{+300}_{-400}$	/
	2018-07-25	1130010123	$0.337^{+0.002}_{-0.002}$	6.0	$\mathbf{21}^{+6}_{-5}$	$\mathbf{-900}^{+1900}_{-2100}$	/	$\mathbf{49 \pm 6}$	$\mathbf{-200}^{+900}_{-1000}$	/
	2018-07-26	1130010124	$0.335^{+0.002}_{-0.002}$	6.0	$\mathbf{18 \pm 6}$	$\mathbf{-800}^{+2500}_{-3200}$	/	$\mathbf{44}^{+7}_{-5}$	$\mathbf{-600}^{+1000}_{-1000}$	/
	2018-07-28	1130010125	$0.34^{+0.003}_{-0.003}$	6.3	$\mathbf{18}^{+8}_{-6}$	$\mathbf{-700}^{+2900}_{-3200}$	/	$\mathbf{38}^{+7}_{-8}$	$\mathbf{-200}^{+1300}_{-1600}$	/
	2018-08-02	1130010126	$0.359^{+0.002}_{-0.002}$	7.3	/	/	/	$\mathbf{38}^{+4}_{-5}$	$\mathbf{-1300}^{+900}_{-900}$	/
	2018-08-04	1130010128	$0.343^{+0.002}_{-0.002}$	6.4	/	/	/	$\mathbf{44}^{+4}_{-5}$	$\mathbf{-500}^{+700}_{-600}$	/
	2018-08-06	1130010130	$0.346^{+0.002}_{-0.002}$	6.6	/	/	/	$\mathbf{40}^{+4}_{-3}$	$\mathbf{-300}^{+900}_{-800}$	/
	2018-08-08	1130010132	$0.327^{+0.001}_{-0.001}$	6.2	$\mathbf{15}^{+1}_{-2}$	$\mathbf{400}^{+800}_{-800}$	/	$\mathbf{44 \pm 2}$	$\mathbf{300}^{+300}_{-200}$	/

Table 7.4: continued

Source	Date	ObsID	$HR_{[6-10]/[3-10]}$	$L_{[3-10]}/L_{Edd}$ $\times 10^{-2}$	Fe xxv Kα			Fe xxvi Kα		
					EW	blueshift	width	EW	blueshift	width
			Bands in keV		eV	km/s	km/s	eV	km/s	km/s
	2018-08-10	1130010134	$0.333^{+0.002}_{-0.002}$	6.0	$\mathbf{17 \pm 4}$	$\mathbf{-100}^{+700}_{-1000}$	/	$\mathbf{47}^{+4}_{-3}$	$\mathbf{0}^{+300}_{-400}$	/
	2018-08-11	1130010135	$0.325^{+0.001}_{-0.002}$	5.8	$\mathbf{19 \pm 3}$	$\mathbf{-600}^{+1000}_{-1100}$	/	$\mathbf{45}^{+3}_{-2}$	$\mathbf{-300}^{+400}_{-500}$	/
	2018-08-20	1130010139	$0.318^{+0.001}_{-0.001}$	5.5	$\mathbf{22 \pm 2}$	$\mathbf{300}^{+300}_{-400}$	/	$\mathbf{47}^{+3}_{-2}$	$\mathbf{100}^{+300}_{-200}$	/
	2018-08-22	1130010141	$0.299^{+0.002}_{-0.002}$	5.3	$\mathbf{26}^{+4}_{-6}$	$\mathbf{-100}^{+700}_{-700}$	/	$\mathbf{46 \pm 5}$	$\mathbf{-100}^{+400}_{-400}$	/
	2018-10-05	1130010148	$0.195^{+0.002}_{-0.001}$	2.4	/	/	/	$\mathbf{28}^{+9}_{-6}$	$\mathbf{1800}^{+1200}_{-1100}$	/
2020	2020-04-01	3130010106	$0.339^{+0.002}_{-0.002}$	7.4	/	/	/	$\mathbf{10}^{+5}_{-4}$	$\mathbf{-1700}^{+1800}_{-1600}$	/
	2020-04-03	3130010108	$0.318^{+0.002}_{-0.002}$	6.1	/	/	/	$\mathbf{24}^{+5}_{-4}$	$\mathbf{600}^{+700}_{-800}$	/
	2020-04-06	3130010110	$0.33^{+0.003}_{-0.003}$	6.1	/	/	/	$\mathbf{29}^{+9}_{-6}$	$\mathbf{-300}^{+1300}_{-1400}$	/
	2020-04-07	3130010111	$0.325^{+0.002}_{-0.002}$	5.8	/	/	/	$\mathbf{22}^{+5}_{-4}$	$\mathbf{-200}^{+800}_{-700}$	/
	2020-04-09	3130010112	$0.335^{+0.002}_{-0.002}$	6.1	/	/	/	$\mathbf{28}^{+4}_{-5}$	$\mathbf{-400}^{+700}_{-600}$	/
	2020-04-13	3130010116	$0.334^{+0.003}_{-0.003}$	6.1	/	/	/	$\mathbf{27}^{+8}_{-5}$	$\mathbf{200}^{+1000}_{-800}$	/
	2020-04-15	3130010118	$0.339^{+0.003}_{-0.003}$	6.7	/	/	/	$\mathbf{24 \pm 7}$	$\mathbf{-400}^{+1000}_{-1600}$	/
	2022-07-30	5130010101	$0.219^{+0.003}_{-0.004}$	2.4	$\mathbf{18}^{+8}_{-9}$	$\mathbf{1200}^{+1800}_{-1300}$	/	$\mathbf{39}^{+10}_{-9}$	$\mathbf{0}^{+900}_{-800}$	/
	2022-07-31	5130010102	$0.208^{+0.005}_{-0.005}$	2.4	/	/	/	$\mathbf{57}^{+30}_{-21}$	$\mathbf{-2000}^{+1600}_{-3000}$	/
	2022-08-06	5130010103	$0.25^{+0.001}_{-0.001}$	3.6	$\mathbf{23}^{+3}_{-5}$	$\mathbf{-900}^{+900}_{-900}$	/	$\mathbf{41}^{+1}_{-8}$	$\mathbf{100}^{+600}_{-500}$	/
	2022-08-07	5130010104	$0.259^{+0.002}_{-0.003}$	3.5	$\mathbf{22}^{+3}_{-8}$	$\mathbf{-1200}^{+900}_{-900}$	/	$\mathbf{39}^{+5}_{-6}$	$\mathbf{-900}^{+700}_{-400}$	/
	2022-08-08	5130010105	$0.273^{+0.002}_{-0.002}$	3.8	$\mathbf{21 \pm 4}$	$\mathbf{-300}^{+1000}_{-1000}$	/	$\mathbf{37}^{+5}_{-4}$	$\mathbf{-600}^{+600}_{-500}$	/
	2022-08-09	5130010106	$0.274^{+0.004}_{-0.005}$	4.2	$\mathbf{28}^{+18}_{-12}$	$\mathbf{-2800}^{+2700}_{-4300}$	/	$\mathbf{46}^{+21}_{-12}$	$\mathbf{200}^{+1700}_{-2400}$	/
	2022-08-14	5130010110	$0.298^{+0.002}_{-0.002}$	4.9	$\mathbf{23 \pm 4}$	$\mathbf{100}^{+800}_{-800}$	/	$\mathbf{41}^{+5}_{-4}$	$\mathbf{-300}^{+300}_{-400}$	/
	2022-08-15	5130010111	$0.297^{+0.002}_{-0.003}$	4.9	$\mathbf{19}^{+8}_{-6}$	$\mathbf{-1300}^{+1800}_{-1700}$	/	$\mathbf{35 \pm 8}$	$\mathbf{-1200}^{+800}_{-1000}$	/
	2022-08-18	5130010112	$0.307^{+0.004}_{-0.004}$	5.3	/	/	/	$\mathbf{36 \pm 11}$	$\mathbf{800}^{+4000}_{-4600}$	/
	2022-08-22	5501010101	$0.327^{+0.003}_{-0.003}$	5.6	$\mathbf{18 \pm 5}$	$\mathbf{-200}^{+1100}_{-1300}$	/	$\mathbf{49 \pm 5}$	$\mathbf{-600}^{+400}_{-400}$	/

Table 7.4: continued

Source	Date	ObsID	$HR_{[6-10]/[3-10]}$	$L_{[3-10]}/L_{Edd}$ $\times 10^{-2}$	Fe xxv Kα			Fe xxvi Kα		
					EW	blueshift	width	EW	blueshift	width
			Bands in keV		eV	km/s	km/s	eV	km/s	km/s
	2022-08-23	5501010102	$0.331^{+0.004}_{-0.004}$	6.0	$\mathbf{20}^{+9}_{-8}$	$\mathbf{-1300}^{+1500}_{-2100}$	/	$\mathbf{32}^{+10}_{-9}$	$\mathbf{-1200}^{+1300}_{-1600}$	/
	2022-08-25	5501010104	$0.331^{+0.001}_{-0.002}$	6.0	$\mathbf{19}^{+3}_{-4}$	$\mathbf{600}^{+700}_{-600}$	/	$\mathbf{47}^{+2}_{-4}$	$\mathbf{0}^{+300}_{-300}$	/
	2022-08-26	5501010105	$0.328^{+0.002}_{-0.002}$	5.6	$\mathbf{25}^{+4}_{-3}$	$\mathbf{100}^{+1200}_{-1100}$	/	$\mathbf{47 \pm 4}$	$\mathbf{-100}^{+700}_{-600}$	/
	2022-08-27	5501010106	$0.344^{+0.002}_{-0.002}$	5.7	$\mathbf{22}^{+5}_{-4}$	$\mathbf{-100}^{+1500}_{-1400}$	/	$\mathbf{47}^{+6}_{-4}$	$\mathbf{0}^{+900}_{-800}$	/
	2022-08-28	5501010107	$0.331^{+0.003}_{-0.003}$	5.7	$\mathbf{26}^{+5}_{-4}$	$\mathbf{-400}^{+900}_{-1300}$	/	$\mathbf{48}^{+5}_{-3}$	$\mathbf{-400}^{+600}_{-500}$	/
	2022-08-29	5501010108	$0.333^{+0.002}_{-0.002}$	5.5	$\mathbf{26}^{+5}_{-4}$	$\mathbf{-1100}^{+1300}_{-1100}$	/	$\mathbf{44}^{+5}_{-3}$	$\mathbf{-700}^{+900}_{-700}$	/
	2022-08-30	5501010109	$0.337^{+0.002}_{-0.002}$	5.8	$\mathbf{22}^{+5}_{-4}$	$\mathbf{-800}^{+1300}_{-1400}$	/	$\mathbf{44 \pm 5}$	$\mathbf{-300}^{+900}_{-800}$	/
	2022-08-31	5501010110	$0.33^{+0.002}_{-0.002}$	5.5	$\mathbf{24 \pm 3}$	$\mathbf{-800}^{+1100}_{-1000}$	/	$\mathbf{44 \pm 3}$	$\mathbf{-1000}^{+700}_{-700}$	/
	2022-09-01	5501010111	$0.316^{+0.003}_{-0.004}$	5.3	$\mathbf{29}^{+10}_{-9}$	$\mathbf{-500}^{+2400}_{-2500}$	/	$\mathbf{61}^{+13}_{-9}$	$\mathbf{-200}^{+1200}_{-1100}$	/
	2022-09-18	5130010114	$0.332^{+0.002}_{-0.003}$	5.2	$\mathbf{31}^{+4}_{-3}$	$\mathbf{-1300}^{+500}_{-500}$	/	$\mathbf{51}^{+5}_{-3}$	$\mathbf{-700}^{+400}_{-300}$	/
	2022-09-20	5130010116	$0.296^{+0.002}_{-0.002}$	4.7	$\mathbf{33}^{+3}_{-5}$	$\mathbf{-700}^{+800}_{-900}$	/	$\mathbf{45}^{+4}_{-7}$	$\mathbf{-1800}^{+800}_{-500}$	/
	2022-09-27	5130010118	$0.341^{+0.003}_{-0.003}$	5.1	$\mathbf{28 \pm 4}$	$\mathbf{-600}^{+1100}_{-1100}$	/	$\mathbf{57 \pm 4}$	$\mathbf{-1400}^{+700}_{-600}$	/
2022/2024	2022-09-30	5130010119	$0.325^{+0.006}_{-0.007}$	5.1	/	/	/	$\mathbf{60}^{+19}_{-16}$	$\mathbf{-2600}^{+2800}_{-2500}$	/
	2022-10-06	5130010120	$0.346^{+0.003}_{-0.003}$	5.1	$\mathbf{38}^{+6}_{-4}$	$\mathbf{-800}^{+1200}_{-1400}$	/	$\mathbf{57}^{+7}_{-6}$	$\mathbf{-1300}^{+800}_{-800}$	/
	2022-10-09	5130010121	$0.319^{+0.003}_{-0.003}$	4.8	$\mathbf{37}^{+5}_{-6}$	$\mathbf{-400}^{+900}_{-1000}$	/	$\mathbf{53 \pm 6}$	$\mathbf{-1100}^{+800}_{-700}$	/
	2022-10-12	5130010123	$0.31^{+0.002}_{-0.002}$	4.4	$\mathbf{33 \pm 6}$	$\mathbf{-400}^{+600}_{-500}$	/	$\mathbf{51 \pm 6}$	$\mathbf{-1500}^{+400}_{-500}$	/
	2023-01-28	5665010201	$0.392^{+0.004}_{-0.004}$	7.3	/	/	/	$\mathbf{31}^{+10}_{-8}$	$\mathbf{-900}^{+2700}_{-2400}$	/
	2023-02-10	5665010301	$0.421^{+0.007}_{-0.008}$	6.5	$\mathbf{23}^{+7}_{-9}$	$\mathbf{-700}^{+3300}_{-4500}$	/	$\mathbf{62}^{+12}_{-9}$	$\mathbf{-800}^{+1100}_{-1300}$	/
	2023-03-09	80801327002	$0.484^{+0.0}_{-0.003}$	12.7	/	/	/	$\mathbf{11 \pm 2}$	$\mathbf{-5700}^{+1400}_{-1400}$	/
	2023-03-10	80902312002	$0.478^{+0.001}_{-0.001}$	12.2	$\mathbf{13}^{+5}_{-3}$	$\mathbf{4600}^{+300}_{-1500}$	/	$\mathbf{8 \pm 3}$	$\mathbf{-6700}^{+2700}_{-2900}$	/
	2023-03-11	80902312004	$0.685^{+0.001}_{-0.003}$	$18.4_{-0.1}$	/	/	/	$\mathbf{9}^{+1}_{-4}$	$\mathbf{-5000}^{+1700}_{-1500}$	/
	2023-03-13	80902312006	$0.641^{+0.001}_{-0.001}$	18.1	/	/	/	$\mathbf{12}^{+4}_{-1}$	$\mathbf{-4400}^{+1700}_{-1200}$	/

Table 7.4: continued

Source	Date	ObsID	$HR_{[6-10]/[3-10]}$	$L_{[3-10]}/L_{Edd}$ $\times 10^{-2}$	Fe xxv Kα			Fe xxvi Kα		
					EW	blueshift	width	EW	blueshift	width
			Bands in keV		eV	km/s	km/s	eV	km/s	km/s
	2023-04-07	5665010407	$0.391^{+0.002}_{-0.002}$	10.2	/	/	/	$\mathbf{10 \pm 3}$	$\mathbf{-1100^{+1300}_{-1400}}$	/
	2023-04-08	5665010408	$0.379^{+0.002}_{-0.002}$	8.7	/	/	/	$\mathbf{15 \pm 6}$	$\mathbf{-1300^{+1200}_{-1400}}$	/
	2023-04-22	6130010111	$0.335^{+0.001}_{-0.001}$	6.6	/	/	/	$\mathbf{23^{+3}_{-5}}$	$\mathbf{-400^{+800}_{-600}}$	/
	2023-05-01	6130010113	$0.323^{+0.002}_{-0.002}$	6.0	/	/	/	$\mathbf{20^{+5}_{-4}}$	$\mathbf{-100^{+900}_{-1200}}$	/
	2023-05-11	6130010115	$0.359^{+0.004}_{-0.004}$	7.1	/	/	/	$\mathbf{16^{+9}_{-7}}$	$\mathbf{-700^{+2200}_{-2700}}$	/
	2023-05-19	5665010411	$0.311^{+0.002}_{-0.002}$	5.5	/	/	/	$\mathbf{25 \pm 5}$	$\mathbf{-1100^{+900}_{-1000}}$	/
	2023-05-28	6130010118	$0.31^{+0.003}_{-0.003}$	5.4	/	/	/	$\mathbf{32^{+10}_{-8}}$	$\mathbf{-1000^{+1300}_{-1200}}$	/
	2023-06-08	6130010119	$0.296^{+0.002}_{-0.002}$	4.7	$\mathbf{22^{+5}_{-4}}$	$\mathbf{-900^{+1000}_{-1100}}$	/	$\mathbf{36 \pm 6}$	$\mathbf{-500^{+700}_{-500}}$	/
	2023-06-16	6130010120	$0.323^{+0.004}_{-0.004}$	4.9	$\mathbf{24^{+13}_{-9}}$	$\mathbf{500^{+4000}_{-6500}}$	/	$\mathbf{30^{+18}_{-11}}$	$\mathbf{-2700^{+6600}_{-5300}}$	/
	2023-06-16	6130010120	$0.301^{+0.004}_{-0.004}$	4.8	$\mathbf{29^{+13}_{-8}}$	$\mathbf{200^{+3000}_{-2900}}$	/	$\mathbf{38^{+15}_{-11}}$	$\mathbf{200^{+2400}_{-2400}}$	/
	2023-06-18	6130010121	$0.302^{+0.002}_{-0.002}$	4.6	$\mathbf{40^{+5}_{-4}}$	$\mathbf{-300^{+900}_{-1100}}$	/	$\mathbf{50^{+7}_{-5}}$	$\mathbf{-600^{+800}_{-1000}}$	/
	2023-06-25	6130010122	$0.314^{+0.005}_{-0.005}$	5.2	/	/	/	$\mathbf{28^{+14}_{-11}}$	$\mathbf{0^{+4900}_{-3400}}$	/
	2023-07-02	6130010123	$0.304^{+0.003}_{-0.003}$	5.4	$\mathbf{21^{+5}_{-7}}$	$\mathbf{-500^{+3600}_{-2300}}$	/	$\mathbf{39^{+9}_{-5}}$	$\mathbf{-2200^{+1500}_{-1500}}$	/

Bibliography

Abbott R., et al., 2020, ApJL, 900, L13

Abbott R., et al., 2023, Physical Review X, 13, 011048

Abe Y., Fukazawa Y., Kubota A., Kasama D., Makishima K., 2005, PASJ, 57, 629

Abolmasov P., Fabrika S., Sholukhova O., Afanasiev V., 2007, Astrophysical Bulletin, 62, 36

Abramowicz M. A., Czerny B., Lasota J. P., Szuszkiewicz E., 1988, ApJ, 332, 646

Aird J., Coil A. L., Georgakakis A., Nandra K., Barro G., Pérez-González P. G., 2015, MNRAS, 451, 1892

Alabarta K., et al., 2021, MNRAS, 507, 5507

Allen J. L., Schulz N. S., Homan J., Neilsen J., Nowak M. A., Chakrabarty D., 2018, ApJ, 861, 26

Altamirano D., Strohmayer T., 2012, ApJL, 754, L23

Altamirano D., et al., 2011, ApJ Letters, 742, L17

Anderson W., 1929, Zeitschrift für Physik, 56, 851

Andrews S. M., et al., 2018, ApJL, 869, L41

Angelini L., White N. E., 2003, ApJL, 586, L71

Armitage P. J., 2022, Lecture notes on accretion disk physics

Arnason R. M., Papei H., Barmby P., Bahramian A., D. Gorski M., 2021, MNRAS, 502, 5455

Arnaud K. A., Arnaud A. K., 1996, ASPC, 101, 17

Astarita S., Kruk S., Reerink J., Gómez P., 2024, arXiv

Athulya M. P., Nandi A., 2023, MNRAS, 525, 489

Atri P., et al., 2020, MNRAS: Letters, 493, L81

Augusteijn T., Kuulkers E., Van Kerkwijk M. H., 2001, A&A, 375, 447

Avakyan A., Neumann M., Zainab A., Doroshenko V., Wilms J., Santangelo A., 2023, A&A, 675, A199

Baade W., Zwicky F., 1934, Proceedings of the National Academy of Sciences, 20, 254

Bachetti M., et al., 2014, Nature, 514, 202

Badnell N. R., Bautista M. A., Butler K., Delahaye F., Mendoza C., Palmeri P., Zeippen C. J., Seaton M. J., 2005, MNRAS, 360, 458

Bahramian A., Degenaar N., 2023, in , Handbook of X-ray and Gamma-ray Astrophysics. Springer Nature Singapore, pp 1–62 (arXiv:2206.10053), doi:10.1007/978-981-16-4544-0_94-1

Bahramian A., et al., 2023, ApJL, 948, L7

Bailey J., 1980, MNRAS, 190, 119

Bailyn C. D., Orosz J. A., Mc Clintock J. E., Remillard R. A., 1995, Nat, 378, 157

Balakrishnan M., et al., 2020, ApJ, 893, 155

Balakrishnan M., Miller J. M., Reynolds M. T., Kammoun E., Zoghbi A., Tetarenko B. E., 2021, ApJ, 909, 41

Balakrishnan M., et al., 2023, ApJ, 947, 38

Balbus S. A., Hawley J. F., 1998, Reviews of Modern Physics, 70, 1

Balbus S. A., Hawley J. F., Balbus S. A., Hawley J. F., 1991, ApJ, 376, 214

Balucinska-Church M., McCammon D., 1992, ApJ, 400, 699

Bambi C., et al., 2021, Space Science Reviews, 217, 1

Baptista R., 2007, in , Astrotomography. Springer Berlin Heidelberg, pp 307–331 (arXiv:0009472), doi:10.1007/3-540-45339-3_23, https://arxiv.org/abs/astro-ph/0009472v1

Barret D., et al., 2023, Experimental Astronomy, 55, 373

Beckwith K., Hawley J. F., Krolik J. H., 2008, ApJ, 678, 1180

Beer M. E., Podsiadlowski P., 2002, MNRAS, 331, 351

Begelman M. C., Armitage P. J., 2014, ApJl, 782, L18

Begelman M. C., McKee C. F., Shields G. A., 1983, ApJ, 271, 70

Behar E., 2009, ApJ, 703, 1346

Bel M. C., et al., 2009, A&A, 501, 1

Belczynski K., Kalogera V., Bulik T., 2002, ApJ, 572, 407

Belczynski K., Done C., Hagen S., Lasota J. P., Sen K., 2023

Bell K. R., Lin D. N. C., 1994, ApJ, 427, 987

Belloni T. M., Motta S. E., 2016, in Bambi C., ed., , Astrophysics of Black Holes: From Fundamental Aspects to Latest Developments. Springer, Berlin, Heidelberg, pp 61–97, doi:10.1007/978-3-662-52859-4_2

Belloni D., Schreiber M. R., 2023, in , Handbook of X-ray and Gamma-ray Astrophysics. pp 1–90 (arXiv:2303.08997), doi:10.1007/978-981-16-4544-0_98-1

Belloni T., Méndez M., King A. R., van der Klis M., van Paradijs J., 1997, ApJ, 479, L145

Belloni T., Klein-Wolt M., Méndez M., Van Der Klis M., Van Paradijs J., 2000, A&A, 355, 271

Belloni T., Psaltis D., van der Klis M., 2002, ApJ, 572, 392

Belmont R., 2009, A&A, 506, 589

Belmont R., Malzac J., Marcowith A., 2008, A&A, 491, 617

Bianchi S., Matt G., 2002, A&A, 387, 76

Bianchi S., Matt G., Nicastro F., Porquet D., Dubau J., 2005, MNRAS, 357, 599

Bianchi S., Ponti G., Muñoz-Darias T., Petrucci P. O., 2017, MNRAS, 472, 2454

Bildsten L., et al., 1997, ApJ Supplement Series, 113, 367

Blandford R. D., Payne D. G., 1982, MNRAS, 199, 883

Blandford R. D., Znajek R. L., 1977, MNRAS, 179, 433

Blandford R., Meier D., Readhead A., 2019, Relativistic Jets from Active Galactic Nuclei (arXiv:1812.06025), doi:10.1146/annurev-astro-081817-051948, www.annualreviews.org

Blum J. L., Miller J. M., Cackett E., Yamaoka K., Takahashi H., Raymond J., Reynolds C. S., Fabian A. C., 2010, ApJ, 713, 1244

Bogdán Á., et al., 2023, Nature Astronomy 2023 8:1, 8, 126

Bogensberger D., et al., 2020, A&A, 641, A101

Bozzo E., et al., 2016, A&A, 589, A42

Bozzo E., Huenemoerder D. P., Produit N., Falanga M., Paltani S., Costantini E., 2023, MNRAS: Letters, 522, L66

Buchner J., et al., 2015, ApJ, 802, 89

Buisson D. J., et al., 2019, MNRAS, 490, 1350

Calcaferro L. M., Althaus L. G., Córsico A. H., 2018, A&A, 614, A49

Callanan P. J., et al., 1995, ApJ, 441, 786

Callister T. A., Miller S. J., Chatziioannou K., Farr W. M., 2022, ApJL, 937, L13

Campana S., Salvo T. D., 2018, pp 149–184 (arXiv:1804.03422), doi:10.1007/978-3-319-97616-7_4, http://arxiv.org/abs/1804.03422http://dx.doi.org/10.1007/978-3-319-97616-7_4

Cantrell A. G., et al., 2010, ApJ, 710, 1127

Cao X., 2016, ApJ, 817, 71

Capitanio F., Belloni T., Del Santo M., Ubertini P., 2009, MNRAS, 398, 1194

Capitanio F., Del Santo M., Bozzo E., Ferrigno C., De Cesare G., Paizis A., 2012, MNRAS, 422, 3130

Capitanio F., Campana R., De Cesare G., Ferrigno C., 2015, MNRAS, 450, 3840

Carotenuto F., Tetarenko A. J., Corbel S., 2022, MNRAS, 511, 4826

Casares J., 2016, ApJ, 822, 99

Casares J., Jonker P. G., 2014, Mass Measurements of Stellar and Intermediate-Mass Black Holes (arXiv:1311.5118), doi:10.1007/s11214-013-0030-6, https://ui.adsabs.harvard.edu/abs/2014SSRv..183..223C/abstract

Casares J., et al., 2009, ApJ, Supplement Series, 181, 238

Casares J., Muñoz-Darias T., Mata Sánchez D., Charles P. A., Torres M. A., Armas Padilla M., Fender R. P., García-Rojas J., 2019, MNRAS, 488, 1356

Casares J., et al., 2022, MNRAS, 516, 2023

Casares J., et al., 2023, MNRAS, 526, 5209

Cash W., 1979, ApJ, 228, 939

Casse F., Ferreira J., 2000, A&A, 361, 1178

Castor J. I., Abbott D. C., Klein R. I., 1975, ApJ, 195, 157

Castro Segura N., et al., 2022, Nat, 603, 52

Castro-Tirado A. J., Brandt S., Lund N., 1992, IAUC, 5590, 2

Chakraborty P., Chatzikos M., Guzmán F., Su Y., Ferland G. J., 2020, ApJ, 901, 69

Chakraborty S., Ratheesh A., Bhattacharyya S., Tomsick J. A., Tombesi F., Fukumura K., Jaisawal G. K., 2021a, MNRAS, 508, 475

Chakraborty P., Ferland G. J., Chatzikos M., Guzmán F., Su Y., 2021b, ApJ, 912, 26

Chakravorty S., Kembhavi A. K., Elvis M., Ferland G., Badnell N. R., 2008, MNRAS: Letters, 384, L24

Chakravorty S., Lee J. C., Neilsen J., 2013, MNRAS, 436, 560

Chakravorty S., et al., 2016, Astron. Nachr., 337, 429

Chakravorty S., et al., 2023, MNRAS, 518, 1335

Chandrasekhar S., 1931, ApJ, 74, 81

Charles P., Matthews J. H., Buckley D. A., Gandhi P., Kotze E., Paice J., 2019, MNRAS: Letters, 489, L47

Chartas G., et al., 2021, ApJ, 920, 24

Chaty S., Bessolaz N., 2006, A&A, 455, 639

Chaty S., Mignani R. P., Israel G. L., 2006, MNRAS, 365, 1387

Chaty S., Fortin F., López-Oramas A., 2020, A&A, 637, A2

Chatzikos M., et al., 2023, Revista Mexicana de Astronomia y Astrofisica, 59, 327

Chauhan J., et al., 2019, MNRAS: Letters, 488, L129

Chen Z.-F., Pan D.-S., 2017, ApJ, 848, 79

Chen W., Shrader C. R., Livio M., 1997, ApJ, 491, 312

Chenevez J., Vandbaek Kroer L., Budtz-Jorgensen C., Brandt S., Lund N., Westergaard N. J., Kuulkers E., Wilms J., 2014, ATel, 6451, 1

Cherepashchuk A. M., Katysheva N. A., Khruzina T. S., Shugarov S. Y., Tatarnikov A. M., Bogomazov A. I., 2019, MNRAS, 490, 3287

Chiang C. Y., Reis R. C., Walton D. J., Fabian A. C., 2012, MNRAS, 425, 2436

Chomiuk L., Metzger B. D., Shen K. J., 2021, Annual Review of A&A, 59, 391

Church M. J., 2001, Advances in Space Research, 28, 323

Coleman M. S., Kotko I., Blaes O., Lasota J. P., Hirose S., 2016, MNRAS, 462, 3710

Connors R. M. T., et al., 2020, ApJ, 892, 47

Connors R. M. T., et al., 2021, ApJ, 909, 146

Contopoulos J., Lovelace R. V. E., 1994, ApJ, 429, 139

Corbel S., et al., 2001, ApJ, 554, 43

Corbel S., Kaaret P., Fender R. P., Tzioumis A. K., Tomsick J. A., Orosz J. A., 2005, ApJ, 632, 504

Cordova F. A., Mason K. O., 1982, ApJ, 260, 716

Coriat M., Corbel S., Buxton M. M., Bailyn C. D., Tomsick J. A., Körding E., Kalemci E., 2009, MNRAS, 400, 123

Coriat M., Fender R. P., Dubus G., 2012, MNRAS, 424, 1991

Corral-Santana J. M., Casares J., Shahbaz T., Zurita C., Martínez-Pais I. G., Rodríguez-Gil P., 2011, MNRAS: Letters, 413, L15

Corral-Santana J. M., Casares J., Muñoz-Darias T., Rodríguez-Gil P., Shahbaz T., Torres M. A., Zurita C., Tyndall A. A., 2013, Science, 339, 1048

Corral-Santana J. M., Casares J., Muñoz-Darias T., Bauer F. E., Martínez-Pais I. G., Russell D. M., 2016, A&A, 587, A61

Corral-Santana J. M., et al., 2018, MNRAS, 475, 1036

Coughenour B. M., et al., 2023, ApJ, 949, 70

Cúneo V. A., et al., 2020, MNRAS, 498, 25

Curran P. A., 2014,] 10.48550/arxiv.1411.3816

Dall'Osso S., Perna R., Stella L., 2015, MNRAS, 449, 2144

Dannen R. C., Proga D., Waters T., Dyda S., 2020, ApJL, 893, L34

Dannen R., Proga D., Waters T., Dyda S., 2024, ApJ, 961, 221

Datta S. R., et al., 2024, A&A, 687, A2

Dauser T., García J., Parker M. L., Fabian A. C., Wilms J., 2014, MNRAS: Letters, 444, L100

Dauser T., Garcia J., Walton D. J., Eikmann W., Kallman T., McClintock J., Wilms J., 2016, A&A, 590, A76

Davis S. W., Tchekhovskoy A., 2020, Magnetohydrodynamics Simulations of Active Galactic Nucleus Disks and Jets, doi:10.1146/annurev-astro-081817-051905, https://www.annualreviews.org/content/journals/10.1146/annurev-astro-081817-051905

De Loore C. W. H., Doom C., 1992. Astrophysics and Space Science Library Vol. 179, Springer Netherlands, Dordrecht, doi:10.1007/978-94-011-2502-4, http://link.springer.com/10.1007/978-94-011-2502-4

Del Santo M., Malzac J., Jourdain E., Belloni T., Ubertini P., 2008, MNRAS, 390, 227

Del Santo M., Malzac J., Belmont R., Bouchet L., De Cesare G., 2013, MNRAS, 430, 209

Del Santo M., et al., 2023, Monthly Notices of the Royal Astronomical Society: Letters, 523, L15

Delgado Mena E., Adibekyan V., Santos N. C., Tsantaki M., González Hernández J. I., Sousa S. G., Bertrán De Lis S., 2021, A&A, 655, 99

Della Valle M., Benetti S., Cappellaro E., Wheeler C., 1997, A&A, 318, 179

Della Valle M., Masetti N., Bianchini A., 1998, A&A, 329, 606

Dermer C. D., Giebels B., 2016, Comptes Rendus Physique, 17, 594

Díaz Trigo M., Boirin L., 2016, Astron. Nachr., 337, 368

Díaz Trigo M., Parmar A. N., Boirin L., Méndez M., Kaastra J. S., 2006, A&A, 445, 179

Díaz Trigo M., Parmar A. N., Miller J., Kuulkers E., Caballero-García M. D., 2007, A&A, 462, 657

Díaz Trigo M., Miller-Jones J. C., Migliari S., Broderick J. W., Tzioumis T., 2013, Nat, 504, 260

Diáz Trigo M., Migliari S., Miller-Jones J. C., Guainazzi M., 2014, A&A, 571

Done C., Gierliński M., Kubota A., 2007, A&A Review, 15, 1

Done C., Tomaru R., Takahashi T., 2018, MNRAS, 473, 838

Draghis P. A., Miller J. M., Zoghbi A., Reynolds M., Costantini E., Gallo L. C., Tomsick J. A., 2023, ApJ, 946, 19

Draghis P. A., Miller J. M., Costantini E., Gallo L. C., Reynolds M., Tomsick J. A., Zoghbi A., 2024, ApJ, 969, 40

Dubus G., Lasota J. P., Hameury J. M., Charles P., 1999, MNRAS, 303, 139

Dubus G., Kim R. S. J., Menou K., Szkody P., Bowen D. V., 2001, ApJ, 553, 307

Dubus G., Done C., Tetarenko B. E., Hameury J. M., 2019, A&A, 632, 40

Duchêne G., Kraus A., 2013, Stellar multiplicity (arXiv:1303.3028), doi:10.1146/annurev-astro-081710-102602, https://ui.adsabs.harvard.edu/abs/2013ARA&A..51..269D/abstract

EHT Collaboration et al., 2019, ApJL, 875, L1

EHT Collaboration et al., 2022, ApJL, 930, L12

Ebbets D., Ebbets D. 1979, PASP, 91, 804

Edgar R., 2004, A review of Bondi-Hoyle-Lyttleton accretion (arXiv:0406166), doi:10.1016/j.newar.2004.06.001, http://arxiv.org/abs/astro-ph/0406166http://dx.doi.org/10.1016/j.newar.2004.06.001

Eggleton P. P., 1983, ApJ, 268, 368

Ekşi K. Y., Andaç I. C., Çikintoğlu S., Gençali A. A., Güngör C., Öztekin F., 2015, MNRAS: Letters, 448, L40

El Mellah I., Sander A. A., Sundqvist J. O., Keppens R., 2019, A&A, 622, A189

Esin A. A., McClintock J. E., Narayan R., 1997, ApJ, 489, 865

Fabian A. C., Ross R. R., 2010, Space Science Reviews, 157, 167

Fabian A. C., et al., 2021, MNRAS, 493, 5389

Farrell S. A., Webb N. A., Barret D., Godet O., Rodrigues J. M., 2009, Nature, 460, 73

Fender R. P., Garrington S. T., McKay D. J., Muxlow T. W., Pooley G. G., Spencer R. E., Stirling A. M., Waltman E. B., 1999a, MNRAS, 304, 865

Fender R., et al., 1999b, ApJl, 519, L165

Fender R. P., Belloni T. M., Gallo E., 2004, MNRAS, 355, 1105

Fender R. P., Homan J., Belloni T. M., 2009, MNRAS, 396, 1370

Ferland G. J., Ferland J. G., 2000, RMxAC, 9, 153

Ferland G. J., et al., 2017, Revista Mexicana de Astronomía y Astrofísica Vol. 53, pp. 385-438 (2017), 53, 385

Ferrarese L., Merritt D., 2000, ApJ, 539, L9

Ferreira J., 1997, A&A, 319, 340

Ferreira J., Pelletier G., 1993, A&A, 276, 625

Ferreira J., Pelletier G., 1995, A&A, 295, 807

Ferreira J., Petrucci P. O., Henri G., Saugé L., Pelletier G., 2006, A&A, 447, 813

Ferreira J., et al., 2022, A&A, 660, 66

Ferrigno C., Bozzo E., Santo M. D., Capitanio F., 2012, A&A, 537, L7

Field G. B., 1965, ApJ, 142, 531

Fijma S., Castro Segura N. C., Degenaar N., Knigge C., Higginbottom N., Hernández Santisteban J. V., Maccarone T. J., 2023, MNRAS: Letters, 526, L149

Filippenko A. V., Leonard D. C., Matheson T., Li W., Moran E. C., Riess A. G., 1999, PASP, 111, 969

Fishbach M., Kalogera V., 2022, ApJL, 929, L26

Fornasini F. M., et al., 2017, ApJ Supplement Series, 229, 33

Fornasini F. M., Antoniou V., Dubus G., Fornasini F. M., Antoniou V., Dubus G., 2023, Technical report, High-mass X-ray Binaries. (arXiv:2308.02645v1)

Fortin F., García F., Simaz Bunzel A., Chaty S., 2024, A&A, 671

Fowler R. H., 1926, MNRAS, 87, 114

Fragile P. C., Liska M., 2024, arXiv, p. arXiv:2404.10052

Frank J., King A. R., Raine D. J., 2002. Cambridge University Press, https://ui.adsabs.harvard.edu/abs/2002apa..book.....F/abstract

Frank A., et al., 2014, Protostars and Planets VI, pp 451–474

Fukumura K., Kazanas D., Contopoulos I., Behar E., 2010, ApJ, 715, 636

Fukumura K., Tombesi F., Kazanas D., Shrader C., Behar E., Contopoulos I., 2014, ApJ, 780, 120

Fukumura K., Tombesi F., Kazanas D., Shrader C., Behar E., Contopoulos I., 2015, ApJ, 805, 17

Fukumura K., Kazanas D., Shrader C., Behar E., Tombesi F., Contopoulos I., 2017, Nat Astronomy, 1, 0062

Fukumura K., Kazanas D., Shrader C., Behar E., Tombesi F., Contopoulos I., 2018a, ApJ, 853, 40

Fukumura K., Kazanas D., Shrader C., Behar E., Tombesi F., Contopoulos I., 2018b, ApJL, 864, L27

Fukumura K., Kazanas D., Shrader C., Tombesi F., Kalapotharakos C., Behar E., 2021, ApJ, 912, 86

Fukumura K., Dadina M., Matzeu G., Tombesi F., Shrader C., Kazanas D., 2022, ApJ, 940, 6

Fuller J., Ma L., 2019, ApJL, 881, L1

Galiullin I., Gilfanov M., 2021, A&A, 646, A85

Gallegos-Garcia M., Jacquemin-Ide J., Kalogera V., 2023

Gallo E., Fender R. P., Pooley G. G., 2003, MNRAS, 344, 60

Gallo E., Degenaar N., Van Den Eijnden J., 2018, MNRAS: Letters, 478, L132

Gandhi P., et al., 2010, MNRAS, 407, 2166

Gandhi P., et al., 2022, Nat Astronomy, 6, 1364

García J., et al., 2014, ApJ, 782, 76

García J. A., et al., 2018, ApJ, 864, 25

Gardenier D. W., Uttley P., 2018, MNRAS, 481, 3761

Gatuzz E., Churazov E., 2018, MNRAS, 474, 696

Gatuzz E., Díaz Trigo M., Miller-Jones J. C. A., Migliari S., Castillo D., 2019, MNRAS, 482, 2597

Gatuzz E., Díaz Trigo M., Miller-Jones J. C., Migliari S., 2020, MNRAS, 491, 4857

Gebhardt K., et al., 2000, ApJ, 539, L13

Gelino D. M., Harrison T. E., 2003, ApJ, 599, 1254

Gelino M. D., 2002, AAS, 200, 08.11

Gelino D. M., Balman S., Kiziloglu U., Yılmaz A., Kalemci E., Tomsick J. A., 2006, ApJ, 642, 438

Gendreau K. C., et al., 2016, in Space Telescopes and Instrumentation 2016: Ultraviolet to Gamma Ray. SPIE, p. 99051H, doi:10.1117/12.2231304, https://ui.adsabs.harvard.edu/abs/2016SPIE.9905E..1HG/abstract

Gerónimo F. C. D., Bertolami M. M. M., Plaza F., Catelan M., 2022, A&A, 659, A150

Gianolli V. E., et al., 2024, A&A, 687, A235

Gierliński M., Zdziarski A. A., Gierliński M., Zdziarski A. A., 1999, ASPC, 161, 64

Gilfanov M., Merloni A., 2014, Space Science Reviews, 183, 121

Gladstone J. C., Roberts T. P., Done C., 2009, MNRAS, 397, 1836

Godet O., Barret D., Webb N. A., Farrell S. A., Gehrels N., 2009, ApJ, 705, 109

Godet O., et al., 2012, ApJ, 752, 34

Gofford J., Reeves J. N., Tombesi F., Braito V., Turner T. J., Miller L., Cappi M., 2013, MNRAS, 430, 60

Gomez S., Mason P. A., Robinson E. L., 2015, ApJ, 809, 9

Gonçalves A. C., Collin S., Dumont A. M., Chevallier L., 2007, A&A, 465, 9

González Hernández J. I., Rebolo R., Israelian G., 2008, A&A, 478, 203

González Hernández J. I., Rebolo R., Casares J., 2014, MNRAS: Letters, 438, L21

González Hernández J. I., Suárez-Andrés L., Rebolo R., Casares J., 2017, MNRAS: Letters, 465, L15

Goodwin A. J., et al., 2020, MNRAS, 498, 3429

Goulding A. D., et al., 2023, ApJL, 955, L24

Gray A., 2024,] 10.1002/leap.1578

Grebenev S. A., Molkov S. V., Revnivtsev M. G., Sunyaev R. A., 2006, in European Space Agency, (Special Publication) ESA SP. No. 622 SP. pp 373–376

Greiner J., Dennerl K., Predehl P., 1996, A&A, 314, L21

Greiner J., Cuby J. G., McCaughrean M. J., Castro-Tirado A. J., Mennickent R. E., 2001, Identification of the donor in the X-ray binary GRS 1915+105 (arXiv:0105467), doi:10.1051/0004-6361:20010771, https://ui.adsabs.harvard.edu/abs/2001A&A...373L..37G/abstract

Guillot S., Servillat M., Webb N. A., Rutledge R. E., 2013, ApJ, 772, 7

Guo X., Dong L., Hao D., 2024, Frontiers in Cell and Developmental Biology, 11, 1339390

Gúrpide A., Godet O., Koliopanos F., Webb N., Olive J.-F., 2021, A&A, 649, A104

Gúrpide A., Parra M., Godet O., Contini T., Olive J. F., 2022, A&A, 666, 100

Hagen S., et al., 2024, MNRAS, 000, 1

Hameury J. M., 2020, Advances in Space Research, 66, 1004

Hameury J. M., Menou K., Dubus G., Lasota J. P., Huré J. M., 1998, MNRAS, 298, 1048

Hameury J. M., Knigge C., Lasota J. P., Hambsch F. J., James R., 2020, A&A, 636, A1

Han Z., BOONRUCKSAR S., QIAN S., XIAOHUI F., WANG Q., ZHU L., DONG A., ZHI Q., 2020, PASJ, 72, 76

Hankla A. M., Zhdankin V., Werner G. R., Uzdensky D. A., Begelman M. C., 2022a, MNRAS, 509, 3826

Hankla A. M., Scepi N., Dexter J., 2022b, MNRAS, 515, 775

Hannikainen D. C., et al., 2005, A&A, 435, 995

Harlaftis E. T., Steeghs D., Horne K., Filippenko A. V., 1997, 114

Harrison F. A., et al., 2013, ApJ, 770, 103

Haswell C. A., et al., 1993, ApJ, 411, 802

Haswell C. A., Hynes R. I., King A. R., Schenker K., 2002, MNRAS, 332, 928

Hawley J. F., Gammie C. F., Balbus S. A., 1995, ApJ, 440, 742

Heida M., Jonker P. G., Torres M. A. P., Chiavassa A., 2017, ApJ, 846, 132

Heil L. M., Vaughan S., Uttley P., 2012, MNRAS, 422, 2620

Heil L. M., Uttley P., Klein-Wolt M., 2015a, MNRAS, 448, 3339

Heil L. M., Uttley P., Klein-Wolt M., 2015b, MNRAS, 448, 3348

Hernández J. I. G., Rebolo R., Casares J., 2013, MNRAS, 438, L21

Higginbottom N., Proga D., Knigge C., Long K. S., 2017, ApJ, 836, 42

Higginbottom N., Knigge C., Long K. S., Matthews J. H., Sim S. A., Hewitt H. A., 2018, MNRAS, 479, 3651

Higginbottom N., Knigge C., Long K. S., Matthews J. H., Parkinson E. J., 2019, MNRAS, 484, 4635

Higginbottom N., Knigge C., Sim S. A., Long K. S., Matthews J. H., Hewitt H. A., Parkinson E. J., Mangham S. W., 2020, MNRAS, 492, 5271

Higginbottom N., Scepi N., Knigge C., Long K. S., Matthews J. H., Sim S. A., 2024, MNRAS, 527, 9236

Hjellming R. M., Rupen M. P., 1995, Nat, 375, 464

Holczer T., Behar E., Kaspi S., 2007, ApJ, 663, 799

Homan J., Miller J. M., Wijnands R., van der Klis M., Belloni T., Steeghs D., Lewin W. H. G., 2005, ApJ, 623, 383

Homan J., Wijnands R., Kong A., Miller J. M., Rossi S., Belloni T., Lewin W. H., 2006, MNRAS, 366, 235

Homan J., Neilsen J., Allen J. L., Chakrabarty D., Fender R., Fridriksson J. K., Remillard R. A., Schulz N., 2016, ApJ, 830, L5

Homan J., et al., 2018, ATel, 11576, 1

Homan J., Neilsen J., Gendreau K., Arzoumanian Z., Remillard R., Steiner J., Altamirano D., Wolff M., 2019, ATel, 13308, 1

Hopkins P. F., et al., 2024, Open Journal of Astrophysics, 7

Hori T., et al., 2014, ApJ, 790, 20

Hori T., Ueda Y., Done C., Shidatsu M., Kubota A., 2018, ApJ, 869, 183

Hu H., Inayoshi K., Haiman Z., Quataert E., Kuiper R., 2022, ApJ, 934, 132

Huenemoerder D. P., et al., 2011, AJ, 141, 129

Hynes R. I., 2002, The Physics of Cataclysmic Variables and Related Objects, 261, 676

Hynes R. I., Haswell C. A., Chaty S., Shrader C. R., Cui W., 2002, MNRAS, 331, 169

Hynes R. I., et al., 2003, MNRAS, 345, 292

Ingram A. R., Motta S. E., 2019, New Astronomy Reviews, 85

Inight K., Gänsicke B. T., Breedt E., Marsh T. R., Pala A. F., Raddi R., 2021, MNRAS, 504, 2420

Ioannou Z., Robinson E. L., Welsh W. F., Haswell C. A., 2004, The Astronomical Journal, 127, 481

Ishibashi K., Dewey D., Huenemoerder D. P., Testa P., 2006, ApJ, 644, L117

Ivanova N., et al., 2013, Common envelope evolution: Where we stand and how we can move forward (arXiv:1209.4302), doi:10.1007/s00159-013-0059-2, https://link.springer.com/article/10.1007/s00159-013-0059-2

Jacquemin-Ide J., Ferreira J., Lesur G., 2019, MNRAS, 490, 3112

Jacquemin-Ide J., Lesur G., Ferreira J., 2021, A&A, 647, 192

Jaisawal G. K., Homan J., Naik S., Jonker P., 2015, ATel, 7361, 1

Jana A., Naik S., Jaisawal G. K., Chhotaray B., Kumari N., Gupta S., 2022, MNRAS, 511, 3922

Jeon M., Pawlik A. H., Bromm V., Milosavljević M., 2014, MNRAS, 440, 3778

Jia N., et al., 2022, MNRAS, 511, 3125

Jiménez-Ibarra F., Muñoz-Darias T., Casares J., Padilla M. A., Corral-Santana J. M., 2019, MNRAS, 489, 3420

Jimenez-Garate M. A., Raymond J. C., Liedahl D. A., 2002, ApJ, 581, 1297

Jin C., Ponti G., Haberl F., Smith R., 2017, MNRAS, 468, 2532

Jin C., Ponti G., Li G., Bogensberger D., 2019, ApJ, 875, 157

Jones C., Forman W., Tananbaum H., Turner M. J. L., Jones C., Forman W., Tananbaum H., Turner M. J. L., 1976, ApJL, 210, L9

Jonker P. G., Nelemans G., 2004, MNRAS, 354, 355

Kaaret P., Feng H., Roberts T. P., 2017, Annual Review of A&A, 55, 303

Kaastra J. S., Bleeker J. A., 2016, A&A, 587, A151

Kaastra J. S., Mewe R., Nieuwenhuijzen H., Kaastra J. S., Mewe R., Nieuwenhuijzen H., 1996, uxsa, pp 411–414

Kalamkar M., Casella P., Uttley P., O'Brien K., Russell D., Maccarone T., van der Klis M., Vincentelli F., 2016, MNRAS, 460, 3284

Kalemci E., Maccarone T. J., Tomsick J. A., 2018, ApJ, 859, 88

Kallman T., Bautista M., 2001, ApJ Supplement Series, 133, 221

Kallman T. R., Bautista M. A., Goriely S., Mendoza C., Miller J. M., Palmeri P., Quinet P., Raymond J., 2009, ApJ, 701, 865

Kallman T., Bautista M., Deprince J., García J. A., Mendoza C., Ogorzalek A., Palmeri P., Quinet P., 2021, ApJ, 908, 94

Kalogera V., Webbink R. F., 1998, ApJ, 493, 351

Kaluzienski L. J., Holt S. S., 1977, IAUC, 3099, 3

Kennea J. A., Skinner G. K., Kennea J. A., Skinner G. K., 1996, PASJ, 48, L117

Keshet N., Behar E., Kallman T. R., 2024, ApJ, 966, 211

Khargharia J., Froning C. S., Robinson E. L., 2010, ApJ, 716, 1105

King A., 2024, MNRAS, 531, 550

King A. R., Davies M. B., Ward M. J., Fabbiano G., Elvis M., 2001, ApJ, 552, L109

King A. L., et al., 2012, ApJL, 746, L20

King A. L., et al., 2014, ApJL, 784, L2

King A. L., Miller J. M., Raymond J., Reynolds M. T., Morningstar W., 2015, ApJL, 813, L37

King A., Lasota J. P., Middleton M., 2023, Ultraluminous X-ray sources (arXiv:2302.10605), doi:10.1016/j.newar.2022.101672, http://creativecommons.org/licenses/by/4.0/

Kitaki T., Mineshige S., Ohsuga K., Kawashima T., 2021, PASJ, 73, 450

Kitamoto S., Tsunemi H., Pedersen H., Ilovaisky S. A., van der Klis M., 1990, ApJ, 361, 590

Klein-Wolt M., Fender R. P., Pooley G. G., Belloni T., Migliari S., Morgan E. H., Van Der Klis M., 2002, MNRAS, 331, 745

Knevitt G., Wynn G. A., Vaughan S., Watson M. G., 2014, MNRAS, 437, 3087

Kobak D., González-Márquez R., Oke-´ E., Horvát A., Lause J., 2024

Koljonen K., Vera R., Lahteenmaki A., Tornikoski M., Koljonen K., Vera R., Lahteenmaki A., Tornikoski M., 2019, ATel, 12839, 1

Koljonen K. I. I., Long K. S., Matthews J. H., Knigge C., 2023, MNRAS, 521, 4190

Kong L. D., et al., 2021, ApJ, 906, L2

Kong L.-D., Ji L., Santangelo A., Zhou M.-L., Shui Q.-C., Zhang S., 2024, A&A

Konigl A., Kartje J. F., Konigl A., Kartje J. F., 1994, ApJ, 434, 446

Kormendy J., Ho L. C., 2013, Coevolution (or not) of supermassive black holes and host galaxies (arXiv:1304.7762), doi:10.1146/annurev-astro-082708-101811, https://ui.adsabs.harvard.edu/abs/2013ARA&A..51..511K/abstract

Kormendy J., Richstone D., 1995, Annual Review of A&A, 33, 581

Kosec P., et al., 2021, MNRAS, 508, 3569

Kosec P., et al., 2023, Nature Astronomy

Kotani T., Ebisawa K., Dotani T., Inoue H., Nagase F., Tanaka Y., Ueda3 Y., 2000, ApJ, 539, 413

Kramida A. R. Y. R. J., NIST ASD Team 2023, NIST Atomic Spectra Database (version 5.11), doi:10.18434/T4W30F, https://physics.nist.gov/asd

Krawczynski H., et al., 2022, Science, 378, 650

Kretschmar P., et al., 2019, New Astronomy Reviews, 86, 101546

Krimm H. A., et al., 2013, ApJ Supplement Series, 209, 14

Krolik J. H., McKee C. F., Tarter C. B., 1981, ApJ, 249, 422

Kubota A., et al., 2007, PASJ, 59, S185

Kumar R., 2024, MNRAS

Kuulkers E., Parmar A. N., Kitamoto S., Cominsky L. R., Sood R. K., 1997, MNRAS, 291, 81

Kuulkers E., Wijnands R., Belloni T., Mendez M., van der Klis M., van Paradijs J., 1998, ApJ, 494, 753

Kuulkers E., et al., 2013, A&A, 552, A32

Kylafis N. D., Belloni T. M., 2015, A&A, 574, A133

Lada C. J., 1985, Annual Rev. Astron. Astrophys., Vol. 23, p. 267-317 (1985), 23, 267

Laha S., Guainazzi M., Chakravorty S., Dewangan G. C., Kembhavi A. K., 2016, MNRAS, 457, 3896

Laha S., Reynolds C. S., Reeves J., Kriss G., Guainazzi M., Smith R., Veilleux S., Proga D., 2020, Nature Astronomy 2020 5:1, 5, 13

Lamer G., Schwope A. D., Predehl P., Traulsen I., Wilms J., Freyberg M., 2021, A&A, 647

Lamers H. J., Levesque E., 2017a, Understanding Stellar Evolution

Lamers H. J., Levesque E. M., 2017b, Understanding Stellar Evolution, pp 26–1–26–7

Lasota J. P., 2001, The disc instability model of dwarf novae and low-mass X-ray binary transients (arXiv:0102072), doi:10.1016/S1387-6473(01)00112-9, http://arxiv.org/abs/astro-ph/0102072http://dx.doi.org/10.1016/S1387-6473(01)00112-9

Lasota J. P., King A., 2023, MNRAS, 526, 2506

Lasota J. P., Dubus G., Kruk K., 2008, A&A, 486, 523

Leahy D. A., Leahy J. C., 2015, Computational Astrophysics and Cosmology, 2, 1

Lebrun F., et al., 2003, A&A, 411, L141

Lee J. C., Reynolds C. S., Remillard R., Schulz N. S., Blackman E. G., Fabian A. C., 2002, ApJ, 567, 1102

Lesur G. R., 2021, A&A, 650, A35

Lesur G., Longaretti P. Y., 2009, A&A, 504, 309

Li L., Zimmerman E. R., Narayan R., McClintock J. E., 2005, ApJ Supplement Series, 157, 335

Lin D., et al., 2018, Nature Astronomy, 2, 656

Liska M., Hesp C., Tchekhovskoy A., Ingram A., van der Klis M., Markoff S., 2018, MNRAS, 474, L81

Liska M. T. P., Musoke G., Tchekhovskoy A., Porth O., Beloborodov A. M., 2022, ApJl, 935, L1

Liu H., et al., 2022, ApJ, 933, 122

Long K. S., Knigge C., 2002, ApJ, 579, 725

López K. M., Jonker P. G., Torres M. A., Heida M., Rau A., Steeghs D., 2019, MNRAS, 482, 2149

Lowell B., Jacquemin-Ide J., Tchekhovskoy A., Duncan A., 2023, ApJ, 960, 82

Lucchini M., et al., 2023, ApJ, 958, 153

Luketic S., Proga D., Kallman T. R., Raymond J. C., Miller J. M., 2010, ApJ, 719, 515

Luminari A., Tombesi F., Piconcelli E., Nicastro F., Fukumura K., Kazanas D., Fiore F., Zappacosta L., 2020, A&A, 633, A55

Luminari A., Nicastro F., Krongold Y., Piro L., Thakur A. L., 2023, A&A, 679

Macdonald R. K., et al., 2014, ApJ, 784, 2

Mall G., Liu H., Bambi C., Steiner J. F., García J. A., 2024, MNRAS, 527, 12053

Mao J., Kaastra J. S., Mehdipour M., Raassen A. J., Gu L., Miller J. M., 2017, A&A, 607, A100

Mapelli M., 2020, in Bambi C., Katsanevas S., Kokkotas K. D., eds, , Handbook of Gravitational Wave Astronomy. Springer, Singapore, pp 1–65, doi:10.1007/978-981-15-4702-7_16-1

Mapelli M., Annibali F., Zampieri L., Soria R., 2013, MNRAS, 433, 849

Marcel G., 2018, Université Grenoble Alpes, https://theses.hal.science/tel-02021327

Marcel G., et al., 2018a, A&A, 615, 57

Marcel G., et al., 2018b, A&A, 617, A46

Marcel G., et al., 2022, A&A, 659

Marino A., et al., 2021, A&A, 656, 63

Markwardt C. B., Swank J. H., 2003, ATel, 133, 1

Markwardt C., Arzoumanian Z., Gendreau K., Hare J., Rutkowski K., Loewenstein M., Team N., 2023, Bulletin of the AAS, 55

Martel É., Lesur G., 2022, A&A, 667, A17

Martin A. C., Casares J., Charles P. A., van der Hooft F., van Paradijs J., 1995, MNRAS, 274, L46

Martin R. G., Nixon C. J., Pringle J. E., Livio M., 2019, New Astronomy, 70, 7

Martocchia A., Matt G., Belloni T., Feroci M., Karas V., Ponti G., 2006, A&A, 448, 677

Massonneau W., Volonteri M., Dubois Y., Beckmann R. S., Beckmann R. S., 2023, A&A, 670, A180

Mata Sánchez D., et al., 2022, ApJL, 926, L10

Mata Sánchez D., Muñoz-Darias T., Armas Padilla M., Casares J., Torres M. A., 2024, A&A, 682, L1

Matthews J. H., Knigge C., Long K. S., Sim S. A., Higginbottom N., 2015, MNRAS, 450, 3331

Matthews J. H., Knigge C., Higginbottom N., Long K. S., Sim S. A., Mangham S. W., Parkinson E. J., Hewitt H. A., 2020, MNRAS, 492, 5540

Matthews J. H., et al., 2023, MNRAS, 526, 3967

Matzeu G. A., et al., 2022, MNRAS, 515, 6172

Mauche C. W., Liedahl D. A., Fournier K. B., 2003, ApJ, 588, L101

McClelland L. A., Eldridge J. J., 2016, MNRAS, 459, 1505

McKinney J. C., Blandford R. D., 2009, MNRAS, 394, L126

Mehdipour M., Kaastra J. S., Kallman T., 2016, A&A, 596, A65

Mendoza C., Kallman T. R., Ballhausen R., Ogorzałek A., Dannen R., García J. A., 2024, The European Physical Journal D, 78, 93

Mestici S., Tombesi F., Gaspari M., Piconcelli E., Panessa F., 2024, MNRAS, 532, 3036

Meyer F., Liu B. F., Meyer-Hofmeister E., 2000, A&A, 354, L67

Mezcua M., Mar 2017, IJMPD, 26, 1730021

Miceli C., et al., 2024, A&A, 684, A67

Middleton M., 2016, pp 99–151 (arXiv:1507.06153), doi:10.1007/978-3-662-52859-4_3

Miller-Jones J. C., Jonker P. G., Dhawan V., Brisken W., Rupen M. P., Nelemans G., Gallo E., 2009, ApJ, 706, L230

Miller-Jones J. C., Jonker P. G., Ratti E. M., Torres M. A., Brocksopp C., Yang J., Morrell N. I., 2011, MNRAS, 415, 306

Miller J. M., et al., 2004, ApJ, 601, 450

Miller J. M., Raymond J., Fabian A., Steeghs D., Homan J., Reynolds C., Van Der Klis M., Wijnands R., 2006a, Nat, 441, 953

Miller J. M., et al., 2006b, ApJ, 646, 394

Miller J. M., Raymond J., Reynolds C. S., Fabian A. C., Kallman T. R., Homan J., 2008, ApJ, 680, 1359

Miller J. M., et al., 2012, ApJL, 759, L6

Miller J. M., et al., 2014, ApJ, 788, 53

Miller J. M., Fabian A. C., Kaastra J., Kallman T., King A. L., Proga D., Raymond J., Reynolds C. S., 2015, ApJ, 814

Miller J. M., et al., 2016, ApJ, 821, L9

Miller J. M., et al., 2020, ApJ, 904, 30

Mineo S., Gilfanov M., Sunyaev R., 2012, MNRAS, 419, 2095

Mitrani S., Behar E., 2023, ApJ, 957, 105

Mitsuda K., et al., 2007, Pasj, 59, S1

Miyakawa T., Yamaoka K., Homan J., Saito K., Dotani T., Yoshida A., Inoue H., 2008, PASJ, 60, 637

Miyasaka H., Tomsick J. A., Xu Y., Harrison F. A., Miyasaka H., Tomsick J. A., Xu Y., Harrison F. A., 2018, ATel, 12340, 1

Morton D. C., 1991, ApJ Supplement Series, 77, 119

Morton D. C., Morton C. D., 1979, MNRAS, 189, 57

Motta S., Belloni T., 2024, A&A, 684, A209

Motta S., Muñoz-Darias T., Casella P., Belloni T., Homan J., 2011, MNRAS, 418, 2292

Motta S., Homan J., Muñoz-Darias T., Casella P., Belloni T. M., Hiemstra B., Méndez M., 2012, MNRAS, 427, 595

Motta S. E., Casella P., Henze M., Muñoz-Darias T., Sanna A., Fender R., Belloni T., 2015, MNRAS, 447, 2059

Motta S. E., et al., 2017, MNRAS, 471, 1797

Motta S. E., et al., 2021, New Astronomy Reviews, 93

Mukai K., 2017, Publications of the Astronomical Society of the Pacific, 129, 062001

Mummery A., Balbus S., 2023, MNRAS, 521, 2439

Mummery A., Ingram A., Davis S., Fabian A., 2024a, MNRAS, 531, 366

Mummery A., Jiang J., Fabian A., 2024b, MNRAS: Letters, 533, L83

Munari U., 2019, The Impact of Binary Stars on Stellar Evolution

Muñoz-Darias T., Ponti G., 2022, A&A, 664, A104

Muñoz-Darias T., Motta S., Belloni T. M., 2011, MNRAS, 410, 679

Muñoz-Darias T., Coriat M., Plant D. S., Ponti G., Fender R. P., Dunn R. J., 2013, MNRAS, 432, 1330

Muñoz-Darias T., Fender R. P., Motta S. E., Belloni T. M., 2014, MNRAS, 443, 3270

Muñoz-Darias T., et al., 2016, Nat, 534, 75

Muñoz-Darias T., Torres M. A., Garcia M. R., 2018, MNRAS, 479, 3987

Muñoz-Darias T., et al., 2019, ApJ, 879, L4

Mushtukov A. A., Suleimanov V. F., Tsygankov S. S., Poutanen J., 2015, MNRAS, 454, 2539

Narayan R., Igumenshchev I. V., Abramowicz M. A., 2003, Pasj, 55, L69

Narayan R., Sadowski A., Penna R. F., Kulkarni A. K., 2012, MNRAS, 426, 3241

Negoro H., et al., 2018, ATel, 1828, 1

Neilsen J., Degenaar N., 2023, in Bambi C., Jiang J., eds, , High-Resolution X-ray Spectroscopy: Instrumentation, Data Analysis, and Science. Springer Nature, Singapore, pp 291–343, doi:10.1007/978-981-99-4409-5_11

Neilsen J., Homan J., 2012, ApJ, 750, 27

Neilsen J., Lee J. C., 2009, Nat, 458, 481

Neilsen J., Remillard R. A., Lee J. C., 2011, ApJ, 737, 69

Neilsen J., Petschek A. J., Lee J. C., 2012, MNRAS, 421, 502

Neilsen J., Coriat M., Fender R., Lee J. C., Ponti G., Tzioumis A. K., Edwards P. G., Broderick J. W., 2014, ApJL, 784, L5

Neilsen J., Rahoui F., Homan J., Buxton M., 2016, ApJ, 822, 20

Neilsen J., et al., 2018a, ApJ, 860, L19

Neilsen J., Stevens A. L., Steiner R. R. J. F., Homan J., Altamirano D., Arzoumanian Z., Gendreau K., 2018b, ATel, 11771, 1

Neilsen J., Homan J., Steiner J. F., Marcel G., Cackett E., Remillard R. A., Gendreau K., 2020, The Astrophysical Journal, 902, 152

Netzer H., 2006, ApJ, 652, L117

Neumann M., Avakyan A., Doroshenko V., Santangelo A., 2023, A&A, 677

Noble S. C., Krolik J. H., Schnittman J. D., Hawley J. F., 2011, ApJ, 743, 115

Novikov I. D., Thorne K. S., 1973, blho, pp 343–450

Oda H., Machida M., Nakamura K. E., Matsumoto R., Narayan R., 2012, PASJ, 64

Ohsuga K., Mlneshige S., Mori M., Kato Y., 2009, PASJ, 61, L7

Orosz J. A., 2003, IAU Symposium, 212, 365

Orosz J. A., Jain R. K., Bailyn C. D., McClintock J. E., Remillard R. A., 1998, ApJ, 499, 375

Orosz J. A., et al., 2001, ApJ, 555, 489

Orosz J. A., McClintock J. E., Remillard R. A., Corbel S., 2004, ApJ, 616, 376

Orosz J. A., Steiner J. F., McClintock J. E., Torres M. A., Remillard R. A., Bailyn C. D., Miller J. M., 2011, ApJ, 730, 75

Ott C. D., O'Connor E. P., Gossan S., Abdikamalov E., Gamma U. C., Drasco S., 2013, Nuclear Physics B - Proceedings Supplements, 235-236, 381

Pacucci F., Volonteri M., Ferrara A., 2015, MNRAS, 452, 1922

Padovani P., et al., 2017, Active Galactic Nuclei: What's in a Name? (arXiv:1707.07134), doi:10.1007/s00159-017-0102-9

Pahari M., Yadav J. S., Rodriguez J., Misra R., Bhattacharyya S., Pandey S. K., 2013a, ApJ, 778, 46

Pahari M., Neilsen J., Yadav J. S., Misra R., Uttley P., 2013b, ApJ, 778, 136

Pahari M., et al., 2018, ApJ, 867, 86

Pakull M. W., Mirioni L., 2002

Pakull M. W., Soria R., Motch C., 2010, Nature, 466, 209

Panizo-Espinar G., et al., 2022, A&A, 664, A100

Panuzzo P., et al., 2024, A&A, 686, L2

Park S. Q., et al., 2004, ApJ, 610, 378

Parker M. L., Alston W. N., Igo Z., Fabian A. C., 2020, MNRAS, 492, 1363

Parker M. L., Matzeu G. A., Matthews J. H., Middleton M. J., Dauser T., Jiang J., Joyce A. M., 2022, MNRAS, 513, 551

Parmar A., Angelini L., Roche P., White N., 1993, A&A, 279, 179

Parra M., Petrucci P.-O., Bianchi S., Gianolli V., Ursini F., Ponti G., 2024, Astronomy & Astrophysics, 681, A49

Parsotan T., Laha S., Palmer D. M., Lien A., Cenko S. B., Krimm H., Markwardt C., 2023, ApJ, 953, 155

Petretti C., Neilsen J., Homan J., Petretti C., Neilsen J., Homan J., 2023, ApJ, 957, 44

Petrucci P. O., et al., 2001, ApJ, 556, 716

Petrucci P.-O., Ferreira J., Henri G., Pelletier G., 2008, MNRAS, 385, L88

Petrucci P. O., et al., 2021, A&A, 649, 128

Piconcelli E., Jimenez-Bailón E., Guainazzi M., Schartel N., Rodríguez-Pascual P. M., Santos-Lleó M., 2004, MNRAS, 351, 161

Pinto C., Kosec P., 2023, Astronomische Nachrichten, 344

Podgorný J., et al., 2023, MNRAS, 526, 5964

Podgorný J., Dovčiak M., Marin F., 2024, MNRAS, 530, 2608

Pons J. A., Reddy S., Prakash M., Lattimer J. M., Miralles J. A., 1998, ApJ, 513, 780

Ponti G., Fender R. P., Begelman M. C., Dunn R. J. H., Neilsen J., Coriat M., 2012, MNRAS: Letters, 422, L11

Ponti G., Bianchi S., Muñoz-Darias T., De K., Fender R., Merloni A., 2016, Astronomische Nachrichten, 337, 512

Ponti G., Bianchi S., Muñoz-Darias T., Nandra K., 2018, MNRAS: Letters, 481, L94

Ponti G., Bianchi S., De Marco B., Bahramian A., Degenaar N., Heinke C. O., 2019, MNRAS, 487, 858

Popham R., Sunyaev R., 2001, ApJ, 547, 355

Porquet D., Reeves J. N., Uttley P., Turner T. J., 2004, A&A, 427, 101

Porquet D., Grosso N., Bélanger G., Goldwurm A., Yusef-Zadeh F., Warwick R. S., Predehl P., 2005, A&A, 443, 571

Porquet D., Dubau J., Grosso N., 2010, Space Science Reviews, 157, 103

Postnov K. A., Yungelson L. R., 2014, Living Reviews in Relativity, 17

Pourmand A., Ivanova N., 2023, ApJ, 952, 126

Prabhakar G., Mandal S., Bhuvana G. R., Nandi A., 2023, MNRAS, 520, 4889

Pradhan A. K., Nahar S. N., 2011, Atomic Astrophysics and Spectroscopy. Vol. 9780521825, Cambridge University Press, doi:10.1017/CBO9780511975349

Pringle J. E., Rees M. J., 1972, AA, 21, 1

Privon G. C., et al., 2020, ApJ, 893, 149

Proga D., Kallman T. R., 2002, ApJ, 565, 455

Proga D., Waters T., Dyda S., Zhu Z., 2022, ApJL, 935, L37

Protassov R., van Dyk D. A., Connors A., Kashyap V. L., Siemiginowska A., 2002, ApJ, 571, 545

Quintin E., Webb N. A., Gúrpide A., Bachetti M., Fürst F., 2021, Monthly Notices of the Royal Astronomical Society, 503, 5485

Rahoui F., Coriat M., Lee J. C., 2014, MNRAS, 442, 1610

Ramsay G., et al., 2018, A&A, 620, A141

Rao A., Vadawale S. V., 2012, ApJL, 757, L12

Ratheesh A., Tombesi F., Fukumura K., Soffitta P., Costa E., Kazanas D., 2021, A&A, 646, A154

Ratheesh A., et al., 2024, The Astrophysical Journal, 964, 77

Ratti E. M., et al., 2012, MNRAS, 423, 2656

Reid M. J., Miller-Jones J. C. A., 2023, ApJ, 959, 85

Reid M. J., McClintock J. E., Steiner J. F., Steeghs D., Remillard R. A., Dhawan V., Narayan R., 2014, ApJ, 796, 2

Reis R. C., Fabian A. C., Ross R. R., Miller J. M., 2009, MNRAS, 395, 1257

Remillard R. A., McClintock J. E., 2006, Annual Review of A&A, 44, 49

Remillard R. A., Orosz J. A., McClintock J. E., Bailyn C. D., Remillard R. A., Orosz J. A., McClintock J. E., Bailyn C. D., 1996, ApJ, 459, 226

Remillard R. A., et al., 1999, ApJ, 522, 397

Repetto S., Davies M. B., Sigurdsson S., 2012, MNRAS, 425, 2799

Reynolds M., al. 2018, 42nd COSPAR Scientific Assembly, E1.4-38-18

Roberts T. P., Warwick R. S., Ward M. J., Goad M. R., Jenkins L. P., 2005, MNRAS, 357, 1363

Rodriguez J., Varnière P., 2011, ApJ, 735, 79

Rodriguez Cavero N., et al., 2023, The Astrophysical Journal Letters, 958, L8

Rogantini D., et al., 2024, The interplay between accretion disk wind and jet in the neutron-star low-mass X-ray binary GX 13+1, doi:10.3847/25c2cfeb.73f78358, https://baas.aas.org/pub/2024n5i502p03/release/1

Russell D. M., Fender R. P., Jonker P. G., 2007, MNRAS, 379, 1108

Russell T. D., Soria R., Motch C., Pakull M. W., Torres M. A., Curran P. A., Jonker P. G., Miller-Jones J. C., 2014, MNRAS, 439, 1381

Russell D. M., et al., 2019a, Astronomische Nachrichten, 340, 278

Russell T. D., et al., 2019b, ApJ, 883, 198

Safier P. N., 1993, ApJ, 408, 115

Saha D., Pal S., Mandal M., Manna A., 2021

Saikia P., Russell D. M., Pirbhoy S. F., Baglio M. C., Bramich D. M., Alabarta K., Lewis F., Charles P., 2023, MNRAS, 524, 4543

Sakurai Y., Inayoshi K., Haiman Z., 2016, MNRAS, 461, 4496

Sala G., Greiner J., Vink J., Haberl F., Kendziorra E., Zhang X. L., 2007a, A&A, 461, 1049

Sala G., Greiner J., Ajello M., Bottacini E., Haberl F., 2007b, A&A, 473, 561

Salpeter E. E., E. E., 1964, ApJ, 140, 796

Salvesen G., Simon J. B., Armitage P. J., Begelman M. C., 2016, MNRAS, 457, 857

Sanchez-Sierras J., Munoz-Darias T., 2020, A&A, 640, L3

Sánchez-Sierras J., et al., 2023a, A&A, 673, A104

Sanchez-Sierras J., Munoz-Darias T., Motta S., Fender R., Bahramian A., 2023b, ATel, No. 16039, 16039, 1

Sánchez D. M., Muñoz-Darias T., Casares J., Corral-Santana J. M., Shahbaz T., 2015, MNRAS, 454, 2199

Sánchez D. M., Rau A., Hernández A. Á., van Grunsven T. F. J., Torres M. A. P., Jonker P. G., 2021, MNRAS, 506, 581

Scepi N., Lesur G., Dubus G., Flock M., 2018a, A&A, 609, A77

Scepi N., Lesur G., Dubus G., Flock M., 2018b, A&A, 620, 49

Scepi N., Dubus G., Lesur G., 2019, A&A, 626, A116

Scepi N., Begelman M. C., Dexter J., 2024, MNRAS, 527, 1424

Schnittman J. D., Krolik J. H., 2010, ApJ, 712, 908

Schwarzschild K., 1916, Sitzungsberichte der Königlich Preussischen Akademie der Wissenschaften, pp 189–196

Seifina E., Titarchuk L., Shaposhnikov N., 2014, ApJ, 789, 57

Servillat M., Farrell S. A., Lin D., Godet O., Barret D., Webb N. A., 2011, ApJ, 743

Shahbaz T., et al., 1996, MNRAS, 282, L47

Shakura N., Sunyaev R., 1973, A&A, 24, 337

Shaw A. W., et al., 2022, MNRAS, 516, 124

Shi Z., Wu Q., Yan Z., Lyu B., Liu H., 2023, MNRAS, 525, 1431

Shidatsu M., Done C., 2019, ApJ, 885, 112

Shidatsu M., et al., 2013, ApJ, 779, 26

Shidatsu M., et al., 2014, ApJ, 789, 100

Siemiginowska A., 2007, in AIP Conference Proceedings. American Institute of PhysicsAIP, pp 764–771, doi:10.1063/1.2774940, http://aip.scitation.org/doi/abs/10.1063/1.2774940

Smith N., 2014, Annual Review of A&A, 52, 487

Smith R. K., Valencic L. A., Corrales L., 2016, ApJ, 818, 143

Smith K., Proga D., Dannen R., Dyda S., Waters T., 2024, ApJ, 970, 150

Sonbas E., Mohamed K., Dhuga K. S., Göğüş E., 2022, MNRAS, 511, 2535

Soria R., Pakull M. W., Broderick J. W., Corbel S., Motch C., 2010, MNRAS, 409, 541

Soria R., Pakull M. W., Motch C., Miller-Jones J. C., Schwope A. D., Urquhart R. T., Ryan M. S., 2021, Monthly Notices of the Royal Astronomical Society, 501, 1644

Soria R., Ma R., Tao L., Zhang S. N., 2022, MNRAS, 515, 3105

Sriram K., Rao A. R., Choi C. S., 2012, A&A, 541, A6

Sriram K., Rao A. R., Choi C. S., 2013, ApJ, 775, 28

Stecchini P. E., Castro M., Jablonski F., D'Amico F., Braga J., 2017, ApJL, 843, L10

Steeghs D., McClintock J. E., Parsons S. G., Reid M. J., Littlefair S., Dhillon V. S., 2013, ApJ, 768, 185

Steiner J. F., McClintock J. E., Remillard R. A., Gou L., ya Yamada Narayan R., 2010, ApJL, 718, 117

Steiner J. F., McClintock J. E., Reid M. J., 2012, ApJL, 745, L7

Steiner A. W., Heinke C. O., Bogdanov S., Li C. K., Ho W. C., Bahramian A., Han S., 2018, MNRAS, 476, 421

Stella L., Vietri M., Morsink S. M., 1999, ApJ, 524, L63

Stiele H., Kong A. K. H., 2021, ApJ, 914, 93

Stiele H., Yu W., 2016, MNRAS, 460, 1946

Stobbart A.-M., Roberts T. P., Wilms J., 2006, MNRAS, 368, 397

Strohmayer T., Bildsten L., 2003, in , Compact Stellar X-Ray Sources, Eds. W.H.G. Lewin and M. van Der Klis, Cambridge University Press. Cambridge University Press, pp 113–156 (arXiv:astro-ph/0301544), doi:10.1017/cbo9780511536281.004

Stuchlík Z., Kološ M., 2016, ApJ, 825, 13

Suh H., et al., 2024, Feeding Hidden Monsters: A Super-Eddington Accreting Black Hole ~1.5 Gyr after the Big Bang (arXiv:2405.05333), doi:10.48550/arXiv.2405.05333

Szkody P., Piche F., Feinswog L., 1990, ApJ Supplement Series, 73, 441

Tanaka Y., Inoue H., Holt S. S., Tanaka Y., Inoue H., Holt S. S., 1994, PASJ, 46, L37

Tarter C. B., Tucker W. H., Salpeter E. E., Tarter C. B., Tucker W. H., Salpeter E. E., 1969, ApJ, 156, 943

Tauris T. M., van den Heuvel E. P. J., Tauris T. M., van den Heuvel E. P. J., 2006, csxs, 39, 623

Tchekhovskoy A., Narayan R., McKinney J. C., 2011, MNRAS, 418, L79

Team X. S., 2020, Science with the X-ray Imaging and Spectroscopy Mission (XRISM) (arXiv:2003.04962), doi:10.48550/arXiv.2003.04962

Tetarenko B. E., Sivakoff G. R., Heinke C. O., Gladstone J. C., 2016, ApJ Supplement Series, 222, 15

Tetarenko B. E., Lasota J. P., Heinke C. O., Dubus G., Sivakoff G. R., 2018, Nature, 554, 69

Tetarenko B. E., Dubus G., Marcel G., Done C., Clavel M., 2020, MNRAS, 495, 3666

Tian P., et al., 2023, Nature, 621, 271

Titarchuk L., Seifina E., 2023, A&A, 669, A57

Tolman R. C., 1939, Physical Review, 55, 364

Tomaru R., Done C., Ohsuga K., Nomura M., Takahashi T., 2019, MNRAS, 490, 3098

Tomaru R., Done C., Ohsuga K., Odaka H., Takahashi T., 2020, MNRAS, 494, 3413

Tomaru R., Done C., Mao J., 2023, MNRAS, 518, 1789

Tomaru R., Done C., Odaka H., 2024, MNRAS, 527, 7047

Tombesi F., 2016, Astronomische Nachrichten, 337, 410

Tombesi F., Cappi M., Reeves J. N., Palumbo G. G., Yaqoob T., Braito V., Dadina M., 2010, A&A, 521, A57

Tomsick J. A., Lapshov I., Kaaret P., 1998, ApJ, 494, 747

Tomsick J. A., Corbel S., Goldwurm A., Kaaret P., 2005, ApJ, 630, 413

Tomsick J. A., Yamaoka K., Corbel S., Kalemci E., Migliari S., Kaaret P., 2014, ApJ, 791, 70

Torres M. A. P., Casares J., Jiménez-Ibarra F., Muñoz-Darias T., Padilla M. A., Jonker P. G., Heida M., 2019, ApJ, 882, L21

Torres M. A. P., Casares J., Jiménez-Ibarra F., Álvarez-Hernández A., Muñoz-Darias T., Padilla M. A., Jonker P. G., Heida M., 2020, ApJ, 893, L37

Torres M. A., Jonker P. G., Casares J., Miller-Jones J. C., Steeghs D., 2021, MNRAS, 501, 2174

Toyouchi D., Hotokezaka K., Inayoshi K., Kuiper R., 2024, MNRAS, 532, 4826

Trudolyubov S. P., Borozdin K. N., Priedhorsky W. C., 2001, MNRAS, 322, 309

Trueba N., Miller J. M., Kaastra J., Zoghbi A., Fabian A. C., Kallman T., Proga D., Raymond J., 2019, ApJ, 886, 104

Truran J. W., 1977, Springer, Dordrecht, pp 145–158, doi:10.1007/978-94-010-1229-4_14, https://link.springer.com/chapter/10.1007/978-94-010-1229-4_14

Tull R. G., Choisser J. P., Snow E. H., 1975, Applied Optics, 14, 1182

Ubertini P., et al., 2003, A&A, 411, L131

Ueda Y., Inoue H., Tanaka Y., Ebisawa K., Nagase F., Kotani T., Gehrels N., 1998, ApJ, 500, 1069

Ueda Y., Yamaoka K., Remillard R., 2009, ApJ, 695, 888

Ueda Y., et al., 2010, ApJ, 713, 257

Urry C. M., Padovani P., 1995, Publications of the Astronomical Society of the Pacific, 107, 803

Uttley P., Klein-Wolt M., 2015, MNRAS, 451, 475

Uttley P., Malzac J., 2023,] 10.48550/arXiv.2312.08302

Vahdat Motlagh A., Kalemci E., Maccarone T. J., 2019, MNRAS, 485, 2744

Van Den Berg M., 2019, in Proceedings of the International Astronomical Union. Cambridge University Press, pp 367–376 (arXiv:1910.07595), doi:10.1017/S1743921319007981

Van Der Hooft F., Heemskerk M. H., Alberts F., Van Paradijs J., 1998, A&A, 329, 538

Van Oers P., et al., 2010, MNRAS, 409, 763

Veledina A., et al., 2023, arXiv, p. arXiv:2303.01174

Verhamme O., Kluska J., Ferreira J., Bollen D., De Prins T., Kamath D., Van Winckel H., 2024, A&A, 684, A79

Vincentelli F. M., et al., 2023, Nature, 615, 45

Volonteri M., Habouzit M., Colpi M., 2021, Nature Reviews Physics, 3, 732

Walton D. J., MacKenzie A. D., Gully H., Patel N. R., Roberts T. P., Earnshaw H. P., Mateos S., 2022, MNRAS, 509, 1587

Wang Y., Méndez M., Altamirano D., Court J., Beri A., Cheng Z., 2018, MNRAS, 478, 4837

Wang Y., et al., 2020, ApJ, 906, 11

Wang F., et al., 2021a, ApJL, 907, L1

Wang J., et al., 2021b, ApJL, 910, L3

Wang W., Bu D. F., Yuan F., 2022a, MNRAS, 513, 5818

Wang J., et al., 2022b, ApJ, 930, 18

Wang S., Kawai N., Shidatsu M., Matsuoka Y., 2023, PASJ, 75, 1072

Wang J., et al., 2024a, The Astrophysical Journal, 963, 118

Wang X.-L., Yan Z., Xie F.-G., Wang J.-F., Ma R.-Y., 2024b, The Astrophysical Journal, 969, 152

Waters T., Proga D., 2018, MNRAS, 481, 2628

Waters T., Proga D., 2023, Frontiers in Astronomy and Space Sciences, 10, 1198135

Waters T., Proga D., Dannen R., 2021, ApJ, 914, 62

Waters T., Proga D., Dannen R., Dyda S., 2022, ApJ, 931, 134

Webb N. A., Naylor T., Ioannou Z., Charles P. A., Shahbaz T., 2000, MNRAS, 317, 528

Weisskopf M. C., Tananbaum H. D., Van Speybroeck L. P., O'Dell S. L., 2000, X-Ray Optics, Instruments, and Missions III, 4012, 2

Welsh W. F., Gallo L., Robinson E. L., 2002, The Physics of Cataclysmic Variables and Related Objects, 261, 571

Weymann R. J., Carswell R. F., Smith M. G., 1981, Annual Review of A&A, 19, 41

Whelan J. A. J., et al., 1977, MNRAS, 180, 657

White N. E., Marshall F. E., White N. E., Marshall F. E., 1983, IAUC, 3806, 2

Wijnands R., et al., 2006, A&A, 449, 1117

Wijnands R., Degenaar N., Armas Padilla M., Altamirano D., Cavecchi Y., Linares M., Bahramian A., Heinke C. O., 2015, MNRAS, 454, 1371

Wilms J., Allen A., McCray R., 2000, ApJ, 542, 914

Wilson-Hodge C. A., et al., 2018, ApJ, 863, 9

Woods D. T., Klein R. I., Castor J. I., McKee C. F., Bell J. B., 1996, ApJ, 461, 767

Wu J., Orosz J. A., McClintock J. E., Hasan I., Bailyn C. D., Gou L., Chen Z., 2016, ApJ, 825, 46

Xu Y., et al., 2017, ApJ, 851, 103

Xu Y., et al., 2018a, ApJ, 865, 18

Xu Y., Kennea J. A., Harrison F. A., Forster K., 2018b, ATel, 11321, 1

Xu Y., Harrison F. A., Tomsick J. A., Walton D. J., Barret D., García J. A., Hare J., Parker M. L., 2020, ApJ, 893, 30

Yamada S., et al., 2024, ApJ Supplement Series, 274, 8

Yanes-Rizo I. V., et al., 2022, MNRAS, 517, 1476

Yanes-Rizo I. V., Torres M. A., Casares J., Monelli M., Jonker P. G., Abbot T., Armas Padilla M., Muñoz-Darias T., 2024, MNRAS, 527, 5949

Yang Z.-x., et al., 2022, ApJ, 937, 33

Yorgancioglu E. S., et al., 2023, A&A, 677

Yoshitake T., et al., 2024, Publications of the Astronomical Society of Japan, 76, 251

Zdziarski A. A., Szanecki M., Poutanen J., Gierlinski M., Biernacki P., 2021a, MNRAS, 492, 5234

Zdziarski A. A., Dziełak M. A., De Marco B., Szanecki M., Niedźwiecki A., 2021b, ApJL, 909, L9

Zdziarski A. A., et al., 2024, ApJ, 962, 101

Zhang S. N., Wilson C. A., Harmon B. A., Fishman G. J., Wilson R. B., Paciesas W. S., Scott M., Rubin B. C., 1994, IAUC, 6046, 1

Zhang W., Dovčiak M., Bursa M., Karas V., Matt G., Ursini F., 2022, MNRAS, 515, 2882

Zhang Z., et al., 2024a, A Variable Ionized Disk Wind in MAXI J1803-298 Revealed by NICER (arXiv:2402.10315), doi:10.48550/arXiv.2402.10315

Zhang Z., et al., 2024b, Modeling X-Ray Multi-Reflection in Super-Eddington Winds (arXiv:2407.08596), doi:10.48550/arXiv.2407.08596

Zhao Q. C., et al., 2023, MNRAS, 524, 3215

Zhu Z., Stone J. M., 2018, ApJ, 857, 34

Ziolkowski J., Ziolkowski J. 2002, MmSAI, 73, 1038

Zoghbi A., et al., 2016, ApJ, 833, 165

Zurita C., Durant M., Torres M. A. P., Shahbaz T., Casares J., Steeghs D., 2008, ApJ, 681, 1458

van den Eijnden J., Ingram A., Uttley P., Motta S. E., Belloni T. M., Gardenier D. W., 2017, MNRAS, 464, 2643

van den Heuvel E. P., Portegies Zwart S. F., de Mink S. E., 2017, MNRAS, 471, 4256